UNIVERSITAT DE BARCELONA

3*d* and/or 4*f* coordination compounds derived from chiral Schiff bases: magnetic and spectroscopic study

Júlia Mayans Ayats

ADVERTIMENT. La consulta d'aquesta tesi queda condicionada a l'acceptació de les següents condicions d'ús: La difusió d'aquesta tesi per mitjà del servei TDX (**www.tdx.cat**) i a través del Dipòsit Digital de la UB (**diposit.ub.edu**) ha estat autoritzada pels titulars dels drets de propietat intel·lectual únicament per a usos privats emmarcats en activitats d'investigació i docència. No s'autoritza la seva reproducció amb finalitats de lucre ni la seva difusió i posada a disposició des d'un lloc aliè al servei TDX ni al Dipòsit Digital de la UB. No s'autoritza la presentació del seu contingut en una finestra o marc aliè a TDX o al Dipòsit Digital de la UB (framing). Aquesta reserva de drets afecta tant al resum de presentació de la tesi com als seus continguts. En la utilització o cita de parts de la tesi és obligat indicar el nom de la persona autora.

ADVERTENCIA. La consulta de esta tesis queda condicionada a la aceptación de las siguientes condiciones de uso: La difusión de esta tesis por medio del servicio TDR (**www.tdx.cat**) y a través del Repositorio Digital de la UB (**diposit.ub.edu**) ha sido autorizada por los titulares de los derechos de propiedad intelectual únicamente para usos privados enmarcados en actividades de investigación y docencia. No se autoriza su reproducción con finalidades de lucro ni su difusión y puesta a disposición desde un sitio ajeno al servicio TDR o al Repositorio Digital de la UB. No se autoriza la presentación de su contenido en una ventana o marco ajeno a TDR o al Repositorio Digital de la UB (framing). Esta reserva de derechos afecta tanto al resumen de presentación de la tesis como a sus contenidos. En la utilización o cita de partes de la tesis es obligado indicar el nombre de la persona autora.

WARNING. On having consulted this thesis you're accepting the following use conditions: Spreading this thesis by the TDX (**www.tdx.cat**) service and by the UB Digital Repository (**diposit.ub.edu**) has been authorized by the titular of the intellectual property rights only for private uses placed in investigation and teaching activities. Reproduction with lucrative aims is not authorized nor its spreading and availability from a site foreign to the TDX service or to the UB Digital Repository. Introducing its content in a window or frame foreign to the TDX service or to the UB Digital Repository is not authorized (framing). Those rights affect to the presentation summary of the thesis as well as to its contents. In the using or citation of parts of the thesis it's obliged to indicate the name of the author.

3*d* AND/OR 4*f* COORDINATION COMPOUNDS DERIVED FROM CHIRAL SCHIFF BASES: MAGNETIC AND SPECTROSCOPIC STUDY

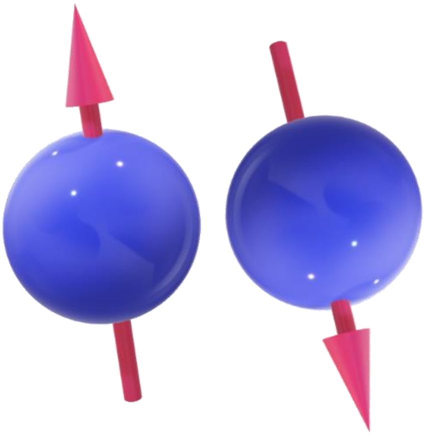

Júlia Mayans Ayats

UNIVERSITAT DE BARCELONA

Doctorat en Nanociències

3*d* AND/OR 4*f* COORDINATION COMPOUNDS DERIVED FROM CHIRAL SCHIFF BASES: MAGNETIC AND SPECTROSCOPIC STUDY

Júlia Mayans Ayats

Director: Albert Escuer Fité
Universitat de Barcelona

Tutor: Ramón Vicente Castillo
Universitat de Barcelona

Als meus pares.

AGRAIMENTS I FESTES.

Haig de començar aquesta part agraint-li al Dr. Albert Escuer que m'acceptés al seu grup, donant-me, sense saber-ho, una de les millors oportunitats de la meva vida. No hagués pensat mai en fer una tesi en química molecular, però està clar que no tenia ni idea de res. També haig d'agrair tota l'ajuda i bons consells de tot el Grup de Magnetisme Molecular i a tot el departament de Química Inorgànica.

A la Núria Clos, que ha tingut la paciència de no dir-me mai que deixés d'intentar fer mesures absurdes i a la Mercè Font, que mai m'ha depreciat cristalls impossibles. A tota la gent que ha passat pel laboratori durant el temps que hi he estat i especialment als seus habitants permanents: a la Saskia, per la guia prestada en tot moment, a la Beltzane perquè és un sol i a la Berta per existir.

To all the people that welcomed me to Firenze. Mi mancherai LAMM, Roberta Sessoli and Andrea Canneschi who accepted me in their lab, Lorenzo Sorace, because he lost one million hours trying to explain me what is a magnet, how they work and what I suppose to do with them. Also to Marie Emmanuelle Boulon for the Italian tequila and to Lorenzo Tesi, for the friendship and for the cantilever nightmare.

No se hace una tesis solamente con conocimiento y horas de trabajo. De hecho, eso es imposible. Se hace una tesis sabiendo que cuando estas hundido en el pozo hay un montón de gente que te da la mano y estira hacia arriba para que salgas y te vayas a tomarte un wiski con ellos. Han estirado fuerte hacia el wiski Uri y Dani, ya sabéis *It yanks you out of your body and your mind and throws you against the wall.* Han estirado fuerte Alberto y Sergi, tan fuerte que me he convertido en una experta en tetas, en gafas y en como el pelo de una mujer siempre debe ser largo y liso. Además, también os he cogido cariño. Han estirado fuerte Cristina y Pablo, que he tenido menos tiempo para conoceros, pero tengo buenos augurios y también Raúl, una consciencia demasiado clarividente para ser un niño rata como los demás. Sobretodo han estirado muy fuerte Almudena, Noe y Sonia, la familia. Almudena, que Tarragona es un coñazo, vuelve que echo de menos a mi *miniyó*. Noe, que vistes de negro y nos haces vivir la vida de colores. Y Sonia, que has sido todo lo que necesitaba. Chicos, *como todos los jóvenes, arrancamos para ser unos genios, pero afortunadamente, la risa intervino.*

Al David, que no se m' acut una persona més bona al món. Que m'ha deixat viure com he volgut i m'ha omplert la vida de tot, sobretot de gats.

Als meus avis. A la iaia, que em va convèncer a base d'abraçades de que no fos peixatera i al meu avi, a qui menys voldria decepcionar.

Als meus pares, que no ens entenem però ens estimem. Qui vol una família podent tenir la millor aventura de la seva vida?

I a l'Albert, ara que ja s'acaben les paraules i que sé que no les necessita per a res.

For nothing worthy proving can be proven,
Not yet disproven. Wherefore thou be wise,
Cleave ever to the sunnier side of doubt,
And cling to Faith beyond the forms of Faith!

Lord Alfred Tennyson

CONTENTS

- LIST OF LIGANDS AND COMPOUNDS
- CHAPTER 0: AIM AND THESIS ORGANIZATION……………………….....I
- CHAPTER 1: INTRODUCTION………………………………………………..1
  - 1.1. MAGNETISM……………………………………………………………..1
    - 1.1.1. A brief history of magnetism………………………………….....1
    - 1.1.2. From molecular magnetism to Single Molecule Magnets……....1
    - 1.1.3. Single Molecule Magnets (SMMs)……………………………..2
      - 1.1.3.1. The memory of molecules………………………………3
      - 1.1.3.2. Magnetic exchange and superexchange………………...5
      - 1.1.3.3. Relaxation in Single Molecule Magnets………………..5
      - 1.1.3.4. Thermal relaxation in SMMs. Arrhenius-like relaxation…………..……………………………………...…..6
      - 1.1.3.5. Spin-lattice relaxation by phonons: Alternatives to Orbach relaxation………………………………………………..7
      - 1.1.3.6. Tunnel relaxation of the magnetization………………..10
    - 1.1.4. Transition metals and lanthanides in molecular magnetism......11
    - 1.1.5. Lanthanides: A curious born in Scandinavia…………………13
    - 1.1.6. Lanthanides: Anisotropy and Crystal Field…………………...16
  - 1.2. SUPRAMOLECULAR CHEMISTRY…………………………………18
    - 1.2.1. Supramolecular chirality……………………………………....19
  - 1.3. EXPERIMENTAL METHODOLOGY……………………………….....20
    - 1.3.1. Magnetic techniques………………………………………...21
      - 1.3.1.1. Susceptometer QUantum Interference Device………..21
      - 1.3.1.2. Cantilever Torque Magnetometry (CTM)……….........24
        - 1.3.1.2.1. Non-collinearity……………………………24
        - 1.3.1.2.2. Theoretical background……………………25
        - 1.3.1.2.3. Experimental setup………………………...27
        - 1.3.1.2.4. Orientations …...…………………………..29
    - 1.3.2 Spectroscopic techniques………………………………………29
      - 1.3.2.1. Electronic Paramagnetic Resonance (EPR)…………29
        - 1.3.2.1.1. CW-EPR………………………….........30
        - 1.3.2.1.2. EPR in lanthanide complexes……………...30
        - 1.3.2.1.3. Instrumentation……………………………31
      - 1.3.2.2. Electronic Circular Dichroism (ECD)………………..31
        - 1.3.2.2.1. Theory……………………………………...31
        - 1.3.2.2.2. Experimental setup………………………...33
    - 1.3.3. Experimental setup for physical measurements……………...33
      - 1.3.3.1. Infrared Spectroscopy (IR)…………………………...33
      - 1.3.3.2. SQUID measurements………………………………..33
      - 1.3.3.3. Monocrystal X-Ray Diffraction (M-XRD)…………...34
      - 1.3.3.4. Powder X-Ray Diffraction (P-XRD)…………………34

        1.3.3.5. ECD……………………………………………………...34
        1.3.4.6. CTM……………………………………………………...34
    1.4. SYNTHESIS……………………………………………………..34
        1.4.1. The ligands: Schiff bases……………………………………35
        1.4.2. The metals…………………………………………………38
        1.4.3. Crystallization techniques……………………………………39
    1.5. OBJECTIVES………………………………………………………41

- CHAPTER 2: NICKEL COMPLEXES……………………………......…43

Publication #1………………………………………………………………45
Publication #2………………………………………………………………47

- CHAPTER 3: AN IRON STAR……………………………………………..49

Publication #3...51

- CHAPTER 4: MANGANESE COMPLEXES…………………………………53

Publication #4………………………………………………………………55
Publication #5………………………………………………………………57
Publication #6………………………………………………………………59
Publication #7………………………………………………………………61

- CHAPTER 5: HETEROMETALLIC CLUSTERS 3*d*/4*f* DERIVED FROM CHIRAL AND RACEMIC SCHIFF BASES. A NEW ISOMERISM TYPE?..63
    5.1. INTRODUCTION……………………………………………………..63
    5.2. SYNTHESIS…………………...………………………………………63
    5.3. STRUCTURAL DESCRIPTON……………………………………….64
    5.4. CHIRAL *vs*. MESO FORMS………………………………………….67
    5.5. FERROELECTRICITY………………………………………………. 69
    5.6. MAGNETIC STUDIES………………………………………………..71
    5.7. OTHER PROPERTIES………………………………………………..73

- CHAPTER 6: FIELD INDUCED SINGLE ION MAGNET COMPLEXES DERIVED FROM KRAMERS IONS……………………………………..…...75
    6.1. INTRODUCTION……………………………………………………..75
    6.2. EXPERIMENTAL……………………………………………………..77
    6.3. SYNTHESES…………………………………………………………..78
        6.3.1. Complex choice…………………………………………………78
        6.3.2. Syntheses of the ligand and complexes…………………………79
    6.4. STRUCTURAL DESCRIPTION………………………………………80
        6.4.1. Ligand conformation……………………………………………85
    6.5. CHIRALITY TRANSFER AND ECD…………………………………85
    6.6. LUMINESCENCE MEASUREMENTS………………………………86
    6.7. MAGNETIC MEASUREMENTS……………………………………..86

- CHAPTER 7: PURELY LANTHANIDE COMPOUNDS...……..……………93
    7.1. SYNTHESIS AND CHARACTERIZATION…………………………93

- 7.1.1. Syntheses……………………………………………………………93
- 7.1.2. Spectroscopic characterization….……………………………….94
- 7.2. DINUCLEAR COMPOUNDS. (THE [Ln_2] FAMILY)……………….95
  - 7.2.1. Structural description………………………………………….…95
  - 7.2.2. Magnetic studies…………………………………………………98
    - 7.2.2.1. Static magnetic studies………………………………….98
    - 7.2.2.2. Dynamic magnetic properties..…………………………..99
  - 7.2.3. EPR studies……………………………………………………..104
  - 7.2.4. CTM…………………………………………………………….107
- 7.3. MONONUCLEAR COMPOUNDS. (The [Ln] FAMILY)…………109
  - 7.3.1. Structural characterization………………………………………109
  - 7.3.2. Magnetic studies………………………………………………...112
    - 7.3.2.1. Dynamic magnetic properties…………………………112
- 7.4. FINAL CONSIDERATIONS……………………………………….117

- CHAPTER 8. FINAL REMARKS……………………………………………119
  - 8.1. THE SCHIFF BASES……………………………........…………..119
    - 8.1.1. Schiff bases with a lonely imine group………………………119
    - 8.1.2. Schiff bases with two imino groups………….…………………123
    - 8.1.3. Compartmental Schiff bases…………………………………124
    - 8.1.4. Solvolysis of the Schiff bases……………….………………126
  - 8.2. EFFECT OF THE COUNTERION AND THE BASE………………127
  - 8.3. ECD FOR STRUCTURAL CHARACTERIZATION………………129
  - 8.4. SUPRAMOLECULAR CHIRALITY. CHIRALITY TRANSFER....130
  - 8.5. MAGNETISM……………………………………………………134
    - 8.5.1. Magnetic behaviour……………………………………………134
      - 8.5.1.1. Static properties………………………………………134
    - 8.5.2. The Magnetic relaxation in lanthanide compounds ……….…..135
    - 8.5.3. Fit of the magnetic measurements ……………………….…136

- CONCLUSIONS………………………………………………………...139

- APPENDIX I……………………………………………………………141
- APPENDIX II…………………………………………………………143
- APPENDIX III…………………………………...……………...145
- APPENDIX IV……………………………………………………..157

RESUM EN CATALÀ…………………………………………………………..159

BIBLIOGRAPHY…..…………………………………………………………..163

Ligand	*Name*	*Structure*
L1	*N,N'-bis(2-pyridylmethilidene)-1,2-(R,R/S,S)-cilohexanediamine*	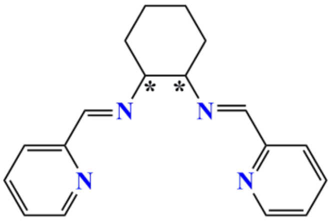
L2	*N, N'-bis(2-quinolylmethilidene)-1,2-(R,R/S,S)-cilohexanediamine*	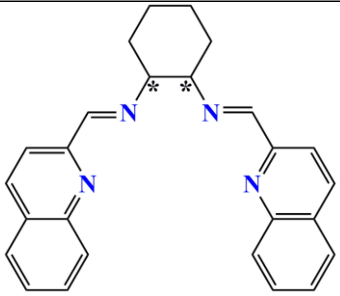
L3	*N,N'-bis(1-(2-pyridyl)ethylidene)-(R/S)-propane-1,2-diamine)*	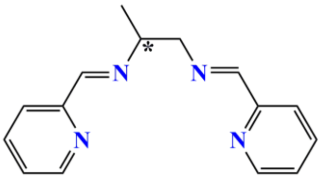
L4	*N,N'-bis(1-(2-quinolyl)ethylidene)-(R/S)-propane-1,2-diamine)*	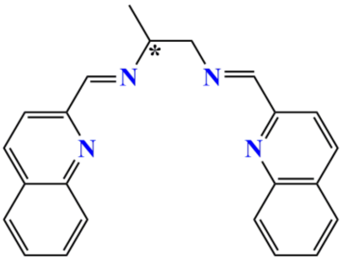
L5	*N,N'-bis(1-(2-pyridyl)ethylidene)-ethyl-1,2-diamine)*	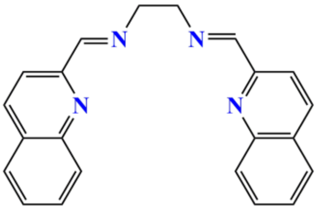
L6	*N,N'-bis((1,2-diphenyl- (pyridin-2-yl)methylene)-(R,R/S,S)-ethane-1,2-diamine)*	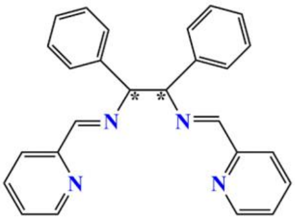

LIST OF LIGANDS AND COMPLEXES

H_2L7	*2-((2-hydroxy-1-(R/S)-phenylethyliminomethyl)phenol)*	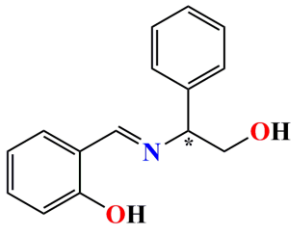
H_2L8	*2-((3-hydroxy-1-(R/S)-phenylpropyliminomethyl)phenol)*	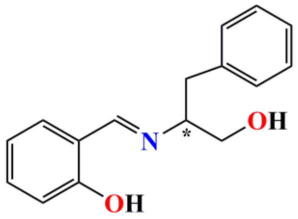
H_2L9	*bis(2-(((2-(hydroxy)-1-(R/S)-phenylethyl)imino)-6-methoxyphenol*	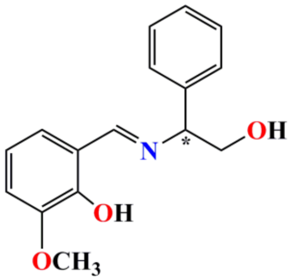
H_2L10	*bis(2-(((2-(hydroxy)-1-(R/S)-isopropylethyl)imino)-6-methoxyphenol*	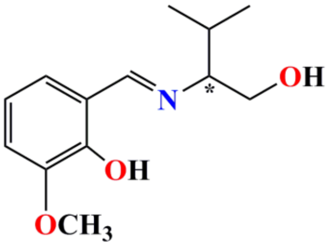
H_2L11	*bis(2-(((2-(hydroxy)-1-(R,S/S,R)-diphenylethyl)imino)-6-methoxyphenol*	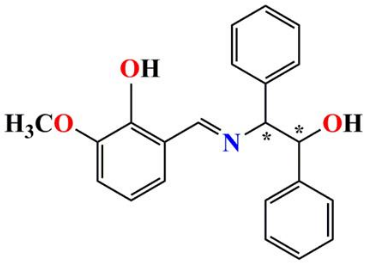
H_2L12	*(m-2-(((2-((2-hydroxy-3-methoxybenzylidene)amino)-(R,R/S,S)-1,2-diphenylethyl)imino)methyl)-6-methoxyphenol)-bis(m-2-(((2-((2-oxido-3-methoxybenzylidene)amino)-1,2-diphenylethyl)imino)methyl)-6-methoxyphenol.*	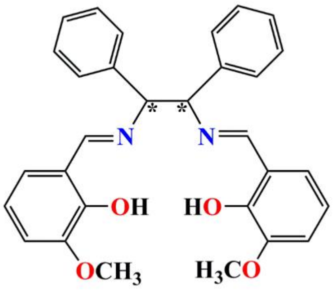

Number,chapter, publication id.	Ligand	Nuclearity	Structure
[1], appears in Chapter 2 and in ***Publication #1*** with name ***1RR/1SS***	**L1**	$[\mathrm{Ni}^{II}_2]$	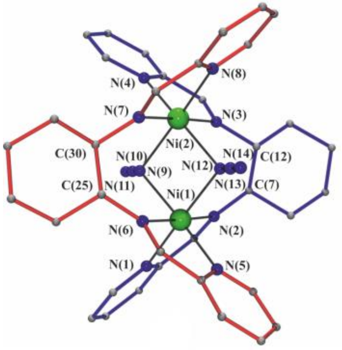
[2], appears in Chapter 2 and in ***Publication #1*** with name ***2RR/2SS***	**L2**	$[\mathrm{Ni}^{II}_2]$	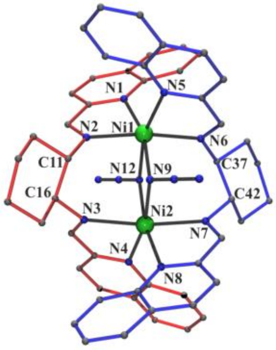
[3], appears in Chapter 2 and in ***Publication #1*** with name ***4R***	**L3**	$[\mathrm{Ni}^{II}_2]$	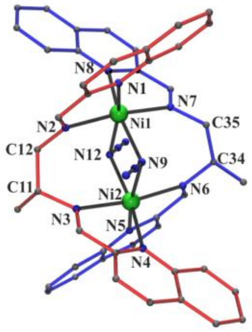
[4], appears in Chapter 2 and in ***Publication #1*** with name ***7A/7B***	**L4**	$[\mathrm{Ni}^{II}_2]$ $[\mathrm{Ni}^{II}_2]$	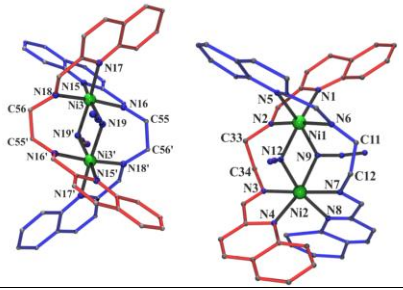
[5], appears in Chapter 2 and in ***Publication #2*** with number ***1R / 1S***	**H_2L9**	$[\mathrm{Ni}^{II}_4]$	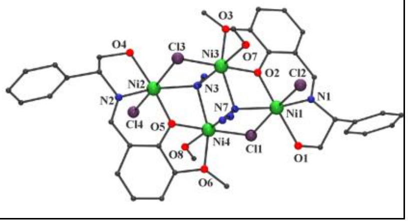

LIST OF LIGANDS AND COMPLEXES

[18], appears in Chapter 3 and in ***Publication #3*** with number ***1R*** / ***1S.***	$\mathbf{H_2L9}$	$[Fe^{III}_4]$	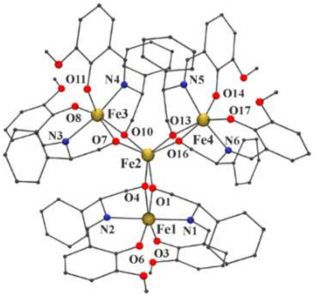 O11 N4 N5 O14 O8 Fe3 O17 O13 N3 O7 O10 Fe4 N6 O16 Fe2 O4 O1 N2 Fe1 N1 O6 O3
[19], appears in Chapter 3 and in ***Publication #3*** with number **2*RS.***	$\mathbf{H_2L11}$	$[Fe^{III}]$	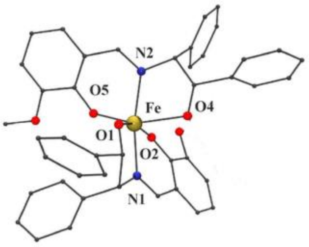 N2 O5 Fe O4 O1 O2 N1
[6], appears in Chapter 4 and in ***Publication #4*** with number (*R*)-**1** and (*S*)-**1.**	$\mathbf{H_2L7}$	$[Mn^{II}Mn_2^{III}]$	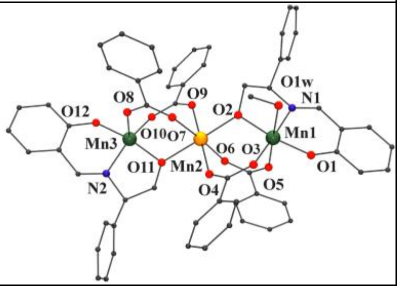 O1w N1 O8 O9 O2 O12 Mn3 O10 O7 O6 O3 Mn1 O11 Mn2 O1 N2 O4 O5
[7], appears in Chapter 4 and in ***Publication #4*** with number (*R*)-**2** and (*S*)-**2.**	$\mathbf{H_2L7}$	$[Mn^{II}Mn_2^{III}]$	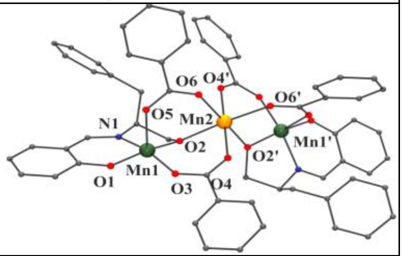 O6 O4' O6' N1 O5 Mn2 Mn1' O2 O2' Mn1 O1 O3 O4
[8], appears in Chapter 4 and in ***Publication #4*** with number (*R*)-**3** and (*S*)-**3.**	$\mathbf{H_2L8}$	$[Mn_3^{III}]$	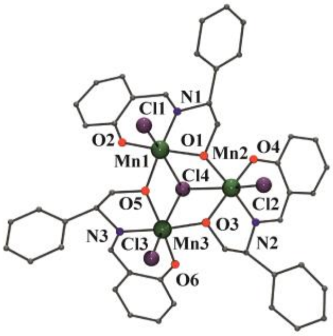 N1 Cl1 O2 O1 Mn1 Mn2 O4 Cl4 O5 Cl2 O3 N3 Cl3 Mn3 N2 O6
[9], appears inChapter 3 and in ***Publication #5*** with number ***2R/2S*** and in ***Publication #7*** with number ***6R/6S***.	$\mathbf{H_2L9}$	$[Mn^{II}Mn_6^{III}Ln^{III}Na_2^{I}]$	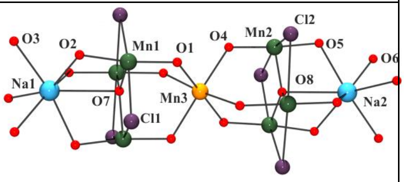 O3 O2 Mn1 O1 O4 Mn2 Cl2 O5 O6 Na1 O7 Mn3 O8 Na2 Cl1
[10], appears in Chapter 3 and in ***Publication #7*** with number ***7R***.	$\mathbf{H_2L9}$	$[Mn^{II}Mn_6^{III}Ln^{III}Na_2^{I}]$	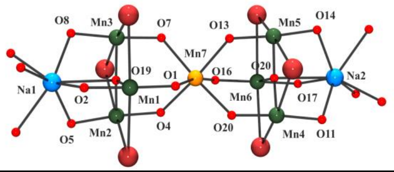 O8 Mn3 O7 O13 Mn5 O14 Mn7 O19 O1 O16 O20 Na1 Na2 O2 Mn1 Mn6 O17 O5 Mn2 O4 O20 Mn4 O11

[11], appears in Chapter 3 and in ***Publication #5*** with number ***1R/1S*** and in ***Publication #7*** with number ***1R/1S***.	**H$_2$L9**	$[\mathrm{Mn^{II}Mn_3^{III}Na^{I}}]$	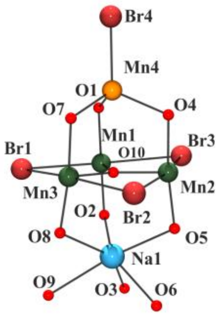 Br4 Mn4 O1 O7 O4 Mn1 Br1 O10 Br3 Mn3 Mn2 O2 Br2 O8 O5 Na1 O9 O3 O6
[12] appears in Chapter 3 and in ***Publication #7*** with number ***4R/4S***	**H$_2$L9**	$[\mathrm{Mn^{II}Mn_3^{III}Na^{I}}]$	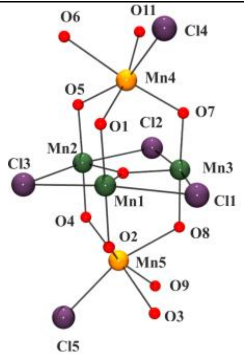 O6 O11 Cl4 Mn4 O5 O7 O1 Cl2 Mn2 Cl3 Mn3 Mn1 Cl1 O4 O2 O8 Mn5 O9 O3 Cl5
[13], appears in Chapter 3 and in ***Publication #7*** with number ***5S***	**H$_2$L9**	$[\mathrm{Mn_2^{II}Mn_3^{III}}]$	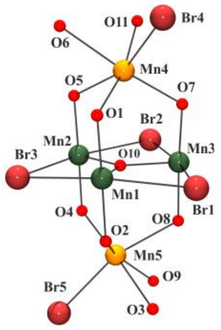 O11 Br4 O6 Mn4 O5 O7 O1 Br2 Mn2 Mn3 Br3 O10 Mn1 Br1 O4 O8 O2 Mn5 O9 Br5 O3
[14], appears in Chapter 3 and in ***Publication #7*** with number ***2R/2S***	**H$_2$L9**	$[\mathrm{Mn^{II}Mn_3^{III}Ca^{II}}]$	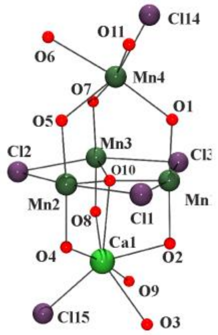 Cl14 O11 O6 Mn4 O7 O1 O5 Mn3 Cl2 Cl O10 Mn2 Mn O8 Cl1 Ca1 O4 O2 O9 Cl15 O3
[15], appears in Chapter 3 and in ***Publication #7*** with number ***3S***	**H$_2$L9**	$[\mathrm{Mn^{II}Mn_3^{III}Ca^{II}}]$	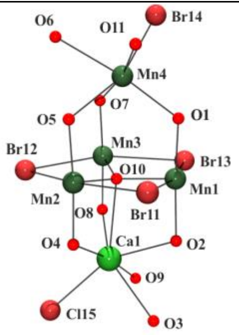 O6 O11 Br14 Mn4 O7 O1 O5 Mn3 Br12 O10 Br13 Mn1 Mn2 O8 Br11 Ca1 O4 O2 O9 Cl15 O3

[16], appears in Chapter 4 and in ***Publication #6*** with number ***1R/1S***	**H_2L10**	[Mn $_2^{II}$Mn$_6^{III}$Na$_2^{II}$]	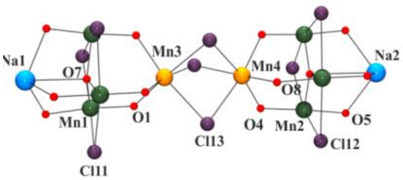 Na1 O7 Mn1 O1 Cl11 Mn3 Cl13 Mn4 O8 O4 Mn2 Cl12 O5 Na2
[17], appears in Chapter 4 and in ***Publication #6*** with number ***2S***	**H_2L10**	[Mn$_2^{II}$Mn$_6^{III}$Na$_2^{II}$]	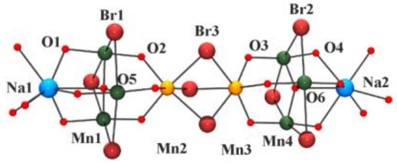 Br1 O1 O2 Br3 O3 Br2 O4 Na1 O5 O6 Na2 Mn1 Mn2 Mn3 Mn4
[20] containing Y. Ln=Ce^{III} **[21]**, Pr **[22],** Nd^{III} **[23]**, Eu^{III} **[24]**, Gd^{III} **[25]**, Tb^{III} **[26]**, Dy^{III} **[27]**, Er^{III} **[28]**, Yb^{III} **[29].** Appear in Chapter 5.	**H_2L9**	[Mn$_6^{III}$Ln^{III}Na$_2^{II}$]	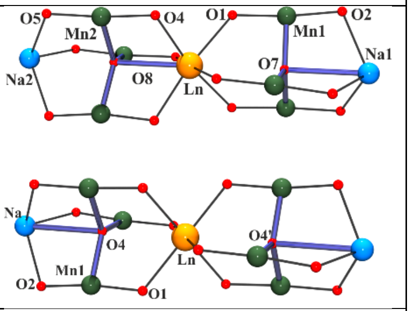 O5 Mn2 O4 O1 Mn1 O2 Na2 O8 Ln O7 Na1 Na O4 Mn1 O2 O1 Ln O4'
Ln=Ce^{III} **[30]**, Nd^{III} **[31]**, Eu^{III} **[32]**, Dy^{III} **[33]**, Er^{III} **[34]**, Yb^{III} **[35].** Appear in Chapter 6.	**L12**	[Zn^{II}Ln^{III}]	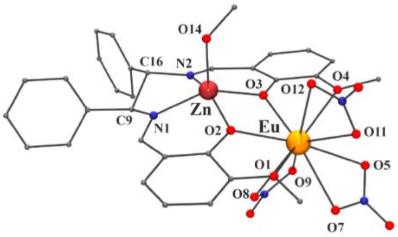 O14 C16 N2 O3 O12 O4 Zn C9 N1 O2 Eu O11 O1 O5 O9 O8 O7
Ln=Ce^{III} **[36]**, Nd^{III} **[37]**, Eu^{III} **[38]**, Dy^{III} **[39]**, Er^{III} **[40]**, Yb^{III} **[41].** Appear in Chapter 6.	**L12**	[Ni^{II}Ln^{III}]	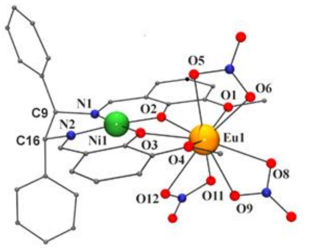 O5 C9 N1 O2 O1 O6 N2 C16 Ni1 O3 Eu1 O4 O8 O12 O11 O9
Ln=Ce^{III} **[42]**, Nd^{III} **[43]**, Sm^{III} **[44]**. Appear in Chapter 7.	**L6**	[Ln$^{III}_2$]	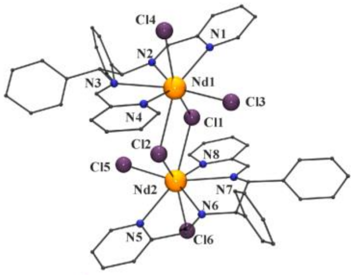 Cl4 N1 N2 N3 Nd1 Cl3 N4 Cl1 Cl2 N8 Cl5 Nd2 N7 N6 N5 Cl6
Ln=Eu^{III} **[45]**, Tb^{III} **[46]**, Dy^{III} **[47]**, Er^{III} **[48]**, Yb^{III} **[49]**, appear in Chapter 7	**L6**	[Ln^{III}]	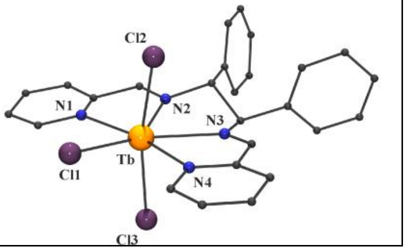 Cl2 N1 N2 N3 Cl1 Tb N4 Cl3

CHAPTER 0. AIM AND THESIS ORGANIZATION

This thesis was performed in the Group of Molecular Magnetism of the University of Barcelona with the aim of synthesizing and characterizing new coordination compounds. The Molecular Magnetism Group has been working for years in the study of the magnetic properties of transition metals, mainly copper, manganese, nickel and lanthanides, but also has interest in supramolecular chemistry.

The main objective of the present thesis was to synthesize multiproperty molecular coordination compounds presenting optical, magnetic and/or ferroelectric properties. The optical properties like the polarized absorption of light or the emission of polarized luminescence are directly linked to chiral structures and specific elements which present the possibility of emission, mainly lanthanides. The polarized absorption of light was achieved in our case directly obtaining the chirality by using enantiopure reactants. Many trials have been done to obtain emissive compounds but the success was only for one europium complex, number **[45]**, which presents luminescence at naked eye but was not measured. On contrary, we were able to study the polarized absorption properties spectroscopically with Electronic Circular Dichroism (ECD) for all the new systems. Ferroelectricity was, and still is, the hard bone of this thesis, because even in principle chirality should help to promote the necessary conditions for a ferroelectric behavior, the measurements of ferroelectricity in molecular compounds are unusual and complicated and the opportune collaborations are currently being developed.

The study of the magnetic properties was primordial in this thesis, and different lines were followed. The objective was to synthesize clusters with magnetic properties, sometimes in the search of Single Molecule Magnet (SMM) or Single Ion Magnet (SIM) behavior, but also to perform magneto-structural correlations and to study the slow magnetic relaxation in lanthanide clusters. The study of the static magnetic properties was performed on all the clusters synthesized, even sometimes was just a routine, because, as will be shown, there were other interesting features in the clusters, like for example in the series presented in the ***Publication #1***, where the main interest is about their supramolecular properties.

The magnetic properties of the clusters were achieved by using specific paramagnetic cations from the first transition raw (Mn^{II}/Mn^{III}, Fe^{III} and Ni^{II}) and from the Rare Earth period, taking advantage of the anisotropy of these ions (Ce^{III}, Nd^{III}, Tb^{III}, Dy^{III}, Er^{III} and Yb^{III}). Gd^{III} derivatives were prepared in some cases to calculate coupling constants with isotropic Hamiltonians.

Because the common thread of this work is the use of chiral Schiff bases, the chapter organization is devoted to the metallic center and no chronological order of the experimental work is followed. To fully understand the whole work and the reasons that brought us to work with a concrete system, a brief introduction and explanation is needed at this point.

Everything began during my master thesis synthesizing cooper and nickel cubanes.[1] The initial idea was to mix *d* and *f* metals within the same molecule. The syntheses did not succeed even series of *d* compounds using chiral and non-chiral ligands were prepared. **Figure 0.1** presents a scheme of this previous work.

Even though we succeed to obtain chiral compounds (using the ligand (*R/S*)-2-(1-hydroxyethyl) pyridine) there was another group that usually collaborates with us was preparing at that time compounds using the same ligand, so we decided to swap to another family of ligands: the Schiff bases.

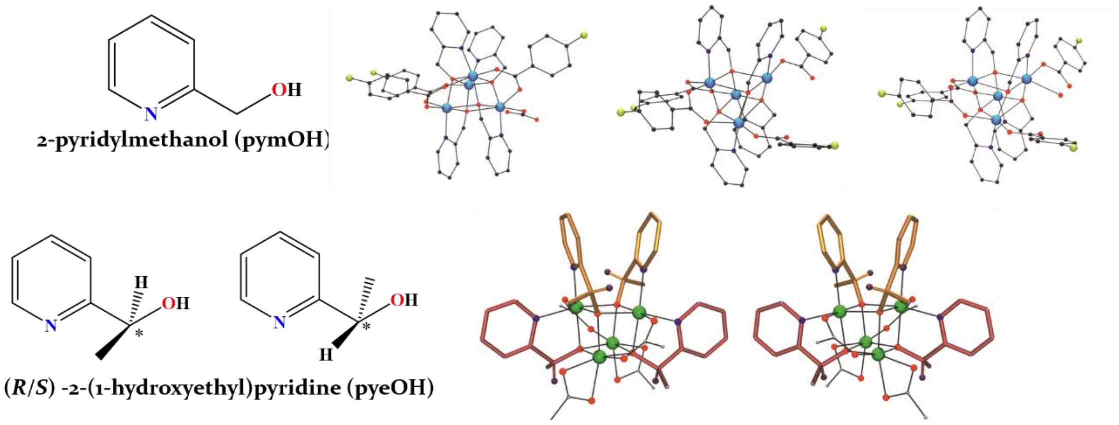
OH
N
2-pyridylmethanol (pymOH)
H
OH
N
*
OH
N
*
H
(R/S) -2-(1-hydroxyethyl)pyridine (pyeOH)

Figure 0.1. Scheme of the two series of compounds which were the initial idea of this thesis. First raw corresponds to non-chiral Cu^{II} cubanes and second raw corresponds to an enantiomeric pair of Ni^{II} cubanes with formula[Ni_4(*R/S*-pyeO)$_4$(MeCOO)$_4$ derived from the chiral ligand (*R/S*)-2-(1-hydroxyethyl) pyridine (pyeOH).

At this point two options were possible: to choose one family of ligands for the whole work or assay a variety of Schiff bases with different charge or donor properties. The second option was preferred in order to have a wide landscape of the possibilities of different families of ligands and widespread the nuclearities and magnetic properties.

The first attempt was with the Schiff bases **H_2L7** and **H_2L8** (**Figure 0.2**) and manganese salts. Manganese is a good candidate to work in molecular magnetism due to its flexible chemistry, the facility to form large polynuclear clusters, which can help to increase the total spin *S*, and due to the introduction of anisotropy by means of the Jahn-Teller distortion. This work resulted in ***Publication #4*** with the structures **[6], [7]** and **[8]** depicted in **Figure 0.5**. This series of three different complexes (three enantiomeric pairs) had Single Molecule Magnet (SMM) behavior in one case, but was decided to give up these first Schiff base ligands because of their complicate and dirty crystallization.

By changing the used aldehyde to condense the Schiff base, a new series of compounds started also using manganese salts and the ligands **H_2L9** and **H_2L10** (starting from *o*-vanillin instead of salicylaldehyde) (**Figure 0.2**). This was a successful combination which allowed to publish the work in ***Publication #5, Publication #6*** and ***Publication #7***. Even these works contain very interesting and beautiful compounds **[9]-[17]** (**Figure 0.5**), none of them has SMM response due to the position of the anisotropy axes of the Mn^{III} cations. As the search of SMMs was one of the objectives of this thesis, we decided to do a small change in these molecules by introducing a lanthanide cation to take advantage of the anisotropy of these ions which could make the slow magnetic relaxation appears. The result was the introduction of a single lanthanide cation in the structures: Mn^{II} from complexes **[9]** and **[10]** was changed by a Ln^{III} (or Y^{III}) yielding in a series of structures which are depicted in **Figure 0.6,** corresponding to compounds **[20], [21], [22], [23], [24], [25], [26], [27], [28]** and **[29].** Even though there was no presence of slow magnetic relaxation, a nice structural characterization has been done due to the differences in the chiral and racemic compounds, which opens the possibility to a new isomerism type that we have named chiral/racemic isomerism.

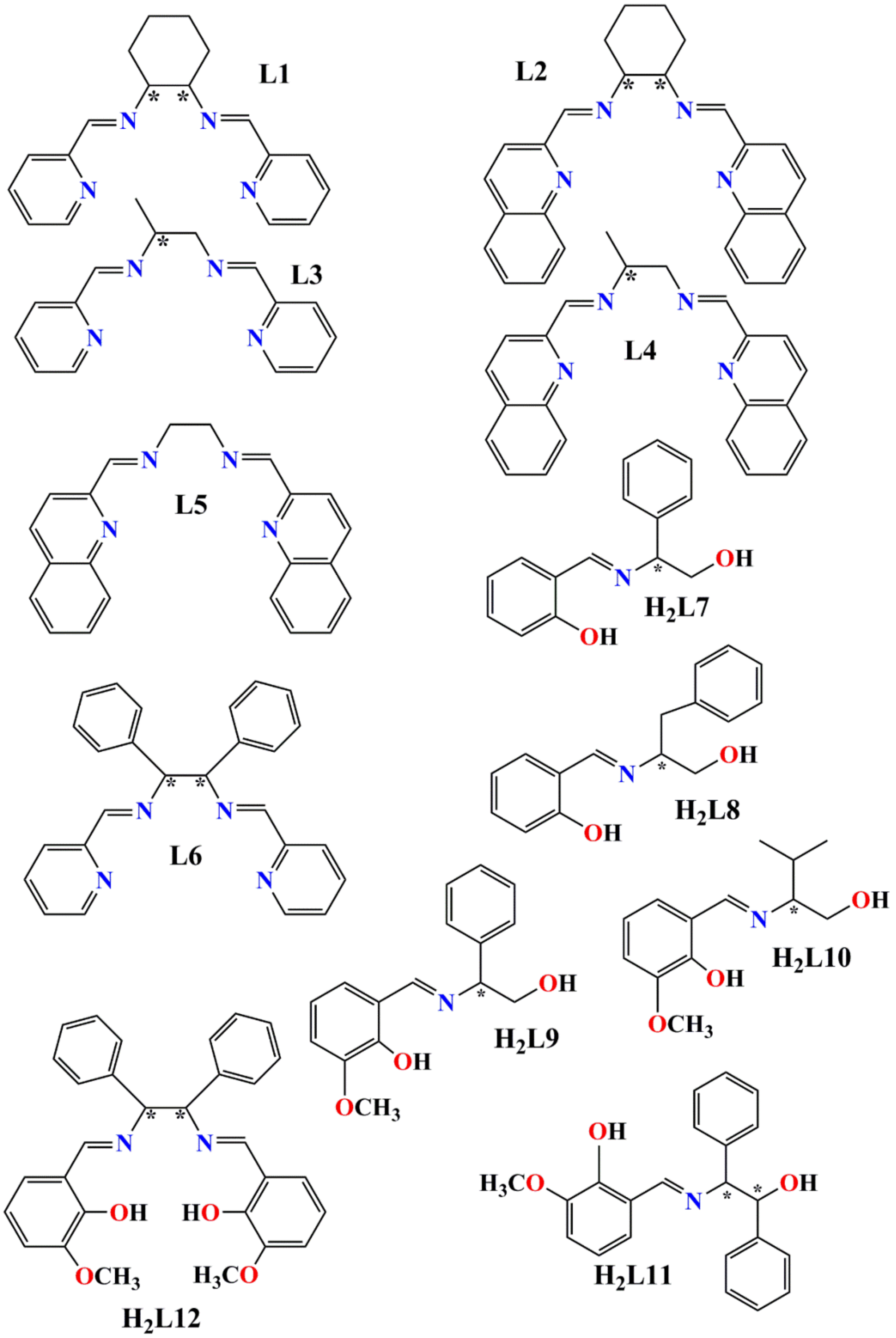
L1
L2
L3
L4
L5
L6
H2L7
H2L8
H2L9
H2L10
H2L11
H2L12
N
OH
HO
OCH3
H3CO
*

Figure 0.2. List of labelled ligands used in this thesis.

Another change that was planned to do in compounds **[9]** and **[10]** was the introduction of a different *d* metal instead of Mn^{III}. The result was the complete change in the structures and the obtention of a compound belonging to a classic family of SMMs known as iron stars, compound **[18]** represented in **Figure 0.4** which has been published in ***Publication #3*** and the synthesis of a lonely enantiomeric nickel pair, which is depicted in **Figure 0.3** as complex **[5]** and published in ***Publication #2***.

Preliminary trials to prepare heterometallic Fe^{III}/Ln^{III} systems to enhance the magnetic relaxation properties, yielded in a series of compounds which remains under study.

At the same time that we were working with $Mn^{II,III}$, Mn^{III}/Ln^{III}, Ni^{II} and Fe^{III}, an independent series of compounds derived from diamine ligands with different aldehydes (**Figure 0.2**, **L1, L2, L3, L4** and **L5,** was developed. These ligands in a reaction with different Ni^{II} salts yielded in compounds **[1], [2], [3]** and **[4]**, which are published in ***Publication #1***.

Using a selected two-cavities dinucleating Schiff base **H_2L12**, a series of mixed Ln^{III}/Zn^{II} and Ln^{III}/Ni^{II} series corresponding to complexes **[30], [21], [32], [33], [34]** and **[35]** for the Zn^{II} derivatives and complexes **[36], [37], [38], [39], [40]** and **[41]** for the Ni^{II} derivatives have been prepared. An example of the Ln^{III}/Zn^{II} and Ln^{III}/Ni^{II} families is depicted in **Figure 0.7.**

The try to synthesize pure lanthanide compounds using the ligands derived from diamines, concretely using **L6**, produced two different series of lanthanide clusters, for which the final structure depends on the used lanthanide, corresponding to compounds **[42], [43], [44], [45], [46], [47], [48]** and **[49], Figure 0.8.**

The organization of this thesis will be as follows.

The first chapter (**CHAPTER 1. INTRODUCTION**) containing a brief introduction about magnetism, supramolecular chemistry and about the theoretical background and the experimental setup of the characterization techniques. There is also an explanation about the choosing of the ligand type and the metallic cations of the synthesized compounds and, finally, the specific objectives of the thesis. The second chapter is about the nickel compounds (**CHAPTER 2. NICKEL COMPLEXES**), the third one is a short chapter about iron complexes (**CHAPTER 3. AN IRON STAR)**, the fourth one is about manganese clusters in (II) and (III) oxidation states and also mixed in some cases with alkaline (Na^{I}) and alkaline earth (Ca^{II}) metals **(CHAPTER 4. MANGANESE COMPLEXES**), the fifth one is about compounds synthesized mixing manganese with lanthanides and also containing sodium (**CHAPTER 5: CHIRAL vs. RACEMIC *3d/4f* COMPLEXES. A NEW ISOMERISM TYPE?**), the sixth chapter is about the search of SIM compounds which are dinuclear complexes containing a lanthanide cation and a diamagnetic *3d* cation (**CHAPTER 6. FIELD INDUCED SINGLE ION MAGNET COMPLEXES DERIVED FROM KRAMERS IONS**), chapter number seven is about purely *4f* compounds which crystallize in different way depending on the used lanthanide cation (**CHAPTER 7. PURELY LANTHANIDE COMPLEXES**). The last part of the thesis contains an overview of the whole work and a discussion about general issues under the title of **CHAPTER 8. FINAL REMARKS**.

Due to the organization in different publications of the main part of this thesis, an independent numeration of the compounds is going to be used in this work. A complete list of the compounds appears in the “LIST OF LIGANDS AND COMPOUNDS” which is available at the very beginning of the thesis. In that list, for the published clusters, there is also indicated the number of the compound in the present thesis, the number of chapter where it is included, the number of publication where the compound is included and finally, the number of the compound in its corresponding publication.

Because of the vast majority of the compounds have been synthesized in their *R*, *S* and racemic form in some cases, the names of the compounds will be presented as the compound number followed by the corresponding isomeric indication, as an example: **[1*R*], [1*S*]** or **[1*RAC*]**, and for the cases with more than one chiral center: **[1*RR*], [1*SS*]** or **[1*RAC*].**

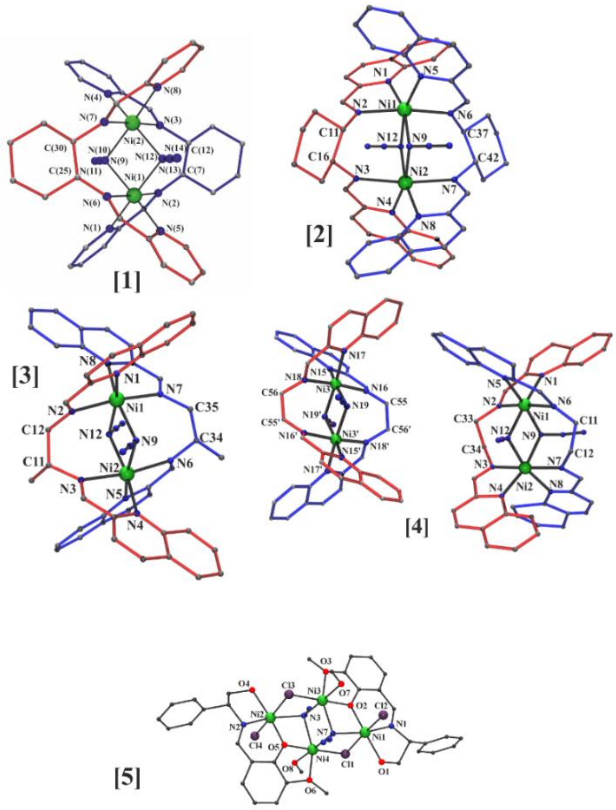
[1]
N(4)
N(8)
N(7)
N(3)
Ni(2)
C(30)
N(10)
N(9)
N(12)
N(14)
C(12)
C(25)
N(11)
N(13)
C(7)
Ni(1)
N(6)
N(2)
N(1)
N(5)
[2]
N1
N5
N2
Ni1
N6
C11
N12
N9
C37
C16
C42
N3
Ni2
N7
N4
N8
[3]
N8
N1
N7
N2
Ni1
C35
C12
N12
C34
N9
C11
Ni2
N6
N3
N5
N4
[4]
N17
N18
N15
N16
C56
N19
C55
C55'
N19'
C56'
N16'
N18'
N15'
N17'
N5
N1
N2
N6
C33
Ni1
C11
N12
N9
C34
C12
N3
N7
N4
Ni2
N8
[5]
O3
O4
Cl3
Ni3
O7
Ni2
O2
Cl2
N2
N3
N1
N7
Ni1
Cl4
O5
Ni4
Cl1
O8
O1
O6

Figure 0.3. Nickel complexes included in ***Publication #1*** and ***Publication #2***. **[1], [2], [3]** and **[5]** have been synthesized in *R* and *S* forms while **[4]** is derived from a non-chiral ligand.

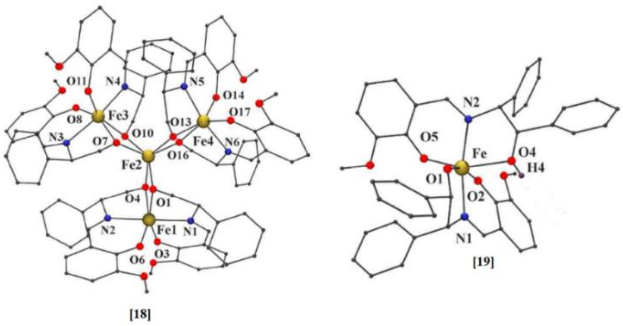
O11
N4
N5
O14
O8
Fe3
O17
O13
N3
O7
O10
Fe4
N6
Fe2
O16
O4
O1
N2
Fe1
N1
O3
O6
[18]
N2
O5
Fe
O4
H4
O1
O2
N1
[19]

Figure 0.4. Complex **[18]** has been synthesized as an enantiomeric pair *R*/*S* derived from **H_2L9** and complex **[19]** is derived from **H_2L12**.

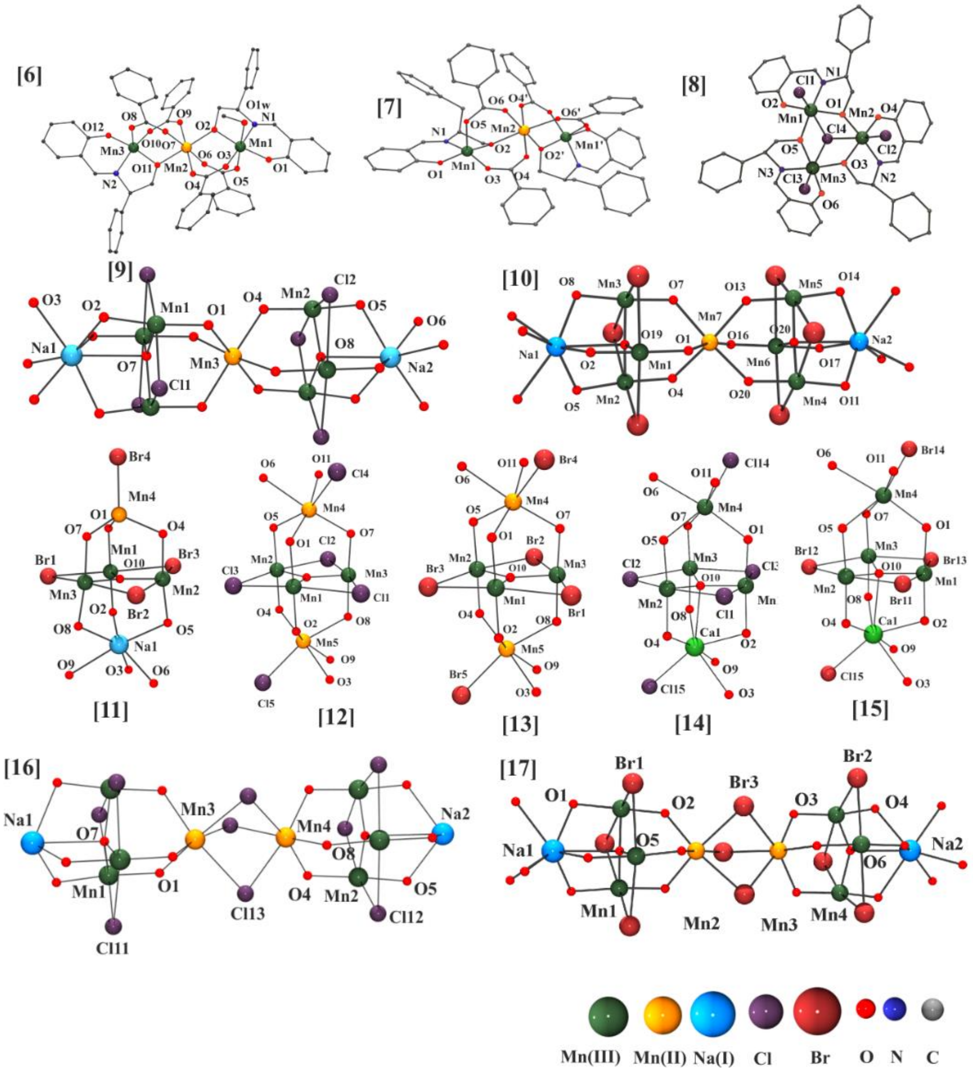
[6]
[7]
[8]
[9]
[10]
[11]
[12]
[13]
[14]
[15]
[16]
[17]
Mn(III)
Mn(II)
Na(I)
Cl
Br
O
N
C

Figure 0.5. Numeration of the manganese clusters presented in this thesis. For clarity, in most of them only the metallic core is depicted while the full structure and molecular formula can be checked in the corresponding publications.

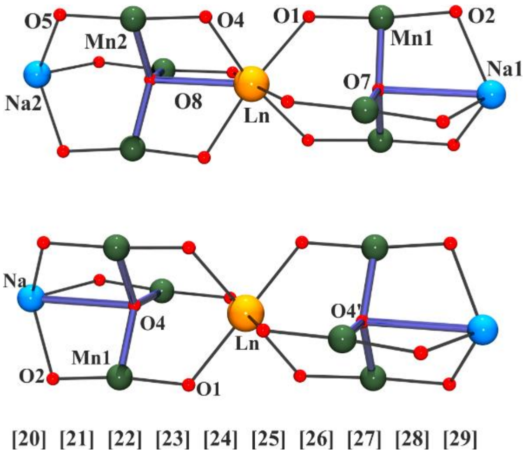
O5
Mn2
O4
O1
Mn1
O2
Na1
Na2
O8
Ln
O7
Na
O4
Mn1
O2
O1
Ln
O4'
[20] [21] [22] [23] [24] [25] [26] [27] [28] [29]

Figure 0.6. Racemic (top) and chiral (down) cores of compounds with general formula $[Y^{III}Mn^{III}_6Na^{I}_2]$ **[20]** and $[Ln^{III}Mn^{III}_6Na^{I}_2]$ (Ln= Ce **[21]**, Pr **[22],** Nd **[23]**, Eu **[24]**, Gd **[25]**, Tb **[26]**, Dy **[27]**, Er **[28]**, Yb **[29]**) derived from **H_2L9**.

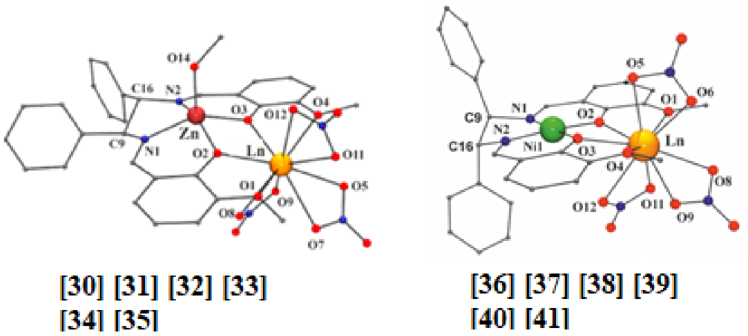
O14
C16
N2
Zn
O3
O12
O4
C9
N1
O2
Ln
O11
O1
O5
O8
O9
O7
C9
N1
O2
O5
O6
O1
N2
Ni1
C16
O3
O4
O8
O12
O11
O9

[30] [31] [32] [33] [34] [35]

[36] [37] [38] [39] [40] [41]

Figure 0.7. Dinuclear compounds with SIM behavior due to the diamagnetism of the *d* metals. Different lanthanides were used in the synthesis: **[30]** and **[36]** are Ce^{III}, **[31]** and **[37]** Nd^{III}, **[32]** and **[38]** Eu^{III}, **[33]** and **[39]** Dy^{III}, **[34]** and **[40]** Er^{III} and **[35]** and **[41]** Yb^{III}.

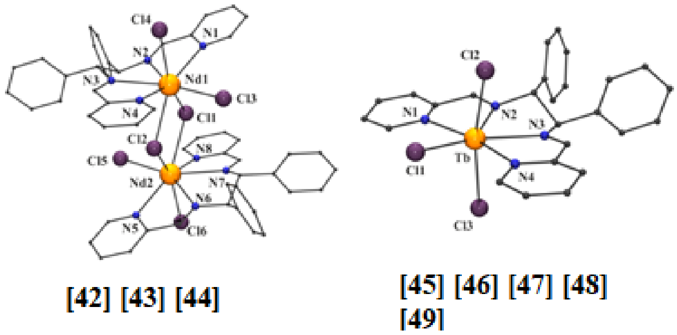
Cl4
N1
N2
N3
Nd1
Cl3
N4
Cl1
Cl2
N8
Cl5
Nd2
N7
N6
N5
Cl6
Cl2
N1
N2
N3
Cl1
Tb
N4
Cl3

[42] [43] [44]

[45] [46] [47] [48] [49]

Figure 0.8. Depending on the used ligand, the final complex is a dinuclear compound for the light lanthanides, [$Ln_2L_2Cl_6$] (Ln= Ce^{III} **[42]**, Nd^{III} **[43], ** Sm^{III} **[44]**) and mononuclear compounds for heavy lanthanides, [$LnLCl_3$] (Ln=Eu^{III} **[45]**, Tb^{III} **[46]**, Dy^{III} **[47]**, Er^{III} **[48]**, Yb^{III} **[49]**.

CHAPTER 1. INTRODUCTION

1.1. MAGNETISM

1.1.1. A brief history of magnetism.

Magnetic phenomena were known in the ancient world and the word *magnet* comes from the Greek μαγνῆτις λίθος, *magnetic lithos*, magnetic stone. Another version says that the word *magnetic* can derivate from the city of Magnesia, where maybe this phenomenon was first observed. According to Plinius the Old, the word comes from the shepherd *Magnes* who first realized that the iron was attracted by loadstone. The first magnetic discussion is attributed to Thales of Miletus (625-545 B.C.) although at the same time, there are evidences that the Indian surgeon Sushruta used the magnetism for medical purposes. Around the 4th century B.C., the concept of magnetism was pointed out in the Chinese book *The Sage of Ghost Valley*, and two hundred years later, the sentence "*Loadstone attracts the iron*" appears in the *Lüshi Chunqiu*, when a rudimentary compass made of loadstone was fashioned. In the 11th century, the Chinese scientist Shen Kuo was the first to apply in astronomy and navigation the concept of *True North*.

After this fresh start of a new phenomenon, many scientists have been attracted by magnetism: Galileo Galilei, Francis Bacon, Descartes and many others. In 1600 William Gilbert (1544-1603) demonstrated that Earth was magnetic by itself. A huge progress must be attributed to Charles-Augustin du Coulomb (1736-1806), who in 1789 wrote a paper named *Du Magnètisme*, where he pointed out that electricity and magnetism were different phenomena but closely related. In 1830, Hans Christian Ørsted (1777-1851) discovered that electric currents create magnetic fields and in 1820, André-Marie Ampère (1775-1836) realized that magnetism is a microscopic phenomenon which, only in some cases, can result into a macroscopic property of the matter. In 1831 Michael Faraday (1791-1867) discovered that a time-varying magnetic flux can induce voltage and, finally, James Clerk Maxwell (1831-1879) related light, electricity and magnetism in his famous equations. Some years later, Paul Langevin (1872-1946) devised the modern interpretation of paramagnetism and diamagnetism in terms of the spins of the electrons in the atoms, extended by Piere Weiss (1865-1940) demonstrating that magnetism is a collective behavior in the formulation of the Molecular Field Theory. So, it was during the 19th and 20th century that the nature of magnetism was understood, but until that moment, magnetic materials were based on metals and oxides. Towards the end of the 20th century the first magnets based on organic matter were discovered, coordination compounds were investigated and, a new field named molecular magnetism was born.

1.1.2. From molecular magnetism to single molecule magnets.

After WWII there was an increasing interest of the inorganic chemists in coordination chemistry: crystals formed by coordination complexes were studied under the perspective of the ligand field theory.[2] Louis Eugène Félix Neél (1904-2000) did an important advance in the field in 1948 in his study about ferrimagnetism[3] and some years later, P. W. Anderson (1923-), described a quantum-mechanical approach to the interaction between the spins in neighboring metal ions.[4] Before that, there were many important contributions by Heisenberg, Dirac or Van Vleck, demonstrating that the magnetic behavior was associated to the chemical bond.[5-7] From a chemical point of view, a significant help arrived with the Goodenough-Kanamori rules[8] which transformed the complicate quantum-mechanical treatment of the problem in a series of symmetry rules. In 1956, the first compound (Prussian Blue Analogue) with ferromagnetic remanence at low temperature was studied at Bell laboratories[9] and also the first molecular coordination compound, the famous dinuclear Cu^{II} acetate with a paddlewheel structure,[10] was magnetically studied under N_2 temperature: the behavior of its magnetic susceptibility response at low temperature allowed Bleaney and Bowers[11] to describe its behavior by using the Heisenberg-Dirac-Van Vleck Hamiltonian. The strong exchange coupling between the Cu^{II} ions is not trough space or through direct Cu^{II}-Cu^{II} interaction: the magnetic interaction involves the ligands, interaction known as *Superexchange* (see below). After that, started a period where many molecular compounds were magnetically studied by means of their magnetization and susceptibility curves, arriving progressively to liquid helium temperatures and, due to the incorporation of X-Ray diffraction for the determination of the structures as a usual technique in the laboratories, the information collected permitted to establish correlations between the magnetic properties and the molecular structures. In the later 80s, Olivier Kahn and co-workers gave a massive contribution to molecular magnetism by publishing a molecular $Mn^{II}Cu^{II}$ bimetallic chain bridged by oxamato groups which was the first chain magnet[12] and, in 1993, Michel Verdaguer published a room temperature ferrimagnetic cyanide-based material.[13] This new comprehension of the relation between structure and magnetic properties in molecular compounds, promoted the change from *magnetochemistry*, which is essentially the use of magnetic techniques to extract structural information, to *molecular magnetism*,[14] which allows the modeling and design of new molecule-based magnetic materials. All the textbooks and personal feelings of people who was involved in that transition, agree that the birth of molecular magnetism can be fixed in a NATO Advanced Study Institute (ASI) held in Castiglione de la Pescaia, Italy, in 1983.[15] From that moment, many laboratories trough the world began to synthesize and characterize molecules which can be useful in designing new magnetic materials because of the growing interest in nanoscience.

At that moment, most of papers about molecular magnetism were about the coupling between the metallic centers, exchange and superexchange, which is only the first term of the spin Hamiltonian (**Equation 1.1**, as an example of a spin Hamiltonian for pairs) that was used as an approximation to describe the molecular systems. Were Dante Gatteschi and co-workers, who in 1993 realized about the second term of such Hamiltonian, to exploit the consequences of the anisotropy, D.[16,17] The discovery of the slow relaxation of the magnetization in the famous Mn_{12}, the elucidation of an anisotropy energy barrier between to bistable states and the fact that it presents magnetic hysteresis, inaugurated the new field of the molecules which behave as tiny magnets, known as Single Molecule Magnets (SMM).

$$\mathcal{H}_{ss} = -J_{12}\boldsymbol{S}_1 \cdot \boldsymbol{S}_2 + \boldsymbol{S}_1 \cdot \boldsymbol{D}_{12} \cdot \boldsymbol{S}_2 + \boldsymbol{d}_{12} \cdot (\boldsymbol{S}_1 \, x \, \boldsymbol{S}_2) \qquad \textbf{(1.1)}$$

1.1.3. Single molecule magnets.

Magnetic materials are very common in our daily life. At the beginning, these materials were basically bulk solids, but, since some years ago, the needed miniaturization and the new properties observed in molecules, started to promote an alternative to bulk magnets. These magnetic molecular materials had been proposed for different applications like spintronics,[18] high-density information storage,[19] and as qubits for quantum computing[20] due to their quantum size effects[21] or Josephson junctions[22] confirming the Copenhagen interpretation of quantum mechanics, supposing that everything started with the Schrödinger's cat. Sadly, for the moment, practical applications remain in a second plane mainly due to the temperature problems, while their study is incredibly useful to better understand their behavior and for, may be one day, apply them in real technologies.

1.1.3.1. The memory of molecules.

The observation of magnetic hysteresis was detected in a twelve-ion mixed-valence manganese cluster, $[Mn_{12}O_{12}(O_2CCH_3)_{16}(H_2O)_4]\cdot 2CH_3COOH\cdot 4H_2O$, and this was the beginning of the Single Molecule Magnets, an evocative name regarding the molecular structure of this first example.[17] Thanks to the use of ac susceptibility measurements and Electronic Paramagnetic Resonance (EPR), was evidenced an S=10 ground state arising from the magnetic coupling between the spins of manganese with different oxidation states. An axial zero-field splitting is present (D) which leads to the splitting of the S=10 levels into 21 levels characterized by a quantum number, m_s, which is the spin projection along z, being $-S\leq m_s\leq +S$ with a separation between them proportional to $2(|m_s|-1)D$. The negative sign of D promotes an energy barrier, U, between the $m_s = -10$ and $m_s = +10$ states (states with the higher absolute value of m_s yielding lower). To flip the spin from $-S$ to $+S$ passing through the perpendicular $m_s = 0$ state, a quantity of energy is needed. This type of *anisotropy (D)* is known as *easy axis anisotropy* (**Figure 1.1**) and it's associated to the spin Hamiltonian:

$$\mathcal{H}_{an} = |D|\, S_z^2 \qquad \textbf{(1.2)}$$

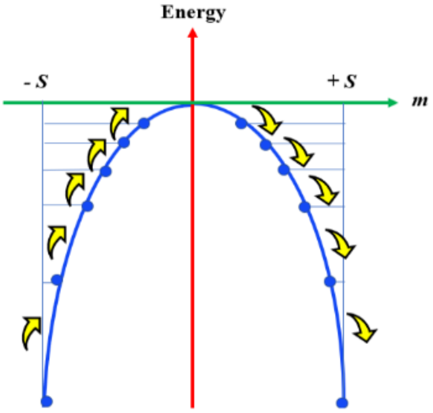

Figure 1.1. Splitting in zero field of the |m> components of a spin state S, according a negative D in **Equation 1.2**. m is the projection of the spin along the z direction (represented in red).

When this energy barrier is large enough, the spin of the molecule can be magnetized in one of the two directions: when the molecule is exposed to a magnetic field, one of the two wells is stabilized in front of the other, moving to the state with S= -10 (or +10). It is say that at this point that the magnetization is saturated, and due to the presence of the energy barrier (**Figure 1.2**), it will remain in this new state: a remnant magnetization is observed. If the thermal energy of the system, k_BT (being k_B the Boltzmann constant) is smaller than U, the system will be unable to reorientate its magnetization and will be trapped in a minimum of potential energy. This energy barrier will depend on DS^2 or (DS^2 – ¼) for integer or half-integer spins, respectively.

The hysteresis in molecular compounds was immediately attributed to these two features: the high ground spin sate and the easy axis magnetic anisotropy,[23] and can be easily understood that the return to equilibrium would require some time, and this time, known as the *relaxation rate*, will be one of the key parameters in molecular magnetism.

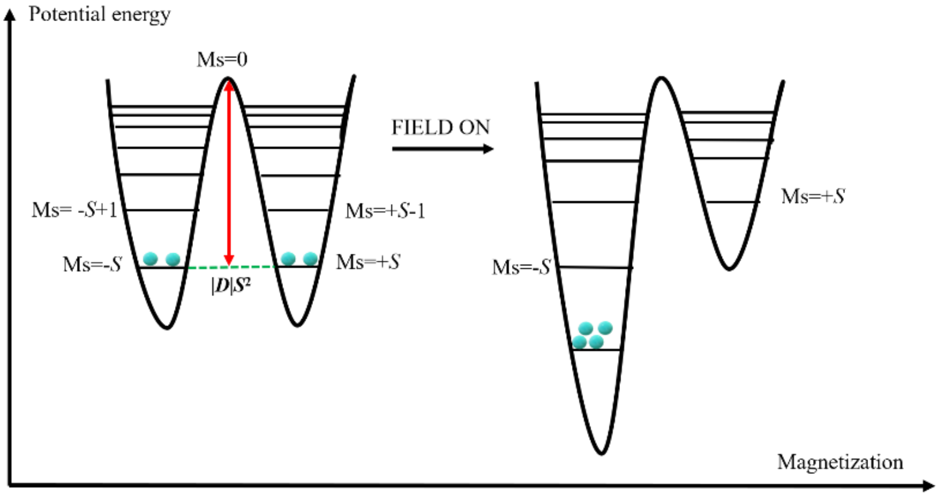

Figure 1.2. Potential energy *vs*. magnetization for a SMM with axial zero field splitting and with an energy barrier proportional to DS_z^2.

The hysteresis loop shows the "history" of the magnetization, and, depending on this "history", at zero field the magnetization can be positive or either negative. Taking profit of this property, we can assume that molecules should be able to have memory (**Figure 1.3**).

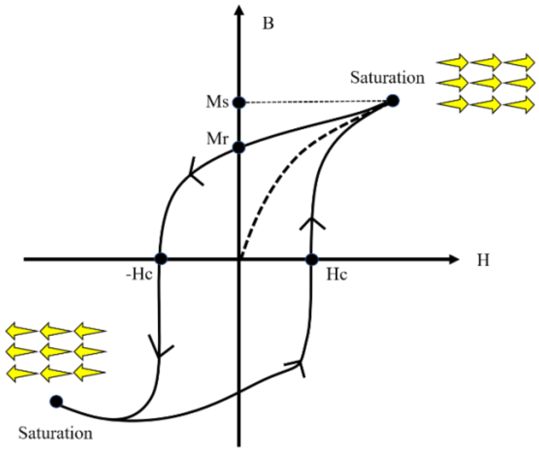

Figure 1.3. Representation of a hysteresis loop with magnetization *vs*. field is plotted. *M*s is the magnetization saturation, *M*r is the remnant magnetization and *H*c is the coercitive field. The coercitive field depends on temperature, and generally, large coercitive fields are only observed at very low temperatures. SMMs only display hysteresis below their blocking temperatures.

If a negative field is not applied, the molecule will tend relatively slowly to its equilibrium situation, which is the state with the same population in both wells. This rate of reversal of the magnetization is expected to follow an Arrhenius-like behavior (**Equation 1.3**) in certain conditions that will be discussed in Section 1.1.2.3.

$$\tau^{-1} = \tau_0^{-1}\exp\left(-\Delta E/k_B T\right) \qquad \mathbf{(1.3)}$$

where τ is the relaxation rate, τ_0 is the preexponential factor and k_B the Boltzmann constant.

1.1.3.2. Magnetic exchange and superexchange.

The origin of the coupling between magnetic centers has two origins: magnetic and electrostatic. The interaction can be described through space or trough bond. The origin of magnetic coupling was described by Kahn in 1993[14] as the formation of a weak bond. This interaction was described at the beginning by the Anderson's theory[4,24]: two metal ions, each one with an unpaired electron, linked by a unity with no unpaired electrons interact, and at this point their electrons are no localized anymore because they are forming the weak bond. This interaction is the sum of a kinetic exchange, a potential exchange and a dipolar exchange. The interaction between the two paramagnetic centers can occur directly (exchange) or through the diamagnetic unity linking them (superexchange). The qualitative features of this weak bonding are described by the Goodenough-Kanamori rules[8,24]:

1. When two ions have the lobes of magnetic orbitals (the orbitals containing the unpaired electrons) pointing towards each other in such a way that the orbitals would have a reasonably large overlap, the exchange is antiferromagnetic.
2. When the orbitals are arranged in such a way that they are expected to be in contact, but they have no overlap, the interaction is ferromagnetic.
3. When the magnetic orbital overlaps an empty orbital, the interaction is ferromagnetic.[25]

1.1.3.3. Relaxation in single molecule magnets.

Molecular magnetism has been paying much attention to the high of the barrier between the two spin states (being U one of the "quality parameters of the SMM"), rather to the structure of this barrier, which would be very useful to study the relaxation in SMMs. The spontaneous transition from one state to another can have two different origins: on one hand, the spin system coupling with lattice vibrations which involves the so called Orbach and Raman relaxations. On the other hand, due to the condition of nanoobjects of the SMM, they can experience the rise of new properties like the existence of quantum effects: SMMs offer the possibility of relaxing trough Quantum Tunneling of the Magnetization (QTM)[26] or thermally activated tunneling (TA-QTM) between m_s substates of the same energy. This last point is related with the rhombic ZFS parameter, E. **Figure 1.4** presents a scheme of the different relaxation mechanisms. Also a direct relaxation is possible under the application of an external static field.[27,28]

Going back to **Figure 1.2**, when the applied field to the system is removed, the system must return to the thermal equilibrium, the *relaxation*, which can be calculated by measuring the magnetization of the system as a function of time, as is shown in **Equation 1.4**.

$$\boldsymbol{M}(t) = \boldsymbol{M}(t=0)\exp(-t/\tau) \qquad \mathbf{(1.4)}$$

Which is related with the coupling of the system with the environment.

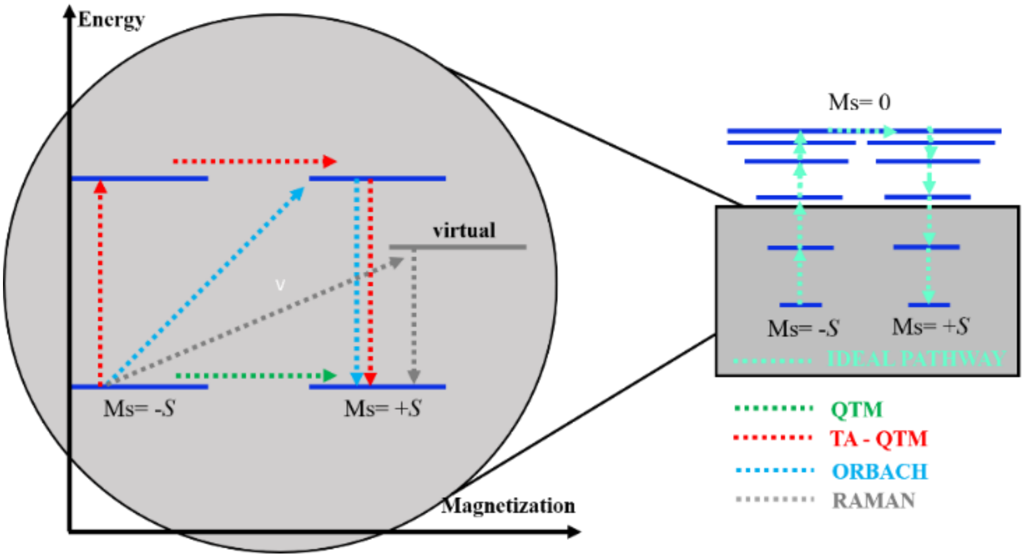
Energy
virtual
v
Ms= -S
Ms= +S
Magnetization
Ms= 0
Ms= -S
Ms= +S
IDEAL PATHWAY
QTM
TA - QTM
ORBACH
RAMAN

Figure 1.4. Schematic representation of the three relaxation processes. Blue lines represent spin states and the grey line represents a virtual state.

1.1.3.4. Thermal relaxation in SMMs. Arrhenius-like relaxation.[29]

The spin-phonon interaction is the main mechanism to exchange thermal energy in the paramagnetic ions (spin system). This energy exchange is the key to understand why the relaxation time varies with temperature and shifts the *g*-values by introducing changes in the spin Hamiltonian.

The energy is transferred by transitions between different energy levels by absorbing or emitting a quantum of energy between the spin system and the surroundings. The paramagnetic substances in a magnetic field is just an example of a system with discrete energy levels exchanging energy with a thermal reservoir (the field), **Figure 1.5.**

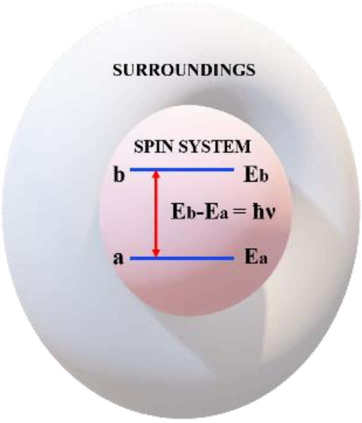
SURROUNDINGS
SPIN SYSTEM
b
Eb
Eb-Ea = ħν
a
Ea

Figure 1.5. Spin system and its surroundings for the energy exchange.

To calculate the relaxation rate, is need to know the transition probability from m_s=*a* with energy E_a to m_s=b with energy E_b, with this transition probability depending on the energy, so is extremely low at low temperature,

When τ is measured at different temperatures, a decrease with temperature is observed, usually represented by Arrhenius formula in **Equation 1.3** or:

$$\tau = \tau_0 exp\frac{T_0}{T} \tag{1.5}$$

And, to have a straight line it's useful to plot $1/\ln(\tau/\tau_0)$ as a function of *T*:

$$\frac{1}{\ln(\frac{\tau}{\tau_0})} = \frac{T}{T_0} \tag{1.6}$$

being the typical behavior for magnetic relaxation of τ in front of temperature the one represented in **Figure 1.6.**, **Equation 1.3**, is only satisfied when *T* is higher than T_1.

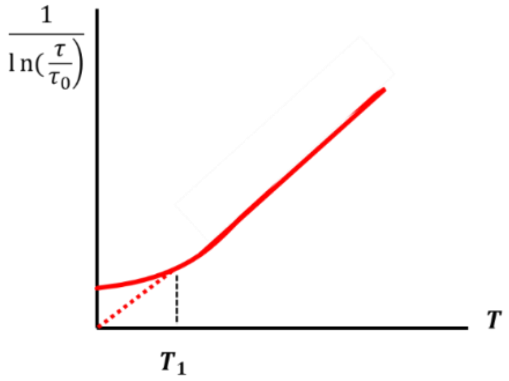

Figure 1.6. Behavior of the relaxation time, τ, of the magnetization represented in front of temperature, *T*. Arrhenius law is verified at relatively large temperatures while τ is constant al low temperature.

This Arrhenius behavior depending on temperature, explains perfectly the over barrier process when the magnetization relaxes. The problem is that, experimentally, there are many examples where the calculated energy barrier by means of this Arrhenius dependency supposes a relaxation *below* the barrier. This behavior is easy to explain through a tunneling relaxation (see Section 1.1.3.6.) but also by means of another thermal processes pointed out by Waller, Koenig, Van Vleck and others. These below-barrier processes are schematized in **Figure 1.4**.

1.1.3.5. Spin-lattice relaxation by phonons. Alternatives to Orbach relaxation.

The application of an oscillatory magnetic field with an appropriate frequency produces transitions in the levels of the two-level simplified example of **Figure 1.7**, in both directions, being the up transition an absorption from the radiation field and the down transition an emission to the radiation field.

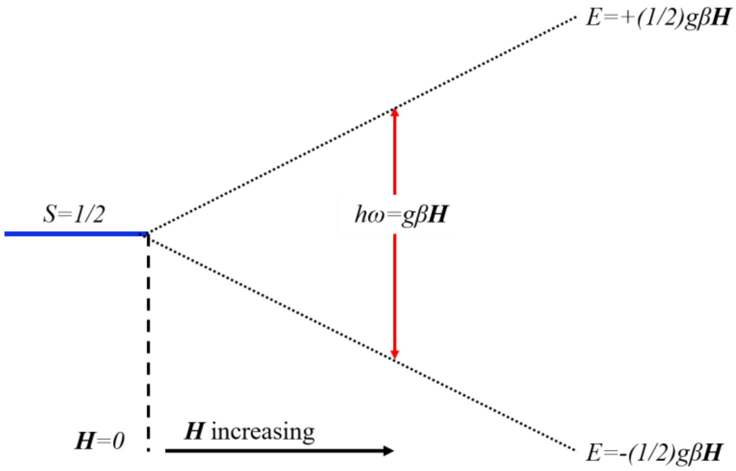

Figure 1.7. Energy levels for *S*=1/2: Zeeman effect under an applied field where the allowed transition is represented.

As has been told before, τ_1 is the *spin-lattice relaxation time*, and as is showed in **Equation 1.6** there is an exponential return to the equilibrium situation. The diverse kind of interactions between the spin system and the lattice determines the spin-spin interaction. And the spin-spin interaction determines τ_1. This point was discussed for a very first time by Waller in 1932.[30] Waller distinguished two processes in such interactions:

a) DIRECT PROCESS. A phonon with the same energy as the needed quantum for the transition is absorbed by the spin system, resulting in an up transition, or is emitted, resulting in a down transition. The process involves one phonon.
b) RAMAN PROCESS. A phonon of any frequency interacts with the spin, causing a transition. The phonon is scattered with a different frequency. The process involves two different phonons.

Direct and Raman processes are represented in **Figure 1.8.**

Raman relaxation will be the most contributive process because can involve phonons with any energy, while a phonon with specific energy is needed for the direct relaxation. This approximation was based on the modulation of the magnetic dipolar spin-spin interactions and the problem was that the experimentally observed relaxation times are much lower than those predicted by theory.

Another theory, unlike that of Waller is independent on the concentration, is the relaxation by the coupling of the system to the environment by spin-phonon interactions which induce modulations in crystal-field. This dependence on the crystal field of the relaxation time is fully controlled by the SOC: spin-lattice relaxation times are lower in 4*f* and 5*f* metals (except the ones with half-filled shells).

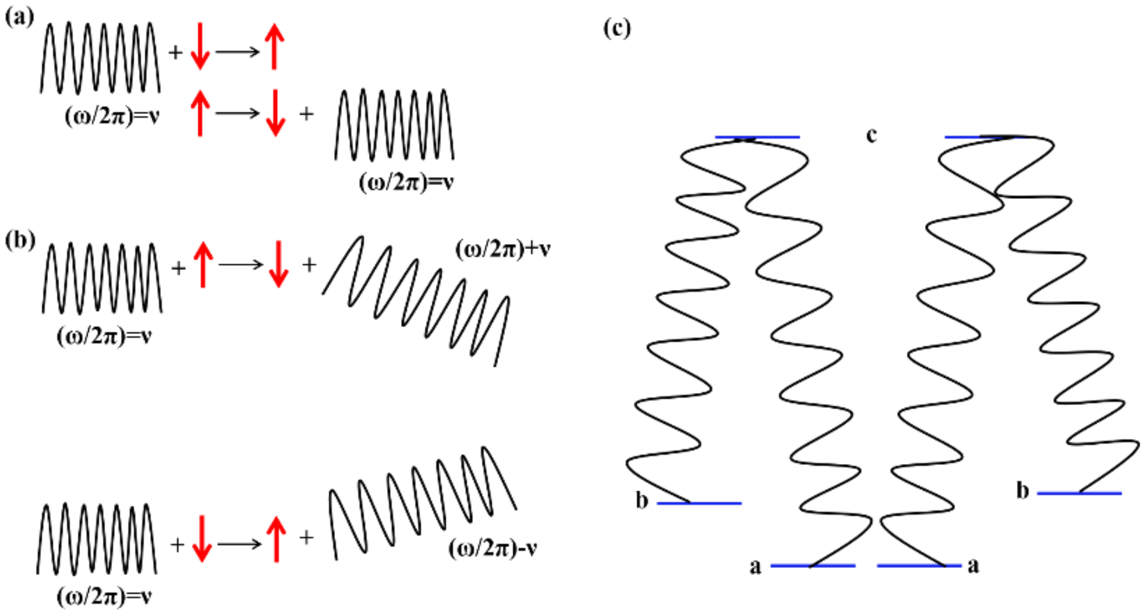

Figure 1.8. (a) represents the direct process: a phonon with a ν frequency absorbs (emits) a phonon with the same frequency. **(c)** Orbach process: The paramagnetic ion has a ground doublet (a/b) with an excited state c separated by an energy *Δ*.

This theory was mainly developed by Kronig and Van Vleck around 1940[31,6] and was extended by Orbach.[26] There is a temperature dependence which can be written as:

$$\frac{1}{\tau_1} = a \coth\left(\frac{h\nu}{2kt_0}\right) + bT_0^n + \frac{c}{exp\left(\frac{\Delta}{kT_0}\right)-1} \qquad \mathbf{(1.7)}$$

Where $1/\tau_1$ has different simultaneous contributions with large contribution variability, which are:

a. DIRECT PROCESS. Corresponds to the first term of **Equation 1.7**. and like in Waller's theory, involves phonons of the same energy as the magnetic resonance.
b. RAMAN PROCESS. All phonons can take part, giving the strongly temperature dependent second term on **Equation 1.7** The value of the exponent changes for Kramers or non-Kramers ions.
c. ORBACH PROCESS, the third term of **Equation 1.7** Consists on the absorption of a phonon by direct process to excite the system to a higher level, followed by the emission of another phonon of different energy.

If the global relaxation presents an exponential decay of spin-phonon coupling is due to the spin-phonon Hamiltonian contains quadratic terms and therefore, the only allowed transitions are from |*Ms*> to |*Ms* ±1> and |Ms±2>. The molecule starts its relaxation by absorbing a quantum which corresponds to the energy difference E (|*Ms* ±1>)- E(|*Ms*>) and so on until *Ms* =0. Each one of these transitions present a *transition probability*, which is extremely small at low temperatures. The complete transition from E(*Ms*=0) to E(*Ms*=±S) in the limit where $kT \ll \Delta E$ have been demonstrated to correspond to **Equation 1.2**. Because the overall rate in a process is determined by the slowest step (in our case this corresponds to the transition trough the top of the barrier), this exponential dependence determines the overall relaxation time of the process.

1.1.3.6. Tunnel relaxation of the magnetization.

As has been previously said, SMMs can present quantum properties due to their size, knows and *quantum size effects*. We suppose the same situation as before, with the double well scheme of our molecule with a negative zero field splitting (**Figure 1.1**), and now, to study the quantum properties of the system, the attention will be focused at very low temperatures, where there are almost no phonons, so the spin cannot jump over the barrier.

In the case of the two wells, a macroscopic object should choose between one of them, and it can change its state by climbing the energy wall. But completely different possibilities arise from the quantum world, because the object has also a waving nature: if the wave function of one of the two wells extends to the other well, the object can be in both wells at the same time, concretely, can be in a superposition of the two states. The situation where the particle can move from one well to another without climbing the barrier is known as Quantum Tunneling of the Magnetization (QTM). When the wavefunctions of the two wells interact, there is a splitting of the degenerate levels, *Tunnel Splitting* (Δ_T) (**Figure 1.9**). The possibility of tunnel depends on the relation between the Δ_T and the height of the barrier and with the degree of interaction with the spin system and the environment (See Section 1.1.3.4).

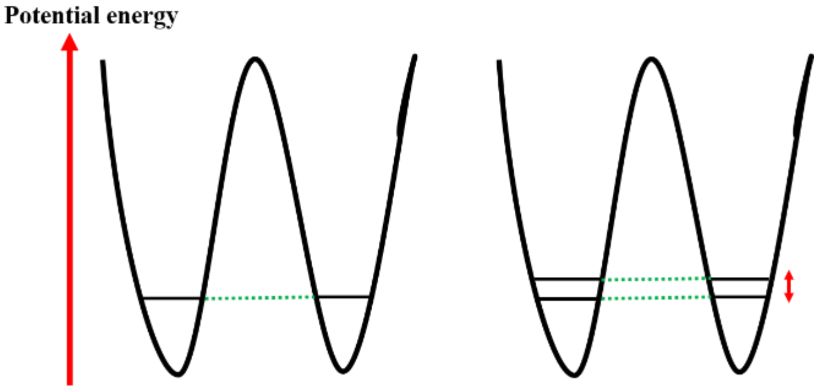

Figure 1.9. Tunneling in a double well. Left, in no interacting states and right, in interacting states which produces splitting.

In the case of zero field and at very low temperature, only the $Ms = \pm S$ are populated, but, because the state $-S$ and $+S$ are orthogonal to each other, no QTM is allowed. To observe QTM, the levels must be mixed by some perturbation (only $|Ms\pm1|$ and $|Ms\pm2|$ can be mixed in first order perturbations), which is named *resonant tunneling*. This perturbation is usually a removal of the axial symmetry: the introduction of anisotropy in the xy plane, known as *transverse anisotropy*, *E*, which must be always lower than the axial anisotropy, *D* ($0 \leq |E/D| \leq ⅓$). Kramers ions don't present Δ_T because *E* does not allow the mixing of the ground states at any order perturbation, so, in principle, QTM is not allowed for Kramers ions at zero field.

Tunneling may occur between degenerate levels different from the ground ones: a phenomenon called phonon-assisted or thermally activated tunneling.

When a magnetic field is applied in the direction of the *z* axis, the energies of the *Ms* levels change (**Figure 1.2**). If the *Ms* levels are no degenerate anymore, how the tunnel operates? What happens is that in the middle of these fluctuations of energy, a random level from the left well has at some point the same energy than a random level of the right well, allowing again the resonant tunneling (**Figure1.4**).

Because relaxation by tunneling is temperature independent, a very easy way to see if a compound presents tunneling or not is by representing the relaxation rate vs. temperature (typically $ln\tau$ vs. $1/T$). When there is no temperature dependence, the relaxation by tunnel is present (**Figure 1.10**).

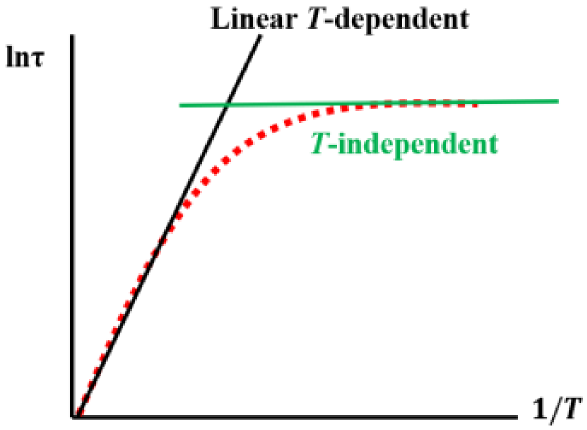

Figure 1.10. *T*-dependent and *T*-independent relaxation rates.

The fingerprints of SMM behavior are the mentioned hysteresis loops, where the Orbach and/or tunnel relaxations can be observed, and the dependence of the magnetic susceptibility (real and imaginary parts) on the frequency of an oscillating magnetic field. These dependency can be fitted in the two dimensional Argand plots to extract the relaxation times, τ, at different temperatures using the so-called Debye model.[33]

1.1.4. Transition metals and lanthanides in molecular magnetism.

At the very beginning, the world of SMMs was dominated by open shell transition metals, especially by the ones of the first row. Manganese was the star of these systems, maybe because a manganese cluster was the first of the family but also because Mn^{III} is the most anisotropic cation without SOC. During years, the mail goal was to increase the height of the barrier by means of constructing larger and larger molecules to maximize the total spin quantum number, S by synthesizing polynuclear clusters with globally ferromagnetic interactions between the paramagnetic centers. But the experience showed that very often, a polynuclear cluster doesn’t has the expected behavior. As an example, Mn_{12} has a D of only 0.46 cm^{-1} while the record Mn_6 cluster has a D value of 0.43 cm^{-1} with an effective energy barrier of 62 cm^{-1}.[34] The major prove was when a cluster of Mn_{19} with a record total spin $S = 83/2$ showed a surprisingly low energy barrier of 4 cm^{-1}. If the strategy of maximizing the spin to achieve high barriers was correct, the Mn_{19} should be, without discussion, the SMMs with the largest energy barrier ever. But, it was realized that due to the specific symmetry inside the molecule, the orientation of the paramagnetic ions "cancelled" the total anisotropy.[35] The surprise is that, if we compare these systems with a Jahn-Teller axially elongated Mn^{III} center, D is typically ~-4.5 cm^{-1}, so, a single ion can provide higher anisotropy than a really large coordination cluster. This experimental behavior leads to establish relations between the possibility of increasing D while increasing S,[36,37] leading to the conclusion that an increasing of S will not be translated in a higher energy barrier for the relaxation if the ions are not in the correct orientation, which is an understandable and logic conclusion because the interaction of two paramagnetic centers cannot lead to spectacular changes in the energy of the systems. As an example,[24] Gatescchi underlines how poorly efficient would be to made an effort to ferromagnetically couple the ions Mn_{12} to achieve a $S = 22$. In fact, comparisons between the same cluster FM or AF coupled, yields to the conclusion that the FM doesn't increases the high of the barrier as much as expected. This makes the ferrimagnetic approach specially interesting. To date, largest anisotropy barrier of a d metal is 67 cm^{-1} for a Co^{II} cluster without the application of an external magnetic field[38] and larger barriers are achieved under an applied external static magnetic field. One can think that may be the perfect SMM will be a large polynuclear compound with a correct orientation of the ions in the molecule but, waiting for the synthesis of this compound, there has been a growing sensation that the anisotropy is the key for the design of SMMs with high energy barriers,[39] and the new equation for the barrier $U=S^0|D|$ instead of $U=S^2|D|$ has been considered more accurate.[40]

Ions of lanthanide elements have demonstrated to have single ion large magnetic anisotropies because their orbital angular momentum remains unquenched and induces Spin Orbit Coupling (SOC) in the LS term resulting in a total angular momentum, J.[41] An increasing amount of papers appeared about lanthanide SMMs since Ishikawa *et al.* demonstrated the promising magnetic properties of single ion compounds in a phthalocyanine "double-decker" complexes $[LnPc_2]^-$ (Ln=Tb, Dy, Ho; H_2Pc_2=phthalocyanine).[42] Lanthanide complexes have demonstrated for the moment that they are able to slow down the magnetization dynamics.

So, are lanthanides the new promise of SMMs?

Even the spectacular results in the molecular magnetism with lanthanide compounds during last years,[43] new challenges appear when working with rare earth ions, mainly due to the fast tunneling.

It has been reported recently that the distribution of the electrons from the ligands with respect to the lanthanide cation is of mainly importance to determine the magnetic properties of the compound,[44,45] so, a precise design of the ligands is needed. For example, for oblate-shaped lanthanides like Dy^{III}, Tb^{III} or Ho^{III}, an axial disposition of the electrons from the ligands around the cation ensures an enhancement of the magnetic relaxation properties (**Figure 1.11**). The problem is that the preferred large coordination numbers of lanthanides (typically 8-10) yield usually in distorted or spherical geometries around the cation, which implies inevitably the apparition of rhombic anisotropy, E. This low symmetry produces the mixing of low lying states which enhances the tunneling effects, the main drawback in lanthanides SMM behavior.

1.1.5. Lanthanides, a curious born in Scandinavia layer by layer.[46]

Lanthanide derives from the Greek word “lanthanien” which means “hidden” and owe their name to the Swiss Chemist Victor Moritz Goldschmidt (1888-1947), who detected strong similarities in the behavior of the elements situated immediately after the lanthanum in the periodic table.

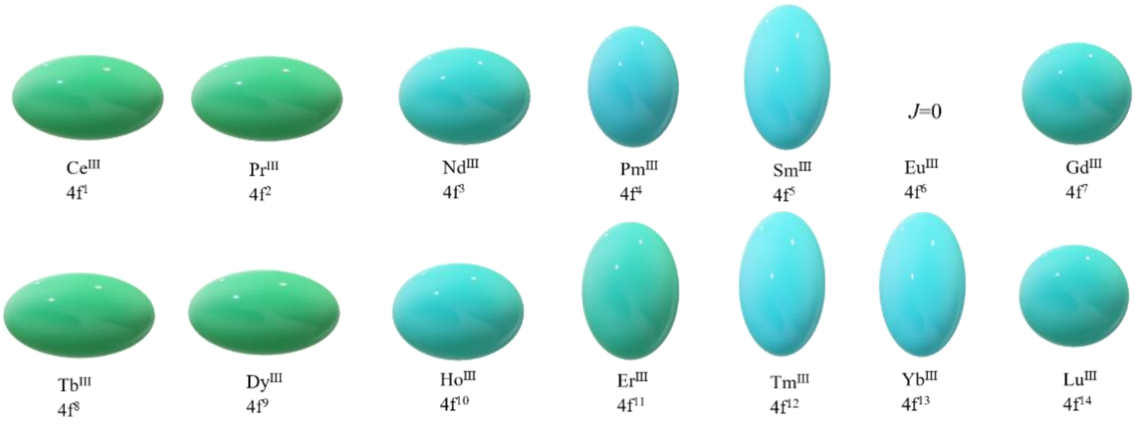

Figure 1.11. Oblate/Prolate shape of the different Ln^{III} cations.

“Lanthanides” were discovered for the very first time at the end of the XVIII century by the Finnish chemist and physicist Johan Gadolin (1760-1852). In 1792, Gadolin received a sample of a heavy and dark mineral which was found in a mine in the Swedish town of Ytterby. Gadolin was able to isolate an oxide that was first called Yttria. After that, it took more than a hundred years to separate and characterize the rest of the non-radioactive lanthanides, being the last one, the lutetium, in 1907, by the obviously Parisian scientific George Urbain (1872-1938). The process of finding and characterizing all the lanthanides was full of unexpected discoveries, because all the lanthanides are chemically similar, and, during years, one after one, appeared in the most unexpected ways. In 1803, Vilhem Hisinger (1766-1852) and Berzelius (1779-1848) started to investigate a sample called “heavy rock of Bastnäs”, a mineral found by the discoverer of Nickel, Axel Friederik Cronstedt (1722-1765). Hisinger and Berzelius were trying to find the already known yttria, but they separated a new oxide, really similar to yttria, which they named ceria, in honor to Ceres, the recently discovered planetoid (1801). Forty years later, was discovered that yttria and ceria were not pure oxides. Carl Gustav Mosander (1797-1858), the young disciple of Berzelius, was sure that ceria had something more. Working with this new compound, Mosander was surprised about a red coloration that sometimes appeared in these new oxides, which could be a sign of something. At the beginning of 1840 Mosander found lanthanum, from the Latin *lanthano*, “the one who remains crouched down” and in 1843 Terbium and Erbium, both names derived from the town of Ytterby, the place where the first mineral containing lanthanides was found.

After that amount of new discovered metals, the investigation in this field was stretched because the growing of organic chemistry eclipsed the inorganic one. Twenty years later, with the introduction of spectral techniques and taking advantage of this, in 1878, the Swiss chemist Jean Charles Galissard de Marignac (1817-1894) discovered that erbia, that was firstly isolated by Mosander, contained another compound, and he called it yterbia. Next year, the Swedish chemist Lars F. Nilson (1840-1899) identified, using spectroscopic techniques, a new element associated to Yterbia, and he named it Scandium, in an obvious allusion to Scandinavia. Another Swedish chemist, Theodor Cleve (1840-1905) suspected that also erbia could contain more than one system, and he discovered holmium, named because of the last syllable of Stockholm, and tulium, name derived from the Latin denomination of Scandinavia, *Tulia*. The discover that also holmia was not alone was made by the French scientist, dedicated to cognac production, Paul Émile Lecoq de Boisbaudran (1838-1912). He was able to separate holmia in holmia and dysprosia. This work required an incredible amount of precipitations with ammonia and oxalate and a detailed spectroscopic study. Some years later, Boisbaudran also found samaria in a mineral called samarskita, and in 1880 was found that samarskita also contained gadolinium, making a perfect loop going back to Johan Gadolin.

In 1901, Eugene Demarçay (1852-1903), one of the most famous spectroscopists and a close collaborator of *The Curies*, achieved the identification of a new element that was present in samples of samarium, and he named the new element, europium. Few years later, the Austrian chemist Auer von Welsbach (1858-1929) found praseodinium, in Greek "green twin" and neodinium, "new twin".

In 1945, Prometium, the synthetic lanthanide, was prepared during investigations in the Manhattan Project.

Even the popular name of the lanthanides, "Rare Earths" (name that includes yttrium and scandium), can remind to something exotic and estrange, they are not really "rare" and the name of "earth" is because of how were named the oxides in alchemy. For example, Ce, Y and Nd are more abundant than Pb, and Tm, the scarcest of the lanthanides, is more abundant than Au or Pt.

At the end of the XIX century, Auer von Welsbach, the discoverer of Pr and Nd, was who gave the first industrial application to lanthanides related with their lightening possibilities, but their period of stardom ended in 1930 when electricity replaced the gas lightening. Around 1960, they had a second period of fame when became the sub products of atomic industry, and, after studying they correct and commercial separation process from their complex mixed oxides, they gain popularity in new technological applications.

Even this interesting and unexpected discovery of lanthanides and interesting applications, the knowledge about their oxides and the new techniques to extract and purify them, they were a little bit forgotten for years by the inorganic chemists. Lanthanides don't have spectacular properties in the chemistry that was most known during the XX century: they early applications were linked to very simple inorganic compounds, mainly salts and oxides, they have a really poor redox chemistry, and, due to the inner nature of 4*f* valence orbitals, ligand field effects are very small, and their spectroscopic properties minimum affected by their coordination environment. For many years, they were considered like the boring brothers of 3*d* metals.

Related to coordination and molecular chemistry, the last twenty years finally gave to lanthanides the opportunity to show their capabilities in many fields like synthesis, catalysis, luminescence, magnetism or bio applications, especially due to their spectroscopic and magnetic properties which are derived from the nature of *4f* orbitals, which are shielded from the coordination environment by the filled 5*s* and 5*p* ones ([Xe] core).

The properties of the lanthanides and their compounds are influenced by the size of the ion and subtle changes in their radius are responsible for the changes in their properties along the period. The ionic radii along the 4*f* period sustain a progressive decrease from La to Lu, which is known as “lanthanide contraction”. The nature of this contraction is the same that for the transition metals, that is, the small shielding effect of one electron in another one of the same subshells. Even the “lanthanide contraction”, lanthanide ions have large ionic radii and this allows large coordination numbers. Today, appear in the literature coordination numbers from 3 to 12, with numbers 8 and 9 being the most usual by far.[47] The arrangement of the ligands around them basically depends upon the inner characteristics of the ligand.

The normal oxidation state for all the lanthanides is +3 being the most stable for all of them (also +4 for Ce and +2 for Eu). Trends in the physical and chemical properties of the elements are generally viewed as a function of the atomic number, is the so-called Z plots. In the case of the lanthanides there is no such a relationship and this effect has been called “The Gadolinium Break”. In the lanthanide series, the correlation of the properties is better considering the ground-state total angular momentum quantum number, L. A general principle in lanthanide chemistry stated by Johnson in 1980 is that in processes which do not involve changes in the number of f electrons, the lanthanides behave similarly.

About the interesting properties of lanthanides, fluorescence is one of the most popular. The luminescence of the lanthanides comes from the Laporte forbidden *f*-*f* transitions (the electrons cannot rearrange in the orbitals of the same subshell) between two spectroscopic levels. In practice, this selection rules are not strict, and some couplings can make forbidden transitions happen. However, they are weak with very low extinction coefficients. Taking this into account, another compound is needed to make the lanthanide to efficiently absorb light. This other compound is called “antenna”, typically an organic ligand, and is the responsible of the energy transfer to the excited state of the lanthanide. This phenomenon is called sensitization. As has been told previously, the crystal field is not very active in lanthanide compounds, so, the electronic levels involved in the light emission are not really dependent of the coordination environment of the cation. That’s why the emission spectra of the lanthanides are not really shifted depending on the environment. This is one of the most interesting properties of the lanthanides because the luminescence for each ones appears always in the same region and with the same color. With this characteristic, emission is a characterization technique for lanthanide cations. As some examples, $\mathrm{Sm^{III}}$, $\mathrm{Eu^{III}}$ and $\mathrm{Tb^{III}}$ emit always in the visible region of the electromagnetic spectra when the emission is unquenched. Other lanthanides like $\mathrm{Nd^{III}}$ or $\mathrm{Yb^{III}}$ emit in the near-IR region, which means that can be very useful for biomedical applications.

Changing to magnetism, lanthanides have been being really popular from few years ago and, studies about achieving a Single Molecular Magnet (SMM) behavior with lanthanide coordination compounds are today at the same levels of popularity that the ones with transition metals. In 3*d* metals magnetic studies was assumed that the combination of two properties is needed to achieve the SMM behavior: A Ising-type magnetic anisotropy, which is described with the zero-field splitting parameter, D, and a high total ground spin state, S. Since the publication of the double-decker $\mathrm{Tb^{III}}$ Single Ion Magnet[42] there has been a growing convincement that single-ion anisotropy is a new crucial property needed to improve the SMMs. The differential fact of 4*f* metals comparing them with the d metals is their intrinsic anisotropy, which is going to be detailed in the magnetic properties of the lanthanides (Section 1.1.6). As an introduction, only to comment that lanthanides are today one of the most important source of magnetic materials, due to their large spin-orbit-coupling and an unquenched orbital angular momentum.

1.1.6. Lanthanides: anisotropy and crystal field.

Anisotropy has a Greek etymology which means “not-equally turned”. In the case of *magnetic anisotropy* means that *magnetization* is not equally distributed in the space. The knowledge of the magnetic anisotropy of a system is useful to understand the magnetic behavior of the material and to predict some of its properties. As has been previously said, anisotropy is a mandatory characteristic for SMM behavior, that is, a preferential direction of the magnetization to lie.
The Hamiltonian of the free ion has three main contributions, as is shown in **Equation 1.8**:

$$\mathcal{H}_{free} = \mathcal{H}_{kin} + \mathcal{H}_{ee} + \mathcal{H}_{SOC} = \sum_i (\frac{\boldsymbol{p}_i^2}{2m} - \frac{Ze^2}{r_i}) + \sum_{i<j} \frac{e^2}{|r_i - r_j|} + \sum_i \xi_i \cdot \boldsymbol{l}_i \cdot \boldsymbol{s}_i \qquad \textbf{(1.8)}$$

where the first term is about the kinetic energy describing the movement of the electrons in an effective spatial region, the orbital, being $\boldsymbol{p}_i$ the linear momentum operator, m and e the electron mass and charge, respectively, Z, the nuclear charge and r_i, the position vector. The second term corresponds to the interelectronic repulsions and the third term corresponds to the SOC, with ξ being the ion SOC strength of the ion, which depends on the partially filled valence orbitals, $\boldsymbol{l}_i$ corresponds to the orbital angular momentum and $\boldsymbol{s}_i$ to the spin angular momentum.

Depending on the nature of the ion we are working on, different order of the energetic perturbations is applied when calculating the total energy Hamiltonian: in Transition Metals (TM), the ligands around the metal *quench* the orbital momentum, reducing the contribution of the SOC while for lanthanides the SOC contribution is high due to the inner nature of 4*f* electrons.

Because the calculation and the interpretation of the anisotropy of lanthanide compounds is one of the main goals of this thesis, an introduction to what promotes anisotropy in molecular lanthanide clusters and how to deal with it to understand the magnetic properties is needed at this point.

Lanthanides present magnetic properties arising from their electronic configuration with unpaired 4*f* electrons which are shielded by the filled 5*s* and 5*p* orbitals. This means that the behavior of lanthanide compounds is much less affected by the ion environment than in transition metal compounds (**Figure 1.12**), so, their magnetic behavior can be studied in a first approach as an isolated single ion.

The Russell-Saunders coupling is applied so interelectronic repulsion is considered to be dominant over SOC and the SOC dominant over the crystal field.

The spin angular momentum of all the electrons is first coupled to obtain a *global* spin S, $S = \sum s_i$ and the same with the orbital angular momentum, $L = \sum l_i$, to give a total momentum J, being $J = |L-S|,\ldots,L+S$. Each J value has a corresponding energy depending on its orientation and gives a number of degenerate states characterized as $^{2S+1}L_J$, with S, P, D, F, ..., etc. symbol corresponding to L=0, 1, 2, 3, …etc. taking into account that sometimes this set of quantum numbers is not enough to characterize the term and the Racah parameters are needed.

If there is no a preferred orientation for the total angular momentum, J, all the directions will present the same energy (this is what happens in an isolated cation). Obviously, in molecular compounds the ion is far from being isolated, so the electrostatic potential of the atoms surrounding the lanthanide cation will break this spherical energy symmetry promoting preferred orientations of the angular momentum. That means that the molecular anisotropy comes from the

SOC, but only when the electrostatic potential around the lanthanide is different from the spherical one.

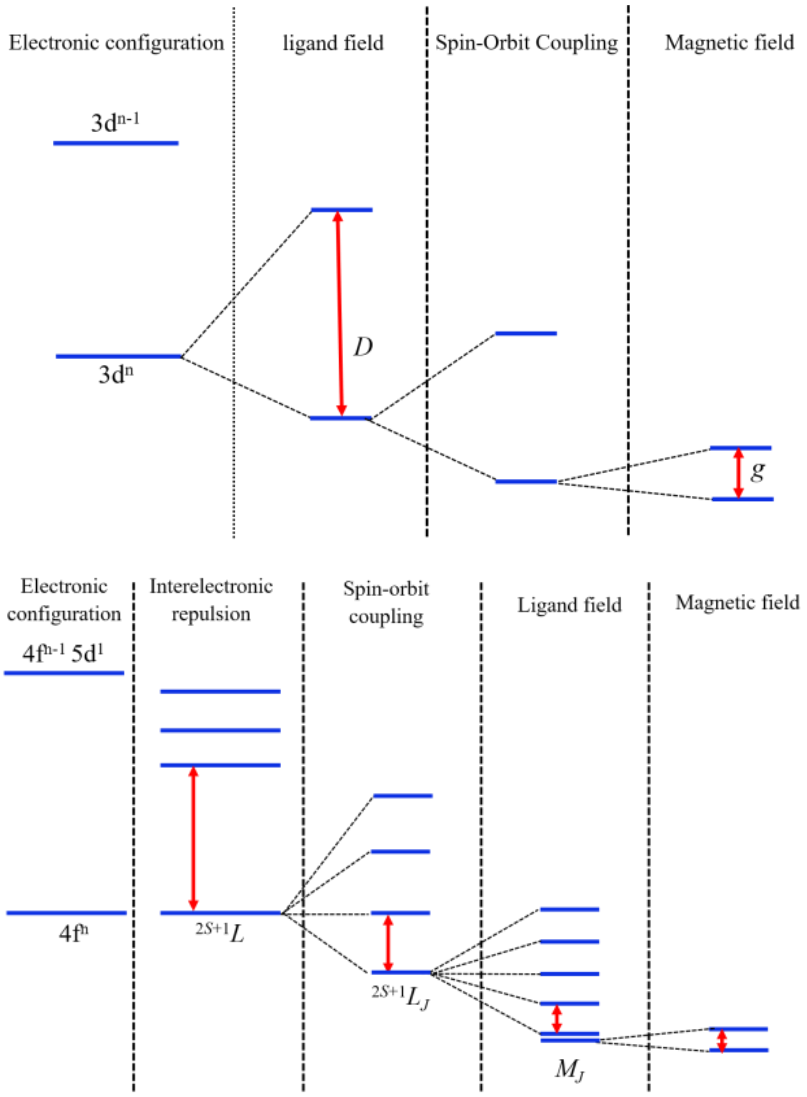
Electronic configuration
ligand field
Spin-Orbit Coupling
Magnetic field
$3d^{n-1}$
$3d^n$
D
g
Electronic configuration
Interelectronic repulsion
Spin-orbit coupling
Ligand field
Magnetic field
$4f^{n-1}\,5d^1$
$4f^n$
^{2S+1}L
$^{2S+1}L_J$
M_J

Figure 1.12. *d*-metals and lanthanides present a different order in the perturbations. Figure shows a scheme of the order of progressively weaker perturbations for both types of metals (*d*- metals on the top and lanthanides below).

The electrostatic potential around the cation is known as the Crystal Field (CF) and is usually described using the CF operators by using Wybourne or Stevens notations (see Appendix I). These formalisms are the responsible of explaining the preferential alignment of the charge perpendicular (prolate ions) or parallel (oblate ions) to the z axis to ensure a proper magnetic anisotropy (**Figure 1.11**).

An alternative notation to describe the effect of the ligands around a cation is using the angular overlap model,[40] which is more intuitive, or also by using the *zero-field splitting* (ZFS) formalism that considers the effect of the ligands as a zero-field splitting (**Eq. 1**). Because D is a tensor, there is the possibility of separating its components in the diagonal components (D) and in the non-diagonal components (E). The complete ZFS Hamiltonian is given in **Equation 1.9**:

$$\mathcal{H}_{ZFS} = D[J_Z^2 - \frac{1}{3}J(J+1) + E(J_x^2 + J_y^2) \tag{\textbf{1.9}}$$

The ZFS and CF approaches are similar when some parameters of the Wybourne and Stevens notations are zero.

When a magnetic field is applied, the degeneracy of the (2J+1) levels of each $^{2S+1}L_J$ multiplet is removed giving different levels labeled with a M_J ($-J \leq M_J \leq +J$). A new term appears in the Hamiltonian, named Zeeman term in honor to the 1902 Nobel Prize Pieter Zeeman (1865-1943), $\mathscr{H}_Z$ (**Equation 1.10**):

$$\mathcal{H}_Z = [\frac{3}{2} + \frac{S(S+1)-L(L+1)}{2J(J+1)}]\mu_B \boldsymbol{J} \cdot \boldsymbol{B} = g_J \mu_B \boldsymbol{J} \cdot \boldsymbol{B} \tag{\textbf{1.10}}$$

Where $\boldsymbol{B}$ is the applied magnetic field, g_J is the Landé factor and μ_B the Bohr magneton. This perturbation removes the m_J degeneracy and populates selectively the $+ m_J$ or the $-m_J$ state.

Because g is also a tensor, its diagonal provides the orientation of the magnetic anisotropy and the magnitude of its components. If $g_z > g_x = g_y$, we have an easy axis anisotropy, while if $g_z < g_x = g_y$, the anisotropy is known as easy plane.

A final perturbation can be added to the Hamiltonian, known as hyperfine coupling resulting from an interaction between electronic and nuclear spins and plays a role in metals with at least one isotope with a nuclear spin different from zero (I):

$$\mathcal{H}_{hyp} = \boldsymbol{J} \cdot \boldsymbol{A} \cdot \boldsymbol{I} \tag{\textbf{1.11}}$$

Where A is the tensor that couples both spins. This interaction is very weak and is almost always neglected.

Taking all of this into account, we can consider than the total Hamiltonian to describe the energy of the atom in the lanthanides approach:

$$\mathcal{H}_{TOT} = \mathcal{H}_{free\ ion} + \mathcal{H}_{CF} + \mathcal{H}_z + \mathcal{H}_{hyp} \tag{\textbf{1.12}}$$

Concluding than the SOC of the single ion defines the more stable orientation between L and S and that the CF orients the magnetic anisotropy depending on the surrounding ions.

1.2. SUPRAMOLECULAR CHEMISTRY.

The field of *supramolecular chemistry* is about to go beyond the covalent bond in the molecular chemistry to gain control over the intermolecular bond. The complexity gets increased going from molecules towards supramolecules, held together by non-covalent interactions.[49] This new chemistry developed at the end of the XX Century, is based on the concept of *molecular recognition*, *self-assembly* and *self-organization*¸ which in words of Jean-Marie Lehn, who won the Nobel Prize for his work in this area in 1987, can be described as "*a sort of molecular sociology!*". It is graphically represented in **Figure 1.13.**

Coordination chemistry is a kind of supramolecular interaction where the covalent molecules (the ligands) are *coordinated* to a metallic cation. Coordination complexes are known since the beginning of modern chemistry, being manly developed by Alfred Werner (1866-1919) by the concept of coordination sphere and by the discover that the spatial arrangement of the ligands involved in the formation of the *coordination complex* was a determinant parameter for the final structure. The ligands surrounding the metal are bounded to it by what it is known as a *dative bond* or coordination bond by donating a lone electron pair.

Supramolecular chemistry is a key concept in molecular magnetism because of different reasons, being the main one that the vast majority of SMM are based on coordination compounds prepared as a *bottom-up* assembly, where the non-covalent interactions between atoms are the key to the molecular magnets.

The properties of the macroscopic matter are obviously related with the properties of its microscopic units: the whole is the sum of its parts, but this sentence lacks sense when we realize that SMMs offer something new impossible to achieve only from "their parts". The properties of SMM arise from both, the nature and the way that the atoms are arranged in space by means of supramolecular chemistry, offers a new field of properties difficult to predict by knowing only the behavior of single atoms. So, in this case we can be sure that the *whole* is more than *the sum of its parts.*[50]

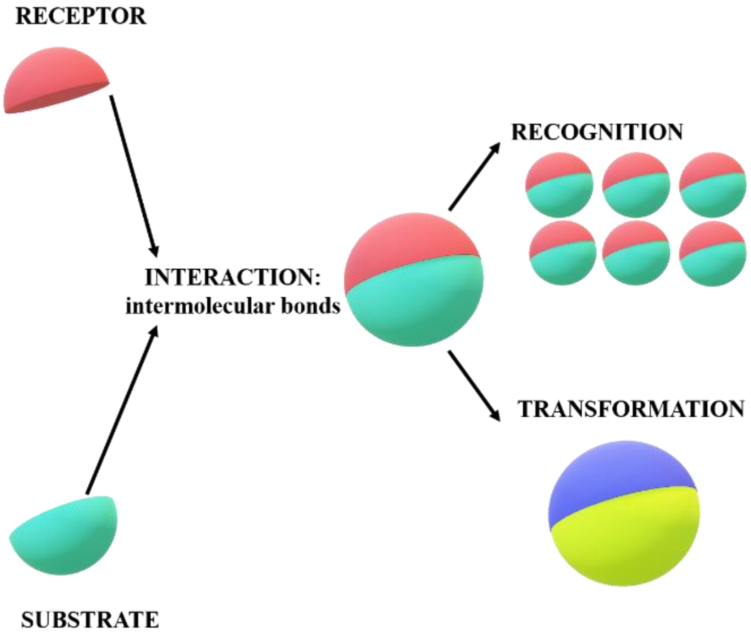

Figure 1.13. From molecular to supramolecular chemistry.

1.2.1. Supramolecular chirality.

Supramolecular chirality defines the chirality at a supramolecular level because of the possibility of the spatial arrangement of the molecules assembling trough non-covalent bonds.

Chirality is a word derived from the Greek (χερι) which means *hand* and is a property related with the asymmetry. A system is *chiral* if it is distinguishable from its mirror image (**Figure 1.14**).

In chemistry, chirality can be expressed in the molecular level (enantiomers) with applications in all the fields of chemistry, but also at the supramolecular level, arising from the arrangement of chelating ligands around the metal ion to generate predetermined topologies. In some cases, the enantiopure coordination complexes are obtained from the syntheses starting from enantiopure reactants used as ligands. The chiral ligands will determine the chirality of *all* the complex: the ligand transfers its chirality to the metal center, and this process is known as *predetermined chirality*. This chirality in the metal center can be propagated trough specific interactions inside the material, achieving a *supramolecular chirality* in coordination complexes. According to von Zalewsky: "*The use of organic ligands, where the configuration can be controlled by known methods, is the main feature by which chiral information can be transferred to the metal center. In this way, a predetermination of the absolute configuration at the metal center can be reached"*.[51] The study and control of this supramolecular chirality can lead to specific properties like the different absorption of the circular polarized light or the emission in opposite directions, that can be studied by means of specific techniques like Electronic Circular Dichroism (ECD), Circularly Polarized Luminescence (CPL), ferroelectricity, etc.

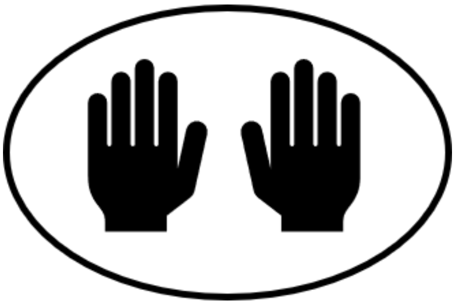

Figure 1.14. Human hands are the most universally recognized example of chirality. The left hand is not superimposable to right hand, no matter the orientation.

1.3. EXPERIMENTAL METHODOLOGY.

The products presented in this thesis have been characterized by means of the conventional characterization techniques (IR, single crystal or powder X-Ray diffraction, Electronic Circular Dichroism (ECD))

The study of the magnetic properties was performed using a Superconducting QUantum Interference Device (SQUID) for the study of the static and dynamic magnetism for all the complexes of this thesis following the procedure that is depicted in **Figure 1.15**, the Cantilever Torque Magnetometry for some lanthanide clusters to take information about the anisotropy and by Electronic Paramagnetic Resonance at different bands to get information about the anisotropy and about the *g* factors. A brief introduction to the theoretical background and about their experimental setup will be described in the following sections for these non-routine magnetic techniques.

This chapter is important to highlight which kind of information is extracted from each of the traditional techniques employed in molecular magnetism.

1.3.1. Magnetic techniques.

1.3.1.1. Susceptometer QUantum Interference Device (SQUID).[52]

SQUID is a variation of the standard magnetometry measurements, where the induced current is indirectly measured by a superconducting ring intercepted by Josephson junctions, which can be tunneled (See **Figure 1.15**).

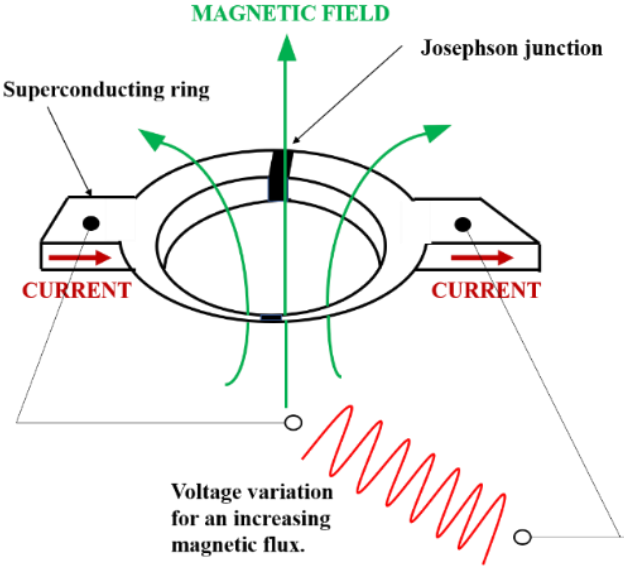

Figure 1.15. Schematic diagram of a SQUID magnetometer. Because it is superconducting, is kept under liquid He.

The measurement of the magnetization (*M*) is done at variable temperature (from 1.5-300 K in commercial SQUIDs). The temperature-dependent measurements are important because when decreasing *T*, the excited spin states are depopulated, and the temperature dependence of the magnetization is related with the energy separation of the levels.

We generally work with the representation of ($M/N\mu_B$) vs. field, where $N\mu_B$ is the magnetic moment of a mol of electrons because in this representation, when g is close to g_e, the value at which ($M/N\mu_B$) tends, is the number of unpaired electrons, which determine the fundamental state of the system, S.

The measurement of the magnetic susceptibility, χ, is done at constant field and variable temperature, and specially representing χT *vs* T, is very useful to extract information about the deviations, at low temperatures, from the paramagnetic behavior of the non-interacting spins, which should follow the Curie law. This representation is used to extract information about the nature of the magnetic exchange interactions.

Another important information that we can extract from SQUID measurements is about the anisotropy of the system by measuring powdered samples and plotting the field-dependence of the magnetization at different temperatures, plotted as reduced magnetization. This information is particularly useful to determine the ground spin state of clusters of *d* elements while is useless for Ln^{III} cations.

More precise information can be obtained from the measurement of the magnetization of single crystals in a procedure very similar to the monocrystal EPR (see Section 1.3.2.1) in the case that the molecules are packed collinear in the crystal.

SQUID allows also time-dependent measurements, what is known as *dynamic magnetic* properties, which consists in measuring the time decay of the remnant magnetization by applying a magnetic field at the temperature where the dynamics is fast. Then is needed to cool down and to measure the time that the magnetization needs to disappear. The demagnetization time follow an exponential law (see **Equation 1.3**).

A way to take information about the dynamic magnetic properties is by measuring the behavior of the samples under an alternating current (ac), which gives information about the magnetic susceptibility. The knowledge about what happens when a sample is putted under an ac field is the key to understand if a molecule presents or not SMM behavior and about the number and type of relaxation processes and is relatively easy to extract the information by the simple process of changing the oscillating frequency of the ac field (ω).

The field that the sample experiments is:

$$H = H_0 + h\cos(\omega t) \qquad \textbf{(1.13)}$$

Where H_0 is the static field that can be applied or not.

Regarding the simple example of a system with two possible states in a thermal bath from Section 1.1.3.4., the equilibrium population from the sates m=1/2 and m=-1/2 oscillates in time following the equation:

$$\frac{p_1}{p_2} = \exp[\frac{g\mu_B(H_0 + hcos\omega t)}{K_B T}] \qquad \textbf{(1.14)}$$

Where the establishment of thermal equilibrium requires the time τ. When ω of the ac field is low ($\omega\tau$<<1) the susceptibility that we are measuring is the *isothermal susceptibility* (χ_T) and when the frequency is so high, and the system has no time to exchange energy with the surroundings ($\omega\tau$>>1), we are measuring the *adiabatic susceptibility* (χ_S) **(Figure 1.16)**.

The following formula was proposed by Casimir du Pré[53] in 1938 to express the measured susceptibility in intermediate conditions (at very low frequencies the dynamic and static susceptibilities are equal and at very high frequencies the isothermal and adiabatic susceptibilities vanish, so we can assume them as reals):

$$\chi(\omega) = \chi_S + \frac{\chi_T - \chi_S}{1 + i\omega\tau} \qquad \textbf{(1.15)}$$

Where we can separate the real and imaginary susceptibilities.

$$\chi' = \frac{\chi_T - \chi_S}{1+\omega^2\tau^2} + \chi_S; \quad \chi'' = \frac{(\chi_T - \chi_{S)}\omega\tau}{1+\omega^2\tau^2} \qquad \textbf{(1.16)}$$

Because of the same development was made for dielectric materials by Debye, this treatment of the data in molecular magnetism is known as the *Debye Model*.[54]

A crucial factor that must be considered when the SMM behavior is analyzed is the α parameter. This parameter gives information about the dispersion in the values of the relaxation rates. The way to obtain α is using the Cole-Cole plots[55,56] proposed at the very beginning for dielectrics. In magnetism, these plots are known as Argand plots[57] and represent χ in the complex plane.

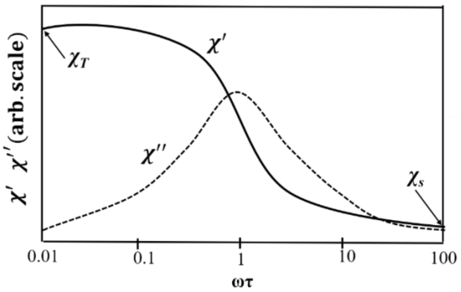

Figure 1.16. Solid line represents the real part of the susceptibility while the dotted line represents the imaginary part. χ' goes to a maximum when $\omega\tau$ =1 while χ'' has limiting values when $\omega \to 0$ and when $\omega \to \infty$.

The Debye model predicts that if the whole magnetization relaxes with a single characteristic time, the Argand plot describes a perfect semicircle (**Equation 1.16** transforms into a semicircle with its center in the x-axis) (**Figure 1.17, a**).

When the relaxation process is not characterized by a unique relaxation time but rather by a distribution of them, the previous **Equation 1.16** must be modified by means of α:

$$\chi(\omega) = \chi_S + \frac{\chi_T - \chi_S}{1+(i\omega\tau)^{1-\alpha}} \qquad \textbf{(1.17)}$$

The wider the distribution times the larger is α, being always $0 \leq \alpha \leq 1$. When α is different from zero, the component χ'' does not reach the maximum value and the Argand plot is flattened (**Figure 1.17, b**).

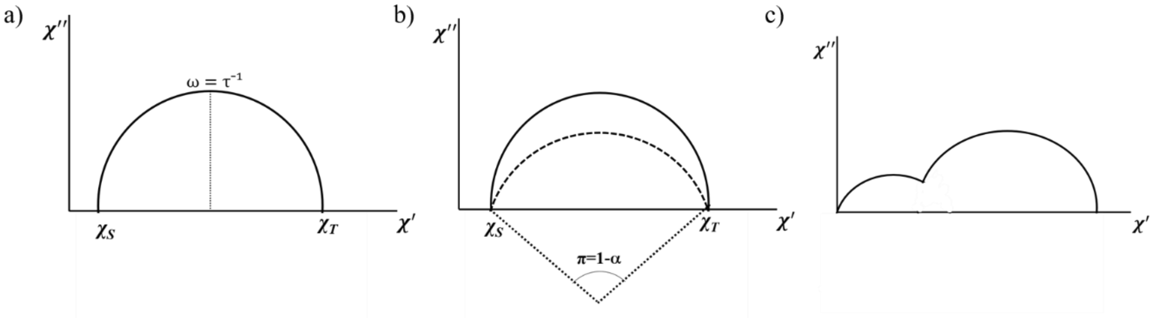

Figure 1.17. Solid line, relaxation process for a single time constant. At the top of the semicircle, the frequency satisfies the relation $\omega = \tau^{-1}$, and the relaxation time can be easily extracted.

More complex can also be observed in the relaxation time behavior. If different contributions of the magnetization relax with different processes, more semicircles appear in the Argand plots. Then the relaxations must be described with the sum of different Debye functions:

$$\chi_{AC}(\omega) = \chi_{S1} + \chi_{S2} + \frac{\chi_{T1} - \chi_{S1}}{1+(i\omega\tau_1)^{(1-\alpha_1)}} + \frac{\chi_{T2} - \chi_{S2}}{1+(i\omega\tau_2)^{(1-\alpha_2)}} \qquad \textbf{(1.19)}$$

Each χ_1 and χ_2 represent a semicircle for each relaxation in an analogous way to the one process semicircle. **Figure 1.17**, **c**.

Figure 1.18 represents the basic procedure performed for every complex in this thesis.

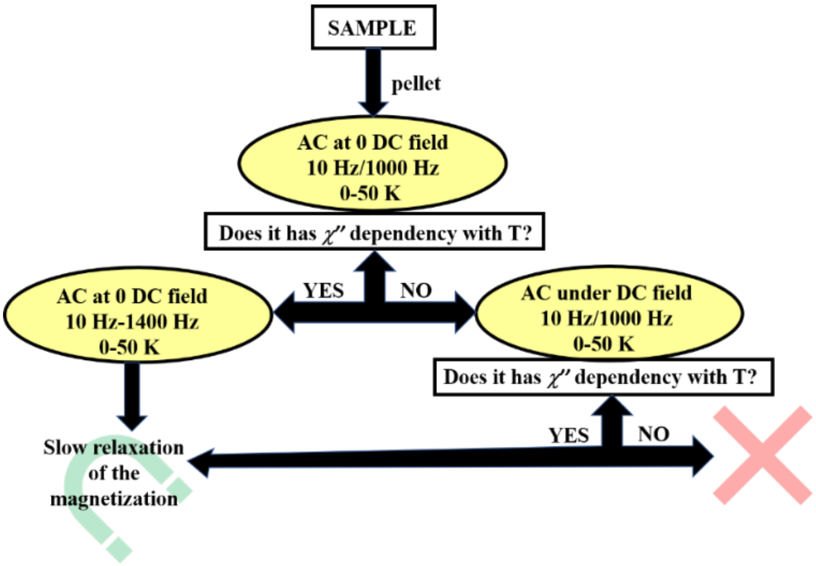
SAMPLE
pellet
AC at 0 DC field
10 Hz/1000 Hz
0-50 K
Does it has χ'' dependency with T?
YES
NO
AC at 0 DC field
10 Hz-1400 Hz
0-50 K
AC under DC field
10 Hz/1000 Hz
0-50 K
Does it has χ'' dependency with T?
YES
NO
Slow relaxation
of the
magnetization

Figure 1.18. General procedure performed in the SQUID for each one of the compounds after the confirmation that the ground state is different from zero.

1.3.1.2. Cantilever torque magnetometry[52,58]

I brief overview of the Cantilever Torque Magnetometry (CTM) is needed to understand how this tool can extract the information about magnetic anisotropy, a key parameter in molecular magnetism. There are other techniques that can extract information about the anisotropy of the systems like Single Crystal Magnetometry (SCM), Electronic Paramagnetic Resonance (EPR), Polarized Neutron Diffraction (PND) or X-Ray Natural Circular Dichroism (XNCD), but all of them present different drawbacks comparing with CTM.

CTM is an extremely sensitive technique that allows the study of all the crystal systems, offers the possibility to investigate all the spin systems (integer or half-integer spins) and allows to work up to room temperature, which is very useful to give information about the energy levels that are populated in a broad temperature range. The main drawback of CTM is that allows a number of solutions equal to the number of non-collinear contributions.

1.3.1.2.1. Noncollinearity.

The difficulty to study a system increases with the number of noncollinear anisotropies, because each one of these anisotropies has a different response in front of an applied external magnetic field. It's not common to work with a crystal system with all the molecules equally oriented in space and containing only one paramagnetic center each one, so, there are several sources of noncollinearity. The sum of all the anisotropies belonging to the different paramagnetic centers in the molecules in known as the *molecular anisotropy* and the sum of the magnetic anisotropies in the crystal packing is known as *crystal anisotropy*. The number of noncollinear anisotropies inside a crystal depends mainly on symmetry and interactions such as Dzyaloshinkii-Moriya (DM)[59] or frustration.

In the case of mononuclear systems, the noncollinearity arises usually from the presence of crystallographic inequivalent molecules and, in the case of polynuclear clusters, the noncollinearity arises from the probable different ligand field around the metals when the sites are not related by symmetry elements.

When the paramagnetic centers interact, we can consider the two interacting spins exchange Hamiltonian (**Equation 1.1** and **1.19**):

$$\mathcal{H}_{exc} = \boldsymbol{S}_1 \cdot \boldsymbol{J}_{exc} \cdot \boldsymbol{S}_2 = -\boldsymbol{J}_{12}\boldsymbol{S_1} \cdot \boldsymbol{S}_2 + \boldsymbol{S_1} \cdot \boldsymbol{D_{12}} \cdot \boldsymbol{S_2} + \boldsymbol{d}_{12}\boldsymbol{S_1}\, x\, \boldsymbol{S}_2 \qquad \textbf{(1.19)}$$

Where $\boldsymbol{J}_{exc}$ represents the exchange matrix. The first term is a scalar and isotropic, known as *Heisenberg contribution*. It aligns the spins parallel (↑↑) or antiparallel (↑↓) and is generally the biggest magnitude. The second terms is a tensor, the anisotropic contribution, depending on the matrix $\boldsymbol{D_{12}}$ which aligns the spins along certain directions, and finally, the vectorial term, known the *antisymmetric* or *Dzyaloshinkii-Moriya* term, which contains the vectorial product between he spins that minimizes the energy when the spins are perpendicular to each other (see also Section 1.1.3.2.).

1.3.1.2.2. Theoretical background

The *torque* (τ), or moment of force is the tendency to a force to transmit a rotation along a certain axis to an object, in an analogous way like for example when we open a door: the *torque* is the derivative of an energy with respect to an angle.

$$\tau_i = \frac{dE}{d\varphi}$$

In the case of magnetism, the analogous to the τ is the *magnetic torque*, defined in **Equation 1.20** for the case of a magnetic dipole moment ($\boldsymbol{m}_\mathbf{i}$, belonging to the atom i-th) interacting with the magnetic induction¸ $\boldsymbol{B}$:

$$\tau_i = \boldsymbol{m}_\mathbf{i} \times \boldsymbol{B} = m_i \cdot B \cdot sin\varphi_i \qquad \textbf{(1.20)}$$

and considering a sample containing *n* equal magnetic moments:

$$\tau = \sum_{i=1}^{N}(m_i x \boldsymbol{B}) = \boldsymbol{M}\, x\, \boldsymbol{B} = M \cdot B \cdot sin\varphi \qquad \textbf{(1.21)}$$

Since **Equation 1.22** contains a vectorial product, τ is orthogonal to $\boldsymbol{M}$ and $\boldsymbol{B}$ (**Figure 1.19**). In a paramagnet, when $\boldsymbol{M}$ is perpendicular to $\boldsymbol{B}$, τ should be equal to zero. However, this is only true in the case of a purely isotropic system and fails when anisotropy is present.

To obtain the equation that defines the magnetic torque in a paramagnetic sample in a homogeneous magnetic field, is necessary to define previously the magnetic susceptibility tensor:

$$\chi_{ij} = \frac{\partial M_j}{\partial H_i} \qquad \textbf{(1.22)}$$

Where *i*, *j*= *X*, *Y*, *Z*. At enough low field and enough elevated temperature, *M* increases linearly with *H*.

At this point two different cases appear: low field and high field.

a) Low field ($k_B T > g\mu_B \boldsymbol{B}$)

Is useful to start from the simplified model of **Figure 1.19**, where there is the plane XZ containing ***M*** and ***B***.

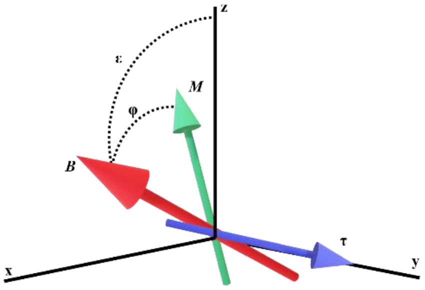

Figure 1.19. Orientation of ***M***, ***B*** and *τ* in an orthogonal frame xyz.

$$M_\alpha = \chi_{\alpha\alpha} H_\alpha + \chi_{\beta\alpha} H_\beta \qquad \textbf{(1.23)}$$

Being α and β *X* and *Z*. Because *τ* must be orthogonal, in these cases it lies along the *Y* axis:

$$\tau_Y = M_Z B_X - M_X B_Z = \frac{1}{\mu_0}\left[\left(\chi_{ZZ} - \chi_{XX}\right) B_X B_Z + \left(B_X^2 - B_Z^2\right)\chi_{XZ}\right] = \frac{1}{\mu_0}\left[B^2\left(\chi_{ZZ} - \chi_{XX}\right)\cos(\varepsilon)\sin(\varepsilon) + B^2\chi_{XZ}\left(2sin^2(\varepsilon) - 1\right)\right] \qquad \textbf{(1.24)}$$

In an axial system (rotating *X* and *Z* to make them coincide with the magnetic variables) the equation can be simplified as:

$$\tau_Y = B^2\left(\chi_{ZZ} - \chi_{XX}\right)\cos(\varepsilon)\sin(\varepsilon) \qquad \textbf{(1.25)}$$

From **Equation 1.25** is extracted that *τ* has a periodic behavior that does not change sign every *kπ* (*k* = 1, 2, 3, .., *n*, integer), as usual in a vectorial product, and that goes to zero every *kπ*/2. When the field is small enough, torque is proportional to $\boldsymbol{B}^2$, allowing to detect signal in small magnetic field. *τ* = 0 when ***B*** is parallel or perpendicular to the easy axis. This feature makes CTM a very useful tool to detect the orientation of the principal axis of the magnetization. When *θ* = 0º, the field is parallel to the easy axis of the molecule, ***B*** and ***M*** are parallels, thus *τ* = 0. This point is called the *easy zero*. When 0º < *θ* < 90º, ***M*** turns anticlockwise towards ***B*** causing a positive torque (maximum when *θ* = 45º). When *θ* = 90º, ***B*** is perpendicular to the *easy axis* contained in the *hard plane*, and *τ* = 0 again, *hard zero* (**Figure 1.20**, left).

b) High field ($k_B T < g\mu_B \boldsymbol{B}$)

If the magnetic field is high enough or temperature low enough, the simple angular dependence of *τ* breaks down. While the zero torque points are maintained, the shape of the curve changes. In a low field, the representation of the magnetization *vs*. the angle has a cosinusoidal shape, when the field is rotated to the easy axis to the hard plane. For high field, when *θ* is close to 0 or 180º, the field can cause saturation and the magnetization can be constant for a wide angular range, and small variations of the energy are expected. Near the hard zero, a small variation of ***B*** causes the appearance of a small component $\boldsymbol{B}_z$, which changes $\boldsymbol{M}_z$. Thus, a massive change in energy occurs. This is the reason why the angle at which the magnetic torque is maximum changes as a function of the field.

When increasing the field the curves are progressively warped: when ***M*** is perpendicular to ***B***, there is the maximum slope in the torque curve.

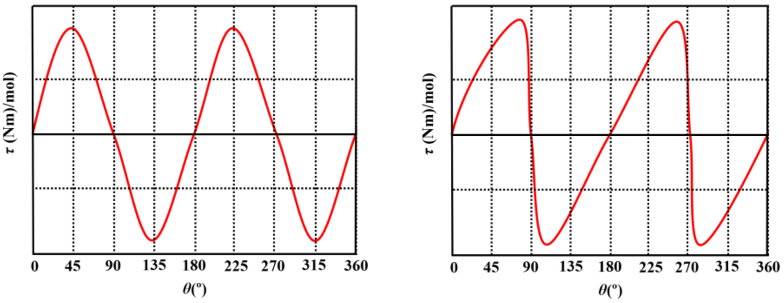

Figure 1.20. Magnetic torque representation in low field, (left) and in high field, (right).

1.3.1.2.3. Experimental setup.

There are different ways to measure the magnetic torque, but the one that was used in this thesis was the capacitive detection.

The capacitance of an ideal parallel plates capacitor is given by:

$$C = \frac{\varepsilon_D \cdot A}{d} \tag{1.26}$$

Being ε_D the permittivity of the dielectric separating the plates, A, the area of the plate (of the cantilever) and d the distance between the plates. The capacitance changes when a force is applied in a proportional way to the *deflection* (Δd), which is in turn proportional to the torque.

The experimental setup can be seen in **Figure 1.21,** left. The instrument is a fixed cooper base (around 300 nm of thickness) separated around 1 mm from the other *plate*, the cantilever, which is easily deflected when a torque is acting in the sample which is fixed to it. This upper plate is made of a cooper-beryllium alloy, which presents many advantages. The support and the spacer are made of epoxy. A wheel is connected to the instrument and performs clockwise rotations. The instrument registers the changes in capacitance (distance) and the value of the torque can be simply obtained by applying a voltage to a gold wire loop fixed in the cantilever. A known magnetic moment is generated.

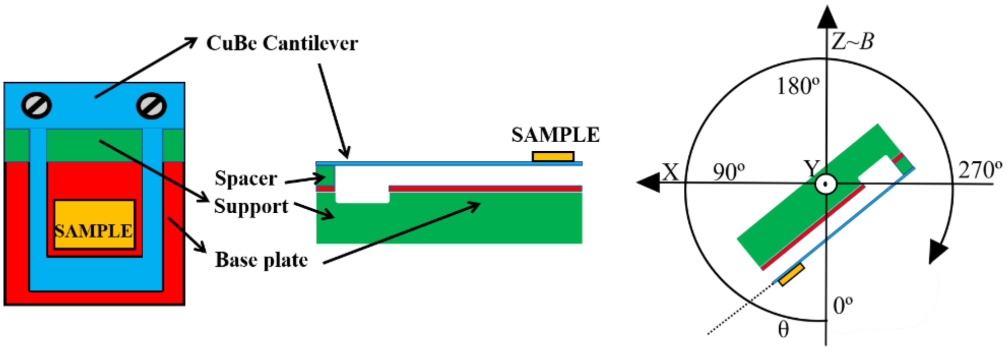

Figure 1.21. View of the main part of a capacitive torque magnetometer.

The sample is glued on a square acetate foil with two distinguishable sides (**Figure 1.22**). Before doing the measurements, all the monocrystals must be indexed using an X-ray diffractometer to know exactly how the crystallographic planes are situated on the top on the acetate.

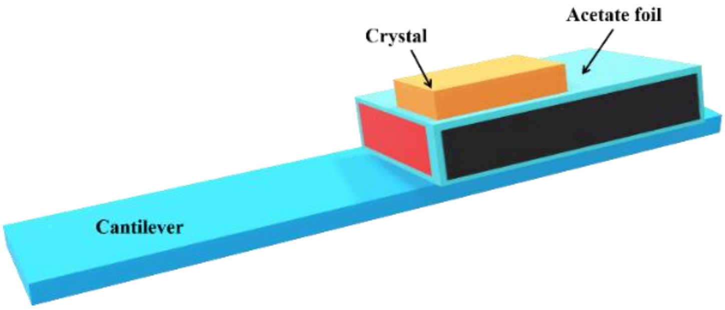

Figure 1.22. An acetate foil with two distinguishable faces (red and black in the picture) is places on the top of the cantilever. The crystalline sample is places on the top of this *indexed* acetate foil.

The physical quantities that are going to be varied during the measurements are:

- Temperature. The temperature dependence of the torque is related with the population of the ground levels inside the *J* ground manifold (lanthanides). A uniform population of the levels would be translated in a magnetic isotropy. *T* dependence is depicted in **Figure 1.23**.
- The angle between the sample and the applied magnetic field.
- The magnitude of the applied magnetic field.

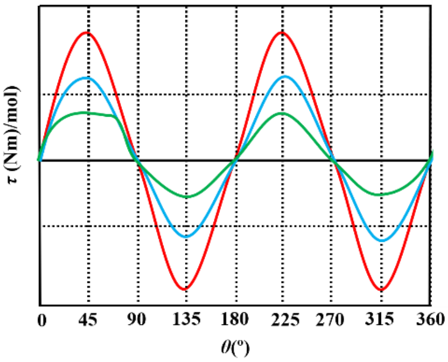

Figure 1.23. Dependency of τ *vs*. angle plots at same field and different temperature. Red line represents the lowest *T*, blue line an intermediate one and green line represents the plot at the highest *T*.

1.3.1.2.4. Orientation of the magnetic anisotropy and crystal field parameters.

Because of the main objective of using CTM is to detect the orientation of the magnetic anisotropy, three possibilities exist in coordination crystal systems: collinear systems, intermolecular noncollinear systems and intramolecular noncollinear systems.

Systems with collinearity are the easiest to study and the rarest ones. This is the case where all the molecular anisotropies inside the crystal are collinear, so CTM provides a unique solution for the anisotropy direction. In the case of intermolecular noncollinearity, the resolution of the system is more complicated due to the presence of symmetry operations that generates another molecule inside the cell, while the most challenging case is when the different contributions to anisotropy come from the same cluster, this means that there is more than one paramagnetic center with different coordination environments. Moreover, the interactions between the paramagnetic centers complicates the treatment of the data.

Finally, is important to mention that CTM is also able to determine the crystal field splitting using the breaking field method or the Maxwell Boltzmann Statistics.

1.3.2. SPECTROSCOPIC TECHNIQUES

1.3.2.1. Electronic Paramagnetic Resonance (EPR).

Electronic Paramagnetic Resonance (EPR) is the oldest magnetic resonance technique being used for the very first time in the 1940s in Kazan by E. K. Zavoisky with $CuCl_2·2H_2O$ samples. Nowadays, EPR has a broad range of applications is physics, chemistry, biology, material science, etc. EPR measures the absorption of electromagnetic radiation by placing a paramagnetic sample (organic radicals, *d* and *f* metals with unpaired electrons, systems with conducting electrons, etc.) in a static magnetic field. EPR induces transitions in the states belonging to a given multiplet and provides information about the chemical environment of the paramagnetic centers, about the anisotropy tensor and about the dynamic magnetic properties, especially when pulsed-EPR is involved. This information can be obtained from single crystal measurements but also from systems in which the tumbling ratio of paramagnetic centers is slow compared to EPR time scale when are the possible orientations of the molecules are present (powder samples).

Regarding the electronic Zeeman effect (**Figure 1.7**), the Zeeman Hamiltonian is expressed as:

$$\mathcal{H}_Z = g\mu_B \boldsymbol{HS} \qquad (\mathbf{1.27})$$

Which is the consequence of an external magnetic field applied on an isolated electron that splits the M_S components of the S=1/2. This external magnetic field produces an electromagnetic radiation, $h\nu$, which creates resonance between the +1/2 and the -1/2 states. Usually, in EPR experiments, this resonance is in the microwave region. The population of these two states is not the same, following a Boltzmann distribution, and this fact promotes a net absorption/emission of radiation.

Generally, EPR experiments are performed at fixed frequency and variable magnetic fields. The oscillating magnetic field of the radiation is perpendicular to the static magnetic field, and in this case, the selection rule is $\Delta M_S = \pm1$.

For a spin system interacting with electromagnetic radiation, an emission or an absorption can be induced, being the ratio of populations given by the Boltzmann distribution. Generally, for the EPR experimental conditions n_a and n_b in eq. X are very similar: $n_a/ n_b \approx 1$ and:

$$\frac{n_b}{n_a} \approx 1 - \frac{g\mu_B B}{kT} \quad \textbf{(1.28)}$$

$$n_b - n_a = n_b\left[1 - \left(1 - \frac{g\mu_B B}{kT}\right)\right] = Ng\mu_B B/2kT \quad \textbf{(1.29)}$$

that is why the EPR sensitivity increases with the total number of spins, N, with the temperature, *T*, and with the increasing magnetic field strength. Because of the field at which the absorption occurs is proportional to the microwave frequency, sensitivity is greater at high frequencies (W-band). However, as high is the frequency smaller are the waveguides, so samples are necessary smaller, and the same concentration contains fewer spins. [60]

1.3.2.1.1. Continuous wave EPR (CW-EPR).

Commercial spectrometers use X-band, Q-band and more unusual are the K-, W-, and D-bands. All the parameters for each band are detailed in **Table 1**. As the frequency is increased, is more difficult to achieve a homogeneous magnetic field inside the cavity and for this reason X-band is the most common even has some drawbacks when the system has *S* > ½.

ν (GHz)	λ (mm)	E (cm^{-1})	B (g=2) (T)
9.5 (X-band)	31.5	0.317	0.34
24 (K-band)	12.5	0.8	0.86
35 (Q-band)	8.55	1.17	1.25
95 (W-band)	3.15	3.17	3.4
130 (D-band)	2.31	4.33	4.6

Table 1.1. Representative EPR microwave frequencies with associated wavelengths, energies and magnetic fields for a resonance at *g*=2.

The advantages of increasing the operating frequency are that can be obtained more resolution, more sensitivity, observation of "silent species EPR" and the determination of the sign of the ZFS.

1.3.2.1.2. EPR spectroscopy of lanthanide complexes

The results obtained in the EPR experiments involving lanthanides are a pillar in the derivation of the Crystal Field theory. Due to their unquenched angular momentum, EPR of lanthanides is only observed at very low temperatures. These spectra are always interpreted supposing that only the lowest levels arising from the ligand field splitting o the ground *J* are EPR active. For the Kramer ions Ln^{3+}, the spectra is interpreted as a doublet with anisotropic *g* values. For low symmetries, two different values of *g* are expected for *x* and *y* directions.

1.3.2.1.3. Instrumentation.

The basic instrumentation for a commercial CW-EPR spectrometer is depicted in **Figure 1.24** and includes:

- A microwave source (klystron or solid-state source).
- A sample resonator, usually a resonant reflection cavity.
- An electromagnet with control of the field.
- A data acquisition system, generally a current detector.
- A data display and processing system.

1.3.2.2. Electronic Circular Dichroism (ECD).

1.3.2.2.1. Theoretical background.

Electronic Circular Dichroism (ECD) is a powerful technique to establish the absolute configuration of compounds. It is a spectroscopic variation of a technique named Optical Rotatory Dispersion (ORD). Electronic Circular dichroism is a spectroscopy based on the different absorption of left- and right- handed circularly polarized visible or near ultraviolet region of the electromagnetic spectrum (200-800 nm).

ECD is based in the so-called Cotton-effect curves which are curves displaying a maximum or a minimum (or both) in the region under study. This curves are called positive or negative curves depending on the sign of the first extreme observed at the longer wavelength[61] as is shown in **Figure 1.25.**

The ECD spectra can present only one type of Cotton curve (positive or negative) when the whole line remains in the same side of the spectra or multiple Cotton effects, when there is more than one Cotton effect in the same spectrum. As an example, the curves from **Figure 1.25** present two different Cotton effects because the line crosses the zero one time. The sign of the Cotton effect depends on the absolute configuration of the nearest stereogenic center to the corresponding absorption line: There is a straightforward correlation between the wavelength of the Cotton effect in ECD spectra and the wavelength of the UV absorption transitions.

In the case of working with organic enantiomeric species, their ECD must be identical except in the region where the ($n \rightarrow \pi^*$) transition is produced, which are of opposite signs for each enantiomer, so, enantiomers exhibit identical ECD spectra with opposite sign.

There are many empirical rules to establish the absolute configuration of the compounds[62] and also non-empirical methods[63] which allow to determine the configuration by straightforward spectroscopic interpretation.

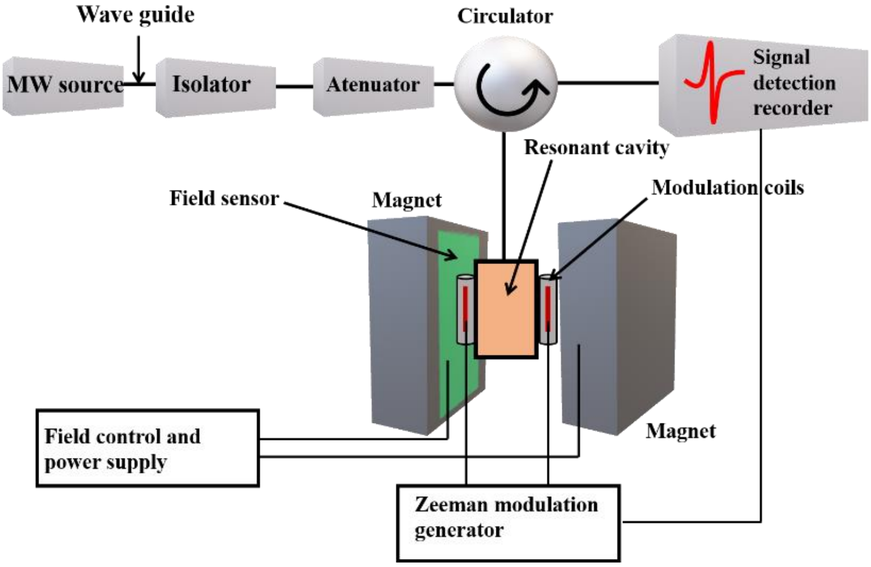
Wave guide
Circulator
MW source
Isolator
Atenuator
Signal detection recorder
Resonant cavity
Field sensor
Magnet
Modulation coils
Field control and power supply
Magnet
Zeeman modulation generator

Figure 1.24. Principal components of a CW-EPR spectrometer. The electromagnetic radiation is transmitted through rectangular waveguides, so there is no electric field component in the propagation direction and the magnetic field has the largest value. This waveguides are designed to transmit radiation over a relatively narrow frequency range. Waveguides look like rectangular cross-section pipes with dimensions on the order of the wavelength to be transmitted. The size of the waveguides depends on the used frequency. The sample cavity is a resonating cavity whose volume is varied trough the adjustment of a metallic iris connected to a screw. Coils are placed around the sample cavity to modulate the intensity of the external magnetic field by coupling to electromagnetic radiation. After a phase sensitive detection, the signal appears in the form of the first derivative.

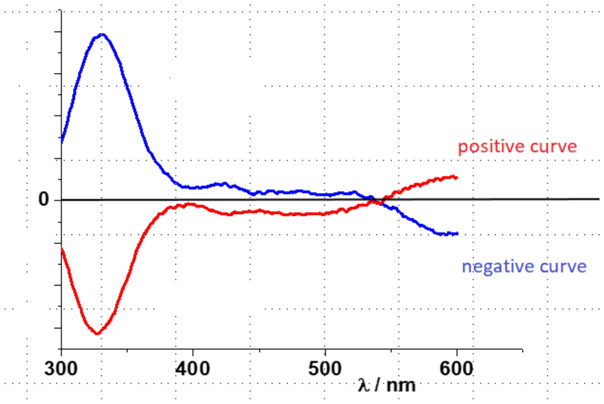

Figure 1.25. The blue line is a negative Cotton curve and the red line is a positive Cotton curve.

What happens physically when a ECD experiment is performed, is that the molecule gets excited from its ground electronic state to an excited electronic state by absorbing a photon with the appropriate energy. Because of the solutions of chiral compounds rotate the plane of polarization, the beam in its initial orientation that passes through the sample exits in a different orientation.

The ECD spectra is usually reported in degrees of ellipticity, θ, which is measure of the polarization, given by the equation **Equation 1.30** (**Figure 1.26**).

$$tan\theta = \frac{E_l - E_r}{E_l + E_r} \tag{1.30}$$

Where *E* is the magnitude of the electric field vector. θ is the angle between the magnitude of the electric field vector at its maximum and its minimum.[64]

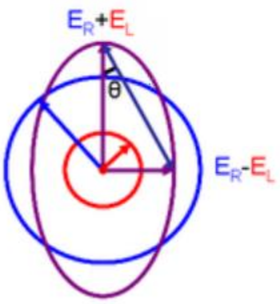

Figure 1.26. Eliptically polarized light (purple), which is the superposition of LCP and RCP.

1.3.2.2.2. Experimental setup

The linearly polarized light passes through a monocromator, and then, the single wavelength passes through a photoelelastic modulator (PEM), which transforms the linear light in circularly polarized light. The incident light enters into the chiral medium switching between left. circularly polarized (LCP) and right circularly polarized (RCP). When the incident light switches the polarization direction, the absorption changes and the absorptivity can be calculated.

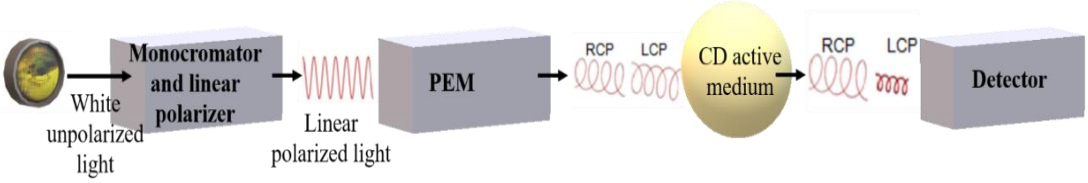

Figure 1.27. Instrumentation of a common ECD spectrometer.

1.3.3. Experimental setup for physical measurements.

1.3.3.1. Infrared spectroscopy (IR)

Infrared spectra (4000-400 cm^{-1}) were recorded from KBr pellets on a Bruker IFS-125 FT-IR spectrophotometer.

1.3.3.2. SQUID measurements

The measure of all the powdered compounds were performed in a MPMS5 Quantum Design susceptometer working in the range 30 - 300 K under magnetic fields of 0.3 T and under a field of 0.03T in the 30 – 2 K range to avoid saturation effects at low temperature. Dc magnetic measurements of complexes from Chapter 7 were measured in pellets using a Quantum Design MPMS SQUID magnetometers on powders pressed in a pellet to avoid field induced orientation of the crystallites. Ac susceptibility was measured using Quantum Design PPMS in ac mode.

Diamagnetic corrections were estimated from Pascal Tables.

1.3.3.3. Monocrystal X-Ray Diffraction.

The X-ray intensity data were measured on a D8 Venture system equipped with a multilayer monochromator and a Mo microfocus (λ = 0.71073 Å). The frames were integrated with the Bruker SAINT software package using a narrow-frame algorithm. Data were corrected for absorption effects using the multi-scan method (SADABS). All the structures in this thesis were solved and refined using the Bruker SHELXTL Software Package. Unit cell parameters and structure solution and refinement data for all the structures are listed in the corresponding chapters or appendixes.
For complexes **[41]** and **[42],** their faces were indexed by using an SCD Oxford Xcalibur3 X-Ray diffractometer.

1.3.3.4. Powder X-Ray Diffraction.

Were performed with a PANalytical X'Pert PRO MPD θ/θ powder diffractometer of 240 millimetres of radius, in a configuration of convergent beam with a focalizing mirror and a transmission geometry with flat samples sandwiched between low absorbing films and Cu $K\alpha$ radiation (λ = 1.5418 Å).

1.3.3.5. Electronic Circular Dichroism

EDC spectra were recorded in dichloromethane or methanolic solutions in a Jasco-815 spectropolarimeter.

1.3.3.6. Cantilever Torque Magnetometry

Cantilever torque measurements were performed by using a home made two-legged CuBe cantilever separated by 0.1 mm from a gold plate. The cantilever was inserted into an Oxford Instruments MAGLAB2000 platform with automated rotation of the cantilever chip in a vertical magnet. The capacitance of the cantilever was detected with a Andeen-Hegerling 2500 A Ultra Precision Capacitance Bridge.

1.4. SYNTHESES.

In coordination chemistry, even the "designed synthesis" is sometimes possible when there is a previous experience with related products or when there is no possibility of changes in the coordination modes and geometries, most of the syntheses are guided but what is known as *serendipity***.** Even the unpredictable nature of this kind of chemistry, it presents the advantage that there is the possibility of achieving new molecular topologies that were not imagined before, and, bonded with this, the possibility of new molecular and unpredictable properties.

This thesis presents the syntheses of poly and mononuclear coordination compounds following the so-called *bottom-up* approach which consists of the synthesis of a material starting from its components. All the compounds of this thesis have Schiff bases as organic ligands combined with different paramagnetic cations.

The general procedure for the synthesis is depicted in **Figure 1.28**. The metals are introduced as salts, the base can be more than one depending on the syntheses and the use of a co-ligand is optional depending on what we want to obtain. The specific solvent (or mixture of solvents) used for a reaction, the temperature, the use or not of a microwave and the specific features of each reaction will be commented in the corresponding chapters. The idea of this scheme is that all the syntheses are bottom-up in solution at open air. Then, a crystallization of the product was needed for the determination of the structure and for other characterization techniques. In some cases, in order to confirm the isostructurality, powder-diffraction measurements have been done.

1.4.1. The ligands: Schiff bases.

Schiff bases are N analogues of aldehydes or ketones, where the C=O is replaced by a C=N group. There are usually formed by the condensation of a primary amine with a carbonyl group, also known as imines or azomethines. Are easily synthesized and form complexes with almost all metallic cations, acting as ligands. Their common name, Schiff bases, comes from their discoverer, Hugo Schiff. And, who was Hugo Schiff? Schiff (1834-1915) was a German chemist who studied in Göttingen with Friederich Wöhler, famous for the synthesis of urea. The years 1848/49 were really convulsed due to the revolutions that brought the end of the feudal structures in Europe, known as the Spring of Europe. Schiff was really involved in the events and because of his political views, he was forced to leave Germany. He moved to Italy in 1863 and spent his career in the University of Florence, which chemistry department bears his name, where he was teaching until the year of his death. Before moving to Florence, he spent some years in Pisa, where he discovered that the reaction of aniline with some aldehydes yielded imines. The designation of these new compounds as bases is valid today, in spite that they are not used as bases in the conventional sense. In Italy, he persisted with his political ideas, and he combined his scientific career with a political and cultural agenda. He was the cofounder of the *Gazzeta Chimica Italiana* and of the socialist newspaper *L'Avanti*, which exists until today.

Schiff bases are used today as one of the most popular organic ligands in coordination chemistry, and the clusters formed with them, exhibit activity in a wide range of fields like biological activity, catalysis or magnetism.

About the synthesis of Schiff bases, the mechanism is a nucleophilic addition to the carbonyl where the nucleophile is the primary amine. The lonely pair of the N atom attacks the carbonyl yielding in an unstable compound called carbinolamine, then a 1,3-hydrogen shift favors the loss of a water molecule (**Figure 1.29**). The geometry of the final imine double bound favors in practically all the cases a *trans* orientation.

The synthesis of Schiff bases in the literature presents a wide variety of proposed methods, from simple mixtures at room temperature in alcoholic solutions from a synthesis that spent many days in different steps and solvents. This variation of conditions in the synthesis probably means that the vast majority of Schiff bases is easy to synthesize and are stable in many conditions. Typically, it requires a protic solvent which is enough dry to prevent the hydrolysis of the formed imine bond.

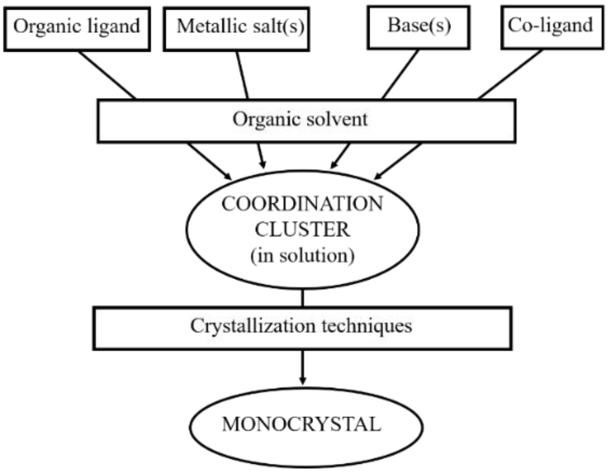
Organic ligand
Metallic salt(s)
Base(s)
Co-ligand
Organic solvent
COORDINATION CLUSTER (in solution)
Crystallization techniques
MONOCRYSTAL

Figure 1.28. General procedure for the syntheses of all the compounds of this thesis.

Schiff bases are popular ligands in coordination chemistry because allow versatility in coordination modes, because are able to coordinate to a wide variety of metals, allow the modulation of the charge in the clusters and, in our particular need of chiral ligands, allow both enantiomers in different stereogenic carbons.

The compounds in the thesis have been synthesized with different Schiff bases, starting from aminoalcohols or diamines as the amino group to be condensed with different aldehydes. All the used ligands are depicted in **Figure 1.30**.

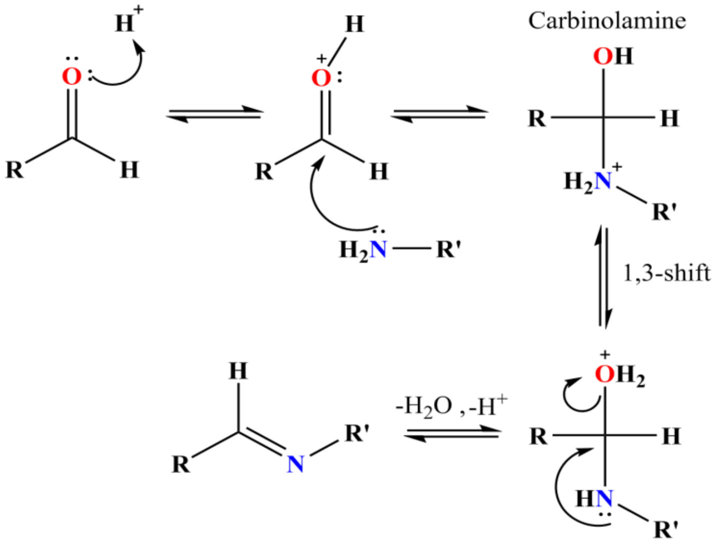
Carbinolamine
1,3-shift
-H₂O , -H⁺

Figure 1.29. Schiff base formation mechanism.

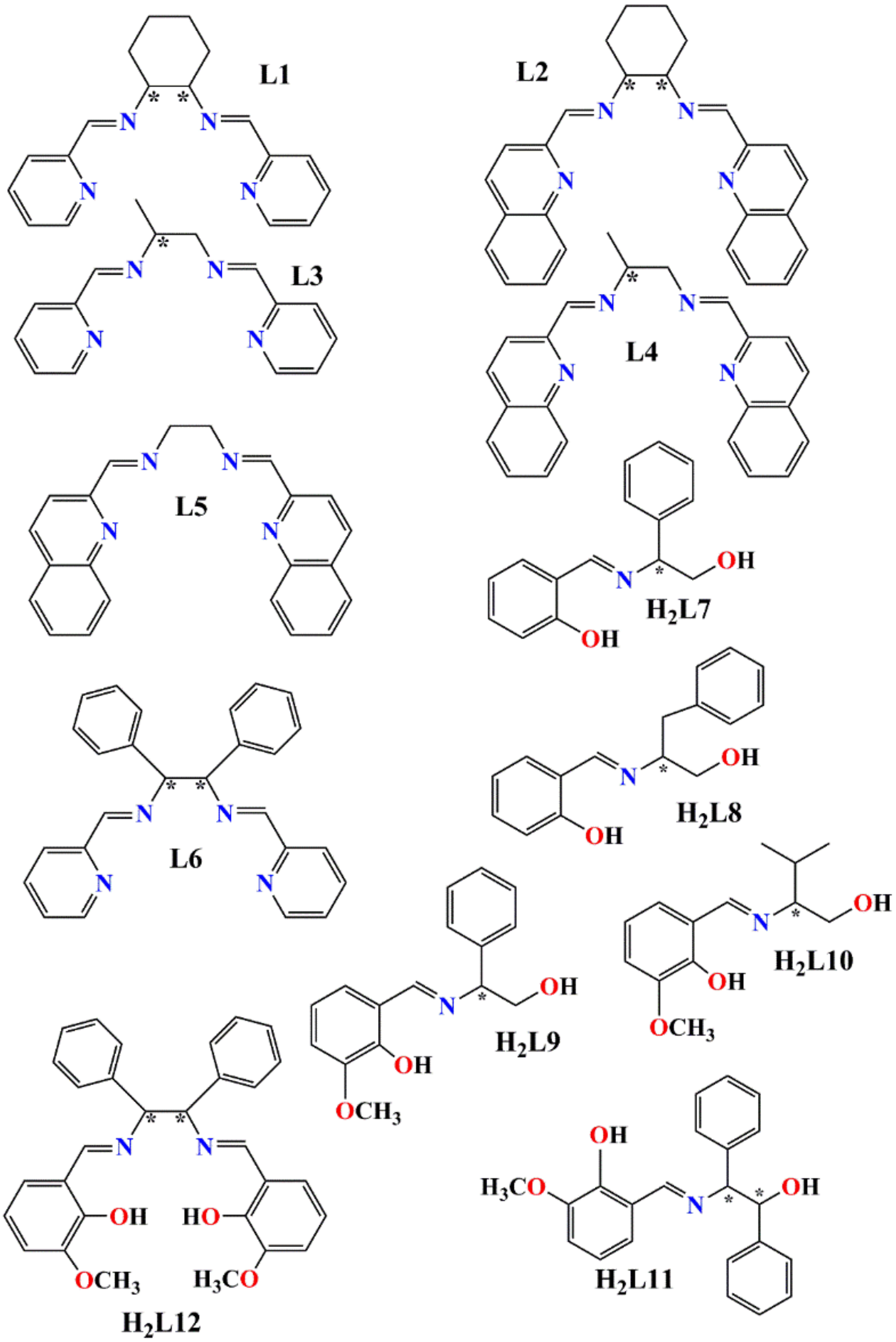
L1
L2
L3
L4
L5
L6
H$_2$L7
H$_2$L8
H$_2$L9
H$_2$L10
H$_2$L11
H$_2$L12

Figure 1.30. Schiff bases used in this work.

1.4.2. The metals.

The first compounds that are going to be presented are Ni^{II} clusters. These compounds suppose a continuity of the clusters presented in my master thesis, which were Cu^{II} and Ni^{II} cubanes using pyridyl-alcohols as ligands and immediately we changed to Schiff base ligands. Even Ni^{II} is not a really good candidate to promote SMM response, a deep supramolecular study was made with compounds derived from **L1, L2, L3, L4** and **L5**, which are presented in ***Publication #1***. To achieve SMM response, we moved to manganese and iron chemistry. Mn^{III} presents a Jahn-Teller distortion and for this reason is usually a good metal to promote slow relaxation of the magnetization. We prepared manganese clusters derived from ligands **H_2L8, H_2L9, H_2L10** and **H_2L11,** which were interesting to elucidate magneto structural correlations and specially to study the chirality transfer from ligand to metal and the supramolecular chirality in the reported structures. However, no slow relaxation of the magnetization was observed in the manganese clusters due to the position of the anisotropy axis, except for one Mn^{III} triangle (see ***Publication #4***), so we decided to introduce lanthanides in the clusters. The introduction of a lanthanide cation could provide slow relaxation of the magnetization to the clusters but also, the introduction of multiproperty due to the intrinsic luminescent features of lanthanide cations. Due to the interesting structures and properties of the mixed *3d-4f* clusters, our goal was to mix also iron with lanthanides. The mixture of Fe^{III} with lanthanides is still under study. Finally, to study the magnetic properties of the lanthanides we decided to prepare, firstly, a series of a *4f* metal with a diamagnetic *3d* cation to achieve Single Ion Magnet (SIM) response with magnetic dilution and secondly, a series of pure *4f* clusters. **Figure 1.31** shows the used metals and a code color to explain the reasons.

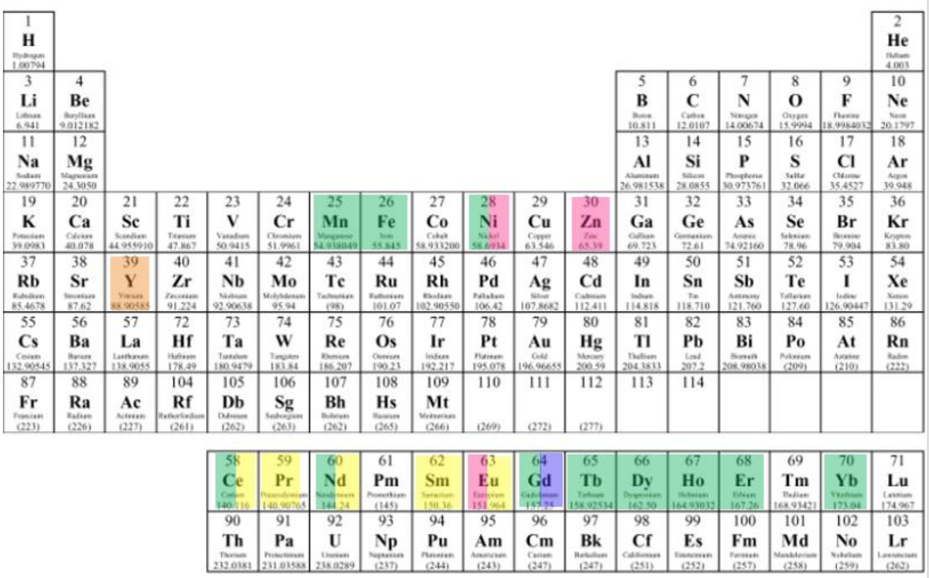

Figure 1.31. In the periodic table some metals are painted with different colors: in green, the metals used as paramagnetic centers searching for a magnetic behavior, in pink, the metals used as a *dilutors*, in yellow, the elements used for the search of luminescent properties, in blue, Gd^{III} that was also used to study the different relaxation of Mn^{III} in NMR and in orange, Y^{III} which has been used as the "diamagnetic lanthanide".

1.4.3. Crystallization techniques.

One of the main goals in magnetochemistry is to be able to know exactly the structure of the compound we are working with. Even there are a wide variety of characterization techniques to elucidate the structure of the compounds, no one is more precise that the Monocrystal X-Ray Diffraction, which gives us, literally, a picture of the structure. The drawback of this technique is the obtention of a monocrystal. A monocrystalline solid is a material in which the crystal lattice of the entire sample is continuous and has no grain boundaries. Because entropic effects favor the presence of imperfections, perfect single crystals of meaningful size are difficult to produce but can be made under controlled conditions in the laboratory.

The used crystallization techniques have been:

- Layer crystallization. Allows the apparition of monocrystals due to the insolubility of the product in the precipitating agent and its slow diffusion into the solvent. At the bottom of the tube there is the densest solution of the desired product and on the top of the tube the precipitating agent. This allows that the mixing between the two solvents is as slow as possible.
- Crystallization by slow evaporation of the solvent. Due to the solvent evaporation, the concentration of the desired product increases in the solution until it arrives to the saturation point.
- Slow vapor diffusion in a double vial. A small vial with the dissolution of the product is placed inside a bigger vial with the precipitant agent. The crystallization principle is the same than in layering.

All the crystallization techniques are depicted in **Figure 1.32**.

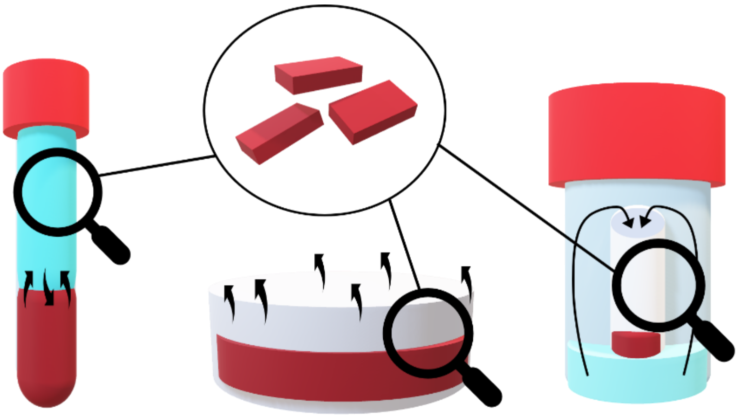

Figure 1.32. Left, the layering method, center, the evaporation of solvent and right, the diffusion in a double vial. The loupe indicates the zone where the crystals form.

1.5. OBJECTIVES.

- The synthesis of chiral polynuclear *3d* systems with slow relaxation of the magnetization to achieve multiproperty systems.

- The synthesis of chiral mononuclear clusters of *4f* metals to achieve Single Ion Magnet Behavior and, due to the presence of the lanthanide, to have also luminescent properties.

- The study of the supramolecular arrangement of all the compounds in order to understand the chirality transfer and the supramolecular chirality.

- The study of the optical properties of the compounds by means of Electronic Circular Dichroism, luminescence and Circularly Polarized Luminescence in the allowed cases.

- The magnetic study of all the compounds.

CHAPTER 2. NICKEL COMPLEXES

This chapter comprises ***Publication #1*** and ***Publication #2***.

Publication #1 *"From Mesocates to Helicates: Structural, Magnetic and Chiro-Optical Studies on Nickel(II) Supramolecular Assemblies Derived from Tetradentate Schiff Bases."* is about complexes $[Ni_2(L1)_2(N_3)_2](NO_3)\cdot 2MeOH$ **[1*RR*] [1*SS*] [1*RAC*],** $[Ni_2(L2)_2(N_3)_2](NO_3)\cdot 3MeOH$ **[2*RR*] [2*SS*],** $[Ni_2(L4)_2(N_3)_2](ClO_4)\cdot xMeOH$ **[3*R*]** and $[Ni_2(L5)_2(N_3)_2](NO_3)\cdot 2H_2O$, 2MeOH **[4]**, which are dinuclear Ni^{II} complexes derived from the tetradentate ligands **L1, L2, L4** and **L5** reacting with $Ni(NO_3)_2$ or $Ni(ClO_4)_2$ and NaN_3. The azido ligands in its μ-(1,1) coordination mode, act as a double bridge between the two Ni^{II} cations.

The idea behind the syntheses of these complexes was the study of the supramolecular structures known as *helicates* and *mesocates*. **Figure 2.1** represents both types of structures which have been largely studied with bis-bidentate ditopic ligands. The key concept in using this type of ligands to produce helicates is that they usually have a flexible spacer that can be twisted to wrap the cations along the M···M axis. Our goal was to modify this flexible spacer to see how long the helicate twist was allowed. **Figure 2.2** shows the differences in the spacer of the ditopic ligands that we have used in these compounds.

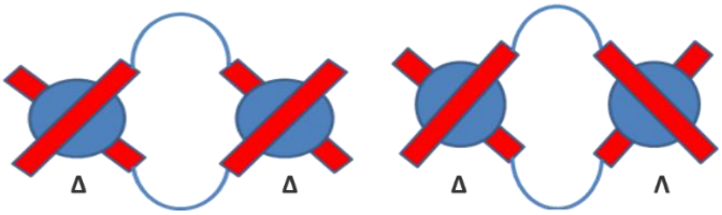

Figure 2.1. Left, double helicate supramolecular structure for two metallic centers. The inner nature of the helicate makes the two centers to have the same configuration (Δ/Δ) or (Λ/Λ) which converts the structure in a chiral supramolecule. Right, the double mesocate structure for two metallic centers with opposite total configurations (Δ/Λ). This configuration of the centers converts the mesocate in a non-chiral supramolecular structure.

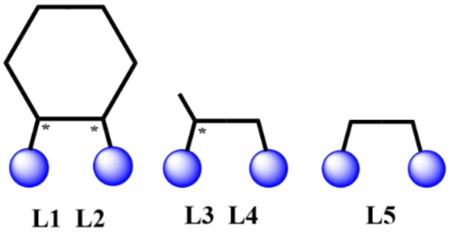

Figure 2. 2. Differences in the spacers of ligands used in ***Publication #1***. While **L1** and **L2** only yield the mesocates, **L3** and **L4** allowed a mixture of both structures and **L5** allowed both structures depending on the aromatic substituents of the aldehyde used to synthesize the Schiff base.

What the experimental results showed is that, as was expected, the torsion is not allowed for the more rigid ligands and the mesocate structures are formed.

Another variable that is analyzed in the text is the influence of the aromatic substituent of the aldehyde used to synthesize the Schiff base.

Examining the literature of previous related compounds synthesized from enantiopure ligands (mainly with tetrahedral Ag^I and Cu^I and with octahedral Zn^{II}, Cu^{II} and Fe^{II}) there is a common characteristic in of all them known as *chirality transfer*. As its name indicates, this phenomenon translates the chirality of the enantiopure ligand to the total configuration of the metal yielding always in a helicate moiety. Because we reach to tune the ligand torsion by using more or less rigid ligands, the helicate form was not allowed, and due to the use of enantiopure ligands, to our knowledge complexes **[1*RR*/1*SS*]** and **[2*RR*/2*SS*]** are the first chiral mesocates in the literature. It deserves a mention the exceptional structure of **[4]** that reach the equilibrium point between both supramolecular structures exhibiting both conformations in the same cell: the helicates (Δ/Δ) and (Λ/Λ) and the mesocate (Δ/Λ) in ratio 2:1 respectively.

Publication #2 "*Chiral tetranuclear Ni^{II} clusters derived from Schiff bases and azido co-ligands*" describes an enantiomeric pair of Ni^{II} double defective cubanes $[Ni_4(HL9)_2Cl_4(\mu_3\text{-}N_3)_2(MeOH)_2]\cdot$solvent synthesized using **H_2L9** and azido co-ligands in its μ-(1,3) coordination mode **[5*R*]** and **[5*S*]**. Magnetic static measurements have been performed in both enantiomers showing a ferromagnetic interaction mediated by the azido bridge that tends to the maximum ground state $S = 4$. $\chi_M T$ *vs.* T plot shows a decay at very low temperature which has been tested as a zJ or D terms. The reduced magnetization experiments were determinant to elucidate that the decay was attributed to a high D positive value.

Publication #1 *"From Mesocates to Helicates: Structural, Magnetic and Chiro-Optical Studies on Nickel(II) Supramolecular Assemblies Derived from Tetradentate Schiff Bases."*

CHEMISTRY
A European Journal

www.chemeurj.org

A Journal of

ChemPubSoc Europe

2018-24/30

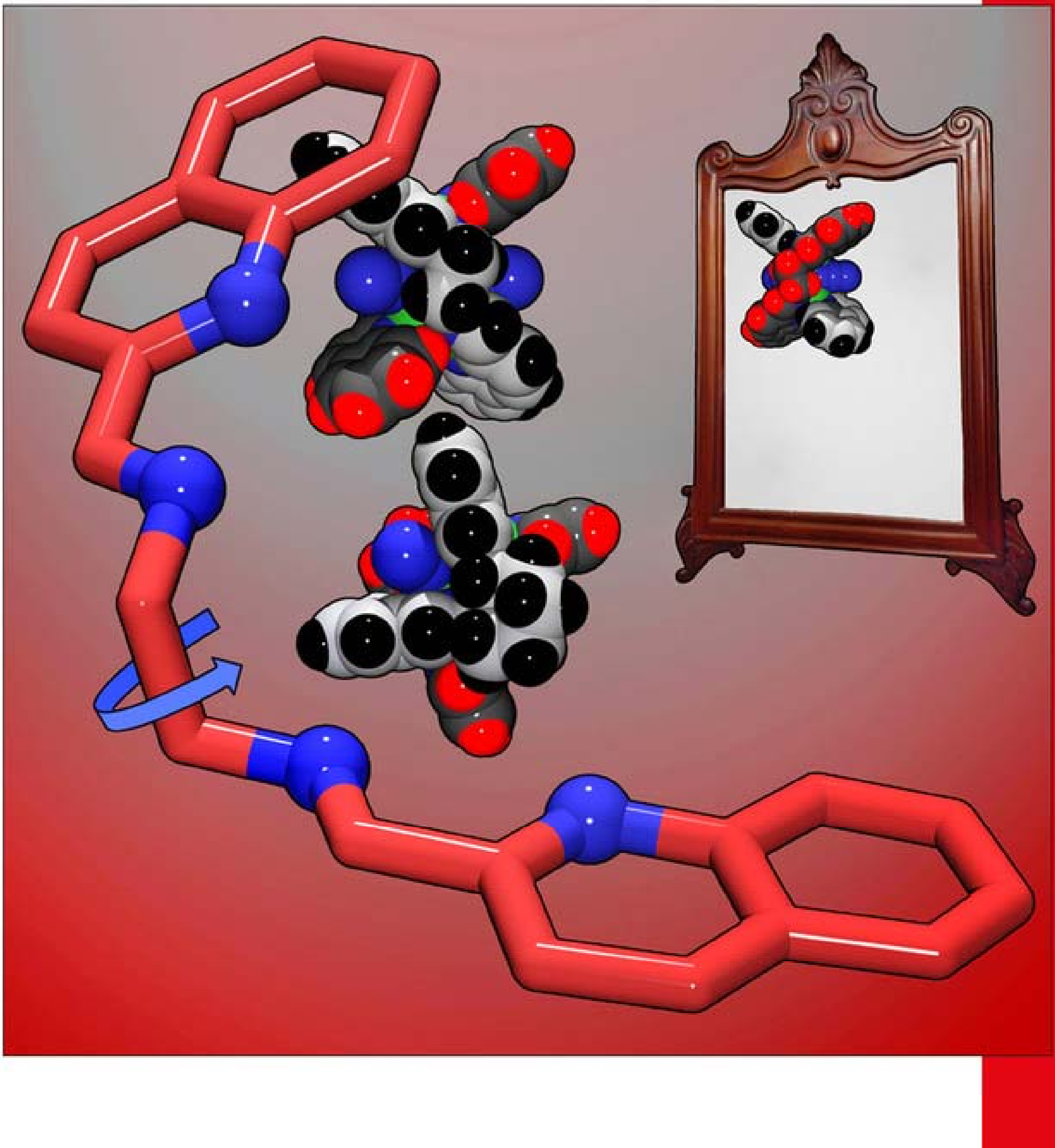

Cover Feature:

A. Escuer et al.

From Mesocates to Helicates: Structural, Magnetic and Chiro-Optical Studies on Nickel(II) Supramolecular Assemblies Derived from Tetradentate Schiff Bases

Supported by

ACES Asian Chemical Editorial Society

WILEY-VCH

ChemPubSoc Europe
DOI: 10.1002/chem.201800323
CHEMISTRY
A European Journal
Full Paper

Solid-State Chirality |Hot Paper|

From Mesocates to Helicates: Structural, Magnetic and Chiro-Optical Studies on Nickel(II) Supramolecular Assemblies Derived from Tetradentate Schiff Bases

Júlia Mayans,[a] Mercè Font-Bardia,[b] Lorenzo Di Bari,[c] Lorenzo Arrico,[c] Francesco Zinna,[c] Gennaro Pescitelli,[c] and Albert Escuer*[a]

Abstract: The systematic reactions of a family of tetradentate pyridyl/imine and quinolyl/imine racemic or enantiopure Schiff bases with $Ni(NO_3)_2$ or $Ni(ClO_4)_2$ in the presence of sodium azide yielded, as a function of the starting racemic, chiral or achiral base, a set of chiral, *meso* or achiral complexes. In all cases, the compounds consist of two Ni^{II} cations linked by a double azido bridge in its end-on coordination mode. All the dimers exhibit a mesocate supramolecular structure and one of them, the unprecedented mix of helicate and mesocate in 2:1 ratio. The transition from mesocate to helicate conformation has been reached by tuning the flexibility of the central spacers of the Schiff bases and the size of the substituents. Electronic circular dichroism (ECD) studies have been performed for two pairs of enantiomers and interpreted by means of DFT calculations. Susceptibility measurements show a ferromagnetic coupling between the Ni^{II} cations mediated by the end-on azido bridges.

Introduction

Enantiopure polynuclear transition-metal complexes are becoming a subject of great interest in coordination chemistry because they open a wide range of possibilities in the synthesis of new materials,[1,2] biochemistry,[3–6] drug design,[7] and catalysis.[8–12]

Control of chirality in supramolecular structures is a way to relate their properties and reactivity to their structure in a predictable way. It allows the design of complexes with a controlled topology and with specific physical properties such as electronic circular dichroism (ECD), circularly polarized luminescence (CPL), non-linear optics, and magneto-chiral effects, etc.

Helicates and mesocates built around hexa- or tetra-coordinated metal cations,[13,14] are among the most studied supramolecular structures, because the self-assembly between the organic ligands and the metal cations allows the parameters that direct the formation of supramolecular structures to be elucidated; such factors include the electronic or steric preferences of the metal, the disposition of the donor atoms in the ligand, or other factors such those postulated by M. Albrecht relating the preference for one or other stereochemistry, for series of ligands with different spacers, with even or odd number of C-atoms[15] of the chain or its flexibility.[16]

Ligands must be chosen carefully to prepare compounds of this kind because they must have the ability to link different metal centers in spite of chelating a single cation. Bis-bidentate or bis -tridentate ditopic ligands, in which the chelating fragments are linked by a flexible spacer, are extremely useful in this field because they can afford complexes with a large variety of cations. In this sense, the first-row transition metals have been specially studied, although structures with other transition metals or even quadruple helicates with rare earths have also been reported.[17] Usually, all the coordination sites around the metal are filled by the ligands, resulting in double helicates ($[M_2L_2]^{n+}$) when the bis-bidentate ligands react with cations that prefer a tetrahedral environment, or when the bis-tridentate ligands react with cations that prefer a octahedral environment. When pyridyl/imine Schiff bases with an ethylene spacer are employed as ligands, systematic characterization of $[M_2L_2]^{n+}$ helicates have been reported and, in both cases, the bidentate or tridentate units around the same cation have an ideal 90° angle between them. Furthermore, in both cases, the torsion angle subtended by the NCCN atoms of the flexible spacer typically lies around 60°, as shown in the analysis of the 30 reported structures with pyridyl/imine ligands and tetrahedral Cu^{I},[18–29] Ag^{I},[24,25,30–35] or with bipyridyl/imine ligands and

---

[a] J. Mayans, Prof. A. Escuer
Departament de Química Inorgànica i Orgànica, Secció Inorgànica and Institut de Nanociència i Nanotecnologia (IN²UB), Universitat de Barcelona
Martí i Franques 1–11, Barcelona 08028 (Spain)
E-mail: albert.escuer@qi.ub.es
Homepage: www.ub.edu/inorgani/recerca/MagMol/magmol.htm

[b] Dr. M. Font-Bardia
Departament de Mineralogia, Cristal·lografia i Dipòsits Minerals and Unitat de Difracció de R-X. Centre Científic i Tecnològic (CCiTUB)
Universitat de Barcelona, Martí Franqués s/n, Barcelona 08028 (Spain)

[c] Prof. L. D. Bari, Dr. L. Arrico, Dr. F. Zinna, Dr. G. Pescitelli
Dipartimento di Chimica e Chímica Industriale, Università di Pisa
Via Moruzzi 13, 56124 Pisa (Italy)

Supporting information and the ORCID identification number(s) for the author(s) of this article can be found under https://doi.org/10.1002/chem.201800323.

© 2018 Wiley-VCH Verlag GmbH & Co. KGaA, Weinheim

octahedral Zn^{II}, Cu^{II} or Fe^{III} cations,[28,36,37] Scheme 1(a) and (b). Double Ni^{II} helicates with the cations in octahedral environment and with two coordination sites occupied by one bidentate ligand and employing the L2 Schiff base (Scheme 2), exhibit similar coordination sites for the *N*-donors and NCCN torsion angles in the same range (Scheme 1c).[38]

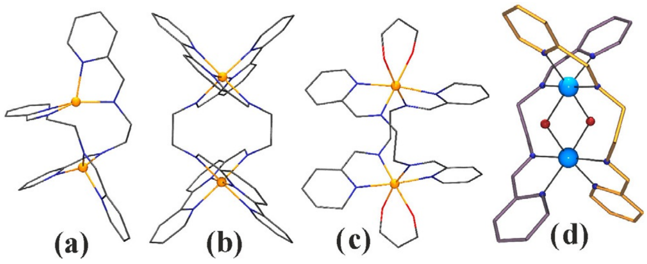

Scheme 1. a) Double helicate with bis-bidentate ligands around tetrahedral cations; b) bis-tridentate ligands around octahedral cations; c) bis-bidentate ligands around octahedral cations and a bidentate co-ligand, and d) bis-bidentate ligands and two bridging co-ligands around octahedral cations.

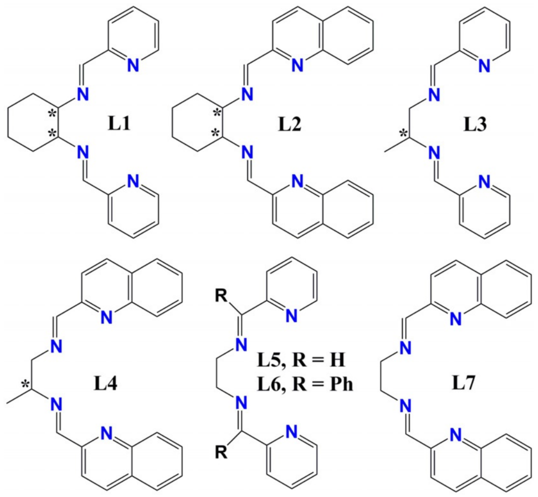

Scheme 2. Ligands employed (L1, L2, L3, L4, L7) or referenced (L5, L6) in the present work. Asterisks denote the chiral C-atoms for ligands L1 to L4.

A special case is provided by double helicates with general formula $[M_2(L)_2X_2]^{n+}$, (Scheme 1d). These systems, in which L corresponds to the bis-bidentate pyridyl/imine Schiff bases L5 or L6 (Scheme 2) and X is a bridging ligand, are scarce and have only been reported for Co^{II} cations with X = oxo, or peroxo,[39] and for Ni^{II} cations with X = azido or cyanate.[40] In all cases, the $[M_2L_2X_2]^{n+}$ dimers exhibit a helicate arrangement and, as a consequence of the relative position of the pyridine ring, the corresponding NCCN torsion angle of the spacer becomes much larger—typically in the 80–90° range. An interesting characteristic of this kind of structure is that, in contrast to the $\Lambda\Delta$ mesocates, the helicity implies homochiral ($\Lambda\Lambda$ or $\Delta\Delta$) stereochemistry around the metallic centers.

With the aim to characterize new $[M_2L_2X_2]^{n+}$ complexes and to study the relationship between helicates and mesocates in this kind of system that requires unusual NCCN torsion angles, we choose for this work a family of bis-bidentate Schiff bases (Scheme 2), containing four N-donor nitrogen atoms with a NCCN spacer able to promote the formation of discrete metal–ligand complexes. Three aspects have been taken into account to understand better the self-assembling of these structures. First, the tuning of the flexibility of the central saturated C–C bond of the spacer permits its influence in the final product to be studied: when the C–C bond presents a high degree of flexibility, the helicate structure should be allowed, whereas for a low degree of flexibility, only the mesocate should be achieved. Second, the steric effect of the aromatic substituents in the ligand was varied to check its influence in the final conformation, and, third, the effect of the chirality was considered as a driving force to form helicates against the former effects, because, as can be found in the literature,[41,42] when an organic ligand with a stereogenic center is used, it usually tends to yield chiral supramolecular helicate structures with the same configuration $\Lambda\Lambda$ or $\Delta\Delta$ for all the octahedral metal centers.

In this work we report the syntheses and characterization of a series of complexes with general formula $[Ni_2L_2(N_3)_2]A_2$ (A = NO_3^-, ClO_4^-), obtained by the reaction of the corresponding NiA_2 salt with the selected L Schiff base in the presence of sodium azide, resulting in various kinds of compounds: the *meso* **1M** and the chiral (**1*SS***, **1*RR***) mesocate complexes with general formula $[Ni_2(L1)_2(N_3)_2](NO_3)_2)$; the chiral mesocates $[Ni_2(L2)_2(N_3)_2](NO_3)_2$ (**2*SS***, **2*RR***); several derivatives of L3 (**3**) with A = NO_3^- or ClO_4^- for which the structure was not fully determined; the mesocate $[Ni_2(R\text{-}L4)_2(N_3)_2](ClO_4)_2$ (**4*R***); and the rare mixing in 1:2 ratio of mesocate and helicate conformations derived from the achiral ligand L7 with formula $[Ni_2(L7)_2(N_3)_2](NO_3)_2$ (**7**).

All the synthesized complexes are dinuclear structures, as was expected, and they join several unusual features: the transition from mesocate to helicate has been tuned by changes in the ligands, showing in one case the unprecedented coexistence of mesocates and helicates in the same network; moreover, we achieved the synthesis of rare chiral mesocates due to the chirality of the ligands. In addition to the structural study, the systems have been characterized by electronic circular dichroism (ECD), DFT calculations and magnetic susceptibility measurements

Results and Discussion

Description of the structures

The structures of the reported complexes are similar in their general trends. To avoid repetitive descriptions, the structure of **1M** will be described in detail and only the more important features will be discussed for the remainder complexes. Intermolecular interactions and the supramolecular arrangement in the network will be discussed separately.

***meso*-$[Ni_2(L1)_2(N_3)_2](NO_3)_2\cdot 2MeOH$ (1M·2MeOH)**: The molecular structure of **1M** consists of a centrosymmetric cationic Ni$^{II}_2$ complex (Figure 1) and two NO_3^- counteranions. The main bond parameters are summarized in Table S1. Each bidentate pocket of the L1 ligand is coordinated to a different Ni^{II} cation,

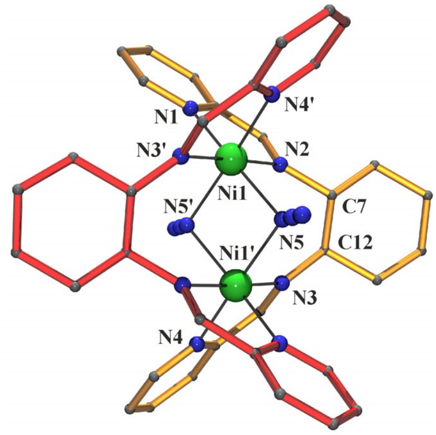

Figure 1. Partially labeled view of the mesocate cationic dinuclear complex **1M**. Color key for all figures: Ni^{II}, green; N, navy blue; C, dark grey.

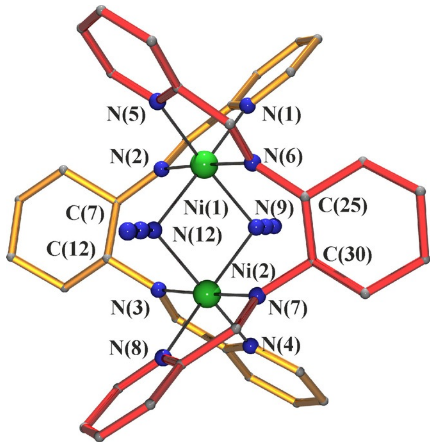

Figure 2. Partially labeled plot of complex **1*RR***. Atom labels are common for **1*RR*** and **1*SS***.

acting as a bis-bidentate ligand. The Ni^{II} cations are octahedrally coordinated in a *cis* fashion by two bidentate fragments of L1 and two azido ligands in its end-on coordination mode. The main distortion of the octahedron is due to the low bite angle of the bidentate fragments that gives N_{imine}-Ni-N_{py} bond angles around 80°. The Ni_2N_2 (Ni-(N_{azido})$_2$-Ni) central ring is planar, with similar distances to the azide bridging atoms, 2.104(1)–2.099(1) Å, with a Ni···Ni distance of 3.0339(3) Å. The azido ligands form an angle of 42.8(2)° with the mean Ni_2N_2 plane. The hexane ring shows a chair conformation, with a N(2)-C(7)-C(12)-N(3) torsion angle of 54.5(3)°. Each L1 ligand possesses two chiral C-atoms related by the inversion center placed in the dinuclear unit, and thus one possesses *RR* and the other *SS* chirality. In this complex, the L1 ligands are surrounding the Ni^{II} cations in a mesocate arrangement and consequently, the two Ni^{II} cations exhibit opposite Λ / Δ stereochemistry. The pyridyl rings linked to the same Ni^{II} cation form a 97.8° angle between mean planes. Intermolecular interactions between dinuclear units are weak CH···N and CH···O H-bonds involving the nitrate counteranions, methanol solvent molecules and terminal *N*-atoms of the azido ligands, and the only stronger OH···O H-bonds present in the network are those between the methanol molecules and the nitrate counterions.

[Ni_2(*RR*-L1)$_2$(N_3)$_2$](NO_3)$_2$·2MeOH (1*RR*·2MeOH) and [Ni_2(*SS*-L1)$_2$(N_3)$_2$](NO_3)$_2$·2MeOH (1*SS*·2MeOH): The structures of both enantiomers are practically identical and thus the following description is centered on **1*RR***, shown in Figure 2. Selected bond angles and distances for **1*RR*** are listed in Table S2. As for the **1M** complex described above, the dimers show a mesocate arrangement but in this case the dimers are not centrosymmetric.

Ni-N_{azide}-Ni bond angles are quasi identical (92.1°/92.5°), with an angle between the azides and the main Ni_2N_2 plane of 43.5°. The octahedral coordination sphere of Ni(1) consists of two bonds to the bridging azido ligands, two N_{imine} and two N_{py} donors with Ni–N bond distances clearly larger for Ni–N_{imine} than for Ni–N_{py}. The situation is reversed around Ni2, which shows Ni–N_{imine} bond distances shorter than the Ni–N_{py} bond distances. The NCCN torsion angles of the central spacer (44.9(3)°/ 49.0(3)°) are lower than for **1M**. As a consequence of these differences, the angle between pyridine rings linked to the same Ni^{II} cation is also asymmetric, with values of 92.4(2)° for the rings linked to Ni1 and 103.8(2)° for the pyridinic rings linked to Ni2. The intermolecular interactions are similar to those of **1M**.

[Ni_2(*RR*-L2)$_2$(N_3)$_2$](NO_3)$_2$·3MeOH (2*RR*·3MeOH) and [Ni_2(*SS*-L2)$_2$(N_3)$_2$](NO_3)$_2$·3MeOH (2*SS*·3MeOH): The mesocate structures of **2*RR*** and **2*SS*** are similar in their general trends to the complexes **1*RR*** and **1*SS*** described above. In the case of **2*RR*** and **2*SS***, there are two similar but nonequivalent dimers in the unit cells, labelled A and B. Selected bond parameters are listed in Table S3 and a view of the A unit of **2*RR*** is shown in Figure 3. The coordination spheres of Ni(1) and Ni(2) are also different, with the Ni–N_{imine} bond distances being clearly shorter than the Ni–N_{py} for Ni(1) (mean values 2.059 and 2.120 Å, respectively), whereas the situation is the opposite for Ni(2), with Ni–N_{imine} mean bond distance of 2.179 Å and Ni–N_{py} of 2.124 Å. The NCCN torsion angles are 48.1(7)°/47.6(6)° for mol-

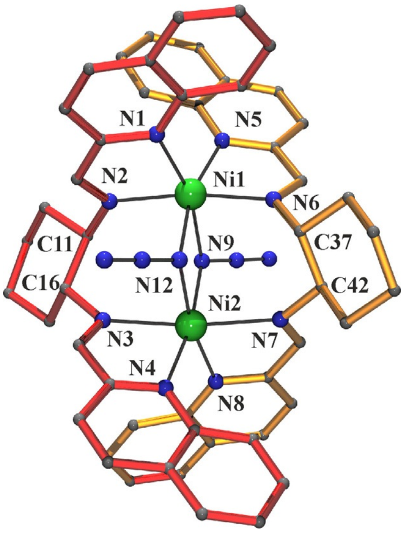

Figure 3. Partially labeled plot of complex **2*SS***, common with **2*RR***.

ecule **2*RR***-A and 52.8(6)°/51.3(6)° for molecule **2*RR***-B, and the angles between the quinolyl mean planes linked to the same Ni^{II} cations are clearly different, with values of 110.5(2)°/106.3(2)° for the A unit and 94.2(2)°/91.0(2)° for the B unit and Ni1/ Ni2, respectively.

$[Ni_2(R\text{-}L4)_2(N_3)_2](ClO_4)_2\cdot x$MeOH (4*R*·*x*MeOH): A labeled plot of **4*R*** is shown in Figure 4 and the main bond parameters are listed in Table S4. The molecular structure of the mesocate complex **4*R*** is very similar to the complexes **2*RR*/*SS*** described above, with two independent dimers (labeled as A or B) in the unit cell, similar Ni-N-Ni bond angles and the same $Ni-N_{imine}$/$Ni-N_{qx}$ bond distances relationship for Ni1 and Ni2. The main differences lie in the lower NCCN torsion bonds, with values of 48.3(9)°/39.3(9)° for the A unit and 39.1(7)°/33.9(8)° for the B dimer. The dihedral angle between mean quinolyl planes linked to the same Ni^{II} cation is similar in both dimers, ranging between 104.9(3)° and 109.9(2)°.

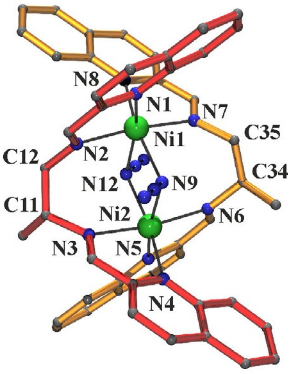

Figure 4. Partially labeled plot of complex **4*R***.

$[Ni_2(L7)_2(N_3)_2](NO_3)_2\cdot 2H_2O,2MeOH$ (7): The exceptional structure of compound **7** consists of two nonequivalent dimers, labeled A and B, one of them with mesocate centrosymmetric arrangement (**7B**) and the other with helicate noncentrosymmetric structure (**7A**). The presence of inversion centers in the network generates two molecules with opposite helicity **7A-Δ** and **7A-Λ**; thus, there are three different dimers in the achiral network. The main bond parameters are listed in Table S5 and a view of the mesocate and one of the helicates is shown in Figure 5. The mesocate unit **7B** is similar to the previously described systems with the same conformation, showing larger $Ni-N_{qx}$ bond distances than the $Ni-N_{imine}$ ones, a NCCN torsion of the central spacer of 50.1(7)°, and a dihedral angle between quinolyl mean planes of 94.0(1)°.

The **7A** helicate molecule shows $Ni-N_{qx}$ are greater than $Ni-N_{imine}$ bond distances for both Ni1 and Ni2 environments, with similar dihedral angles between the quinolyl planes (110.8(2)°/108.0(2)°). The key difference with the precedent mesocates lies, as expected, in the larger NCCN torsion angles, which take values of 83.7(6)° and 81.2(5)°. Ni-N-Ni bond angles are 99.3(2)° and 100.5(2)°.

$[Ni_2(L3)_2(N_3)_2]A_2\cdot$solvent ($A=NO_3^-$, ClO_4^-) (3): Diffraction data were collected for multiple crystals of the complexes derived from *rac*-L3 or chiral-L3 ligand and nitrate or perchlorate counteranions but trials to solve the structure were unsuccessful. The complexes crystallize in nice polyhedral crystals that diffract correctly but fail in the refinement process. The obtained molecules show images in which both conformations seem to overlap and with disordered azido ligands with large deviation from linearity (Figure S1). In light of the partial structural results, the presence of both mesocate and helicate conformations seems to be consistent, although caution must be assumed.

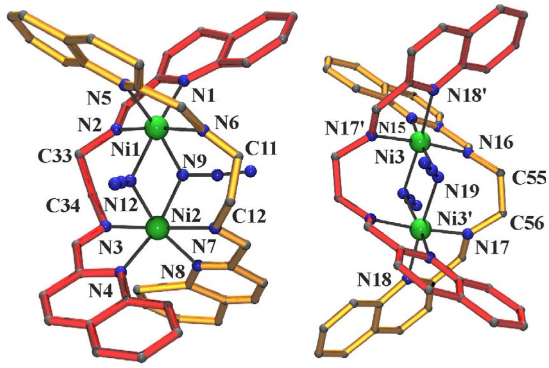

Figure 5. Partially labeled plot of the helicate **7A** (left) and the mesocate **7B** (right) complexes.

Network supramolecular arrangement

The most conventional noncovalent interaction forces that determine the network supramolecular arrangement for systems containing aromatic rings are typically π-π stacking. In addition and equally important, electron-deficient aromatic rings such as those containing coordinated N-donors, can promote other interactions that were found to be determinant in biological systems, but rarely studied in cluster chemistry, such as anion-π or lone pair-π interactions.[43] The weaker CH···π interaction has also been revealed as a determinant in the crystal packing.[44] Complexes **1M**, **1*RR***, and **1*SS***, containing pyridyl rings, do not show remarkable interdimer interactions in the network. In contrast, when the quinolyl aromatic fragment is present in the structures, it promotes intermolecular interactions, which determines the spatial arrangement of the molecules. Intermolecular interactions in complexes **2*RR*** and **2*SS*** are dominated by the π-π stacking of the aromatic rings of the quinolyl groups, which show a distance between the centroids of the phenyl fragments of 3.645 Å. In addition, there are two CH···π interactions between one of the H-atoms of the phenyl ring and one phenyl fragment of the neighbor molecule (H-centroid distances of 2.565 and 3.152 Å). As a consequence of these interactions, the molecules are ordered forming parallel chains where the A and B nonequivalent dimers present in the unit cell are arranged in an ABABA alternating sequence along the chains (Figure 6).

As in the previous case, the structure of **4*R*** contains two nonequivalent dimers (named A and B). The network consists of layers of parallel chains of B molecules and noninteracting A

© 2018 Wiley-VCH Verlag GmbH & Co. KGaA, Weinheim

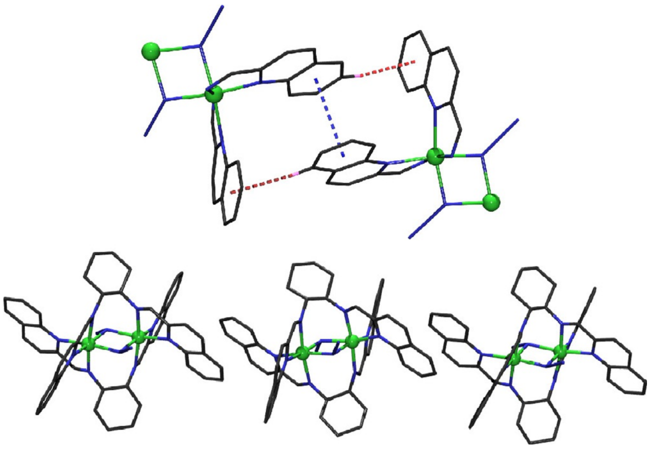

Figure 6. (Top) Intermolecular interactions found in compounds **2*RR*** and **2*SS***. π-π stacking is indicated as blue dotted lines between centroids and H-ring contacts as red dotted lines. (Bottom) Lateral view of the 1D arrangement of the dimers.

dimers between the layers, which are surrounded by perchlorate anions and solvent molecules, giving a complex set of weak C–H···O H-bonds. The interaction that generates the B chains is the π-π stacking of the quinolyl fragments, with interplanar distance of around 3.3 Å, and a distance between the centroids of the phenyl and the pyridyl fragments of 3.542 Å. In this case, one O-atom of the perchlorate counteranion gives an anion-π ring interaction with a distance between the O-donor and the centroid of the pyridyl ring of 2.900 Å. This interaction avoids the possibility of CH···π interactions (Figure 7).

The structure of complex **7** contains a centrosymmetric mesocate and two helicates with opposite Δ/Λ helicity. The intermolecular interactions provide an exceptional example of chiral recognition in an achiral network. The mesocates form layers of parallel chains of dimers linked by the same kind of intermolecular interactions as have been described above for compounds **2*RR***/**2*SS*** (Figure 6); namely, π-π stacking of the aromatic rings of the quinolyl groups, with a distance of 3.424 Å between main planes and of 3.715 Å between centroids, plus symmetric CH···π ring interactions (H-centroid of the phenyl ring distance of 2.866 Å). Between the mesocate planes, there are layers of helicates formed by homochiral parallel chains of ΛΛ and ΔΔ dimers related by inversion centers (Figure 8). In these helical chains the intermolecular interactions are dominated by double CH···π ring interactions with H-ring(pyridyl) distance to centroids of 2.643 Å and H-ring(phenyl) of 2.901 Å. The π-π stacking is less effective than for the mesocates because the aromatic rings are not parallel.

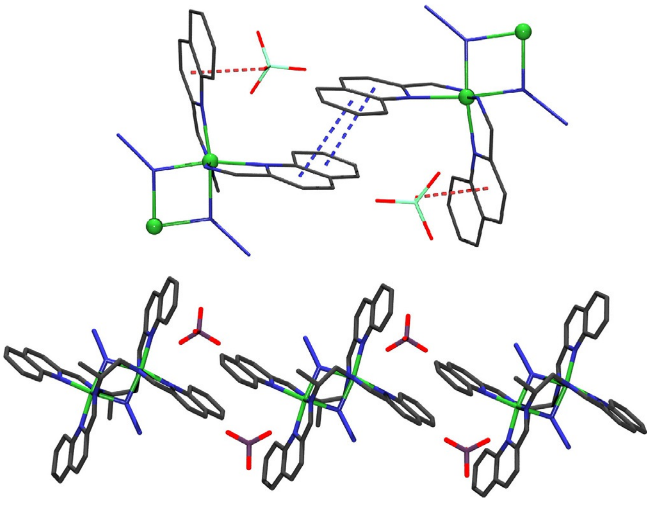

Figure 7. (Top) Intermolecular interactions found in compound **4*R***. π-π stacking is indicated as blue dotted lines between centroids and O-ring contacts as red dotted lines. (Bottom) Lateral view of the 1D arrangement of dimers.

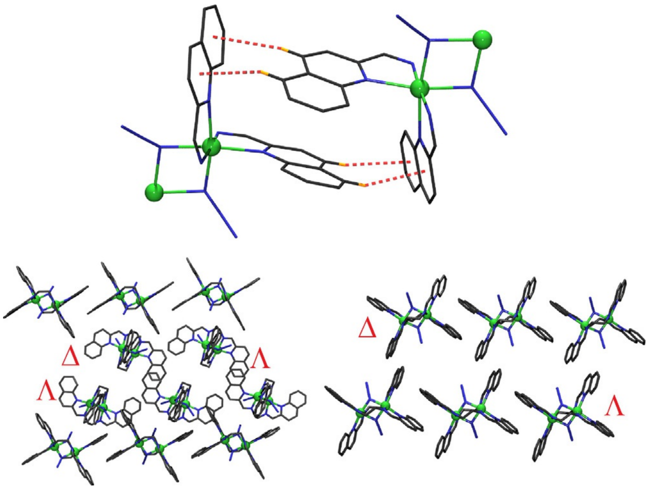

Figure 8. (Top) Intermolecular interactions found in compound **7A-Λ** and **7A-Δ**. CH···π ring contacts are indicated as red dotted lines. (Bottom, left) One layer of chains of Δ and Λ dimers between layers of parallel chains of mesocates. (Bottom, right) A lateral view of the parallel Δ and Λ chains of helical dimers.

Electronic and vibrational circular dichroism

Vibrational circular dichroism (VCD) of **1*RR*/*SS*** and **2*RR*/*SS*** in the solid state (KCl pellets) was preliminarily investigated with the aim of identifying metal-induced VCD enhancements.[45,46] However, no VCD enhancement was observed, probably because there are no *d-d* transitions of suitable energy to effectively mix with the vibrational transitions.[47] Under these conditions, the VCD signals are too weak with respect to the artifacts due to linear anisotropies in the solid state; therefore, it was not possible to obtain reliable VCD spectra.

Solid-state ECD spectra were measured as KCl pellets for **1*RR*** and **1*SS*** in the 350–900 nm region. They display several bands with non-negligible rotational strength (Figure 9, top). These bands have an expected main *d-d* character; however, their nature is in fact more complex (see the computational analysis section). The spectra measured on the two enantiomers are perfect mirror images, ensuring that there are no significant contributions from linear dichroism/linear birefringence.[48] In this case, it was not possible to obtain a disc of sufficient quality to penetrate below 350 nm. Solution spectra measured in acetonitrile display several relatively intense

© 2018 Wiley-VCH Verlag GmbH & Co. KGaA, Weinheim

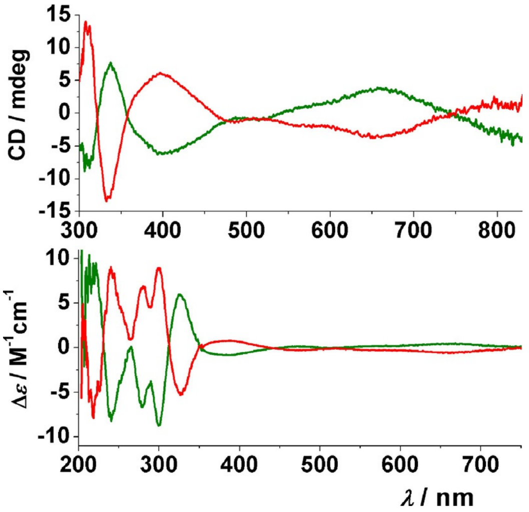

Figure 9. (Top) Solid-state ECD spectra recorded for the **1*RR*** (green line) and **1*SS*** (red line) enantiomers. The spectra were recorded on KCl pellets. (Bottom) Normalized solution ECD spectra in CH_3CN recorded for **1*RR*** and **1*SS*** enantiomers. The spectra were recorded using a 0.1 cm cell for the 200–380 nm region and a 1 cm cell for the 380–900 nm region.

bands also in the 200–350 nm region, where the character of the transitions is mainly, although not exclusively, ligand centered (Figure 9, bottom).

For complexes **2*RR*/*SS***, it was possible to obtain KCl discs suitable to penetrate down to 250 nm (Figure 10, top). We note that the intensity ratio between long-wavelength and short-wavelength transitions is lower than in the **1*RR*/*SS*** case. This fact is appreciable both in the solid state and in the solution spectra (Figure 10, bottom), and is related to the stronger electronic transitions of the quinoline chromophores with respect to the pyridine ones.

It is interesting to compare the solution and the solid-state ECD spectra. It is apparent from Figure 11 that the two pairs of spectra are almost perfectly superimposable in the longer wavelength region, 400–900 nm, whereas shorter wavelength transitions (above 350 nm) maintain the same shape and sign in the two media but with different relative intensity; a higher intensity is observed in solution than in the solid state. This indicates that, although small ligand rearrangements can occur upon solvation, Ni-centered transitions are not significantly affected. Furthermore, intermolecular interactions that may occur in the microcrystalline solid-state samples are more effective for ligand-centered transitions, because of their stronger electric-dipole allowed character.[49]

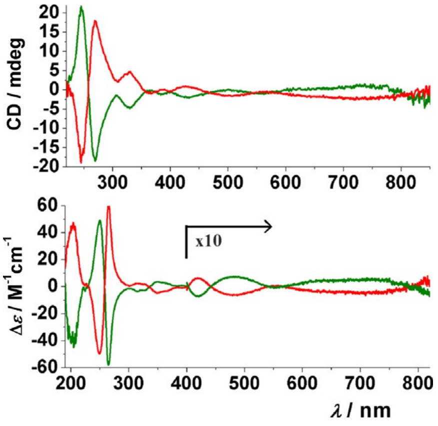

Figure 10. (Top) Solid-state ECD spectra recorded for the two **2*RR*** (green line) and **2*SS*** (red line) enantiomers. The spectra were recorded on KCl pellets. (Bottom) Normalized solution ECD spectra in CH_3CN recorded for **2*RR*** and **2*SS*** enantiomers. The spectra were recorded using a 0.1 cm cell for the 200–380 nm region and a 1 cm cell for the 380–900 nm region.

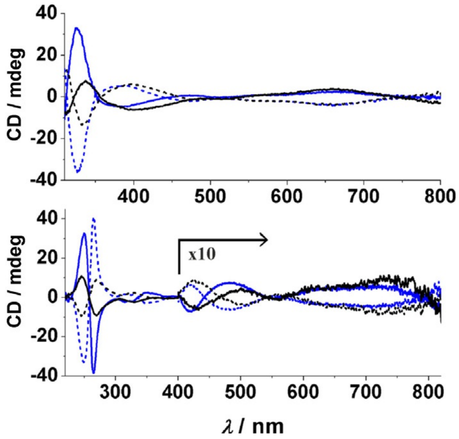

Figure 11. Comparison between solid state (blue lines) and solution (black lines) ECD spectra for **1*RR*** and **1*SS*** (top) and for **2*RR*** and **2*SS*** (bottom). *RR* enantiomers, continuous lines; *SS* enantiomers, dotted lines.

Time-dependent density functional theory (TDDFT) was employed to simulate the ECD spectra of compounds **1*SS***.[50] It must be stressed that excited-state calculations of open-shell Ni complexes with high spin are very demanding.[51,52] In the current case, the situation is further complicated by the presence of four chromophores, each with several transitions. In fact, a very high number of transitions needed to be considered; however, TDDFT calculations are intrinsically less accurate for high-lying states.[53] As a consequence, only a portion of the ECD/UV spectra may be investigated (above ca. 300 nm), and our analysis is not expected to perfectly reproduce the experimental spectra. In Figure 12 we show the absorption and CD spectra calculated for **1*SS*** at CAM-B3LYP/LanL2DZ level, which gave the best results (see the Computational Section). The input structure was obtained by reoptimizing the X-ray geometry with DFT at the B3LYP/6-31G(d) level of theory; an input structure with +2 charge (devoid of counteranions) and quintet spin state was used in all calculations.

Many distinct transitions contribute to the observed absorption and ECD bands; moreover, orbital and population analysis reveal that each transition is due to several different single excitations. This renders a full spectrum assignment impossible in terms of easily identified transitions, especially because there is no clear separation between metal- and ligand-centered transitions, and metal-centered transitions occur deeply in the UV region of the spectrum. We have already observed this behavior before for high-spin Ni complexes with chromophoric ligands.[52] As an example, we summarize the assignment of the two transitions contributing most to the two observed nega-

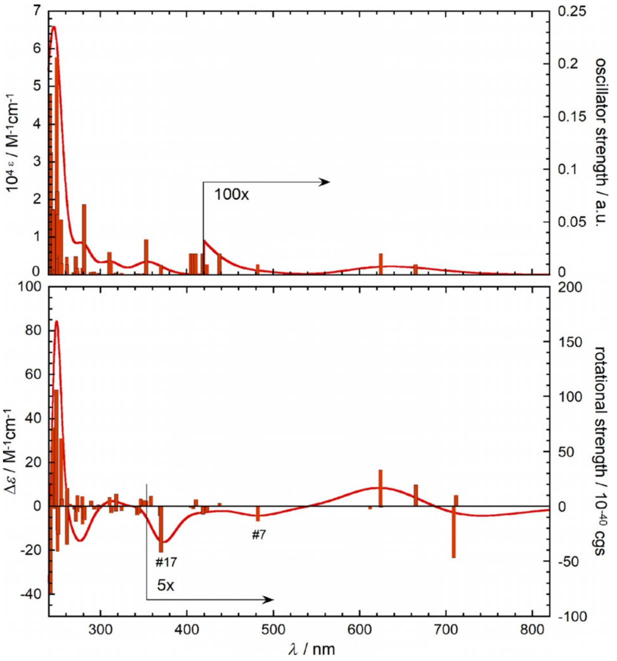

Figure 12. TDDFT calculated absorption (top) and ECD (bottom) spectra for compound **1*SS*** at CAM-B3LYP/LanL2DZ level. Vertical bars represent calculated transitions with respective rotational and oscillator strengths. Spectra were plotted as sums of Gaussian with exponential band-width of 0.3 eV.

tive ECD bands observed around 650 and 480 nm of **1*SS***, calculated at 482 (transition labeled #7 in Figure 12) and 370 nm (#17), respectively. The former band is a mixing of several excitations, the dominant ones being those from the $\pi_{C=N}$, $\pi_{py\ C=N}$, and d_{xz} orbitals to a mixed $\pi_{N3}{}^* + d_{yz}$ orbital (the *z* axis is along the Ni-Ni direction). The latter band is also a mixing of many excitations, the dominant ones being those from a mixed $\pi_{py\text{-}C=N} + d_{y2+z2}$ orbital to the two mixed $\pi_{py}{}^*/d_{yz}$ and $\pi_{py}{}^*/d_{x2}$ orbitals. One clear result from the calculations is that the apparent baseline drift above 800 nm in the ECD spectra is due to a real ECD band, and possibly a further ECD signal with opposite sign is present at even longer wavelengths.

Helicate versus mesocate conformation

Helicates and mesocates are supramolecular structures formed by the self-assembly of metallic centers and bridging ligands, as has been described previously. Double helicates with M_2L_2 and triple helicates with M_2L_3 stoichiometry are formed by bis-bidentate ligands bound to two tetrahedral or octahedral metal centers, respectively. In the latter case, this arrangement generates a homochiral ($\Lambda\Lambda$ or $\Delta\Delta$) helical structure. For a dinuclear double helix built with these types of ligand, it is postulated that the spacer must have an adequate size, enough rigidity to sterically favor the coordination of the two bidentate fragments to different cations, and it also needs enough flexibility to permit the wrap around the M⋯M axis of the molecule.

For cations showing octahedral coordination, the triple M_2L_3 helicates with C_3 symmetry are the most common structures (Figure 13, left). In this case, the main axis of the molecule is placed on the center of opposite triangular faces of the octahedra and NCCN torsions around 60° are enough to satisfy the helicate requirements. A large number of M_2L_2 (M = tetrahedral Cu^{I}, Cu^{II}, Ag^{I}) helicates have been reported for ligands with a two-C spacer like those employed in the present work, with NCCN torsion angles also around 60°.[18–35] In contrast, for the less common ML_2X_2 double helicates with monoatomic or small double M-X-M bridges, the symmetry is reduced to C_2, with the main molecular axis along the center of opposite edges of the octahedra (Figure 13, right).

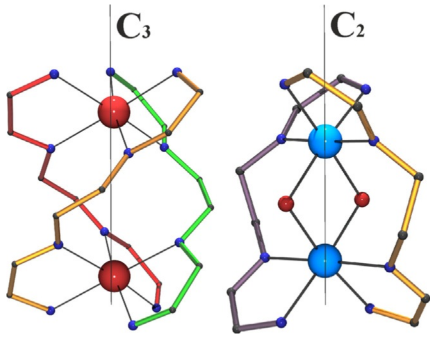

Figure 13. Main axial symmetry for triple M_2L_3 (lower NCCN torsion) and ML_2X_2 double helicates (larger NCCN torsion).

This arrangement requires larger NCCN torsion angles closer to 90°, as has been experimentally proved for $[Ni_2(L5)_2(\mu_{11}\text{-}N_3)_2](ClO_4)_2$ (NCCN = 78(1)°/80.0(9)°), $[Ni_2(L6)_2(\mu_{11}\text{-}N_3)_2](ClO_4)_2$ (NCCN = 92.8(4)°/93.4(4)°), $[Ni_2(L6)_2(\mu_{11}\text{-}NCO)_2](ClO_4)_2$ (NCCN = 93.8(4)°/94.0(4)°),[38] $[Co_2(L5)_2(\mu\text{-}O)(\mu\text{-}(O_2)]A_2$ (A = BF_4^-, NCCN = 80.2(5)°/81.1(5)°; A = ClO_4^-, NCCN = 80.5(3)°/81.1(3)°).[39,40]

In light of these data, our aim was to explore the reactivity of ligands with different flexibility or aromatic donors with different size in order to tune the selective syntheses of homochiral ($\Lambda\Lambda$ or $\Delta\Delta$) helicate or heterochiral ($\Lambda\Delta$) mesocate structures for the ML_2X_2 case and to obtain experimental evidence of the factors that determine the formation of one or another type of structure.

Steric requirements were centered on the flexibility of the C–C central spacer and size of the aromatic rings. Our starting point was the analysis of the experimentally reported torsion angles on the C–C=NCCN=C–C fragment belonging to any kind of Schiff bases for the spacers cyclohexane (690 structures), methylethyl (72 structures) and ethyl (2865 structures). From these data emerge two interesting features: first, the preferred NCCN torsion angle of the spacer lies around 40–50°, with practically 50 % of the structures falling in this range and, second, the ethyl fragment appears to be more flexible than the cyclohexane or methylethyl fragments, showing several structures with NCCN torsion angles larger than 80° (Figure S2). The same analysis for the pyridyl ligands L1 (46 structures), L3 (9 structures), and L5 (95 structures) reflect the same general trends; that is to say, the same preferred torsion angle and the larger flexibility of the ethyl fragment. For L1 in all cases the NCCN torsion is comprised between 39.5° and 73.8° with one unique case reaching 78°; for L3 the torsion lies in the very short range of 45.2–66.6°; whereas, for L5 it spans all values between 0° and 93.8° (Figure S3). There are a few reported complexes for the quinolyl ligands L2 (12 structures), L4 (zero structures), and L7 (3 structures), and although the available information is scarce, it indicates that the NCCN torsion for L1 is limited to a short range of angles comprised between 53–66°. From this structural analysis, the larger flexibility of the ligand for unsubstituted spacers and smaller ring size can be inferred.

As could be expected, the most rigid ligands are those containing the cyclohexane ring, which prevents extreme torsions; effectively, L1 and L2 are not flexible enough in the spacer to produce the helicate. As experimental confirmation, the mesocate arrangement was obtained for **1M**, **1*SS***, **1*RR***, **2*SS***, and **2*RR***.

L3 and L4 should, in principle, be slightly more flexible in the spacer than their analogous L1 and L2 with cyclohexane spacer, and, according to the previous analysis, L3 should be more flexible than L4. Then, is not surprising that the mesocate arrangement is the preferred form for **4*R***, whereas both helicate and mesocate forms seem to be equally preferred for L3. In the same way and following the same tendencies, both forms seem to be equally favored for the quinolyl ligand L7 with an ethyl spacer, whereas the helicate is exclusively formed for the previously reported[38–40] most flexible ligands L5 and L6.

Thus, we can conclude that the combination of the flexibility of the spacer and the difference in the volume of the aromatic chromophore, promotes a well-established effect on the resulting supramolecular arrangement, showing a perfect transition from mesocate to helicate arrangement for the $ML_2(\mu\text{-}X)_2$ case. The combination of both effects can be graphically seen in Scheme 3.

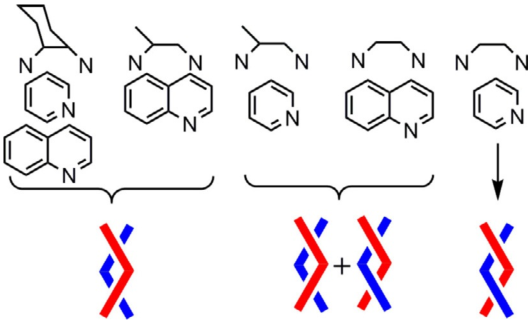

Scheme 3. Helicate to mesocate transition as function of the spacer and ring size of the Schiff bases.

On the other hand, the transfer of chirality from the chiral center of the ligands to the cations or the whole supramolecular assembly is a common fact and it is widely accepted that chiral molecules (ligands in the particular case of coordination chemistry) generate chiral supramolecular systems. This interesting feature, where the ligand transfers its chirality to the metal centers, has been called predetermined chirality,[9,41,42] with the $\Lambda\Lambda$ or $\Delta\Delta$ configurations of the stereogenic metal centers being completely controlled by the chiral configuration of the ligands.[54] In our case, this assumption means that the employment of enantiomerically pure ligands should lead to the formation of homochiral helicates with homochirality at the level of the metal centers and helicity of the molecules. However, in contrast with these rules, for compounds **1*SS***, **1*RR***, **2*SS***, **2*RR***, and **4*R*** for which chiral ligands were employed, the mesocate configuration was obtained. These results highlight the possibility that even when the ligand has a stereodefined chiral center and the bridging mode of the ligand allows for conformational chirality, the final structure cannot present an overall chirality by rational control of the properties of the ligand. On the other hand, the final mesocates retain the chirality only through the presence of asymmetric C-atoms of the ligands, resulting in the extremely unusual chiral mesocates.

Susceptibility studies

The magnetic response for double azido bridges with Ni-N-Ni bond angles has been well established, giving strong ferromagnetic interaction for bond angles around 100°.[55] To check the magnetic properties of the reported compounds, susceptibility measurements were performed for the series of compounds **1** and **2. 1M**, **1*RR***, and **1*SS*** show quasi identical plots, as does the pair of **2*RR*** and **2*SS*** isomers. Therefore, only one measurement for each family of enantiomers will be discussed. The room-temperature $\chi_M T$ value for compound **1*RR*** of 2.62 $cm^3 mol^{-1} K$ is larger than the expected value for two isolated $S=1$ centers (2.0 $cm^3 mol^{-1} K$ for $g=2.00$). Upon cooling, the $\chi_M T$ product increases gradually to 16 K (3.56 $cm^3 mol^{-1} K$). Below this temperature, the $\chi_M T$ product decreases to 3.15 $cm^3 mol^{-1} K$ at 2 K (Figure 14). Complex **2*RR*** has a similar response, with a room-temperature $\chi_M T$ value of 2.77 $cm^3 mol^{-1} K$, a maximum value of 3.56 $cm^3 mol^{-1} K$ at 20 K and a final value of 3.23 $cm^3 mol^{-1} K$ at 2 K. The $\chi_M T$ plots evidence strong intramolecular ferromagnetic interactions between the Ni^{II} centers. Considering that the structural data do not show relevant intercluster interactions, the decay of $\chi_M T$ at low temperature should be attributed to *D* effects.

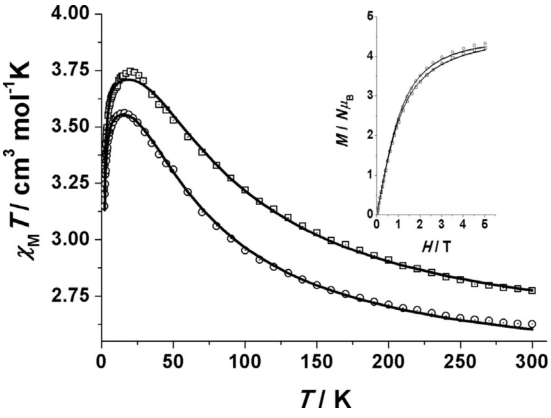

Figure 14. Plot of the $\chi_M T$ product versus *T* for compounds **1*RR*** (circles) and **2*RR*** (squares). Inset, magnetization plots. Solid lines show the best fits of the experimental data.

A fit of the experimental data was performed in the full range of temperature by using the PHI program[56] based on the Hamiltonian $H=-2J_1(S_1 \cdot S_2)$ and including a D_{ion} term.

The best fit of the experimental data gave $J=+14.9$ cm^{-1}, $g=2.18$ and $D_{ion}=2.07$ cm^{-1} for **1*RR*** ($R=8.1\times10^{-6}$), and $J=+19.2$ cm^{-1}, $g=2.23$ and $D_{ion}=2.30$ cm^{-1} for **2*RR*** ($R=1.8\times10^{-5}$). From these *J* values it can be inferred that the ground state is a well isolated $S=2$ level. The magnetization data show quasi-saturated values of 4.32 and 4.24 Nμβ for **1*RR*** and **2*RR***, respectively. These results show good agreement with the expected magnetic response and the reported values for $[Ni_2(L5)(N_3)_2](ClO_4)_2$ and $[Ni_2(L5)(N_3)_2](ClO_4)_2$.[40]

Conclusion

A complete family of Ni^{II} dimers built from bis-bidentate Schiff bases with the general formula $[Ni_2(L)_2(N_3)_2]^{2+}$, showing the transition from mesocate to helicate conformation, has been structurally characterized and related to the flexibility of the central spacer of the ligands and the size of the substituents of the Schiff base (pyridyl/quinoxalyl). The ECD spectra in both the solid state and solution have been measured for two pairs of enantiomers showing that the systems are stable in solution and their spectra have been rationalized by DFT calculations. Notably, the unprecedented structure of complex **7** shows simultaneous crystallization of both conformations in the same unit cell and enables the characterization of the first coordination compound derived from the imine-quinoxalyl ligand L4.

Experimental Section

Physical measurements: Magnetic susceptibility measurements were carried out on polycrystalline samples with a MPMS5 Quantum Design susceptometer working in the range 30–300 K under magnetic fields of 0.3 T and under a field of 0.03 T in the 30–2 K range to avoid saturation effects at low temperature. Diamagnetic corrections were estimated from Pascal Tables. Infrared spectra (4000–400 cm^{-1}) were recorded from KBr pellets with a Bruker IFS-125 FT-IR spectrophotometer. ECD spectra were recorded with a Jasco J-710 spectropolarimeter. Solution spectra were recorded in 2×10^{-4} M CH_3CN solutions; solid-state spectra were recorded using the KCl pellet technique. To rule out the occurrence of contributions from linear dichroism/linear birefringence due to preferential orientation of the solid sample, the disc was rotated by 90°, 180°, 270° and then flipped around its C_2 axis. A spectrum was recorded after each rotation to check that no significant difference depending on the rotation angle was present. VCD spectra were recorded with a Jasco FVS 6000 spectropolarimeter on KCl discs.

DFT calculations: Calculations were run with Gaussian09, rev. D01,[57] starting from the X-ray geometry of **1*SS***, which was fully re-optimized at B3LYP/6-31G(d) level to a true energy minimum (no imaginary frequencies). A structure with +2 charge and quintet spin state was used in all calculations. Excited states TDDFT calculations were run with several different functionals, including B3LYP, CAM-B3LYP, X3LYP, BH&HLYP, PBE-1/3, and basis sets, including SVP, TZVP and LanL2DZ (with ECP for Ni), including up to 100 excited states (roots).

Single-crystal X-ray structure analyses: Prism-like specimens of **1M**, **1*SS***, **1*RR***, **2*SS***, **2*RR***, **4*R***, and **7** and multiple crystals of the complexes derived from L3 were used for the X-ray crystallographic analysis. The X-ray intensity data were measured with a D8-Venture system equipped with a multilayer monochromator and a Mo microfocus ($\lambda=0.71073$ Å). The frames were integrated with the Bruker SAINT software package using a narrow-frame algorithm. The final cell constants were based upon the refinement of the XYZ-centroids of reflections above 20 σ(*I*). Data were corrected for absorption effects by using the multi-scan method (SADABS). The structures were solved using the Bruker SHELXTL Software Package, and refined using SHELXL.[58] Details of crystal data, collection and refinement are summarized in Tables S6–S9. Analyses of the structures and plots for publication were performed with Ortep3[59] and POVRAY programs.

Syntheses

Schiff bases L1 and L2 were isolated as solids, whereas L3, L4, and L7 were prepared in situ and the ligand solution was employed directly to synthesize the corresponding complexes.

***Rac*-L1, *RR*-L1, and *SS*-L1**: Syntheses were common for the racemic or enantiomerically pure ligands *rac*-L1, *RR*-L1, and *SS*-L1. A solution of 2-pyridinecarboxaldehide (3.9 mmol) and the corresponding diaminociclohexane isomer (1.75 mmol) in methanol (20 mL) was stirred for 2 h at room temperature. Concentration in vacuo afforded ligands L1 as white solids that were recrystallized in diethyl ether.

***RR*-L2 and *SS*-L2**: A similar procedure was employed for *RR*-L2 and *SS*-L2. A solution of the corresponding isomer of 1,2-cyclohexanediamine (0.5 mmol) and 2-quinolinecarboxaldehide (1 mmol) were mixed in dichloromethane (20 mL) and stirred at room temperature for 24 h. After concentration to one half volume, the solution was mixed with *n*-hexane (20 mL). L2 was collected as a yellowish powder. Recrystallization in diethyl ether afforded the yellowish crystals used for syntheses. IR spectra are shown in Figure S4.

$[Ni_2(L)_2(N_3)_2](NO_3)_2 \cdot n$MeOH (L=L1, 1M·2MeOH, 1*RR*·2MeOH, 1*SS*·2MeOH; L=L2, 2*RR*·3MeOH, 2*SS*·3MeOH): The complexes were synthesized by following the same experimental procedure: The corresponding L1 or L2 ligand (1 mmol) and $Ni(NO_3)_2 \cdot 6H_2O$ (1 mmol) were solved in methanol (20 mL) and stirred for some minutes. To this solution was added sodium azide (1 mmol) solved in methanol (5 mL). Crystallization by vapor diffusion of diethyl ether afforded well-formed reddish crystals after one to two days. Anal. Calcd/found (%) for **1*M*/1*RR*/1*SS*** as $C_{38}H_{48}N_{16}Ni_2O_8$: C, 46.85/46.8/464/46.5; H, 4.97/4.6/4.3/5.1; N, 23.00/22.9/23.2/23.4. Calc/found (%) for **2*RR*/2*SS*** as $C_{55}H_{60}N_{16}Ni_2O_9$: C, 54.75/53.9/54.3/54.2; H, 5.01/4.8/4.7/5.2; N, 18.57/18.9/18.3/18.5. IR spectra are shown in Figure S4.

$[Ni_2(R\text{-}L4)_2(N_3)_2](ClO_4)_2 \cdot H_2O$ (4*R*·0.25H$_2$O): Synthesized by preparing the ligand in situ by mixing *R*- or *S*-1,2-diaminopropane hydrochloride (0.25 mmol) with triethilamine (0.5 mmol) and quinoline carboxaldehyde (0.5 mmol). The mixture was heated to reflux in MeOH for 1 h. After cooling, $Ni(ClO_4)_2 \cdot 6H_2O$ (0.25 mmol) and NaN_3 (0.25 mmol) were added. The mixture was stirred at room temperature for 30 min and filtered. Crystallization by vapor diffusion of diethyl ether produced well-formed reddish crystals after a few days. Anal. Calcd/found (%) for **4*R*** as $C_{46}H_{40.5}Cl_2N_{14}Ni_2O_{8.25}$: C, 49.79/49.3; H, 3.67/3.8; N, 17.67/17.4. IR spectra are shown in Figure S5.

$[Ni_2(L3)_2(N_3)_2](X)_2$ (3) ($X=NO_3^-$, ClO_4^-): The six complexes derived from L3 (*meso*, *R* and *S*) were synthesized in the search for adequate crystals to obtain structural information, but all data collection were unsuccessful. The syntheses were performed by following the same procedure employed for **4*R***. IR spectra are shown in Figure S6.

© 2018 Wiley-VCH Verlag GmbH & Co. KGaA, Weinheim

$[Ni_2(L7)_2(N_3)_2](NO_3)_2 \cdot 2\,H_2O \cdot 2MeOH$ (7·$2\,H_2O \cdot 2MeOH$): Prepared by synthesizing the ligand in situ by mixing ethylenediamine (0.025 mmol) and quinoline carboxaldehide (0.5 mmol) and heating to reflux for 1 h. After cooling, $Ni(NO_3)_2 \cdot 6\,H_2O$ (0.25 mmol) and sodium azide (0.25 mmol) were added and the mixture was stirred at room temperature 30 min. The solution was filtered and layered with diethyl ether. Red crystals were obtained after a few days. Anal. Calcd/found (%) for **7** as $C_{67}H_{61}N_{24}Ni_3O_{11}$: C, 51.77/51.5; H, 3.96/3.8; N, 21.63/21.8. IR spectrum is shown in Figure S5.

Acknowledgements

JM and AE thank the Ministerio de Economia *y* Competitividad (Project CTQ2015-63614-P) for financial support.

Conflict of interest

The authors declare no conflict of interest.

Keywords: chirality · circular dichroism · solid-state structures · helicate · mesocate · nickel

[1] O. Mamula, A. von Zelewsky, *Coord. Chem. Rev.* **2003**, *242*, 87 – 95.
[2] D. Amabilino, *Chirality at the Nanoscale, Nanoparticles, Surfaces, Materials and More*, Wiley-VCH, Weinheim, **2009**.
[3] A. Myari, N. Hadjiliadis, A. Garoufis, *J. Inorg. Biochem.* **2005**, *99*, 616 – 626.
[4] E. Francotte, W. Lindner, *Chirality in Drug Research*, Wiley-VCH, Weinheim, **2006**.
[5] K. Szacilowski, W. Mazyk, A. Drzewiecka-Matuszek, M. Brindell, G. Stochel, *Chem. Rev.* **2005**, *105*, 2647 – 2694.
[6] E. Yashima, N. Ousaka, D. Taura, K. Shimomura, T. Ikai, K. Maeda, *Chem. Rev.* **2016**, *116*, 13752 – 13990.
[7] Y. Inoue, V. Ramamurthy, *Chiral Photochemistry*, Marcel Dekker, New York **2004**, pp. 261 – 313.
[8] K. Mikami, M. Lantens, *New Frontiers in Asymmetric Catalysis*, Wiley, Hoboken, **2007**.
[9] R. Gómez Arrayás, J. Adrio, J. C. Carretero, *Angew. Chem. Int. Ed.* **2006**, *45*, 7674 – 7715; *Angew. Chem.* **2006**, *118*, 7836 – 7878.
[10] G. C. Fu, *Acc. Chem. Res.* **2006**, *39*, 853 – 860.
[11] T. Katsuki, *Chem. Soc. Rev.* **2004**, *33*, 437 – 444.
[12] G. Chelucci, R. P. Thummel, *Chem. Rev.* **2002**, *102*, 3129 – 3170.
[13] J. M. Lehn, *Supramolecular Chemistry: Concepts and Perspectives*, VCH, Weinheim, **1995**.
[14] J. W. Steel, J. L. Atwood, *Supramolecular Chemistry*, 2nd ed., Wiley, Chichester, **2009**.
[15] M. Albrecht, *Chem. Eur. J.* **2000**, *6*, 3485 – 3489.
[16] B. W. Ding, R. Keese, H. Stoeckli-Evans, *Angew. Chem. Int. Ed.* **1999**, *38*, 375 – 376; *Angew. Chem.* **1999**, *111*, 387 – 388.
[17] J. Xu, K. N. Raymond, *Angew. Chem. Int. Ed.* **2006**, *45*, 6480 – 6485; *Angew. Chem.* **2006**, *118*, 6630 – 6635.
[18] M. A. Masood, E. J. Enemark, T. D. P. Stack, *Angew. Chem. Int. Ed.* **1998**, *37*, 928 – 932; *Angew. Chem.* **1998**, *110*, 973 – 977.
[19] V. Amendola, L. Fabbrizzi, L. Linati, C. Mangano, P. Pallavicini, V. Pedrazzini, M. Zema, *Chem. Eur. J.* **1999**, *5*, 3679 – 3688.
[20] V. Amendola, L. Fabbrizzi, C. Mangano, P. Pallavicini, E. Roboli, M. Zema, *Inorg. Chem.* **2000**, *39*, 5803 – 5806.
[21] P. K. Pal, S. Chowdhury, P. Purkayastha, D. A. Tocher, D. Datta, *Inorg. Chem. Commun.* **2000**, *3*, 585 – 589.
[22] V. Amendola, L. Fabbrizzi, L. Gianelli, C. Maggi, C. Mangano, P. Pallavicini, M. Zema, *Inorg. Chem.* **2001**, *40*, 3579 – 3587.
[23] R. Ziessel, P. Nguyen, L. Douce, M. Cesario, C. Estournes, *Org. Lett.* **2004**, *6*, 2865 – 2868.
[24] G. K. Patra, I. Goldberg, *New J. Chem.* **2003**, *27*, 1124 – 1131.
[25] N. C. Habermehl, P. M. Angus, N. L. Kilah, L. Noren, A. D. Rae, A. C. Willis, S. B. Wild, *Inorg. Chem.* **2006**, *45*, 1445 – 1462.
[26] A. Ouali, M. Taillefer, J. F. Spindler, A. Jutand, *Organometallics* **2007**, *26*, 65 – 74.
[27] P. Pallavicini, M. Boiocchi, G. Dacarro, C. Mangano, *New J. Chem.* **2007**, *31*, 927 – 935.
[28] V. Amendola, M. Boiocchi, V. Brega, L. Fabbrizzi, L. Mosca, *Inorg. Chem.* **2010**, *49*, 997 – 1007.
[29] M. Boiocchi, V. Brega, C. Ciarrocchi, L. Fabbrizzi, P. Pallavicini, *Inorg. Chem.* **2013**, *52*, 10643 – 10652.
[30] G. C. van Stein, G. van Koten, K. Vrieze, C. Brevard, A. L. Spek, *J. Chem. Soc., Chem. Commun.* **1980**, 1016 – 1018.
[31] G. C. van Stein, G. van Koten, K. Vrieze, C. Brevard, A. L. Spek, *J. Am. Chem. Soc.* **1984**, *106*, 4486 – 4492.
[32] P. K. Bowyer, K. A. Porter, A. D. Rae, A. C. Willis, S. B. Wild, *Chem. Commun.* **1998**, 1153 – 1154.
[33] V. Amendola, Y. D. Fernandez, C. Mangano, M. Montalti, P. Pallavicini, L. Prodi, N. Zaccheroni, M. Zema, *Dalton Trans.* **2003**, 4340 – 4345.
[34] A. D. Amirnasr, M. Khalaji, R. Welter, *Anal. Sci.* **2006**, *22*, x151 – x152.
[35] E. C. Constable, G. Zhang, C. E. Housecroft, J. A. Zampese, *CrystEngComm* **2010**, *12*, 3724 – 3732.
[36] E. C. Constable, G. Zhang, C. E. Housecroft, M. Neuburger, J. A. Zampese, *Eur. J. Inorg. Chem.* **2010**, 2000 – 2011.
[37] E. C. Constable, G. Zhang, C. E. Housecroft, J. A. Zampese, *Dalton Trans.* **2010**, *39*, 5332 – 5340.
[38] T. Takeda, S. Harada, A. Nishida, *Org. Lett.* **2015**, *17*, 5184 – 5187.
[39] Y. I. Cho, D. M. Joseph, M. J. Rose, *Inorg. Chem.* **2013**, *52*, 13298 – 13300.
[40] M. Habib, T. K. Karmakar, G. Aromi, J. Ribas-Arino, H.-K. Fun, S. Chantrapromma, S. K. Chandra, *Inorg. Chem.* **2008**, *47*, 4109 – 4117.
[41] J. Crassous, *Chem. Soc. Rev.* **2009**, *38*, 830 – 845.
[42] M. Liu, L. Zhang, T. Wang, *Chem. Rev.* **2015**, *115*, 7304 – 7397.
[43] A. Frontera, P. Gamez, M. Mascal, T. J. Mooibroek, J. Reedijk, *Angew. Chem. Int. Ed.* **2011**, *50*, 9564 – 9583; *Angew. Chem.* **2011**, *123*, 9736 – 9756.
[44] M. Nishio, *CrystEngComm* **2004**, *6*, 130 – 158.
[45] R. Berardozzi, E. Badetti, N. A. Carmo dos Santos, K. Wurst, G. Licini, G. Pescitelli, C. Zonta, L. Di Bari, *Chem. Commun.* **2016**, *52*, 8428 – 8431.
[46] S. R. Domingos, H. J. Sanders, F. Hartl, W. J. Buma, S. Woutersen, *Angew. Chem. Int. Ed.* **2014**, *53*, 14042 – 14045; *Angew. Chem.* **2014**, *126*, 14266 – 14269.
[47] L. A. Nafie, *J. Phys. Chem. A* **2004**, *108*, 7222 – 7231.
[48] G. Pescitelli, T. Kurtán, U. Flörke, K. Krohn, *Chirality* **2009**, *21*, E181 – E201.
[49] D. Padula, S. Di Pietro, M. A. M. Capozzi, C. Cardellicchio, G. Pescitelli, *Chirality* **2014**, *26*, 462 – 470.
[50] M. Srebro-Hooper, J. Autschbach, *Annu. Rev. Phys. Chem.* **2017**, *68*, 399 – 420.
[51] A. Ipatov, F. Cordova, L. J. Doriol, M. E. Casida, *J. Mol. Struct.* **2009**, *914*, 60 – 73.
[52] M. Enamullah, M. A. Quddus, M. R. Hasan, G. Pescitelli, R. Berardozzi, G. Makhloufi, V. Vasylyeva, C. Janiak, *Dalton Trans.* **2016**, *45*, 667 – 680.
[53] M. E. Casida, C. Jamorski, K. C. Casida, D. R. Salahub, *J. Chem. Phys.* **1998**, *108*, 4439 – 4449.
[54] A. Lützen, M. Hapke, J. Griep-Raming, D. Haase, W. Saak, *Angew. Chem. Int. Ed.* **2002**, *41*, 2086 – 2089; *Angew. Chem.* **2002**, *114*, 2190 – 2194.
[55] A. Escuer, J. Esteban, S. P. Perlepes, T. C. Stamatatos, *Coord. Chem. Rev.* **2014**, *275*, 87 – 129.
[56] N. F. Chilton, R. P. Anderson, L. D. Turner, A. Soncini, K. S. Murray, *J. Comput. Chem.* **2013**, *34*, 1164 – 1165.
[57] Gaussian 09, Revision D.01, M. J. Frisch, G. W. Trucks, H. B. Schlegel, G. E. Scuseria, M. A. Robb, J. R. Cheeseman, G. Scalmani, V. Barone, B. Mennucci, G. A. Petersson, H. Nakatsuji, M. Caricato, X. Li, H. P. Hratchian, A. F. Izmaylov, J. Bloino, G. Zheng, J. L. Sonnenberg, M. Hada, M. Ehara, K. Toyota, R. Fukuda, J. Hasegawa, M. Ishida, T. Nakajima, Y. Honda, O. Kitao, H. Nakai, T. Vreven, J. A. Montgomery, Jr., J. E. Peralta, F. Ogliaro, M. Bearpark, J. J. Heyd, E. Brothers, K. N. Kudin, V. N. Staroverov, R. Kobayashi, J. Normand, K. Raghavachari, A. Rendell, J. C. Burant, S. S. Iyengar, J. Tomasi, M. Cossi, N. Rega, J. M. Millam, M. Klene, J. E. Knox, J. B. Cross, V. Bakken, C. Adamo, J. Jaramillo, R. Gomperts, R. E. Stratmann, O. Yazyev, A. J. Austin, R. Cammi, C. Pomelli, J. W. Ochterski, R. L. Martin, K. Morokuma, V. G. Zakrzewski, G. A. Voth, P. Salvador, J. J. Dannenberg,

S. Dapprich, A. D. Daniels, Ö. Farkas, J. B. Foresman, J. V. Ortiz, J. Cioslowski, D. J. Fox, Gaussian, Inc., Wallingford CT, 2009.
[58] G. M. Sheldrick, *Acta Crystallogr. Sect. A* **2008**, *64*, 112 – 122.
[59] L. J. Farrugia, *J. Appl. Crystallogr.* **1997**, *30*, 565.

Manuscript received: January 22, 2018
Accepted manuscript online: March 8, 2018
Version of record online: April 27, 2018

© 2018 Wiley-VCH Verlag GmbH & Co. KGaA, Weinheim

CHEMISTRY
A European Journal

Supporting Information

From Mesocates to Helicates: Structural, Magnetic and Chiro-Optical Studies on Nickel(II) Supramolecular Assemblies Derived from Tetradentate Schiff Bases

Júlia Mayans,[a] Mercè Font-Bardia,[b] Lorenzo Di Bari,[c] Lorenzo Arrico,[c] Francesco Zinna,[c] Gennaro Pescitelli,[c] and Albert Escuer*[a]

chem_201800323_sm_miscellaneous_information.pdf

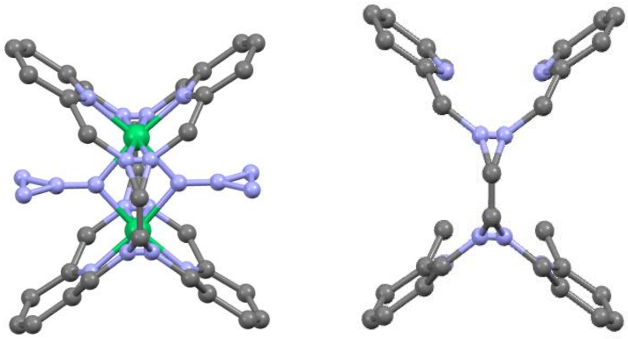

Figure S1. View of one image of one of the trials to solve the structure of one L3 derivative (left) and plot of the isolated ligand fragment (right) showing the mix of helicate/mesocate conformations. All trials to solve the structure of L3 derivatives shows the same disorder on the azide ligand.

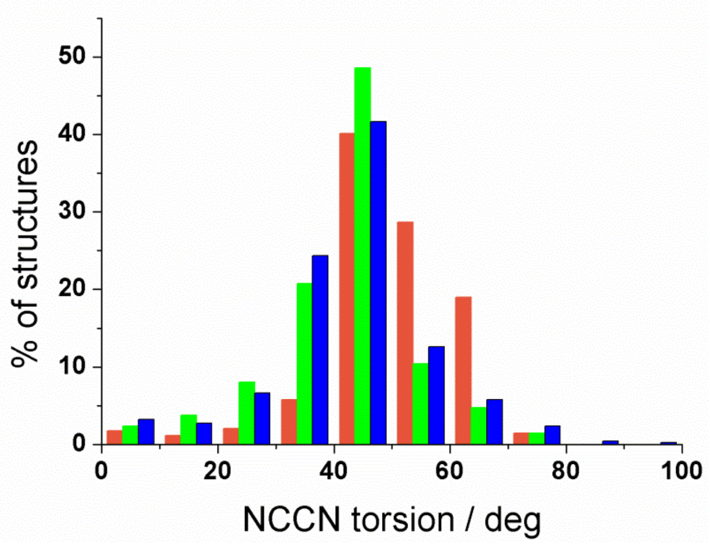

Figure S2. Plot of the number of structures (%) versus NCCN torsion angle for any kind of Schiff base with cyclohexane (over 690 structures, orange), Me-en (over 72 structures, green) and ethylene spacers (over 2865 structures, blue).

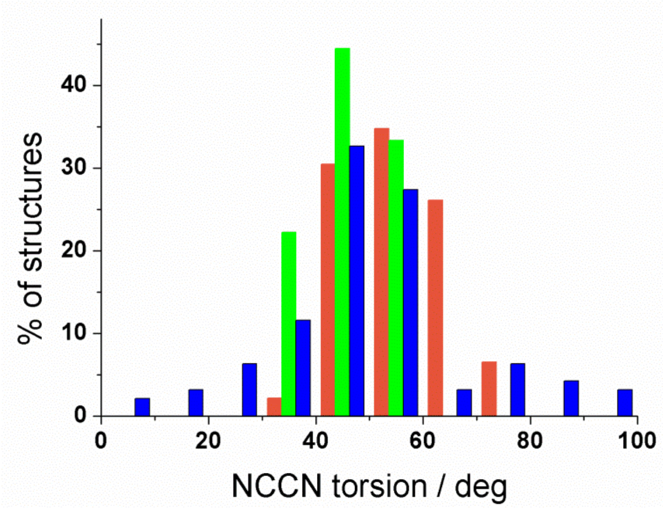

Figure S3. Plot of the number of structures (%) versus NCCN torsion angle for the Schiff bases L1 (over 46 structures, orange), L3 (over 9 structures, green) and L5 (over 95 structures, blue) evidencing the larger flexibility of L5.

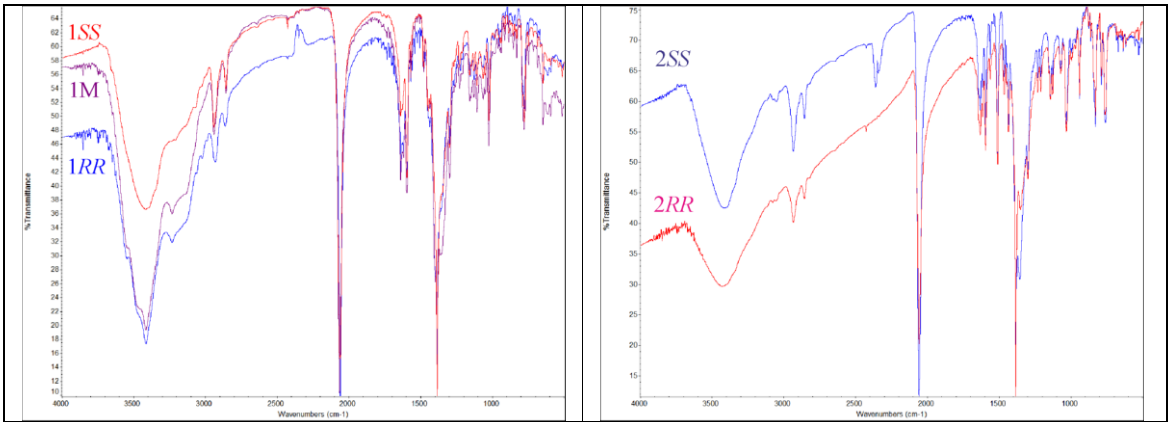

Figure S4. IR spectra for complexes **1M**, **1*RR*** and **1*SS*** (left) and **2*RR*** and **12*S*** (right).

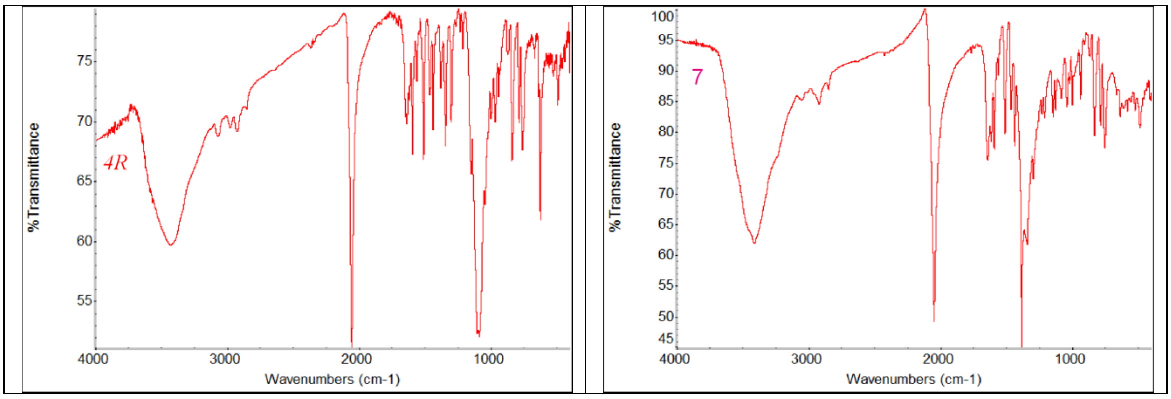

Figure S5. IR spectra for complexes **4*R*** (left) and **7** (right).

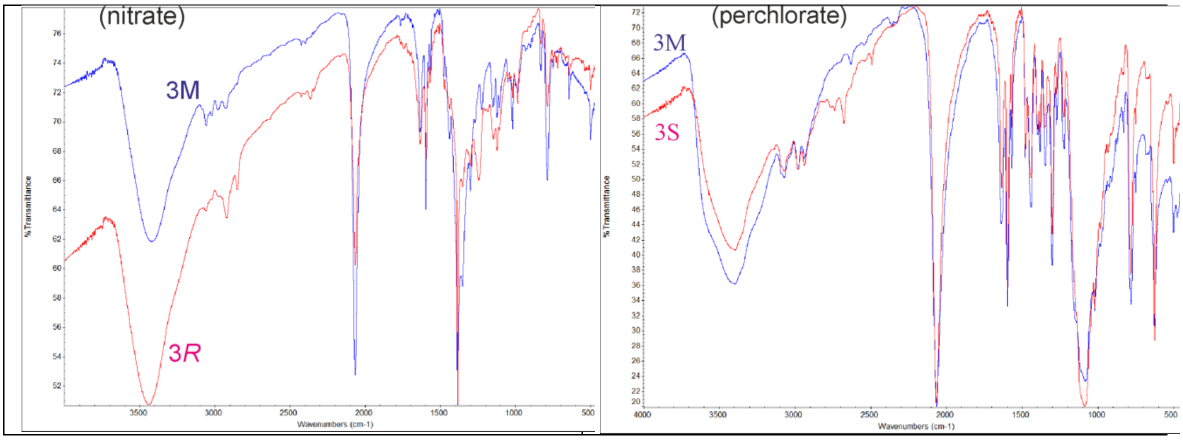

Figure S6.IR spectra for *meso* or chiral complexes derived from ligand L3 with nitrate or perchlorate counteranions. All spectra show similar trends such the aliphatic or aromatic C-H peaks, the asymmetric stretching of the end-on azido bridge around 2060 cm^{-1}, the C=N strtching over 1600 cm-1 and the strong bands due to the ionic nitrate (1, 2, 3 and 7) or perchlorate for 3 and 4*R*.

Table S1. Selected distances (Å) and angles (º) for the Ni^{II} environment of compound **1M**.

Ni(1)-N(1)	2.050(1)	Ni(1)-N(4‘)	2.050(1)
Ni(1)-N(2)	2.079(1)	Ni(1)-N(5)	2.104(1)
Ni(1)-N(3‘)	2.112(1)	Ni(1)-N(5‘)	2.099(1)
N(1)-Ni(1)-N(2)	80.26(4)	N(1)-Ni(1)-N(5)	170.28(4)
N(3‘)-Ni(1)-N(4‘)	79.80(4)	N(2)-Ni(1)-N(3‘)	176.54(4)
N(1)-Ni(1)-N(4‘)	94.03(4)	N(4‘)-Ni(1)-N(5‘)	172.66(4)
Ni(1)-N(5)-Ni(1‘)	92.41(4)		

Table S2. Selected distances (Å) and angles (º) for the Ni^{II} environment of compound **1*RR***.

Ni(1)-N(1)	2.058(2)	Ni(2)-N(3)	2.052(2)
Ni(1)-N(2)	2.153(2)	Ni(2)-N(4)	2.060(2)
Ni(1)-N(5)	2.045(2)	Ni(2)-N(7)	2.056(2)
Ni(1)-N(6)	2.131(2)	Ni(2)-N(8)	2.055(2)
Ni(1)-N(9)	2.090(2)	Ni(2)-N(9)	2.110(2)
Ni(1)-N(12)	2.094(2)	Ni(2)-N(12)	2.120(2)
N(1)-Ni(1)-(N2)	79.93(9)	N(3)-Ni(2)-(N4)	80.10(9)
N(5)-Ni(1)-(N6)	80.6(1)	N(7)-Ni(2)-(N8)	79.9(1)
N(1)-Ni(1)-(N5)	91.44(9)	N(4)-Ni(2)-(N8)	97.27(9)
N(1)-Ni(1)-(N12)	173.5(1)	N(4)-Ni(2)-(N12)	168.37(9)
N(5)-Ni(1)-(N9)	172.5(1)	N(8)-Ni(2)-(N9)	169.63(9)
N(2)-Ni(1)-(N6)	177.8(1)	N(3)-Ni(2)-(N7)	177.3(1)
Ni(1)-N(9)-Ni(2)	92.5(1)	Ni(1)-N(12)-Ni(2)	92.1(1)

Table S3. Selected distances (Å) and angles (º) for the Ni^{II} environment of compound **2*RR*** (A).

Ni(1)-N(1)	2.121(4)	Ni(2)-N(3)	2.176(4)
Ni(1)-N(2)	2.059(4)	Ni(2)-N(4)	2.125(5)
Ni(1)-N(5)	2.115(4)	Ni(2)-N(7)	2.158(4)
Ni(1)-N(6)	2.054(4)	Ni(2)-N(8)	2.117(4)
Ni(1)-N(9)	2.137(4)	Ni(2)-N(9)	2.098(4)
Ni(1)-N(12)	2.122(4)	Ni(2)-N(12)	2.107(4)
N(1)-Ni(1)-(N2)	78.2(2)	N(3)-Ni(2)-(N4)	78.3(2)
N(5)-Ni(1)-(N6)	78.8(2)	N(7)-Ni(2)-(N8)	78.3(2)
N(1)-Ni(1)-(N5)	100.1(2)	N(4)-Ni(2)-(N8)	97.2(2)
N(1)-Ni(1)-(N9)	163.6(2)	N(4)-Ni(2)-(N9)	166.6(2)
N(5)-Ni(1)-(N12)	163.9(2)	N(8)-Ni(2)-(N12)	168.9(2)
N(2)-Ni(1)-(N6)	171.9(2)	N(3)-Ni(2)-(N7)	172.0(2)
Ni(1)-N(9)-Ni(2)	99.0(2)	Ni(1)-N(12)-Ni(2)	99.2(2)

T**able S4.** Selected distances (Å) and angles (º) for complex **4*R*** (A).

Ni(1)-N(1)	2.105(6)	Ni(2)-N(3)	2.080(7)
Ni(1)-N(2)	2.189(7)	Ni(2)-N(4)	2.124(6)
Ni(1)-N(7)	2.172(6)	Ni(2)-N(5)	2.126(6)
Ni(1)-N(8)	2.157(6)	Ni(2)-N(6)	2.064(6)
Ni(1)-N(9)	2.093(6)	Ni(2)-N(9)	2.084(6)
Ni(1)-N(12)	2.109(5)	Ni(2)-N(12)	2.111(5)
N(1)-Ni(1)-(N2)	78.5(2)	N(3)-Ni(2)-(N4)	78.3(3)
N(7)-Ni(1)-(N8)	77.9(2)	N(5)-Ni(2)-(N6)	78.4(2)
N(1)-Ni(1)-(N8)	100.3(2)	N(4)-Ni(2)-(N5)	100.1(2)
N(1)-Ni(1)-(N12)	165.8(3)	N(5)-Ni(2)-(N9)	162.4(3)
N(8)-Ni(1)-(N9)	167.7(2)	N(4)-Ni(2)-(N12)	163.8(3)
N(2)-Ni(1)-(N7)	173.2(2)	N(3)-Ni(2)-(N6)	171.9(2)
Ni(1)-N(9)-Ni(2)	98.3(2)	Ni(1)-N(12)-Ni(2)	96.9(2)

T**able S5.** Selected distances (Å) and angles (º) for complex **7**.

7A (Helicate)			
Ni(1)-N(1)	2.169(4)	Ni(2)-N(3)	2.060(5)
Ni(1)-N(2)	2.063(4)	Ni(2)-N(4)	2.185(4)
Ni(1)-N(5)	2.178(4)	Ni(2)-N(7)	2.069(4)
Ni(1)-N(6)	2.072(4)	Ni(2)-N(8)	2.164(5)
Ni(1)-N(9)	2.095(4)	Ni(2)-N(9)	2.118(4)
Ni(1)-N(12)	2.125(4)	Ni(2)-N(12)	2.123(4)
N(1)-Ni(1)-(N2)	79.1(2)	N(3)-Ni(2)-(N4)	79.19(17)
N(5)-Ni(1)-(N6)	78.0(2)	N(7)-Ni(2)-(N8)	79.9(2)
N(1)-Ni(1)-(N5)	100.2(2)	N(4)-Ni(2)-(N8)	100.1(2)
N(1)-Ni(1)-(N12)	168.9(2)	N(4)-Ni(2)-(N9)	168.8(2)
N(5)-Ni(1)-(N9)	169.0(2)	N(8)-Ni(2)-(N12)	169.3(2)
N(2)-Ni(1)-(N6)	176.3(2)	N(3)-Ni(2)-(N7)	177.2(2)
Ni(1)-N(9)-Ni(2)	100.5(2)	Ni(1)-N(12)-Ni(2)	99.3(2)
7B (Mesocate)			
Ni(3)-N(15)	2.120(4)	Ni(3)-N(18')	2.159(4)
Ni(3)-N(16)	2.035(4)	Ni(3)-N(19)	2.127(4)
Ni(3)-N(17')	2.113(4)	Ni(3)-N(19‘)	2.143(4)
N(15)-Ni(1)-N(16)	79.0(2)	N(15)-Ni(1)-N(19)	164.8(2)
N(17')-Ni(1)-N(18')	80.1(2)	N(18')-Ni(1)-N(19‘)	173.4(2)
N(15)-Ni(1)-N(18')	94.7(2)	N(16)-Ni(1)-N(17')	171.1(2)
Ni(3)-N(19)-Ni(3')	98.5(2)		

Table S6. Crystal data for coordination compounds **1*M*, 1*RR*** and **1*SS***

	1*M*	**1*RR***	**1*SS***
Formula	$C_{38} H_{48} N_{16} Ni_2 O_8$	$C_{38} H_{48} N_{16} Ni_2 O_8$	$C_{38} H_{48} N_{16} Ni_2 O_8$
FW	974.34	974.34	974.34
System	Triclinic	Triclinic	Triclinic
Space group	P-1	P1	P1
a/Å	9.6190(4)	9.7099(5)	9.7152(4)
b/Å	11.4185(6)	11.4058(6)	11.3990(5)
c/Å	11.9517(6)	11.9551(7)	11.9432(5)
α/deg.	98.989(2)°	98.915(2)°	98.935(2)°
ß/deg.	113.520(2)°	113.944(2)°	113.915(2)°
γ/deg.	109.217(2)°	109.171(2)°	109.278(2)°
V/ Å^3	1072.05(9)	1077.4(1)	1075.30(8)
Z	1	1	1
T, K	100(2)	100(2)	100(2)
λ(MoKα), Å	0.71073	0.71073	0.71073
ρcalc, g·cm-3	1.509	1.502	1.505
μ(MoK$_α$), mm^{-1}	0.950	0.945	0.947
Flack parameter	---	0.024(8)	0.028(9)
R	0.0377	0.0267	0.0271
ω*R*^{2}	0.0885	0.0649	0.0636

Table S7. Crystal data for coordination compounds **2*RR*** and **2*SS***

	2*RR*	**2*SS***
Formula	$C_{55} H_{60} N_{16} Ni_2 O_9$	$C_{55} H_{60} N_{16} Ni_2 O_9$
FW	1206.61	1206.61
System	Monoclinic	Monoclinic
Space group	P21	P21
a/Å	13.6384(4)	13.6681(7)
b/Å	18.8741(5)	18.8226(9)
c/Å	21.4093(6)	21.403(1)
α/deg.	90	90
ß/deg.	94.732(1)°	94.680(2)°
γ/deg.	90	90
V/ Å^3	5492.2(3)	5488.0(5)
Z	4	4
T, K	100(2)	100(2)
λ(MoKα), Å	0.71073	0.71073
ρcalc, g·cm-3	1.459	1.460
μ(MoK$_α$), mm^{-1}	0.759	0.759
Flack parameter	0.007(4)	0.003(2)
R	0.0418	0.0325
ω*R*^{2}	0.1017	0.0765

Table S8. Crystal data for coordination compounds **4*R*** and **7.**

	4*R*	**7**
Formula	$C_{184} H_{162} Cl_{8} N_{56} Ni_{8} O_{33}$	$C_{134} H_{122} N_{48} Ni_{6} O_{22}$
FW	4438.97	3109.05
System	Monoclinic	Triclinic
Space group	C2	P-1
a/Å	38.669(2)	11.9937(8)
b/Å	12.5528(5)	12.993(1)
c/Å	22.1896(11)	22.696(2)
α/deg.	90	84.965(4)°
ß/deg.	112.110(2)°	81.822(4)°
γ/deg.	90	73.178(3)°
V/ Å^3	9978.9(8)	3346.8(4)
Z	2	1
T, K	100(2)	100(2)
λ(MoKα), Å	0.71073	0.71073
ρcalc, g·cm-3	1.477	1.543
μ(MoK$_\alpha$), mm^{-1}	0.925	0.917
Flack parameter	0.47(4)	---
R	0.0360	0.0655
ωR^2	0.0700	0.1956

Table S9. Cell parameters for coordination compounds derived from ligand L3 (**3).**

	3*S* (NO$_3$)	**3M (ClO$_4$)**	**3*S* (ClO$_4$)**
Space group	I23	Im-3	R3
a/Å	17.9506(4)	18.2178(9)	25.866(1)
b/Å	17.9506(4)	18.2178(9)	25.866(1)
c/Å	17.9506(4)	18.2178(9)	15.8095(8)
α/deg.	90	90	90
ß/deg.	90	90	90
γ/deg.	90	90	120
V/ Å^3	5784.1	6046.3	9159.9
T, K	100(2)	100(2)	100(2)

Publication #2 "*Chiral tetranuclear Ni^{II} clusters derived from Schiff bases and azido co-ligands*"

Polyhedron 150 (2018) 10–14

Contents lists available at ScienceDirect

Polyhedron

journal homepage: www.elsevier.com/locate/poly

Chiral tetranuclear Ni^{II} clusters derived from Schiff bases and azido co-ligands

J. Mayans [a], A. Martin [a], M. Font-Bardia [b], A. Escuer [a,*]

[a] *Departament de Química Inorgànica i Orgànica, Secció Inorgànica and Institut de Nanociència i Nanotecnologia (IN²UB), Universitat de Barcelona, Martí i Franqués 1-11, Barcelona 08028, Spain*

[b] *Departament de Mineralogia, Cristal·lografia i Dipòsits Minerals, Universitat de Barcelona, Martí Franqués s/n, Barcelona-08028, and Unitat de Difracció de R-X. Centre Científic i Tecnològic de la Universitat de Barcelona (CCiTUB), Solé i Sabarís 1-3, Barcelona 08028, Spain*

ARTICLE INFO

Article history:
Received 28 February 2018
Accepted 2 May 2018
Available online 9 May 2018

Dedicated to Prof. Spyros P. Perlepes, great friend and maestro of scientists.

Keywords:
Nickel
Schiff base
Magnetism
Chirality
Circular dichroism

ABSTRACT

Chiral tetranuclear clusters have been obtained employing enantiomerically pure Schiff bases and azido coligands. The core of the new clusters shows defective dicubane topology with two vertices occupied by two $\mu_{1,1,1}$-N_3 ligands. Linkage between the Ni^{II} cations is completed with two μ-O(phenoxo) and two μ-Cl bridging ligands. The new systems have been characterized by single crystal X-ray analysis, electronic circular dichroism and susceptibility/magnetization measurements that reveal ferromagnetic response and strong positive zero field splitting of the $S = 4$ ground state.

© 2018 Elsevier Ltd. All rights reserved.

1. Introduction

Polytopic Schiff bases derived from *o*-vanillin and aminoalcohols are popular ligands in 3*d* and 4*f* chemistry due to their good chelating ability (around 180 entries in CCDC database). The 2-amino-1-ethanol (60 entries) and 3-amino-1-propanol (48 entries) are the most employed precursors but the large number of available substituted aminoalcohols has provided a wide family of Schiff bases. Among them, those derived from substituted 2-amino-1-ethanol (monosubstituted such 1-R and 2-R or disubstituted 1,2-R_2) are chirals, and become adequate precursors to obtain chiral coordination clusters. These systems attracted the attention of the synthetic chemists because they can be useful in the search of systems combining chirality with Single Molecule Magnet (SMM) response [1] and/or emissive 4*f* properties such Circular Polarized Luminescence (CPL) and/or ferroelectricity [2–5]. Reaction of *o*-vanillin with enantiomerically pure (*R*)- or (*S*)-2-phenylglycinol yields the chiral 2-(((2-hydroxy-1-phenylethyl)imino)methyl)-6-methoxyphenolato) (H_2L) base, Scheme 1, for which only one Cd^{2+}mononuclear derivative of the monodeprotonated HL^- ligand, [6] some pairs of enantiomers with $Mn^{III}_6Mn^{II}Na^{I}_2$ and Cu^{II}_6 nuclearity [2,7] or one *meso*-Ni^{II} cubane [8] complexes, derived of the fully deprotonated L^{2-} ligand, have been reported.

Metal–azide complexes have been extensively studied in recent years and the combination of Schiff bases with the azido co-ligands has been an interesting source of 3*d* transition Cu^{II}, Ni^{II}, Co^{II} and $Mn^{II,III}$ [9] or 4*f* Dy^{III} [10] clusters, usually presenting a ferromagnetic coupling due to the interactions mediated by $\mu_{1,1}$-N_3 or $\mu_{1,1,1}$-N_3 bridges.

The presence of $\mu_{1,1,1}$-N_3 bridges in nickel chemistry is often related to defective cubane fragments that span from Ni_3 [11] to larger assemblies that involve Ni_4, [12–16] Ni_5, [17] Ni_6, [18–21] Ni_7, [22] Ni_8, [23] Ni_{10} [24,25] and Ni_{13} [26] nuclearities. The scarce tetranuclear clusters with double defective dicubane core and two $\mu_{1,1,1}$-N_3 ligands show a variety of bridges between the central and peripheral Ni^{II} cations: two systems containing four Ni–O–Ni bridges [14,15], four systems with two Ni–O–Ni and two Ni–(N_3)–Ni bridges [13,16] and one rare complex with only azido bridges [12] have been reported, Fig. 1a–c.

In this work we present the characterization of a pair of enantiomeric Ni^{II} clusters obtained by the reaction of nickel chloride and sodium azide with the H_2L chiral Schiff base obtained by condensation of *o*-vanillin and (*R*)- or (*S*)-2-phenylglycinol, with molecular formula $[Ni_4(HL)_2Cl_2(\mu\text{-}Cl)_2(\mu_3\text{-}N_3)_2(MeOH)_2]$ (**1*R***, **1*S***).

---

* Corresponding author.
E-mail address: albert.escuer@ub.edu (A. Escuer).

https://doi.org/10.1016/j.poly.2018.05.002
0277-5387/© 2018 Elsevier Ltd. All rights reserved.

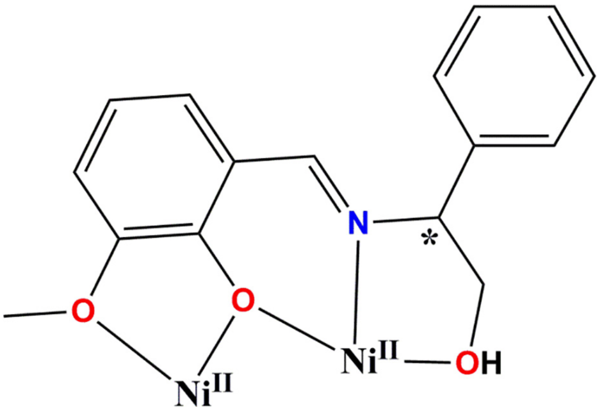

Scheme 1. Coordination of HL^- ligand to two Ni^{II} cations found in complexes **1*R*** and **1*S***. Asterisk denotes the chiral C-atom.

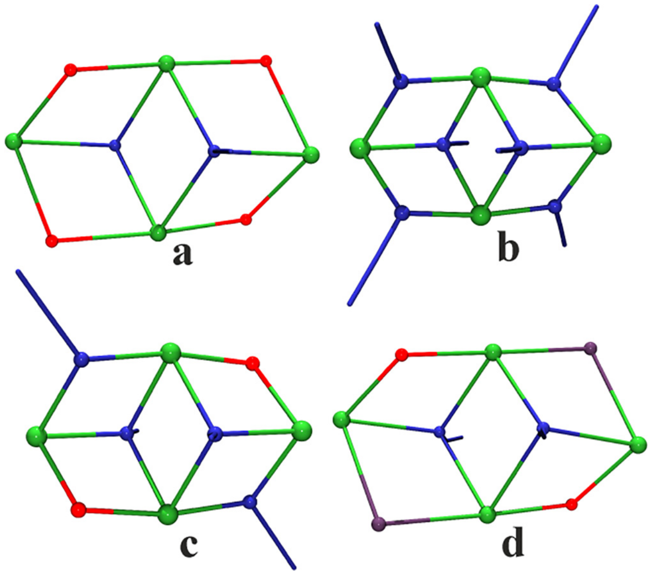

Fig. 1. Schematic representation of the reported defective dicubane Ni^{II} cores with double $\mu_{1,1,1}$-N_3 bridges. Core d corresponds to the complexes reported in this work. Color key for all figures: Ni^{II}, green; O, red; N, blue; Cl, violet. (Color online.)

The defective dicubane structure of these compounds exhibits a novel $\{Ni_4(\mu\text{-}Cl)_2(\mu_3\text{-}N_3)_2(\mu\text{-}O)_2\}$ core, Fig. 1d. Magnetic measurements reveal ferromagnetic interaction between the Ni^{II} cations, mediated by the μ_{111}-N_3 bridges and a large and positive anisotropy of the $S = 4$ ground state.

2. Experimental

2.1. Physical measurements

Magnetic measurements were carried out on polycrystalline samples with a MPMS5 Quantum Design susceptometer. Susceptibility data was measured working under magnetic fields of 0.3 T between 30–300 K and 0.03 T in the 300–2 K range of temperature to avoid saturation effects. Magnetization experiments were performed in the 0–5 T field range. Fit of the experimental data was calculated with PHI program [27]. Fit R quality factor was parametrized as $R = (\chi_M T_{\text{exp}} - \chi_M T_{\text{calc}})^2/(\chi_M T_{\text{exp}})^2$. Diamagnetic corrections were estimated from Pascal Tables. Infrared spectra (4000–400 cm^{-1}) were recorded from KBr pellets on a Bruker IFS-125 FT-IR spectrophotometer. EDC spectra were recorded in methanolic solutions in a Jasco-815 spectropolarimeter.

2.2. Syntheses

$[Ni_4(HL)_2Cl_2(\mu\text{-}Cl)_2(\mu_3\text{-}N_3)_2(MeOH)_2]\cdot$solvents (**1*R***$\cdot 0.75H_2O\cdot 0.25MeOH$ and **1*S***$\cdot 0.25MeOH\cdot 0.25H_2O$). The syntheses were the same for both complexes but starting from the corresponding enantiomerically pure (*R*)- or (*S*)-aminoalcohol.

Equimolecular amounts of (*R*)- or (*S*)-2-phenylglycinol (0.2 mmol, 0.034 g) and *o*-vanillin (0.2 mmol, 0.027 g) were solved in 10 mL of methanol and refluxed for one hour. Then, the resulting solution was cooled down to room temperature. $NiCl_2\cdot 6H_2O$ (0.095 g, 0.2 mmol) and sodium azide (0.015 g, 0.22 mmol) were solved in 15 mL of acetonitrile and mixed with the previously prepared ligand solution, resulting in a light green solution. Slow vapor diffusion with diethylether allows to the formation of green crystals in few days. *Anal.* Calc./found for **1*R***$\cdot 0.75H_2O\cdot 0.25MeOH$ ($C_{34.25}H_{40.5}Cl_4N_8Ni_4O_9$): C, 37.85/37.2, N, 10.31/10.6; H, 3.94/3.6. IR spectra for both compounds (cm^{-1}): 3058, 3025, 2943, 2850 (w, aromatic and aliphatic C–H st.), 2087 (s, assymm. st. N_3), 1630 (s, st. C═N), 1604 (m), 1472 (s), 1315, 1236 (m), 1216 (s), 1164, 1076, 1045, 1000 (w), 969 (m), 917, 862 (w), 771, 748, 702, 539 (w).

3. Crystallographic measurements

Green prism-like specimens of dimensions 0.081 mm × 0.130 mm × 0.259 mm (**1*R***) and 0.058 mm × 0.079 mm × 0.120 mm (**1*S***) were used for the X-ray crystallographic analysis. The X-ray intensity data were measured on a D8 Venture system equipped with a multilayer monochromator and a Mo microfocus (λ = 0.71073 Å).

The frames were integrated with the Bruker SAINT software package using a narrow-frame algorithm. The integration of the data using a monoclinic unit cell yielded a total of 23453 reflections to a maximum θ angle of 24.48 (0.86 Å resolution), of which 7567 were independent (average redundancy 3.099, completeness = 99.6%, R_{int} = 5.61%, R_{sig} = 6.12%) and 5687 (75.16%) were greater than $2\sigma(F^2)$ for **1*R*** and 22 669 reflections to a maximum θ angle of 26.42° (0.80 Å resolution), of which 9349 were independent (average redundancy 2.425, completeness = 99.3%, R_{int} = 7.74%, R_{sig} = 10.53%) and 5732 (61.31%) were greater than $2\sigma(F^2)$ for **1*S***. The final cell parameters are based upon the refinement of the XYZ-centroids of reflections above $20\sigma(I)$. Data were corrected for absorption effects using the multi-scan method (SADABS). The calculated minimum and maximum transmission coefficients (based on crystal size) are 0.6053 and 0.7451 for **1*R*** and 0.6285 and 0.7454 for **1*S***. The structures were solved and refined using the Bruker SHELXTL Software Package. Crystal and structure refinement data are summarized in Table 1.

4. Results and discussion

4.1. Structural description

The structures of the two enantiomers are identical and only minor differences in some bond parameters can be found. Thus, to avoid repetitive descriptions the following structural comments will be referred to the **1*R*** enantiomer assuming that can be applied to **1*S***.

The labeled molecular structure of **1*R*** is shown in Fig. 2 and selected bond parameters are summarized in Table 2. The structure consists of tetranuclear Ni^{II} clusters with defective face-sharing dicubane topology. The Ni^{II} cations are linked by two $\mu_{1,1,1}$-N_3

Table 1
Crystal data and structure refinement for coordination compounds **1*R*** and **1*S***.

	1*R*·0.75H_2O·0.25CH_3OH	**1*S***·0.25CH_3OH·0.25H_2O
Formula	$C_{137}H_{162}Cl_{16}N_{32}Ni_{16}O_{36}$	$C_{137}H_{150}Cl_{16}N_{32}Ni_4O_{34}$
Formula weight	4339.54	4295.44
System	monoclinic	monoclinic
Space group	C 2	C 2
a (Å)	25.561(1)	25.588(2)
b (Å)	17.5744(6)	17.445(1)
c (Å)	10.2380(4)	10.2804(7)
α (°)	90	90
β (°)	92.435(2)	92.383(3)
γ (°)	90	90
V (Å^3)	4595.0(3)	4584.9(5)
Z	1	4
T (K)	293(2)	100(2)
λ (Mo Kα), Å	0.71073	0.71073
ρ_{calc} (g·cm^{-3})	1.568	1.556
μ (Mo Kα), (mm^{-1})	1.903	1.906
Variables	405	462
Maximum/minimum peaks (e Å^{-3})	1.236/−0.861	0.614/−0.498
Flack parameter	0.05(4)	0.05(3)
R	0.0456	0.0374
ωR^2	0.1116	0.0824

ligands, two μ-Cl and two μ-O(phenoxo) bridges that occupy the vertex of the dicubane. The deprotonated phenoxo group of the Schiff base acts as a bridging ligand whereas the protonated alcohol function acts as a terminal O-donor. Thus, charge balance of the neutral tetramers is achieved with two azides, four chloro donors and two HL^- ligands. Ni1 and Ni2 are hexacoordinated with a *trans*-$NiN_2O_2Cl_2$ environment formed by three terminal donors (O-alcoxo, N-iminic from the HL^- and one chloro donor) and three bridging ligands (O-phenoxo, chloro and azido). The central Ni3 and Ni4 cations are also hexacoordinated with a NiN_2O_3Cl environment formed by two terminal ligands (O-methoxide from HL^- and one coordinated methanol molecule) and bridging groups (two azides, one O-phenoxo and one chloro). The dicubane core is strongly distorted, with two large Ni–O–Ni bond angles (109.2° and 110.3°) and two shorter Ni–Cl–Ni bond angles (90.0°). The Ni–N3–Ni and Ni–N7–Ni bond angles mediated by the $\mu_{1,1,1}$-N_3 bridges range between 89.2° and 99.2°. In particular the double azido bridge between Ni3 and Ni4 exhibit low bond angles of 89.2° and 92.3°. The coordinated methanol molecules and the terminal chloro ligands are linked by two intramolecular H-bonds (Cl4···O8, 2.974 Å; Cl2···O7, 3.080 Å). Intermolecular double H-bonds between the terminal chloro ligands and the protonated alcoxo fragment of the Schiff base (Cl2···O4′, 2.295 Å; O1···Cl4′, 3.022 Å) determine the 1D arrangement of clusters along the *c* crystallographic axis in the network, Fig. 2, bottom.

4.2. Electronic circular dichroism

ECD spectra of the enantiomeric pair of pure **1*R*** and **1*S*** complexes were measured in methanolic solutions and show perfect mirror image among them as should be expected for a pair of enantiomers, Fig. 3. The spectrum of the H_2L base was previously reported [2] and the absorptions in the UV region were assigned to π–π^* transitions of the aromatic groups of the Schiff base and a band around 400 nm to a n–π^* transition with origin in the azomethine cromophore. The spectra of the **1*R*** and **1*S*** show similar π–π^* transitions in the UV region (213, 238 and 283 nm) and the

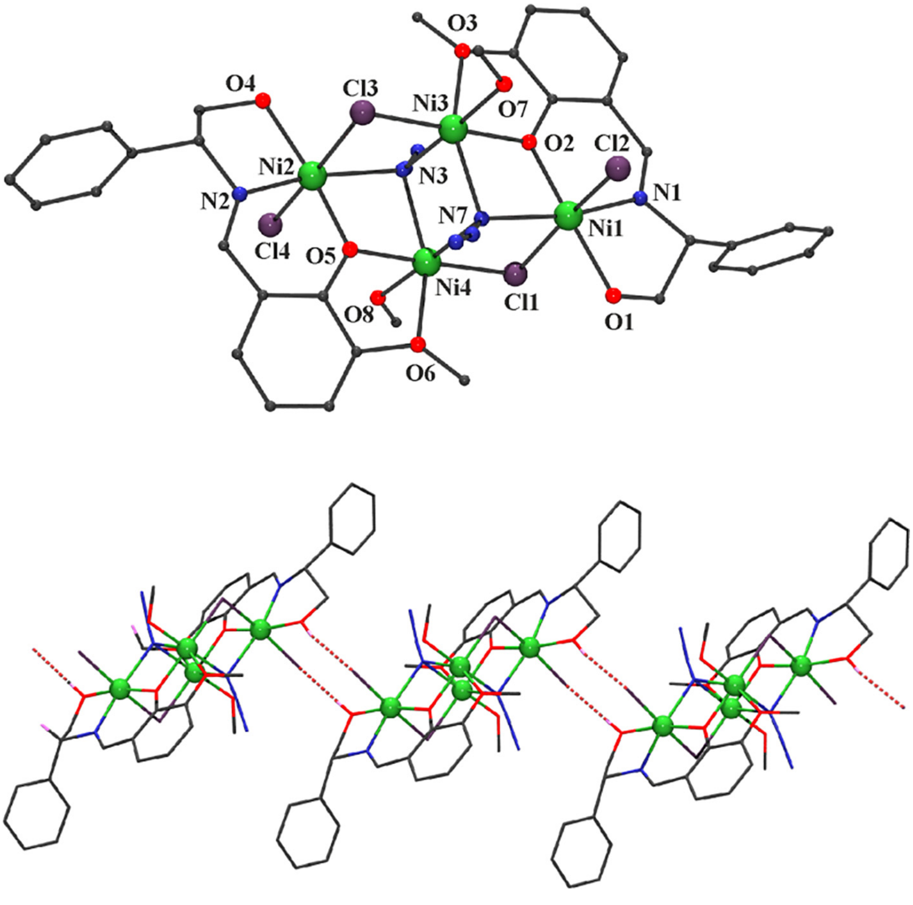

Fig. 2. Top, labeled plot of the molecular structure of **1*R***. Bottom, 1-D arrangement of tetramers linked by double OH···Cl H-bonds.

Table 2
Selected bond parameters for complex **1*R***.

Ni1–O1	2.058(8)	Ni2–O4	2.076(9)
Ni1–O2	1.978(8)	Ni2–O5	1.951(7)
Ni1–N1	2.016(8)	Ni2–N2	1.998(9)
Ni1–N7	2.204(11)	Ni2–N3	2.262(9)
Ni1–Cl1	2.460(4)	Ni2–Cl3	2.419(4)
Ni1–Cl2	2.370(4)	Ni2–Cl4	2.446(4)
Ni3–O2	1.968(8)	Ni4–O5	1.976(8)
Ni3–O3	2.176(9)	Ni4–O6	2.132(8)
Ni3–O7	2.072(9)	Ni4–O8	2.051(9)
Ni3–N3	2.121(10)	Ni4–N7	2.267(12)
Ni3–N7	2.224(12)	Ni4–N3	2.250(11)
Ni3–Cl3	2.301(4)	Ni4–Cl1	2.312(3)
Ni1–O2–Ni3	109.2(4)	Ni2–O5–Ni4	110.3(3)
Ni1–Cl1–Ni4	90.0(1)	Ni2–Cl3–Ni3	90.0(1)
Ni1–N7–Ni3	93.2(4)	Ni2–N3–Ni3	99.2(4)
Ni1–N7–Ni4	98.1(5)	Ni2–N3–Ni4	91.1(4)
Ni3–N7–Ni4	89.2(3)	Ni3–N3–Ni4	92.3(4)

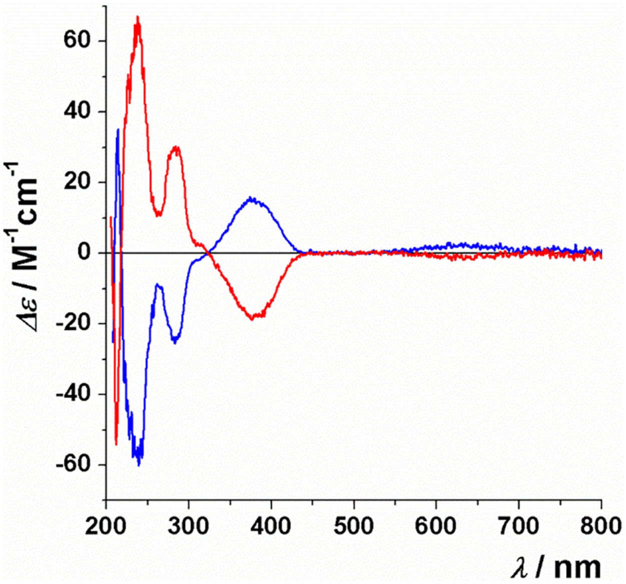

Fig. 3. ECD spectra for complexes **1*R*** (blue line) and **1*S*** (red line). (Color online.)

n–π^* at 378 nm. The Ni^{II} environment is not chiral and a weak participation of Ni^{II} cations molecular orbitals which are not directly linked to the aromatic rings, should be expected, and thus, only the weak absorption centered around 630 nm can be related to the Ni^{II} contribution.

4.3. Magnetic properties

The $\chi_M T$ versus T plots for the pair of enantiomers **1*R*** and **1*S*** are shown in Fig. 4, top. The room temperature values are 5.17 cm^3 mol^{-1} K (**1*R***) and 5.30 cm^{3}mol^{-1} K (**1*S***), very close to the expected value for four non-interacting Ni^{II} cations (g ~2.25). On cooling, $\chi_M T$ increases up to a well defined maximum at 20 K and below this temperature abruptly decreases down to 2.81 cm^3 mol^{-1} K (**1*R***) and 3.32 cm^3 mol^{-1} K (**1*S***). The shape of the plots and the value of the maximum evidences a dominant ferromagnetic interaction that tends to the maximum ground state $S = 4$. Magnetization experiments revealed a continuous increase of magnetization for increasing external field until unsaturated values of 4.7 (**1*R***) and 5.0 N μβ (**1*S***) under the maximum field of 5 T. These values are much lower than the expected value of 9.7 N μβ equivalent to eight electrons (g value around 2.2).

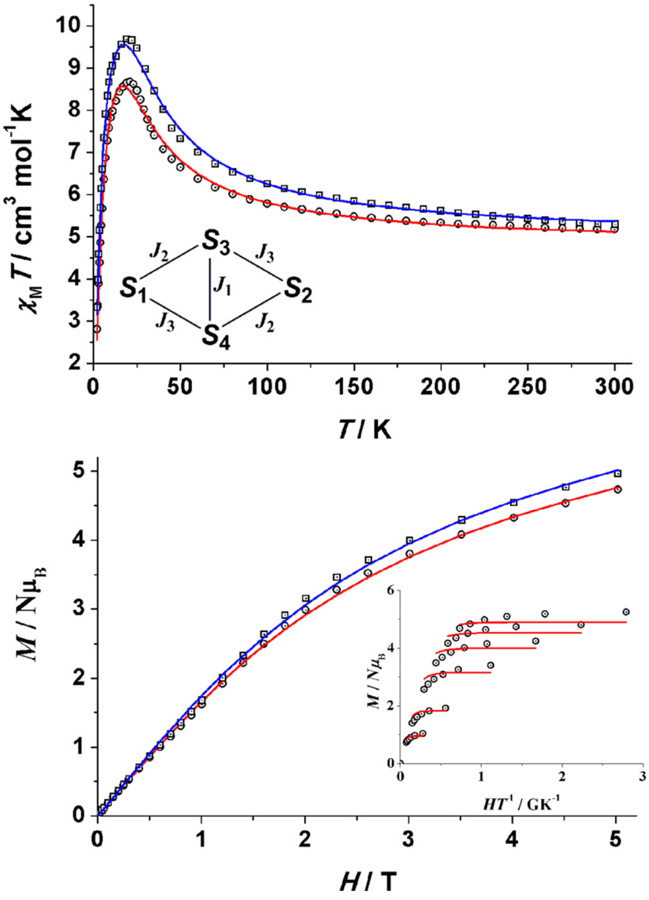

Fig. 4. $\chi_M T$ product vs. T (top) and magnetization data for compounds **1*R*** (circles) and **1*S*** (squares). Insets, coupling scheme and reduced magnetization for **1*R***. Solid lines show the best fit for both measurements.

In basis on the structural information, a 3-J Hamiltonian in which J_1 parametrizes the interaction mediated by the double azido bridge and J_2 and J_3 the chloro/azido or oxo/azido bridges (Fig. 4, inset), was employed to fit the experimental data:

$$\mathrm{H} = -2J_1(S_3 \cdot S_4) - 2J_2(S_1 \cdot S_3 + S_2 \cdot S_4) - 2J_3(S_1 \cdot S_4 + S_2 \cdot S_3)$$

The fit of ferromagnetic systems with a low temperature decay of the susceptibility and unsaturated magnetization is not routine because these facts can be either due to intermolecular interactions (zJ) or to the effect of the zero field splitting (D), often mathematically correlated. To try to elucidate the reason of the low temperature magnetic response, two previous fits with the above Hamiltonian were performed for complex **1*R***, one with a variable zJ term and fixing $D_{\mathrm{ion}} = 0$ and a second one fixing $zJ = 0$ and a variable D_{ion} parameter. The result gave almost superimposable simulations (best fit parameters Table 3), showing that the $\chi_M T$ measurements can not differentiate between these two effects. In contrast, the magnetization experiments were determinant because the experimental data can not be reproduced with a weak zJ parameter even supposing unrealistic low g values. In contrast, an excellent fit was obtained when supposing that the low temperature response is attributed to the zero field splitting. In light of these preliminary simulations the susceptibility and magnetization plots were fitted according the $zJ = 0$ and a variable D_{ion} option. The best fitting parameters are summarized in Table 3. From these results we realize relatively low J values for all the superexchange pathways and a high ZFS effect.

To confirm this assumption and to have a more reliable determination of the ZFS parameter, reduced magnetization

Table 3
Best fit parameters obtained from susceptibility or magnetization data for complexes **1*R*** and **1*S***.

	J_1	J_2	J_3	g	D_{ion}	zJ	R
1*R* ($\chi_M T$)	+2.3	+5.3	+5.3	2.20	–	-0.11	$5.9 \cdot 10^{-4}$
1*R* ($\chi_M T$)	+5.3	+4.0	+4.0	2.19	8.4	–	$3.1 \cdot 10^{-4}$
1*R* (M)	+5.5	+3.7	+3.7	2.19	9.1	–	$2.0 \cdot 10^{-4}$
1*S* ($\chi_M T$)	+2.4	+6.0	+6.0	2.22	8.6	–	$1.8 \cdot 10^{-4}$
1S (M)	+1.5	+4.3	+6.7	2.21	9.9	–	$3.4 \cdot 10^{-4}$

experiments were performed. The plot of the magnetization versus HT^{-1} shows non coincident plots for the different applied fields and temperatures, evidencing a strong ZFS in the $S = 4$ spin level which is the only one populated at 2–6 K. Fit of this plot gives a $D_{(S4)} = +13.6\ \text{cm}^{-1}$ when $g = 2.08$. The shape of the plot and the obtained fit values confirm a very high positive anisotropy of the $S = 4$ ground state and consequently, that the low magnetization and the decay of the susceptibility at low temperature is attributable to the depopulation of the higher m_s levels. From this data, the $m_s = 0/\pm 4\ DS^2$ gap is close to 200 wavenumbers but unfortunately, the positive sign of D excludes any SMM response as was experimentally checked. The calculated D value is apparently very high for a $S = 4$ spin level but has previously been reported [16] for related ferromagnetic dicubanes with $\mu_{1,1,1}$-N_3 bridges (calculated from $\chi_M T$ measurements) and should be attributed to the very strongly distorted field around the nickel cations. Interestingly, for the related core with μ_3-OR bridges, antiferro [28] or ferromagnetic [29–33] response has been reported and in the latter case, the calculated D values are always lower than in the case of the azido bridge with only one exception, in which positive D values around $8\ \text{cm}^{-1}$ were calculated in spite that the decay of the $\chi_M T$ plot was not evident and the data was non supported by reduced magnetization experiments [32].

Comparison of the coupling constants of the reported compounds with other defective dicubane nickel clusters with $\mu_{1,1,1}$-N_3 bridges is limited to the dominant ferromagnetic behavior [12–16] because of the variety of superexchange pathways Ni–O–Ni, Ni–N–Ni or Ni–Cl–Ni exclude this analysis. The only common point between these structures is the central Ni–$(N_3)_2$–Ni bridge but it becomes quite surprising that the reported J values for similar Ni–N–Ni and Ni–N bond angles and distances, covers a wide range of values between 2.5 and $22\ \text{cm}^{-1}$.

5. Concluding remarks

The use of enantiomerically pure ligands leads to chiral clusters adding optical properties and proving that is a good way to obtain multiproperty/multifunctional systems. Combination of Schiff bases with azido co-ligands yielded tetranuclear clusters in which the presence of $\mu_{1,1,1}$-N_3 bridges promotes defective cubanes based structures. End-on azido bridges becomes determinant in the ferromagnetic response of the new clusters independently of the remaining Ni–X–Ni bridges present in the molecules. In addition to the ferromagnetic exchange in these tetramers, its $S = 4$ ground state possesses a high zero field splitting due to the low symmetric environment around the Ni^{II} cations.

Acknowledgement

Support from Ministerio de Economía y Competitividad-Spain, Project CTQ2015-63614-P are acknowledged.

References

[1] M. Liu, L. Zhang, T. Wang, Chem. Rev. 115 (2015) 7304.
[2] L.-L. Fan, F.-S. Guo, L. Yun, Z.-J. Lin, R. Herchel, J.-D. Leng, Y.-C. Ou, M.-L. Tong, Dalton Trans. 39 (2010) 1771.
[3] S. Nayak, H.P. Nayek, S. Dehnen, A.K. Powell, J. Reedijk, Dalton Trans. 40 (2011) 2699.
[4] C. Ding, C. Gao, S. Ng, B. Wang, Y. Xie, Chem. Eur. J. 19 (2013) 9961.
[5] Y. Song, G. Zhang, X. Qin, Y. Gao, S. Ding, Y. Wang, C. Du, Z. Liu, Dalton Trans. 43 (2014) 3880.
[6] S. Yuan, Y.-J. Zhang, J.-Y.N. Hou, Q.-L. Liu, D.-P. Li, Y.-X. Li, J. Huaxue, Chin. J. Struct. Chem. 35 (2016) 965.
[7] A. Escuer, J. Mayans, M. Font-Bardia, M. Gorecki, L. Di Bari, Dalton Trans. 46 (2017) 6514.
[8] Q.-Y. Lian, H.-N. Hu, C.-H. Li, D.-P. Li, X.-Y. Jiao, Y.-X. Li, Chin. J. Struct. Chem. 36 (2017) 273.
[9] A. Escuer, J. Esteban, S.P. Perlepes, T.C. Stamatatos, Coord. Chem. Rev. 275 (2014) 87.
[10] Y.-Z. Zheng, Y. Lan, C.E. Anson, A.K. Powell, Inorg. Chem. 47 (2008) 10813.
[11] C.J. Milios, A. Prescimone, J. Sanchez-Benitez, S. Parsons, M. Murrie, E.K. Brechin, Inorg. Chem. 45 (2006) 7053.
[12] T.K. Karmakar, S.K. Chandra, J. Ribas, G. Mostafa, T.-H. Lu, B.K. Ghosh, Chem. Commun. (2002) 2364.
[13] L. Botana, J. Ruiz, A.J. Mota, A. Rodriguez-Dieguez, J.M. Seco, I. Oyarzabal, E. Colacio, Dalton Trans. 43 (2014) 13509.
[14] I. Oyarzabal, J. Ruiz, A.J. Mota, A. Rodriguez-Dieguez, J.M. Seco, E. Colacio, Dalton Trans. 44 (2015) 6825.
[15] L. Jiang, D.-Y. Zhang, J.-J. Suo, W. Gu, J.-L. Tian, X. Liu, S.-P. Yan, Dalton Trans. 45 (2016) 10233.
[16] S.S. Tandon, S.D. Bunge, N. Patel, J. Sanchiz, Polyhedron 123 (2017) 361.
[17] C. Papatriantafyllopoulou, T.C. Stamatatos, W. Wernsdorfer, S.J. Teat, A.J. Tasiopoulos, A. Escuer, S.P. Perlepes, Inorg. Chem. 49 (2010) 10486.
[18] X.-T. Wang, B.-W. Wang, Z.-M. Wang, W. Zhang, S. Gao, Inorg. Chim. Acta 361 (2008) 3895.
[19] D. Mandal, V. Bertolasi, J. Ribas-Arino, G. Aromi, D. Ray, Inorg. Chem. 47 (2008) 3465.
[20] S.S. Tandon, S.D. Bunge, R. Rakosi, Z. Xu, L.K. Thompson, Dalton Trans. (2009) 6536.
[21] Y.-J. Liu, X.-J. Fu, X.-F. Li, T.-B. Qiu, H.-X. Yang, Acta Crystallogr., Sect. E 67 (2011) m307.
[22] D.I. Alexandropoulos, L. Cunha-Silva, A. Escuer, T.C. Stamatatos, Chem. Eur. J. 20 (2014) 13860.
[23] A. Bell, G. Aromi, S.J. Teat, W. Wernsdorfer, R.E.P. Winpenny, Chem. Commun. (2005) 2808.
[24] G. Aromi, S. Parsons, W. Wernsdorfer, E.K. Brechin, E.J.L. McInnes, Chem. Commun. (2005) 5038.
[25] R.T.W. Scott, L.F. Jones, I.S. Tidmarsh, B. Breeze, R.H. Laye, J. Wolowska, D.J. Stone, A. Collins, S. Parsons, W. Wernsdorfer, G. Aromi, E.J.L. McInnes, E.K. Brechin, Chem. Eur. J. 15 (2009) 12389.
[26] G. Brunet, F. Habib, C. Cook, T. Pathmalingam, F. Loiseau, I. Korobkov, T.J. Burchell, A.M. Beauchemin, M. Murugesu, Chem. Commun. 48 (2012) 1287.
[27] N.F. Chilton, R.P. Anderson, L.D. Turner, A. Soncini, K.S. Murray, J. Comput. Chem. 34 (2013) 1164.
[28] C.G. Efthymiou, C.P. Raptopoulou, A. Terzis, R. Boca, M. Korabic, J. Mrozinski, S.P. Perlepes, E.G. Bakalbassis, Eur. J. Inorg. Chem. (2006) 2236.
[29] P. King, R. Clerac, W. Wernsdorfer, C.E. Anson, A.K. Powell, Dalton Trans. (2004) 2670.
[30] S. Liu, S. Wang, F. Cao, H. Fu, D. Li, J. Dou, RSC Adv. 2 (2012) 1310.
[31] S. Banerjee, M. Nandy, S. Sen, S. Mandal, G.M. Rosair, A.M.Z. Slawin, C.J.G. Garcia, J.M. Clemente-Juan, E. Zangrando, N. Guidolin, S. Mitra, Dalton Trans. 40 (2011) 1652.
[32] R. Herchel, I. Nemec, M. Machata, Z. Travnicek, Dalton Trans. 45 (2016) 18622.
[33] T. Nakajima, K. Seto, A. Scheurer, B. Kure, T. Kajiwara, T. Tanase, M. Mikuriya, H. Sakiyama, Eur. J. Inorg. Chem. (2014) 5021.

CHAPTER 3. AN IRON STAR

This chapter comprises ***Publication #3***.

Publication #3 *"Chiroptical and magnetic properties of star-shaped Fe^{III}_4 complexes from chiral Schiff bases. Structural and magnetic correlations based on continuous shape measurements."* describes the synthesis, the magnetic characterization of an enantiomeric pair of iron stars derived from **H_2L9** with formula $[Fe^{III}_4(L9)_6]$ **[18*R*]/[18*S*]** and the mononuclear complex **[19*RS*]** derived from the ligand **H_2L11**. A discussion about structural correlations of the iron star family is included in the paper.

The paper shows how a slight change in the substituents of the ligand completely changes the final structure of the products. It is important to mention that many other substituents have been used to try the synthesis of other iron clusters and no one of them yielded in reproducible and/or clean syntheses. This list of ligands is depicted in **Figure 3.1.**

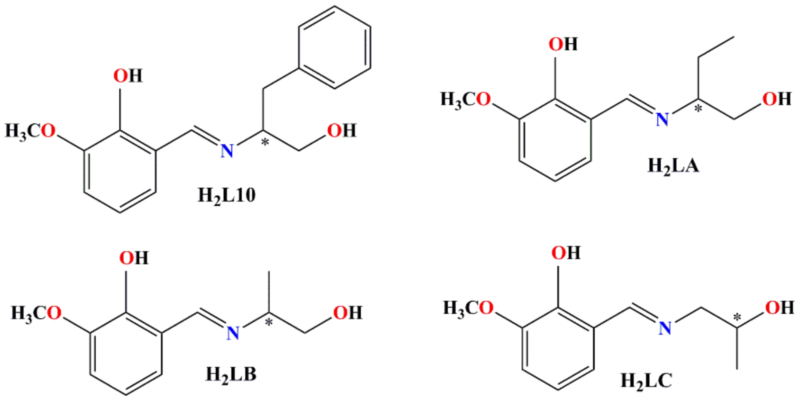

Figure 3.1. List of ligands used in the attempts to synthesize other iron complexes. One of the attempts was with the ligand **H_2L10**, which has been used in another complexes of the thesis. Ligands **H_2LA, H_2LB** and **H_2LC** were not successful in any synthesis.

Iron stars are a family of complexes that have been deeply magnetically studied by R. Sessoli *et al*. This kind of clusters present an isolated $S = 5$ ground state with a global ferrimagnetic behavior, as is shown in the magnetic susceptibility measurements. The strong decay at low temperatures has been tested by fittings including D and zJ. Reduced magnetization measurements showed that D is the main parameter in the low temperature decay while the intercluster interaction is very small. The study of the dynamic magnetic properties of the $[Fe^{III}_4]$ clusters yield in no out-of-phase susceptibility peaks above 1.8 K in χ_M'' vs. temperature plots but strong enough tails are observed so a Debye relaxation was used to calculate the magnetic relaxation parameters.

The use of Continuous Shape Measures (CShM) to study the degree of the polyhedral distortion was used to do a qualitative comparison with all the similar clusters in the literature by dividing the structural types in types I-VIII, performing analysis in the central and in peripheral Fe^{III} cations to try to elucidate what mostly affects the magnetic response.

Publication #3 *“Chiroptical and magnetic properties of star-shaped* Fe^{III}_4 *complexes from chiral Schiff bases. Structural and magnetic correlations based on continuous shape measurements.”*

Dalton Transactions

PAPER

Cite this: *Dalton Trans.*, 2018, **47**, 8392

Chiroptical and magnetic properties of star-shaped Fe_4^{III} complexes from chiral Schiff bases. Structural and magnetic correlations based on continuous shape measures†

Julia Mayans,[a] Mercè Font-Bardia[b] and Albert Escuer *[a]

Received 27th April 2018,
Accepted 25th May 2018

DOI: 10.1039/c8dt01684d

rsc.li/dalton

New chiral Fe_4^{III} star-shaped complexes have been synthesized starting from enantiomerically pure Schiff bases and chiroptically and magnetically characterized. The structural and magnetic properties of the complete family of 40 Fe_4 complexes reported in the literature have been analyzed in the search for synthetic and magnetostructural correlations.

Introduction

Fe_4 star shaped clusters comprise an aesthetically pleasant family of complexes that show moderately strong antiferromagnetic interaction between the central and the three peripheral Fe^{III} cations with an overall ferrimagnetic response and a well isolated $S = 5$ ground state. In spite of the ^6S ground term of the high spin Fe^{III} cations, they become moderately anisotropic by the distortion of the coordination polyhedron and usually exhibit slow relaxation of the magnetization. The star-shaped topology has been reported from the employment of substituted tris(hydroxymethyl)ethane,[1–13] alkoxides,[14,15] *N*-methyldiethanolamine,[16–18] Schiff bases[19–25] and one isolated case from the tartrate ligand.[26]

After the discovery of the single molecule magnet (SMM) phenomenon in 1993,[27–29] the complex $[Fe_4(MeO)_6(dpm)_6]$ (dpm = dipivaloylmethane) was studied early in 1999 by Gatteschi *et al.*[14] and from the characterization of the $[Fe_4(thme)_2(dpm)_6]$ complex,[1] in which dpm is the deprotonated form of the tripodal ligand tris(hydroxymethyl)ethane, a large number of $[Fe_4(R\text{-thme})_2(dpm)_6]$ clusters (R-H_3thme = substituted tris(hydroxymethyl)ethane) were synthesized and magnetically studied, becoming one of the most well-known families of SMMs.

Fe_4 complexes built from Schiff bases obtained by condensation of salicylaldehyde and 1,2-aminoethanol or their substituted derivatives have been reported more recently by S. Gao *et al.*[21–23]

These types of complexes with the formula $[Fe_4L_6]$ become of interest because in addition to having similar magnetic properties and SMM response, they allow the possibility to modify the different substituents either on the aromatic ring or on the aliphatic C-atoms of the hydroxyethyl fragment. In the latter case, monosubstituted carbon atoms become chiral centres that open the possibility of incorporating optical properties or the study of chiral supramolecular effects.[30–32]

The employment of *o*-vanillin instead of salicylaldehyde remains unexplored with the exception of the Fe_4 complex with the formula $[Fe_4(L)_4(MeO)_2Cl_2]$ prepared with the Schiff base derived from 1,3-aminopropanol which yielded a very asymmetric complex, probably due to the large bite and steric hindrance of the propyl fragment.[25] With this idea in mind, we decided to prepare enantiomerically pure Schiff bases derived from the condensation of *o*-vanillin and several chiral derivatives of 1,2-aminoethanol. Positive results were obtained for the ligands H_2L1 (derived from (R)- or (S)-phenylglycinol) and H_2L2 (derived from ($1R$,$2S$)-diphenylaminoethanol), Scheme 1, that allowed the characterization of a pair of star-shaped enantiomers with the formula $[Fe_4(L1)_6]$ (**1*R*** and **1*S***) and one mononuclear derivative of H_2L2 with the formula $[Fe(L2)(HL2)]$ (**2*RS***). The tetranuclear systems have been characterized by electronic circular dichroism and static and dynamic susceptibility measurements.

Bibliographic data show that the coordination polyhedra around the Fe^{III} cations can vary from octahedral to trigonal prismatic; on the one hand, we have analyzed all the reported structures of the Fe_4 complexes with star topology using SHAPE software and the continuous shape measures (CShM)

---

[a] *Departament de Química Inorgànica i Orgànica, Secció Inorgànica and Institute of Nanoscience and Nanotechnology (IN^2UB), Universitat de Barcelona, Av. Diagonal 645, Barcelona-08028, Spain. E-mail: albert.escuer@qi.ub.es*

[b] *Departament de Mineralogia, Cristal·lografia i Dipòsits Minerals and Unitat de Difracció de R-X. Centre Científic i Tecnològic de la Universitat de Barcelona (CCiTUB). Universitat de Barcelona, Solé i Sabarís 1-3, 08028 Barcelona, Spain*

† Electronic supplementary information (ESI) available: Synthetic and structural description. CCDC 1839483–1839485. For ESI and crystallographic data in CIF or other electronic format see DOI: 10.1039/c8dt01684d

This journal is © The Royal Society of Chemistry 2018

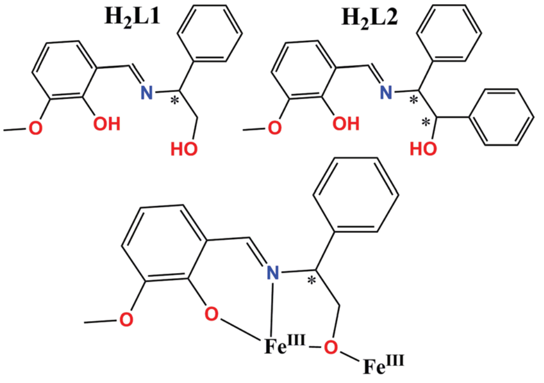

Scheme 1 Structural formula of the Schiff bases employed in this work and the coordination mode for $L1^{2-}$ in the star-shaped Fe_4 complexes. Asterisks denote the chiral centres.

as a tool to study the relationship between the ligands and the distortion of the coordination polyhedra around the Fe^{III} cations and, on the other hand, have examined whether there is a correlation between the aforementioned distortion of the coordination environment of the cations and the main magnetic parameters *J* and *D* or their SMM response.

Experimental

Materials and methods

IR spectra (4000–400 cm^{-1}) were recorded using a Bruker IFS-125 FT-IR spectrometer with samples prepared as KBr pellets. Variable-temperature magnetic studies were performed using an MPMS5 Quantum Design magnetometer operating at 0.03 T in the 300–2.0 K range. Diamagnetic corrections were applied to the observed paramagnetic susceptibility using Pascal's constants. The fit of the experimental data was performed with the PHI program.[33] The quality factor was parametrized with the parameter $R = (\chi_M T_{exp} - \chi_M T_{calc})^2/(\chi_M T_{exp})^2$. EDC spectra were recorded in dichloromethane solution in a Jasco-815 spectropolarimeter.

Single-crystal X-ray crystallography

Red prism-like specimens of dimensions 0.055 mm × 0.130 mm × 0.213 mm (**1*R***), 0.111 mm × 0.201 mm × 0.202 mm (**1*S***) or 0.058 mm × 0.113 mm × 0.195 mm (**2*S***) were used for X-ray crystallographic analysis. The X-ray intensity data were obtained on a D8 Venture system equipped with a multilayer monochromator and a Mo microfocus (λ = 0.71073 Å).

The frames were integrated with the Bruker SAINT software package using a narrow-frame algorithm. The final cell constants were based upon the refinement of the XYZ-centroids of reflections above 20 $\sigma(I)$. The structure was solved and refined using the Bruker SHELXTL software package. Details of the crystal data, collection and refinement for **1*R***, **1*S*** and **2*RS*** are summarized in Table 1.

Table 1 Crystal data, collection and structure refinement details for the X-ray structure determination of complexes **1*R***, **1*S*** and **2*RS***

	1*R*	**1*S***	**2*RS***
Formula	$C_{98}H_{94}Cl_4Fe_4N_6O_{18}$	$C_{100}H_{96}Fe_4N_8O_{18}$	$C_{49}H_{49}FeN_4O_7$
FW	2008.99	1921.24	861.77
System	Monoclinic	Monoclinic	Monoclinic
Space group	*P*21	*P*21	*P*21
a/Å	12.1916(5)	12.2369(6)	10.7824(6)
b/Å	27.895(1)	27.772(2)	18.1395(8)
c/Å	14.2943(6)	14.252(1)	11.3010(6)
α/°	90	90	90
β/°	111.665(2)	112.288(2)	99.806(2)
γ/°	90	90	90
$V/Å^3$	4517.9(3)	4481.7(5)	2178.0(2)
Z	2	2	2
T/K	100(2)	100(2)	100(2)
Θ range/°	2.316–26.467	2.321–26.459	2.662–23.859
Reflex. collected	60 409	145 485	22 062
Reflex. indep.	18 333	18 383	6642
Parameters	1171	1179	554
λ(MoKα)/Å	0.71073	0.71073	0.71073
$\rho_{calc}/g\ cm^{-3}$	1.477	1.424	1.314
$\mu(MoK_\alpha)/mm^{-1}$	0.822	0.710	0.403
Flack parameter	0.011(4)	0.004(3)	0.009(4)
R	0.0515	0.0331	0.0228
ωR^2	0.1391	0.0750	0.0553

Synthetic procedure

$[Fe_4(L1)_6]$·solvents (1*R*·2CH_2Cl_2 and 1*S*·2MeCN). Complex **1*S***·2MeCN was accidentally crystallized in very low yield from a methanol/acetonitrile solution of $FeCl_2$, $LnCl_3$ and H_2L in a basic medium during the trials to synthesize mixed iron/lanthanide complexes. In light of the structure, the direct synthesis was optimized to obtain complex **1*R***·2CH_2Cl_2 in a high yield. A solution of 0.5 mmol (0.069 g) of the corresponding (*R*) or (*S*)-phenylglycinol and 0.5 mmol (0.076 g) of *o*-vanillin in 15 mL of methanol was heated for 30 minutes at 80° in a microwave furnace. The yellow solution of the H_2L ligand was added to 0.101 g (0.25 mmol) of $Fe(NO_3)_3·9H_2O$ dissolved in 10 mL of acetonitrile. The color of the solution turned to deep blue and changed immediately to dark red after the addition of 0.101 g (1.0 mmol) of Et_3N. The mixture was stirred for 30 minutes and filtered to collect the complex as a brown microcrystalline powder in a practically quantitative yield. The crude complex was dissolved in 10 mL of dichloromethane and diffused with a vapour of diethyl ether. Well-formed crystals were collected after three days in 70% yield. IR spectra are shown in the ESI, Fig. S1.† Elemental analysis for **1*R*** as a solvent free complex: calc. C, 62.69; N, 4.57; H, 4.93%. Found: C, 62.1; N, 4.4; H, 5.1%.

$[Fe(L2)(HL2)_2]$·solvents (2*RS*). The ligand was prepared following the same procedure as that of H_2L1 but starting from (1*R*,2*S*)-2-amino-1,2-diphenylethanol instead of phenylglycinol. To a methanolic solution of 0.5 mmol of H_2L2 were added 0.032 g (0.25 mmol) of anhydrous $FeCl_2$ and 0.101 g (1 mmol) of Et_3N. Slow evaporation of the final dark red solution gave crystals useful for X-ray diffraction in a few days. Elemental analysis for **2*RS***: calc. C, 70.69; N, 3.75; H, 5.26%. Found: C, 70.3; N, 4.0; H, 5.3%.

Results and discussion

Structural description

[$Fe_4(L1)_6$]·solvents (1*R*·2CH_2Cl_2 and 1*S*·2MeOH). The two enantiomers were obtained with two molecules of different solvents, but the crystallization molecules are placed in the same voids in the network, and the two samples are isostructural, Table 1. The molecular structures of the tetrameric complexes show minor differences in their bond parameters, and thus to avoid repetitive descriptions, the following data refer to **1*S***.

The tetranuclear clusters consist of three peripheral [$Fe(L1)_2$]$^-$ fragments that act as bidentate *complex-as-ligand* linking the central Fe^{III} cation to form a star-shaped cluster, Fig. 1. The central Fe^{III} ion is hexacoordinated by six bridging alkoxide donors that define a coordination polyhedron close to a trigonal prism, whereas the peripheral cations are placed in a distorted octahedral [FeN_2O_4] environment. A detailed analysis of the coordination polyhedron for the two environments is provided in the following sections. The Fe–O distances (range 1.924–2.075 Å) are shorter than the Fe–N distances (range of 2.114–2.159 Å), and thus the peripheral Fe^{III} ions are slightly elongated along the N–Fe–N axis. The Fe–O–Fe bond angles are different for each peripheral cation, being shorter for Fe2–O–Fe3 (104.1/104.8°), larger for Fe2–O–Fe4 (108.0/109.0°) and intermediate for Fe2–O–Fe1 (104.4/107.3°). The four iron cations are placed in the same plane. The angles between the mean iron plane and the planes determined by the Fe–$(O)_2$–Fe atoms (helical pitch) range between 77.2 and 83.9°. The main planes of the $L1^{2-}$ ligands form a mean angle of around 56° with the Fe_4 plane determining the propeller-shape of the cluster. Main bond parameters are summarized in Table 2.

[Fe(L2)(HL2)]·2MeCN·MeOH (2*RS*·2MeCN·MeOH). The mononuclear complex **2*RS*** shows an Fe^{III} cation in a distorted [FeN_2O_4] octahedral environment, coordinated by one deprotonated $L2^{2-}$ and one monodeprotonated $HL2^-$ ligand, Fig. 2. Fe–O bond distances to the deprotonated O-donors are between 1.900 and 1.963 Å and are shorter than the distance to the protonated alkoxide (Fe–O4, 2.206 Å). As is usual for this type of ligands, the Fe–N distances are larger than 2.1 Å. The crystallization methanol molecule establishes a strong O1w···H4–O4 H-bond with an O4···O1w distance of 2.618 Å. Selected bond parameters are summarized in Table S1.†

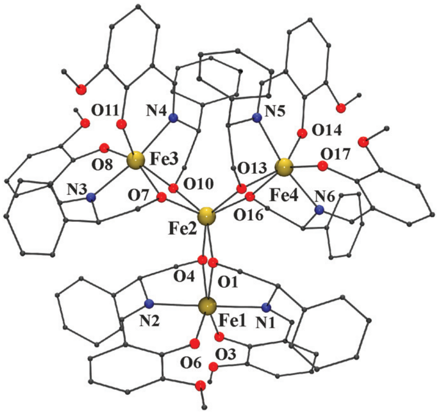

Fig. 1 Partially labeled plot of complex **1*S*** (common labels for **1*R***).

Table 2 Main bond distances (Å) and angles (°) for complex **1*S***

Fe2–O1	2.075(2)	Fe3–O7	2.001(3)
Fe2–O4	1.984(2)	Fe3–O8	1.934(3)
Fe2–O7	2.011(3)	Fe3–O10	2.001(3)
Fe2–O10	2.020(2)	Fe3–O11	1.924(3)
Fe2–O13	1.998(3)	Fe3–N3	2.114(3)
Fe2–O16	2.040(3)	Fe3–N4	2.115(3)
Fe1–O1	2.001(3)	Fe4–O13	2.016(3)
Fe1–O2	1.924(3)	Fe4–O14	1.925(3)
Fe1–O4	2.016(3)	Fe4–O16	2.000(3)
Fe1–O5	1.927(3)	Fe4–O17	1.927(3)
Fe1–N1	2.136(3)	Fe4–N5	2.158(3)
Fe1–N2	2.136(3)	Fe4–N6	2.159(3)
Fe2–O1–Fe1	104.4(1)	Fe2–O13–Fe4	109.0(1)
Fe2–O4–Fe1	107.3(1)	Fe2–O16–Fe4	108.0(1)
Fe2–O7–Fe3	104.1(1)		
Fe2–O10–Fe3	104.8(1)		

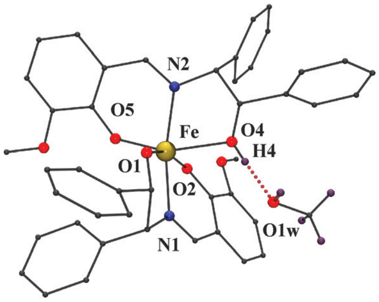

Fig. 2 Partially labeled plot of complex **2*RS***. The dotted line shows the H-bond between HL^- and the crystallization methanol molecule.

Synthetic aspects

The reaction of H_2L1 with iron nitrate in a basic medium yielded compounds **1*R***/**1*S***, and in light of these results, similar reactions under the same conditions were tried with the Schiff bases derived from the condensation of *o*-vanillin and 2-amino-1-butanol or phenylalaninol. In contrast with compounds **1*R***/**1*S***, the final products were soluble in the mother liquor, and no solid product was obtained upon layering with diethyl ether. All trials to obtain the solid complexes in a variety of solvents (methanol, acetonitrile, and dichloromethane) and by diffusion of diethyl ether or hexane gave oils. Susceptibility measurements performed on the crude product obtained by removing the solvent of the mother solution show the typical shape expected for an Fe_4 star but with a lower *g* value that evidences logical impurities.

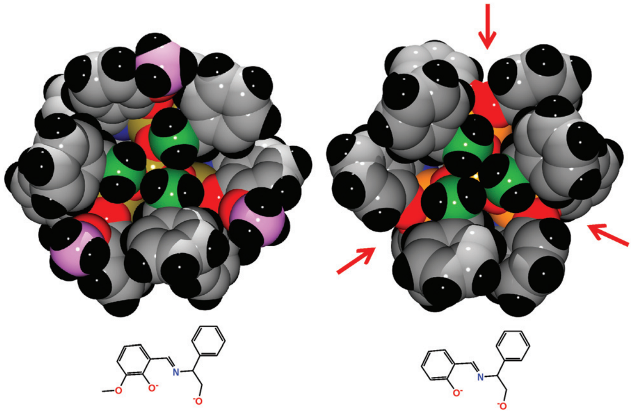

Fig. 3 Left, axial view of complexes **1*R*** or **1*S*** showing the C-atoms of the methoxide functions (pink colour) and the C-atoms adjacent to the O-donor of the aliphatic arm (green color). Right, the same view for the analogous complex built from the related Schiff base without the methoxide substituent (CCDC: UVIPUL).

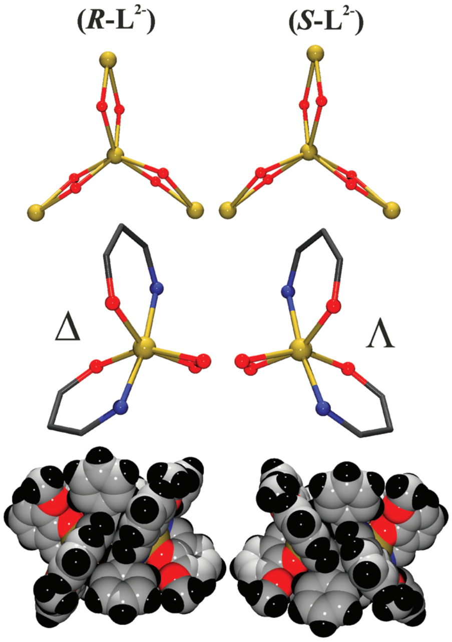

Fig. 4 Chirality transfer to the central (top) and peripheral (middle) Fe^{III} cations in complexes **1*R*** (left) and **1*S*** (right). The same Λ or Δ helicity is transferred to the whole complexes (bottom).

The complexes derived from L1^{2-} exhibit a sand-glass shape with two cavities above and below the Fe$_4$ plane, Fig. 3. The walls of the cavity are formed by the aromatic rings and the methoxide functions of the *o*-vanillin fragments with the aliphatic ethoxide bridging arm placed inside the cavity. This arrangement evidences that the –CH$_2$– fragment fits inside the cavity but substitution of the H-atoms by a larger function must lead to a loss of the stability of the structure. The reaction with H$_2$L2 with one phenyl group in this position effectively makes the Fe$_4$ structure impossible, and the simple mononuclear complex was obtained, showing that this type of structure can be obtained with any substituent on the C-atom adjacent to the imine and that the aforementioned structures become impossible when the substitution is on the carbon adjacent to the O-donor.

Comparison with the structure of the related complex with the Schiff base without the methoxide group (L3^{2-}) (reported by S. Gao, CCDC code UVIPUL)[21] shows that this substituent is not innocent. For this complex with the [Fe(L3)$_6$] formula, there is enough free space to rotate the ligands giving a quasi-perfect trigonal prism environment for the central Fe^{III} cations, with a mean helical pitch of 88.5°. The steric hindrance produced by the methoxide substituent reduces the helical pitch to a mean value of 80.1°, distorting the environment of the Fe^{III} cations and, as is explained in the following sections, has influence on its magnetic response.

Chirality transfer and electronic circular dichroism

The employment of chiral ligands in coordination chemistry usually induces the phenomenon of chirality transfer which produces structures with pre-determined supramolecular chirality that can be observed at several hierarchical levels, from the Λ/Δ absolute configuration of the coordination sphere of the cations to the arrangement of the molecule or the whole network.[30–32]

In our case, the transference of chirality in **1*R*/1*S*** can be observed on the central cation that, in spite of its small deviation from the trigonal prism topology, shows the opposite distortion sense for each enantiomer, Fig. 4, top. The same feature occurs for the peripheral Fe^{III} cations which show an octahedral environment and opposite configurations for the two enantiomers, Fig. 4, middle. The tilted planes of the L1^{2-} ligands with a main Fe$_4$ plane determine, as was described above, the propeller-shape of the cluster which also shows opposite helicity for **1*R*** and **1*S***, Fig. 4, bottom, resulting in a supramolecular helicate arrangement. The sense of the molecular helicity and the environments of the central and the three peripheral Fe^{III} cations show a Δ configuration for **1*R***, whereas Λ is the configuration for the enantiomer **1*S***.

Electronic circular dichroism confirms the enantiomeric nature of **1*R*** and **1*S***. The spectrum of **1*R*** collected in dichloromethane solution exhibits positive Cotton effects at λ_{max} = 244 and 398 nm and negative Cotton effects at 272, 312, 451 and 560 nm, whereas **1*S*** shows a mirror image at the same wavelengths and with opposite sign, Fig. 5.

Several enantiomeric pairs of Fe$_4$ clusters have been reported, but the dichroism studies are rare. S. Gao *et al.*[21] reported the DFT simulation for several related [Fe$_4$L$_6$] complexes (L^{2-} = Schiff bases derived from salicylaldehyde and phenylglycinol) as the sum of the contribution of L^{2-} and the chirality transfer to the coordination spheres of the central and the peripheral Fe^{III} cations, confirming that the intense absorptions below 300 nm are attributable to the chiral ligand, whereas the absorptions with the opposite Cotton effect around 300 and 400 nm have a main contribution from the central Fe^{III}, and the bands above 450 nm are due to the peripheral cations and are attributed to d–d transitions and ligand

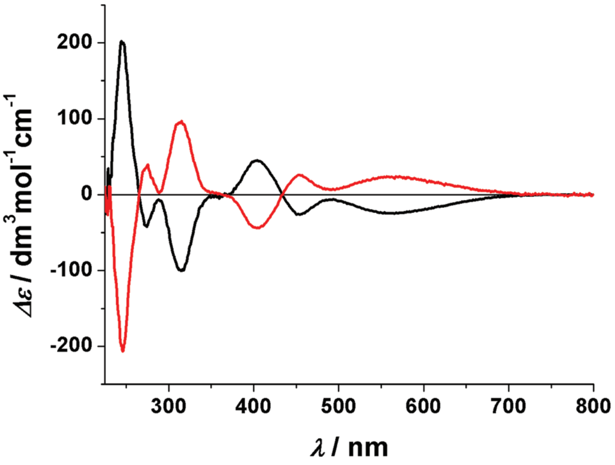

Fig. 5 Dichloromethane solution ECD spectra for the pair of Fe_4 enantiomers (black line, **1*R***; red line, **1*S***).

to metal charge transfer. The close similitude above 300 nm of the spectra of **1*R*/1*S*** with those previously reported gives a clear signature for this type of cluster with Schiff bases and the trigonal prism (central cation) and octahedral (peripheral cations) environments.

Magnetic properties

The $\chi_M T$ *vs.* T plot for complex **1*R*** shows a room temperature value of 13.05 cm^3 K mol^{-1}, lower than the expected value of 17.50 cm^3 K mol^{-1} for four non-interacting Fe^{III} cations, each one with $S = 5/2$. On cooling, the $\chi_M T$ value decreases down to a minimum of 12.12 cm^3 K mol^{-1} at 150 K and, below this temperature, increases up to a maximum value of 14.99 cm^3 K mol^{-1} at 16 K and decreases to a final value of 13.96 cm^3 K mol^{-1} at 2 K, Fig. 6. The shape of the plot and the $\chi_M T$ values indicate a ferrimagnetic-like behavior as a consequence of an anti-ferromagnetically coupled system without a full compensation of the spins.

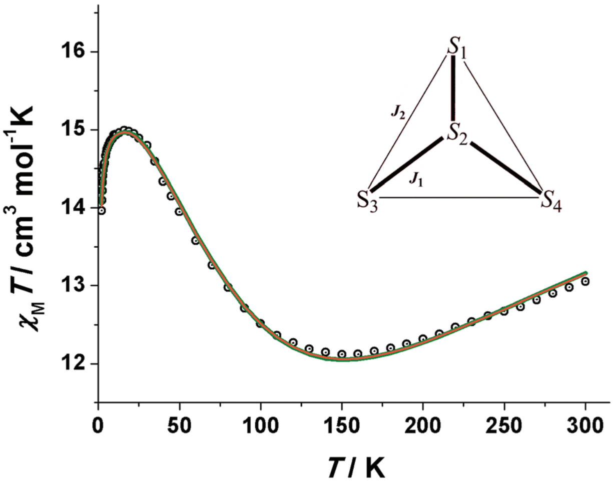

Fig. 6 $\chi_M T$ *vs.* T plot for complex **1*R***. The superimposed red or green continuous lines show the best fit obtained simulating the low T decay from intermolecular interactions or D effect (see text). Inset, coupling scheme.

The $\chi_M T$ decay at low temperatures can be either due to the anisotropy of the cations (zero field splitting in the $S = 5$ ground state) or antiferromagnetic intercluster interactions, which usually are strongly correlated in the fitting procedure.

On the basis of the coupling scheme shown in Fig. 6 (inset), in which J_1 corresponds to the interaction between the central and peripheral Fe^{III} cations and J_2 parametrizes the weak interaction between the external cations and the derived Hamiltonian:

$$H = -2J_1(S_2 \cdot S_1 + S_2 \cdot S_3 + S_2 \cdot S_4) - 2J_2(S_1 \cdot S_3 + S_3 \cdot S_4 + S_1 \cdot S_4)$$

two independent fits were performed to simulate the experimental data, assuming that $D_{ion} = 0$ and variable zJ intercluster interactions or variable D_{ion} and $zJ = 0$. The fit neglecting the zero field splitting effect gave the best fitting values $J_1 = -9.6$ cm^{-1}, $J_2 = +1.3$ cm^{-1}, $g = 2.01$, and $zJ = -0.0026$ cm^{-1}, whereas the fit assuming a D value different from zero and neglecting zJ yields gave the values $J_1 = -9.5$ cm^{-1}, $J_2 = +1.4$ cm^{-1}, $g = 2.00$, and $D = 0.39$ cm^{-1}. The two fits were equally good and the fit curves were superimposable (R quality factors, 1.35×10^{-5} *vs.* 1.06×10^{-5}), confirming that in this case, the fit of the susceptibility plot gives reliable values for the superexchange interactions but, in any case, can be applied to obtain an unambiguous approach to the D/zJ values.

To elucidate which is the dominant effect of the low temperature $\chi_M T$ decay, reduced magnetization experiments were performed, Fig. 7. In this case, the magnetization should be sensitive to the zero field splitting whereas, at medium-high fields, it becomes insensitive to very small intercluster zJ interactions.

The reduced magnetization shows non-coincident plots for the explored fields and temperatures, and a satisfactory fit for all fields was obtained for D (ground state) $= -0.29$ cm^{-1}, $g = 1.98$ and $R = 6.2 \times 10^{-5}$.

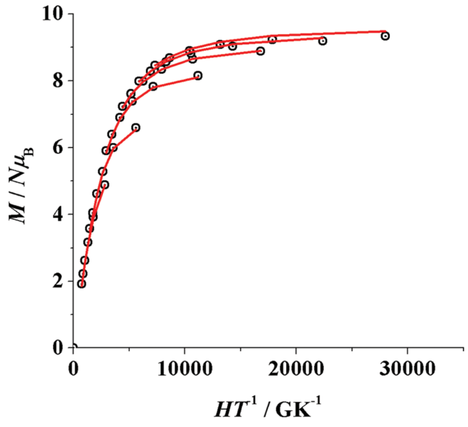

Fig. 7 Reduced magnetization plots in the 1.8–6.8 K range with 1 K increment for complex **1*R***. Solid lines show the best fit assuming an $S = 5$ ground state.

In light of the above data, the ground state should be described as S = 5 derived from the strong J_1 interaction and with a moderately weak ground state anisotropy.

Alternate field (ac) susceptibility measurements performed at zero field do not show out-of-phase signals above 2 K, but measurements at 1000 Hz under transverse fields between 0 and 4000 G exhibit a strong dependence of the applied field, ESI Fig. S2,† evidencing strong quantum tunneling of magnetization. From these data, the static field of 1500 G was selected to perform the ac measurements in the 1488–200 Hz frequency range which shows frequency dependence signals corresponding to peak tails with the maxima below the lower temperature limit of the instrument, Fig. 8.

For well-defined signals for which the maxima of the peaks are not available and the Arrhenius law cannot be applied, the analysis of the data, assuming one relaxation process and one U_{eff} barrier, can be performed by means of the Debye relation:

$$\ln(\chi''_{\mathrm{M}}/\chi'_{\mathrm{M}}) = \ln(\omega\tau_0) - U_{\mathrm{eff}}/k_{\mathrm{B}}T$$

The fit of the experimental data for all frequencies except the lower one at 200 Hz that shows a too weak signal, Fig. 8, inset, gives a consistent set of values (ESI, Table S2†), and the mean parameters $\tau_0 = 5.9 \times 10^{-7}$ s and U_{eff} = 15.4 K in good agreement with the normal values found for these types of complexes.

Structural correlations

Despite the simplicity of the $[\mathrm{Fe_4(\mu\text{-}O)_6}]$ core, the coordination environment of the $\mathrm{Fe^{III}}$ cations exhibits large variations that are strongly dependent on the linking properties of the ligands. Continuous shape measures (CShM), proposed by Avnir and others,[34,35] provide a quantitative evaluation of the degree of distortion from a given ideal polyhedron and, if there are two defined polyhedra, can evaluate it along the minimal distortion pathway that connects the ideal regular polyhedra. Parametrization of the coordination environments has been performed by means of the SHAPE program,[36] which compares the real shape with the coordinates of the ideal polyhedron P, corresponding the S(P) = 0 value to the full agreement of the problem and the ideal coordinates.

The search in the CCDC database returns 40 $\mathrm{Fe_4}$ stars, but some of them correspond to pairs of enantiomers or structures measured at different temperatures, and thus the structural dataset was reduced to 35 independent structures. Shape measurements were performed for the central and peripheral iron cations and the only close shapes were the octahedron (Oh) and the trigonal prism (TPr), and thus the minimal distortion pathway between these structures was selected for the analysis, the extreme points being S(Oh) = 0 and S(TPr) = 16.737 for an ideal octahedron and S(Oh) = 16.737 and S(TPr) = 0 for the ideal trigonal prism. For the systems that follow the distortion path, the structure is intermediate between the ideal polyhedra, whereas deviations from the path indicate other distortions (elongation, compression, short or long bond angles as a consequence of the bite of the ligands, *etc.*). The 35 structures have been classified into eight groups as a function of the ligands that are involved in the Fe–O–Fe bonds. The S(P) values are summarized in the ESI, Table S3.†

Practically one half of the $\mathrm{Fe_4}$ ferric stars (16 structures, type **I**) are built from the tripodal ligand tris(hydroxymethyl) ethane ($\mathrm{H_3}$thme) or a variety of the *R*-substituted ligand (*R*-$\mathrm{H_3}$thme) and acetylacetonate or dipivaloylmethane (*R*-acac) to fulfill the remaining coordination sites of the peripheral $\mathrm{Fe^{III}}$, with the general formula [$\mathrm{Fe_4}$(*R*-thme)$_2$(*R*-acac)$_6$], Scheme 2.

Also, with acetylacetonate peripheral ligands we have the type **II** (one structure) with the formula [$\mathrm{Fe_4}$(*R*-thme)(EtO)$_3$(*R*-acac)$_6$] and type **III** (two structures) with the formula [$\mathrm{Fe_4}$(MeO)$_6$(*R*-acac)$_6$].

Four complexes were derived from *N*-methyldiethanolamine ($\mathrm{H_2}$mdea) with the formula [$\mathrm{Fe_4(mdea)_6}$] (type **IV**) and eight

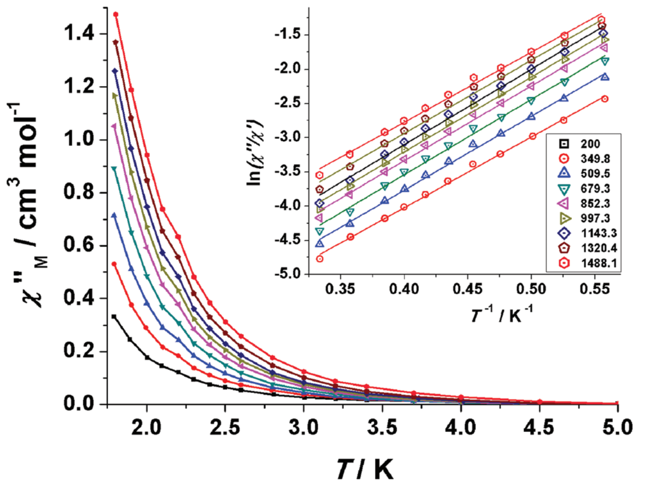

Fig. 8 Alternate current out-of-phase susceptibility plot *vs.* T for complex **1*R***. Inset, natural logarithm of χ''/χ' *vs.* $1/T$ for the indicated frequencies.

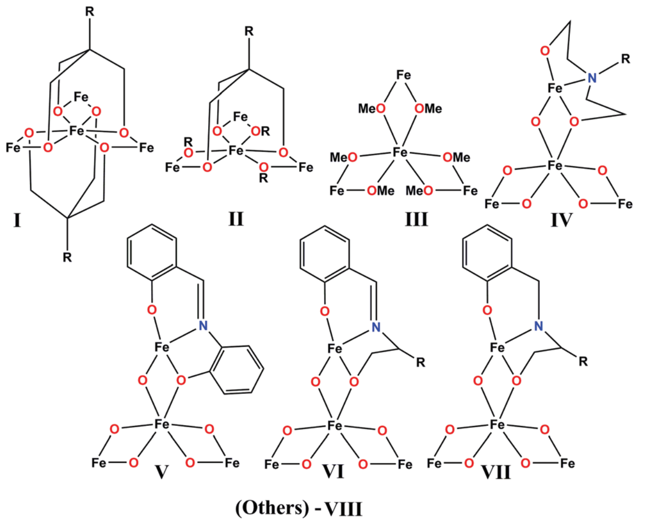

Scheme 2 Structural types of the $\mathrm{Fe_4}$ stars reported in the literature as a function of the ligands that provide the Fe–O–Fe bridges.

from Schiff bases (H_2Schiff) were derived from the condensation of salicylaldehyde with 2-aminophenol (two structures, type **V**) or 2-aminoethanol or their 2-*R*-substituted analogues (six structures, type **VI**) with the [Fe_4(Schiff)$_6$] formula. Finally, one system with one reduced Schiff base with the same [$Fe_4(L)_6$] formula (type **VII**) and three complexes with very asymmetric cores (type **VIII**) complete the set of structures.

The SHAPE analysis of the central Fe^{III} cations shows a wide distribution of their coordination environments from the octahedral shape for type **V** to quasi-perfect trigonal prisms for the Schiff base derivatives, type **VI**, Fig. 9. The shape of the coordination polyhedra follows the Oh–TPr minimal pathway, revealing that this type of distortion becomes the most relevant for all the Fe_4 stars. In particular, the most studied series **I** and **VI** fit quasi-perfectly on the pathway. Other distortions become relevant for the octahedral **II**–**V** and **VII** complexes, with very close shape characteristics for each kind of ligand.

In particular, the steric hindrance promoted by the methoxide group in **1*R*/1*S***, Fig. 3, induces a larger distortion from the trigonal prism environment around the central cation for the type **VI** complexes.

The same analysis for the peripheral Fe^{III} cations shows that the distorted octahedron is the preferred environment in most of the cases, but with the exception of the type **I**–**III** complexes that follow the Oh–TPr pathway, and the remaining systems show important distortions related with the donor properties of the coordinated ligands, Fig. 10. In fact, for type **I**, the two acetylacetonate ligands coordinated to the iron cations provide a comfortable bite angle (~85°) that favors a low distorted octahedral arrangement, whereas, for types **IV** and **VII**, the *fac*-coordination of the tridentate ligands with bite angles ~75–79° determine very distorted environments that are relatively close to the trigonal prism.

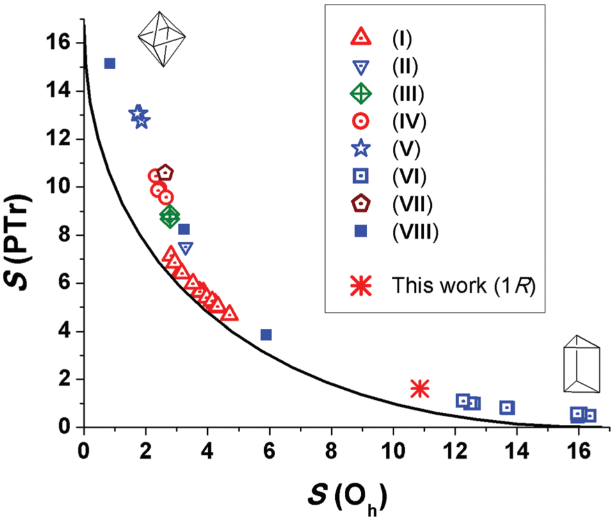

Fig. 9 *S*(TPr) *vs.* *S*(Oh) for the central Fe^{III} cation of the 35 Fe_4 independent structures reported to date. (I)–(VIII) refer to the structural types described in Scheme 2. The distortion pathway between the octahedral and the trigonal prism is shown as a solid black line.

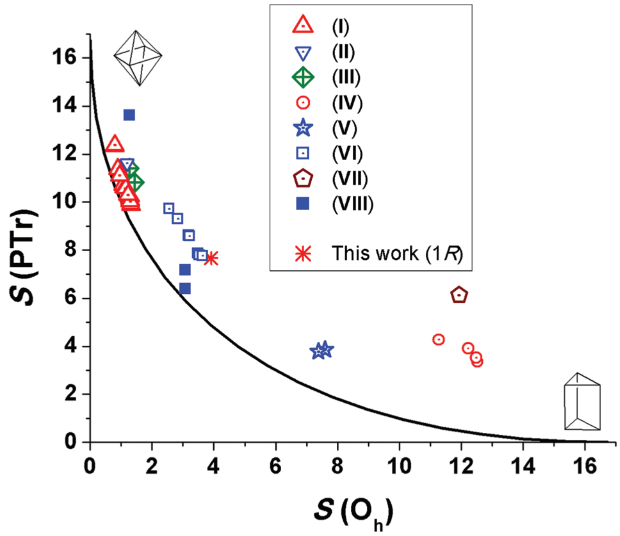

Fig. 10 *S*(TPr) *vs.* *S*(Oh) for the peripheral Fe^{III} cations (mean values) of the 35 Fe4 independent structures reported to date. (I)–(VIII) refer to the structural types described in Scheme 2. The distortion pathway between the octahedral and the trigonal prism is shown as a solid black line.

It is worth noting that, for the two larger series **I** and **VI**, for which there are enough complexes to extract conclusions, we realize that the environment of the peripheral cations for type **I** is quasi-constant with an *S*(Oh) in the short range 0.79–1.31 for the complexes derived from the rigid Schiff bases (type **VI**), and there is a clear correlation between the degree of *S*(TPr) of the central cation and the distortion of the octahedral environment of the peripheral cations, that is to say, the more prismatic the central cation, the more octahedral the peripheral Fe^{III} cations become, Table S3 and Fig. S3.†

One of the most interesting conclusions of this analysis is that each type of ligand produces, either for the central or the peripheral cations, Fe_4 stars with a well-defined environment, and that the coordination around the Fe^{III} cations for new members of the aforementioned structural types can be effectively predicted with a low margin of surprise by the adequate selection of the ligands.

Magnetic correlations. The main structural and magnetic parameters for the 30 complexes for which there is available information in the literature are summarized in Table 3. This series of complexes is specially adequate to analyze magneto-structural correlations because they are quite an unusual case in which the magnetic parameters are highly reliable: the value of the J coupling constants is a function, with low error margin, of the position of the minimum of $\chi_M T$,and the D parameter has been determined in practically all cases from reduced magnetization or/and high field EPR. From these data, two independent correlations can be obtained, one for the J coupling constant between the central and peripheral cations and a second for their SMM response.

The superexchange between Fe^{III} cations mediated by oxo bridges shows a moderate dependence of the bond angle (larger interactions for larger angles) and a strong dependence

Table 3 Main coupling constant and range of structural parameters for the reported Fe_4 complexes

CCDC CODE	Type	J^c	Fe–O–Fe^d (°)	Fe–O^d (Å)	D (cm^{-1})	U_{eff} (K)	AC peaks	Ref.
AGAQIJ	**I**	−16.2	102.1–103.3	1.976–1.996	$-0.43^{a,b}$	15.7	>2 K	5
DUFNUO	**I**	−17	101.8–102.4	1.960–1.984	-0.35^{a}	12.6	<2 K	8 and 9
DUFPAW	**I**	−16.4	101.6–102.6	1.977–1.983	-0.34^{a}	12.2	<2 K	8 and 9
DUPSAK	I	−15.9	101.9–102.6	1.963–1.992	-0.439^{a}	14.9/17.2	>2 K	12
ICOCIN	I	−15.3	102.0–102.4	1.972–1.981	-0.42^{b}	15.6	>2 K	2
ITAKUJ	I	−16.5	102.8–103.0	1.963–1.983	$-0.45^{a,b}$	17	>2 K	1
KAXGUN	I	−16.9	101.9–102.6	1.970–1.989	$-0.42^{a,b}$	15.0	>2 K	11
NIPJEC	I	−16.9	102.2–103.0	1.970–1.983	-0.45^{a}–0.43^{b}	15.9	>2 K	3
TACFUA	I	−13.7	102.1–102.4	1.968–1991	-0.407^{a} 0.414^{b}	11.1	>2 K	10
TACGAH	I	−16.7	101.8–102.6	1.970–1.993	-0.403^{a}–0.421^{b}	11.14	>2 K	10
VOBXUG	I	−16	101.6–102.6	1.972–1.994	-0.42^{a}–0.41^{b}	—	—	4
XUBVUM	I	−17.7	102.0–103.2	1.965–1.995	-0.42^{b}	15.9	>2 K	7
XUBWAT	I	−17.2	102.1–102.8	1.967–1.997	-0.45^{b}	11.9	>2 K	7
XUBWEX	I	−15.6	102.2–103.0	1.961–2.005	-0.44^{b}	12.9/9.5	>2 K	7
XUBWIB	I	−15.9	101.4–101.9	1.973–1.988	-0.41^{b}	16.1	>2 K	7
ICOCOT	II	−21.4	103.0–105.5	1.938–2.016	-0.27^{a}	6.0	<2 K	2
DEKPAK	III	−21.1	104.3–104.4	1.950–2.016	$-0.20^{a,b}$	3.5	<0.8 K	14
GANWEA	III	−17.9	104.4–105.0	1.952–2.011	-0.18^{a}	—	—	15
MEMKAR	IV	−20.8	105.1–106.7	1.982–2.030	-0.40^{b}	—	—	17
CUHJEW	V	−15.7	106.0–107.1	1.997–2.098	—	—	—	19
JORWAQ	VI	−23.4	105.6	2.003–2.021	-0.38^{a}–0.37^{b}	14.1	<2 K	22
UVIPUL	VI	−23.6	105.3–107.4	2.014–2.041	-0.34^{a}	5.9/9.9	<2 K	21
XOKDEI	VI	−24.8	105.1–107.1	1.993–2.049	-0.33^{a}	7.0	<2 K	23
XOKDIM	VI	−23.2	104.9–107.5	1.982–2.047	-0.36^{a}	11.0	<2 K	23
XOKDOS	VI	−26.4	105.5–107.2	1.992–2.052	-0.29^{a}	—	<0.5	23
XOKQAR	VI	−22.8	105.6–108.0	2.003–2.046	-0.29^{a}	—	<0.5	23
1*S*	VI	−19.0	104.1–109.0	1.924–2.075	-0.29^{a}	15.4 K	<2 K	This work
AHOTEX	VII	−21.9	107.2–108.5	1.970–2.009	$\sim 0^{a}$	—	<1.8 K	24
DAMREQ	VIII	−5.5	99.9–101.0	2.030–2.045	—	—	—	25
GAGREM	VIII	−28.2	105.0–105.3	1.984–1.995	-0.32^{a}–0.33^{b}	8.5	<0.8 K	13
LEBRIU	VIII	−29.2	104.4–107.1	1.942–2.050	-0.31^{a}	—	NO	26

[a] Value calculated from reduced magnetization measurements. [b] Value calculated from EPR data. [c] Referred to the $H = JS_iS_j$ convention. [d] Maximum and minimum value for each parameter.

of the Fe–O distances in the bridging region (larger interactions for shorter distances) and several empirical methods have been proposed to predict the magnitude of the Fe^{III}–O–Fe^{III} interaction.[37,38] From these models, it can be seen that few degrees of difference (102–106° range as an example) in the Fe–O–Fe bond angle are poorly relevant and suppose an increment of less than 1.5 cm^{-1} in the J value whereas the magnitude of the interaction changes drastically in the 1.95–2.05 range for the Fe–O distance. On this basis, a simple inspection of Table 3 shows that complexes with similar bond parameters have different J values and that the larger interactions correspond to the systems with Fe–O bond distances larger than 2.0 Å, and thus the reported complexes do not follow these well-established correlations. In the same way, there is no correspondence between the S(Oh) (central or peripheral cations) and the J parameter, ESI, Fig. S4.† This fact is not surprising because the magnitude of the superexchange interaction between the central and the peripheral cations of the Fe_4 systems must be assumed as a complicated multifactor problem that, in addition to bond lengths and angles at the bridging region, includes the donor properties of each type of O-donor (alcoxo, phenoxo, *etc.*) and the extreme differences in the stereochemistry around the cations with the concomitant change of the atomic orbitals that participate in the superexchange pathway, from $d_{x^2-y^2}/d_{z^2}$ for an ideal octahedron (Oh, e_g) to d_{xz}/d_{yz} for an ideal trigonal prism (D_{3h}, e'') environments.

However, some general conclusions can be drawn from the experimental evidence: (a) the J parameter is coherent and characteristic for each type of compound following the order of the AF interaction type **I** ~ **V** < **II** ~ **III** < **VI** ~ **VII**. This means that the Schiff bases with alkoxo bridging arms promote larger interactions than the phenoxo ones and that the intermediate interactions correspond to the complexes with MeO^- or EtO^- bridges, Table 3. The only complex that does not follow this order is one type **III** system with a low J value attributable to the larger electronegativity of the fluorinated dipivaloylmethane ligands, and all type **VIII** complexes which show extreme asymmetric environments or even square pyramidal penta-coordination for the peripheral cations.

The dependence of D with the structural distortion of the octahedral polyhedron was studied by Gatteschi *et al.*, proposing that the trigonal compression of the octahedron along the C_3 axis contributes to larger and negative D values and that the trigonal rotation (from Oh towards TPr) also contributes to negative D values.[14,39]

Type **I** complexes have been exhaustively studied by R. Sessoli and others[1–13] and the D parameter has been correlated to several distortion parameters such as the trigonal compression, trigonal rotation or the helical pitch defined as the dihedral angle between the main Fe_4 and the Fe–(O_2)–Fe planes. This latter parameter joins with the trigonal compression (larger pitch means lower compression) and trigonal rotation (larger pitch means larger rotation) and proved to be useful in a series of twelve type **I** complexes.[7] For this type of complexes, with the same dipivaloylmethane ligands coordinated to the peripheral cations and a very similar Oh environment for the central Fe^{III} cations placed on the distortion pathway (triangles in Fig. 9 and 10), the parameter S(Oh) joins both distortions and consequently yields to the same conclusion, it is to say, larger negative D for larger S(Oh), Fig. 11.

The trial to extend the correlation obtained for the homogeneous series of type **I** complexes to types **II** and **III** fails as was pointed out by the same authors and others.[7,25] If the relationship is extended to all Fe_4 types, the lack of correspondence between both parameters becomes evident. This fact seems logical because, as occurs for the *J* parameter, the correlation fails due to multiple factors that can tune the *D* parameter as a consequence of the completely different coordination polyhedron for the central and/or the peripheral cations. In fact, larger *D* values (~0.4 cm^{-1}) are provided for type **I** complexes with intermediate/Oh environments for the central/peripheral cations and lower values (~0.2 cm^{-1}) with a similar environment for type **III**, whereas similar *D* values of around ~0.3 cm^{-1} are found for completely different coordination polyhedra such as intermediate/Oh (type **II**), TPr/intermediate (type **VI**) or highly distorted as type **VIII**. On the other hand, it becomes evident that each type of complex possesses a characteristic *D* value.

A final aspect concerns the SMM response and particularly the U_{eff} barrier calculated for these complexes. In a quasi-systematic fashion, type **I** complexes exhibit χ''_M peaks at zero field and above 2 K (typically between 2 and 3 K), whereas the other types, and in particular, those derived from Schiff bases (type **VI**) show peaks clearly below 2 K and, in some cases, even with the application of a static field to suppress the quantum tunneling of magnetization, do not overcome this temperature. In the same way, the U_{eff} values for type **I** agree in general terms with the DS^2 value but much lower values have been reported for the other types measured at zero field, confirming the large tunneling of the magnetization.

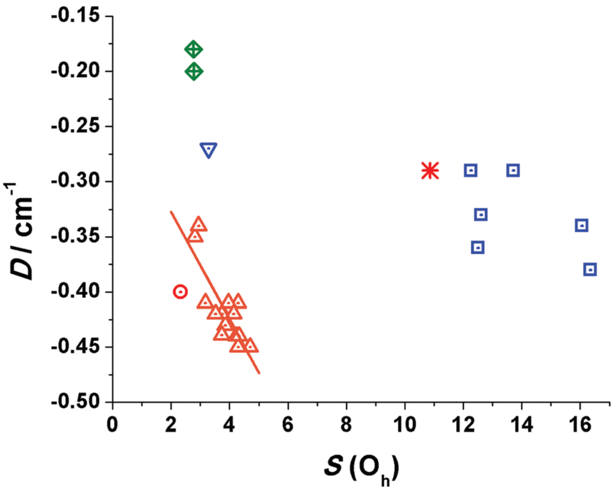

Fig. 11 *D vs. S*(Oh) of the central Fe^{III} cation for the I, II, III, IV and VI type complexes. The solid line shows the tendency for type I complexes.

As a consequence of the steric restrictions for **1*R*/1*S***, the new compounds show larger distortion from the regular trigonal prism for the type **VI** complexes, showing low *J* and *D* values in comparison with the rest of the members of the family of $[Fe(L)_6]$ (L = Schiff base) complexes.

Conclusions

Two new tetranuclear, star-shaped Fe^{III} complexes derived from enantiomerically pure Schiff bases obtained by the reaction of *o*-vanillin and phenylglycinol have been characterized. EDC spectra confirm characteristic peaks and the sign for the systems with the central cation in a trigonal prism environment. Magnetic analysis reveals an SMM response with a moderate *D* value and large tunneling. The previously published Fe_4 complexes with the same topology have been reviewed in light of continuous shape measures with SHAPE software for eight types of Fe_4 clusters, concluding that there are predetermined coordination environments for the central and peripheral Fe^{III} cations for each type of ligand reported to date. In the same way, the distortion parameter *S*(Oh) proved to be adequate to establish structural and magnetic correlations for these types of complexes and *J* and *D* values are strongly dependent on the employed ligands, showing characteristic values for each type of complex and allowing the design of future clusters with predetermined magnetic properties.

Conflicts of interest

There are no conflicts to declare.

Acknowledgements

Financial support from the Ministerio de Economía y Competitividad-Spain, Project CTQ2015-63614-P is acknowledged.

References

1 A. Cornia, A. C. Fabretti, P. Garrisi, C. Mortalo, D. Bonacchi, D. Gatteschi, R. Sessoli, L. Sorace, W. Wernsdorfer and A. L. Barra, *Angew. Chem., Int. Ed.*, 2004, **43**, 1136.

2 S. Accorsi, A. L. Barra, A. Caneschi, G. Chastanet, A. Cornia, A. C. Fabretti, D. Gatteschi, C. Mortalo, E. Olivieri, F. Parenti, P. Rosa, R. Sessoli, L. Sorace, W. Wernsdorfer and L. Zobbi, *J. Am. Chem. Soc.*, 2006, **128**, 4742.

3 A. L. Barra, F. Bianchi, A. Caneschi, A. Cornia, D. Gatteschi, L. Gorini, L. Gregoli, M. Maffini, F. Parenti, R. Sessoli, L. Sorace and A. M. Talarico, *Eur. J. Inorg. Chem.*, 2007, 4145.

4 G. G. Condorelli, A. Motta, G. Pellegrino, A. Cornia, L. Gorini, I. L. Fragala, C. Sangregorio and L. Sorace, *Chem. Mater.*, 2008, **20**, 2405.

5 A. Cornia, L. Gregoli, C. Danieli, A. Caneschi, R. Sessoli, L. Sorace, A. L. Barra and W. Wernsdorfer, *Inorg. Chim. Acta*, 2008, **361**, 3481.

6 L. Bogani, C. Danieli, E. Biavardi, N. Bendiab, A. L. Barra, E. Dalcanale, W. Wernsdorfer and A. Cornia, *Angew. Chem., Int. Ed.*, 2009, **48**, 746.

7 L. Gregoli, C. Danieli, A. L. Barra, P. Neugebauer, G. Pellegrino, G. Poneti, R. Sessoli and A. Cornia, *Chem. – Eur. J.*, 2009, **15**, 6456.

8 C. Schlegel, J. van Slageren, M. Manoli, E. K. Brechin and M. Dressel, *Polyhedron*, 2009, **28**, 1834.

9 C. Schlegel, E. Burzuri, F. Luis, F. Moro, M. Manoli, E. K. Brechin, M. Murrie and J. van Slageren, *Chem. – Eur. J.*, 2010, **16**, 10178.

10 M. J. Rodriguez-Douton, A. Cornia, R. Sessoli, L. Sorace and A. L. Barra, *Dalton Trans.*, 2010, **39**, 5851.

11 T. K. Prasad, G. Poneti, L. Sorace, M. J. Rodriguez-Douton, A. L. Barra, P. Neugebauer, L. Constantino, R. Sessoli and A. Cornia, *Dalton Trans.*, 2012, **41**, 8368.

12 A. Nava, L. Rigamonti, E. Zangrando, R. Sessoli, W. Wernsdorfer and A. Cornia, *Angew. Chem., Int. Ed.*, 2015, **54**, 8777.

13 M. Moragues-Canovas, E. Riviere, L. Ricard, C. Paulsen, W. Wernsdorfer, G. Rajaraman, E. K. Brechin and T. Mallah, *Adv. Mater.*, 2004, **16**, 1101.

14 A. L. Barra, A. Caneschi, A. Cornia, F. Fabrizi de Biani, D. Gatteschi, C. Sangregorio, R. Sessoli and L. Sorace, *J. Am. Chem. Soc.*, 1999, **121**, 5302.

15 L. Rigamonti, M. Piccioli, A. Nava, L. Malavolti, B. Cortigiani, R. Sessoli and A. Cornia, *Polyhedron*, 2017, **128**, 9.

16 R. W. Saalfrank, I. Bernt, M. M. Chowdhry, F. Hampel and G. B. M. Vaughan, *Chem. – Eur. J.*, 2001, **7**, 2765.

17 R. W. Saalfrank, A. Scheurer, I. Bernt, F. W. Heinemann, A. V. Postnikov, V. Schunemann, A. X. Trautwein, M. S. Alam, H. Rupp and P. Muller, *Dalton Trans.*, 2006, 2865.

18 S. Mishra, E. Jeanneau, M. Rolland and S. Daniele, *RSC Adv.*, 2016, **6**, 1738.

19 K. Takahashi, K. Kawamukai, T. Mochida, T. Sakurai, H. Ohta, T. Yamamoto, Y. Einaga, H. Mori, Y. Shimura, T. Sakakibara, T. Fujisawa, A. Yamaguchi and A. Sumiyama, *Chem. Lett.*, 2015, **44**, 840.

20 A. K. Dutta, S. Biswas, S. Dutta, L. N. Dawe, C. Robert Lucas and B. Adhikary, *Inorg. Chim. Acta*, 2016, **444**, 141.

21 Y.-Y. Zhu, X. Guo, C. Cui, B.-W. Wang, X.-M. Wang and S. Gao, *Chem. Commun.*, 2011, **47**, 8049.

22 Y.-Y. Zhu, T.-T. Yin, S.-Da Jiang, A.-L. Barra, W. Wernsdorfer, P. Neugebauer, R. Marx, M. Dorfel, B.-Wu Wang, Z.-Q. Wu, J. van Slageren and S. Gao, *Chem. Commun.*, 2014, **50**, 15090.

23 Y.-Y. Zhu, C. Cui, K. Qian, J. Yin, B.-W. Wang, Z.-M. Wang and S. Gao, *Dalton Trans.*, 2014, **43**, 11897.

24 R. Singh, A. Banerjee, E. Colacio and K. K. Rajak, *Inorg. Chem.*, 2009, **48**, 4753.

25 N. T. Madhu, J.-K. Tang, I. J. Hewitt, R. Clerac, W. Wernsdorfer, J. van Slageren, C. E. Anson and A. K. Powell, *Polyhedron*, 2005, **24**, 2864.

26 Q. Gao, X. Wang, M. T. Conato, T. Makarenko and A. J. Jacobson, *Cryst. Growth Des.*, 2011, **11**, 4632.

27 R. Sessoli, H. L. Tsai, A. R. Schake, S. Wang, J. B. Vincent, K. Folting, D. Gatteschi, G. Christou and D. N. Hendrickson, *J. Am. Chem. Soc.*, 1993, **115**, 1804.

28 R. Sessoli, D. Gatteschi, A. Canesch and M. A. Novak, *Nature*, 1993, **365**, 141.

29 D. Gatteschi, A. Caneschi, L. Pardi and R. Sessoli, *Science*, 1994, **265**, 1054.

30 J. Crassous, *Chem. Soc. Rev.*, 2009, **38**, 830.

31 H. Miyake, *Symmetry*, 2014, **6**, 880.

32 M. Liu, L. Zhang and T. Wang, *Chem. Rev.*, 2015, **115**, 7304.

33 N. F. Chilton, R. P. Anderson, L. D. Turner, A. Soncini and K. S. Murray, *J. Comput. Chem.*, 2013, **34**, 1164.

34 S. Zabrodsky, D. J. Peleg and D. J. Avnir, *J. Am. Chem. Soc.*, 1992, **114**, 7843.

35 J. Cirera, P. Alemany and S. Alvarez, *Chem. – Eur. J.*, 2004, **10**, 190.

36 M. Llunell, D. Casanova, J. Cirera, P. Alemany and S. Alvarez, *SHAPE version 2.0*, Barcelona, 2010, the program can be obtained by requesting the authors.

37 S. M. Gorun and S. J. Lippard, *Inorg. Chem.*, 1991, **30**, 1625.

38 K. J. Mitchell, K. A. Abboud and G. Christou, *Inorg. Chem.*, 2016, **55**, 6597.

39 D. Gatteschi and L. Sorace, *J. Solid State Chem.*, 2001, **159**, 253.

Electronic Supplementary Information (ESI) for

" ***Chiroptical and magnetic properties of star-shaped Fe^{III}_4 complexes from chiral Schiff bases. Structural and magnetic correlations based on continuous shape measurements*** "

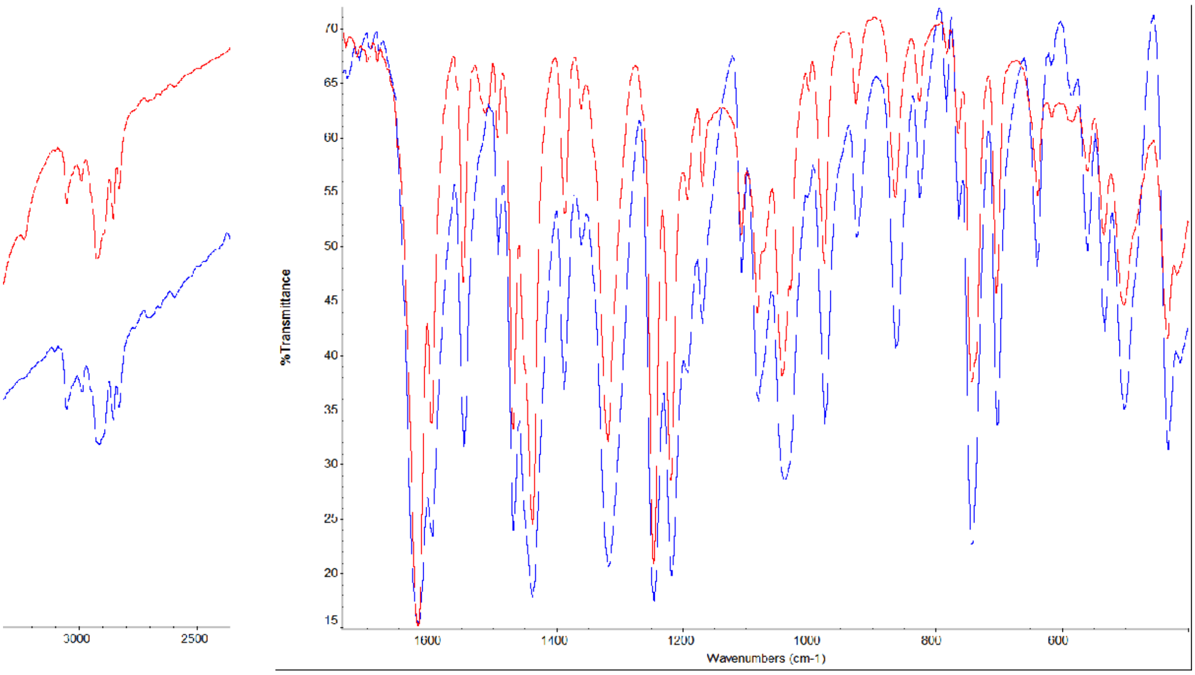

Fig S1. IR spectra for the enantiomers of **1*R*** (red) and **1*S*** (blue).

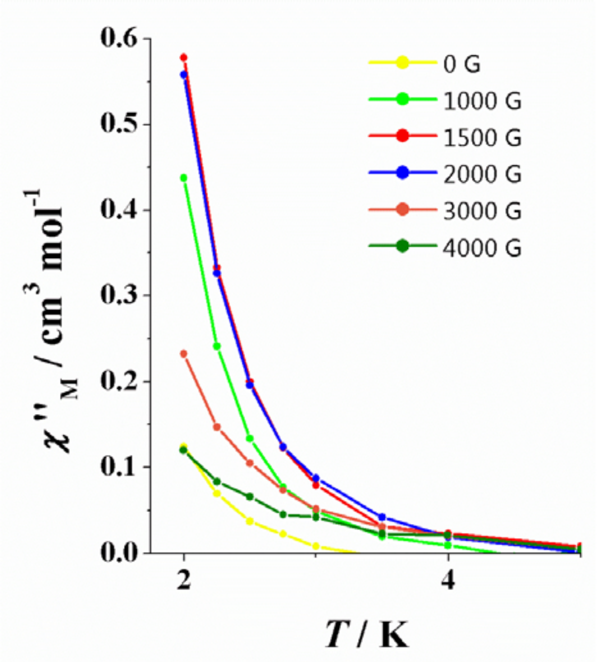

Fig S2. AC response of the under different static fields and at the 1000 Hz frequency for complex **1*R***. From these data the 1500 G field was selected for the alternate current measurements.

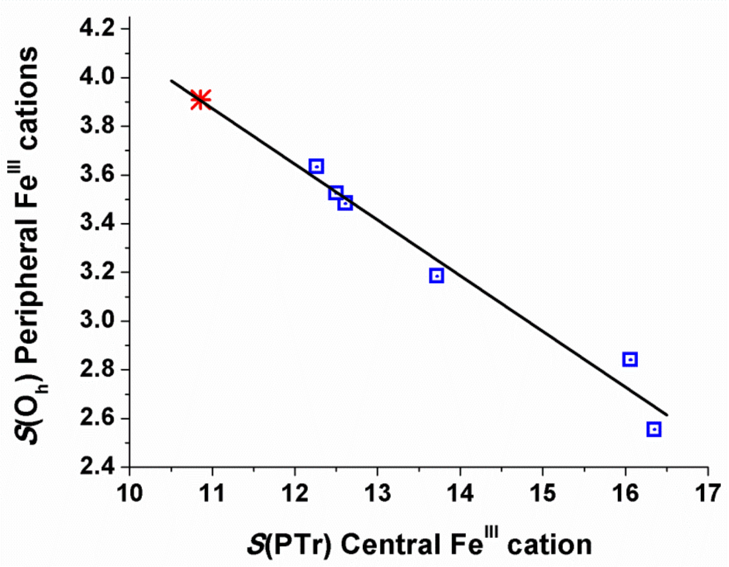

Fig S3. *S*(PTr) for the central Fe^{III} cations versus *S*(O*h*) for the peripheral ones, showing the correspondence between both distortions for the reported complexes type **VI**. (Red star shows the values for complex **1*S*** that shows the larger distortion from the regular polyhedra.

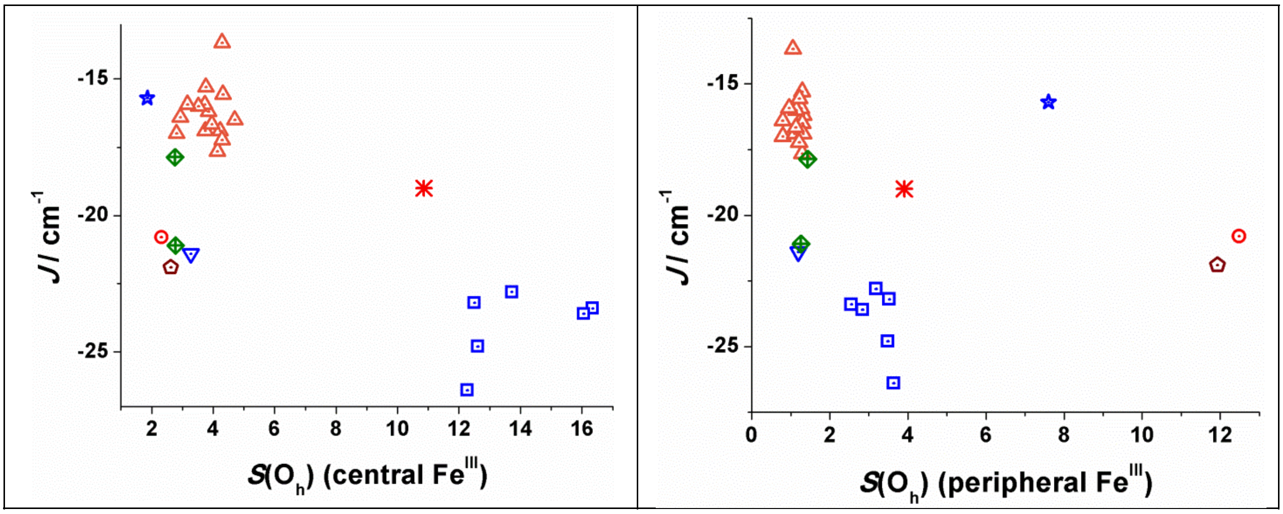

Fig S4 *S*(O*h*) vs. *J* for the all the reported Fe_4 complexes. Any direct correlation can be extracted between the distortion of the central or peripheral environments and the magnitude of the interaction. However, each type of complexes shows a range of characteristic values.

Table S1. Selected bond distances (Å) and angles (°) for the core of compound **2*RS***.

Fe1-O1	1.901(2)	Fe1-O5	1.931(2)
Fe1-O2	1.963(2)	Fe1-N1	2.137(2)
Fe1-O4	2.206(2)	Fe1-N2	2.128(2)
O1-Fe1-O2	161.22(7)	O4-Fe1-O5	154.56(7)
O1-Fe1-O4	95.76(7)	O4-Fe1-N1	92.23(7)
O1-Fe1-O5	99.53(8)	O4-Fe1-N2	73.90(7)
O1-Fe1-N1	78.31(8)	O5-Fe1-N1	110.66(8)
O1-Fe1-N2	91.09(8)	O5-Fe1-N2	85.55(8)
O2-Fe1-O4	83.07(7)	N1-Fe1-N2	161.75(8)
O2-Fe1-O5	88.70(7)		
O2-Fe1-N1	82.99(8)		
O2-Fe1-N2	106.45(8)		

Table S2. Fit values for the τ_0 and U_{eff} parameters from the ln(χ''/χ') vs. 1/*T* plots.

Frequency (Hz)	τ_0	U_{eff}
1488.1	7.02 E-07	10.22
1320.4	5.61 E-07	10.68
1143.3	4.77 E-07	11.03
997.3	5.06 E-07	10.96
852.3	5.24 E-07	10.94
679.3	5.19 E-07	11.02
509.5	6.02 E-07	10.81
349.8	8.29 E-07	10.31

Table S3 *S*(O*h*) and *S*(PTr) values calculated for the central and peripheral cation of the reported $\mathrm{Fe_4}$ star-shaped systems.

		Central $\mathrm{Fe^{III}}$		Peripheral $\mathrm{Fe^{III}}$						Peripheral $\mathrm{Fe^{III}}$	
CCDC	**Type**	***S*(O*h*)**	***S*(PTr)**	**S_1(O*h*)**	**S_1(PTr)**	**S_2(O*h*)**	**S_2(PTr)**	**S_3(O*h*)**	**S_3(PTr)**	**Mean *S*(O*h*)**	**Mean *S*(TPr)**
AGAQIJ	**I**	3.849	5.630	1.263	10.096	1.274	10.006	1.445	9.557	1.327	9.886
DOPKAV	**I**	3.114	6.488	1.120	10.559	0.868	11.381	0.696	12.199	0.895	11.380
DUFNUO	**I**	2.809	7.149	0.991	11.613	0.601	13.051			0.796	12.332
DUFPAW	**I**	2.936	6.860	0.958	11.876	0.623	12.875			0.790	12.375
DUPSAK	**I**	3.727	5.658	1.382	10.119	1.149	10.358			1.265	10.239
ICOCIN	**I**	3.767	5.619	1.443	10.081	1.130	10.430			1.287	10.255
ITAKUJ	**I**	4.701	4.676	1.295	10.102					1.295	10.102
KAXGUN	**I**	3.746	5.644	1.141	10.627	1.061	10.632			1.101	10.630
NIPJEC	**I**	4.228	5.161	1.346	9.674	1.286	10.163			1.316	9.919
TACFUA	**I**	4.292	4.990	1.005	10.822	1.105	10.634			1.055	10.728
TACGAH	**I**	3.957	5.396	1.380	9.613	0.873	11.646			1.127	10.629
VOBXUG	**I**	3.520	5.983	1.226	10.391	1.050	10.768			1.138	10.580
XUBVUM	**I**	4.140	5.254	1.576	9.171	1.093	10.725	1.207	10.210	1.292	10.036
XUBWAT	**I**	4.294	5.043	1.395	9.577	1.033	11.023			1.214	10.300
XUBWEX	**I**	4.317	5.026	1.405	9.581	1.036	11.026			1.220	10.304
XUBWIB	**I**	3.167	6.414	0.921	11.156	0.992	11.060			0.956	11.108
ICOCOT	**II**	3.277	7.523	1.193	11.619					1.193	11.619
DEKPAK	**III**	2.780	8.687	1.413	10.391	1.113	12.439			1.263	11.415
GANWEA	**III**	2.766	8.882	1.630	9.762	1.229	11.867			1.430	10.814
ABOKIL	**IV**	2.449	9.947	11.733	3.734	10.817	4.824			11.275	4.279
ABOLEI	**IV**	2.400	9.858	12.439	3.632	12.606	3.094			12.522	3.363
MEMKAR	**IV**	2.318	10.452	14.082	3.413	11.412	3.981	11.953	3.190	12.482	3.528
SAGBOU	**IV**	2.654	9.572	13.013	3.816	11.868	3.911	11.790	4.008	12.224	3.912
CUHJEW	**V**	1.859	12.764	5.124	5.882	9.085	2.769	8.593	2.919	7.601	3.857
TACHIR	**V**	1.792	13.075	6.953	4.008	6.617	4.035	8.570	3.298	7.380	3.780
JORWAQ	**VI**	16.350	0.466	2.554	9.721					2.554	9.721
UVIPUL	**VI**	16.059	0.550	2.800	9.166	3.114	9.172	2.608	9.559	2.841	9.299
XOKDEI	**VI**	12.611	0.975	3.444	8.048	3.725	7.148	3.283	8.419	3.484	7.872
XOKDIM	**VI**	12.502	0.987	3.913	6.941	3.262	8.389	3.401	8.032	3.525	7.787
XOKDOS	**VI**	12.266	1.094	3.668	7.857	4.273	7.018	2.961	8.416	3.634	7.763
XOKQAR	**VI**	13.718	0.790	3.332	8.486	3.087	8.528	3.134	8.819	3.184	8.611
1*S*	**VI**	10.861	1.618	4.082	7.147	2.421	9.530	5.225	6.318	3.909	7.665
AHOTEX	**VII**	2.624	10.588	11.628	6.205	11.684	6.228	12.476	6.001	11.929	6.144
DAMREQ	**VIII**	0.843	15.123	3.305	6.029	2.844	6.771			3.074	6.400
GAGREM	**VIII**	5.888	3.855	1.284	13.660	1.270	13.577			1.277	13.619
LEBRIU	**VIII**	3.234	8.247	3.078	7.170	PyQ*		PyQ*		3.078	7.170

* Square pyramidal environment.

CHAPTER 4. MANGANESE COMPLEXES

This chapter comprises ***Publication #4***, ***Publication #5***, ***Publication #6*** and ***Publication #7***.

Publication #4 *"Trinuclear complexes derived from R/S Schiff bases - Chiral Single-Molecule Magnets"* is about the synthesis and the magnetic characterization of three enantiomeric pairs of trinuclear manganese clusters labelled as **[6*R*]**, **[6*S*]** **[7*R*]**, **[7*S*]** and **[8*R*]** and **[8*S*]** by the reaction of **H_2L7** and **H_2L8** with different manganese salts, ($Mn(PhCOO)_2$ for **[6]** and **[7]** and $MnCl_2·4H_2O$ for **[8]**).

Complexes **[6]** and **[7]** show a typical structure of Mn clusters with carboxylates presenting a trinuclear configuration with the linear core $\{Mn^{II}Mn^{III}_2(\mu\text{-}RO)_2(RCOO)_4\}$ with the Mn^{II} in the middle of the other two Mn^{III} cations. In contrast, complex **[8]** has a triangular $[Mn^{III}_3]$ core with the three manganese cations linked by an unusual μ_3-Cl bridge, being the first example in discrete triangular Mn^{III} systems. While **[6]** and **[7]** present an antiferromagnetic coupling between manganese cations, complex **[8]** shows a moderate intramolecular ferromagnetic interaction with negative ZFS. The dynamic magnetic properties of **[8]** were explored and slow relaxation of the magnetization was observed under an applied field of 1000 G due to the favorable alignment of the Mn^{III} easy axis.

Publication #5 **"***Syntheses, structures and chiroptical and magnetic properties of chiral clusters built from Schiff bases: a novel $[Mn^{II}Mn_6^{III}Na_2^{I}]$ core*" and ***Publication #7*** *"Chiral $[Mn^{II}Mn^{III}M']$ ($M'=Na^{I}$, Ca^{II}, Mn^{II}) and $[Mn^{II}Mn_6^{III}Na_2^{I}]$ clusters built from an enantiomerically pure Schiff base: synthetic, chiroptical and magnetic properties*" are closely related because one of them is a previous communication while the other is the full paper. Complexes **[9]-[15]** are described in these papers yielding in a series of Mn clusters using **H_2L9** for all the syntheses. Aim of the work was to observe differences in the products by changing the alkaline/alkaline earth cation (Na^{I}/Ca^{II}) and the bridging halides (Cl^-/Br^-).

[9*R*]/[9*S*] and **[10*R*]/[10*S*]** are nonanuclear complexes with core $[Mn^{II}Mn_6^{III}Na_2^{I}]$ containing μ-Cl^- or μ-Br^- bridges, respectively. By slightly changing the synthesis conditions, a variation of structure **[8],** which corresponds to the Br^- derivative, is obtained, yielding the structure **[11*R*]/[11*S*]** with core $[Mn^{II}Mn_3^{III}Na^{I}]$. Trying to replace the alkaline cation, syntheses with K^+ and Cs^+ were tried showing that both were too big for the cavity, and yielding in all the cases complexes **[12*S*]** and **[13*R*]/[13*S*]** with unprecedented core $[Mn_2^{II}Mn_3^{III}]$, demonstrating that the cavity is size selective for cations equal or smaller than Na^+.

Taking profit of this, a synthesis using $Ca(CH_3O)_2$ allowed to obtain complexes **[14*R*]/[14*S*]** and **[15*S*]**, with core $[Mn_4^{III}Ca^{II}]$ due to the similar size of Na^{I}, Mn^{II} and Ca^{II}. Complexes **[14]** and **[15]** have a very similar structure to the one proposed for the Photosystem II.

About the magnetic properties of these series of compounds, no one of them presents slow relaxation of the magnetization due to the unfavorable orientation of the anisotropy axes of the Mn^{III} cations, but the magnetostructural correlations are really interesting. The triangular arrangement of the Mn^{III} subunits has a ferromagnetic behavior yielding to a $S = 6$ for each triangle, except for complexes **[12]** and **[13]** where one of the ligands has an inverted position. In the case of complexes **[9]** and **[10]**, each one of these triangles is antiferromagnetically coupled with the Mn^{II} cation, and there is also a weak coupling between the two triangles that influences the low temperature susceptibility. This intertriangle coupling is the key factor to justify the susceptibility and magnetization curves.

Publication #6 "*Triple halide bridges in chiral*$[Mn_2^{II}Mn_6^{III}Na_2^{I}]$ *cages: structural and magnetic characterization*", describes the synthesis and the magnetic behavior of the enantiomeric pairs with core $[Mn_2^{II}Mn_6^{III}Na_2^{I}]$ **[16*R*]/[16*S*]** and **[17*R*]/[17*S*]** and using **H_2L10** with $MnCl_2$ and $MnBr_2$, respectively. In these clusters, there a triple halide bridge between the two Mn^{II} cations. For the case of the Cl^- derivative, this is the second example in molecular complexes in the literature, while is the first one for the Br^- derivative. In both cases, this paper is the first magnetic study of the triple halide bridge Mn^{II}-$(X)_3$-Mn^{II} in discrete complexes.

These compounds present a ferromagnetic coupling inside the Mn^{III} triangle and are antiferromagnetically coupled with the Mn^{II}. The triple halide bridge presents a very weak antiferromagnetic coupling between the two Mn^{II} cations and in the case of the Br^- derivative is almost zero, making that the compound practically behaves as two independent $[Mn^{II}Mn_3^{III}]$ units.

Is opportune to mention at this point that the complex represented in **Figure 4.1** can be obtained when azide ions are added to the reaction mixture. This complex has two different connections inside the two Mn^{III} triangles (chloro or methoxide bridges in the axial positions of the trivalent manganeses). It has a magnetic behavior similar to **[16]** and **[17]** with antiferromagnetic coupling mediated by the triple azido bridge. This complex was excluded of the work due to the crystallization problems.

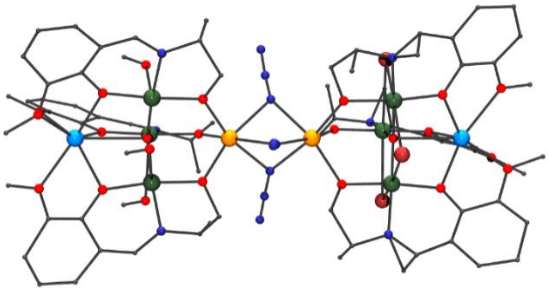

Figure 4.1. Obtained complex when NaN_3 is added to the reaction mixture. Color code: green, Mn^{III}; yellow, Mn^{II}; light blue, Na^{I}; red, oxygen; blue, nitrogen. The picture corresponds to the Br^- derivative.

The complexes reported in ***Publication #6*** point out that the pendant R group on the adjacent C-atom to the imine function is not innocent and that has a strong influence on the final structures, probably due to changes in the solubility of the systems. In fact, changing the phenyl for the isopropyl group the nuclearity and connectivity becomes different.

Publication #4 *"Trinuclear complexes derived from R/S Schiff bases - Chiral Single-Molecule Magnets"*

EurJIC
European Journal of Inorganic Chemistry

A Journal of
ChemPubSoc Europe

6/2017
www.eurjic.org

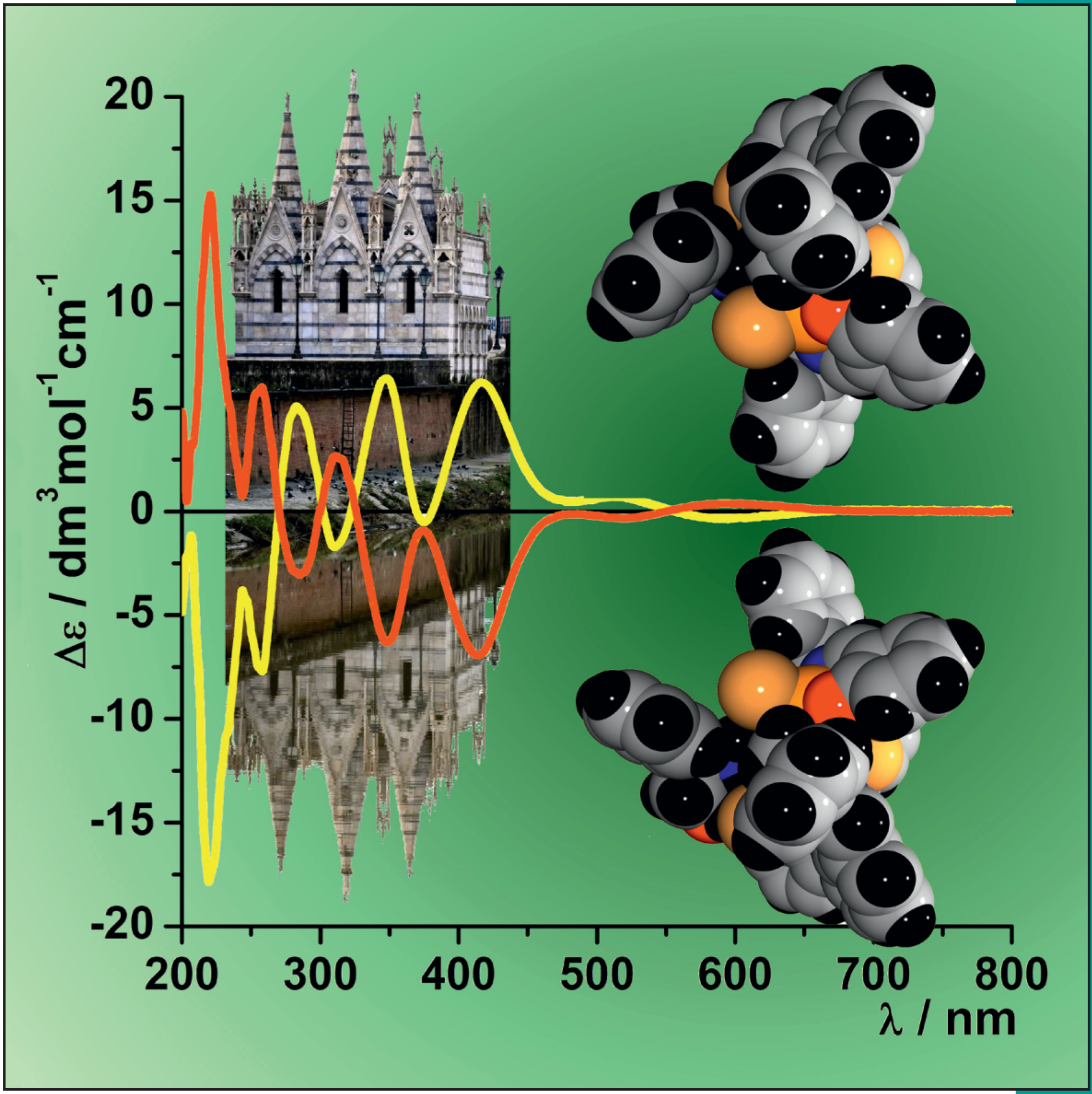

Front Cover

Albert Escuer et al.
Trinuclear Complexes Derived from *R*/*S* Schiff Bases –
Chiral Single-Molecule Magnets

WILEY-VCH

ChemPubSoc Europe
EurJIC European Journal of Inorganic Chemistry
Cover Profile

DOI: 10.1002/ejic.201700078

Read the full text of the article at 10.1002/ejic.201601138

Trinuclear Complexes Derived from *R*/*S* Schiff Bases – Chiral Single-Molecule Magnets

A. Escuer

J. Mayans

M. Font-Bardia

L. Di Bari

M. Górecki

UNIVERSITAT DE BARCELONA

UNIVERSITÀ DI PISA

Invited for the cover of this issue is the group of Albert Escuer from Universitat de Barcelona, Spain, in collaboration with the group of Lorenzo Di Bari from Università di Pisa, Italy. The cover image shows the space-filling plots of two enantiomeric Mn^{III} triangles and their electronic circular dichroism (ECD) spectra against a background of an enantiomeric image from the macroscopic world.

What was the inspiration for this cover design?

We had some discussion on what landmark to use. Interestingly, our colleagues from Pisa voted for places in Barcelona and vice versa. The final selection was made on the basis of the unique perspective of the natural mirror image of the gothic spires on the Arno waters, reflecting the inversion of the ECD spectra of the two enantiomers.

What role did international collaboration play in this work?

We strongly believe that sharing knowledge and expertise is the most relevant added value of research. Transnational relations have always played a major role in Europe. Learning from each other, sharing our cultural backgrounds, and, importantly, joining the specialized skills and resources of different teams lead to innovation.

What is the inspiration for this work?

Even with complicated molecular structures, dealing with chiral elements is easy, for example, the effect of branching in a simple 1,2-bidentate ligand, like our own iminoalcohol. Observing molecular magnetism with chiroptical methods was a natural consequence. With similar systems, we hope to investigate more complex phenomena such as magnetochiral spectroscopy.

Is your current research mainly fundamental or rather applied?

Our research is mainly devoted to synthesis and magnetic (mainly single-molecule magnets) or optical properties. Nevertheless, quantum-mechanical phenomena, at a few degrees Kelvin, lead to applications in real devices. Moreover, chiral emissive complexes are promising materials in fields as diverse as medical diagnosis, new-generation 3D screens, or security devices.

Did serendipity play a part in this work?

Serendipity is one of the main tools in cluster chemistry. In spite of the constant discussion on serendipity versus design, only in few cases is it possible to predict the full design of a polynuclear complex, as there are many variables to account for (solvents, stoichiometry, solubility, counterions, etc.). Serendipitous findings are not random findings, as was pointed out in the original definition by Warpole "*always making discoveries, by accidents and sagacity, of things which they were not in quest of*". Successful synthesis of clusters with specific properties requires the correct choice of variables based on knowledge and experience… and often, something better is discovered on the way!

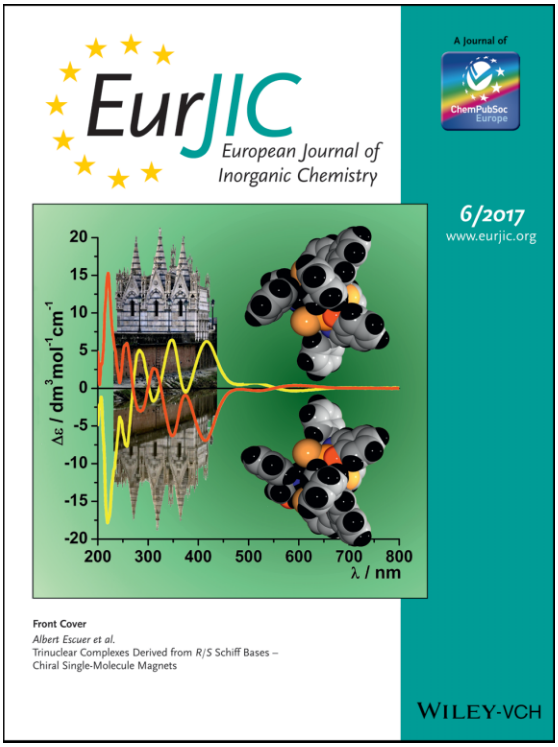

Front Cover
Albert Escuer et al.
Trinuclear Complexes Derived from *R*/*S* Schiff Bases – Chiral Single-Molecule Magnets

© 2017 Wiley-VCH Verlag GmbH & Co. KGaA, Weinheim

DOI: 10.1002/ejic.201601138

Chiral Magnets

Trinuclear Complexes Derived from *R*/*S* Schiff Bases – Chiral Single-Molecule Magnets

Albert Escuer,*[a] Julia Mayans,[a] Merce Font-Bardia,[b] Lorenzo Di Bari,[c] and Marcin Górecki[c]

Abstract: The employment of enantiomerically pure Schiff bases in manganese chemistry is revealed to be an excellent method to obtain chiral single-molecule magnets and has allowed the characterization of several pairs of enantiomers, for which the magnetic properties were investigated. The reported systems consist of $Mn^{III}–Mn^{II}–Mn^{III}$ linear trimers or Mn^{III}_3 cations in a triangular arrangement including the first example of a μ_3-Cl bridge in an isolated manganese triangle.

Introduction

Research on coordination clusters of paramagnetic 3d or 4f cations has been key in the search for single-molecule magnets (SMMs) or single-ion magnets (SIMs)[1] and more recently for their catalytic,[2] bioinorganic,[3] and optical[4] properties. The exploration of molecular systems that crystallize in chiral space groups is still an emerging field, and the possible chiral organization of magnetic moments can produce quite exotic properties such as the predicted skyrmions[5] or chiral solitons.[6] The spontaneous crystallization of nonchiral components in chiral groups or the resolution of racemic mixtures are unusual[7] or experimentally difficult; therefore, syntheses with enantiomerically pure chiral ligands have become the optimal method to reach systems of this kind.[8]

The condensation of salicylaldehyde and 1,2-aminoethanol yields the Schiff base 2-[(2-hydroxyethyl)iminomethyl]phenol (H_2sae, Scheme 1). H_2sae is a popular ligand and has been employed widely in transition-metal and lanthanide coordination chemistry (around 110 entries in the CCDC) owing to its good chelating properties and its ability to generate polynuclear systems through the potentially bridging *O*-phenolate and *O*-alkoxido donors.

The chemistry of manganese with nonchiral Schiff bases such as H_2sae or their substituted analogs has been partially explored in the recent past to yield a variety of systems such as neutral mononuclear Mn^{IV} complexes,[9] one Mn^{III} 1D system,[10] and several homometallic $Mn^{II}Mn^{III}_2$,[11] Mn^{III}_4 (ring),[12] Mn^{III}_4 (butterfly),[12c,13] Mn^{III}_6, $Mn^{II}_2Mn^{III}_4$, and Mn^{III}_8 clusters[13,14] as well as heterometallic[15] $Cu^{II}_3Mn^{III}$ and $Ni^{II}_2Mn^{III}_2$ clusters. Among them, the magnetic properties of the tetranuclear cyclic systems with general formula $[Mn^{III}_4X_4L_4]$ (X = Cl, Br) have been the most interesting, as they display ferromagnetic interactions and SMM responses.[12b]

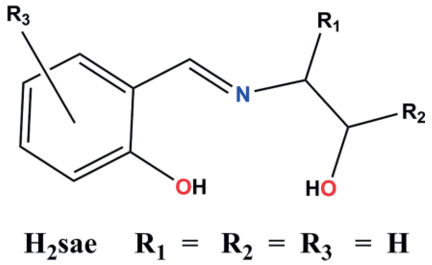

Scheme 1. General structural formula for the H_2sae ligand and its substituted derivatives. The variation of the R1 and R2 groups allows the synthesis of chiral ligands.

The substitution on the aromatic ring or the C atoms of the ethyl fragment can increase the number of Schiff bases enormously, and chirality can be induced if the substitution occurs at the 1- or 2-position of the hydroxyethyl group (Scheme 1).

Following our work in this field, we have explored the reactivity in manganese chemistry of the enantiomerically pure ligands (*R*)- and (*S*)-2-[(2-hydroxy-1-phenylethyliminomethyl)-phenol] (H_2**L1**) and (*R*)- and (*S*)-2-[(3-hydroxy-1-phenylpropyliminomethyl)phenol] (H_2**L2**, Scheme 2).

The reactions of these ligands with different manganese salts under appropriate reaction conditions allowed the characterization of the first polynuclear derivatives of H_2**L1**/H_2**L2** consisting of three pairs of trinuclear chiral clusters with formulas $[Mn_3(\mathbf{L1})_2(PhCOO)_4(MeOH)]$ [(*R*)-**1**·MeOH and (*S*)-**1**·MeOH], $[Mn_3(\mathbf{L2})_2(PhCOO)_4]$ [(*R*)-**2**·5H_2O and (*S*)-**2**·2MeCN·MeOH·1.5H_2O], and (Phgly)$[Mn_3(\mathbf{L1})_3(\mu_3\text{-Cl})(Cl)_3]$ [(*R*)-**3**·0.5MeCN·0.25MeOH·0.5H_2O and (*S*)-**3**·0.5MeCN·0.5H_2O; Phgly = phenyl-

---

[a] Departament de Química Inorgànica i Orgànica,
Secció Inorgànica and Institute of Nanoscience (IN^{2}UB)
and Nanotecnology, Universitat de Barcelona,
Av. Diagonal 645, 08028 Barcelona, Spain
E-mail: albert.escuer@ub.edu
http://www.ub.edu/inorgani/recerca/MagMol/magmol.htm
[b] Departament de Mineralogia, Cristallografia i Dipòsits Minerals and
Unitat de Difracció de R-X, Centre Científic i Tecnològic de la Universitat
de Barcelona (CCiTUB), Universitat de Barcelona,
Solé i Sabarís 1–3 08028 Barcelona, Spain
[c] Dipartimento di Chimica e Chímica Industriale, Università di Pisa,
Via Moruzzi 13, I-56124 Pisa, Italy

Supporting information and ORCID(s) from the author(s) for this article are available on the WWW under http://dx.doi.org/10.1002/ejic.201601138.

© 2017 Wiley-VCH Verlag GmbH & Co. KGaA, Weinheim

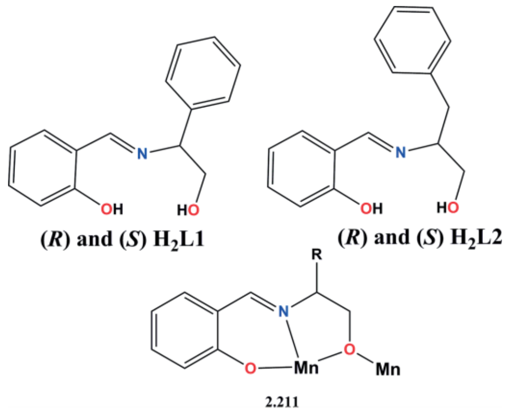

Scheme 2. Structures of H_2**L1** and H_2**L2** ligands (top) and their crystallographically established coordination mode in complexes **1**–**3** (bottom).

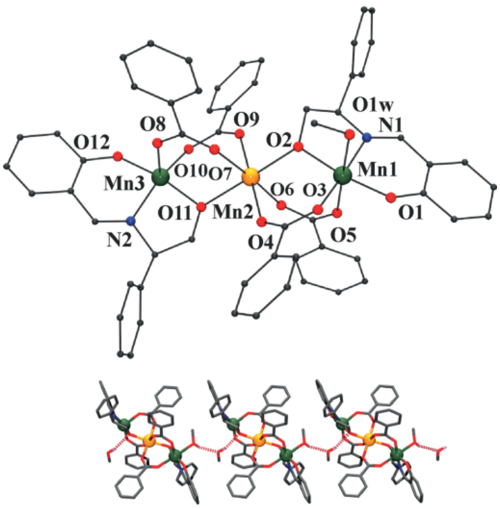

Figure 1. Top: partially labeled plot of **1** [common labels for (*R*)-**1** and (*S*)-**1**]. Bottom: 1D arrangement of trinuclear units linked by intermolecular H bonds (red dashed bonds). H atoms omitted for clarity. Color key: Mn^{II} orange, Mn^{III} dark green, O red, N navy, C grey.

glycinate]. Complexes **1** and **2** have linear $\{Mn^{II}Mn^{III}_2(\mu\text{-}O)_2(RCOO)_4\}$ cores, whereas **3** has a triangular arrangement with an unprecedented $\{Mn^{III}_3(RO)_3(\mu_3\text{-}Cl)\}$ linkage and SMM response.

Results and Discussion

Structural Descriptions

Each pair of enantiomers is very similar; therefore, a common structural description is provided for the corresponding *R* enantiomer. The oxidation states of the manganese atoms have been assigned on the basis of structural considerations and bond valence sum (BVS) calculations. The bond parameters for each pair of enantiomers are summarized in Table S2 for (*R*)-**1** and (*S*)-**1**, Table S3 for (*R*)-**2** and (*S*)-**2**, and Table S4 for (*R*)-**3**. Some significant bond parameters for (S)-**3** are also provided in Table S4.

[Mn$_3$(L1)$_2$(PhCOO)$_4$(MeOH)]·MeOH [(R)-1·MeOH and (S)-1·MeOH]

Compounds (*R*)-**1** and (*S*)-**1** can be described as linear trinuclear $Mn^{III}_2Mn^{II}$ systems, in which the Mn^{II} cation is in the central position and linked to both Mn^{III} cations by two *syn–syn* carboxylate bridges and one alkoxido bridge. A view of the complex is shown in Figure 1, and the main bond parameters are summarized in Table S2. The trinuclear system is almost linear [the Mn(1)···Mn(2)···Mn(3) angle is close to 178°]. The divalent Mn(2) cation shows an MnO_6 octahedral environment, whereas the trivalent Mn(1) cation exhibits an octahedral MnO_5N coordination with the elongated Jahn–Teller axis directed toward the O(5)-carboxylato atom and the coordinated methanol molecule, and Mn(3) shows a square-pyramidal MnO_4N environment with the apical position occupied by the O(8) donor from one of the carboxylate groups.

The angle between the main O10–O11–O12–N2 and O1–O2–O3–N1 planes is 6.2°; thus, the easy axes of the two Mn^{III} cations, defined by the Mn3–O8 and O5–Mn1–O1w directions, are approximately parallel.

The crystallization methanol molecule establish two H bonds with the coordinated methanol molecule and the O(11) alkoxido atom of the neighboring clusters to afford a 1D arrangement of trimers. The O(1w)···O(2 W) and O(1w)···O(11) distances are 2.764 and 2.984 Å, respectively.

[Mn$_3$(L2)$_2$(PhCOO)$_4$(MeOH)]·Solvent [(R)-2·5H$_2$O, (S)-2·2MeCN·MeOH·1.5H$_2$O]

The trinuclear compounds (*R*)-**2** and (*S*)-**2** show the same general formulas and connectivities as (*R*)-**1** and (*S*)-**1** but significant differences in the manganese coordination spheres and the arrangement of the ligands. A view of the complex is shown in Figure 2, and the main bond parameters are summarized in Table S3.

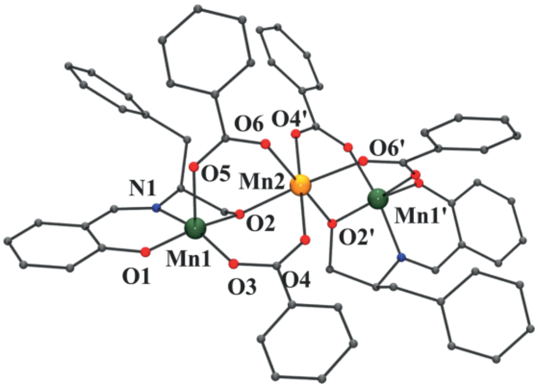

Figure 2. Partially labeled plot of **2** [common labels for (*R*)-**2** and (*S*)-**2**].

For **2**, the two moieties of the complex are related by one C_2 axis, which results in a more symmetrical molecule than **1**. In this case, the trinuclear complex has a Mn(1)···Mn(2)···Mn(1′) angle of 135°, and the carboxylate ligands are placed on the same side of the mean trimer plane. Mn(1) and symmetry-related Mn(1′) are pentacoordinate with MnO_4N square-pyramidal environments, whereas the divalent Mn(1) cation is octahedrally coordinated.

© 2017 Wiley-VCH Verlag GmbH & Co. KGaA, Weinheim

The angle determined by the mean planes that define the base of the square pyramids (O1–O2–O3–N1 and the symmetry-related counterpart) is 44.6°; consequently, the angle between the easy axes of the Mn^{III} cations is also close to 45°.

(Phgly)[$Mn_3(L1)_3(\mu_3\text{-}Cl)(Cl)_3$]·0.5MeCN·0.5$H_2O$·0.25MeOH [(*R*)-3·0.5MeCN·0.5H_2O·0.25MeOH]

Complex (*R*)-**3** can be described as a triangular arrangement of three Mn^{III} ions linked by *O*-alkoxido donors and one μ_3-Cl bridge. A view of the complex is shown in Figure 3, and the main bond parameters are summarized in Table S4. The Mn^{III} cations are octahedrally coordinated with a $MnCl_2O_3N$ environment. One **L1**$^{2-}$ Schiff base is coordinated to each manganese atom through their three donor atoms and acts as an *O*-alkoxido bridge to the neighboring cation. The coordination sphere is completed by two chlorido ligands in *trans* positions, one of which acts as a μ_3-Cl bridge. The easy axis corresponding to the elongated axis of the octahedron follows the Cl–Mn–Cl direction, and the mean O_3N planes of the Mn^{III} cations are tilted by ca. 58° as consequence of this arrangement.

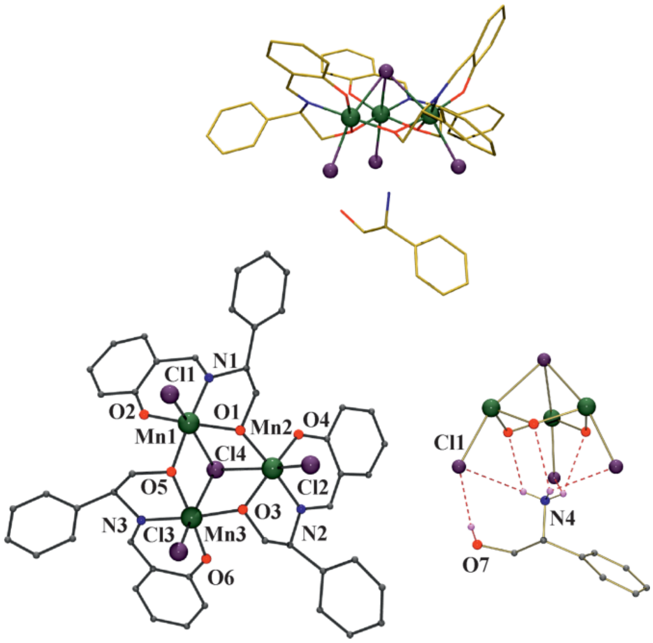

Figure 3. Left: partially labeled plot of (*R*)-**3**. The partial resolution of the structure confirmed the same core for (*S*)-**3**. Right: H bonds involving the trimeric complex and the protonated $Phgly^+$ cation. Color scheme: Mn^{III} dark green, O red, N navy, Cl violet, C grey, H pink.

The trinuclear entity is monoanionic, and charge balance is provided by one protonated phenylglycinate cation [(*R*)- or (*S*)-$Phgly^+$ for (*R*)-**3** or (*S*)-**3**, respectively], which is linked to the three terminal chlorido ligands and the *O*-alkoxido atoms through six H bonds promoted by the RNH_3^+ fragment. No relevant intermolecular interactions were found.

It should be emphasized that complexes **3** are the only examples of discrete triangular Mn^{III} systems with one μ_3-Cl bridge. This kind of bridge has been reported previously for cubanes with {Mn_4O_3Cl} cores in which one corner[16] is occupied by the chlorido ligand or as a fragment of a larger cluster.

Comments on the Syntheses

The reactions of H_2**L1** and H_2**L2** with manganese carboxylates yielded the trinuclear $Mn^{II}Mn^{III}_2$ systems **1** and **2**, which show the very stable {$Mn^{II}Mn^{III}_2(\mu\text{-}O)_2(RCOO)_4$} core. This kind of complex is well known for most transition-metal cations; for manganese, they often form from the reactions of manganese carboxylates with bi- or tridentate ligands. Notably, the cores of **1** and **2** are closely related, and the main difference lies in the rotation of one of the moieties by ca. 60° (Figure 4).

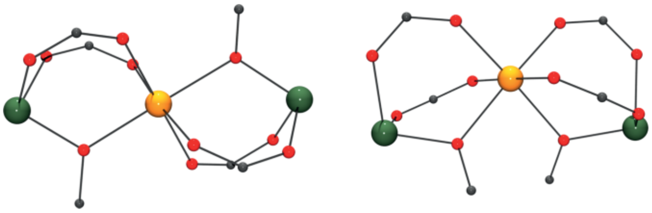

Figure 4. Cores of **1** (left) and **2** (right).

More interesting are the reactions of H_2L (H_2sae or substituted derivatives) with $MnCl_2$ (Scheme 3). Tetranuclear rings with four μ-O and four μ-Cl bridges formed through the reactions of $MnCl_2$ and the Schiff base (1:1) in ethanol followed by recrystallization in acetonitrile/diethyl ether.[12a,12b]

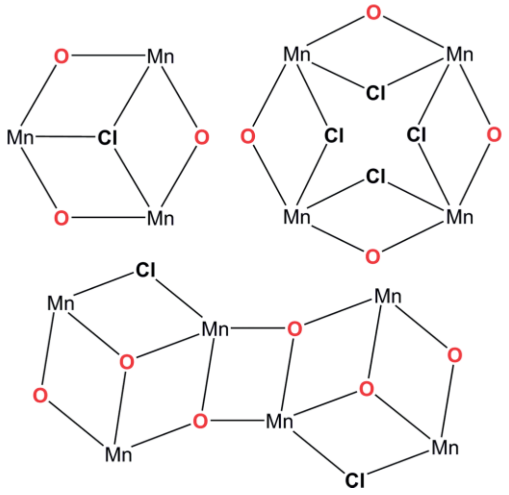

Scheme 3. Tri-, tetra-, and hexanuclear cores of the clusters reported previously through the reactions of $MnCl_2$ and H_2sae (or substituted derivatives). All oxygen bridges are provided by the *O*-alkoxido atoms of the sae^{2-} ligands.

In that case, the deprotonation of the ligand was induced by the trivalent manganese centers because no base was added. The same core was also formed through the reaction of $MnCl_2$, the Schiff base, and sodium benzoate (in a 4:2:1 ratio) in hot acetonitrile.[12c] In contrast, a hexanuclear $Mn^{II}_2Mn^{III}_4$ core was obtained through the reaction of $MnCl_2$, the Schiff base, and triethylamine (in a 1:1:2 ratio) in methanol.[14] In our case, (*R*)-**3** and (*S*)-**3** were obtained through the reaction of $MnCl_2$, the chiral Schiff base, and sodium benzoate (in a 1:1:1 ratio) in acetonitrile under reflux.

The deprotonation of the H_2L ligands occurs in neutral and basic media, and a comparison of the reaction conditions suggests that it is hard to extract any justification for the different nuclearities. The most probable factor that allows the formation of triangular systems **3** is the partial breaking of the ligand during the heating of the reaction mixture under reflux to regenerate the Phgly$^+$ cation, which helps to stabilize the structure. The only conclusion is that these systems are very sensitive to small changes in the synthetic procedures, and a rich cluster chemistry can be advanced by the systematic study of reactions with the variation of the strength of the basic medium, the H_2sae substituents, or the solvent.

Electronic Circular Dichroism Spectra

Electronic circular dichroism (ECD) spectroscopy represents a crucial tool in structural studies of chiral coordination compounds.[17] Generally, the chirality in such systems may be induced by a chiral ligand, by the intrinsic chirality of metal coordination, or both. The ECD and absorption (UV/Vis) spectra of the complexes in solution (CH_3CN) and in the solid state (KCl pellets) were measured. The solid-state ECD spectra of both enantiomers of **1**–**3** (Figure 5) and those recorded in acetonitrile solution for both enantiomers of **2** and **3** are perfect mirror images of each other (see Supporting Information, Figures S1 and S2); this confirms the enantiomeric purity and also artefact-free character of the solid-state spectra. The solid-state ECD spectra again showed some regularities. For (*S*)-**1** and (*S*)-**3**, there is a common sequence of ECD bands: negative in the range λ = 650–800 nm, positive at $\lambda \approx$ 550 nm, and negative at $\lambda \approx$ 400 nm [also present for (*S*)-**2**]. Owing to the low solubility of **1**, the acetonitrile solution was prepared by heating for several minutes, and we noticed that the spectra for the two enantiomers were not exact mirror images (Figure S3). The sum of the two ECD spectra should give zero or, for different enantiomeric purity, a spectrum identical to that of one of the two enantiomers. This is not the case, as shown in Figure S4; therefore, some inequivalent decomposition occurs during the heating process.

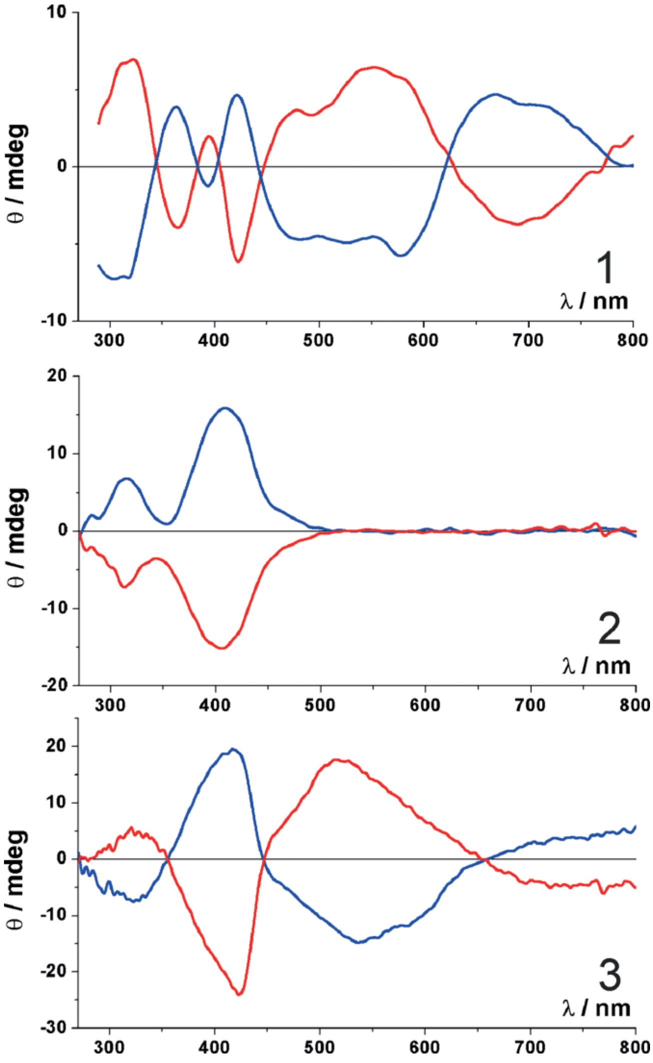

Figure 5. Solid-state ECD spectra for the pairs of enantiomers of **1**–**3** (red lines, *S* enantiomers; blue lines, *R* enantiomers).

All of the absorption spectra of the complexes in acetonitrile solution are fairly similar to each other (see Figures S1–S3). The spectra show a very weak band at $\lambda \approx$ 470 nm (this band is not developed for **3**), a moderately intense band at $\lambda \approx$ 390 nm, and two intense bands at λ = 270 and $\lambda \approx$ 230 nm. Similarly to the absorption spectra, the ECD spectra display a few common features, especially in the range λ = 300–800 nm. All of the complexes with the *S* ligand configuration, that is, (*S*)-**1**, (*S*)-**2**, and (*S*)-**3**, show three negative bands: one in the range λ = 500–550 nm, the second at $\lambda \approx$ 400 nm, and the third one in the range λ = 300–350 nm. Furthermore, for (*S*)-**1** and (*S*)-**3**, a weak positive broad band appears in the visible range centered at λ = 675 and 595 nm, respectively. As expected, this range is not readily detectable in the absorption spectra (in the concentration range $2.0–2.7 \times 10^{-4}$ M) as the transitions have mainly d–d character.

In summary, although the chiral complexes show very different structures, the presence of the aforementioned correlations support the hypothesis that the ECD spectrum is directed mainly by the chirality of the chelating ligands rather than the chirality of the manganese coordination sphere by itself. To obtain more evidence, we compared the solution and solid-state ECD spectra. Such comparisons will give a pronounced view into the differences between the molecular species in both states and shed more light on the origin of the transitions in such complex systems. For clarity, the comparisons were done for one enantiomer for each pair of compounds.

For (*S*)-**1**, the solid-state and solution ECD spectra show significant variations (Figure S5); in particular, the signs of two bands in the visible region at $\lambda \approx$ 550 and 675 nm are opposite. This demonstrates that the solid-state ECD spectra are governed by intercrystalline interactions and the measured spectrum does not reflect the most stable conformer(s) in solution.

Time-dependent DFT (TDDFT) calculations of high-spin coordination compounds are still very demanding and were not performed because of the complexity of the system as a result of the complicated relationship between the geometry and the electronic configuration.[18]

In contrast to the previous case, complexes **2**, which are more symmetric than **1** (as stated above), exhibits rather similar ECD spectra in both media (Figure 6). The only difference is the

© 2017 Wiley-VCH Verlag GmbH & Co. KGaA, Weinheim

relative intensity of the band λ = 300 nm, which suggests that the dominant conformation in solution is similar to that in the solid state. Furthermore, one can notice that the intensity of the ECD bands (in solution) are the highest among the studied set of Mn complexes.

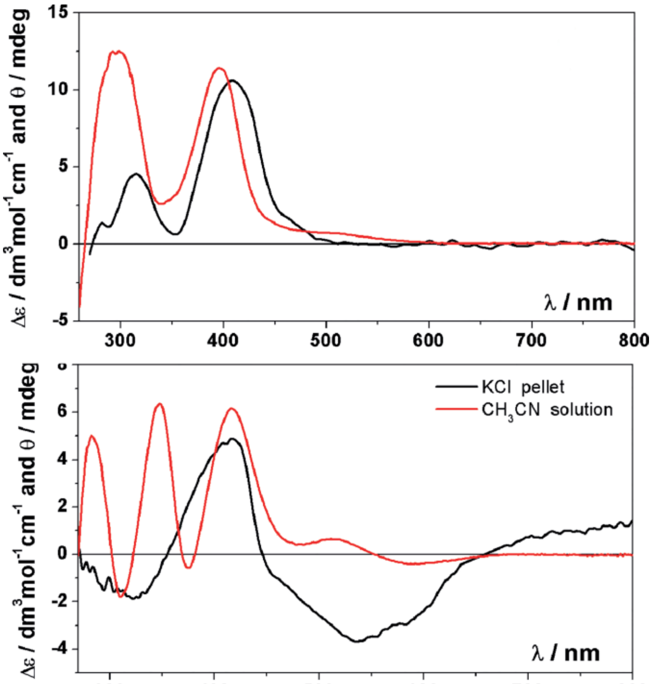

Figure 6. Comparison between the solid-state and solution ECD spectra for (*R*)-**2** (top) and (*R*)-**3** (bottom). Note that the solid-state spectrum of (*R*)-**2** is divided by 1.5 and that of (*R*)-**3** is divided by 4.

It is apparent from Figure 6 that the spectra for (*R*)-**3** in the solid state and solution are different. This suggests that the crystal structure is not close to the predominant structure(s) in acetonitrile solution, as could be expected from the weak H-bond interactions between the triangular cluster and the phenylglycinate counteraction, which could be broken readily by interactions with the solvent.

We noticed that the studied complexes in solution and the solid state are characterized by several well-developed ECD bands. In the solution spectra, ECD bands are good indicators of the absolute configuration of the ligand, both for linear (**1** and **2**) and triangular (**3**) Mn cores. The geometry of the most prevalent conformer(s) in solution is in good agreement with the solid-state structure only for **2**. Additionally, significant differences between the ECD spectra of **1** and **3** in the two media suggest a strong overlap of electronic transitions between the manganese coordination spheres and the arrangement of the ligands.

Magnetic Properties

The $\chi_M T$ versus T plots for the pairs of enantiomers of **1**–**3** are shown in Figure 7. The room-temperature $\chi_M T$ values for the enantiomers (*R*)-**1** and (*S*)-**1** are 8.62 and 8.41 cm^3 mol^{-1} K respectively, clearly lower than the expected value of 10.375 cm^3 mol^{-1} K for two Mn^{II} and one Mn^{III} isolated cations (g = 2.00). On cooling, the $\chi_M T$ values decreases continuously to a plateau at 1.5 cm^3 mol^{-1} K at ca. 6 K. At very low temperatures, the decrease is more pronounced, probably because of a mixing of the intermolecular coupling mediated by H bonds, the D effect induced by the Mn^{III} cations, or the weak interaction between the terminal Mn^{III} ions.

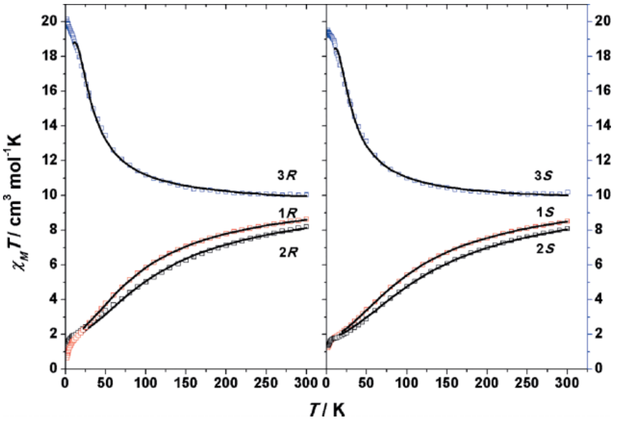

Figure 7. Plots of $\chi_M T$ versus T for (*R*)-**1**, (*R*)-**2**, (*R*)-**3** (left) and (*S*)-**1**, (*S*)-**2**, (*S*)-**3** (right). The solid lines are the fits of the data; see the text for the fit parameters.

To avoid overparameterization, the fit of the experimental data was performed in the 300–15 K temperature range with the conventional isotropic Hamiltonian for a linear arrangement of three S = 2, 5/2, 2 spins [Equation (1)]:

$$H = -2J(S_1 \cdot S_2 + S_2 \cdot S_3) \quad (1)$$

The best fit parameters were J = –5.7 cm^{-1} and g = 2.00 with $R = 1.53 \times 10^{-5}$ for (*R*)-**1** and J = –6.7 cm^{-1} and g = 2.01 with $R = 5.17 \times 10^{-6}$ for (*S*)-**1**.

As expected from their bond parameters, complexes (*R*)-**2** and (*S*)-**2** exhibit similar magnetic responses to that of **1**, and the room-temperature $\chi_M T$ values are 8.19 and 8.09 cm^3 mol^{-1} K, respectively. The fit of the experimental data was performed with the same Hamiltonian and conditions used for (*R*)-**1** and (*S*)-**1**. The best fit parameters were J = –7.1 cm^{-1} and g = 2.00 with $R = 2.95 \times 10^{-4}$ for (*R*)-**2** and J = –8.1 cm^{-1} and g = 2.02 with $R = 8.71 \times 10^{-5}$ for (*S*)-**2**. The magnetization under the maximum field of 5 T reached an unsaturated value close to 2.25 Nμ_B for the four complexes. These values are in agreement with those reported previously for similar Schiff bases and carboxylate bridges.[11a] The small difference between the values for each pair of enantiomers must be attributed to the different solvent molecules in the structures. Complexes (*R*)-**3** and (*S*)-**3** show room-temperature $\chi_M T$ values of 10.03 and 10.20 cm^3 mol^{-1} K. respectively, higher than the expected value of 9.00 cm^3 mol^{-1} K for three isolated Mn^{III} cations. As the temperature decreases, the $\chi_M T$ products of both compounds increase to a maximum value of ca. 20 cm^3 mol^{-1} K, which indicates a moderate intramolecular ferromagnetic coupling.

© 2017 Wiley-VCH Verlag GmbH & Co. KGaA, Weinheim

As the Mn–Cl–Mn and Mn–O–Mn bond angles show minor differences, the system was modeled as an equilateral triangle. A first attempt to fit the experimental data isotropically in the 10–300 K temperature range was made with one J coupling constant with the Hamiltonian shown in Equation (2):

$$H = -J(S_1{\cdot}S_2 + S_1{\cdot}S_3 + S_2{\cdot}S_3) \quad (2)$$

However, the experimental plots were not reproduced; thus, a D_{ion} term was also taken into account. An excellent match to the experimental data was obtained under these conditions with the best fit parameters $J = +1.6$ cm^{-1}, $D_{ion} = 3.5$ cm^{-1}, and $g = 2.03$ with $R = 9.4 \times 10^{-5}$ for (*R*)-**3** and $J = +1.5$ cm^{-1}, $D_{ion} = 3.4$ cm^{-1}, and $g = 2.03$ with $R = 1.3 \times 10^{-4}$ for (*S*)-**3**. From these data, an $S = 6$ ground state can be proposed.

Magnetization measurements performed at 2 K show a nonsaturated value of 10.6 Nμ_B for (*R*)-**3** and 10.7 electrons for (*R*)-**3** under the maximum field of 5 T. The fits of the magnetizations for an isolated $S = 6$ ground state were satisfactory for $D = -0.42$ cm^{-1} and $g = 1.95$ for both compounds (Figure S6). These data confirm the $S = 6$ state and indicate a significant ground-state anisotropy.

A more precise determination of the D parameter was performed through reduced magnetization experiments (Figure 8). These measurements nicely confirmed the anisotropic character of the ground state, and excellent fits of the experimental data were obtained for $D = -0.39$ cm^{-1} and $g = 1.93$ for (*R*)-**3** and $D = -0.37$ cm^{-1} and $g = 1.92$ for (*S*)-**3**.

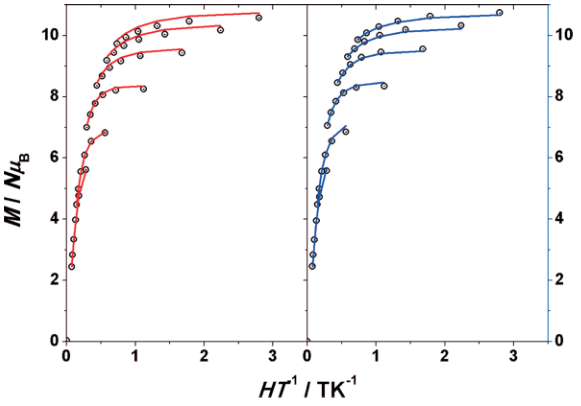

Figure 8. Reduced magnetization plots for (*R*)-**3** (left) and (*S*)-**3** (right). The solid lines show the best fits of the data.

In light of the above results, the SMM properties were explored. Alternating-current (ac) measurements at zero field only showed the tails of the out-of-phase signals, but measurements performed under a transverse magnetic field of 0.1 T broke the tunneling of the magnetization and allowed the observation of well-defined ac peaks above 2 K. The ac peaks for (*R*)-**3** and (*S*)-**3** were compared at the arbitrary frequency of 1000 Hz. They were exactly identical (Figure S7) and, thus, the complete set of measurements was performed for only one of the enantiomers [(*S*)-**3**, Figure 9]. The Arrhenius fit of the positions of the peak maxima gives a barrier for the reversal of the magnetization of $E_a = 17.1$ cm^{-1} and $\tau_o = 9.3 \times 10^{-9}$. The D value of 0.48 cm^{-1} from the $E_a = DS^2$ relationship is in agreement with the values obtained from the magnetization experiments.

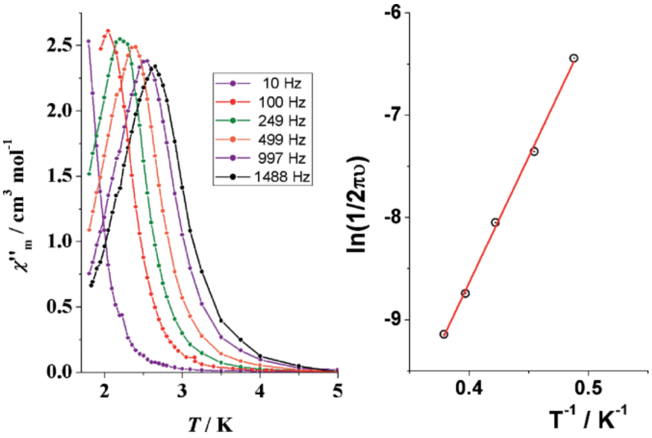

Figure 9. Left: out-of-phase peaks for (*S*)-**3** under a 0.1 T field at the indicated frequencies. Right: Arrhenius plot.

Among other factors, a parallel alignment of the easy axis of the Mn^{III} cations contributes to the enhanced global anisotropy of the system and the SMM response. Low-temperature studies (0.04–2 K) of ferromagnetic tetranuclear [Mn$_4$(sae)$_4$Cl$_4$] rings, which show a quasiperpendicular easy axes, revealed a weak anisotropy and energy barriers of ca. 5 cm^{-1}. The triangular systems derived from Schiff bases with one μ_3-O ligand displaced from the Mn$_3$ plane are scarce,[19] and an $S = 6$ ground state has been reported for only one of them.[19b] As in the above case, the easy axes of the Mn^{III} cations are roughly perpendicular, the ground state was weakly anisotropic, and no SMM response was observed. In contrast, the easy axes for (*R*)-**3** and (*S*)-**3** are directed towards the μ_3-Cl ligand and form a mean angle close to 65°, which allows a moderate total anisotropy and an appreciable E_a barrier.

Conclusions

The employment of enantiomerically pure Schiff bases is an excellent method to produce chiral clusters and chiral SMMs. The reported systems are the first polynuclear derivatives of the employed ligands, and a discrete triangular arrangement of Mn^{III} cations linked by one μ_3-Cl bridge was isolated for the first time and gives unambiguous evidence of its ferromagnetic response. Complexes **3** exhibit the largest energy barriers for this family of clusters. Electronic circular dichroism is a fundamental tool for the full characterization of these kind of compounds, and a comparison between the solid and solution spectra provided information about the stabilities of the complexes in different media.

Experimental Section

Materials and Methods: The IR spectra ($\tilde{\nu}$ = 4000–400 cm^{-1}) were recorded with a Bruker IFS-125 FTIR spectrometer with samples prepared as KBr pellets. Variable-temperature magnetic studies were

© 2017 Wiley-VCH Verlag GmbH & Co. KGaA, Weinheim

performed with a Quantum Design MPMS-5 magnetometer operating at 0.03 T in the 300–2.0 K range. Diamagnetic corrections were applied to the observed paramagnetic susceptibilities by using Pascal's constants. The analysis of the magnetic data was performed with the PHI program.[20] The qualities of the fits were parametrized by the value of $R = (\chi_M T_{exp} - \chi_M T_{calcd.})^2/(\chi_M T_{exp})^2$.

The ECD and UV/Vis spectra were recorded with a Jasco J-715 spectrometer at room temperature with samples in spectroscopy-grade acetonitrile. Solutions in the concentration range $2.0–2.7 \times 10^{-4}$ mol dm^3 (i.e., 1.33–1.50 mg of sample per 5 mL of acetonitrile) were measured in three quartz cells with pathlengths of 2 cm (λ = 850–450 nm), 1 cm (λ = 450–315 nm), and 0.1 cm (λ = 315–200 nm). In each case, a tiny amount of the sample would not dissolve. All spectra were recorded at a scanning speed of 100 nm min^{-1}, a step size of 0.1 nm, a bandwidth of 2 nm, a response time of 0.5 s, and averaged over four accumulations. The baselines of the spectra were corrected with the solvent (acetonitrile) spectrum recorded under the same conditions immediately before or after the sample measurement. The ECD spectra were normalized to the UV/Vis spectra. The solid-state ECD spectra were obtained by placing a pellet in a rotating holder as close as possible to the photomultiplier tube of a Jasco J-715 spectrometer. Freshly prepared pellets with KCl as a matrix were measured in the range λ = 240–800 nm. In all cases, it was not possible to obtain a good quality spectrum below λ = 270 nm. The following measurement parameters were applied: scanning speed 100 nm min^{-1}, step size 0.1 nm, bandwidth 2 nm, response time 0.5 s, and four scans. The backgrounds of the resulting spectra were corrected. In each case, several spectra were obtained for one pellet, for which the disk was rotated around the incident axis direction and then flipped. The spectra were very similar, and no major differences were observed on the variation of rotation angle; therefore, the absence of spectral artefacts from linear dichroism and birefringence was confirmed.

Single-Crystal X-ray Crystallography: Prismlike specimens of the *R* and *S* enantiomers of **1**–**3** were used for the X-ray crystallographic analysis. The X-ray intensity data were measured with a Bruker D8-Venture system equipped with a multilayer monochromator and a Mo microfocus source (λ = 0.71073 Å). The frames were integrated with the Bruker SAINT software package with a narrow-frame algorithm. The final cell constants were based upon the refinement of the *xyz* centroids of reflections above $20\sigma(I)$. The data were corrected for absorption effects by the multiscan method (SADABS). The structures were solved with the Bruker SHELXTL software package and refined with SHELXL.[21] Details of the crystal data, collection, and refinement for the pairs of enantiomers **1**–**3** are summarized in Table S1. The analyses of the structures and the preparation of the plots for publication were performed with the Ortep3[22] and POVRAY programs.

The quality of the structure for (*S*)-**3** was below the quality standard for publication; thus, the complete structural data are not included in the work but unambiguous characterization was provided by the cell parameters and space group (Table S1), which agree with those obtained for (*R*)-**3**, and the partial data of the cluster confirms an identical structure.

CCDC 1492960 [for (*R*)-**1**], 1492961 [for (*S*)-**1**], 1492962 [for (*R*)-**2**], 1492963 [for (*S*)-**2**], 1492964 [for (*R*)-**3**], and 1492965 [for (*S*)-**3**] contain the supplementary crystallographic data for this paper. These data can be obtained free of charge from The Cambridge Crystallographic Data Centre.

Synthetic Procedures: Mn(PhCOO)$_2$ was synthesized in high yield (>80 %) by mixing stoichiometric amounts of aqueous solutions of Na(PhCOO) and Mn(NO$_3$)$_2$. Mn(PhCOO)$_2$ precipitated immediately as a white powder, which was washed with cold water to remove soluble ions and air-dried. (*R*)- and (*S*)-2-phenylglycinol and (*R*) and (*S*)-phenylalaninol were purchased from TCI chemicals and used without further purification. Each pair of enantiomers was prepared by the same procedure; thus common syntheses will be described. The yields for **1**–**3** were ca. 25 %, and well-formed crystals were obtained and employed for instrumental measurements. The samples for analysis were dried gently to remove volatile solvents.

H$_2$L1 and H$_2$L2 Schiff Bases: Equimolar amounts of (*R*)- or (*S*)-2-phenylglycinol (for H$_2$**L1**) or phenylalaninol (for H$_2$**L2**) and salicylaldehyde were mixed in ethanol, and the mixture was heated under reflux for 1 h. The ligands were collected as yellowish solids in high yields after the concentration of the mother solutions.

[Mn$_3$(L1)$_2$(PhCOO)$_4$(MeOH)]·MeOH [(*R*)-1·MeOH and (*S*)-1·MeOH]: Mn(PhCOO)$_2$ (0.5 mmol, 0.167 g) and (*R*)- or (*S*)-H$_2$**L1** (0.5 mmol, 0.121 g) were mixed in MeOH/MeCN (1:1), and the mixture was stirred for 1 h at room temperature. The resulting dark brown solution was filtered and left to diffuse slowly with Et$_2$O. Dark brown crystals suitable for XRD appeared after 24 h. $C_{58}H_{46}Mn_3N_2O_{12}$: calcd. C 61.77, H 4.11, N 2.48; found [(*R*)-**1**/(*S*)-**1**] C 60.9/61.3, H 4.2/4.0, N 2.3/2.3. IR: $\tilde{\nu}$ = 3423.67 (br), 2925.21 (br), 1598.48 (s), 1565.85 (s), 1538.66 (m), 1445.84 (w), 1395.35 (s), 1338.50 (m), 1287.31 (m), 1201.53 (w), 1147.38 (w), 1023.48 (m), 865.77 (s), 724.00 (m), 704.36 (w), 675.43 (w), 630.21 (w), 584.37 (w), 549.39 (m), 452.23 (w) cm^{-1}.

[Mn$_3$(L2)$_2$(PhCOO)$_4$]·Solvent [(*R*)-2·5H$_2$O, (*S*)-2·2MeCN·MeOH·1.5H$_2$O]: Mn(PhCOO)$_2$ (0.5 mmol, 0.167 g) and (*R*)- or (*S*)-H$_2$**L2** (0.5 mmol) were mixed in MeOH/MeCN (1:1), and the mixture was stirred for 1 h at room temperature. The resulting solution was filtered and left to evaporate slowly. Dark brown crystals appeared after 24 h. $C_{61}H_{54}Mn_3N_2O_{13}$: calcd. C 61.68, H 4.58, N 2.36; found [(*R*)-**2**/(*S*)-**2**] C 62.0/61.5, H 4.3/4.4, N 2.3/2.5. IR: $\tilde{\nu}$ = 3434.23 (br), 3059.21 (w), 2930.64 (w), 1598.78 (s), 1569.96 (s), 1540.78 (s), 1491.65 (w), 1469.41 (w), 1446.43 (s), 1374.50 (s), 1299.23 (m), 1149.83 (w), 1051.26 (w), 1023.34 (w), 764.13 (w), 754.62 (w), 721.38 (m), 672.72 (w), 577.72 (m), 453.71 (w) cm^{-1}.

(Phgly)[Mn$_3$(L1)$_3$(μ$_3$-Cl)(Cl)$_3$]·Solvent [(*R*)-3·0.5MeCN·0.25MeOH·0.5H$_2$O, (*S*)-3·0.5MeCN·0.5H$_2$O]: MnCl$_2$·4H$_2$O (0.5 mmol, 0.197 g), (*R*)- or (*S*)-H$_2$**L1** (0.5 mmol, 0.121 g), and Na(PhCOO) (0.5 mmol, 0.036 g) were dissolved in MeCN (20 mL), and the mixture was heated under reflux for 30 min. The solution was filtered and left to evaporate slowly. Dark brown crystals suitable for XRD appeared after two weeks.

The same product was obtained from an attempt to introduce an azide ion into the cluster with Na(PhCOO) replaced with NaN$_3$ (0.5 mmol, 0.033 g). $C_{53}H_{51}Cl_4Mn_3N_4O_7$: calcd. C 54.75, H 4.42, N 4.81; found [(*R*)-**3**/(*S*)-**3**] C 55.1/55.4, H 4.1/4.5, N 4.9/4.6. IR: $\tilde{\nu}$ = 3446.7 (br), 2926.72 (br), 1607.85 (s), 1541093 (m), 1492.22(w), 1441.13 (m), 1384.07 (w), 1293.49 (m), 1149.25 (w), 981.56 (w), 757.49 (m), 703.00 (m), 643.11 (w), 591.05 (m), 553.57 (s) cm^{-1}.

Supporting Information (see footnote on the first page of this article): Structural and ECD data.

Acknowledgments

Funding from the Ministerio de Economía y Competitividad, Project CTQ2015-63614-P, is acknowledged. M. G. thanks the Polish Ministry of Science and Higher Education ("Mobilnosc Plus" grant no. 1286/MOB/IV/2015/0) for support.

© 2017 Wiley-VCH Verlag GmbH & Co. KGaA, Weinheim

Keywords: Manganese · Schiff bases · Single-molecule magnets · Chirality · Cluster compounds

[1] a) D. N. Woodruff, R. E. P. Winpenny, R. A. Layfield, *Chem. Rev.* **2013**, *113*, 5110–5148; b) J. D. Rinehart, J. R. Long, *Chem. Sci.* **2011**, *2*, 2078–2085; c) L. Ungur, S.-Y. Lin, J. Tang, L. F. Chibotaru, *Chem. Soc. Rev.* **2014**, *43*, 6894–6905.
[2] a) K. Griffiths, C. W. D. Gallop, A. Abdul-Sada, A. Vargas, O. Navarro, G. E. Kostakis, *Chem. Eur. J.* **2015**, *21*, 6358–6361; b) G. Maayan, G. Christou, *Inorg. Chem.* **2011**, *50*, 7015–7021; c) N. C. Anastasiadis, D. A. Kalofolias, A. Philippidis, S. Tzani, C. P. Raptopoulou, V. Psycharis, C. J. Milios, A. Escuer, S. P. Perlepes, *Dalton Trans.* **2015**, *44*, 10200–10209.
[3] J.-C. G. Bünzli, S. V. Eliseeva, *Chem. Sci.* **2013**, *4*, 1939–1949.
[4] J.-C. G. Bünzli, S. V. Eliseeva, *Chem. Soc. Rev.* **2010**, *39*, 189–227.
[5] a) S. Muhlbauer, B. Binz, F. Jonietz, C. Pfleiderer, A. Rosch, A. Neubauer, R. Georgii, P. Boni, *Science* **2009**, *323*, 915–919; b) X. Z. Yu, Y. Onose, N. Kanazawa, J. H. Park, J. H. Han, N. Nagaosa, Y. Tokura, *Nature* **2010**, *465*, 901–904.
[6] a) J. Kishine, K. Inoue, Y. Yoshida, *Prog. Theor. Phys. Suppl.* **2005**, *159*, 82–95; b) Y. Togawa, T. Koyama, K. Takayanagi, S. Mori, Y. Kousaka, J. Akimitsu, S. Nishihara, K. Inoue, A. S. Ovchinnikov, J. Kishine, *Phys. Rev. Lett.* **2012**, *108*, 107202.
[7] a) H. Asada, M. Ozeki, M. Fujiwara, T. Matsushita, *Chem. Lett.* **1999**, *28*, 525–526; b) H. Asada, M. Ozeki, M. Fujiwara, T. Matsushita, *Polyhedron* **2002**, *21*, 1139–1148; c) M. Dey, C. P. Rao, P. K. Saarenketo, K. Rissanen, E. Kolehmainen, P. Guionneau, *Polyhedron* **2003**, *22*, 3515–3521; d) C. P. Pradeep, T. Htwe, P. S. Zacharias, S. K. Das, *New J. Chem.* **2004**, *28*, 735–739; e) C. P. Pradeep, P. S. Zacharias, S. K. Das, *Polyhedron* **2005**, *24*, 1410–1416; C. P. Pradeep, P. S. Zacharias, S. K. Das, *J. Chem. Sci.* **2006**, *118*, 311–317; f) S.-Z. Zhan, Y.-J. Zhang, J.-G. Wang, *Acta Crystallogr., Sect. E: Struct. Rep. Online* **2006**, *62*, m2713–m2714; g) C. P. Pradeep, P. S. Zacharias, S. K. Das, *Inorg. Chem. Commun.* **2008**, *11*, 89–93.
[8] R. Inglis, F. White, S. Piligkos, W. Wernsdorfer, E. K. Brechin, G. S. Papaefstathiou, *Chem. Commun.* **2011**, *47*, 3090–3092.
[9] a) Y.-Y. Zhu, C. Cui, Y.-Q. Zhang, J.-H. Jia, X. Guo, C. Gao, K. Qian, S.-D. Jiang, B.-W. Wang, Z.-M. Wang, S. Gao, *Chem. Sci.* **2013**, *4*, 1802–1806; b) Y.-Y. Zhu, C. Cui, K. Qian, J. Yin, B.-W. Wang, Z.-M. Wang, S. Gao, *Dalton Trans.* **2014**, *43*, 11897–11907.
[10] L.-F. Zhang, Z.-H. Ni, Z.-M. Zong, X.-Y. Wei, C.-H. Ge, H.-Z. Kou, *Acta Crystallogr., Sect. C: Cryst. Struct. Commun.* **2005**, *61*, m542–m544.
[11] a) Y.-G. Li, L. Lecren, W. Wernsdorfer, R. Clerac, *Inorg. Chem. Commun.* **2004**, *7*, 1281–1284; b) H.-C. Yao, M.-M. Li, L.-M. Zheng, Z.-J. Li, *J. Coord. Chem.* **2008**, *61*, 2814–2822.
[12] a) C. Boskovic, E. Rusanov, H. Stoeckli-Evans, H. U. Gudel, *Inorg. Chem. Commun.* **2002**, *5*, 881–886; b) C. Boskovic, R. Bircher, P. L. W. Tregenna-Piggott, H. U. Gudel, C. Paulsen, W. Wernsdorfer, A.-L. Barra, E. Khatsko, A. Neels, H. Stoeckli-Evans, *J. Am. Chem. Soc.* **2003**, *125*, 14046–14058; c) S. Nayak, G. Novitchi, S. Muche, D. Luneau, S. Dehnen, *Z. Anorg. Allg. Chem.* **2012**, *638*, 1127–1133.
[13] Y.-G. Li, Q. Wu, L. Lecren, R. Clerac, *J. Mol. Struct.* **2008**, *890*, 339–345.
[14] N. Hoshino, T. Ito, M. Nihei, H. Oshio, *Inorg. Chem. Commun.* **2003**, *6*, 377–380.
[15] a) Q. Wu, Q. Shi, Y.-G. Li, E.-B. Wang, *J. Coord. Chem.* **2008**, *61*, 3080–3091; b) Y. Ding, J. Xu, Z. Pan, H. Zhou, X. Lou, *Inorg. Chem. Commun.* **2012**, *22*, 40–43.
[16] a) Q. Li, J. B. Vincent, E. Libby, H.-R. Chang, J. C. Huffman, P. D. W. Boyd, G. Christou, D. N. Hendrickson, *Angew. Chem. Int. Ed. Engl.* **1988**, *27*, 1731–1733; *Angew. Chem.* **1988**, *100*, 1799; b) S. Wang, K. Folting, W. E. Streib, E. A. Schmitt, J. K. McCusker, D. N. Hendrickson, G. Christou, *Angew. Chem. Int. Ed. Engl.* **1991**, *30*, 305–306; *Angew. Chem.* **1991**, *103*, 314; c) D. N. Hendrickson, G. Christou, E. A. Schmitt, E. Libby, J. S. Bashkin, S. Wang, H.-L. Tsai, J. B. Vincent, P. D. W. Boyd, J. C. Huffman, K. Folting, Q. Li, W. E. Streib, *J. Am. Chem. Soc.* **1992**, *114*, 2455–2471; d) M. W. Wemple, H.-L. Tsai, K. Folting, D. N. Hendrickson, G. Christou, *Inorg. Chem.* **1993**, *32*, 2025–2031; e) S. Wang, H.-L. Tsai, E. Libby, K. Folting, W. E. Streib, D. N. Hendrickson, G. Christou, *Inorg. Chem.* **1996**, *35*, 7578–7589.
[17] T. Wu, X.-Z. You, P. Bouř, *Coord. Chem. Rev.* **2015**, *284*, 1–18.
[18] a) A. Ipatov, F. Cordova, L. J. Doriol, M. E. Casida, *J. Mol. Struct.* **2009**, *914*, 60–73; b) M. Enamullah, M. A. Quddus, M. R. Hasan, G. Pescitelli, R. Berardozzi, G. Makhloufi, V. Vasylyeva, Ch. Janiak, *Dalton Trans.* **2016**, *45*, 667–680.
[19] a) M. Nihei, N. Hoshino, T. Ito, H. Oshio, *Chem. Lett.* **2002**, *31*, 1016–1017; b) P. Chaudhuri, R. Wagner, T. Weyhermuller, *Eur. J. Inorg. Chem.* **2010**, 1339–1342; c) C.-M. Liu, D.-Q. Zhang, D.-B. Zhu, *Dalton Trans.* **2010**, *39*, 1781–1785.
[20] N. F. Chilton, R. P. Anderson, L. D. Turner, A. Soncini, K. S. Murray, *J. Comput. Chem.* **2013**, *34*, 1164–1175.
[21] G. M. Sheldrick, *Acta Crystallogr., Sect. A: Fundam. Crystallogr.* **2008**, *64*, 112–122.
[22] Ortep-3 for Windows: L. J. Farrugia, *J. Appl. Crystallogr.* **1997**, *30*, 565.

Received: September 15, 2016
Published Online: December 9, 2016

© 2017 Wiley-VCH Verlag GmbH & Co. KGaA, Weinheim

Eur. J. Inorg. Chem. **2016** · ISSN 1099–0682

SUPPORTING INFORMATION

DOI: 10.1002/ejic.201601138

Title: Trinuclear Complexes Derived from *R*/*S* Schiff Bases – Chiral Single-Molecule Magnets

Author(s): Albert Escuer,* Julia Mayans, Merce Font-Bardia, Lorenzo Di Bari, Marcin Górecki

Table S1. Crystal data and structure refinement for coordination compounds **1 - 3**

	1*R*	**1*S***	**2*R***	**2*S***	**3*R***	**3*S***
Formula	$C_{60}H_{54}Mn_3N_2O_{14}$	$C_{60}H_{54}Mn_3N_2O_{14}$	$C_{60}H_{60}Mn_3N_2O_{17}$	$C_{66}H_{73}Mn_3N_4O_{15.5}$	$C_{217}H_{218}Mn_{12}N_{18}O_{31}$	--
FW	1191.87	1191.87	1245.92	1329.07	4800.56	--
System	Triclinic	Triclinic	Trigonal	Trigonal	Monoclinic	Monoclinic
Space group	P1	P1	P3221	P3121	P21	P21
a/Å	10.7290(5)	10.7345(5)	15.2041(16)	15.4793(6)	11.791(4)	11.800(3)
b/Å	11.6229(5)	11.5502(5)	15.2041(16)	15.4793(6)	21.506(7)	21.390(6)
c/Å	12.6156(5)	12.6278(6)	24.725(3)	24.9201(9)	22.497(7)	22.402(6)
α/deg.	66.924(2)	67.363(2)	90	90	90	90
β/deg.	78.315(2)	78.448(2)	90	90	90.470(9)	91.012(9)
γ/deg.	74.547(2)	74.587(2)	120	120	90	90
V/ Å^3	1386.4(1)	1384.6(1)	4950(1)	5171.1(4)	5704(3)	5653(3)
Z	1	1	3	3	1	1
T, K	100(2)	100(2)	293(2)	100(2)	100(2)	100(2)
λ(MoKα), Å	0.71073	0.71073	0.71073	0.71073	0.71073	0.71073
ρcalc, g·cm-3	1.428	1.429	1.254	1.286	1.397	--
μ(MoK$_\alpha$), mm^{-1}	0.741	0.742	0.629	0.606	0.895	--
R	0.0379	0.0387	0.0528	0.0437	0.0595	--
ωR^2	0.0995	0.1026	0.1126	0.1275	0.1486	--

Table S2. Selected bond distances (Å) and angles (°) for compounds **1*R*** and **1*S***.

d Å	(**1*R***)	(**1*S***)
Mn1-O1	1.879(2)	1.874(3)
Mn1-O2	1.885(2)	1.887(3)
Mn1-O3	1.951(2)	1.951(2)
Mn1-O5	2.165(2)	2.159(2)
Mn1-O1w	2.358(3)	2.345(3)
Mn1-N1	1.998(3)	1.998(3)
Mn2-O2	2.150(3)	2.156(3)
Mn2-O4	2.162(3)	2.159(3)
Mn2-O6	2.104(3)	2.103(3)
Mn2-O7	2.128(3)	2.136(3)
Mn2-O9	2.162(3)	2.161(3)
Mn2-O11	2.230(2)	2.230(3)
Mn3-O8	2.056(2)	2.054(2)
Mn3-O10	1.950(2)	1.949(3)
Mn3-O11	1.878(2)	1.882(3)
Mn3-O12	1.877(2)	1.876(2)
Mn3-N2	1.996(2)	1.995(3)
Angles (º)	(**1*R***)	(**1*S***)
Mn1-O2-Mn2	117.0(1)	116.8(1)
Mn2-O11-Mn3	115.2(1)	115.1(1)

Table S3. Selected bond distances (Å) and angles (°) for compounds **2*R*** and **2*S***.

d Å	(**2-*R***)	(**2-S**)
Mn1-O1	1.857(5)	1.873(3)
Mn1-O2	1.881(5)	1.870(3)
Mn1-O3	1.929(6)	1.938(3)
Mn1-O5	2.076(6)	2.122(4)
Mn1-O7		
Mn1-N1	1.979(7)	1.978(4)
Mn2-O2	2.169(5)	2.167(3)
Mn2-O4	2.173(6)	2.171(3)
Mn2-O6	2.114(5)	2.119(3)
Angles (º)	(**2-R**)	(**2-S**)
Mn1-O2-Mn2	117.9(3)	117.7(2)

Table S4. Selected bond distances (Å) and angles (°) for compounds **3*R***. Some selected parameters for **3*S*** are shown to check that, in addition to the agreement of the cell parameters, the core of both complexes is equivalent.

d Å	(**3*R***)-A	(**3*R***)-B	(**3*S***)-A	(**3*S***)-B
Mn1-O1	1.946(3)	1.904(4)		
Mn1-O2	1.919(4)	1.833(4)		
Mn1-O5	2.005(5)	1.922(4)		
Mn1-N1	1.934(5)	2.014(4)		
Mn1-Cl1	2.544(2)	2.477(2)	*2.493(5)*	*2.501(4)*
Mn1-Cl4	2.680(2)	2.748(2)	*2.779(4)*	*2.736(4)*
Mn2-O1	1.985(4)	2.008(4)		
Mn2-O3	1.890(4)	1.949(3)		
Mn2-O4	1.865(4)	1.855(4)		
Mn2-N2	1.999(5)	1.954(5)		
Mn2-Cl2	2.491(2)	2.528(2)	*2.521(4)*	*2.499(5)*
Mn2-Cl4	2.744(2)	2.738(2)	*2.705(4)*	*2.746(4)*
Mn3-O3	1.995(3)	1.970(4)		
Mn3-O5	1.927(4)	2.013(4)		
Mn3-O6	1.852(5)	1.843(4)		
Mn3-N3	1.991(5)	2.008(5)		
Mn3-Cl3	2.483(2)	2.512(2)	*2.480(4)*	*2.499(4)*
Mn3-Cl4	2.765(2)	2.716(2)	*2.732(4)*	*2.707(4)*
Angles (º)	(**3*R***)-A	(**3*R***)-B	(**3*S***)-A	(**3*S***)-B
Mn1-Cl4-Mn2	78.10(4)	77.34(5)	*77.7(1)*	*77.5(1)*
Mn1-Cl4-Mn3	78.15(5)	78.07(4)	*76.0(1)*	*77.4(1)*
Mn2-Cl4-Mn3	75.79(4)	77.22(4)	*77.7(1)*	*77.5(1)*
Mn1-O1-Mn2	120.8(2)	122.4(2)	*123.4(5)*	*122.5(4)*
Mn1-O5-Mn3	121.6(2)	121.9(2)	*123.9(5)*	*122.3(4)*
Mn2-O3-Mn3	121.1(2)	120.6(2)	*121.2(4)*	*121.6(4)*

ECD measurements

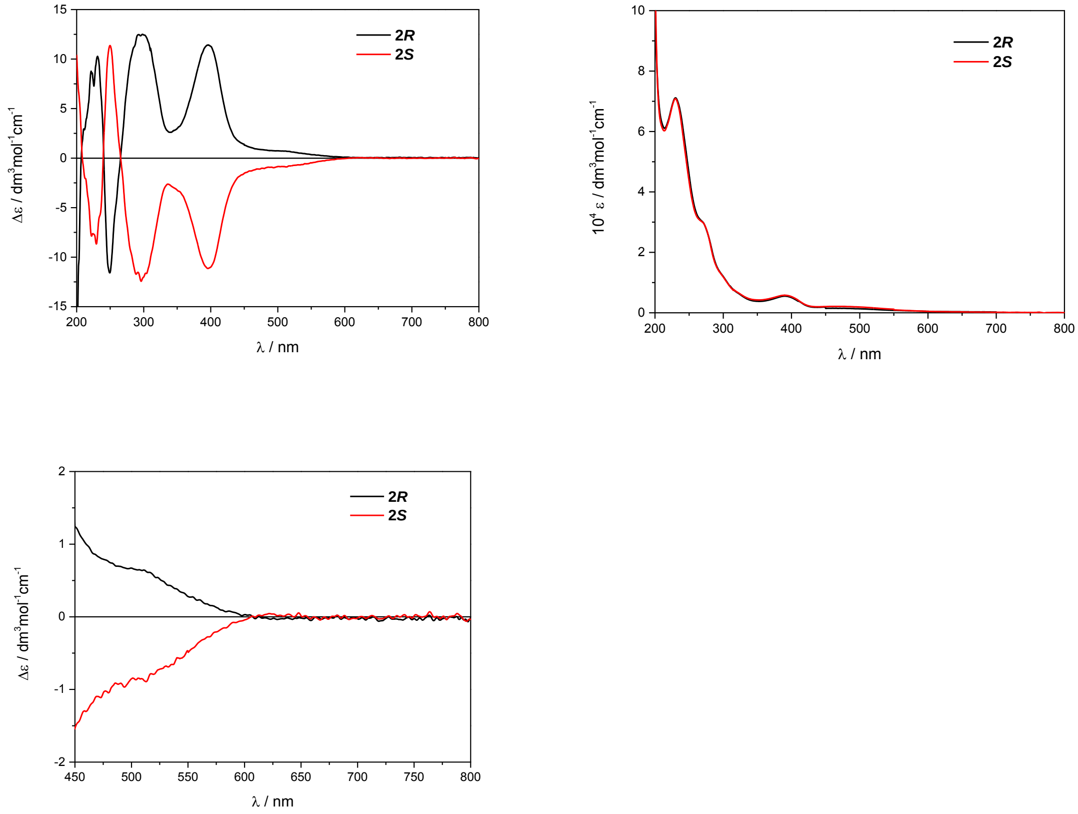

Figure S1. **Top,** ECD and UV-Vis spectra of **2*R*** and **2*S*** recorded in CH_3CN. **Bottom**, ECD spectrum in the visible region.

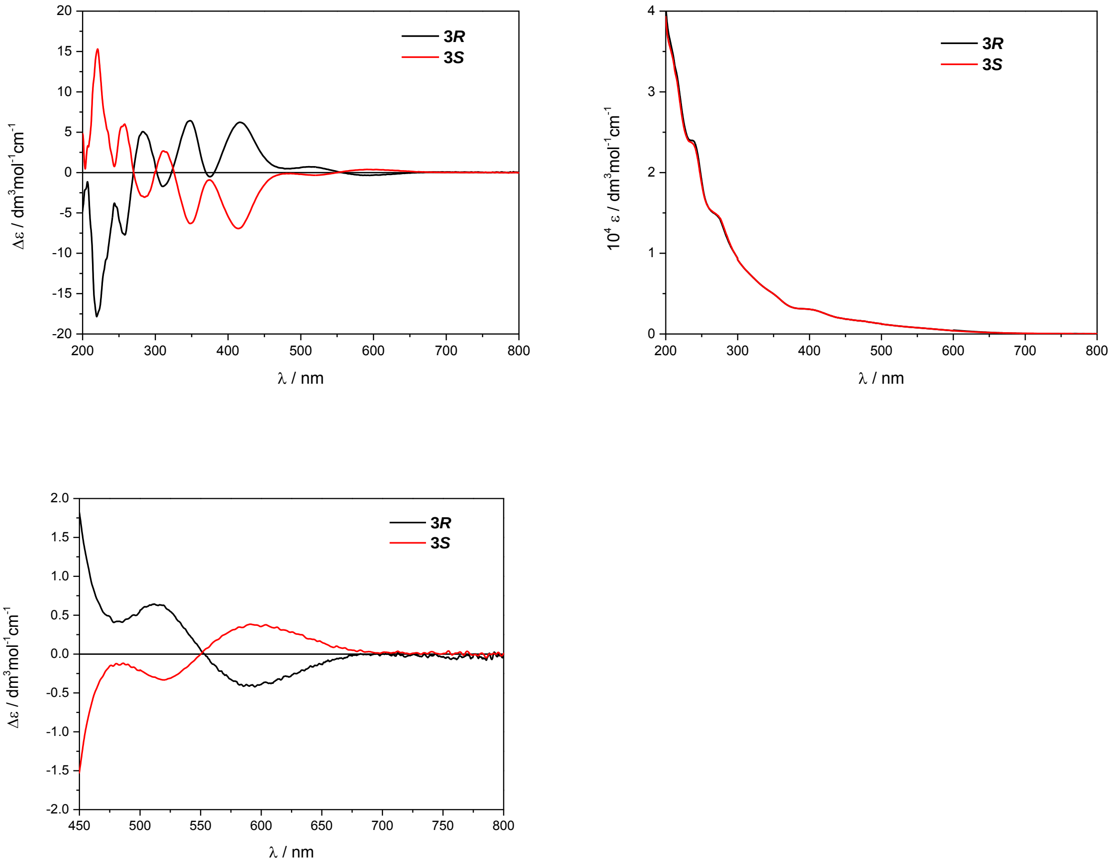

Figure S2. **Top**, ECD and UV-vis spectra of **3*R*** and **3*S*** recorded in CH_3CN. **Bottom**, ECD spectrum in the visible region.

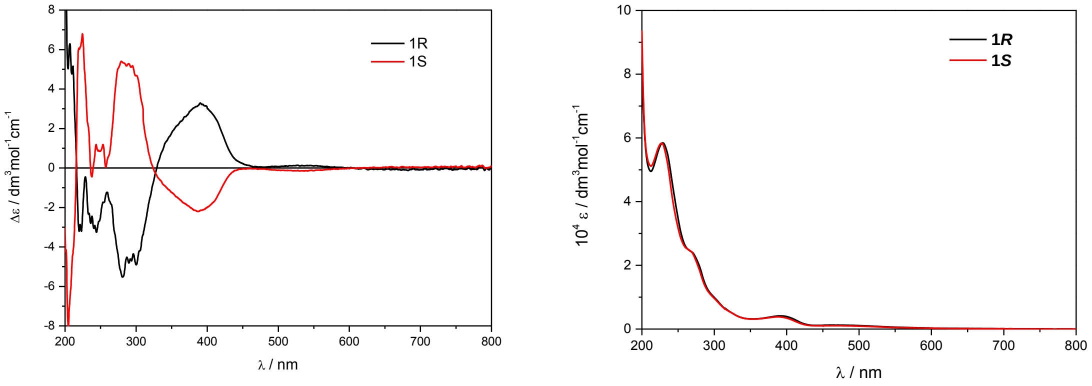

Figure S3. ECD and UV-vis spectra of **1*R*** and **1*S*** recorded in CH_3CN.

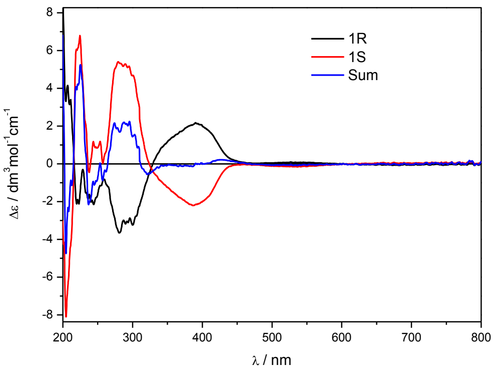

Figure S4. ECD spectra of **1*R*** and **1*S*** recorded in CH_3CN and their arithmetic sum. After normalisation, using UV-vis as a reference, the obtained ECD spectra are not mirror image. As one can see, the obtained curve (blue) after adding up the spectra of two enantiomers is not flat/zero, as one would expect, in particular in the range of 200-450 nm. This clearly shows some differences between both enantiomers attributable to partial decomposition by heating during the dissolution of the sample.

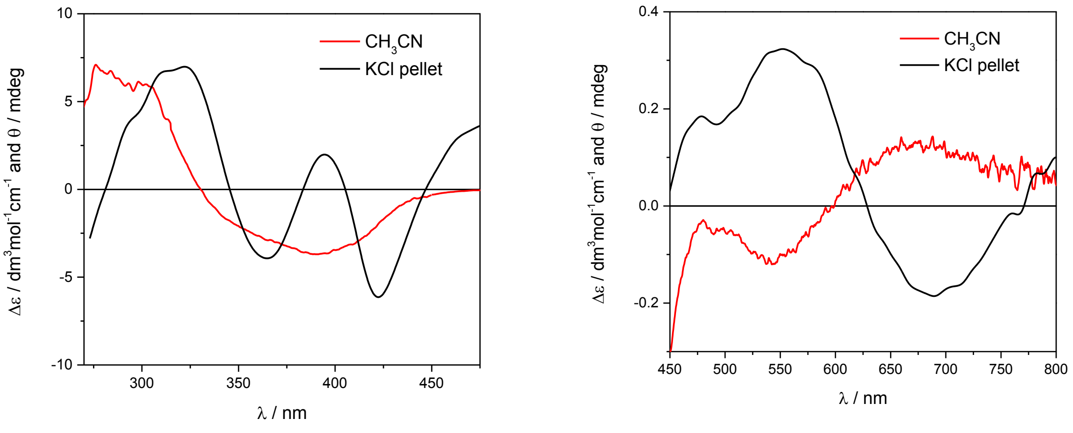

Figure S5. Comparison between the solid-state (range 450-800 nm divided by 20) and the solution ECD spectra for **1*S***.

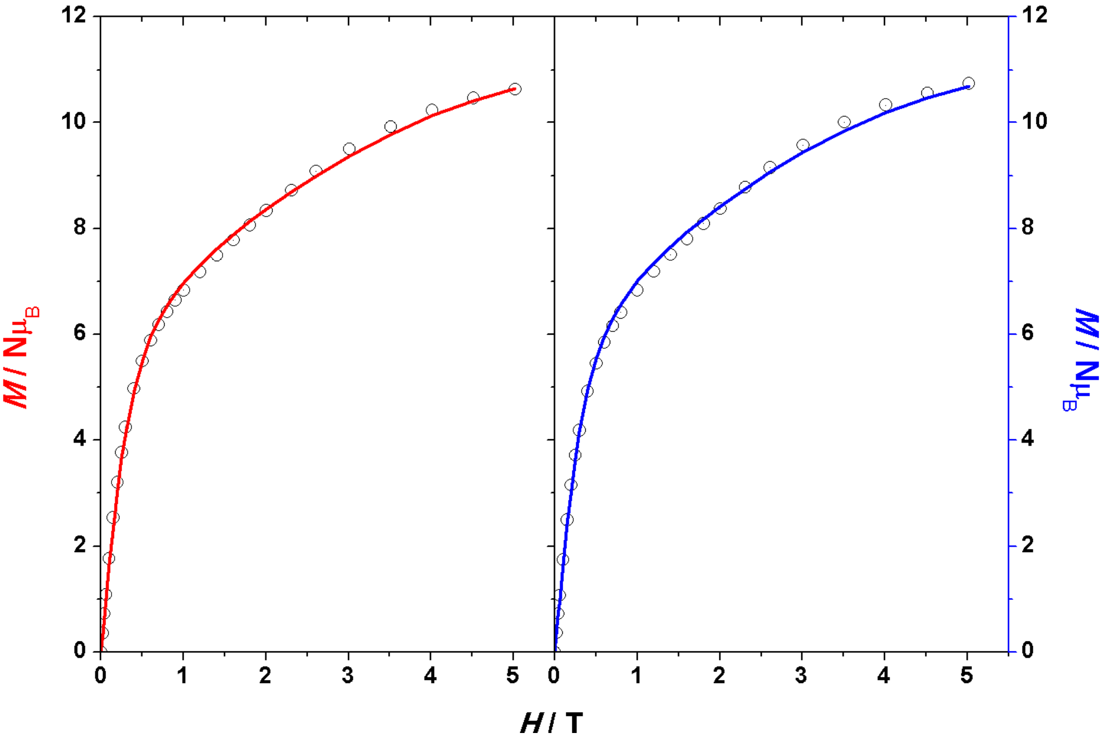

Figure S6. Magnetization plots for **3*R*** (left) and **3*S*** (right). Solid lines show the best fit as an anisotropic $S = 6$ isolated ground state.

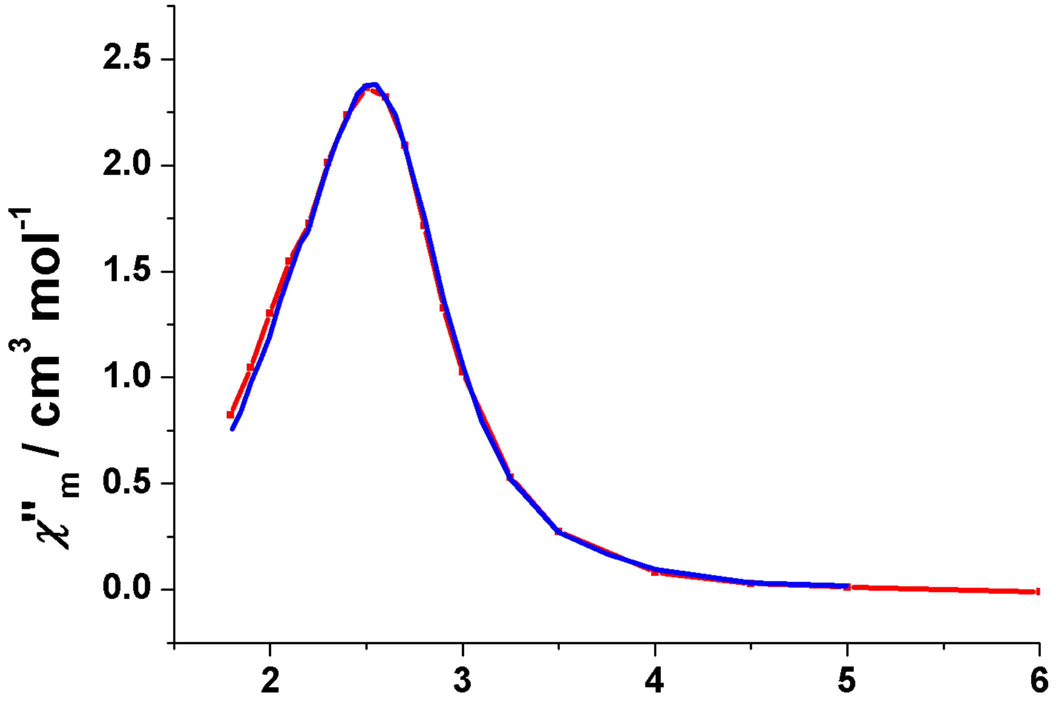

Figure S7. Ac plots for **3*R*** (red) and **3*S*** (blue) measured under a transverse field of 0.1 T and 1000 Hz, showing the identical out-of-phase signals for both enantiomers.

Publication #5 *“Syntheses, structures and chiroptical and magnetic properties of chiral clusters built from Schiff bases: a novel* $[Mn^{II}Mn^{III}_6Na^{I}_2]$ *core”*

Dalton Transactions

COMMUNICATION

Check for updates

Cite this: *Dalton Trans.*, 2017, **46**, 6514

Received 6th March 2017,
Accepted 3rd April 2017

DOI: 10.1039/c7dt00811b

rsc.li/dalton

Syntheses, structures, and chiroptical and magnetic properties of chiral clusters built from Schiff bases: a novel $[Mn^{II}Mn_6^{III}Na_2^{I}]$ core†

A. Escuer, *[a] J. Mayans,[a] M. Font-Bardia,[b] M. Górecki[c] and L. Di Bari[c]

Chiral clusters with $Mn^{II}Mn_3^{III}Na^{I}$ and the new $Mn^{II}Mn_6^{III}Na_2^{I}$ cores have been synthesised employing enantiomerically pure Schiff bases and halide ligands. The new compounds have been characterized by electronic circular dichroism (ECD) and magnetic susceptibility.

Supramolecular chirality has received a great deal of attention over the last few years in several research fields such as chiral catalysis, recognition and sensing or CPL emission[1] as well due to its potentially different reactivity in biological environments.[2] As a subfield, chiral self-assembled coordination compounds revealed to be attractive in the study of transfer of chirality, chiroptical properties (often lanthanide complexes), or magnetochemistry in close relationship with the search for chiral SMM or extended magnets.[3] Employment of enantiomerically pure ligands allows the direct syntheses of chiral coordination compounds that can be useful in the search for multifunctional systems in which optical or emissive properties could be combined with their magnetic response. Among them, Schiff bases constitute an appropriate family of ligands to reach this target due to its ability to generate large nuclearity or high spin clusters and because these ligands can be easily functionalized to incorporate chiral centres. In this communication we report preliminary results from the employment of the *R*/*S* chiral Schiff base H_2L obtained by condensation of *o*-vanilline and *R*- or *S*-phenylglycinol in manganese chemistry and the characterization of enantiomeric pairs of $Mn^{II}Mn_3^{III}Na^{I}$ penta and the new $Mn^{II}Mn_6^{III}Na_2^{I}$ nonanuclear complexes, in which the dianionic form of H_2L links three different cations, Scheme 1.

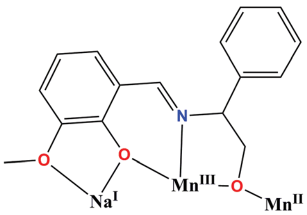

Scheme 1 Coordination to one Mn^{III}, one Mn^{II} and one Na^{I} cations found in complexes **1–3** for the L^{2-} ligand employed in this work.

Reaction of *R*- or *S*-H_2L with manganese bromide and sodium azide yields the pentanuclear complexes $[Mn_4NaOL_3Br_4]\cdot[Mn_4NaOL_3Br_4(H_2O)]\cdot[Mn_4NaOL_3Br_3(MeOH)(MeCN)(H_2O)]\cdot[Mn_4NaOL_3Br_3(MeOH)(MeCN)_2]Br_2\cdot 6CH_3CN\cdot 5CH_3OH$ (**1*R***) and $[Mn_4NaOL_3Br_4(H_2O)]\cdot[Mn_4NaOL_3Br_3(MeOH)(H_2O)_2]Br\cdot 6CH_3CN\cdot CH_3OH$ (**1*S***) which exhibit a core similar to some previously reported systems with azido or other ligands instead of halides and related Schiff bases.[4] In contrast, the reaction in basic NaOH medium yields the nonanuclear clusters $[Mn_7Na_2(O)_2L_6X_6]$·solvents (X = Cl, **2*R*** and **2*S***, X = Br, **3*R***), that exhibit an unprecedented core, (synthetic details are in the ESI†). To our knowledge, the $\{(\mu_3\text{-}O)Mn_3^{III}\text{–}Mn^{II}\text{–}Mn_3^{III}(\mu_3\text{-}O)\}$ core has only been reported as a fragment of larger Mn_{19} clusters[5] and in one Mn_7 system built from salicyloximate ligands.[6] However, in this latter case, the core was closer to two pseudocubanes sharing the central Mn^{II} cation and becomes less comparable.

The structures (ESI, Tables S1–S5†) of **1*R*** and **1*S*** contain pentanuclear $Mn^{II}Mn_3^{III}Na^{I}$ discrete units linked by three L^{2-} ligands. The metallic cations determine a trigonal bipyramidal arrangement with the three Mn^{III} ions in the equatorial plane and the Mn^{II} and Na^{I} cations at the apical positions, Fig. 1. The *O*-phenoxide and *O*-methoxide donors form an octahedral cavity that holds the Na^{I} cation, which is bridged by means of the *O*-phenoxides to the Mn^{III} cations whereas the *O*-alcoxide donors link the Mn^{III} cations with the Mn^{II} ions. An additional

---

[a] *Departament de Química Inorgànica i Orgànica, Secció Inorgànica and Institute of Nanoscience (IN^2UB) and Nanotechnology, Universitat de Barcelona, Av. Diagonal 645, Barcelona-08028, Spain. E-mail: albert.escuer@ub.edu*

[b] *Departament de Mineralogia, Cristal·lografia i Dipòsits Minerals and Unitat de Difracció de R-X. Centre Científic i Tecnològic de la Universitat de Barcelona (CCiTUB). Universitat de Barcelona, Solé i Sabarís 1-3, 08028 Barcelona, Spain*

[c] *Dipartimento di Chimica e Chímica Industriale, Università di Pisa, Via Moruzzi 13, I-56124 Pisa, Italy*

† Electronic supplementary information (ESI) available: Synthetic and structural description. CCDC 1536187–1536191. For ESI and crystallographic data in CIF or other electronic format see DOI: 10.1039/c7dt00811b

This journal is © The Royal Society of Chemistry 2017

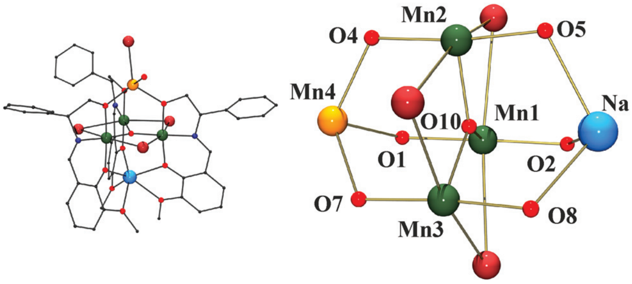

Fig. 1 Left, view of one of the non-equivalent clusters of **1*R***. Right, the partially labelled common core of complexes **1*R*** and **1*S***. Color code: Mn^{III}, dark green; Mn^{II}, orange; Na^{I}, light blue; N, navy; O red; Br, firebrick.

μ_3-O donor is placed at the centre of the triangle determined by the trivalent manganese cations.

Noteworthily, the complicated structure of **1*R*** contains four different clusters that differ in how the coordination sphere of the Mn^{II} cation is fulfilled: three *fac*-coordination sites are occupied in all cases by three *O*-alcoxide donors from the L^{2-} ligands but the remaining positions can be occupied by one bromide (tetracoordinated), three solvent molecules (hexacoordinated) or by one water molecule and one bromo ligand (pentacoordinated). For **1*S*** a similar fact was observed with the presence of two independent units with the Mn^{II} cations in octahedral or pentacoordinated environments (ESI, Fig. S2†). The main structural consequence consists of the increase of the Mn^{III}–O–Mn^{II} bond angles, which are close to 122° (octahedral Mn^{II}), 118° (pentacoordinated Mn^{II}) and 111° (tetrahedral Mn^{II}). The remaining angles or distances of the cluster core are similar in all units (ESI, Table S3†).

The chirality transfer for complexes **1*R*** and **1*S*** can be observed at the level of the inner Na^{I} cations that exhibit Λ (**1*R***) or Δ (**1*S***) configuration or at the whole helical shape of the molecule due to the tilted arrangement of the ligands with respect to the main axis of the molecule, Fig. 2.

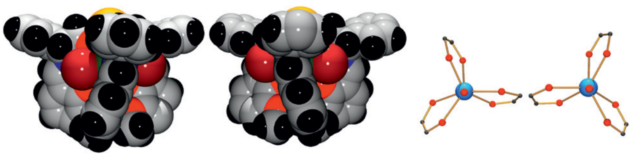

Fig. 2 Left, a spacefill view of the two pentanuclear enantiomers of **1*R*** and **1*S*** showing the helical arrangement of the ligands. Right, Na^{I} environment for **1*R*** (Λ) and **1*S*** (Δ) viewed along the O10–Na direction.

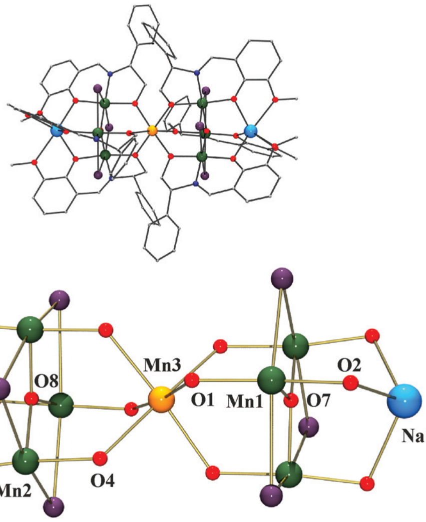

Fig. 3 Top, a view of cluster **2**. Bottom, the partially labelled common core of complexes **2*R*** and **2*S***. Color code: as Fig. 1; Cl, violet.

The ***R*** and ***S*** pairs of enantiomers of **2** consist of two pentanuclear units (similar to those described for **1**), sharing the Mn^{II} cation, resulting a nonanuclear $Mn^{II}Mn^{III}_6Na^{I}_2$ core, Fig. 3. The 22 positive charges are balanced by the six dianionic Schiff bases, six halides and two μ_3-oxo donors. The L^{2-} ligands and the Mn^{III} cations in each pentanuclear subunit are related by one C_3 axis (*R*3 space group) but the lack of symmetry between them determines different bond parameters around Mn3 in each subunit: Mn2–O4–Mn3 bond angles take a mean value of 125.8(3)° whereas Mn1–O1–Mn3 is 122.9(3)°. Surprisingly, the helicity of each $Mn^{II}Mn^{III}_3Na^{I}$ moiety turns in the opposite sense and thus, the Na^{I} cations show also the opposite Λ/Δ configuration. Complex **3*R***, prepared to check if this structure can be extended to other halides, exhibits the same core than **2*R*** and with the logical exception of the larger Mn^{III}–Br bond distances, all bond parameters of the cluster core are very similar to **2** (ESI, Tables S4 and S5†).

Noteworthily, in all cases the oxo ligand is slightly displaced out of the Mn^{III}_3 plane towards the Na^{I} cation, with a Na–O distance of around 2.7 Å and thus, the coordination of the sodium ions can be formally described as an apicated octahedron and the oxo donors can be assumed as μ_4-O ligands.

ECD spectra of the pairs of enantiomers **1*R*/1*S*** and **2*R*/2*S*** measured in the solid phase and acetonitrile solution show perfect mirror images of each other, which confirm the enantiomeric purity of samples, Fig. 4. The spectra of the penta and nonanuclear complexes are closely related as can be

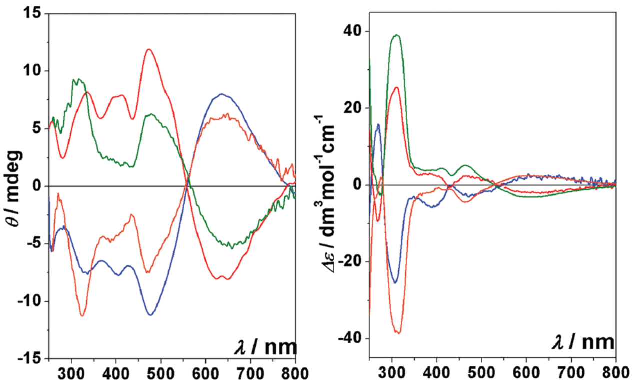

Fig. 4 Solid state (left) and acetonitrile solution (right) ECD spectra for the pair of enantiomers of the $Mn^{II}Mn^{III}_3Na^{I}$ complexes **1** (***S*** green line; ***R*** orange line) and $Mn^{II}Mn^{III}_6Na^{I}_2$ complexes **2** (***S*** red line; ***R*** blue line, X10).

expected for systems in which the ECD spectrum is directed mainly by the chirality of the chelating ligands. Comparison between the solid and solution spectra in the 250–800 range suggest that the crystal structure is pretty close to the predominant conformer(s) in acetonitrile solution.

As expected from the structural data the magnetic response for each kind of core is very similar and independent of the enantiomer or the halide donors. Thus, we provide a general description of their magnetic behaviour. The room temperature $\chi_M T$ value for the complexes with the $Mn^{II}Mn^{III}_3Na^I$ core is close to 10.5 cm^3 mol^{-1} K, slightly lower than the expected value for three isolated Mn^{III} and one Mn^{II} cations (13.375 cm^3 mol^{-1} K) and this value decreases continuously on cooling down to a plateau between 25 and 5 K, with a low T fall down to 6 cm^3 mol^{-1} K at 2 K. In contrast, the complexes with the $Mn^{II}Mn^{III}_6Na^I_2$ core exhibit a room temperature $\chi_M T$ value close to 19 cm^3 mol^{-1} K, also lower than the expected value for six non-interacting Mn^{III} and one Mn^{II} cations (22.375 cm^3 mol^{-1} K). On cooling, $\chi_M T$ decreases down to a well-defined minimum around 120 K with a further increase up to a maximum value close to 28 cm^3 mol^{-1} K at 10–15 K with a final decrease below these temperatures indicating a ferrimagnetic response, Fig. 5.

Previously reported related systems with the $Mn^{II}Mn^{III}_3Na^I$ core have different ligands at the elongated coordination sites of the Mn^{III} cations[4] but in our case the clusters are close or possess a strict C_3 symmetry with halide donors at these positions, simplifying the coupling scheme. Fit of the experimental data was performed with the PHI program[7] applying a 2-J model in which J_1 corresponds to the interaction between the Mn^{III} cations inside the triangular subunits and J_2 corresponds to the $Mn^{III}\cdots Mn^{II}$ interactions according the Hamiltonians and coupling scheme shown in Fig. S3.†

Excellent fits were obtained with consistent FM coupling for the Mn^{III}–Mn^{III} interactions (J_1 in the +0.8/+0.9 cm^{-1} range) and AF coupling for the Mn^{II}–Mn^{III} interactions (J_2 in the −2.3/−3.7 cm^{-1} range) and g around 1.9.

Noteworthily, the new Mn_7 core of **2–3** is similar to the central fragment of the S = 83/2 ground state supertetrahedral vertex-sharing Mn_{19} clusters, Fig. S4.† [5] In contrast with **2–3**, the Mn^{II}–O–Mn^{III} interaction for Mn_{19} was ferromagnetic contributing to reach the maximum spin. A close inspection of the bond parameters for both systems shows that the Mn^{II}–O–Mn^{III} bond angle for **2–3** is much larger than for Mn_{19} (≈124° *vs.* ≈110°), and consequently the $Mn^{II}\cdots O_{oxo}$ distance increases by about 0.75 Å and the Mn^{II} environment for **2–3** becomes closer to a regular octahedron instead of the pseudo octacoordination observed in Mn_{19}, resulting in interactions of the opposite sign.

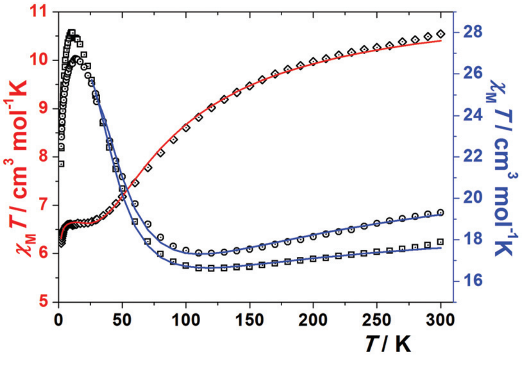

Fig. 5 Plot of $\chi_M T$ product *vs.* T for one of the enantiomers of complexes **1*S*** (diamonds, red axis), **2*S*** and **3*R*** (squares and circles, blue axis). Solid lines show the best fit of the data.

The easy axis of the Mn^{III} cations lies in the $\{\mu_3O\text{-}Mn^{III}_3\}$ plane directed towards the chloro ligands forming angles of around 60° between them. This easy axis arrangement is unfavourable to reach high anisotropy and, as was experimentally checked, no out-of-phase response was found in AC experiments.

Conclusions

Reaction of manganese halides with enantiomerically pure Schiff bases obtained from the condensation of *o*-vanilline and (*R*) or (*S*)-phenylglycinol leads to the characterization of chiral penta and nonanuclear complexes with $Mn^{II}Mn^{III}_3Na^I$ and the rare $Mn^{II}Mn^{III}_6Na^I_2$ cores. Current efforts to fully characterize a series of related complexes changing the Na^I cations by other monovalent or divalent cations, its role as oxygen evolving systems and a wide magnetostructural correlation are in progress and will be reported in a forthcoming full paper.

Acknowledgements

Funds from Ministerio de Economía y Competitividad, Project CTQ2015-63614-P are acknowledged. MG thanks support from the Polish Ministry of Science and Higher Education ("Mobilnosc Plus" grant no. 1286/MOB/IV/2015/0).

References

1 M. Liu, L. Zhang and T. Wang, *Chem. Rev.*, 2015, **115**, 7304.

2 R. Carr, N. H. Evans and D. Parker, *Chem. Soc. Rev.*, 2012, **41**, 7673.

3 (*a*) J. Crassous, *Chem. Soc. Rev.*, 2009, **38**, 830; (*b*) H. Miyake, *Symmetry*, 2014, **6**, 880.

4 (*a*) L.-L. Fan, F.-S. Guo, L. Yun, Z.-J. Lin, R. Herchel, J.-D. Leng, Y.-C. Ou and M.-L. Tong, *Dalton Trans.*, 2010, **39**, 1771; (*b*) S. Nayak, H. P. Nayek, S. Dehnen, A. K. Powell and J. Reedijk, *Dalton Trans.*, 2011, **40**, 2699; (*c*) P.-P. Yang, C.-Y. Shao, L.-L. Zhu and Y. Xu, *Eur. J. Inorg. Chem.*, 2013, 5288; (*d*) P.-P. Yang, L.-L. Zhu and Y. Xu, *Z. Anorg. Allg. Chem.*, 2013, **639**, 1821; (*e*) C. Ding, C. Gao, S. Ng, B. Wang and Y. Xie, *Chem. – Eur. J.*, 2013, **19**, 9961; L. Cong, X. Qin, W. Sun, Y. Wang, S. Ding and Z. Liu, *New J. Chem.*, 2014, **38**, 545; (*f*) B. Gole, K. C. Mondal and P. S. Mukherjee, *Inorg.*

This journal is © The Royal Society of Chemistry 2017

Chim. Acta, 2014, **415**, 151; Y. Song, G. Zhang, X. Qin, Y. Gao, S. Ding, Y. Wang, C. Du and Z. Liu, *Dalton Trans.*, 2014, **43**, 3880.

5 (*a*) A. M. Ako, I. J. Hewitt, V. Mereacre, R. Clerac, W. Wernsdorfer, C. E. Ansonand and A. K. Powell, *Angew. Chem., Int. Ed.*, 2006, **45**, 4926; (*b*) S. Nayak, M. Evangelisti, A. K. Powell and J. Reedijk, *Chem. – Eur. J.*, 2010, **16**, 12865; J.-L. Liu, J.-D. Leng, Z. Lin and M.-L. Tong, *Chem. – Asian J.*, 2011, **6**, 1007; (*c*) A. M. Ako, Y. Lan, O. Hampe, E. Cremades, E. Ruiz, C. E. Anson and A. K. Powell, *Chem. Commun.*, 2014, **50**, 5847.

6 C. J. Milios, I. A. Gass, A. Vinslava, L. Budd, S. Parsons, W. Wernsdorfer, S. P. Perlepes, G. Christou and E. K. Brechin, *Inorg. Chem.*, 2007, **46**, 6215.

7 N. F. Chilton, R. P. Anderson, L. D. Turner, A. Soncini and K. S. Murray, *J. Comput. Chem.*, 2013, **34**, 1164.

This journal is © The Royal Society of Chemistry 2017

Electronic Supplementary Material (ESI) for Dalton Transactions.
This journal is © The Royal Society of Chemistry 2017

Electronic Supplementary Material (ESI) for "*Syntheses, structures, chiroptical and magnetic properties of chiral clusters built from Schiff bases: a novel* $[Mn^{II}Mn^{III}_6Na^{I}_2]$ *core* "

Syntheses and methods.

H_2L ligand: A solution 0.072 M of the H_2L ligand was previously prepared following the procedure: 0.5 g (3.64 mmols) of the corresponding *R* or *S* enantiomer of 2-phenylglycinol and 0.55 g (3.64 mmols) of 2-hydroxy-3-methoxybenzaldehyde in 20 mL of methanol. The yellow mixture was refluxed for 1 h and diluted to 50 mL with methanol. This solution was employed directly in the synthesis of the derived complexes.

Complexes 1*R* and 1*S*: $MnBr_2{\cdot}4H_2O$ (0.104 g, 0.365 mmols) and NaN_3 (0.024 g, 0.365 mmols) dissolved in 20 mL of acetonitrile were added to 5 mL of the previous prepared ligand solution of H_2L (0.365 mmols). The mixture was stirred at room temperature for three hours, filtered and layered with diethylether. Dark brown crystals were collected after a week. Analogous reaction starting from $MnCl_2{\cdot}4H_2O$ lead to complexes **2**. Anal. Calcd for $C_{217}\ H_{233}\ Br_{16}\ Mn_{16}\ N_{21}\ Na_4\ O_{49}$ (**1*R***): C, 42.25; H, 3.81; N, 4.77%. Found: C, 42.0; H, 3.6; N, 4.4%, (corresponding to the partial loss of around 2 ACN). Anal. Calcd for $C_{220}\ H_{234}\ Br_{16}\ Mn_{16}\ N_{24}\ Na_4\ O_{53}$ (**1*S***): C, 41.86; H, 3.74; N, 5.33%. Found: C, 41.6; H, 3.7; N, 4.7%,(corresponding to the partial loss of around 4 ACN).

Complexes 2*R* and 2*S*: $MnCl_2{\cdot}4H_2O$ (0.072 g., 0.365 mmols) and NaOH (0.015 g, 0.365 mmols) were dissolved in 20 mL of acetonitrile and stirred for 5 minutes. After that, 5 mL of the H_2L ligand solution (0.365 mmols) were added. The resulting mixture was stirred at room temperature for 3 h and filtered. The resulting solution was layered with diethylether and dark brown crystals were obtained after few days. Anal. Calcd for $C_{105}\ H_{111}Cl_6\ Mn_7\ N_6\ Na_2\ O_{23}$ (**2*R***): C, 50.24; H, 4.46; N, 5.02%. Found: C, 50.5; H, 4.1; N, 4.8% (corresponding to the partial loss of around 2 ACN and one methanol). Anal. Calcd for $C_{97.5}\ H_{100}\ Cl_6\ Mn_7\ N_6\ Na_2\ O_{23.5}$ (**2*S***): C, 49.30; H, 4.24; N, 3.542%. Found: C, 49.4; H, 3.7; N, 4.3%.

Complex 3*R*: was obtained following the same procedure, starting from $MnBr_2{\cdot}4H_2O$ instead $MnCl_2{\cdot}4H_2O$. Anal. Calcd for $C_{108}\ H_{112}\ Br_6\ Mn_7\ N_{10}\ Na_2\ O_{21}$ (**3*R***): C, 46.03; H, 3.94; N, 4.13%. Found: C, 45.8; H, 3.8; N, 4.3% (corresponding to the loss of the diethylether and partial loss of around 2 ACN).

The reaction that allow to the pentanuclear complexes **1*R***/**1*S*** was also performed starting from manganese chloride but this reaction produces in all cases compounds **2*R***/**2*S*** instead the pentanuclear clusters. In contrast, the syntheses of the enneanuclear complexes **2*R***/**2*S***/**3*R*** is not sensitive to the starting halide salt.

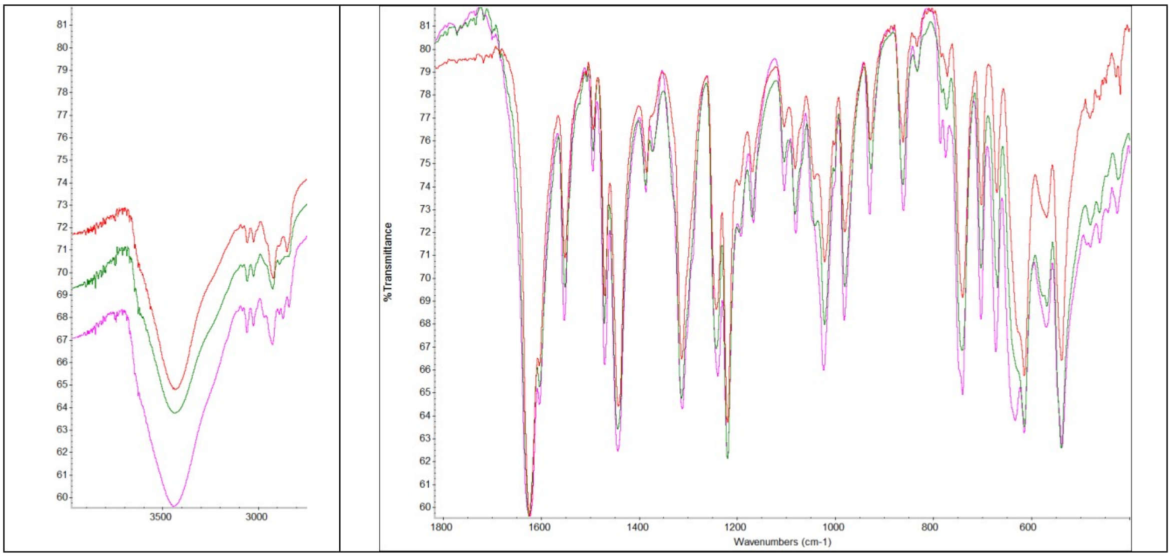

Fig S1. IR spectra for one of the enantiomers of **1** (red), **2** (violet) and **3** (green). As can be expected from the similar subunits and analogous coordination of the Schiff base, the spectra do not show differences between the penta and nonanuclear complexes. The only relevant difference corresponds to the peak at 635 cm^{-1} for the chloro complex **2** that shifts to 614 cm^{-1} for the bromo complexes **1** and **3**.

Instrumental measurements

IR spectra (4000-400 cm-1) were recorded using a Bruker IFS-125 FT-IR spectrometer with samples prepared as KBr pellets. Variable-temperature magnetic studies were performed using a MPMS-5 Quantum Design magnetometer operating at 0.03 T in the 300-2.0 K range. Diamagnetic corrections were applied to the observed paramagnetic susceptibility using Pascal's constants. Analysis of the magnetic data were performed with PHI program. ECD and UV-Vis spectra were recorded using a Jasco J-715 spectrometer at room temperature in spectroscopy grade acetonitrile in three quartz cells with path-length of 2 cm (850-450 nm), 1 cm (450-315 nm), and 0.1 cm (315-200 nm). The solid-state ECD spectra were obtained by placing a KBr pellet in a rotating holder as close as possible to the photomultiplier tube of a Jasco J-715 spectrometer. The X-ray intensity data were measured on a D8-Venture system equipped with a multilayer monochromator and a Mo microfocus (λ = 0.71073 Å). The frames were integrated with the Bruker SAINT software package using a narrow-frame algorithm. The final cell constants were based upon the refinement of the XYZ-centroids of reflections above 20 σ(I). Data were corrected for absorption effects using the multi-scan method (SADABS). The structures were solved using the Bruker SHELXTL Software Package, and refined using SHELXL.

Table S1. Crystal data and structure refinement for coordination compounds **1*R*** and **1*S***.

	1*R*	**1*S***
Formula	$C_{217}H_{233}Br_{16}Mn_{16}N_{21}Na_{4}O_{49}$	$C_{220}H_{234}Br_{16}Mn_{16}N_{24}Na_{4}O_{53}$
FW	6168.79	6311.86
System	Triclinic	Monoclinic
Space group	P1	P21
a/Å	16.545(2)	20.2507(7)
b/Å	19.911(2)	16.3807(6)
c/Å	20.663(2)	20.7092(8)
α/deg.	114.549(4)	90
β/deg.	91.914(5)	115.848(1)
γ/deg.	90.337(4)	90
V/ Å^3	6187(1)	6182.4(4)
Z	1	1
T, K	100(2)	100(2)
λ(MoKα), Å	0.71073	0.71073
ρcalc, g·cm-3	1.656	1.695
μ(MoK$_\alpha$), mm^{-1}	3.450	3.456
R	0.0536	0.0361
ωR^2	0.1344	0.0762

Table S2. Crystal data and structure refinement for coordination compounds **2*R***, **2*S*** and **3*R***.

	2*R*	**2*S***	**3*R***
Formula	$C_{105}H_{111}Cl_{6}Mn_{7}N_{6}Na_{2}O_{23}$	$C_{97.5}H_{100}Cl_{6}Mn_{7}N_{6}Na_{2}O_{23.5}$	$C_{108}H_{112}Br_{6}Mn_{7}N_{10}Na_{2}O_{21}$
FW	2510.28	2375.09	2796.09
System	Trigonal	Trigonal	Triclinic
Space group	R3	R3	P1
a/Å	19.6260(7)	19.686(1)	14.2067(6)
b/Å	19.6260(7)	19.686(1)	14.5629(7)
c/Å	28.7679(9)	28.677(2)	16.5401(8)
α/deg.	90	90	91.435(2)
β/deg.	90	90	112.245(2)
γ/deg.	120	120	110.988(2)
V/ Å^3	9596.3(7)	9624(2)	2905.6(2)
Z	3	3	1
T, K	100(2)	100(2)	100(2)
λ(MoKα), Å	0.71073	0.71073	0.71073
ρcalc, g·cm-3	1.303	1.229	1.598
μ(MoK$_\alpha$), mm^{-1}	0.864	0.857	2.876
R	0.0572	0.0441	0.0304
ωR^2	0.1654	0.1137	0.0730

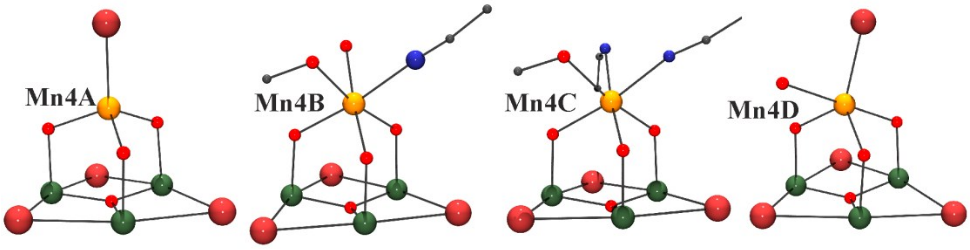

Fig S2. Detail of the coordination of the divalent atom Mn4 in the four non-equivalent units of **1*R***. The structure of **1*S*** contains two non-equivalent units similar to B and D.

Table S3. Selected bond distances (Å) and angles (°) for the core of compounds **1*R*** and **1*S***.

	(1*R*)-A	**(1*R*)-B**	**(1*R*)-C**	**(1*R*)-D**	**(1*S*)-A**	**(1*S*)-B**
Coordination number for Mn4	4	6	6	5	5	6
Mn1-O10	1.928(8)	1.893(9)	1.931(9)	1.891(8)	1.890(4)	1.905(5)
Mn2-O10	1.880(8)	1.884(9)	1.894(9)	1.898(9)	1.895(4)	1.887(5)
Mn3-O10	1.915(9)	1.873(9)	1.844(9)	1.877(8)	1.905(5)	1.894(5)
Mn1-O1	1.905(10)	1.875(9)	1.899(8)	1.881(8)	1.900(5)	1.892(4)
Mn2-O4	1.895(10)	1.878(10)	1.899(8)	1.898(9)	1.901(5)	1.897(5)
Mn3-O7	1.893(10)	1.881(9)	1.879(9)	1.886(9)	1.904(5)	1.880(4)
Mn4-O1	2.079(9)	2.145(9)	2.160(9)	2.183(8)	2.166(5)	2.157(5)
Mn4-O4	2.082(9)	2.133(11)	2.153(8)	2.059(9)	2.086(5)	2.151(5)
Mn4-O7	2.017(11)	2.136(10)	2.100(10)	2.076(9)	2.071(5)	2.148(5)
Mn1-O10-Mn2	121.5(5)	119.1(5)	117.3(5)	116.2(4)	2.128(3)	118.0(2)
Mn1-O10-Mn3	119.5(4)	118.0(5)	120.4(4)	118.7(5)	2.162(3)	118.7(2)
Mn2-O10-Mn3	118.6(4)	120.5(5)	120.3(5)	123.1(4)	2.230(2)	120.6(2)
Mn1-O1-Mn4	110.3(4)	121.4(5)	121.7(4)	117.6(4)	118.6(2)	121.8(2)
Mn2-O4-Mn4	109.4(4)	121.0(5)	120.9(4)	118.5(4)	118.3(2)	122.4(2)
Mn3-O7-Mn4	113.7(5)	124.4(5)	123.3(4)	119.8(4)	118.3(2)	122.7(2)
Mn1-O2-Na	111.0(4)	106.1(4)	106.3(4)	109.4(4)	108.6(2)	107.2(2)
Mn2-O5-Na	109.8(4)	107.6(4)	108.9(4)	108.1(4)	108.7(2)	117.2(6)
Mn3-O8-Na	107.9(4)	104.8(4)	109.3(4)	108.7(4)	108.4(2)	107.0(2)

Table S4. Selected bond distances (Å) and angles (°) for compounds **2*R*** and **2*S***.

d Å	(**2**-***R***)	(**2**-**S**)
Mn1-O1	1.893(6)	1.852(8)
Mn1-O2	1.903(6)	1.894(7)
Mn1-O7	1.881(1)	1.882(2)
Mn1-N1	1.979(6)	1.984(7)
Mn1-Cl1	2.601(2)	2.581(3)
Mn1-Cl1'	2.686(2)	2.711(3)
Mn2-O4	1.887(6)	1.894(8)
Mn2-O5	1.911(6)	1.880(8)
Mn2-O8	1.880(1)	1.879(2)
Mn2-N2	1.981(6)	1.968(7)
Mn2-Cl2	2.648(2)	2.665(3)
Mn2-Cl2'	2.717(2)	2.730(3)
Mn3-O1	2.214(5)	2.207(7)
Mn3-O4	2.195(5)	2.196(7)
Mn1-O1-Mn3	122.5(3)	123.4(3)
Mn2-O4-Mn3	125.5(3)	126.1(3)
Mn1-O7-Mn1'	119.51(7)	119.56(9)
Mn2-O8-Mn2'	118.8(1)	119.1(1)
Mn1-O2-Na1	107.0(3)	108.4(3)
Mn2-O5-Na2	108.1(3)	107.9(3)

Table S5. Selected bond distances (Å) and angles (°) for compound **3*R***.

Mn1-O1	1.881(3)	Mn5-O13	1.888(3)
Mn1-O2	1.908(3)	Mn5-O14	1.904(3)
Mn1-O19	1.882(3)	Mn5-O20	1.887(3)
Mn1-N1	1.998(3)	Mn5-N5	1.985(3)
Mn1-Br1	2.8328(7)	Mn5-Br4	2.8059(7)
Mn1-Br2	2.8271(7)	Mn5-Br5	2.8003(7)
Mn2-O4	1.891(3)	Mn6-O16	1.885(3)
Mn2-O5	1.912(3)	Mn6-O17	1.910(3)
Mn2-O19	1.885(3)	Mn6-O20	1.878(3)
Mn2-N2	1.980(3)	Mn6-N014	1.992(3)
Mn2-Br2	2.8023(7)	Mn6-Br5	2.8312(7)
Mn2-Br3	2.8005(7)	Mn6-Br6	2.7905(7)
Mn3-O7	1.891(3)	Mn7-O1	2.200(3)
Mn3-O8	1.903(3)	Mn7-O4	2.189(3)
Mn3-O19	1.885(3)	Mn7-O7	2.209(3)
Mn3-N3	1.985(3)	Mn7-O10	2.215(3)
Mn3- Br1	2.8457(7)	Mn7-O13	2.190(3)
Mn3-Br3	2.7937(7)	Mn7-O16	2.195(3)
Mn4-O10	1.884(3)		
Mn4-O11	1.911(3)		
Mn4-O20	1.888(3)		
Mn4-N4	1.987(3)		
Mn4-Br4	2.8145(7)		
Mn4-Br6	2.8808(7)		
Mn1-O1-Mn7	127.6(1)	Mn1-O19-Mn2	118.56(14)
Mn2-O4-Mn7	127.6(1)	Mn1-O19-Mn3	120.03(14)
Mn3-O7-Mn7	126.3(1)	Mn2-O(19-Mn3	117.83(13)
Mn4-O10-Mn7	128.2(1)	Mn4-O20-Mn5	118.0(1)
Mn5-O13-Mn7	127.7(1)	Mn4-O20-Mn6	120.3(1)
Mn6-O16-Mn7	127.9(1)	Mn5-O20-Mn6	117.3(1)

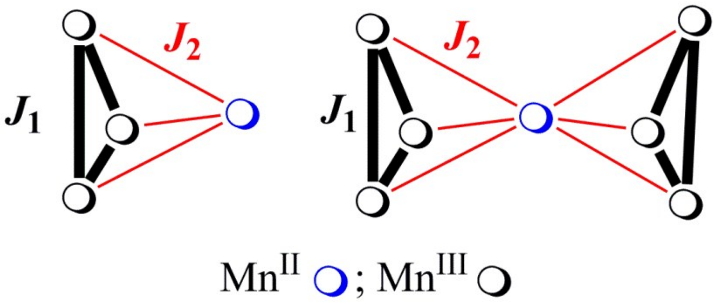

Fig. S3 Coupling scheme for complexes **1** (left), **2** and **3** (right). The derived Hamiltonians are :

$H = -2J_1(S_1 \cdot S_2 + S_1 \cdot S_3 + S_2 \cdot S_3) - 2J_2(S_1 \cdot S_4 + S_2 \cdot S_4 + S_3 \cdot S_4)$ for **1** and

$H = -2J_1(S_1 \cdot S_2 + S_1 \cdot S_3 + S_2 \cdot S_3 + S_4 \cdot S_5 + S_4 \cdot S_6 + S_5 \cdot S_6) - 2J_2(S_1 \cdot S_7 + S_2 \cdot S_7 + S_3 \cdot S_7 + S_4 \cdot S_7 + S_5 \cdot S_7 + S_6 \cdot S_7)$ for complexes **2** and **3**.

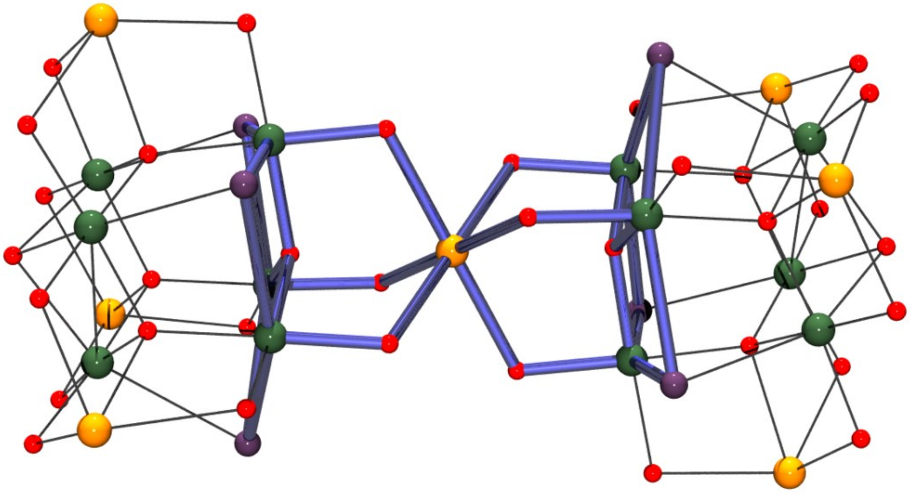

Fig. S4 Core of one typical Mn$^{III}_{12}$Mn$^{II}_{7}$ cluster[5]. The central {(μ_3-O)Mn$^{III}_3$-Mn^{II}-Mn$^{III}_3$(μ_3-O)} fragment and in some case even the axial chloride ligands (enlighted as blue bonds) are equivalent to the core of complexes **2**-**3**. Note the out-of plane position of the μ_3-O donors, towards the central Mn^{II} cation.

Publication #6 *“Triple halide bridges in chiral $[Mn^{II}_2Mn^{III}_6Na^{I}_2]$ cages: structural and magnetic characterization”*

Inorganic Chemistry
Cite This: Inorg. Chem. 2018, 57, 926−929
Communication
pubs.acs.org/IC

Triple Halide Bridges in Chiral $Mn^{II}_2Mn^{III}_6Na^I_2$ Cages: Structural and Magnetic Characterization

Júlia Mayans,[†] Mercè Font-Bardia,[‡,§] and Albert Escuer*,[†]

[†]Departament de Química Inorgànica i Orgànica, Secció Inorgànica and Institut de Nanociència i Nanotecnologia, Universitat de Barcelona, Martí i Franqués 1−11, Barcelona 08028, Spain

[‡]Departament de Mineralogia, Cristal·lografia i Dipòsits Minerals, Universitat de Barcelona, Martí Franqués s/n, 08028 Barcelona, Spain

[§]Unitat de Difracció de R-X, Centre Científic i Tecnològic de la Universitat de Barcelona, Solé i Sabarís 1−3, 08028 Barcelona, Spain

Supporting Information

ABSTRACT: A family of decanuclear chiral clusters with a $Mn^{II}_2Mn^{III}_6Na^I_2$ core have been synthesized from enantiomerically pure Schiff bases. The new systems consist of two $Mn^{II}Mn^{III}_3Na^I$ units linked by rare triple chloro or bromo bridges between the divalent Mn cations. Susceptibility measurements point out the weak antiferromagnetic interaction mediated by these kinds of bridges and afford the first magnetic measurements for the $(\mu\text{-Br})_3$ case.

Multidentate Schiff bases obtained from the condensation of *o*-vanillin and amino alcohols have been widely employed in coordination chemistry (around 180 entries in CCDC) because of their good chelating properties with 3d or 4f cations. The large variety of easily available amino alcohols has been useful in modulating the size, charge, or number of O-atom donors resulting in H_2L, H_3L, or H_4L Schiff bases as a function of the adequate choice of the starting reagent 2-amino-1-ethanol,[1−5] 3-amino-1,2-propanediol,[6−10] 2-amino-2-methyl-1,3-propanediol,[3] or tris(hydroxymethyl)aminomethane.[11]

One characteristic kind of complex derived of these ligands in manganese chemistry consists of $[Mn^{III}_3Mn^{II}Na^I]$ cages, in which the cations determine a trigonal bipyramid defined by one $\{(\mu_3\text{-}O)Mn^{III}_3\}$ triangle with Na^I and Mn^{II} cations in the apical positions. Among them, two kinds of complexes can be differentiated as a function of the employed Schiff base: the H_3L ligands derived from condensation with 3-amino-1,2-propanediol,[6−10] which generate two octahedral cavities that satisfy all of the coordination sites of the apical Mn^{II} and Na^I cations (Chart 1; H_3L-A type) and the H_2L ligands derived from 2-amino-1-ethanol, or in some random cases H_3L or H_4L, which maintain the cavity for the Na^I ion but not for the Mn^{II} cation, which, after formation of the cage, still has an open face capable of coordinating additional ligands (Chart 1, H_2L-B type). Usually, these coordination sites are occupied by anions or solvent molecules, but two pentanuclear units are able to share their open faces by means of triple bridges, as has been reported in two cases for the $\mu_{1,1}\text{-}N_3$ ligand.[4,10]

Chart 1. Schematic Drawing of the Typical $[Mn^{III}_3Mn^{II}Na^I]$ Cages with a Closed Pocket around the Mn^{II} Cation (H_3L-A) or Open-Face Mn^{II} Cation (H_2L-B)[a]

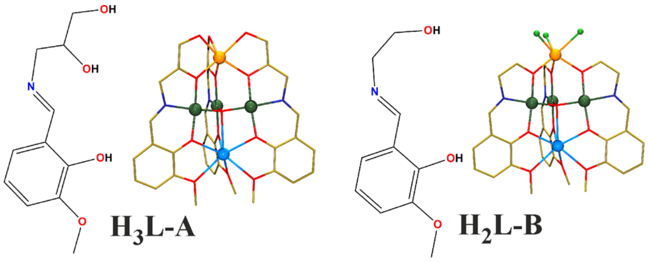

[a]Color code for all plots: O, red; N, navy blue; Na^I, blue; Mn^{II}, orange; Mn^{III}, dark green; Cl, violet.

An additional interest of H_2L-B kinds of ligands is that chirality can be incorporated by substitution on the C atoms of the hydroxyethyl fragment and enantiomerically pure chiral bases can be easily obtained from the substituted (*R*)- or (*S*)-2-amino-1-ethanol.

Following our work in this field,[5,12] we have explored the reactivity in manganese chemistry of the enantiomerically pure (*R*)- and (*S*)-H_2L ligands derived from the condensation of *o*-vanillin and 2-amino-3-methyl-1-butanol (Chart 2), which remains unexplored in 3d coordination chemistry (only one *meso*-$[Ni_4L_4]$ cubane[13] has been reported to date). The reason for this choice was to check its reactivity in comparison with other members of this family of ligands because the substituent is not innocent and different clusters or nuclearities can be obtained.

Chart 2. Schematic Drawing of the Anionic Form of the H_2L Ligand Employed in This Work and Its Coordination to the Metallic Centers[a]

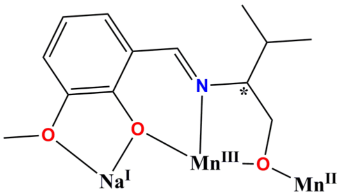

[a]The asterisk denotes the chiral C atom.

Received: December 12, 2017
Published: January 25, 2018

© 2018 American Chemical Society

DOI: 10.1021/acs.inorgchem.7b03125
Inorg. Chem. 2018, 57, 926−929

The reaction of H_2L with manganese halides in a methanolic solution allowed characterization of the first manganese derivatives of H_2L consisting of two enantiomeric decanuclear anionic clusters with the formula $Na[Mn_8Na_2(L)_6(O)_2(Cl)_9]$ (**1*R*** and **1*S***) and the pair of enantiomers of the related complex with bromo ligands $Na[Mn_8Na_2(L)_6(O)_2(Br)_9]$ (**2*R*** and **2*S***). See the Supporting Information for synthetic details. The core of these complexes consists of two $[Mn^{III}_3Mn^{II}Na^{I}]$ cages linked by the extremely unusual triple halide $Mn^{II}-(X)_3-Mn^{II}$ bridge. The new compounds have been characterized by X-ray diffraction, electronic circular dichroism (ECD), and magnetic susceptibility measurements.

The structures are very similar; therefore, only a common description based on **1*R*** is provided. Crystal data for **1*R*** and **1*S*** are summarized in Table S1. Selected bond parameters for **1*R*** and **1*S*** are listed in Tables S2 and S3. The cell and some significant bond parameters for the isostructural complex **3*S*** are also provided in Tables S1 and S5. The oxidation states of the Mn atoms have been assigned by structural considerations and bond-valence-sum calculations (Table S4).

Compound **1*R*** consists of two trigonal-bipiramidal $[Mn^{III}_3Mn^{II}Na^{I}]$ clusters joined by a triple μ-Cl bridge that links the Mn^{II} cations. A view of the cluster and a labeled core can be seen in Figure 1. Each pentanuclear subunit consists of a μ_3-O-centered equilateral triangle of Mn^{III} cations, one Mn^{II} cation, and one Na^{I} cation in the apical positions of the trigonal bipyramid. These cations are held together by three L^{2-} ligands that link the Na^{I} cation with the Mn^{III} ions by means of the phenoxide O atom and the Mn^{III} with the Mn^{II} cations with the alkoxide O-atom donors (Chart 2). The coordination polyhedron around the Mn^{III} cations is an elongated octahedron with two *trans*-μ-Cl ligands in the axial coordination sites. Coordination is completed with one μ_3-O donor placed in the center of the triangle. The three methoxide and phenoxide O-atom donors form a cavity that holds the Na^{I} cations.

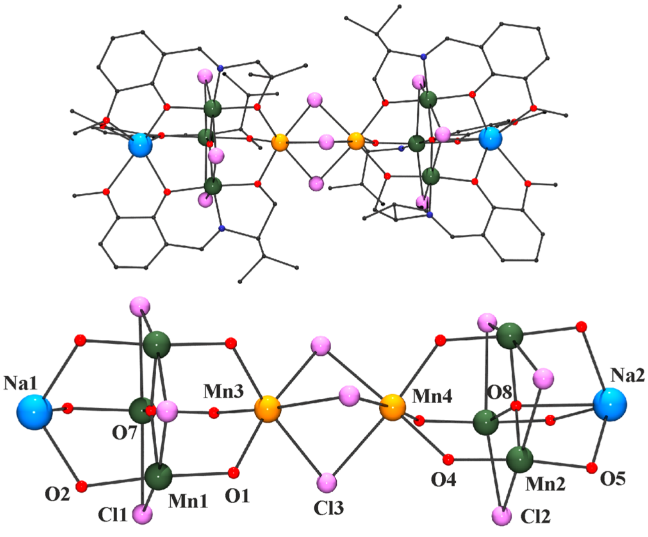

Figure 1. (Top) View of complex **1*R***. (Bottom) Labeled core of **1*R***.

The two $[Mn^{III}_3Mn^{II}Na^{I}]$ subunits are not equivalent and show different bond parameters (Table S2). The oxo donor O7 is placed in the center of the triangle determined by Mn1 (and symmetry-related cations) and acts as a μ_3-O, whereas O8 is displaced by 0.262 Å out of the mean Mn^{III}_3 plane determined by Mn2 (and symmetry-related cations) toward the Na^{I} cation, resulting in a Na2–O8 distance of 2.605 Å and, thus, O8 can be assumed as a μ_4-O bridge. *SHAPE*[14] measurements show that the coordination polyhedron around Na1 is very close to a trigonal prism, but it is closer to an octahedron for Na2 (Figure 2 and Table S6). An axial view of the clusters shows that, taking the $[OMn^{III}_3Cl_3]$ mean plane as a reference, the two subunits are slightly deviated from an eclipsed configuration (determined by the sharing of one face of the Mn^{II} coordination polyhedra), in contrast with the related systems that consist of two $[Mn^{III}MNa^{I}]$ units sharing the M cation (M = Mn^{II}, Ln^{III}),[5,15] which always show a staggered conformation.

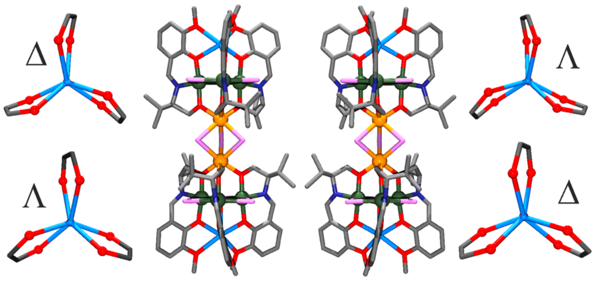

Figure 2. Mirror image of the helical arrangement of the ligands for **1*R*** (left) and **1*S*** (right) and a view of the coordination of the corresponding Na1 (top) and Na2 (bottom) cations.

Transfer of the chirality from the chiral centers to the coordination sphere of the cations or the whole molecule is a common effect that, in this case, can be seen at the level of opposite helicity of the propeller-shaped $[Mn^{III}_3Mn^{II}Na^{I}]$ units or the opposite Δ/Λ conformation of the chiral Na^{I} cations (Figure 2).

These structural results point out that the resulting complexes are sensitive to the substituents on the hydroxyethyl C atoms. Equivalent reactions with the ligand with one phenyl group instead of isopropane produce one nonanuclear system formed by the same subunits but sharing the Mn^{II} cation.[5] Interestingly, the reported systems with triple bridges (azido) have also been obtained from ligands with methyl or alkoxo substituents.[4,10]

The ECD spectra for the two pairs of enantiomers **1*R***/**1*S*** and **2*R***/**2*S*** measured in a methanolic solution show similar plots and are perfect mirror images among them, as must be expected from isostructural enantiomerically pure compounds (Figure 3). The spectrum of (*R*)-H_2L shows two positive absorptions centered at 213 and 275 nm, three negative bands at 227, 248(w), and

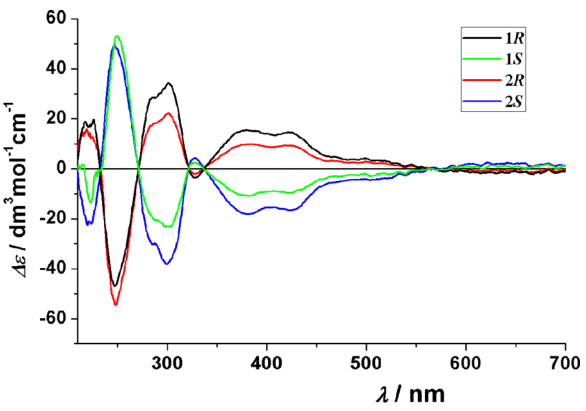

Figure 3. ECD spectra in a methanolic solution for complexes **1*R***, **1*S***, **2*R***, and **2*S***.

314(w) nm associated with the $\pi-\pi^*$ transitions, and no bands in the visible region. The spectra of the reported complexes exhibit bands with the same sign in the UV region due to the coordinated L^{-2} ligand, strong new absorptions around 380 and 425 nm, and weak broad absorptions up to 700 nm that suggest the participation of molecular orbitals, with contribution of the Mn^{III} cations that are directly linked to the aromatic groups. A comparison between the spectra of the chloro or bromo complexes shows identical spectra, and thus any effect related with these ligands or the Mn^{II} cation, linked to the aliphatic moiety of the ligand, must be expected.

Susceptibility measurements were performed on powdered samples of one chloro and one bromo complexes. The room temperature $\chi_M T$ values for **1*R*** and **2*S*** are 21.8 and 24.0 $cm^3 \cdot mol^{-1} \cdot K$, respectively, lower than the calculated value of 26.75 $cm^3 \cdot mol^{-1} \cdot K$ for two Mn^{II} and six Mn^{III} isolated cations ($g = 2.00$; Figure 4). Upon cooling, $\chi_M T$ decreases continuously to values of 3.60 or 9.91 $cm^3 \cdot mol^{-1} \cdot K$ at 2 K for **1*R*** or **2*S***, respectively.

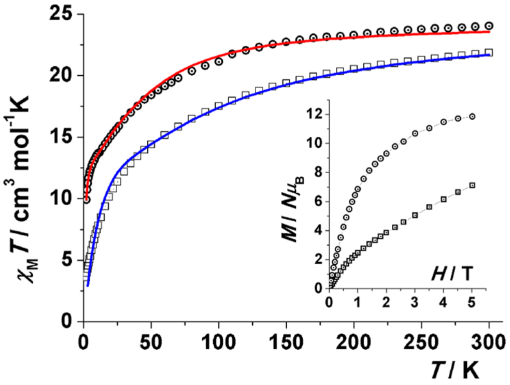

Figure 4. $\chi_M T$ product vs. temperature for complexes **1*R*** (squares) and **2*S*** (circles). Inset, magnetization plot for **1*R*** and **2*S***.

The complexes possess C_3 symmetry, and assuming that both subunits contribute equally to the magnetic response, a simplified coupling scheme with only three different superexchange pathways ($Mn^{III} \cdots Mn^{III}$, J_1; $Mn^{II} \cdots Mn^{III}$, J_2; $Mn^{II} \cdots Mn^{II}$, J_3) can be proposed to fit the experimental data (see Figure S3 for the coupling scheme and the applied isotropic Hamiltonian).

Fitting of the experimental data was performed with the *PHI*[16] program in the 300−2 K range of temperatures, and best-fit parameters were $J_1 = +2.0$ cm^{-1}, $J_2 = -7.8$ cm^{-1}, $J_3 = -2.6$ cm^{-1}, and $g = 1.91$ with $R = 8.5 \times 10^{-4}$ for **1*R*** and $J_1 = +7.2$ cm^{-1}, $J_2 = -6.4$ cm^{-1}, $J_3 = -0.3$ cm^{-1}, and $g = 1.89$ with $R = 1.9 \times 10^{-4}$ for **2*S***. These values indicate ferromagnetic interaction inside the Mn^{III}_3 triangles and antiferromagnetic (AF) interaction with the Mn^{II} cations, resulting in a local $S = {}^7/_2$ for each subunit. The weak AF interaction mediated by the triple halide bridge led to a final $S = 0$ ground state with very close $S \neq 0$ levels for **1*R***, whereas the response of **2*S*** is closer to the sum of two quasi-isolated $Mn^{II}Mn^{III}_3$ fragments. In agreement with these data, the magnetization plot for **1*R*** shows a continuous increase of the magnetization with a change of slope around 1 T, reaching the unsaturated value of 7.1 Nμ_β under the maximum field of 5 T, whereas the magnetization plot for **2*S*** tends to a quasi-saturated value of 11.8 Nμ_β, slightly lower than the sum of two isolated $\{(\mu_3\text{-}O)Mn^{II}Mn^{III}Na^{I}\}$ fragments (12.6 Nμ_β for the $g = 1.90$ value found in the susceptibility measurement).

Magnetic measurements for triple chloro bridges between Mn^{II} cations have only been reported for three $[MnCl_3]^-$ chains[17−19] with Mn−Cl−Mn bond angles comprised between 77.5 and 78.4° and similar *J* values (−4.8/−5.5 cm^{-1}) and for one discrete molecular dimer reported by Wieghardt et al.[20] for which a *J* value of −11.6 cm^{-1} was found for an average Mn−Cl−Mn bond angle of 74.4°. Our value of −2.6 cm^{-1} for the bond angle of 76.2° is comparable with these data. In contrast, any measure has never been reported for structurally characterized triple bromo bridges and thus any comparison can be made. The only data for a $Mn-(Br)_3-Mn$ fragment were reported in a partially characterized dimer for which a weak AF interaction was proposed.[20] In light of our results, there is evidence for a weak AF interaction promoted by triple chloro or bromo bridges, being clearly lower for the bromo case.

The Mn^{III} coordination polyhedron is elongated toward the chloro donors and, thus, the easy axis lies in the $\{\mu_3O-Mn_3^{III}\}$ plane, forming angles of around 60° between them. This arrangement cancels the anisotropy, and as was experimentally checked, no out-of-phase response was found in alternating-current experiments.

In conclusion, the reported systems reveal or confirm several unusual features: (a) evidence of the versatility of these kinds of ligands as a function of the substituents on the aliphatic C atoms; (b) the first examples of manganese complexes with H_2L and their first chiral derivatives; (c) the second molecular compound with a triple chloro bridge between Mn atoms and the first one with triple bromo bridges; (d) magnetic susceptibility measurements confirming the ferromagnetic response for the unusual $\{Mn^{III}_3(\mu\text{-}Cl)_3(\mu_3\text{-}O)\}$ triangles and evidence of the weak AF interaction promoted by the triple bridge, with the interaction being stronger for $(\mu\text{-}Cl)_3$ than for $(\mu\text{-}Br)_3$.

■ ASSOCIATED CONTENT

Ⓢ Supporting Information

The Supporting Information is available free of charge on the ACS Publications website at DOI: 10.1021/acs.inorgchem.7b03125.

Synthetic details (PDF)

Accession Codes

CCDC 1810689−1810690 contain the supplementary crystallographic data for this paper. These data can be obtained free of charge via www.ccdc.cam.ac.uk/data_request/cif, or by emailing data_request@ccdc.cam.ac.uk, or by contacting The Cambridge Crystallographic Data Centre, 12 Union Road, Cambridge CB2 1EZ, UK; fax: +44 1223 336033.

■ AUTHOR INFORMATION

Corresponding Author

*E-mail: albert.escuer@ub.edu.

ORCID

Albert Escuer: 0000-0002-6274-6866

Notes

The authors declare no competing financial interest.

■ ACKNOWLEDGMENTS

Funds from the Ministerio de Economia y Competitividad under Project CTQ2015-63614-P are acknowledged.

■ REFERENCES

(1) Gole, B.; Mondal, K. C.; Mukherjee, P. S. Tuning nuclearity of clusters by positional change of functional group: Synthesis of polynuclear clusters, crystal structures and magnetic properties. *Inorg. Chim. Acta* **2014**, *415*, 151−164.

(2) Fan, L.-L.; Guo, F.-S.; Yun, L.; Lin, Z.-J.; Herchel, R.; Leng, J.-D.; Ou, Y.-C.; Tong, M.-L. Chiral transition metal clusters from two enantiomeric schiff base ligands. Synthesis, structures, CD spectra and magnetic properties. *Dalton Trans.* **2010**, *39*, 1771−1780.

(3) Hewitt, I. J.; Tang, J.-K.; Madhu, N. T.; Clerac, R.; Buth, G.; Anson, C. E.; Powell, A. K. A series of new structural models for the OEC in photosystem II. *Chem. Commun.* **2006**, 2650−2652.

(4) Song, Y.; Zhang, G.; Qin, X.; Gao, Y.; Ding, S.; Wang, Y.; Du, C.; Liu, Z. Chiral $[NaMn^{II}Mn^{III}_3]$ and $[Na_2Mn^{II}_2Mn^{III}_6]$ clusters constructed by chiral multidentate Schiff-base ligands: synthesis, structures, CD spectra and magnetic properties. *Dalton Trans.* **2014**, *43*, 3880−3887.

(5) Escuer, A.; Mayans, J.; Font-Bardia, M.; Górecki, M.; Di Bari, L. Syntheses, structures, chiroptical and magnetic properties of chiral clusters built from Schiff bases: a novel $[Mn^{II}Mn^{III}_6Na^I_2]$ core. *Dalton Trans.* **2017**, *46*, 6514−6517.

(6) Nayak, S.; Nayek, H. P.; Dehnen, S.; Powell, A. K.; Reedijk, J. Trigonal propeller-shaped $[Mn^{III}_3M^{II}Na]$ complexes (M = Mn, Ca): structural and functional models for the dioxygen evolving centre of PSII. *Dalton Trans.* **2011**, *40*, 2699−2702.

(7) Ding, C.; Gao, C.; Ng, S.; Wang, B.; Xie, Y. Polynuclear complexes with alkoxo and phenoxo bridges from in situ generated hydroxy-rich Schiff base ligands: syntheses, structures, and magnetic properties. *Chem. - Eur. J.* **2013**, *19*, 9961−9972.

(8) Cong, L.; Qin, X.; Sun, W.; Wang, Y.; Ding, S.; Liu, Z. A series of $[NaMn^{III}_3Mn^{II}]$ clusters constructed using a multidentate Schiff-base ligand and decorated with different auxiliary ligands. *New J. Chem.* **2014**, *38*, 545−551.

(9) Yang, P.-P.; Zhu, L.-L.; Xu, Y.; Shao, C.-Y. Synthesis, crystal structures, and magnetic properties of two tetrahedral $Mn^{II}Mn^{III}_3$ complexes. *Z. Anorg. Allg. Chem.* **2013**, *639*, 1821−1826.

(10) Yang, P.-P.; Shao, C.-Y.; Zhu, L.-L.; Xu, Y. Syntheses, crystal structures, and magnetic properties of a family of tetra- and octanuclear mixed-valent manganese clusters. *Eur. J. Inorg. Chem.* **2013**, *2013*, 5288−5296.

(11) Liu, D.; Zhou, Q.; Chen, Y.; Yang, F.; Yu, Y.; Shi, Z.; Feng, S. Constructing octa- and hexadecanuclear manganese clusters from tetrahedral $Mn^{III}_3Mn^{II}$ cores bridged by quinquedentate Schiff base and versatile azide groups. *Dalton Trans.* **2010**, *39*, 5504−5508.

(12) Escuer, A.; Mayans, J.; Font-Bardia, M.; Di Bari, L.; Górecki, M. Mn_3^{III} complexes derived from *R*/*S*-Schiff bases: chiral Single-Molecule-Magnets. *Eur. J. Inorg. Chem.* **2017**, *2017*, 991−998.

(13) Karmakar, S.; Khanra, S. Polynuclear coordination compounds: a magnetostructural study of ferromagnetically coupled Ni_4O_4 cubane core motif. *CrystEngComm* **2014**, *16*, 2371−2383.

(14) Llunell, M.; Casanova, D.; Cirera, J.; Alemany, P.; Alvarez, S. *SHAPE*, version 2.0; Barcelona, 2010. The program can be obtained by request to the authors.

(15) Yang, P.-P.; Wang, X.-L.; Li, L.-C.; Liao, D.-Z. Synthesis, structure and magnetic properties of a novel family of heterometallic nonanuclear $Na^I_2Mn^{III}_6Ln^{III}$ (Ln = Eu, Gd, Tb, Dy) complexes. *Dalton Trans.* **2011**, *40*, 4155−4161.

(16) Chilton, N. F.; Anderson, R. P.; Turner, L. D.; Soncini, A.; Murray, K. S. PHI: a powerful new program for the analysis of anisotropic monomeric and exchange-coupled polynuclear d- and f-block complexes. *J. Comput. Chem.* **2013**, *34*, 1164−1175.

(17) Caputo, R. E.; Roberts, S.; Willett, R. D.; Gerstein, B. C. Crystal structure and magnetic susceptibility of $[(CH_3)_3NH]_3Mn_2Cl_7$. *Inorg. Chem.* **1976**, *15*, 820−823.

(18) Caputo, R. E.; Willett, R. D. Crystal structure and magnetic susceptibility of $(CH_3)_2NH_2MnCl_3$ (DMMC): A low-symmetry analog of $(CH_3)_4NMnCl_3$ (TMMC). *Phys. Rev. B* **1976**, *13*, 3956−3961.

(19) Tancharakorn, S.; Fabbiani, F. P. A.; Allan, D. R.; Kamenev, K. V.; Robertson, N. Combined magnetic and single-crystal X-ray structural study of the linear chain antiferromagnet $[(CH_3)_4N][MnCl_3]$ under varying pressure. *J. Am. Chem. Soc.* **2006**, *128*, 9205−9210.

(20) Bossek, U.; Nuhlen, D.; Bill, E.; Glaser, T.; Krebs, C.; Weyhermuller, T.; Wieghardt, K.; Lengen, M.; Trautwein, A. X. Exchange coupling in an isostructural series of face-sharing bioctahedral complexes $[LM^{II}(\mu\text{-}X)_3M^{II}L]BPh_4$ (M = Mn, Fe, Co, Ni, Zn; X = Cl, Br; L = 1,4,7-trimethyl-1,4,7-triazacyclononane). *Inorg. Chem.* **1997**, *36*, 2834−2843.

DOI: 10.1021/acs.inorgchem.7b03125
Inorg. Chem. 2018, 57, 926−929

Supporting Information

Triple halide bridges in chiral $Mn^{II}_2Mn^{III}_6Na^I_2$ cages. Structural and magnetic characterization

Júlia Mayans,[‡] Mercè Font-Bardia,[#] Albert Escuer,[*,‡]

[‡] Departament de Química Inorgànica i Orgànica, Secció Inorgànica and Institut de Nanociència i Nanotecnologia (IN²UB), Universitat de Barcelona, Martí i Franqués 1-11, Barcelona-08028, Spain.

[#] Departament de Mineralogia, Cristal·lografia i Dipòsits Minerals, Universitat de Barcelona, Martí Franqués s/n, 08028 Barcelona (Spain) and Unitat de Difracció de R-X. Centre Científic i Tecnològic de la Universitat de Barcelona (CCiTUB), Solé i Sabarís 1-3. 08028 Barcelona.

Experimental

Physical measurements: Magnetic susceptibility measurements were carried out on polycrystalline samples with a MPMS5 Quantum Design susceptometer working in the range 30-300 K under magnetic fields of 0.3 T and under a field of 0.03T in the 30 – 2 K range to avoid saturation effects at low temperature. Diamagnetic corrections were estimated from Pascal Tables. Infrared spectra (4000-400 cm–1) were recorded from KBr pellets on a Bruker IFS-125 FT-IR spectrophotometer. EDC spectra were recorded in methanolic solutions in a Jasco-815 spectropolarimeter

Synthetic procedure.

Compounds **1*R***, **1*S***, **2*R*** and **2*S*** were obtained following the same procedure and thus a common description of the syntheses will be detailed:

0.5 mmols (0.076g) 2-hydroxy-3-methoxybenzaldehyde and 0.5 mmols (0.051g) of (*R* or *S*)-valinol were refluxed for one hour in 20 mL of MeOH. The resulting yellow solution of H_2L was employed directly for the syntheses of the corresponding complexes without isolation of the ligand. 0.5 mmols of $MnCl_2\cdot4H_2O$ (0.099g) or $MnBr_2\cdot4H_2O$ (0.143g) and 0.5 mmols (0.02g) of NaOH in acetonitrile were mixed with the methanolic solution of H_2L and stirred for three hours. The mixture becomes progresively darker by air oxidation and the resulting dark brown solution was layered with diethylether. Small dark crystals were collected after two days.

IR spectra are shown in Figure S1.

Anal. calculated/found (%) for the complex formula·$7.5H_2O$: **1*R***, C, 38.93/38.1; H 4.90/5.0; N 3.49/3.40; **1*S***, C, 38.93/38.4; H 4.90/5.1; N 3.49/3.4; **2*R***, C, 33.38/33.0; H 4.20/4.3; N 2.99/2.96; **2*S***, C,33.38/32.6; H 4.20/4.4; N 2.99/2.92.

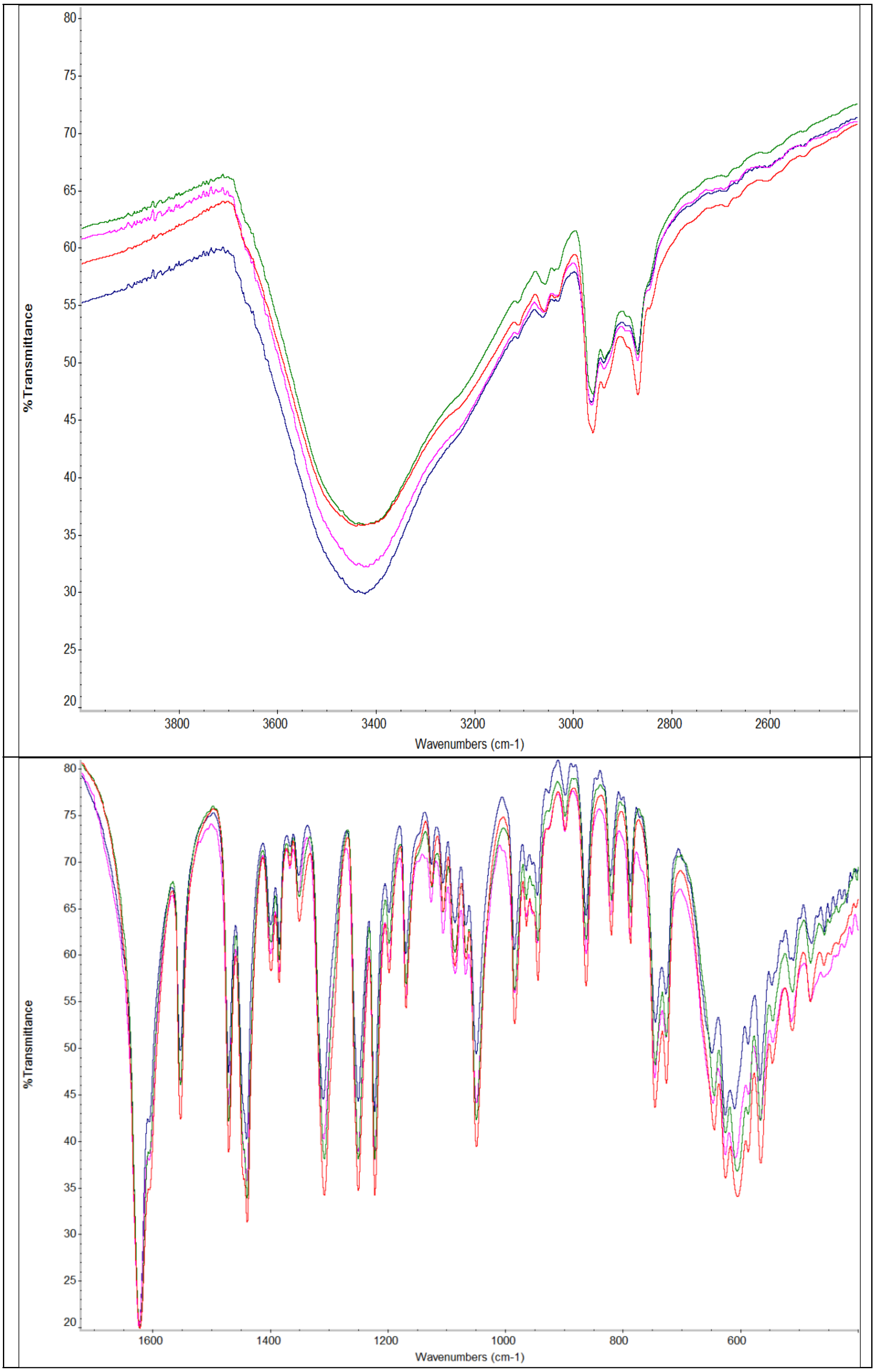

Figure S1.IR spectra for the four reported complexes showing the position of the bands and the full similarity of the four molecular systems **1R** (blue), **1S** (pink), **2R** (red) and **2S** (green).

Complementary information:

Other reactions were tried, in particular including the azido co-ligand and the system with triple azido bridges was also characterized. This compound is similar to two complexes previously reported in the literature obtained from similar Schiff bases. This compound do not has the novelty component and thus is less interesting than the chloro- or bromo- systems. **As information for the reader** we report some details about this system:

The synthesis performed with 0.5 mmols of sodium azido instead NaOH produces the same compounds but with a more or less pronounced band of azido at 2050 cm^{-1}. Several reactions with different Mn^{II}:H$_2$L:NaN$_3$ stechiometries were tried and increasing the amount of sodium azide was posible to isolate the complex with three azido bridges starting from manganese bromide in methanol and employing the 1:1:4 ratio. Its IR spectrum is practically identical to the halo- complexes with a very strong band at 2045 cm^{-1} which corresponds to the asymmetric stretching of the end-on azido ligands. Noteworthy, the isolation of the triple azido bridges required a larger amount of sodium azide in comparison with the two previously reported systems with other Schiff bases.

Crystals were of very bad quality. Several crystals were analyzed and in one case it was possible to obtain a partial structure for the (*S*) enantiomer. The system crystallizes in the P2$_1$3 space group with a = b = c = 23.7051(9) Å and $\alpha = \beta = \gamma = 90^o$. Mn^{II}-N$_{azide}$-Mn^{II} bond angle is 88.8º. The structure is similar to their analogous with chloro or bromo bridges and its magnetic response also indicates ferromagnetic interactions inside the triangular Mn$^{III}_3$ fragments, antiferromagnetic interaction between Mn^{II}-Mn^{III} and weak antiferromagnetic interaction mediated by the triple azido bridges in agreement with the related systems previously reported.

Crystal structure report

A red prism-like specimens of **1*R*** (0.048 x 0.090 x 0.156 mm^3) or **1*S*** (0.095 x 0.112 x 0.189 mm^3) were used for the X-ray crystallographic analysis. The X-ray intensity data were measured on a D8 Venture system equipped with a multilayer monochromator and a Mo microfocus (λ = 0.71073 Å).

The frames were integrated with the Bruker SAINT software package using a narrow-frame algorithm. The integration of the data using a hexagonal unit cell yielded a total of 43175 reflections to a maximum θ angle of 26.38° (0.80 Å resolution), of which 3949 were independent (average redundancy 10.933, completeness = 99.8%, R$_{int}$ = 10.06%, R$_{sig}$ = 8.78%) and 3104 (78.60%) were greater than 2σ(F^2) for **1*R*** or a total of of 37267 reflections to a maximum θ angle of 26.42° (0.80 Å resolution), of which 7696 were independent (average redundancy 4.842, completeness = 99.7%, R$_{int}$ = 11.00%, R$_{sig}$ = 10.50%) and 5528 (71.83%) were greater than 2σ(F^2) for **1*S***. The final cell constants are based upon the refinement of the XYZ-centroids of reflections above 20 σ(I). Data were corrected for absorption effects using the multi-scan method (SADABS).

The structures were solved and refined using the Bruker SHELXTL Software Package. The final anisotropic full-matrix least-squares refinement on F^2 with 402 variables converged at R1 = 4.79%, for the observed data and wR2 = 12.77% for all data. The goodness-of-fit was 1.040. The largest peak in the final difference electron density synthesis was 0.791 e^-/Å^3 and the largest hole was -0.676 e^-/Å^3 with an RMS deviation of 0.089 e^-/Å^3 for **1*R*** and with 294 variables converged at R1 = 7.32%, for the observed data and wR2 = 19.79% for all data. The goodness-of-fit was 1.007. The largest peak in the final difference electron density synthesis was 2.877 e^-/Å^3 and the largest hole was -5.240 e^-/Å^3 with an RMS deviation of 0.147 e^-/Å^3 for **1*S***.

Quality of the crystals of **2*S*** was low and several crystals from different syntheses or crystallization methods were measured to try to solve its structure. The collected data was poor in all cases but the isostructurality with the analogous complexes **1** was proved with the unambiguous determination of their cell parameters. In one case it was possible a partial resolution of the structure, with poor detail of the solvent molecules or the isopropyl groups but with enough resolution to confirm, in addition to the cell parameters, that the core of complexes **2*R*/*S*** is fully equivalent to **1*R*/*S***.

Table S1. Crystal data and structure refinement for coordination compounds **1*R*, 1*S*** and cell parameters for **2*S***

	1*R*	**1*S***	**2*S***
Formula	$C_{78}H_{109}Cl_9Mn_8N_6Na_3O_{27.5}$	$C_{156}H_{220}Cl_{18}Mn_{16}N_{12}Na_6O_{51}$	--
FW	2398.74	4734.48	--
System	Hexagonal	Hexagonal	Hexagonal
Space group	P3	P63	P63
a/Å	13.7006(7)	13.6540(9)	13.8009(5)
b/Å	13.7006(7)	13.6540(9)	13.8009(5)
c/Å	34.892(2)	34.845(2)	35.519(2)
α/deg.	90	90	90
ß/deg.	90	90	90
γ/deg.	120	120	120
V/ Å^3	5671.9(6)	5625.9(8)	5858.8(6)
Z	2	1	--
T, K	100(2)	100(2)	100(2)
λ(MoKα), Å	0.71073	0.71073	0.71073
ρcalc, g·cm-3	1.405	1.397	--
μ(MoK$_\alpha$), mm^{-1}	1.149	1.156	--
R	0.0479	0.0732	--
ωR^2	0.1226	0.1848	--

Table S2. Selected bond distances (Å) and angles (°) for compound **1*R***.

d Å (**1*R***)			
Mn1-O1	1.903(6)	Mn2-O4	1.871(6)
Mn1-O2	1.859(6)	Mn2-O5	1.910(6)
Mn1-O7	1.879(1)	Mn2-O8	1.893(1)
Mn1-N1	1.970(5)	Mn2-N2	1.983(6)
Mn1-Cl1	2.712(2)	Mn2-Cl2	2.657(2)
Mn1-Cl1'	2.686(2)	Mn2-Cl2'	2.666(2)
Mn3-O1	2.127(5)	Mn4-O4	2.122(5)
Mn3-Cl3	2.605(4)	Mn4-Cl3	2.614(4)
Na1-O2	2.365(6)	Na2-O5	2.329(5)
Na1-O3	2.444(6)	Na2-O6	2.492(5)
Na1-O7	2.883(9)	Na2-O8	2.605(8)
Angles (º) (**1*S***)			
Mn1-O7-Mn1'	119.89(3)	Mn2-O8-Mn2'	118.1(1)
Mn1-O1-Mn3	120.5(2)	Mn2-O4-Mn4	123.0(3)
Mn1-O2-Na1	111.1(3)	Mn2-O5-Na2	107.4(2)
Mn1-Cl1-Mn1'	74.09(6)	Mn2-Cl2-Mn2'	75.2(1)
Mn3-Cl3-Mn4	78.2(1)		

Table S3. Selected bond distances (Å) and angles (°) for compound **1*S***.

d Å (**1*S***)			
Mn1-O1	1.880(9)	Mn2-O4	1.850(4)
Mn1-O2	1.895(8)	Mn2-O5	1.899(9)
Mn1-O7	1.879(2)	Mn2-O8	1.895(3)
Mn1-N1	1.977(9)	Mn2-N2	1.965(10)
Mn1-Cl1	2.710(4)	Mn2-Cl2	2.687(4)
Mn1-Cl1'	2.675(4)	Mn2-Cl2'	2.632(4)
Mn3-O1	2.157(9)	Mn4-O4	2.107(8)
Mn3-Cl3	2.669(5)	Mn4-Cl3	2.604(5)
Na1-O2	2.322(9)	Na2-O5	2.362(9)
Na1-O3	2.408(10)	Na2-O6	2.478(10)
Na1-O7	2.873(17)	Na2-O8	2.617(18)
Angles (º) (**1*S***)			
Mn1-O7-Mn1'	119.93(4)	Mn2-O8-Mn2'	118.1(2)
Mn1-O1-Mn3	120.0(4)	Mn2-O4-Mn4	125.4(4)
Mn1-O2-Na1	110.6(4)	Mn2-O5-Na2	107.1(4)
Mn1-Cl1-Mn1'	74.3(1)	Mn2-Cl2-Mn2'	75.3(1)
Mn3-Cl3-Mn4	76.1(1)		

Table S4. BSV calculation for compounds **1*R***, **1*S*** and partial data for **2*S***.

	1*R*			**1*S***			**2*S***
	Mn^{II}	Mn^{III}	Mn^{IV}	Mn^{II}	Mn^{III}	Mn^{IV}	
Mn1	*3.35*	**3.15**	*3.23*	*3.32*	**3.12**	*3.20*	--
Mn2	*3.31*	**3.11**	*3.19*	*3.40*	**3.20**	*3.28*	**3.05**
Mn3	**1.96**	*1.89*	*1.92*	**1.75**	*1.67*	*1.71*	**2.07**
Mn4	**1.96**	*1.88*	*1.92*	**2.03**	*1.94*	*1.99*	**2.07**

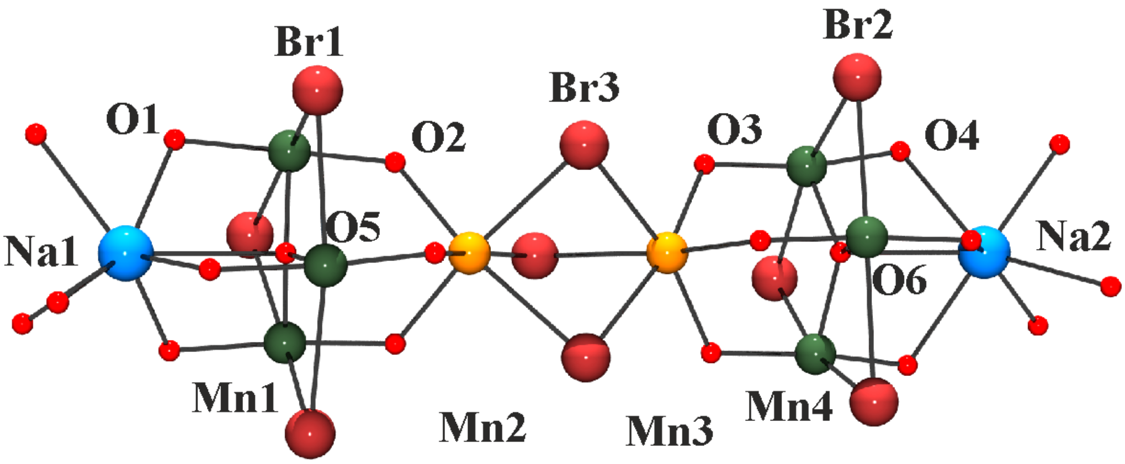

Figure S2. Core of **2*S*** from the partially solved structure.

Table S5. Selected parameters for **2*S*** are shown to check that, in addition to the agreement in the cell parameters, the core of both complexes is fully equivalent, including the differences in the bond angles in the two moieties of the complex..

Mn1-O5	1.898(9)	Mn4-O6	1.93(1)
Na1-O5	2.714	Na2-O6	2.664
Mn1-O5-Mn1'	118.5(7)	Mn4-O6-Mn4'	118.9(8)
Mn1-O2-Mn2	123(2)	Mn4-O3-Mn3	119(1)
Mn1-O1-Na1	110(1)	Mn4-O4-Na2	108(1)
Mn2-Br3-Mn3	80.8(3)		

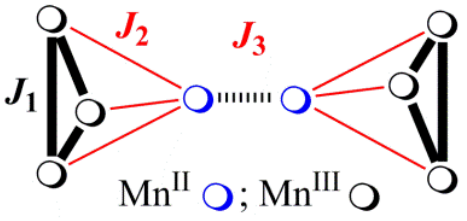

Figure S3. Coupling scheme applied for the fit of compounds **1*R*** and **2*S***. The derived isotropic Hamiltonian is:

$$H = -J_1(S_1\cdot S_2 + S_2\cdot S_3 + S_1\cdot S_3 + S_4\cdot S_5 + S_5\cdot S_6 + S_4\cdot S_5)$$
$$-J_2(S_1\cdot S_7 + S_2\cdot S_7 + S_3\cdot S_7 + S_4\cdot S_8 + S_5\cdot S_8 + S_6\cdot S_8)\ -J_3(S_7\cdot S_8)$$

Table S6. SHAPE measures for the Na^I cations parametrized as *S*(OC-6), *S*(TPR-6) for the six closer O-donors and *S*(COC-7), *S*(CTPR-7). S(P) = 0 corresponds to a structure fully coincident in shape with the reference polyhedron P, regardless of size and orientation. OC-6, octahedron; TPR-6, trigonal prism; COC-7, capped octahedon; CTPR-7, capped trigonal prism

	Na1 (**1*R***)	Na2 (**1*R***)	Na1 (**1*S***)	Na2 (**1*S***)	Na1 (**2*S***)	Na2 (**2*S***)
S(OC-6)	10.540	**5.490**	10.318	**5.675**	7.466	**4.325**
S(TPR-6)	**3.419**	7.831	**3.605**	7.877	**4.755**	10.537
S(COC-7)	10.369	7.451	9.748	7.354	7.409	9.911
S(CTPR-7)	11.513	8.788	11.080	8.700	8.737	11.200

1R and **1*S***: The above data confirms that, for the six O-donors with the shorther Na-O distances, Na1 has a coordination environment close to the trigonal prism. For Na2, the environment is intermediate between the octahedron and the trigonal prism but slightly closer to the octahedron. Inclusion of the seventh O-donor at larger distance is irrelevant for Na1 but shows that the better description for Na2 is an intermediate between octahedron and capped octahedron.

2*S*: The bromo clomplex **2*S*** shows more distortion around the Na^I cations but maintains the preferred trigonal prism (Na1) and octahedral (Na2) polyhedra.

Publication #7 *“Chiral [$Mn^{II}Mn^{III}_3M'$] ($M'=Na^I$, Ca^{II}, Mn^{II}) and [$Mn^{II}Mn^{III}_6Na^I_2$] clusters built from an enantiomerically pure Schiff base: synthetic, chiroptical and magnetic properties*”

ChemPubSoc Europe

DOI: 10.1002/chem.201803730

CHEMISTRY
A European Journal
Full Paper

Chiral Complexes

Chiral [$Mn^{II}Mn^{III}_3M'$] ($M' = Na^I$, Ca^{II}, Mn^{II}) and [$Mn^{II}Mn^{III}_6Na^I_2$] Clusters Built from an Enantiomerically Pure Schiff Base: Synthetic, Chiroptical, and Magnetic Properties

Júlia Mayans,[a] Mercé Font-Bardia,[b] Lorenzo Di Bari,[c] Marcin Górecki,[c] and Albert Escuer*[a]

Abstract: From the reaction of manganese halides with the chiral Schiff bases obtained by condensation of *o*-vanillin and (*R*)- or (*S*)-phenylglycinol, 11 complexes based on pentanuclear cages with trigonal bipyramidal [$Mn^{II}Mn^{III}_3M'$] ($M' = Na^I$, Ca^{II}, Mn^{II}) or enneanuclear [$Mn^{II}Mn^{III}_6Na^I_2$] cores were synthesized. Structural, supramolecular chirality, and optical properties were explored. The magnetic properties of related systems were reviewed, and the magnetic response of the new systems was rationalized to the bond parameters.

Introduction

The characterization of the single-molecule magnet (SMM) response of anisotropic systems with high spin[1] or the modelization of the oxygen evolving center[2] (OEC) have been relevant driving forces of the research on polynuclear manganese clusters during the last two decades. Syntheses of cluster compounds often follow a serendipitous self-assembly process, but Schiff bases have attracted the attention of magnetochemists because of their polynucleating properties with the 3d transition of 4f lanthanide cations and because the adequate arrangement of the N- and O-donors, combined with the relative rigidity of the ligand, can allow predetermined shapes and/or nuclearities.

Condensation of *o*-vanillin and aminoalcohols yields multidentate Schiff bases for which a characteristic family of [$Mn^{II}Mn^{III}_3M^{n+}$] clusters with $M^{n+} = Na^I$ and a trigonal bipyramidal arrangement of the cations has been reported,[3–10] together with a few examples in which $M^{n+} = Ca^{2+}$ or Ln^{3+}.[3,11] All of these clusters are characterized by the triangular arrangement of the trivalent manganese cations and the other two cations in apical positions resulting in a trigonal bipyramidal cage, in which the cations are held by three dianionic ligands.

Schiff bases derived from the condensation of 3-amino-1,2-propanediol with *o*-vanillin gives H_3L ligands that satisfy all the coordination sites of the apical cations, which are hosted in two predetermined octahedral cavities[6–9] (Scheme 1-**I**). On the contrary, the H_2L ligands derived from 2-amino-1-ethanol with only three O donors keep the octahedral cavity around the Na^+ cation, whereas they generate an open face on the Mn^{II} cation[3–5,10] that usually fulfills its coordination sphere with anions or solvent molecules (Scheme 1-**II**). In addition, this coordination gives the possibility to share the central cation or the open faces by means of bridging ligands that can join the pentanuclear units, resulting in larger nuclearities.[10,12,13] In these systems, the three ligands are parallel, and only one example with the divalent cation Ca^{2+} instead of Na^+ has been reported as the OEC model[3] with one of the ligands inverted with respect to the other two (Scheme 1-**III**). A common point in these structures is the presence of three additional bridging ligands on the elongated coordination sites of the trivalent

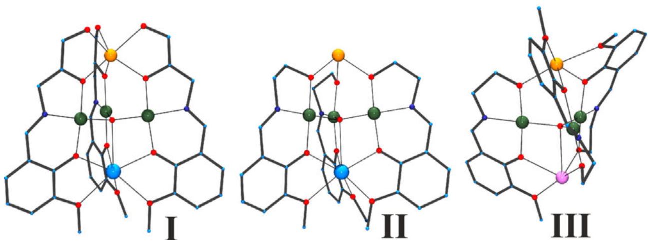

Scheme 1. Arrangement of the ligands in pentanuclear cages based on the Schiff bases obtained by condensation of *o*-vanillin and 3-amino-1,2-propanediol (**I**, literature data) or 2-amino-1-ethanol (**II** and **III**, this work). See Figure 1 for the color key.

---

[a] J. Mayans, Prof. A. Escuer
Departament de Química Inorgànica i Orgànica
Secció Inorgànica and Institut de Nanociència i Nanotecnologia (IN^{2}UB)
Universitat de Barcelona, Martí i Franques 1–11, Barcelona 08028 (Spain)
E-mail: albert.escuer@qi.ub.es
Homepage: http://www.ub.edu/inorgani/recerca/MagMol/magmol.htm

[b] Dr. M. Font-Bardia
Departament de Mineralogia, Cristal·lografia i Dipòsits Minerals
and Unitat de Difracció de R-X. Centre Científic i Tecnològic (CCiTUB)
Universitat de Barcelona, Martí Franqués s/n, Barcelona 08028 (Spain)

[c] Prof. L. Di Bari, Dr. M. Górecki
Dipartimento di Chimica e Chímica Industriale
Università di Pisa, Via Moruzzi 13, 56124 Pisa (Italy)
and
Current address:
Institute of Organic Chemistry, Polish Academy of Sciences
Kasprzaka 44/52 St., 01-224 Warsaw (Poland)

Supporting information and the ORCID identification number(s) for the author(s) of this article can be found under: https://doi.org/10.1002/chem.201803730.

© 2018 Wiley-VCH Verlag GmbH & Co. KGaA, Weinheim

manganese cations. These co-ligands are usually carboxylates, halides, or pseudohalides (especially azide) in the search of ferromagnetic interactions and high-spin ground states.[14]

The employment of chiral 2-amino-1-ethanol aminoalcohols with substituents on the hydroxoethyl fragment generates chiral Schiff bases. Supramolecular chirality[15] is a growing field, which is of interest in chiral catalysis and Circular Polarized Luminescence (CPL) emission,[16] in the search for chiral magnets with d or f cations,[17,18] or by its role in biological environments.[19] The synthesis of chiral clusters from enantiomerically pure ligands becomes of interest to reach multiproperty or multifunctional systems, in which optical, ferroelectric, or emissive properties can be combined with magnetic response. On the other hand, chiral clusters provide interesting examples of chirality transfer, chiral supramolecular arrangement, and chiral recognition.[20]

Following our work in this field[13], we chose the Schiff bases obtained from the condensation of *o*-vanillin with (*R*)- or (*S*)-phenylglycinol (Scheme 2, top) to explore their reactivity in manganese chemistry, with focus on the characterization of new chiral systems based on the $[Mn^{II}Mn^{III}_3M^{n+}]$ pentanuclear fragment. We report the characterization of 11 new chiral complexes with $[Mn^{II}Mn^{III}_3Na^{I}]$, $[Mn^{II}Mn^{III}_3Ca^{II}]$, $[Mn^{II}_2Mn^{III}_3]$, and $[Mn^{II}Mn^{III}_6Na^{I}_2]$ nuclearity with formula $[Mn_4NaOL_3Br_4]\cdot[Mn_4NaOL_3Br_4(H_2O)]\cdot[Mn_4NaOL_3Br_3(MeOH)(MeCN)(H_2O)]\cdot[Mn_4NaOL_3Br_3(MeOH)(MeCN)_2]Br_2\cdot6CH_3CN\cdot5CH_3OH$ (**1*R***) and $[Mn_4NaOL_3Br_4(H_2O)]\cdot[Mn_4NaOL_3Br_3(MeOH)(H_2O)_2]Br\cdot6CH_3CN\cdot CH_3OH$ (**1*S***), $[Mn_4CaOL_3X_5]\cdot$solvents (X=Cl, **2*R*** and **2*S***; X=Br, **3*S***), $[Mn_5OL_3X_5]\cdot$solvents (X=Cl, **4*R*·** and **4*S*·**1.5MeCN; X=Br, **5*S***), and $[Mn_7Na_2(O)_2L_6X_6]\cdot$solvents (X=Cl, **6*R*** and **6*S***; X=Br, **7*R***), respectively. This series of compounds includes one enantiomeric pair of the chloro complexes for each nuclearity (**2*R*/2*S***, **4*R*/4*S***, and **6*R*/6*S***), and for comparative purposes, one example each of the corresponding bromo derivatives (**3*S***, **5*S***, and **7R**). Structural trends and the confirmation of stability in solution for complexes **1** and **6** were reported in a previous communication.[13b] The new systems were structurally characterized and their chiroptical and magnetic properties studied, pointing out the different response of the types **II** and **III** (Scheme 1) classes of clusters. It is remarkable that compounds **2** and **3** with $[Mn^{II}Mn^{III}_3Ca^{II}]$ nuclearity join the scarce number of similar complexes with this topology and that the $[Mn^{II}_2Mn^{III}_3]$ and $[Mn^{II}Mn^{III}_6Na^{I}_2]$ nuclearities with trigonal bipyramidal or double trigonal bipyramidal topology, respectively, are the first members of this family of complexes.

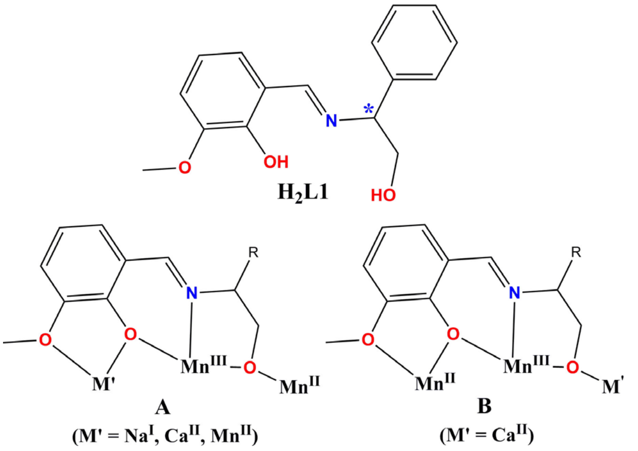

Scheme 2. H_2L Schiff bases employed in this work (top), and their coordination modes linking three cations (bottom). The asterisk denotes the chiral C atom.

Results and Discussion

Structural description

General trends

The reported complexes show some common features that will be described before the detailed comments of each structural type to avoid repetitive text. Several structures contain similar but nonequivalent molecules in the unit cell, and thus to simplify the discussion, all data in the main text are in relation to the "A" labeled molecule. All compounds possess a common core that can be described as a trigonal bipyramidal arrangement of three Mn^{III} cations in the equatorial plane and two cations in the apical sites, resulting in the discrete $[Mn^{II}Mn^{III}_3Na^{I}]$ (**1*R***, **1*S***), $[Mn^{II}Mn^{III}_3Ca^{II}]$ (**2*R***, **2*S***, **3*S***), $[Mn^{II}_2Mn^{III}_3]$ (**4*R***, **4*S***, **5*S***), and the sharing vertex $[Mn^{II}Mn^{III}_6Na^{I}_2]$ (**6*R***, **6*S***, **7*R***) metallic cores. In all cases, an oxo donor is placed in the center of the triangle determined by the Mn^{III} ions with Mn^{III}—O bond distances about 1.9 Å. Also, two μ-Cl (complexes **2**, **4**, and **6**) or μ-Br donors (complexes **1**, **3**, **5**, and **7**) are in all complexes and are coordinated in the elongated coordination sites of the trivalent manganese cations. Each pentanuclear unit is assembled by three Schiff bases in the deprotonated dianionic form, linking three different cations (Scheme 1-**II** and -**III**). The deprotonated O-alkoxo and O-phenoxo donors act as bridges between the equatorial cations and the cations in the apical sites. The oxidation state of the manganese cations was assigned according to the shape of the coordination polyhedra and bond valence sum (BSV) calculations (Table S1). The supramolecular aspects derived from the chiral character will be described for all compounds in the next section.

$[Mn^{II}Mn^{III}_3Na^{I}]$ complexes 1R and 1S

Complexes **1*R*** and **1*S*** show the above described core with three L^{2-} ligands in the type-**II** molecular arrangement. The main bond parameters are summarized in Table 1, and a view of the pentanuclear unit is shown in Figure 1. O-phenoxide and O-alcoxide donors form a distorted octahedral pocket that hosts the Na^{I} cation, which is linked to the three Mn^{III} ions by means of Na^{I}-$O_{phenoxide}$-Mn^{III} bridges, whereas the linkage between the divalent and trivalent manganese ions is provided by three Mn^{II}-$O_{alcoxide}$-Mn^{III} bridges.

In the center of the equatorial plane, one μ_4-O ligand links the three Mn^{III} cations and the Na^{I} cation. This oxo donor is slightly shifted from the center of the triangle toward the Na^{I} cation, which can be assumed as heptacoordinated. Three *fac*-coordination sites of the divalent manganese cation are occupied by three O-alkoxo donors, but the remaining coordination

Table 1. Selected bond distances [Å] and bond angles [°] for complexes **1*R*** and **1*S***. A–D notation refers to the labels of the nonequivalent molecules found in the unit cell.

	1*RA*	**1*RB***	**1*RC***	**1*RD***	**1*SA***	**1*SB***
Coord. No. for Mn4	4	6	6	5	5	6
Na1···O10	2.82(1)	2.67(1)	2.71(1)	2.76(1)	2.747(5)	2.675(5)
Mn4···O10	2.712(1)	3.145(9)	3.133(9)	3.03(1)	3.041(4)	3.175(5)
Mn1–O10	1.928(8)	1.893(9)	1.931(9)	1.891(8)	1.890(4)	1.905(5)
Mn2–O10	1.880(8)	1.884(9)	1.894(9)	1.898(9)	1.895(4)	1.887(5)
Mn3–O10	1.915(9)	1.873(9)	1.844(9)	1.877(8)	1.905(5)	1.894(5)
Mn1-O10-Mn2	121.5(5)	119.1(5)	117.3(5)	116.2(4)	119.4(3)	118.0(2)
Mn1-O10-Mn3	119.5(4)	118.0(5)	120.4(4)	118.7(5)	117.7(2)	118.7(2)
Mn2-O10-Mn3	118.6(4)	120.5(5)	120.3(5)	123.1(4)	120.8(2)	120.6(2)
Mn1-O1-Mn4	110.3(4)	121.4(5)	121.7(4)	117.6(4)	118.6(2)	121.8(2)
Mn2-O4-Mn4	109.4(4)	121.0(5)	120.9(4)	118.5(4)	118.3(2)	122.4(2)
Mn3-O7-Mn4	113.7(5)	124.4(5)	123.3(4)	119.8(4)	118.3(2)	122.7(2)
Mn1-O2-Na1	111.0(4)	106.1(4)	106.3(4)	109.4(4)	108.6(2)	107.2(2)
Mn2-O5-Na1	109.8(4)	107.6(4)	108.9(4)	108.1(4)	108.7(2)	117.2(6)
Mn3-O8-Na1	107.9(4)	104.8(4)	109.3(4)	108.7(4)	108.4(2)	107.0(2)
O10–Ct(Mn^{III}_3)[a]	0.036	0.167	0.153	0.156	0.161	0.177

[a] Distance from the μ_3-O donor to the centroid of the Mn_3 plane.

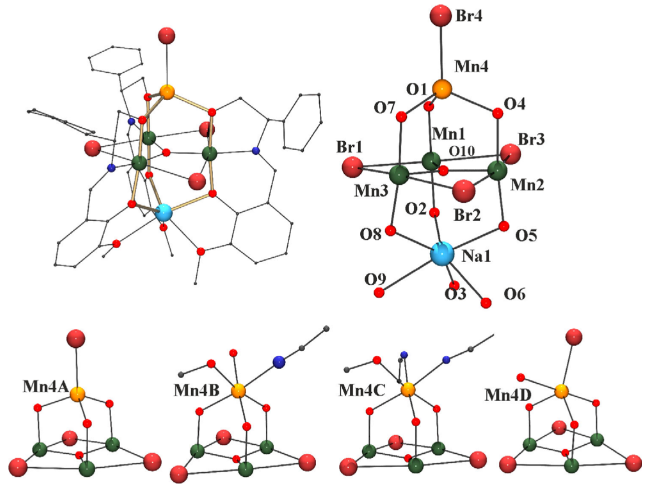

Figure 1. A view of the **1*RA*** molecule and its labeled core (top). Tetra-, penta-, and hexacoordinate environments for the divalent Mn4 cation (bottom). Color key for all figures: Mn^{III} dark green; Mn^{II} orange; Ca^{II} forest green; Na^{I} blue; Cl violet; Br firebrick; O red; N navy; C dark gray.

sites are fulfilled in multiple forms that differ in the coordination of the Mn^{II} cation. Structure **1*R*** contains four nonequivalent clusters that contain one tetrahedral Mn4A cation (MnO_3Br environment), two hexacoordinated Mn4B and Mn4C cations (MnO_5N and MnO_4N_2 environments, respectively), and one pentacoordinated Mn4D (MnO_4Br environment). Complex **1*S*** also exhibits two nonequivalent units with Mn4A and Mn4B in MnO_4Br and MnO_6 coordination environments, respectively. Consequently, Mn^{III}-O-Mn^{II} bond angles show characteristic values as a function of the Mn4 coordination number, which are close to 122° (octahedral Mn^{II}), 118° (pentacoordinated Mn^{II}), and 111° (tetrahedral Mn^{II}) (Figure 1 and Table 1).

Units **1*RA***, **1*RD***, and **1*SA*** are neutral but **1*RB***, **1*RC***, and **1*SB*** are cationic, and thus, the charge balance is fulfilled with two (**1*R***) or one (**1*S***) Br^- counteranion.

Compounds **1*R*** and **1*S*** are not enantiomers in a strict sense because they crystallize in different space groups (*P*1 and *P*2$_1$, respectively), but on the other hand, cell parameters, bond parameters for the cage, and its helicity follow the similitude or mirror image that must be expected for a normal pair of enantiomers. These differences are due to the plasticity of the Mn^{II} coordination sphere, which links different solvents or Br^- ligands and is limited to the Mn4 environment.

[$Mn^{II}Mn^{III}_3Ca^{II}$] complexes **2*R***, **2*S***, *and* **3*S***

Complexes **2*R***, **2*S***, and **3*S*** show the trigonal bipyramidal metallic core described above with three Mn^{III} cations in the equatorial plane, however for these compounds, the apical sites are occupied by one Mn^{II} and one Ca^{II} cation (Figure 2). The main bond parameters are collected in Table 2. The three structures contain two nonequivalent clusters, but in this case, there are only minor differences between them. The main difference with the previously described complexes consists in the reversed coordination of one of the ligands and the concomitant

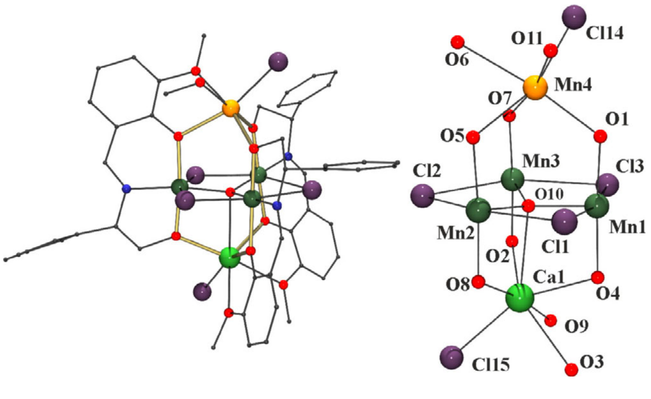

Figure 2. A view of the representative **2*RA*** molecule (left) and its labeled core (right).

© 2018 Wiley-VCH Verlag GmbH & Co. KGaA, Weinheim

Table 2. Selected bond distances [Å] and bond angles [°] for the A molecules of complexes **2*R***, **2*S***, and **3*S***. Bond parameters for the B molecule in the unit cell are similar.

	2*R*	**2*S***	**3*S***
Mn4···O10	3.119(8)	3.224(8)	3.18(2)
Ca1–O10	2.737(8)	2.630(7)	2.67(2)
Mn1–O10	1.926(6)	1.902(7)	1.93(1)
Mn2–O10	1.893(7)	1.905(7)	1.93(1)
Mn3–O10	1.870(3)	1.884(7)	1.85(2)
Mn1-O10-Mn2	118.2(4)	121.2(4)	119.3(8)
Mn1-O10-Mn3	120.2(4)	116.3(4)	117.4(8)
Mn2-O10-Mn3	120.0(4)	118.4(3)	120.0(8)
Mn1-O5-Mn4	114.9(3)	117.1(3)	116.8(7)
Mn2-O7-Mn4	120.5(3)	123.3(4)	120.1(8)
Mn3-O1-Mn4	119.7(3)	123.1(4)	124.3(8)
Mn1-O4-Ca1	110.7(3)	109.2(3)	107.6(2)
Mn2-O8-Ca1	108.8(3)	106.7(3)	107.9(7)
Mn3-O2-Ca1	109.3(4)	107.5(3)	109.7(7)
O10–Ct(Mn$^{III}_3$)[a]	0.136	0.221	0.199

[a] Distance from O10 to the centroid of the Mn_3 plane.

loss of the C_3 symmetry (type-**III** arrangement in Scheme 1). As in the previous case, the oxo donor placed in the center of the triangle defined by the three Mn^{III} cations is also shifted toward the Ca^{II} ion, which is assumed to be heptacoordinated, and then the O donor is a μ_4-O ligand. The environment of Mn4 is defined by two O-alkoxo donors, one phenoxo/methoxide bidentate group, one solvent molecule, and one chloro donor, whereas the environment for Ca1 is defined by two phenoxo/methoxide bidentate groups, one O-alkoxo donor, one coordinated chloro ligand, and contact with the μ_4-O donor resulting in neutral clusters in all the cases. The important asymmetry derived from the 2:1 reversed Schiff bases is translated to the Mn^{II}-O-Mn^{III} bond angles which show significant differences with respect to complexes **1*R*** and **1*S***; the Mn^{II}-O$_{alkoxo}$-Mn^{III} bond angles are larger than the Mn^{II}-O$_{phenoxo}$-Mn^{III} bond angles. In the same way, the Mn$^{III}_3$ triangle becomes scalene. The main intermolecular contacts consist of weak CH···Cl hydrogen bonds involving the chloro ligands coordinated to the Mn^{II} cations.

[Mn$^{II}_2$Mn$^{III}_3$] complexes 4R*, 4S, and* 5S

The neutral complexes **4** and **5** show the same structure as that of the analogous **2** and **3** complexes but with one Mn^{II} cation in the position that was occupied before by the calcium ion (Figure 3). In contrast with the Ca^{II} analogues, the oxo donor is centered in the Mn$^{III}_3$ plane and should be assumed strictly as a μ_3-O ligand. The coordination of the cations and the intermolecular contacts are very similar to those of the isostructural Ca^{II} complexes. The two Mn^{II} cations show an octahedral MnO_5X (X = Cl, Br) environment but are not equivalent because Mn4 links two O-alkoxo donors and one O-phenoxo donor, whereas Mn5 links one O-alkoxo and two O-phenoxo donors with the consequent asymmetry and different Mn^{III}-O-Mn^{II} bond angles as a function of each kind of bridge (Table 3).

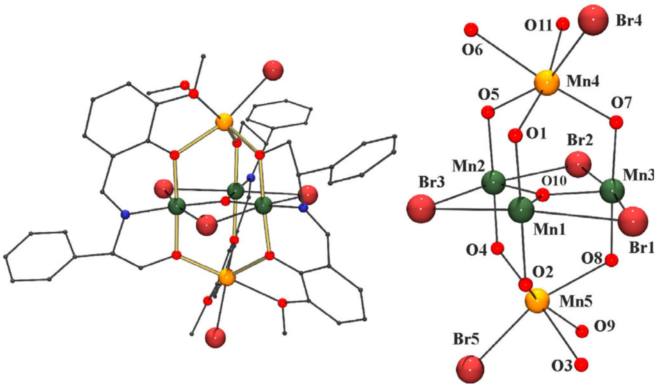

Figure 3. A view of the representative **4*RA*** molecule (left) and its labeled core (right).

Table 3. Selected bond distances [Å] and bond angles [°] for the A molecules of complexes **4*R***, **4*S***, and **5*S***. Bond parameters for the B molecule in the unit cell are similar.

	4*R*	**4*S***	**5*S***
Mn4···O10	3.10(1)	3.073(4)	2.95(1)
Mn5···O10	2.75(1)	2.769(4)	2.89(1)
Mn1–O10	1.883(7)	1.857(3)	1.856(9)
Mn2–O10	1.857(8)	1.866(3)	1.886(11)
Mn3–O10	1.866(7)	1.872(3)	1.868(10)
Mn1-O10-Mn2	117.9(4)	122.0(2)	119.0(5)
Mn1-O10-Mn3	118.6(4)	118.9(2)	120.3(6)
Mn2-O10-Mn3	122.1(4)	119.0(2)	120.6(5)
Mn1-O1-Mn4	117.8(4)	118.3(2)	116.7(4)
Mn2-O5-Mn4	116.2(3)	115.5(2)	114.8(5)
Mn3-O7-Mn4	121.7(4)	117.7(2)	119.0(5)
Mn1-O2-Mn5	111.3(3)	113.4(2)	114.9(5)
Mn2-O4-Mn5	113.9(4)	115.7(2)	116.2(5)
Mn3-O8-Mn5	112.6(3)	113.8(2)	113.2(4)
O10–Ct(Mn$^{III}_3$)[a]	0.126	0.101	0.020

[a] Distance from O10 to the centroid of the Mn_3 plane.

[Mn^{II}Mn$^{III}_6$Na$^{I}_2$] complexes 6R*, 6S, and* 7R

The nonanuclear [Mn^{II}Mn$^{III}_6$Na$^{I}_2$] core of the (*R*) and (*S*) pair of enantiomers of **6** consists of two pentanuclear units (similar to those described for complex **1**) sharing the octahedral Mn^{II} cation (Figure 4). The main bond parameters are summarized in Table 4.The 22 positive charges are balanced by the six dianionic Schiff bases, two μ_3-oxo donors, and six μ-Cl bridges in the axial coordination sites of the Mn^{III} cations. The L^{2-} ligands and the Mn^{III} cations in each pentanuclear subunit are related by one C_3 axis (*R*3 space group), but the lack of inversion center between them determines different bond parameters around the divalent Mn3 in each subunit; the Mn2-O4-Mn3 bond angle takes a mean value of 125.8(3)°, whereas the mean bond angle for Mn1-O1-Mn3 is 122.9(3)°.

Complex **7*R*** exhibits the same core and similar bond parameters to those of complex **6**, except for the logically larger Mn^{III}–Br bonds. However, in this case the complex crystallizes in the triclinic $P\bar{1}$ space group, the C_3 symmetry is lost, and the Mn^{III}-O-Mn^{III} bond angles are slightly different, ranging be-

© 2018 Wiley-VCH Verlag GmbH & Co. KGaA, Weinheim

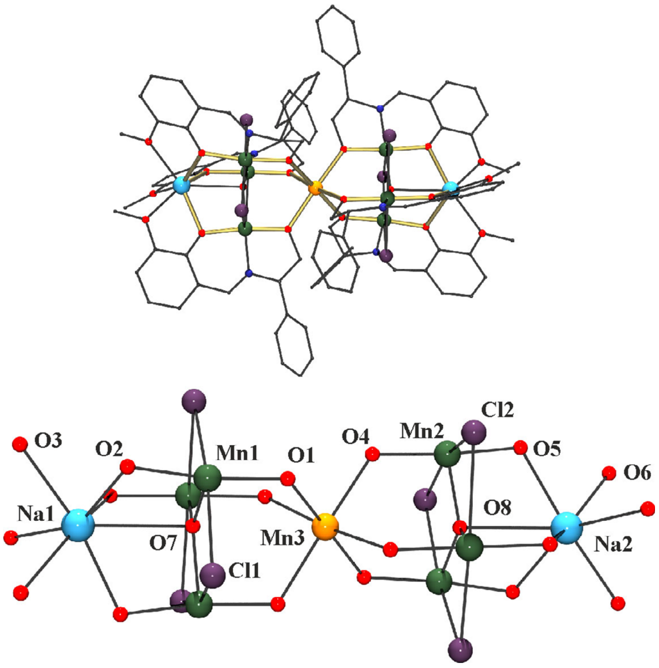

Figure 4. A view of the representative **6*R*** molecule (top) and its labeled core (bottom).

Table 4. Selected bond distances [Å] and bond angles [°] for complexes **6*R*** and **6*S***.

	6*R*	**6*S***
Mn1–O7	1.881(1)	1.852(1)
Mn2–O8	1.880(1)	1.879(2)
Mn3–O1	2.214(5)	2.207(7)
Mn3–O4	2.195(5)	2.196(7)
Na1–O7	2.72(1)	2.74(1)
Na2–O8	2.68(1)	2.67(1)
Mn1-O7-Mn1′	119.51(7)	119.56(9)
Mn2-O8-Mn2′	118.8(1)	119.1(1)
Mn1-O1-Mn3	122.5(3)	123.4(3)
Mn2-O4-Mn3	125.5(3)	126.1(3)
Mn1-O2-Na1	107.0(3)	108.4(3)
Mn2-O5-Na2	108.1(3)	107.9(3)
O7–Ct(Mn^{III}_3)[a]	0.131	0.125
O8–Ct(Mn^{III}_3)[a]	0.204	0.181

[a] Distance from the μ_3-O donor to the centroid of the Mn_3 plane.

tween 117.3–120.3°. The main bond parameters and a labeled plot are shown in Table S2 and Figure S1, respectively.

Notably, in all cases the oxo ligands are slightly shifted out of the Mn^{III}_3 plane toward the Na^{I} cation, with Na–O bond distances of about 2.7 Å, and thus, the coordination of the sodium ions can be formally described as an apicated octahedron, and the oxo donors can be assumed as μ_4-O ligands.

Chirality transfer

The employment of enantiopure chiral ligands determines the configuration of the derived complexes. Chirality can be transferred to the environment of the cations, to the overall complex or even to the crystalline network. This "predetermined chirality" is propagated in the opposite sense by the corresponding enantiomeric ligands, resulting in mirror-image clusters or networks.[15] The reported complexes offer a variety of situations, from the conventional chirality transfer to some unusual responses.

For compounds **1*R*** and **1*S***, the L^{2-} ligands are tilted in the same sense with respect to the main axis of the complex, and thus, the whole molecule shows a helical arrangement that turns in opposite sense for each cluster (Λ for **1*R*** and Δ for **1*S***), as shown in Figure 5. Locally, the environment of the manganese cations is not chiral but the tris-bidentate donors around the Na^{I} cation define a propeller shape, with chirality also Λ for **1*R*** and Δ for **1*S***. In this case, the different orientation in the network of the nonequivalent molecules does not transfer the chirality to the network.

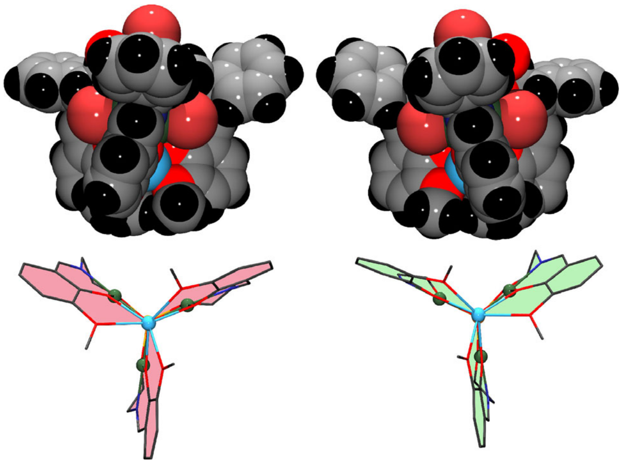

Figure 5. Space-fill view of complex **1** showing the opposite helicity for **1*R*** and **1*S*** (top). Arrangement of the bidentate fragments around the Na^{I} cations (bottom). Fragments depicted as red rings turn Δ, and fragments depicted as green rings turn Λ. Left, *R* enantiomer; right, *S* enantiomer.

The related complexes **2**–**5** also show a helical arrangement of the Schiff bases, but surprisingly, the helicity of the two parallel ligands turns in opposite sense with respect to the reversed ligand, and thus, the propeller shape of the cluster is not achieved.

The two nonequivalent molecules in the network also turn in opposite sense to one another, that is, the parallel ligands in molecule A turn Δ and the reversed ligand turns Λ, whereas for the molecule labeled B, these ligands turn Λ and Δ, respectively (Figure 6). As a direct consequence, the cations linked to three bidentate fragments (Ca^{II} for **2** and **3** or one of the Mn^{II} cations for **4** and **5**) also show opposite conformation that cannot be classified as purely Λ or Δ. The reason for this highly unusual feature can be found in the packing of the clusters, which show a parallel arrangement in the cell with the nonequivalent units rotated 180° relative to each other. This arrangement shows an equivalent distribution of the pending phenyl groups at each side of the molecules, probably favoring a most effective packing of the clusters. This structure is ex-

© 2018 Wiley-VCH Verlag GmbH & Co. KGaA, Weinheim

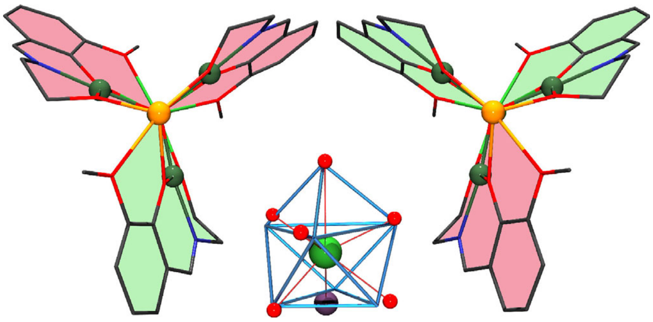

Figure 6. Plot of the coordination of the O donors around the Ca^{II} cations and the ideal apicated octahedron polyhedron for complexes **2**–**5**. The bidentate fragments show two mirror images of opposite helicities around the cation. Fragments depicted as red rings turn Δ, and fragments depicted as green rings turn Λ.

tremely unusual because the presence of two quasi mirror-image molecules in the same cell for a chiral system means that there is a poor chiral induction from the ligand onto the system. This configuration has been observed only once for the related Ca^{II} complex reported by Powell et al.[3]

Finally, complexes **6** and **7** also offer an unusual feature: in this case, the three ligands are parallel, similar to that which occurs in complexes **1*R*** and **1*S***, and thus, the [Mn^{II}Mn$^{III}_3$Na^{I}] subunits show the expected propeller shape but the two fragments turn in the opposite sense, and consequently, the tris-bidentate environment of the Na1 and Na2 cations of the same cluster show opposite Δ and Λ configurations. However, some degree of transference of chirality arises from the central Mn^{II} cation, which is slightly distorted from O_h symmetry to trigonal prism, and this trigonal rotation is transferred to the two moieties of the molecule, breaking a strict regular alternate shape for the two [Mn_3OCl_3] triangular planes. This rotation takes place in the opposite sense for each enantiomer, as well as in the arrangement of the phenyl groups in the molecular shell, which also show a mirror image between them (Figure 7).

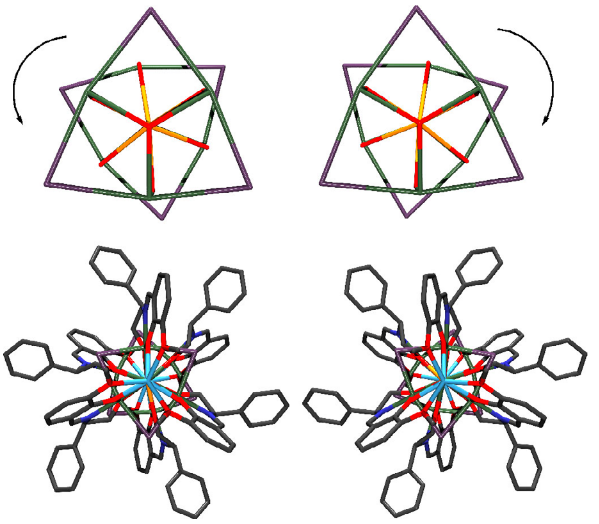

Figure 7. Trigonal rotation of the central Mn^{II} coordination sphere (top) that determines a Λ or Δ conformation (bottom) for **6*R*** (left) and **6*S*** (right), respectively.

Comments on the syntheses

The reaction of the Schiff base H_2L with manganese halides and further air oxidation led to the formation of [Mn^{II}Mn^{III}M′] mixed-valent pentanuclear cages with trigonal bipyramidal shapes. Notably, the syntheses of isolated or fused cages or the nature of M′ is related to the reaction conditions (Scheme 3). Reaction of manganese bromide with the (*R*)- or (*S*)-H_2L ligand in the presence of sodium azide allowed the crystallization of compounds **1*R*** and **1*S***, which contain μ-Br donors in the elongated coordination sites of the Mn^{III} cations and one Mn^{II} and one Na^{I} cation in the apical sites of the core. In this reaction, the azide anion is not coordinated, and its role is then limited to provide basic medium and to contribute to deprotonation of the organic ligand. However, the base is not innocent because complex **7*R***, which consists of two pentanuclear units sharing the Mn^{II} cation, was obtained when sodium hydroxide was employed instead of sodium azide. In contrast, when manganese chloride was employed as the starting salt, only the nonanuclear [Mn^{II}Mn$^{III}_6$Na$^{I}_2$] cages were obtained in all cases.

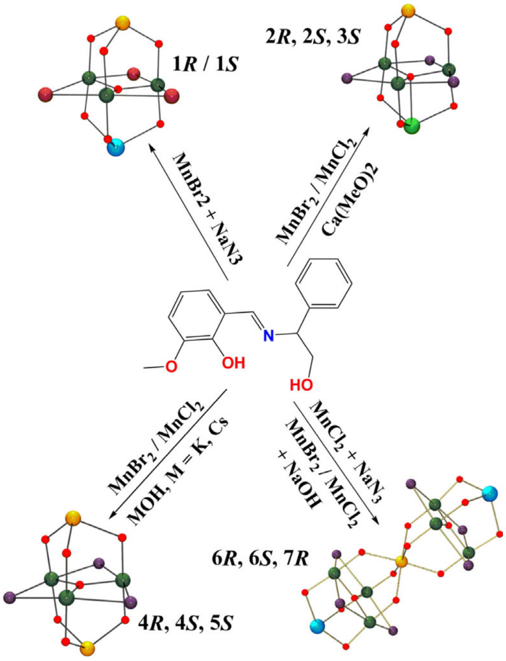

Scheme 3. Reaction scheme showing the conditions that lead to four different systems from the H_2L ligand.

In these cages with the [Mn^{II}Mn$^{III}_3$Na^{I}] core, the sodium cation is placed in a NaO_6 cavity determined by the bidentate phenoxo/methoxide fragments of the ligands. This cavity seems a priori quite flexible, and thus, the reaction with larger cations such as K^{I} or Cs^{I} was tried by employing the corresponding hydroxides to deprotonate the ligands. The result of this reaction, independent of the starting manganese halide, was the characterization for the first time of the related pentanuclear [Mn$^{II}_2$Mn$^{III}_3$] systems (complexes **4*R***, **4*S***, **5*S***). This fact proves that the size of the O_6 pocket is selective for sodium

© 2018 Wiley-VCH Verlag GmbH & Co. KGaA, Weinheim

cations and that the system prefers the coordination of a second Mn^{II} cation instead of the larger alkaline ions.

Given that the size of the cations plays a determinant role in the conformation of the final cage, the Ca^{II} cation, which has a similar ionic radius to that of Na^{I} (close to 1 Å in a hexacoordinated environment), was selected to attempt the characterization of new $[Mn^{II}Mn^{III}_3Ca^{II}]$ cages. The employment of calcium methoxide as a base to deprotonate the organic ligands led effectively to the desired core in complexes **2*R***, **2*S***, and **3*S***.

When the cavity is occupied by Na^{I}, the three Schiff bases exhibit a parallel arrangement along the main axis of the molecule. However, the substitution by a divalent cation induces the antiparallel coordination of one of the ligands, in agreement with the same type-**II** ligand arrangement reported by Powell et al.[3] for a related cage containing the calcium cation instead of sodium.

All samples were prepared at room temperature, and during the different syntheses, we realized that they were poorly sensitive to changes in the manganese/ligand ratio and to the source of basic medium if alkaline ions were present. The complexes are stable at room temperature in the mother solution for weeks.

UV/Vis and ECD spectroscopy

Tong et al.[4] previously reported the UV/Vis and electronic circular dichroism (ECD) spectra for the H_2L ligand; the absorptions in the UV region were assigned to the transitions of the aromatic groups (π–π*) of the Schiff base, and the less intense band at about 400 nm was assigned to the n–π* transition of the azomethine chromophore. As expected, the UV/Vis spectra for **1**–**7** show common absorptions for all complexes that are attributable to ligand transitions (Figure S2).

ECD spectra confirm the enantiomeric nature of the reported systems, with mirror images of the spectra for all the reported pairs of clusters. Complexes **1**–**7** exhibit several structural variables such as the choro or bromo donors at the axial coordination sites of the Mn^{III} cations, different cations in one of the core sites (Na^{I}, Ca^{II}, or Mn^{II}) or different nuclearity (complexes **6** and **7**). To elucidate the factors that can influence the resulting spectra, an inspection of the shape of the spectra evidences a clear similitude between the plots for the **1** and **6** pairs of enantiomers, which show a practically identical distribution of absorptions and intensities in the 275–800 nm range (with a minor difference in the intensity of the 275 nm band) and a different response for complexes **2** and **4**, which show an intense transition centered at 400 nm and apparently no features above 450 nm (Figure 8). These data indicate that halide or cation substitutions are irrelevant and that the main differences in the ECD spectra must be related to the relative position of the ligands for **1**, **6**, and **7** compared to that of **2**–**5**. This assumption is reinforced by the perfect agreement between the spectra of complexes **2** and **4** which contain two very electronically different cations such as Ca^{II} or Mn^{II}, suggesting that the weak absorptions at larger wavelengths involves transitions between the iminic fragments and the Mn^{III} cations.

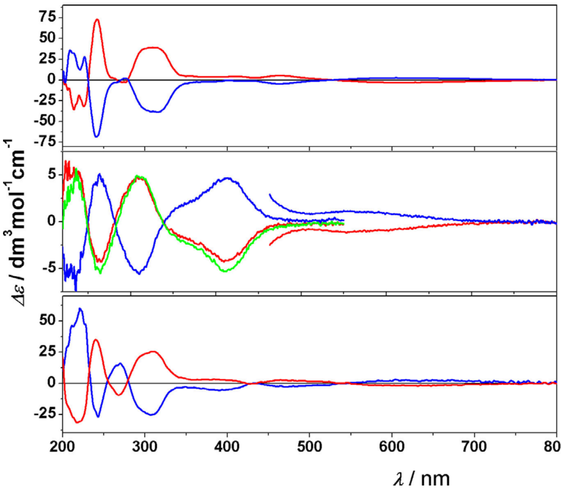

Figure 8. ECD spectra for the pairs of enantiomers of complexes **1** (top), **2** (middle), and **6** (bottom). (*R*)-enantiomers, red lines; (*S*)-enantiomers, blue lines. The spectrum of **4*R*** (green line) appears to be identical to that of **2*R***.

It becomes relevant that the EDC spectra can unambiguously differentiate the type-**II** and **III** topologies (Scheme 1), and thus, provide a new example of the application of this technique to obtain structural information of complexes in solution.

Magnetic properties

The magnetic properties for complexes **1**–**7** were measured for powdered samples in the 2–300 K temperature range. The high number of superexchange pathways (from 6 for **1** to 12 for **6**–**7**), the zero field splitting (*D*) of the anisotropic Mn^{III} cations, and the intermolecular interactions imply a large number of variables that, unless the symmetry is simplified, bring overparametrized Hamiltonians. Therefore, the fit of the experimental data requires rational criteria to employ simplified Hamiltonians to extract significant information about the values of the *J* coupling constants and to rationalize the magnetic response.

The interaction between the apical Mn^{II} cation and each Mn^{III} cation is mediated by a single Mn^{II}-$O_{alkoxide}$-Mn^{III} bridge that gives antiferromagnetic interactions in this type of cluster. The Mn^{III} cations are held together by one μ_3-O bridge with short Mn^{III}–O bond distances and additional μ_2 ligands that link the coordination sites on the elongated Jahn–Teller axis. Thus, the interaction between these cations seems apparently mediated by the main superexchange Mn^{III}-O-Mn^{III} pathway, for which previous studies have shown that the ferromagnetic-antiferromagnetic (FM/AF) limit for a $[Mn^{III}_3(\mu_3\text{-O})]$ fragment is found around the 120° Mn^{III}-O-Mn^{III} bond angle and that the shift of the central μ_3-O from the Mn_3 plane favors the ferromagnetic interactions.[21,22] The assumption of one AF interaction between the Mn^{II} and the Mn^{III} cations and the FM/AF bond-angle dependence of the interaction between the Mn^{III} cations has been systematically applied as general criterion to rationalize the magnetic properties of $[Mn^{II}Mn^{III}_3M']$ systems,[3–10] although these correlations were performed for Mn^{III} triangles with the elongated axis perpendicular to the Mn^{III}_3

© 2018 Wiley-VCH Verlag GmbH & Co. KGaA, Weinheim

plane and with μ_2 ligands (oximate and others) in the triangular edges which strongly contribute to the superexchange mechanism.

Preliminary attempts to fit the reported systems applying this usual criterion were satisfactory for complex **1** but were unable to adequately reproduce the experimental data for the new topologies of **2**–**7**.

To check the commonly accepted explanation of the magnetic response of these systems, we reviewed and analyzed the main bond and magnetic parameters for the 12 $[Mn^{II}Mn^{III}_3Na]$ complexes reported up until now; this is summarized in Table 5 (see also Scheme 4). A simple inspection of the reported data points out several facts: 1) the Mn^{II}-O-Mn^{III} interaction is effectively antiferromagnetic in all cases; 2) the shift of the μ_3-O donor from the Mn_3 plane is very similar in all cases, and thus, its influence is not a relevant variable; 3) often the systems have low symmetry due to the μ_2 additional ligands that, in some cases, induces large deviations from 120° for the Mn^{III}-O-Mn^{III} bond angle (usually lower than 120° for monoatomic bridges such as Cl^-, $\mu_{1,1}$-N_3, etc. or much larger than 120° for *syn-syn* carboxylates or $\mu_{1,3}$-N_3).

Surprisingly, it becomes evident that there is a complete dispersion of *J* values versus the Mn^{III}-O-Mn^{III} bond angle (Figure S3) and that very different *J* values have been reported for the same μ_2 ligand and bond angle as is the case for the μ_2-Cl ligand (LIQXOA compared with WIMBIF) or the pairs of complexes with $\mu_{1,1}$-N_3, $\mu_{1,1}$-N_3, $\mu_{1,3}$-N_3 μ_2 ligands (XIJMAG compared with RILZAP) and the pair of complexes with H_2O, H_2O, $PhCOO^-$ ligands (XIJMIO compared with RILZUJ), as shown in Table 5.

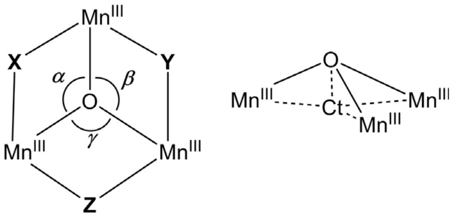

Scheme 4. Key for the structural parameters summarized in Table 5.

We also realized that some fits were poorly reliable because they were unable to reproduce the full experimental susceptibility plots and were performed with the discarding of data below 25–50 K. This lack of correlation points out that the problem is more complex and cannot be reduced to a simple correlation with the Mn^{III}-O-Mn^{III} parameter and also that the contribution of the μ_2-ligand pathway and the differentiation of different values for the Mn^{II}-O-Mn^{III} interactions cannot be discarded.

Considering these features and taking into account that in our case the contribution of the μ_2-Cl additional ligands is constant for all complexes, our procedure was: 1) to employ isotropic Hamiltonians, to employ a *zJ* parameter for the low *T* deviations to reduce computational requirements in the $\chi_M T$ fits, and to take into account the *D* effect in the more sensitive magnetization simulations; 2) to join under the same *J* parameter the pathways mediated by the same kind of bridges independently of slight differences in the bond parameters. This means to assume one common J_1 coupling constant between Mn^{III}-Mn^{III} cations inside the μ_3-O centered triangles, one common J_2 coupling constant between Mn^{III}-Mn^{II} cations linked by O-alkoxo bridges, and a different J_3 coupling constant between Mn^{III}-Mn^{II} cations linked by O-phenoxo bridges in the case of compounds **2**–**5**.

On the basis of the above considerations, the interactions can be described as is shown in Scheme 5.

As is expected from the structural data, the magnetic behavior of the reported complexes is similar for each core, independently of the chirality of the Schiff base, and thus, one example of each core and bridging halide placed in the axial coordination sites of the Mn^{III} cations will be discussed.

The room-temperature $\chi_M T$ value for complex **1*S*** is 10.5 $cm^3\,mol^{-1}\,K$, lower than the value expected for three Mn^{III} and one Mn^{II} isolated cation (13.375 $cm^3\,mol^{-1}\,K$ for $g = 2.00$). On cooling, $\chi_M T$ decreases continuously down to a plateau between 25–5 K and finally decreases slightly at lower temperatures, reaching a value of 6.2 $cm^3\,mol^{-1}\,K$ at 2 K (Figure 9). Assuming a common *J* constant for each Mn^{III}-Mn^{III} or Mn^{III}-Mn^{II} pathway, and according to Scheme 5, the two-*J* Hamiltonian is given by Equation (1):

Table 5. Structural and magnetic parameters for previously reported clusters with the $[Mn^{II}Mn^{III}_3Na^{I}]$ core. Structural parameters are in relation to that shown in Scheme 4.

CCDC code	X, Y, Z	α, β, γ	O–Ct(Mn^{III}_3)[a]	J_1, J_2, J_3	J_4	S_T	Ref.
MEJKES	1,1-N_3, 1,1-N_3, $MeCOO^-$	111.9, 114.0, 133.2	0.103	0, 0, −5.6	−2.1	1/2	[3]
LIQXOA	Cl^-	118.2, 118.2, 118.2	0.259	+15.1	−10.5	7/2	[8]
FUMSIQ^Chiral	1,1-N_3, MeOH, MeOH	114.3, 120.6, 120.8	0.227	−6.4, −7.4, −7.4	−1.65	3/2	[4]
XIWCAJ	Cl^-, Cl^-, EtOH	114.1, 114.4, 127.9	0.206	+0.4, +0.4, −1.2	−3.2	7/2	[10]
XIJLUZ 2	$HOCO^-$, $HOCO^-$, $HCOO^-$	112.5, 112.6, 130.4	0.229	+3.1, +3.1, −10.3	−5.5	1/2	[6]
XIJMAG 1	1,1-N_3, 1,1-N_3, 1,3-N_3	108, 111, 136	0.213	+3.8, +3.8, −15.0	−5.5	1/2	[6]
XIJMIO 3	H_2O, H_2O, $PhCOO^-$	115.8, 116.3, 123.5	0.231	+2.0, +2.0, −13.0	−5.6	1/2	[6]
RILYUI 1	1,1-N_3	117.2, 117.3, 119.8	0.261	−0.7, −0.7, −0.7	−4.5	7/2	[9]
RILZAP 2	1,1-N_3, 1,1-N_3, 1,3-N_3	108.2, 110.6, 136.9	0.221	−4.4, −4.4, −4.7	−5.5	1/2	[9]
RILZUJ 4	H_2O, H_2O, $PhCOO^-$	115.9, 116.6, 123.0	0.223	−9.9, −9.9, −16.6	−6.1	1/2	[9]
WIMZID	1,1-(NCS)	118.1, 118.1, 118.1	0.263	−2.3, −2.3, −2.3	−5.4	3/2	[7]
WIMBIF	Cl^-	116, 116, 122	0.273	+1.9, +1.9, −0.9	−5.3	7/2	[7]

[a] Distance from the O donor to the centroid of the Mn_3 plane. *J* values in cm^{-1}, referred to the 2*J* Hamiltonian.

© 2018 Wiley-VCH Verlag GmbH & Co. KGaA, Weinheim

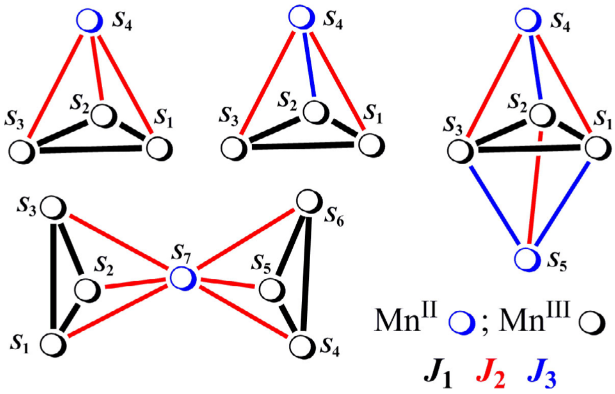

Scheme 5. Coupling scheme for complexes **1** (top, left), **2** and **3** (top, middle), **4** and **5** (top, right), and **6** and **7** (bottom).

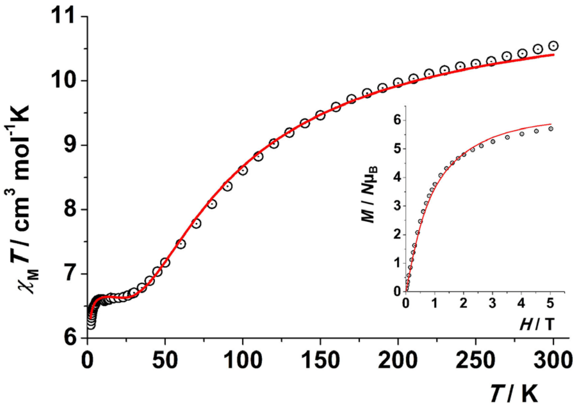

Figure 9. $\chi_M T$ versus T and magnetization (inset) plots for complex **1*S***. Solid lines show the fit of the experimental data.

$$H = -2J_1(S_1 \cdot S_2 + S_2 \cdot S_3 + S_1 \cdot S_3) - 2J_2(S_1 \cdot S_4 + S_2 \cdot S_4 + S_3 \cdot S_4) \quad (1)$$

Fit of the experimental data gave an excellent fit for $J_1 = 0.96$ cm^{-1}, $J_2 = -3.1$ cm^{-1}, $g = 1.86$, and $R = 1.3\times10^{-5}$ (corrected with a $zJ = -0.005$ cm^{-1} for the low T decay). The calculated energy of the spin levels shows a well-isolated $S = 7/2$ ground state with a gap of 27 cm^{-1} to the first $S = 9/2$ excited state. This ground state, which comes from the antiferromagnetic interaction of the Mn^{II} ($S = 5/2$) with the local $S = 6$ from the Mn$^{III}_3$ triangle, is confirmed by the magnetization measurement that tends to an unsaturated value of 5.7 Nμ$_B$ under the maximum applied field of 5 T, in agreement with data reported for related [Mn^{II}Mn$^{III}_3$Na] systems with $S_T = 7/2$.[8,10] This value is close to that expected for seven electrons, assuming the calculated g value from the susceptibility fit (6.5 Nμ$_B$). The difference must be attributed to a D effect, and the fit of the magnetization data as an isolated 7/2 spin was satisfactory for a D value of -0.4 cm^{-1} (inset of Figure 9).

Room-temperature $\chi_M T$ values for complexes **2*R*** and **3*S*** are 12.4 and 12.7 cm^3 mol^{-1} K, respectively. On cooling, $\chi_M T$ decreases down to well-defined minimums at 12 K (8.9 cm^3 mol^{-1} K for **2*R*** and 9.0 cm^3 mol^{-1} K for **3*S***). Below the minimum, $\chi_M T$ increases to reach 10.2 cm^3 mol^{-1} K for **2*R*** and 11.2 cm^3 mol^{-1} K for **3*S*** at 2 K (Figure 10).

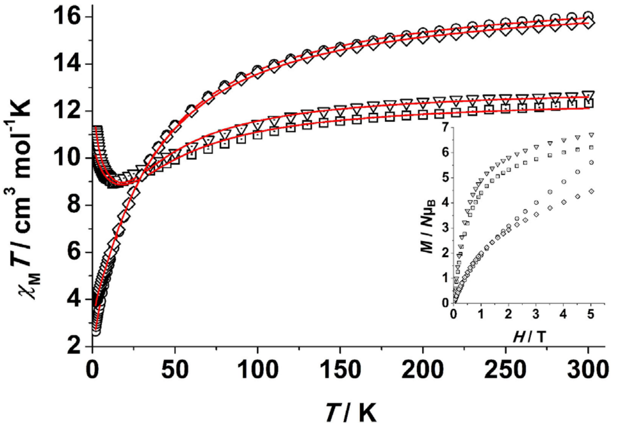

Figure 10. $\chi_M T$ versus T and magnetization (inset) plots for complexes **2*R*** (squares), **3*S*** (triangles), **4*R*** (circles), and **5*S*** (diamonds). Solid lines show the fit of the experimental data.

The core of complexes **2*R*** and **3*S*** is similar to that of the above described complexes **1*R*** and **1*S***, but in this case, the system is fully asymmetric due to the antiparallel orientation of one of the Schiff bases. The Mn^{III}-O-Mn^{III} bond angles are slightly different, and there are two alkoxo and one phenoxo Mn^{III}-O-Mn^{II} bridge. Assuming one J coupling constant for each kind of superexchange pathway, and according to Scheme 5, the resulting 3J-Hamiltonian is given by Equation (2):

$$H = -2J_1(S_1 \cdot S_2 + S_2 \cdot S_3 + S_1 \cdot S_3) - 2J_2(S_1 \cdot S_4 + S_3 \cdot S_4) - 2J_3(S_2 \cdot S_4) \quad (2)$$

Fit of the experimental data in the full temperature range of 2–300 K was satisfactory for $J_1 = -2.7$ cm^{-1}, $J_2 = 2.1$ cm^{-1}, $J_3 = -1.8$ cm^{-1}, $g = 1.94$, and $R = 8.1\times10^{-5}$ for **2*R*** and $J_1 = -1.1$ cm^{-1}, $J_2 = 1.3$ cm^{-1}, $J_3 = -3.4$ cm^{-1}, $g = 1.97$, and $R = 8.2\times10^{-5}$ for **3*S***. A simple analysis of the shape of these plots evidence the following facts. First, the increase of $\chi_M T$ at low temperature discards a response similar to that of complex **1*S*** because for a ferromagnetic Mn$^{III}_3$ triangle (local $S = 6$) interacting with one Mn^{II} cation, only monotonically increasing or decreasing plots tending to $S = 17/2$ or 7/2 should be expected ($S = 6 \pm 5/2$ possible ground levels). Second, the $\chi_M T$ increase at low temperature suggests that low-lying S levels with larger spin must be very close to the S ground state. Calculation of the energy of the S levels for the calculated J values shows two quasi-degenerated ground spin levels $S = 7/2$ and $S = 9/2$ that are highly populated at 2 K (49.8 % and 49.3 %, respectively, for **2*R*** and 24.9 % and 73.1 %, respectively, for **3*S***, Table S3). The population of the larger spin level determines the increase of $\chi_M T$ at low temperatures, and in fact, the experimental $\chi_M T$ values at 2 K are intermediate between 7.875 cm^3 mol^{-1} K ($S = 7/2$) and 12.375 cm^3 mol^{-1} K ($S = 9/2$). Magnetization experiments reveal unsaturated plots tending to 6.21 and 6.72 Nμ$_B$ for **2*R*** and **3*S***, respectively, under the maximum explored field of 5 T (inset of Figure 10). The similar and close S levels in the vicinity of the ground state exclude the accurate fit of the magnetization. In this case, there is only one similar complex reported by Powell et al.,[3] with $\mu_{1,1}$-N_3 and $\mu_{1,3}$-N_3 bridges, which shows an $S=1/2$ ground state that was related to the AF interaction attributed to the end-to-end azido bridge and the large Mn^{III}-O-Mn^{III} angle. Trials to fit the systems by adding different superexchange parameters for the different Mn^{III}-O-Mn^{III} bond angles did not improve the quality of the fits.

The χ_MT plots for complexes **4*R*** and **5*S*** show very similar room-temperature values of 16.0 and 15.8 cm^3 mol^{-1} K, close to the expected χ_MT value for three Mn^{III} and two Mn^{II} isolated cations (17.75 cm^3 mol^{-1} K for $g=2.00$). On cooling, χ_MT decreases continuously down to 2.7 and 3.9 cm^3 mol^{-1} K for **4*R*** and **5*S***, respectively (Figure 10). According to the low symmetry and alkoxo/phenoxo distribution of the Mn^{III}-O-Mn^{II} bridges, the proposed Hamiltonian based on Scheme 5 is given by Equation (3):

$$H=-2J_1(S_1\cdot S_2+S_2\cdot S_3+S_1\cdot S_3)-2J_2(S_1\cdot S_4+S_3\cdot S_4+S_2\cdot S_5)-2J_3(S_2\cdot S_4+S_1\cdot S_5+S_3\cdot S_5) \tag{3}$$

Best fit of the experimental data was obtained for $J_1=-1.7$ cm^{-1}, $J_2=-0.57$ cm^{-1}, $J_3=-1.2$ cm^{-1}, $g=1.96$, and $R=8.7\times10^{-6}$ for **4*R*** and $J_1=-1.6$ cm^{-1}, $J_2=-1.0$ cm^{-1}, $J_3=-0.82$ cm^{-1}, $g=1.96$, and $R=1.8\times10^{-5}$ for **5*S***. As a consequence of the competitive interactions in all the triangular faces of the core of these complexes, the ground state becomes not evident. The calculation of the energy of the S states shows an $S=2$ ground state for these two compounds but with several very close $S=1$, $S=2$, and $S=3$ spin levels. As a function of their population, the χ_MT value at 2 K is closer to an $S=2$ for **4*R*** or intermediate between $S=2$ and $S=3$ for **5*S*** (Table S3). In agreement, the magnetization plots show a continuous increase that corresponds to the population of larger S levels under higher fields (inset of Figure 10), reaching the unsaturated values of 5.61 and 4.46 Nμ_B for **4*R*** and **5*S***, respectively. The large number of close spin levels exclude the fit of the magnetization. Trials to fit the systems by adding different superexchange parameters for the different Mn^{III}-O-Mn^{III} bond angles did not improve the quality of the fits.

The χ_MT plots for complexes **6*R*** and **7*R*** show, as in the previous cases, similar response for the μ-chloro or μ-bromo complexes. The room-temperature χ_MT values of 19.3 and 17.9 cm^3 mol^{-1} K for **6*R*** and **7*R***, respectively, are close to the expected values for six Mn^{III} and one Mn^{II} noninteracting cation of 22.375 cm^3 mol^{-1} K ($g=2.00$). On cooling, χ_MT decreases down to a well-defined minimum around 110 K, followed by an increase up to 27.7 cm^3 mol^{-1} K (**6*R***) or 26.7 cm^3 mol^{-1} K (**7*R***) at 13 K. At lower temperature, the χ_MT plot decreases to reach values around 22 cm^3 mol^{-1} K (Figure 11). Complex **6*R*** possesses one C_3 axis, and consequently, all the Mn^{III}-Mn^{III} or Mn^{III}-Mn^{II} pathways are strictly equivalent by symmetry, and the system can be simulated with only two coupling constants, J_1, joining all the $Mn^{III}\cdots Mn^{III}$ interactions and J_2, joining all the $Mn^{II}\cdots Mn^{III}$ interactions. The same coupling scheme was applied to compound **7*R***. The applied two-*J* Hamiltonian is given by Equation (4):

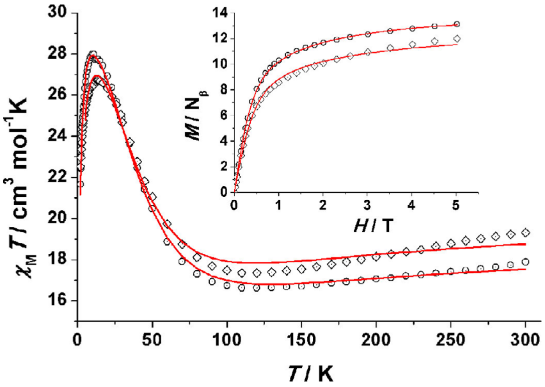

Figure 11. χ_MT versus T plots for complexes **6*R*** (circles) and **7*R*** (diamonds). Solid lines show the fit of the experimental data.

$$H=-2J_1(S_1\cdot S_2+S_2\cdot S_3+S_1\cdot S_3+S_4\cdot S_5+S_4\cdot S_6+S_5\cdot S_6)-2J_2(S_1\cdot S_7+S_2\cdot S_7+S_3\cdot S_7+S_4\cdot S_7+S_5\cdot S_7+S_6\cdot S_7) \tag{4}$$

Fitting by employing the above Hamiltonian and taking into account the *zJ* parameter to include the decay of χ_MT below 15 K was unable to correctly reproduce the low T region, and thus, the isotropic fit was performed in the 25–300 K range. Best fit parameters for these limited fits were $J_1=1.65$ cm^{-1}, $J_2=-2.85$ cm^{-1}, $g=1.96$, and $R=4.2\times10^{-5}$ for **6*R*** and $J_1=0.77$ cm^{-1}, $J_2=-3.74$ cm^{-1}, $g=1.96$, and $R=5.2\times10^{-5}$ for **7*R***.

Magnetization experiments show a continuous increase in the magnetization, reaching the unsaturated values of 11.95 and 12.21 Nμ_B for **7*R*** and **6*R***, respectively. These values are far from the expected values corresponding to the ground state $S=19/2$ derived from the antiferromagnetic interaction of the central $S=5/2$ ion with two ferromagnetic Mn^{III} triangles with $S=6$ local spins. Surprisingly, the fit of the experimental data as isolated spins is satisfactory for a $S=15/2$, $D=0.2$, and $g=1.83$ for **6*R*** and $S=13/2$, $D=0.3$, and $g=1.87$ for **7*R***, which seems to be not compatible with the values derived from the susceptibility data. Considering the lack of consistence of the magnetization and the difficulties to fit the low-temperature χ_MT data, and that any other simplification cannot be proposed because of the strict C_3 symmetry of the complexes, we decided to explore the effect of the interaction between the two ferromagnetic triangles through the Mn^{II} cation in a similar manner to the typical interaction between the peripheral cations in a simple linear trinuclear system, which in this case is equivalent to a $S=5/2$ central ion and two peripheral $S=6$ fragments.

The inclusion of the interactions between the Mn^{III} cations of the two triangles revealed to be extremely important, and as can be seen in Figure 12, the $S=19/2$ spin level remains the ground state until an interaction value close to -0.5 cm^{-1}, however, for larger AF interactions, the ground state changes quickly to lower values.

In the same way, low-temperature χ_MT decreases and the magnetization strongly decreases when the $S=19/2$ and 17/2 spin levels increase in energy.

© 2018 Wiley-VCH Verlag GmbH & Co. KGaA, Weinheim

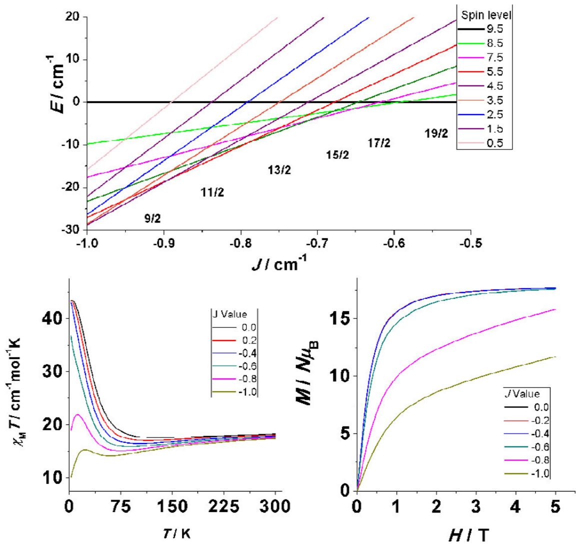

Figure 12. Evolution of the ground state for the $Mn^{II}Mn^{III}_6Na^{I}_2$ system versus the intertriangle interaction, in relation to the 19/2 spin state (top). Effect on the $\chi_M T$ and M response of the intertriangle interaction (bottom).

In light of these calculations, a new fit including the intertriangle interaction for the J value corresponding to the ground state suggested by the fit of the magnetization yield is an excellent fit for the whole range of temperatures for an intertriangle interaction of $-0.7\ cm^{-1}$ and $J_1=3.3\ cm^{-1}$, $J_2=-3.4\ cm^{-1}$, $g=1.84$, and $R=8.8\times10^{-5}$ for **6*R*** and an intertriangle interaction of -0.75 and $J_1=3.3\ cm^{-1}$, $J_2=-3.2\ cm^{-1}$, $g=1.90$, and $R=2.0\times10^{-4}$ for **7*R***.

Absolute J and g values for this system must be assumed with caution because of the number of superexchange parameters, but independently of the fit approach, the sign of the interactions is always AF between $Mn^{II}\cdots Mn^{III}$ and FM inside the triangular Mn^{III} unit. Complexes **6*R*** and **7*R*** can be envisaged as two fused $[Mn^{II}Mn^{III}_3Na^{I}]$ fragments with similar C_3 symmetry and bond parameters, and as should be expected, the sign of the coupling constants is the same as that in compound **1** and the two complexes with μ_2-Cl bridges reported in the literature.[8,13]

Alternate current measurements were performed for all the complexes, but no out-of-phase signals were observed either at zero field or under static fields, discarding a SMM response, probably as a result of the sum of several factors such as the unfavorable arrangement of the easy axis of the Mn^{III} cations, low D values, or the mixing of multiple spin states in the vicinity of the ground state that provide fast relaxation.

The magnetic response of the reported systems and the successful rationalization of their magnetic response provide some conclusions: first, in this case, the μ_2-ligands (Cl or Br) have a negligible influence on the magnetic properties, and second, the generally assumed criterion to justify the magnetic response of related complexes is dubious. The magnetic properties of these systems can be explained without the employment of different J constants for different Mn^{III}-O-Mn^{III} bond angles for a constant μ_2 ligand.

Conclusion

The chiral Schiff base derived from the condensation of *o*-vanillin and phenylglycinol proved to be a versatile ligand that, in adequate experimental conditions, is able to generate a variety of nuclearities and conformations based on the pentanuclear fragment $[Mn^{II}Mn^{III}_3M'(\mu_3\text{-}O)_2L_3]$. New examples of the $M'=Na^{I}$ family, some rare $M'=Ca^{II}$ complexes, and the first clusters with $M'=Mn^{II}$ or the enneanuclear systems $[Mn^{II}Mn^{III}_6Na^{I}_2(\mu_3\text{-}O)_2L_3]$ were characterized. ECD and IR spectroscopy proved to be able to differentiate the parallel or reversed arrangement of the ligands, with the latter related to the inclusion of divalent cations in the M′ position. The reversed arrangement is associated with the anomalous loss of molecular helicity for both enantiomers. A review of the previously published data for the $[Mn^{II}Mn^{III}_3Na^{I}]$ family of clusters revealed that the usually accepted dependence of the Mn^{III}-O-Mn^{III} bond angle of the triangular fragments is poorly reliable to analyze their magnetic properties and that the superexchange role of the axial ligands must be considered.

Experimental Section

Experimental details

IR spectra (4000–400 cm^{-1}) were recorded with a Bruker IFS-125 FTIR spectrometer with samples prepared as KBr pellets. Variable-temperature magnetic studies were performed with a MPMS-5 Quantum Design magnetometer operating at 0.03 T in the 300–2.0 K range. Diamagnetic corrections were applied to the observed paramagnetic susceptibility using Pascal's constants. Analysis of the magnetic data was performed with the PHI program.[23] Quality of the fits was parametrized as the $R=(\chi_M T_{exptl}-\chi_M T_{calcd})^2/(\chi_M T_{exptl})^2$ factor.

The solution ECD and UV/Vis spectra were recorded with a Jasco J-715 spectrometer at RT in spectroscopic grade CH_3CN (10^{-5} M, compounds **1** and **6**) or CH_3OH (10^{-6} M, compounds **2** and **4**). The solutions were measured in quartz cells with a path length between 2 and 0.1 cm. All spectra were recorded by using a scanning speed of 100 nm min^{-1}, a step size of 0.1 nm, a bandwidth of 2 nm, a response time of 0.5 s, and averaged over four accumulations. The spectra were baseline-corrected by using the solvent spectrum under the same conditions and immediately before or after the sample measurement. For all compounds, the yields of the syntheses were about 30–40% of crystalline product that was employed for the instrumental measurements.

Single-crystal X-ray crystallography

Prismlike specimens of the 11 (*R*) and (*S*) enantiomers of **1**–**7** were used for the X-ray crystallographic analyses. The X-ray intensity data were measured with a D8-VENTURE system equipped with a multilayer monochromator and a Mo microfocus ($\lambda=0.71073$ Å). The frames were integrated with the Bruker SAINT software package using a narrow-frame algorithm. The final cell constants were based upon the refinement of the XYZ-centroids of reflections above 20 $\sigma(I)$. Data were corrected for absorption effects using the multi-scan method (SADABS). The structures were solved with the Bruker SHELXTL Software Package and refined using SHELXL.[24] Details of crystal data, collection, and refinement for **1*R*** and **1*S*** are summarized in Table S4, **2*R***, **2*S***, and **3*S*** in Table S5, **4*R***, **4*S***, and **5*S***

© 2018 Wiley-VCH Verlag GmbH & Co. KGaA, Weinheim

in Table S6, and **6R**, **6S**, and **7R** in Table S7. Analyses of the structures and plots for publication were performed with Ortep3[25] and POVRAY programs.

Synthetic procedures

H_2L Schiff bases: The corresponding (*R*)- or (*S*)-enantiomer of 2-phenylglycinol (0.5 g, 3.64 mmol) and 2-hydroxy-3-methoxybenzaldehyde (0.55 g, 3.64 mmol) were dissolved in methanol (20 mL), and the solution was refluxed for 1 h and diluted to 50 mL with methanol. The resulting 0.072 M yellow solutions of the H_2L ligands were employed directly in the synthesis of the derived complexes.

Complexes with [Mn_4Na] core (1*R* and 1*S*): $MnBr_2\cdot 4H_2O$ (0.104 g, 0.365 mmol) and NaN_3 (0.024 g, 0.365 mmol) were dissolved in acetonitrile (20 mL), and the solution was added to a sample of the previously prepared ligand solution of the corresponding enantiomer of H_2L (5 mL, 0.365 mmol). The mixture was stirred at RT for 3 h, filtered, and layered with diethyl ether. Dark-brown crystals were collected after a week. The analogous reaction starting from $MnCl_2\cdot 4H_2O$ led to complex **6**. Elemental analysis calcd (%) for $C_{217}H_{233}Br_{16}Mn_{16}N_{21}Na_4O_{49}$ (**1*R***): C 42.25, H 3.81, N 4.77; found: C 42.0, H 3.6, N 4.4; elemental analysis calcd (%) for $C_{220}H_{234}Br_{16}Mn_{16}N_{24}Na_4O_{53}$ (**1*S***): C 41.86, H 3.74, N 5.33; found: C 41.6, H 3.7, N 4.7. A representative IR spectrum is shown in Figure S4.

Complexes with [Mn_4Ca] core (2*R*, 2*S*, and 3*S*): $MnCl_2\cdot 4H_2O$ (0.099 g, 0.5 mmol) and a sample of the previously prepared ligand solution of the corresponding enantiomer of H_2L (6 mL, 0.438 mmol) were mixed with $Ca(MeO)_2$ (0.026 g, 0.25 mmol) in acetonitrile (20 mL) and stirred at RT for 3 h. The resulting solution was filtered and layered with diethyl ether. Dark-brown crystals of **2*R*** or **2*S*** were obtained after a few days. The same reaction but starting from $MnBr_2\cdot 4H_2O$ (instead of $MnCl_2\cdot 4H_2O$) led to complex **3*S***. Elemental analysis calcd (%) for $C_{100}H_{107.5}Ca_2Cl_{10}Mn_8N_7O_{26.25}$ (**2*R***): C 44.46, H 4.01, N 3.63; found: C 43.9, H 3.8, N 3.8; elemental analysis calcd (%) for $C_{103.5}H_{113}Ca_2Cl_{10}Mn_8N_9O_{25.5}$ (**2*S***): C 44.95, H 4.12, N 4.56; found: C 44.3, H 3.9, N 4.3; elemental analysis calcd (%) for $C_{103}H_{109.5}Br_{10}Mn_8N_9O_{25.25}$ (**3*S***): C 38.71, H 3.45, N 3.94; found: C 37.4, H 3.7, N 4.1. A representative IR spectrum is shown in Figure S4.

Complexes with [Mn_5] core (4*R*, 4*S*, and 5*S*): The same procedure described for complexes **2** and **3** but employing KOH or CsOH (2 mmol) as base led to **4*R***, **4*S***, or **5*S***. Elemental analysis calcd (%) for $C_{101}H_{104}Cl_{10}Mn_{10}N_8O_{23}$ (**4*R***): C 43.90, H 3.88, N 4.15; found: C 42.5, H 4.0, N 4.0; elemental analysis calcd (%) for $C_{105.5}H_{115}Cl_{10}Mn_{10}N_9O_{24.5}$ (**4*S***): C 45.17, H 4.13, N 4.49; found: C 44.1, H 3.8, N 4.3; elemental analysis calcd (%) for $C_{107}H_{116}Br_{10}Mn_{10}N_8O_{24.75}$ (**5*S***): C 39.10, H 3.56, N 4.26; found: C 40.5, H 4.0, N 4.6. A representative IR spectrum is shown in Figure S4.

Complexes with [Mn_7Na_2] core (6*R*, 6*S*, and 7*R*): $MnCl_2\cdot 4H_2O$ (0.072 g, 0.365 mmol) and NaOH (0.015 g, 0.365 mmol) were stirred for 5 min in acetonitrile (20 mL). After that, a sample of the H_2L ligand solution (5 mL, 0.365 mmol) was added. The resulting mixture was stirred at RT for 3 h and filtered. The resulting solution was layered with diethyl ether, and dark-brown crystals were obtained after a few days. The same reaction but starting from $MnBr_2\cdot 4H_2O$ (instead of $MnCl_2\cdot 4H_2O$) led to complex **7*R***. Elemental analysis calcd (%) for $C_{105}H_{111}Cl_6Mn_7N_6Na_2O_{23}$ (**6*R***): C 50.24, H 4.46, N 5.02; found: C 50.5, H 4.1, N 4.8; elemental analysis calcd (%) for $C_{97.5}H_{100}Cl_6Mn_7N_6Na_2O_{23.5}$ (**6*S***): C 49.30, H 4.24, N 3.54; found: C 49.4, H 3.7, N 3.7; elemental analysis calcd (%) for $C_{108}H_{112}Br_6Mn_7N_{10}Na_2O_{21}$ (**7*R***): C 46.03, H 3.94, N 4.13; found: C 45.8, H 3.8, N 4.3. A representative IR spectrum is shown in Figure S4.

Acknowledgements

J.M. and A.E. thank the financial support from the Ministerio de Economia y Competitividad (Project CTQ2015-63614-P). M.G. thanks the Polish Ministry of Science and Higher Education ("Mobilnosc Plus" grant no. 1286/MOB/IV/2015/0) for support.

Conflict of interest

The authors declare no conflict of interest.

Keywords: chirality · circular dichroism · magnetic properties · manganese · Schiff bases

[1] a) R. Sessoli, D. Gatteschi, A. Caneschi, M. Novak, *Nature* **1993**, *365*, 141 – 143; b) J. Villain, F. Hartman-Benton, R. Sessoli, A. Rattori, *Europhys. Lett.* **1994**, *27*, 159 – 164.

[2] a) E. S. Koumousi, S. Mukherjee, C. M. Beavers, S. J. Teat, G. Christou, T. C. Stamatatos, *Chem. Commun.* **2011**, *47*, 11128 – 11130; b) D. R. J. Kolling, N. Cox, G. M. Ananyev, R. J. Pace, G. C. Dismukes, *Biophys. J.* **2012**, *103*, 313 – 322; c) C. Zhang, C. Chen, H. Dong, J.-R. Shen, H. Dau, J. A. Zhao, *Science* **2015**, *348*, 690 – 693.

[3] I. J. Hewitt, J.-K. Tang, N. T. Madhu, R. Clerac, G. Buth, C. E. Anson, A. K. Powell, *Chem. Commun.* **2006**, 2650 – 2652.

[4] L.-L. Fan, F.-S. Guo, L. Yun, Z.-J. Lin, R. Herchel, J.-D. Leng, Y.-C. Ou, M.-L. Tong, *Dalton Trans.* **2010**, *39*, 1771 – 1780.

[5] S. Nayak, H. P. Nayek, S. Dehnen, A. K. Powell, J. Reedijk, *Dalton Trans.* **2011**, *40*, 2699 – 2702.

[6] P.-P. Yang, C.-Y. Shao, L.-L. Zhu, Y. Xu, *Eur. J. Inorg. Chem.* **2013**, 5288 – 5296.

[7] P.-P. Yang, L.-L. Zhu, Y. Xu, C.-Y. Shao, *Z. Anorg. Allg. Chem.* **2013**, *639*, 1821 – 1826.

[8] C. Ding, C. Gao, S. Ng, B. Wang, Y. Xie, *Chem. Eur. J.* **2013**, *19*, 9961 – 9972.

[9] L. Cong, X. Qin, W. Sun, Y. Wang, S. Ding, Z. Liu, *New J. Chem.* **2014**, *38*, 545 – 551.

[10] Y. Song, G. Zhang, X. Qin, Y. Gao, S. Ding, Y. Wang, C. Du, Z. Liu, *Dalton Trans.* **2014**, *43*, 3880 – 3887.

[11] a) V. Chandrasekhar, A. Dey, S. Das, S. Kundu, *CrystEngComm* **2014**, *16*, 1304 – 1310; b) P.-P. Yang, X.-L. Wang, L.-C. Li, D.-Z. Liao, *Dalton Trans.* **2011**, *40*, 4155 – 4161.

[12] D. Liu, Q. Zhou, Y. Chen, F. Yang, Y. Yu, Z. Shi, S. Feng, *Dalton Trans.* **2010**, *39*, 5504 – 5508.

[13] a) A. Escuer, J. Mayans, M. Font-Bardia, L. Di Bari, M. Górecki, *Eur. J. Inorg. Chem.* **2017**, 991 – 998; b) A. Escuer, J. Mayans, M. Font-Bardia, M. Górecki, L. Di Bari, *Dalton Trans.* **2017**, *46*, 6514 – 6517; c) J. Mayans, A. Martin, M. Font-Bardia, A. Escuer, *Polyhedron* **2018**, *150*, 10 – 14; d) J. Mayans, M. Font-Bardia, A. Escuer, *Inorg. Chem.* **2018**, *57*, 926 – 929; e) J. Mayans, M. Font-Bardia, A. Escuer, *Dalton Trans.* **2018**, *47*, 8392 – 8401; f) J. Mayans, M. Font-Bardia, L. Di Bari, L. Arrico, F. Zinna, G. Pescitelli, A. Escuer, *Chem. Eur. J.* **2018**, *24*, 7653 – 7663.

[14] A. Escuer, J. Esteban, S. P. Perlepes, T. C. Stamatatos, *Coord. Chem. Rev.* **2014**, *275*, 87 – 129.

[15] a) J. Crassous, *Chem. Soc. Rev.* **2009**, *38*, 830 – 845; b) H. Miyake, *Symmetry* **2014**, *6*, 880 – 895.

[16] a) K. Mikami, M. Lautens, *New Frontiers in Asymmetric Catalysis*, Wiley, Germany, **2007**; b) J. Kumar, T. Nakashima, T. Kawai, *J. Phys. Chem. Lett.* **2015**, *6*, 3445 – 3452.

[17] a) S. Muhlbauer, B. Binz, F. Jonietz, C. Pfleiderer, A. Rosch, A. Neubauer, R. Georgii, P. Boni, *Science* **2009**, *323*, 915 – 919; b) X. Z. Yu, Y. Onose, N. Kanazawa, J. H. Park, J. H. Han, N. Nagaosa, Y. Tokura, *Nature* **2010**, *465*, 901 – 904; c) Y. Togawa, T. Koyama, K. Takayanagi, S. Mori, Y. Kousaka, J. Akimitsu, S. Nishihara, K. Inoue, A. S. Ovchinnikov, J. Kishine, *Phys. Rev. Lett.* **2012**, *108*, 107202.

[18] a) S.-Y. -Lin, Y.-N. Guo, L. Zhao, P. Zhang, H. Ke, *Chem. Commun.* **2012**, *48*, 6924 – 6926; b) S.-Y- Lin, C. Wang, L. Zhao, J. Tang, *Chem. Asian J.*

2014, *9*, 3558–3564; c) S.-Y. Lin, C. Wang, L. Zhao, J. Wu, J. Tang, *Dalton Trans.* **2015**, *44*, 223.

[19] J.-C. G. Bünzli, S. V. Eliseeva, *Chem. Sci.* **2013**, *4*, 1939–1949.

[20] M. Liu, L. Zhang, T. Wang, *Chem. Rev.* **2015**, *115*, 7304–7397.

[21] a) M. Viciano-Chumillas, S. Tanase, I. Mutikainen, U. Turpeinen, L. J. de Jongh, J. Reedijk, *Inorg. Chem.* **2008**, *47*, 5919–5929; b) T. C. Stamatatos, D. Foguet-Albiol, S. C. Lee, C. C. Stoumpos, C. P. Raptopoulou, A. Terzis, W. Wernsdorfer, S. O. Hill, S. P. Perlepes, G. Christou, *J. Am. Chem. Soc.* **2007**, *129*, 9484–9499; c) J. Cano, T. Cauchy, E. Ruiz, C. J. Milios, C. C. Stoumpos, T. C. Stamatatos, S. P. Perlepes, G. Christou, E. K. Brechin, *Dalton Trans.* **2008**, 234–240.

[22] C. Lampropoulos, K. A. Abboud, T. C. Stamatatos, G. Christou, *Inorg. Chem.* **2009**, *48*, 813–815.

[23] N. F. Chilton, R. P. Anderson, L. D. Turner, A. Soncini, K. S. Murray, *J. Comput. Chem.* **2013**, *34*, 1164–1165.

[24] G. M. Sheldrick, SHELXL-2014/7: Program for the Solution of Crystal Structures, University of Göttingen, Göttingen, Germany, **2014**.

[25] L. J. Farrugia, *J. Appl. Crystallogr.* **1997**, *30*, 565.

Manuscript received: July 20, 2018
Accepted manuscript online: September 19, 2018
Version of record online: ■■ ■■, 0000

FULL PAPER

Chiral Complexes

*J. Mayans, M. Font-Bardia, L. Di Bari, M. Górecki, A. Escuer**

■■ – ■■

Chiral [$Mn^{II}Mn^{III}_3M'$] ($M' = Na^I, Ca^{II}, Mn^{II}$) and [$Mn^{II}Mn^{III}_6Na^I_2$] Clusters Built from an Enantiomerically Pure Schiff Base: Synthetic, Chiroptical, and Magnetic Properties

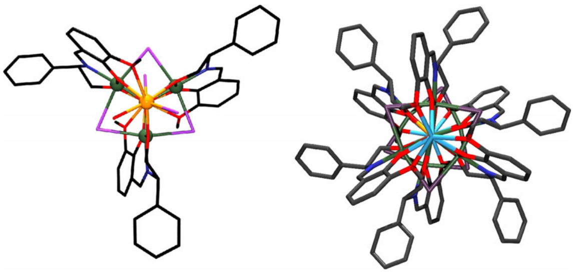

Mirror, mirror: A family of chiral clusters with [$Mn^{II}Mn^{III}_3M'$] or [$Mn^{II}Mn^{III}_6Na^I_2$] cores (see figure) was obtained from enantiomerically pure Schiff bases. Structural characteristics, optical properties, and magnetic response were studied for these complexes.

CHEMISTRY
A European Journal

Supporting Information

Chiral $[Mn^{II}Mn^{III}_3M']$ ($M' = Na^I$, Ca^{II}, Mn^{II}) and $[Mn^{II}Mn^{III}_6Na^I_2]$ Clusters Built from an Enantiomerically Pure Schiff Base: Synthetic, Chiroptical, and Magnetic Properties

Júlia Mayans,[a] Mercé Font-Bardia,[b] Lorenzo Di Bari,[c] Marcin Górecki,[c] and Albert Escuer*[a]

chem_201803730_sm_miscellaneous_information.pdf

Table S1. BVS calculation for the manganese cations of complexes **1-7**. For the complexes with two non-equivalent molecules the data refers to the molecule labelled as “A”. For **1*R*** and **1*S*** the data refers to the molecule with Oh environment for Mn4. The numbers highlighted in red corresponds to the assigned oxidation state.

Complex 1*R*			
	Mn^{II}	Mn^{III}	Mn^{IV}
Mn1	3.39	**3.03**	3.15
Mn2	3.34	**2.98**	3.11
Mn3	3.46	**3.10**	3.22
Mn4	**2.02**	1.86	1.94

Complex 1*S*			
	Mn^{II}	Mn^{III}	Mn^{IV}
Mn1	3.33	**2.99**	3.10
Mn2	3.29	**2.94**	3.06
Mn3	3.36	**3.00**	3.12
Mn4	**1.96**	1.79	1.89

Complex 2*R*			
	Mn^{II}	Mn^{III}	Mn^{IV}
Mn1	3.12	**2.94**	3.00
Mn2	3.33	**3.14**	3.21
Mn3	3.36	**3.17**	3.24
Mn4	**1.77**	1.65	1.72

Complex 2*S*			
	Mn^{II}	Mn^{III}	Mn^{IV}
Mn1	3.25	**3.07**	3.13
Mn2	3.29	**3.09**	3.17
Mn3	3.36	**3.17**	3.24
Mn4	**1.92**	1.80	1.87

Complex 3*R*			
	Mn^{II}	Mn^{III}	Mn^{IV}
Mn1	3.35	**3.00**	3.11
Mn2	3.65	**3.26**	3.40
Mn3	3.34	**2.99**	3.10
Mn4	**2.04**	1.80	1.88

Complex 4*R*			
	Mn^{II}	Mn^{III}	Mn^{IV}
Mn1	3.43	**3.24**	3.31
Mn2	3.53	**3.32**	3.40
Mn3	3.34	**3.13**	3.21
Mn4	**1.88**	1,77	1.83
Mn5	**1.80**	1.70	1.76

Complex 4*S*			
	Mn^{II}	Mn^{III}	Mn^{IV}
Mn1	3.34	**3.14**	3.22
Mn2	3.36	**3.16**	3.23
Mn3	3.31	**3.12**	3.19
Mn4	**1.91**	1.79	1.86
Mn5	**1.87**	1.77	1.83

Complex 5*S*			
	Mn^{II}	Mn^{III}	Mn^{IV}
Mn1	3.48	**3.11**	3.24
Mn2	3.39	**3.04**	3.15
Mn3	3.47	**3.10**	3.22
Mn4	**1.96**	1.70	1.81
Mn5	**1.94**	1.67	1.77

Complex 6*R*			
	Mn^{II}	Mn^{III}	Mn^{IV}
Mn1	3.34	**3.14**	3.22
Mn2	3.28	**3.09**	3.16
Mn3	**1.83**	1.67	1.77

Complex 6*S*			
	Mn^{II}	Mn^{III}	Mn^{IV}
Mn1	3.43	**3.23**	3.30
Mn2	3.34	**3.14**	3.22
Mn3	**1.84**	1.69	1.79

Complex 7*R*			
	Mn^{II}	Mn^{III}	Mn^{IV}
Mn1	3.34	**2.99**	3.11
Mn2	3.38	**3.02**	3.14
Mn3	3.36	**3.01**	3.13
Mn4	3.31	**2.97**	3.09
Mn5	3.39	**3.03**	3.15
Mn6	3.38	**3.02**	3.14
Mn7	**1.85**	1.70	1.79

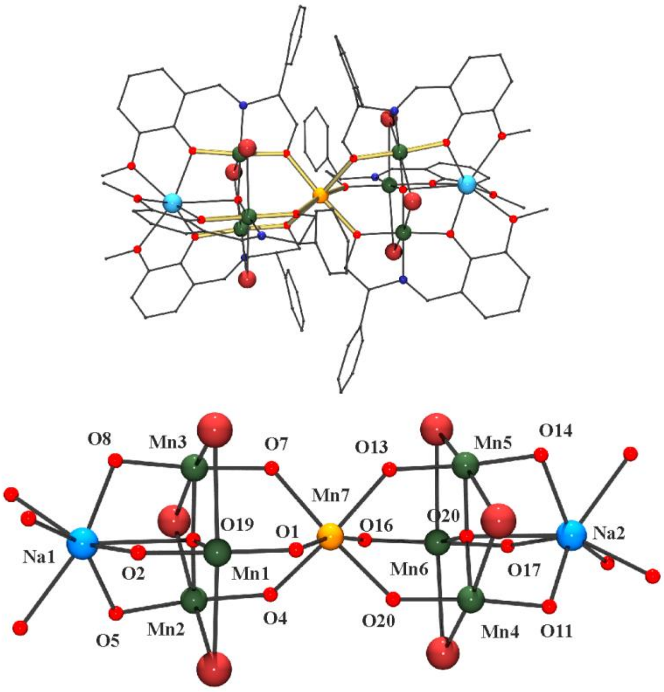
O8
Mn3
O7
O13
Mn5
O14
Mn7
O19
O1
O16
O20
Na1
O2
Mn1
Mn6
O17
Na2
O5
Mn2
O4
O20
Mn4
O11

Figure S1. A view of the representative **7*R*** molecule (top) and its labeled core (down).

Table S2. Selected bond distances (Å) and angles (°) for compound **7*R***.

Mn1-O19	1.882(3)	Mn4-O20	1.888(3)
Mn2-O19	1.885(3)	Mn5-O20	1.887(3)
Mn3-O19	1.885(3)	Mn6-O20	1.878(3)
Mn7-O1	2.200(3)	Mn7-O10	2.215(3)
Mn7-O4	2.189(3)	Mn7-O13	2.190(3)
Mn7-O7	2.209(3)	Mn7-O16	2.195(3)
Mn1-O1-Mn7	127.6(1)	Mn1-O19-Mn2	118.6(1)
Mn2-O4-Mn7	127.6(1)	Mn1-O19-Mn3	120.0(1)
Mn3-O7-Mn7	126.3(1)	Mn2-O(19-Mn3	117.8(1)
Mn4-O10-Mn7	128.2(1)	Mn4-O20-Mn5	118.0(1)
Mn5-O13-Mn7	127.7(1)	Mn4-O20-Mn6	120.3(1)
Mn6-O16-Mn7	127.9(1)	Mn5-O20-Mn6	117.3(1)

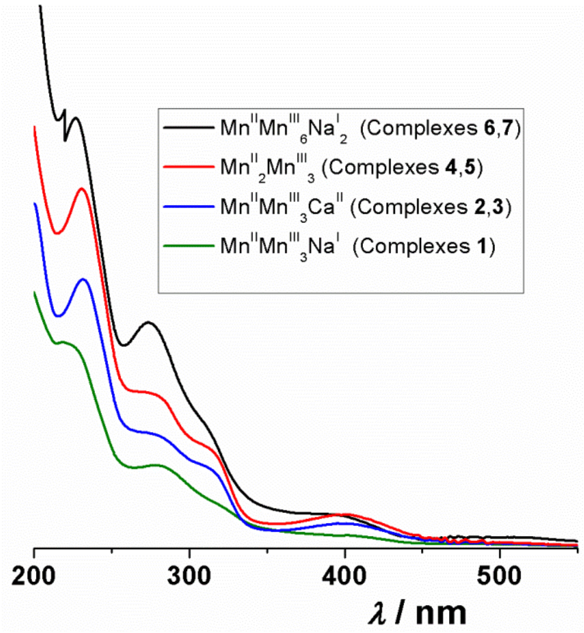

Figure S2. Representative Vis-Uv spectra for the four nuclearities of complexes **1**-**7**. The absorbance values are arbitrary and factorized for clarity.

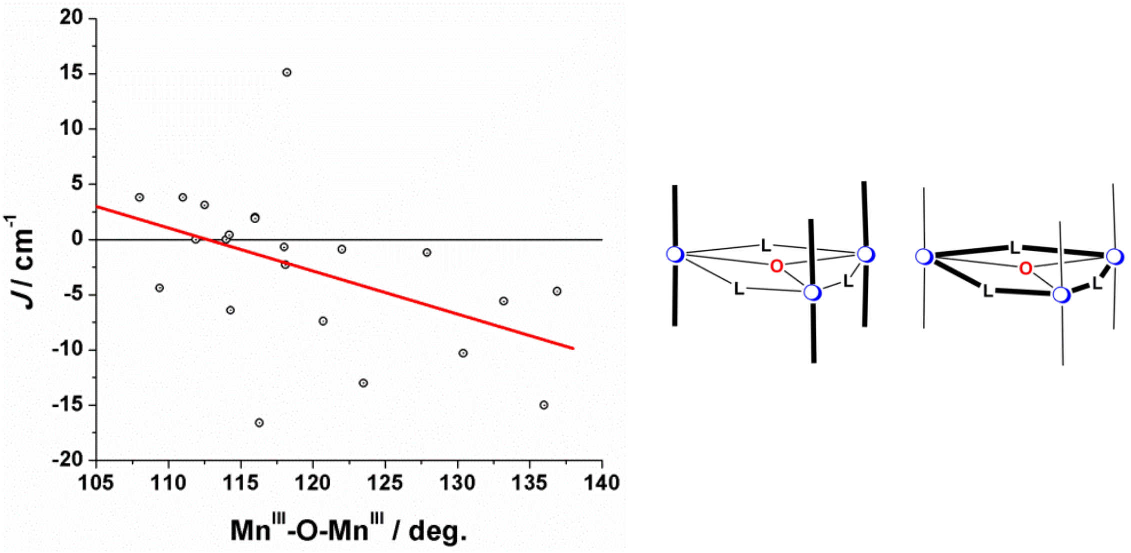

Figure S3. Left, Plot of the bibliographic J values for the $Mn^{III}\cdots Mn^{III}$ interaction *vs*. the Mn^{III}-O-Mn^{III} bond angle, showing the lack of correlation between these parameters for the $Mn^{II}Mn^{III}_3Na^I$ pentanuclear cages. There is a slight correlation for the extreme larger and shorter bond angles but the dispersion is too high to justify any clear relationship. The reason lies in the trial to apply a model developed for a triangular arrangement with the easy axis perpendicular to the manganese plane to systems with the reversed orbitals and the easy axis on plane, right.

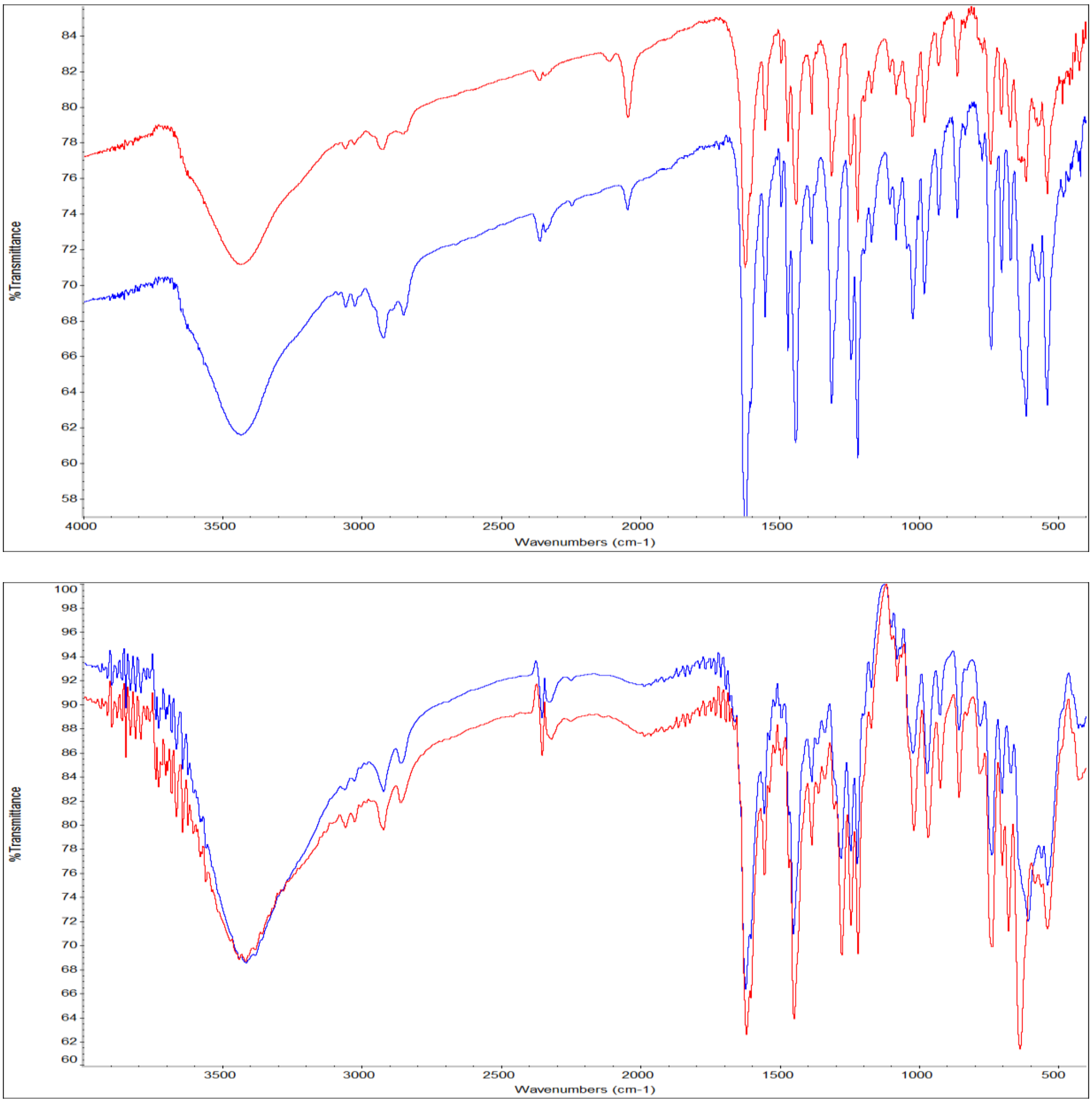

Figure S4. Representative IR spectra for the four nuclearities of complexes **1**-**7**. Spectra for **1** and **7** (top) and **3** and **5** (down). Systems **1** and **7** with the common $Mn^{II}Mn^{III}_3Na^{I}$ core and the three parallel Schiff bases are practically identical and clearly different of the $Mn^{II}Mn^{III}_3Ca^{II}$ and $Mn^{II}_2Mn^{III}_3$ systems (**3** and **5**) with reversed arrangement of the Schiff bases.

Table S3. Spin ground state and energy and population at 2 K for the low laying spin levels for complexes **2*R***, **3*R***, **4*R*** and **5*S*** that justify the susceptibility and magnetization response.

2*R* ($Mn^{II}Mn_3^{III}$Ca core, μ-Cl axial bridges)

Spin	Energy(cm^{-1})	Population at 2K
3.5	0.00000E+00	50.37
4.5	0.48200E-01	48.65
2.5	0.54761E+01	0.98

Gap to the next spin level 16 cm-1

3*R* ($Mn^{II}Mn_3^{III}$Ca core, μ-Br axial bridges)

Spin	Energy(cm^{-1})	Population @ 2K
4.5	0.00000E+00	73.06
3.5	0.14972E+01	24.88
2.5	0.49949E+01	2.01

Gap to the next spin level 10 cm-1

4*R* ($Mn_2^{II}Mn_3^{III}$ core, μ-Cl axial bridges)

Spin	Energy(cm^{-1})	Population at 2K
2.0	0.00000E+00	21.47
1.0	0.69338E-01	20.43
2.0	0.38447E+00	16.28
1.0	0.94117E+00	10.91
2.0	0.15943E+01	6.82
1.0	0.22483E+01	4.26
3.0	0.24625E+01	3.65
0.0	0.30151E+01	2.45
3.0	0.33087E+01	1.99
3.0	0.34097E+01	1.85
0.0	0.35623E+01	1.66
1.0	0.36543E+01	1.55
2.0	0.38145E+01	1.38
2.0	0.42276E+01	1.03
0.0	0.46340E+01	0.77
2.0	0.46937E+01	0.73

5*S* ($Mn_2^{II}Mn_3^{III}$ core, μ-Br axial bridges)

Spin	Energy	Population @ 2K
2.0	0.00000E+00	14.82
2.0	0.11153E-01	14.71
2.0	0.12599E+00	13.54
2.0	0.27496E+00	12.16
3.0	0.12436E+01	6.06
3.0	0.12987E+01	5.82
3.0	0.14011E+01	5.41
3.0	0.14215E+01	5.33
3.0	0.15086E+01	5.01
1.0	0.19011E+01	3.78
1.0	0.20211E+01	3.46
1.0	0.22466E+01	2.94
2.0	0.48010E+01	0.47
2.0	0.48034E+01	0.47

Table S4. Crystal data for compounds **1*R*** and **1*S*.**

	1*R*	**1*S***
Formula	$C_{217}\,H_{233}\,Br_{16}\,Mn_{16}\,N_{21}\,Na_4\,O_{49}$	$C_{220}\,H_{234}\,Br_{16}\,Mn_{16}\,N_{24}\,Na_4\,O_{53}$
FW	6168.79	6311.86
System	Triclinic	Monoclinic
Space group	P1	P21
a/Å	16.545(2)	20.2507(7)
b/Å	19.911(2)	16.3807(6)
c/Å	20.663(2)	20.7092(8)
α/deg.	114.549(4)	90
ß/deg.	91.914(5)	115.848(1)
γ/deg.	90.337(4)	90
V/ Å^3	6187(1)	6182.4(4)
Z	1	1
T, K	100(2)	100(2)
λ(MoKα), Å	0.71073	0.71073
ρcalc, g·cm-3	1.656	1.695
μ(MoKα), mm^{-1}	3.450	3.456
Flack param.	0.025(7)	0.005(2)
R	0.0536	0.0361
ωR^2	0.1344	0.0762

Table S5. Crystal data for compounds **2*R*, 2*S*** and **3*R*.**

	2*R*	**2*S***	**3*R***
Formula	$C_{100}H_{107.5}Ca_2Cl_{10}\,Mn_8\,N_7O_{26.25}$	$C_{103.5}\,H_{113}\,Ca_2Cl_{10}\,Mn_8N_9\,O_{25.5}$	$C_{103}H_{109.5}Br_{10}Ca_2Mn_8N_9\,O_{25.25}$
FW	2701.60	2765.20	3196.27
System	Triclinic	Triclinic	Triclinic
Space group	P1	P1	P1
a/Å	14.019(1)	13.9951(5)	14.0278(8)
b/Å	16.063(1)	15.8813(7)	16.069(1)
c/Å	17.605(1)	17.4719(8)	17.806(1)
α/deg.	105.887(3)	104.472(2)	104.419(3)
ß/deg.	109.488(3)	110.321(2)	110.416(3)
γ/deg.	95.593(3)	95.441(2)	95.512(3)
V/ Å^3	3515.8(5)	3454.8(3)	3568.584)
Z	1	1	1
T, K	100(2)	100(2)	100(2)
λ(MoKα), Å	0.71073	0.71073	0.71073
ρcalc, g·cm-3	1.276	1.329	1.487
μ(MoKα), mm^{-1}	1.016	1.036	3.615
Flack param.	0.16(2)	0.08(3)	0.27(2)
R	0.0596	0.0556	0.0812
ωR^2	0.01617	0.1429	0.2082

Table S6. Crystal data for compounds **4*R***, **4*S*** and **5*S*. 4*R*** was a 62% / 38% twin and due to the size of the crystal and the common reflections was not possible to discard the lower component, yielding an anomalous Flack parameter.

	4*R*	**4*S***	**5S**
Formula	$C_{101.2}\,H_{105.5}Cl_{10}\,Mn_{10}\,N_8O_{23.5}$	$C_{105.5}\,H_{115}\,Cl_{10}\,Mn_{10}\,N_9\,O_{24.5}$	$C_{107}\,H_{116.5}\,Br_{10}\,Mn_{10}\,N_{10}\,O_{24.75}$
FW	2713.73	2804.96	3287.10
System	Triclinic	Triclinic	Triclinic
Space group	P1	P1	P1
a/Å	13.9055(5)	13.9826(6)	14.011(1)
b/Å	15.6344(7)	15.7416(6)	16.019(1)
c/Å	17.5072(8)	17.6505(7)	18.112(2)
α/deg.	104.730(2)	105.673(2)	106.807(4)
ß/deg.	110.605(2)	109.964(2)	109.473(4)
γ/deg.	95.210(2)	95.271(2)	95.522(4)
V/ Å^3	3376.5(3)	3442.3(2)	3584.2(6)
Z	1	1	1
T, K	100(2)	100(2)	100(2)
λ(MoKα), Å	0.71073	0.71073	0.71073
ρcalc, g·cm-3	1.335	1.353	1.523
μ(MoKα), mm^{-1}	1.159	1.140	3.697
Flack param.	0.38(5)	0.05(2)	0.04(1)
R	0.0350	0.0274	0.0494
ωR^2	0.0645	0.0777	0.1344

Table S7. Crystal data for compounds **6*R*, 6*S*** and **7*R*.**

	6*R*	**6*S***	**7*R***
Formula	$C_{105} H_{111}Cl_6 Mn_7 N_6 Na_2 O_{23}$	$C_{97.5} H_{100} Cl_6 Mn_7 N_6 Na_2 O_{23.5}$	$C_{108} H_{112} Br_6 Mn_7 N_{10} Na_2 O_{21}$
FW	2510.28	2375.09	2796.09
System	Trigonal	Trigonal	Triclinic
Space group	R3	R3	P1
a/Å	19.6260(7)	19.686(1)	14.2067(6)
b/Å	19.6260(7)	19.686(1)	14.5629(7)
c/Å	28.7679(9)	28.677(2)	16.5401(8)
α/deg.	90	90	91.435(2)
ß/deg.	90	90	112.245(2)
γ/deg.	120	120	110.988(2)
V/ Å^3	9596.3(7)	9624(2)	2905.6(2)
Z	3	3	1
T, K	100(2)	100(2)	100(2)
λ(MoKα), Å	0.71073	0.71073	0.71073
ρcalc, g·cm-3	1.303	1.229	1.598
μ(MoKα), mm^{-1}	0.864	0.857	2.876
Flack param.	0.022(9)	0.004(15)	0.010(2)
R	0.0572	0.0441	0.0304
ωR^2	0.1654	0.1137	0.0730

CHAPTER 5. HETEROMETALLIC CLUSTERS 3*d*/4*f* DERIVED FROM CHIRAL AND RACEMIC SCHIFF BASES. A NEW ISOMERISM TYPE?

In this Chapter a series of novel compounds with $[Ln^{III}Mn^{III}_6Na^{I}_2]$ core derived from the Schiff base ligand $\mathbf{H_2L9}$ will be described by means of their syntheses, structural characterization and magnetic properties. Moreover, a supramolecular study related with the observed differences in the chiral and meso forms of the compounds is presented, being the unique case of chiral/meso isomers with C_3/D_{3h} symmetry respectively, involving the rearrangement of the cluster and the change in the coordination environment of the Ln^{III} cation. These structural differences were observed for the complete lanthanide period (excluding Pm, Sm, Ho and Tm).

5.1. INTRODUCTION

As is mentioned in the CHAPTER I of this thesis, supramolecular chemistry has been defined as the *chemistry of molecular assemblies and intermolecular bonds,*[49] based on the molecular recognition as a key concept. Moreover, *supramolecular chirality*[65] is an emerging field which focuses its attention on the same concept of self-assembly but when the reactants or the products are chiral that provides specific properties to the conventional supramolecular chemistry. In principle, this chirality can be achieved in different manners, and, in the same way that in the rest of the products, we followed the system of using enantiopure reactants. Among this, the final arrangement of the clusters in the whole network can also be determined by the chirality of the building blocks.[66,67]

This chapter summarizes the results about the unexpected and unprecedented relationship between the chiral and meso forms of the complexes with $[Ln^{III}Mn^{III}_6Na^{I}_2]$ core and including the yttrium derivative, (Y^{III} **[20],** Ln^{III} = Ce **[21],** Pr **[22],** Nd **[23],** [Eu **[24]**, Gd **[25]**, Tb**[26]**, Dy **[27]**, Er **[28]** and Yb **[29]**). ´

5.2. SYNTHESIS.

A solution 0.073 M of the $\mathbf{H_2L9}$ (**Figure 5.1)** was previously prepared according the following procedure: 3.64 mmols (0.5 g) of (*S*/*R*/*rac*)-2-phenylglycinol and 3.64 mmols (0.55g) of 2-hydroxy-3-methoxybenzaldehyd were solved in in 20 mL of methanol and the resulting yellow mixture was refluxed for 1 h and flushed to 50 mL with methanol.

$LnCl_3{\cdot}xH_2O$ (0.243 mmols), $MnCl_2{\cdot}4H_2O$ (0.243 mmols, 0.048g), NaBzO (0.243 mmols, g) and NaN_3 (0.243 mmols, g) were dissolved in 20 mL of acetonitrile and stirred for 15 minutes. After that, 10 mL of the ligand solution (0.73 mmols) were added. The resulting mixture was stirred at room temperature for 24 hours and filtered. The resulting solution was layered with diethyl ether and dark brown crystals were obtained after a few days for the pure enantiomeric species and after two weeks for the more soluble racemic compounds. Complete synthesis is depicted in **Figure 5.1,** ligand coordination mode and a general view of a representative cluster is represented in **Figure 5.2**.

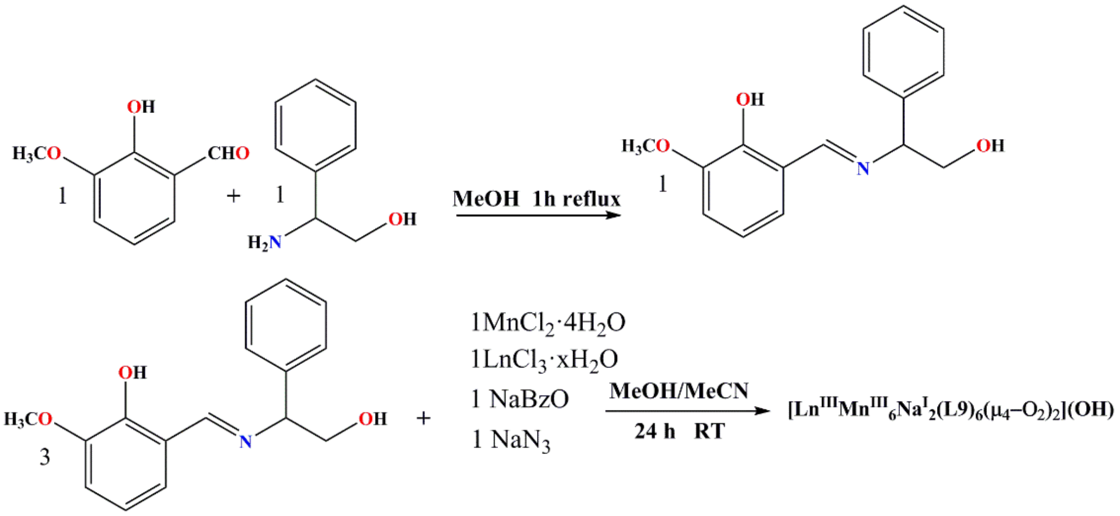
OH
H$_3$CO
CHO
1
+
1
H$_2$N
OH
MeOH 1h reflux
OH
H$_3$CO
1
N
OH
OH
H$_3$CO
3
N
OH
+
1MnCl$_2$·4H$_2$O
1LnCl$_3$·xH$_2$O
1 NaBzO
1 NaN$_3$
MeOH/MeCN
24 h RT
$[Ln^{III}Mn^{III}_6Na^I_2(L9)_6(\mu_4{-}O_2)_2](OH)$

Figure 5.1. Synthetic scheme for complexes **[20]-[29]**

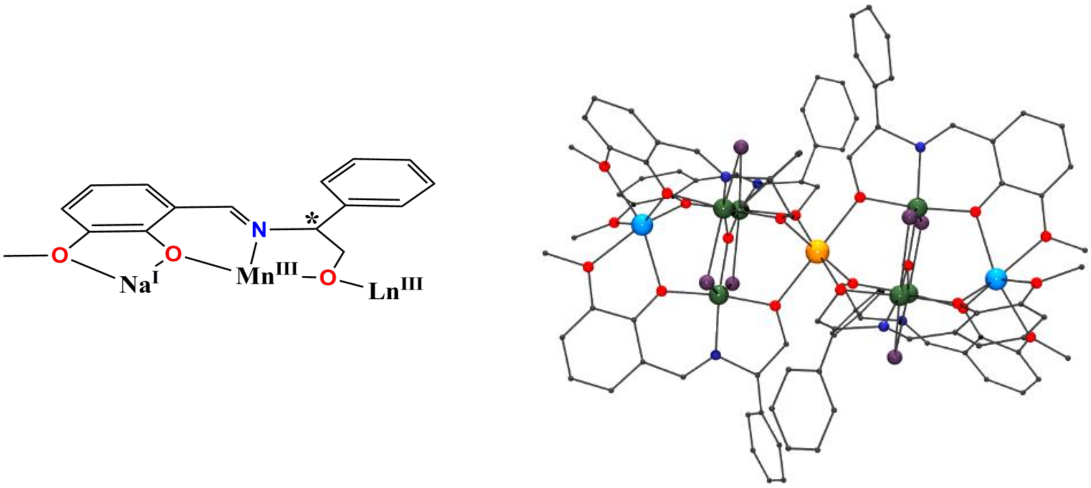
O
O
Na^I
N
*
Mn^{III}
O
Ln^{III}

Figure 5.2. Left, coordination mode of the Schiff base ligand L9^{2-} in compounds **[20]-[29]**. Right, view of cluster showing the coordination of the ligands, the Mn$^{III}_3$ triangles and the bridging chloro ligands in their axial coordination sites. Color code: Mn^{III}, dark green; Ln^{III}, orange; Na^I, light blue; N, navy; O red; Cl, violet.

5.3. STRUCTURAL DESCRIPTION.

Single crystal structural information for the chiral clusters has been collected for Ln^{III} = Ce, Nd, Pr, Eu, Gd, Tb, Dy, Er, and Yb and for racemic clusters for Ln^{III} = Ce, Gd and Tb. The analogous complex with Y^{III} were synthesized to study the magnetic response of the isolated Mn$^{III}_3$ subunits.

One Tb^{III} complex with bromo ligands instead chloro donors was also prepared in order to check if that the observed core is common to a larger series of complexes.

To avoid repetitive descriptions, only the *S* enantiomer and the meso form of the Gd^{III} derivative (compounds **[25*RAC*]** and **[25*S*]**, respectively) are going to be described. All the compounds crystallize in the trigonal space groups *R3* for the chiral derivatives and *R-3* for the meso forms.

Complex **[25*S*]** can be envisaged as two heterometallic [Gd^{III}Mn$^{III}_3$Na^{I}] trigonal bipyramidal subunits sharing the Gd^{III} cation which is placed in one of the apical sites, resulting in a nonanuclear [Gd^{III}Mn$^{III}_6$Na$^{I}_2$] cluster, **Figure 5.3, Table 5.1**.
Each subunit contains three (***S***)-**L9**$^{2-}$ ligands linking the lanthanide, the manganese and the sodium cations. The Mn^{III} cations are linked by one central μ_3-oxo or μ_4-oxo donor and become equivalent inside each subunit by a C_3 axis.
The Mn^{III} cations are coordinated by the μ_4-oxo donor, the iminic nitrogen from one **L9**$^{2-}$ ligand, one O-alcoxo donor that links each manganese atom with the lanthanide, one O-phenoxo atom that bridges with the sodium cation and two μ-Cl bridges with the neighbouring Mn^{III} cations, resulting in an octahedral coordination with the Jahn-Teller elongation directed towards the *trans*-chloro donors. The Gd^{III} cation is heptacoordinated with six shorter Gd-O bond distances to the six O-alcoxo donors from the six **L9**$^{2-}$ ligands (Gd-O4 2.277(6) Å, Gd-O1 2.322(6) Å) and one larger Gd-O8 distance of 2.694(11) Å to one of the μ_4-oxo ligands, resulting one apicated octahedral polyhedron. This distance contrasts with the Gd···O7 distance of 3.300 Å, showing the clear displacement of the Gd^{III} cation from the centre of the complex towards the μ_4-O oxo donor O8. The coordination sphere of the lanthanide cation is distorted to accept the coordination of the oxo donor, opening the O4-Gd-O4' bond angles up to 102.9(2) °, larger than O1-Gd-O1' which is 90.6(2) °. Also to favour the coordination of O8, the Mn2-O4-Gd bond angles are much shorter than Mn1-O1-Gd (111.5(3)° *vs*. 124.1(3)°) and the O8 oxo donor is displaced 0.186 Å out of the plane defined by the three Mn(2) cations towards the Gd^{III} cation. In the other side of the molecule, O7 is placed 0.076 Å out of the plane defined by the three Mn(1) cations towards the Na(1) cation. Consequently, Na(1) can be assumed as heptacoordinated whereas Na(2) remains strictly hexacoordinated. The cluster is monocationic and the charge is balanced by one OH$^-$ counteranion.

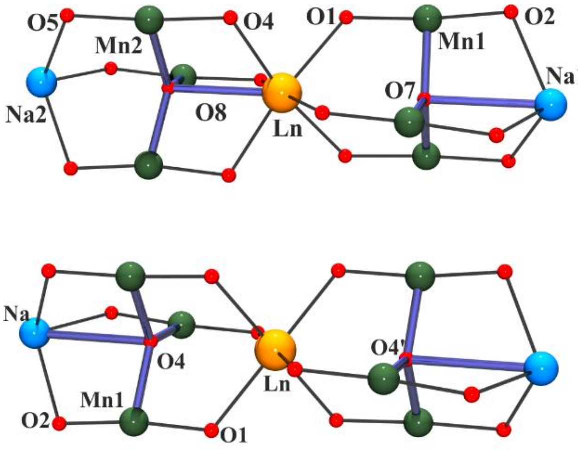

Figure 5.3. Top, labelled view of the core of cluster **[25*S*]**. Bottom, labelled core of complex **[25*RAC*]**.

[25*S*]		**[25*RAC*]**	
Gd(1)-O(1)	2.322(6)	Gd(1)-O(1)	2.287(4)
Gd(1)-O(4)	2.277(6)		
Gd(1)-O(8)	2.694(11)	Gd(1)···O(4)	
Gd(1)····O(7)		Gd(1)···O(4)'	
Mn(1)-O(1)	1.900(6)	Mn(1)-O(1)	1.893(4)
Mn(1)-O(2)	1.902(6)	Mn(1)-O(2)	1.893(5)
Mn(1)-O(7)	1.888(1)	Mn(1)-O(4)	1.9093(9)
Mn(1)-N(1)	1.997(7)	Mn(1)-N(1)	1.982(6)
Mn(1)-Cl(1)	2.673(3)	Mn(1)-Cl(1)	2.603(2)
Mn(1)-Cl(1)#1	2.648(3)	Mn(1)-Cl(1)#1	2.687(2)
Mn(2)-O(4)	1.906(6)		
Mn(2)-O(5)	1.907(6)		
Mn(2)-O(8)	1.936(2)		
Mn(2)-N(2)	1.994(6)		
Mn(2)-Cl(2)	2.641(3)		
Mn(2)-Cl(2)#1	2.602(3)		
Na(1)-O(5)	2.317(6)		
Na(1)-O(6)	2.369(7)		
Na(2)-O(2)	2.322(7)	Na(1)-O(2)	2.306(5)
Na(2)-O(3)	2.363(7)	Na(1)-O(3)	2.378(5)
Na(2)-O(7)	2.810(12)	Na(1)-O(4)	2.928(9)
Na(1)···O(8)		Na(1)'-O(4)'	2.928(9)
O(4)-Gd(1)-O(4) #1	102.9(2)	O(1)-Gd(1)-O(1)#1	82.8(1)
O(1)-Gd(1)-O(1)#1	90.6(2)		
O(1)-Gd(1)-O(4)	79.8(2)	O(1)-Gd(1)-O(1)#2	97.2(1)
Mn(1)-O(1)-Gd(1)	124.1(3)	Mn(1)-O(1)-Gd(1)	117.7(2)
Mn(2)-O(4)-Gd(1)	111.5(3)	Mn(1)'-O(1)'-Gd(1)	117.7(2)
Mn(1)-O(7)-Mn(1) #1	119.84(4)	Mn(1)-O(4)-Mn(1)'	119.96(2)
Mn(2)-O(8)-Mn(2) #1	119.1(1)		
Mn(1)-O(2)-Na(2)	109.1(3)	Mn(1)-O(2)-Na(1)	110.8(2)
Mn(2)-O(5)-Na(1)	111.6(3)		

Table 5.1. Selected bond distances (Å) and angles (°) for compounds **[25*S*]** and **[25*RAC*]**.

The overall shape of the racemic complex **[25*RAC*]** is similar to the chiral complex **[25*S*]** but in this case the cluster is centrosymmetric (D_{3h}), **Figure 5.3**. One of the pentanuclear subunits links three (*R*)-**L9**$^{2-}$ ligands and three (*S*)-**L9**$^{2-}$ ligands are coordinated to the other subunit and thus the inversion centre is placed on the Gd^{III} ion. Consequently, all the Mn-O1-Gd bond angles are identical (117.7(2) º) and the Gd^{III} cation is equidistant to O4 and O4' (2.996 Å). The Gd^{III} ion becomes hexacoordinated and its coordination polyhedron consists of a compressed octahedron along C_3 axis, (structural details in **Table 5.1**). Single crystal structural data have been collected for the analogous complexes with Ln^{III} = Ce and Tb, (Appendix II). The same **[25*RAC*]** structure was obtained from a mixture containing an enantiomeric excess of of (*S*)-**H$_2$L9**, showing that the centrosymmetric arrangement is preferred to the chiral cluster, in a similar way to related systems built from achiral Schiff bases. Thus, it becomes crucial to note that this arrangement is the *consequence* of the possibility to be centrosimmetric but not the *reason* because the alternative arrangement in the network of **[25*S*]** and **[25*R*]** clusters related by inversion centres keeping the most usual heptacoordination of the Gd^{III} cation could be equally possible (or even more probable *a priori*) in light of the structure of the chiral clusters and the flexibility of **L9**$^{2-}$.

The synthesis using $TbBr_3$ instead of $TbCl_3$ yield in a product very similar to complex **[26]** in distances and bond parameters, demonstrating that the Br^- series would be isostructural to complexes **[20]-[29]**.

Moving forward on the lanthanides period, the same structures were obtained for Ce^{III}, Pr^{III}, Nd^{III}, Eu^{III}, Gd^{III}, Tb^{III}, Dy^{III}, Er^{III} and Yb^{III}, while a trial with La^{III} yield in complex **[9]** of this thesis (with one Mn^{II} cation instead the lanthanide) probably due to the too larger size of the La^{III} cation. For the rest of the lanthanides, a structural tracking has been done to see how the size of the lanthanide cation affects the final structure.

As can be seen in the represented graphs of **Figure 5.5** the parameters $d2$, $d3$, $\underline{\alpha}2$ and $\alpha3$ (defined in **Figure 5.4**), have been represented for each complex in its chiral form. $d2$ represents the side of the compounds where the lanthanide is directly linked to the μ_4-O while $d3$ is on the size where the μ_4-O is bonded to the Na^+ cation (in blue) and not bonded to the central lanthanide. $\alpha2$ and $\alpha3$ are the corresponding angles that vary with $d2$ and $d3$. What is easely observed from the representations in **Figure 5.5** is that as the size of the lanthanide decreses, the complex get more and more assymetric until Gd^{III}.

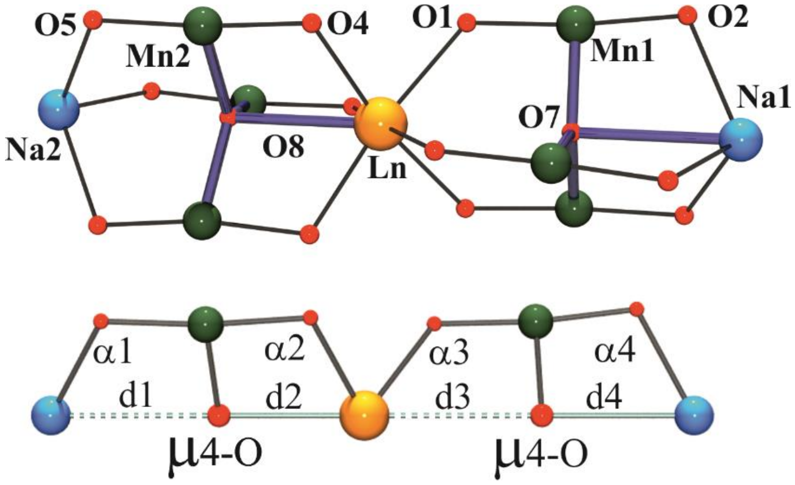

Figure 5.4. Definition of the bond parameters for complexes **[20]-[29]** in their chiral forms. Dashed green line indicates only distances, not bonds.

5.4. CHIRAL vs. MESO FORMS.

The comparison between clusters obtained from chiral or racemic ligands are rarely performed because, generally, the interest in these complexes is directly related to the chirality and to its associated properties like asymmetric catalysis,[68] synthesis of materials,[69] biochemistry,[70] or photochemistry,[71] and also because of the general assumption that the complex obtained from the racemic ligand will be a symmetric meso form or a simple mixing of both enantiomers related by inversion centres or planes in the network but always maintaining the shape, geometry and very similar bond parameters. Nevertheless, this assumption is not a rule and, in a few cases, radical differences have been found.

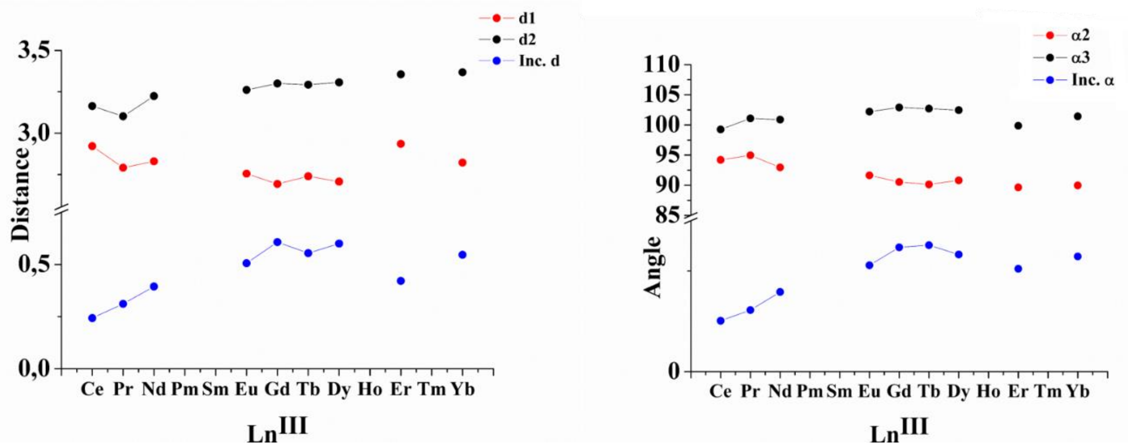

Figure 5.5. Representation of the distances and angles represented in **Figure 5.**4 for each lanthanide complex. Left, the figure shows the absolute values of *d1* and *d2* and the increment between them. Right, the figure shows *α1*, *α2* and the increment.

Relation between chiral and achiral clusters is a fascinating field of supramolecular chirality in which different approaches have been reported: on one hand there is the change from meso to chiral forms[72] and on the other, the difference between chiral and meso identical chemical reactions, widely applied in catalysis by example. As unique examples in the literature, it's interesting the transformation of the aquiral cluster [Dy$_6$Mo$_4$] to a chiral one by the reduction of S_4 symmetry to C_2 symmetry due to the interactions promoted by the cation[73] that yields to a very similar meso and chiral forms. However, in other examples radical differences are found between chiral and meso forms. The reaction of [Ni^{II}(pabn)Cl$_2$] with [Fe^{III}(CN)$_3$(tp)]$^{2+}$ yields in a meso tetranuclear [Ni$^{II}_2$Fe$^{III}_2$] ring for *rac*-pabn and in a [Ni$^{II}_2$Fe$^{III}_2$]$_n$ chain when *R/S*-pabn are employed (pabn=N^2-N^{2}'-bis(pyridine-2-ylmethil)-1,1'-binaphthyl-2,2'-diamine , Htp= hydrotris(pyrazoly) borate).[74] In a similar manner, one meso tetranuclear ring *vs*. 1-D system were characterized for the Cu-Ln complexes, [Cu^{II}(Ldpen)(*1R,2R/1S,2S)*-Ln^{III}(NO$_3$)$_2$]$_2$ and [Cu^{II}(Ldpen)(*1R,2R*)-Ln^{III}(NO$_3$)$_2$(CH$_3$CN)]$_n$, respectively (Ldpen= 2-(((E)-3-ethoxy-2-oxybenzylidene)amino)1,2-diphenylethyl)-2-oxybenzamide), example in **Figure 5.6**.[75]

Interestingly, in these examples, the differences between the meso and the chiral forms go beyond structural and symmetric considerations and it is also reflected in their physical properties, concretely in magnetism: while the 0-D systems have SMM behaviour, the 1-D systems have Single Chain Magnet (SCM) behaviour. Noteworthy, the different dimensionality is based in how the building blocks are spatially arranged but always maintaining the inner structure and the connectivity between them. The driving force that determines the different arrangement of the subunits is unclear, but it could be related to the spatial arrangement of the ligands, which favours one or other dimensionality. Modifications on the substituents of the ligands is a usual tool to obtain different compounds in bases of the involved packing forces or intermolecular interactions, and these examples of meso/chiral isomerism could be assumed as a subtle but similar effect.

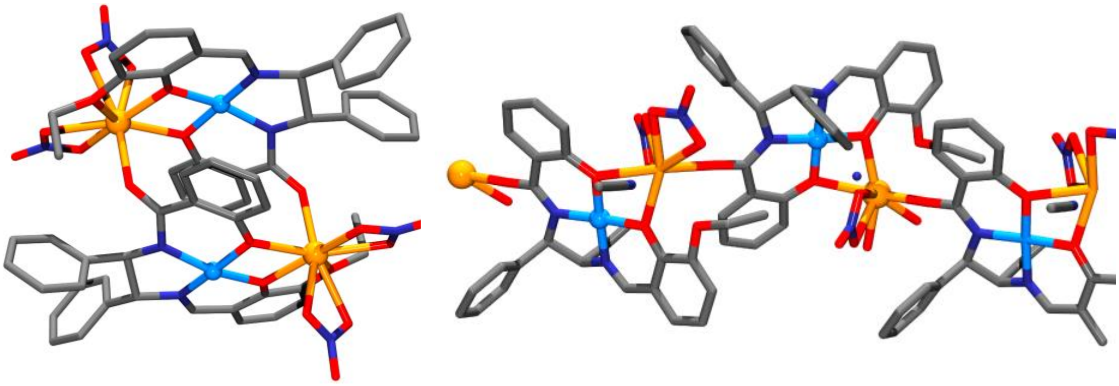

Figure 5.6. Example of meso-chiral isomerism based on a molecular centrosymmetric $[Cu^{II}_2Tb^{III}_2]$ ring with one (*RR*) and one (*SS*) ligand (left) and the 1D arrangement when all the ligands are homochiral (right). Noteworthy, all coordination spheres and bond~~s~~ parameters are very close in both cases. (From reference [75]).

In contrast, the phenomenon observed in the reported **[20]-[29]** complexes provides an unprecedented example in coordination chemistry of chiral vs. meso isomerism that, among others, involves changes in the coordination number of the lanthanide cation and do not fit with the conventional definitions of isomerism, see **Figure 5.7**.[76]

The first division of isomers is related with the question: *do they have the same connectivity?* At this point is difficult to answer because what we have one extra bond between atoms placed in the same way for the chiral and meso form. Let’s suppose that we answer “yes” to this question, so chiral/meso isomers would be a kind of *stereoisomers*. The next question would be if they are interconvertible by the rotation of a single bond, and at this point the answer is very ambiguous, because we can interconvert from one to another by “changing” a bond, but not by rotation. In our case, the ligands are identical and the packing of the racemic/chiral complexes is also identical. The only difference in the network is the symmetry group *R-3* vs. *R3* (with an inversion centre or not) and thus the phenomenon appears to be strictly intramolecular. A common point with the [NiFe] and [CuLn] complexes described above, is that the difference in energy between the chiral and the racemic systems is small. We think that, in our case, the employment of lanthanide cation is favourable because due to its weak crystal field their coordination spheres are very plastic. Among this, the size of the cation is a determinant factor: the analogous $[Mn^{II}Mn^{III}_6Na^{I}_2]$, complex **[9]** of this thesis, with a smaller cation (Mn^{II} instead of Ln^{III}) exhibits a $Mn^{II}O_6$ octahedral environment [77] whereas the complexes **[20]-[29]** made with lanthanides are large enough to establish the contact with the seventh O-donor at distances around 2.7 Å.

5.5. FERROELECTRICITY

The search of multiferrocity is a changeling and desirable coexistence of properties due to the possibility of controlling the magnetization by electronic fields and to develop electronic tuneable magnetic devices. Usually, the multiferrocity has been achieved in solid-state chemistry in oxides and thin-films[78] mainly in perovskite oxides ABO_3 where the ferroelectricty and ferromagnetism cannot rely in the same cation because the ferroelectricity is related with the mobility of the metal ion, the so-called displacive type.

Molecular materials can offer the possibility of multiferrocity in another way[79] or the observation of ferromagnetism in Prussian-Blue Analogues (PBA)[13] or by the use of interpenetrating networks to design multiferroic hybrid materials based on molecular precursors assembled in a 2-D structure.[80]

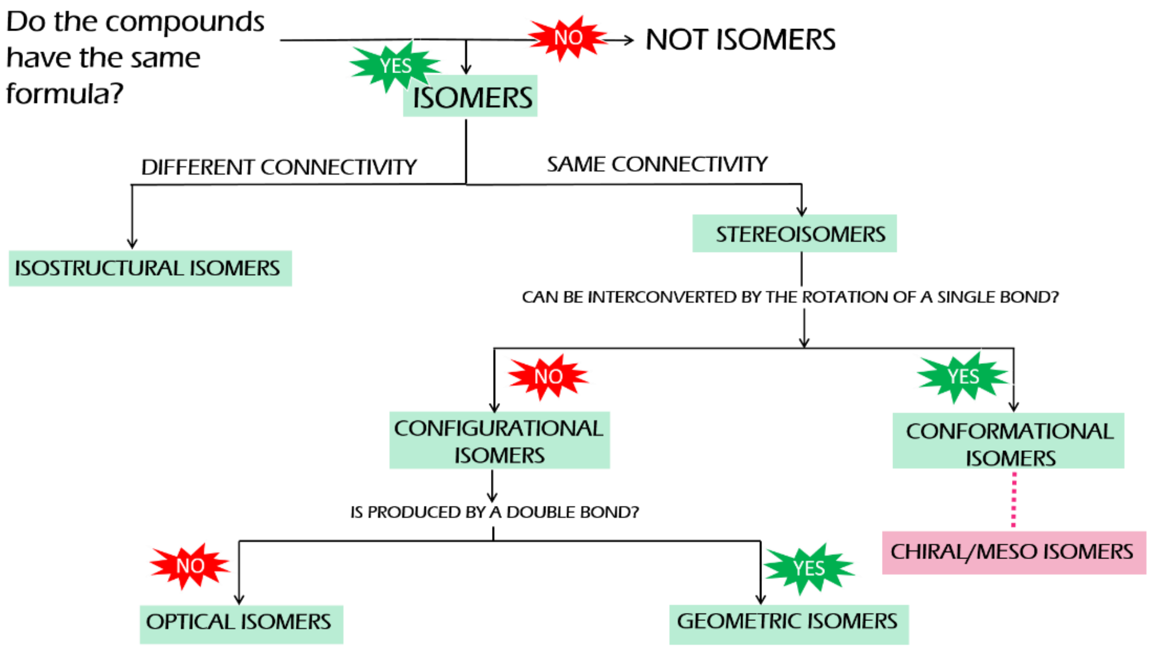
Do the compounds have the same formula?
NO
NOT ISOMERS
YES
ISOMERS
DIFFERENT CONNECTIVITY
SAME CONNECTIVITY
ISOSTRUCTURAL ISOMERS
STEREOISOMERS
CAN BE INTERCONVERTED BY THE ROTATION OF A SINGLE BOND?
NO
YES
CONFIGURATIONAL ISOMERS
CONFORMATIONAL ISOMERS
IS PRODUCED BY A DOUBLE BOND?
CHIRAL/MESO ISOMERS
NO
YES
OPTICAL ISOMERS
GEOMETRIC ISOMERS

Figure 5.7. Classic graph of the isomers classification with the position of the new isomerism type proposed.

One of the characteristics of molecular systems with respect to oxides is the crystallization in generally lower symmetry systems and in the possibility of non-centrosymmetric space groups (with no improper symmetry operations). This allows the resulting materials to exhibit specific physical properties related with their point group symmetry depicted in **Figure 5.8.** The relationship between the space group and the property is a direct consequence of the Curie Principle.[81] For this reason and because complex **[25*S*]** crystallizes in a space group that allows ferroelectricity, it was thought that the investigation of this property was a subject of interest in this thesis.

Due to the differences in the structure of the enantiomeric vs. the meso forms, a ferroelectric response can be expected derived from the transition from the apolar D_{3h} symmetry for **[25*RAC*]** to the polar C_3 symmetry of **[25*S*].** This phase transition is especially important in the search of ferroelectric properties because of the symmetry breaking, which will allow a paraelectric ↔ ferroelectric transition. Another possible approach to ferroelectricity is in a very similar way to the perovskites behaviour by changing the position of the lanthanide, **Figure 5.9.**

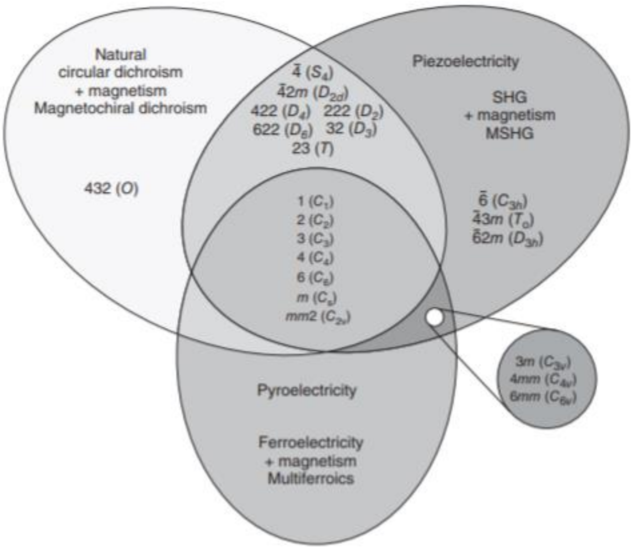
Natural
circular dichroism
+ magnetism
Magnetochiral dichroism
432 (O)
$\bar{4}$ (S_4)
$\bar{4}2m$ (D_{2d})
422 (D_4) 222 (D_2)
622 (D_6) 32 (D_3)
23 (T)
Piezoelectricity
SHG
+ magnetism
MSHG
$\bar{6}$ (C_{3h})
$\bar{4}3m$ (T_d)
$\bar{6}2m$ (D_{3h})
1 (C_1)
2 (C_2)
3 (C_3)
4 (C_4)
6 (C_6)
m (C_s)
mm2 (C_{2v})
3m (C_{3v})
4mm (C_{4v})
6mm (C_{6v})
Pyroelectricity
Ferroelectricity
+ magnetism
Multiferroics

Figure 5.8. Crystal classes and specific physical properties that could arise in non-cetrosymmetric molecules.[82]

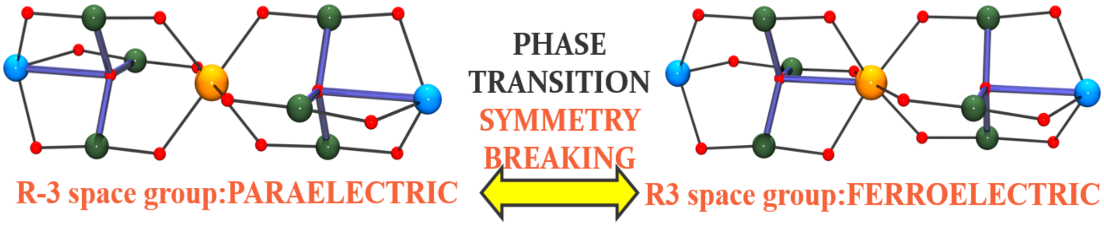
PHASE
TRANSITION
SYMMETRY
BREAKING
R-3 space group:PARAELECTRIC
R3 space group:FERROELECTRIC

Figure 5.9. Schematic representation of the possible paraelectric/ferroelectric transition for complexes **[20]-[29]**.

5.6. MAGNETIC STUDIES.

Preliminary magnetic studies have been performed on this series of compounds. The O-centered equilateral Mn^{III}_3 triangles with axial bridging chloro ligands are scarce but revealed to give typically ferromagnetic coupling, as has been demonstrated in ***Publication #5*** and ***Publication #7*** of this thesis[77, 83] and in another bibliographic examples.[84] Susceptibility measurement for the complex with the diamagnetic yttrium or europium cations in the central position of the cluster evidences ferromagnetic interaction inside the isolated triangular fragments and magnetic measurements for **[25*S*]** and **[25*RAC*]** compounds confirm antiferromagnetic interactions between the ferromagnetic Mn^{III}_3 units and the central lanthanide.

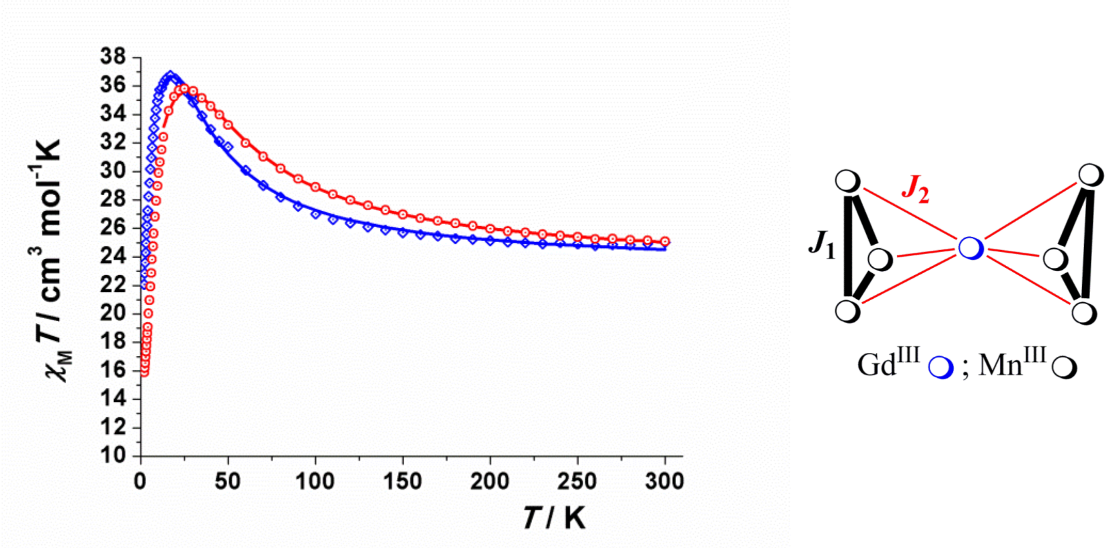

Figure 5.10. Figure 3. Left, plot of $\chi_M T$ product vs. T for **[25*S*]** (red) and [25***RAC***] (blue). Solid lines show the best fit of the data obtained with PHI program[11]. Right, coupling scheme for the Gd^{III} complexes. For the Eu^{III} and Y^{III} derivatives J_2 is zero.

As can be expected from the structural information the chiral and racemic clusters exhibit a similar but not identical susceptibility due to the relatively small changes induced in the bond parameters of the Mn$^{III}{}_3$ triangles and the Ln-O-Mn angles. **Figure 5.10** represents the susceptibility curves for the Gd^{III} derivatives **[25*S*]** and **[25*RAC*]**.

The coupling scheme inside the compound is shown in **Figure 5.10**, and the derived Hamiltonian is:

$$H = -2J_1(S_1 \cdot S_2 + S_1 \cdot S_3 + S_2 \cdot S_3 + S_4 \cdot S_5 + S_4 \cdot S_6 + S_5 \cdot S_6) - 2J_2(S_1 \cdot S_7 + S_2 \cdot S_7 + S_3 \cdot S_7 + S_4 \cdot S_7 + S_5 \cdot S_7 + S_6 \cdot S_7)$$

Isotropic fit of the experimental $\chi_M T$ data was performed with PHI program[85] in the 12-300 K range of temperature for complexes **[25*S*]** and **[25*RAC*]** in order to avoid the low T effects (D, intercluster interactions). Best fit J values are represented in **Table 5.2**. Even with the favourable C_3 axis that reduces the number of J constants, the anisotropy of the Mn$_3$ triangles (with slightly different bond parameters for the chiral systems) plays an important role at low temperature.

	[25*S*]	**[25*RAC*]**
J_1	3.4 cm^{-1}	2.3 cm^{-1}
J_2	-0.19 cm^{-1}	-0.1 cm^{-1}
G	1.90	1.90

Table 5.2. J and g values for the Gd^{III} derivatives **[25*S*]** and **[25*RAC*]**.

To ensure the ferromagnetic behaviour of the Mn^{III} triangles, the Y^{III} and the Eu^{III} derivatives **[20*R*]** and **[23*R*]** respectively, have been measured, **Figure 5.9**. The fit of the data was performed in the complete range of temperature for the Y^{III} complex and only below 60 K for the Eu^{III} complex, which at low temperature becomes diamagnetic. In these cases, we are measuring the Mn^{III} triangles for which a D contribution and/or intercluster interactions could be taken into account. These parameters are usually dependent and good fits of the experimental data were obtained considering D and neglecting zJ' or neglecting D and considering zJ'. However, the J value is always ferromagnetic and close to 3 cm^{-1} in good agreement with the values obtained for the [Gd^{III}Mn$^{III}_6$Na$^{I}_2$] clusters or the previously described [Mn^{II}Mn$^{III}_6$Na$^{I}_2$] or [Mn^{II}Mn$^{III}_3$Na^{I}] systems.

AC measurements show very weak out-of-phase signals for some of the enantiopure complexes: while the measured meso derivatives show a higher dependency of the imaginary component of the susceptibility with temperature and frequency. As an example, Dy^{III} derivatives measurements are shown in Appendix II. The anisotropic contribution of the Mn$_3$ triangles is expected to be low due to the arrangement of their easy axis, but a lanthanide contribution in the total magnetic relaxation must exist. However, the signals are too weak to deserve a more complete ac analysis.

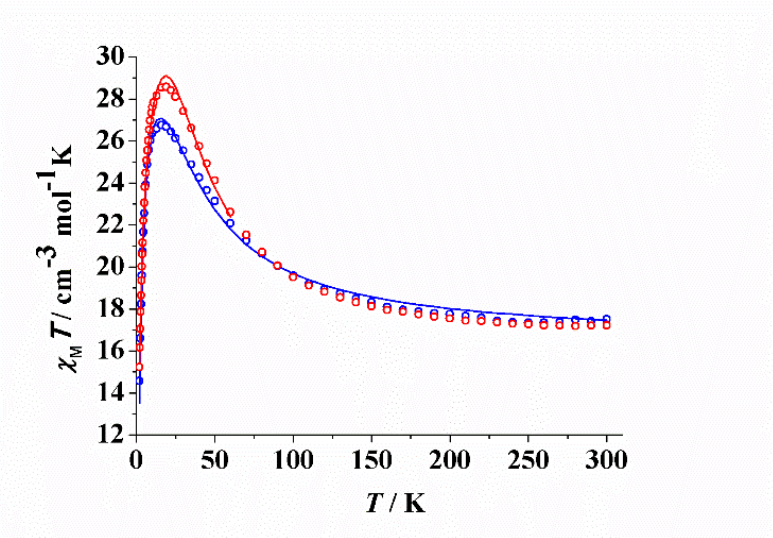

Figure 5.11. Blue circles represent the experimental curve of the Y^{III} derivative **[20],** while the blue line represents the best fit as two isolated ferromagnetic triangles. Red circles correspond to the measure for the Eu^{III} derivative, **[24]**. The red line corresponds to the best fit below 50 K where Eu^{III} has a diamagnetic behaviour.

5.7. OTHER PROPERTIES.

As a final remark, Gd^{III} complexes are known to be characterized by very broad Nuclear Magnetic Resonance (NMR) lines for all active nuclei. This is due to electronic relaxation times which are 3-5 orders of magnitude longer for this ion than for the rest of Ln^{III}. The spherical symmetry of the f^7 electronic configuration ($^8S_{7/2}$) is responsible for a relaxation typically around 1-10 ns. On the contrary, Mn^{III} has a relaxation rate in the 10-100 ps range.[86] In the heterobimetallic complex **[25]**, even neglecting direct electronic exchange between Gd^{III} and Mn^{III}, the distance between the two paramagnetic centres is short enough to determine the through-space dipolar coupling with a resulting shortening of the effective relaxation rate compared to Gd^{III}.[86] The consequence is that the proton signals of the ligand are relatively resolved and –although broad- they can be easily detected. This was observed recently in the metallocrowns systems where four Mn^{III} ions are kept in close vicinity to Ln^{III} centre.[87] Interestingly, in that case, having the complete set of ^{1}H-NMR data for the whole Ln^{III} series gave us the possibility to separate contact and pseudocontact contributions for each and every Ln^{III} complex, including Gd^{III}. This separation method which was used avoids any knowledge of the magnetic anisotropy term of the Ln^{III} ions.[88] The result of this operation confirmed that the pseudocontact shifts of Gd^{III} are indeed totally negligible and this can be considered as experimental evidence of the expected spherical symmetry of this ion. Attempts to measure the relaxation of the Gd^{III} derivative, complex **[25]** are being measured at this moment with similar results.

CHAPTER 6. FIELD INDUCED SINGLE ION MAGNET COMPLEXES DERIVED FROM KRAMERS IONS.

The complexes described in this chapter have been submitted for publication and the structure of this chapter follows the submitted text. The numbering of the complexes follows the numeration of this thesis. The chapter will present complexes **[30]-[41]** derived from the ligand **H_2L12**. Supplementary material corresponds to Appendix III.

6.1. INTRODUCTION

Research on coordination compounds containing lanthanide cations is a growing field due to their applications as magnetic resonance contrast agents,[89-91] catalysts in a wide range of reactions,[92] molecular magnetic coolers (mainly related to Gd^{III})[93] or due to their luminescent properties in the near infrared (NIR)[91,94] or in the visible regions.[95] Regarding its interesting property to exhibit slow relaxation of magnetization[96-99] with potential interest in spintronics[18] and quantum computing.[20] an increasing amount of papers have appeared since the discovery made by Ishikawa *et. al.*[42] about the magnetic properties of a single Tb^{III} complex. Lanthanides are especially good candidates for the preparation of Single Ion Magnets (SIMs) because the required large anisotropy comes from the single ion contribution. Lanthanide cations allow this features due to the relative small radius of the 4*f* shell, almost isolated from the environment: as a result, the orbital moment remains unquenched and induces spin-orbit coupling in the ground LS term. Although spin-orbit coupling is a crucial factor for the magnetic anisotropy, crystal field has also an important effect in the SIM response of lanthanide compounds as has been postulated recently by Reinhart and Long,[44] and, the fine tuning of the crystal field around the cation influences the magnetic behaviour. Low coordination numbers, proper symmetry as possible and the dilution of the paramagnetic canters to avoid intermolecular interactions are the goals to enhance the magnetic properties by avoiding the Quantum Tunneling of the Magnetization (QTM), which is the drawback in lanthanides magnetism. Control of the coordination spheres is not easy for the Ln^{III} cations because of its tendency to prefer large coordination numbers that often yields to low symmetry. Magnetic dilution has been largely explored in lanthanide clusters to take profit of the single ion contributions, specially by incorporating to the cluster a diamagnetic divalent 3*d* cation using compartmental ligands,[100] which is one the best ways to control the number and nature of metal ions in the same molecule. There is a wide variety of ligands, which allows the binucleation by using sets of different donor atoms. The hexadentate Schiff base N,N'-ethylenebis(3-ethoxysalicylaldiimine) is a popular ligand (more than 300 entries in the CCDC) by several reasons like its easy syntheses by the condensation of ethylenediamine and *o*-vanillin and its compartmental structure, with two well differentiated cavities, which allows easy and reproducible syntheses: the $O_2O'_2$ compartment can easily accommodate the large oxophilic lanthanide and the inner and smaller N_2O_2 pocket hosts adequately the 3*d* metal. Moreover, parallel syntheses starting from substituted diamines with chiral centres (cyclohexanediamine, 1,2-propanediamine or 1,2-diphenyl-ethilendiamine) become an interesting route for the synthesis of chiral ligands potentially useful for enantioselective catalysis or for introducing optical properties into the clusters. The most usual syntheses for these types of complexes is by a two-step reaction that consist of the formation of a mononuclear complex with the ligand and the 3*d* metal followed by the reaction of the mononuclear precursor with the lanthanide salt. The diamagnetic Zn^{II} cation has been the preferred 3*d* ion with this kind of ligands to promote a magnetic dilution because when the 3*d* metal is diamagnetic, the larger size of the dinuclear compounds can diminish the intermolecular interactions, mainly the dipolar ones.[101] This technique has been used with Zn^{II}/Ln^{III} clusters with Schiff bases showing different topologies and nuclearities, the vast majority of them being trinuclear $Zn^{II}\cdots Dy^{III}\cdots Zn^{II}$ systems[102a-d] and in some other few cases to other Ln^{III} cations.[102a,b,e,f] allowing a good isolation between Ln^{III} cations and SIM response. In contrast, the dinuclear systems have been studied exclusively for the $[Zn^{II}Dy^{III}]$ and $[Zn^{II}Tb^{III}]$ cases.[103] On the other hand, also has been demonstrated recently that the diamagnetic Zn^{II} can influence the electronic density distribution of the coordinating ligands around the lanthanide cation[104] (mainly for the bridging O-donors), influencing the SMM response and specially the direction of the *g* tensor of the lanthanide by modifying its environment.[44,45,105] However, the drawback of this magnetic dilution method is that the coordination of Zn^{II} in the case of salen-type ligands is square pyramidal with the four basal sites occupied by the Schiff base and one axial site linking anions or solvent molecules favouring the presence of hydrogen bonds between molecules and reducing the effective magnetic isolation. For this reason, we decided to try a better magnetic dilution for $[M^{II}Ln^{III}]$ systems with salen-type Schiff bases and trying to reduce the intermolecular interactions by replacing the Zn^{II} cation, with usually five coordination positions, by the Ni^{II} cation, which prefers the square-planar coordination with these types of ligands and avoids the undesired intermolecular H-bonds. Even the core with diamagnetic Ni^{II} and this kind of Schiff bases has been prepared before, dynamic magnetic measurements have been reported only in one case[106] for Ln = Dy^{III} and Tb^{III}. In general terms, magnetic dilution has been tried with Zn^{II}, Mg^{II}, Ca^{II}, $Al^{III,}$, low-spin Co^{III} or square-planar Ni^{II}, being the later the less studied.[104a]

On the basis on the above considerations and to explore the dynamic magnetic properties of the $[M^{II}Ln^{III}]$ core for the complete *f*-series with the two diamagnetic Zn^{II} and Ni^{II} cations, we decided to design chiral heterometallic $[M^{II}Ln^{III}]$ systems using the mentioned two steps sequential reaction of enantiomerically pure **H_2L12** Schiff base (**Figure 6.1**) with Ni^{II} or Zn^{II} followed by the binucleation with the lanthanide.

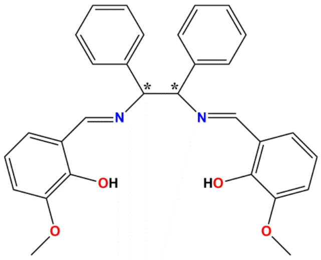

Figure 6.1. Structural formula of **H_2L12** ligand. Asterisks denote the chiral centres.

The procedure allowed the characterization of two series of $[Ni^{II}Ln^{III}(L12)(NO_3)_3]$ neutral complexes in which Ln^{III} = Ce **[36*RR*]**, Nd **[37*RR*]**, Eu **[38*RR*]**, **[38*SS*]**, Dy **[39*RR*]**, Er **[40*SS*]** and Yb **[41*SS*]** and $[Zn^{II}Ln^{III}(L12)(MeOH)(NO_3)_3]\cdot MeOH$ dimers in which Ln^{III} = Ce **[30*RR*]**, Nd **[31*RR*]**, Eu **[32*RR*], [32*SS*]**, Dy **[33*SS*]**, Er **[34*SS*]**, Yb **[35*RR*]**. Single crystal X-ray diffraction demonstrates that the Zn^{II} family of complexes suffers a two-step loss of solvents, yielding to the intermediate [Zn^{II}Eu^{III}(L12)(MeOH)(NO$_3$)$_3$]·1/2 MeOH **[32*RR*b]** and a further loss of the coordinated methanol and the incorporation of two water molecules [Zn^{II}Ln^{III}(L12)(H$_2$O)(NO$_3$)$_3$]·H$_2$O **[32*RR*c]**. The new complexes have been characterized by ECD spectroscopy and susceptibility measurements which revealed slow relaxation of the magnetization under an applied external magnetic field in the two series for the oblate Ce^{III}, Nd^{III} and Dy^{III} complexes whereas the prolate Er^{III} and Yb^{III} show only clear out-of-phase signals for the [Ni^{II}Ln^{III}] core, suggesting that Ni^{II} diamagnetic cation promotes a most efficient magnetic dilution by reducing the intermolecular interactions.

6.2. EXPERIMENTAL

X-ray Crystallography. Prismatic crystals of **[32*RR*]**, **[32*SS*]**, **[38*RR*]** and **[38*SS*]** were used for the single crystal X-ray crystallographic analysis. **[32*SS*b]** and **[32*SS*c]** were measured on the same crystal after exposure of **[32*SS*]** at open air for 48 h and one week, respectively. Crystal data are summarized in Appendix III, **Tables AIII.1 and AIII.2**.
Comparison between the calculated spectrum from the single crystal structure of the enantiomers of compounds **[38*RR*]** / **[38*SS*]** and the experimental spectra for the whole series of powdered [Ni^{II}Ln^{III}] samples gives a perfect match which confirms the isostructurality among them, **Figure 6.2**.

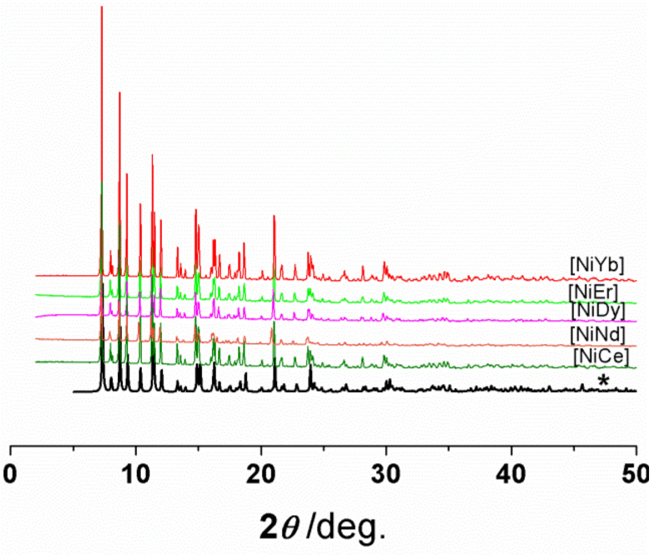

Figure 6.2. Powder X-ray spectra for the [Ni^{II}Ln^{III}] series of complexes **[36]-[41]**. (*) indicates the spectrum calculated from the single crystal data of the [Ni^{II}Eu^{III}] complexes **[38].**

The powdered samples of the series of complexes [Zn^{II}Ln^{III}] **[30]-[35]** revealed to be also isostructural among them but, surprisingly, their spectra were completely different of the calculated spectrum from single crystal diffraction of **[32*RR*]** /[32*SS*], **Figure 6.3.**

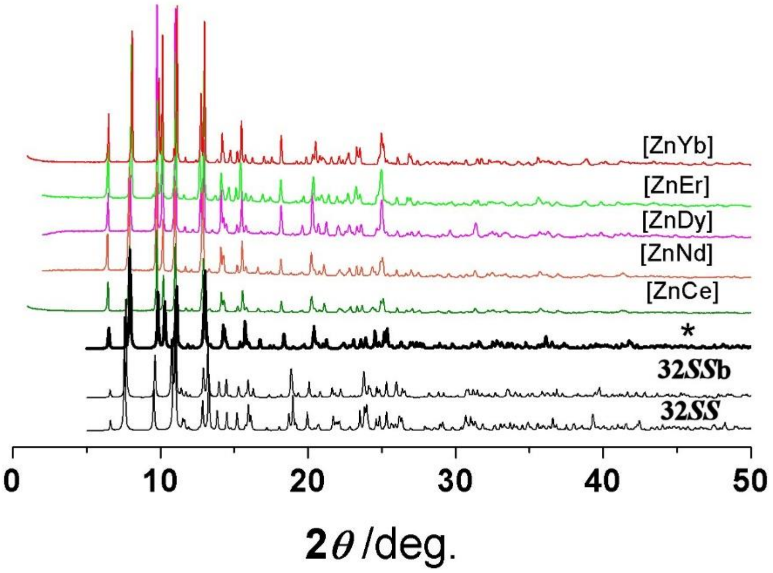

Figure 6.3. Powder X-ray spectra for the [Zn^{II}Ln^{III}] series of complexes **[30]-[35]**. The spectra plotted in black, bold (*) was calculated from single crystal data of the [Zn^{II}Eu^{III}] structure **[32*SS*c]**. Simulated spectra from single crystal structures **[32*SS*]** and **[32*SS*b]** are shown below **[32*SS*c]**.

To check if the problem was due to the loss of solvent molecules, a new crystal of **[32*SS*]** was measured immediately after extraction of the mother liquor and after checking that the structure was the same, another single crystal measurement was made after 48 h of exposure at open air. The new structure **[32*SS*b]** shows a partial loss of the one half of the crystallization methanol molecules but the simulated powder spectra was quite similar to **[32*SS*]**, **Figure 6.3**. This brought us to do a third collection of data after one week of exposure at open air and the resulting structure **[32*SS*c]** revealed the complete removal of the crystallization solvent and also that the coordinated methanol molecules were substituted by water from the ambient moisture. The calculated powder spectra agreed with those obtained from the powdered samples employed for the instrumental measurements, **Figure 6.3**. From these data, the last structure **[32*SS*c]** and its corresponding molecular weight must be assumed as the most adequate to analyse the further measurements.

6.3. SYNTHESES

6.3.1. Complex choice.

One cation of intermediate size (Eu^{III}) was selected to obtain the X-ray single crystal structures. The remainder complexes were characterized by powder X-ray diffraction showing to be isostructural and thus, the full resolution of the remainder structures was not necessary for the purposes of this work. For the selected Eu^{III} complexes both enantiomers were synthesized and structurally characterized whereas for the other cations only one enantiomer was synthesized to check their emissive properties. Magnetic measurements were performed for one of the enantiomers because they must give identical response. Following the same experimental procedure, the Pr^{III}, Sm^{III}, Tb^{III}, Ho^{III} and Tm^{III} derivatives also were prepared but they do not gives any spectroscopic (VIS or NIR luminescence) or out-of-phase magnetic response (for the non-Kramer cations Tb^{III}, Ho^{III} and Tm^{III}) and to avoid unnecessary text, have not been included in the list of reported complexes.

6.3.2. Synthesis of the ligand **H$_2$L12** and complexes **[30]-[41]**.

H$_2$L12. A solution of 0.304 g (2 mmol) of *o*-vanillin and 0.212 g (1 mmol) of (*RR*) or (*SS*)-1,2-diphenyl ethylenediamine in 10 mL of methanol was refluxed for six hours. The resulting solution of the Schiff base was diluted to a volume of 40 mL and employed directly to synthesize the derived complexes without the isolation of the solid ligand. Similar syntheses were previously reported.[102, 103]

[NiLn(L12)(NO$_3$)$_3$]: the syntheses are common for all the lanthanide complexes **[36]-[41]**. 0.062 g (0.25 mmol) of nickel acetate tetrahydrate were solved in the minimum amount of methanol, and to this solution were added 10 mL (0.25 mmol) of the previously prepared solution of **H$_2$L12**. The resulting dark orange solution was refluxed for 1 hour. Over this solution 0.25 mmol of the corresponding lanthanide nitrate n-hydrate were added in solid. After the dissolution of the lanthanide salt, the colour changes to light orange and, after some minutes, it starts to precipitate a red powder of the corresponding complex. Well-formed orange crystals for X-ray diffraction of the europium complex were obtained by vapour diffusion with diethyl ether after a few days. Elemental analysis for **[38*RR*]**: C, 41.17; N, 8.00; H, 2.99%. Found: C, 41.3; N, 7.8; H, 3.1%. Relevant IR bands: weak C-H bands at 3058/3030/2955/2853 cm^{-1}, the C=N stretching varying from 1610 to 1630 cm^{-1} for the whole series of compounds and the N-O stretching of the nitrate at 1384 cm^{-1}. One representative spectrum is shown in Appendix III, **Figure AIII.1.**

[ZnLn(L12)(MeOH)(NO$_3$)$_3$]·MeOH: the syntheses were common for all the lanthanide complexes **[30]-[35]**. 0.074 g (0.25 mmol) of zinc nitrate were solved in the minimum amount of methanol and added to 10 mL (0.25 mmol) of the previously prepared solution of **H$_2$L12** and the resulting yellow solution was refluxed for 1 hour. 0.25 mmol of the corresponding hydrated lanthanide nitrate were added in solid. Well-formed yellow crystals for X-ray diffraction of the **[32*RR*]** and **[32*SS*]** complexes were obtained by vapour diffusion with diethylether. The solubility of some of the [Zn^{II}Ln^{III}] complexes is slightly different than of the [Ni^{II}Ln^{III}] systems, and they only crystallize by vapour diffusion when the solutions were previously reduced to one third of their original volume under reduced pressure. Elemental analysis for **[32*SSc*]**: C, 39.26; N, 7.63; H, 3.29%. Found: C, 40.1; N, 7.7; H, 3.1%. IR spectra are similar but not identical to the Ni^{II} complexes. One representative spectra of each series is shown in **Figure AIII.1.**

A faster synthesis can be performed heating a methanolic solution of *o*-vanillin and the 1,2-diphenyl ethylendiamine at 80° in a microwave furnace, followed by ten minutes at the same temperature after the addition of the 3*d* salt and ten additional minutes at the same temperature after the addition of the lanthanide salt.

6.4. STRUCTURAL DESCRIPTION

The image-mirror structures of the pairs of the enantiomeric [$Ni^{II}Eu^{III}$] **[38*RR*]** / **[38*SS*]** and [$Zn^{II}Eu^{III}$] **[32*RR*]** / **[32*SS*]** complexes contain two non-equivalent A/B molecules in the unit cell with minor differences in the bond parameters. To avoid repetitive text, the following description will be referred to the A-molecule of one of the enantiomers, assuming that there are minimal differences with the corresponding B-molecule or respect the other enantiomer.

[NiEu(L12)(NO_3)$_3$] [38]. A partially labelled plot of **[38*RR*]** is shown in **Figure 6.4** and selected bond parameters are summarized in **Table 6.1**. The representative structure of **[38*RR*]** consist of neutral [$Ni^{II}Eu^{III}$] dinuclear complexes in which the Ni^{II} cation is coordinated to the inner N_2O_2 pocket of the Schiff base while the most hard Eu^{III} cation is coordinated to the external phenoxo/methoxy O_2O_2' pocket. The Ni^{II} cation is tetracoordinated (square planar) with Ni-N / Ni-O distances in the short 1.806-1.843 Å range and N-Ni-O bond angles larger than N-Ni-N and O-Ni-O angles (~95º vs ~85º), whereas the Eu^{III} cation completes its coordination sphere with three bidentate nitrato ligands, being the Eu^{III}-O(nitrate) slightly larger than Eu^{III}-O(phenoxo) and Eu^{III}-O(methoxy) distances. SHAPE[107] calculations indicate that the coordination polyhedron around the Eu^{III} cation is close to an ideal sphenocorona (C_{2v}, CShM = 3.24, **Table AIII.3**), distorted due to the low bite of the bidentate nitrato ligands, **Figure 6.4**.

The Ni^{II}-Schiff base fragment is essentially planar. Dihedral angle between the mean [NiN_2O_2] molecular plane and the plane defined by O2/O3/Eu1 is 15.9º and consequently the Eu^{III} ion is displaced 0.56 Å out of the [NiN_2O_2] plane.

The molecules are well isolated and in addition to weak C-H···O H-bonds the only intermolecular interactions consist of CH-π (ring) contacts, **Figure 6.5**. This kind of supramolecular interaction between aromatic rings acting as H-bond acceptor and -CH groups as H-donor plays an important role in biological systems and often is determinant in the crystal packing of molecular compounds.[108] In this case, the interaction is established between one H-atom of one of the methyl groups of the **L12^{2-}** ligands which is directed towards the centroid of one phenyl group of the neighbouring molecule.

Noteworthy, this interaction generates chains of strictly A or B molecules. Distance between H30B to the centroid of the phenyl ring C17A/C22A is 2.644 Å with a C30A-H30B···centroid angle of 148.9º. The non-equivalent B molecules show similar parameters, being 2.596 Å the distance between H1BC to the centroid of the phenyl ring C17B/C22B and 163.3º the C30A-H30B···centroid angle.

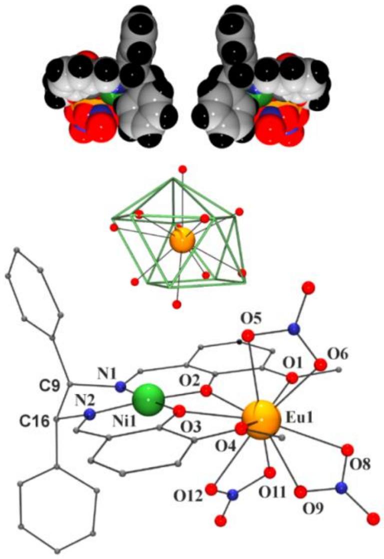

Figure 6.4. Top, spacefill mirror image of the enantiomeric **[38*RR*]** and **[38*SS*]** complexes. Down, ideal coordination polyhedron *vs*. real O-donors sites for the Eu^{III} cation and partially labelled plot of complex **[38*RR*]**. Colour key for all figures: Zn^{II} firebrick, Ni^{II} green, Eu^{III} orange, O red, N navy, C grey.

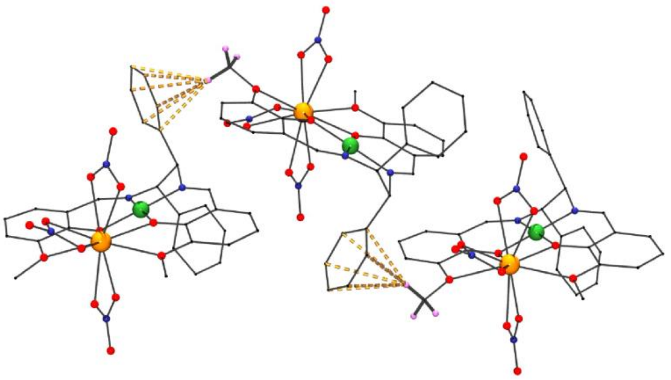

Figure 6.5. CH-π(ring) interactions between the dinuclear Ni^{II}Eu^{III} complexes that determines its 1-D arrangement in the network.

Eu(1)-O(1)	2.552(7)	Ni(1)-N(1)	1.806(7)
Eu(1)-O(2)	2.389(6)	Ni(1)-N(2)	1.840(6)
Eu(1)-O(3)	2.417(4)	Ni(1)-O(2)	1.838(6)
Eu(1)-O(4)	2.550(6)	Ni(1)-O(3)	1.843(6)
Eu(1)-O(5)	2.504(6)	Ni(1)-O(2)-Eu(1)	106.7(3)
Eu(1)-O(6)	2.421(5)	Ni(1)-O(3)-Eu(1)	105.4(2)
Eu(1)-O(8)	2.593(6)	Ni(1)···Eu(1)	3.406(1)
Eu(1)-O(9)	2.480(6)		
Eu(1)-O(11)	2.472(6)		
Eu(1)-O(12)	2.538(5)		

Table 6.1. Selected bond distances (Å) and angles (º) for the A-molecule of **[38*RR*]**.

[ZnEu(L12)(MeOH)(NO_3)$_3$]·MeOH [32*RR*/32*SS*·MeOH]. As in the above described [$Ni^{II}Eu^{III}$] complexes, the structures of the enantiomers **[32*RR*]** and **[32*SS*]** contain two similar but non-equivalent dimers (labelled A/B) in the unit cell and the description will also be cantered on **[32*RR*]**(A) molecule. The Zn^{II} cation is pentacoordinated with a square pyramidal environment, which is defined by the N_2O_2 donors of the Schiff base and one methanol molecule in the apical coordination site, **Figure 6.6**. Main bond parameters are summarized in **Table 6.2**. As consequence of this coordination, the Zn^{II} ion is placed 0.540 Å out of the plane defined by the N_2O_2 atoms. Bond distances are slightly larger than for the Ni^{II} case, ranging between 1.984-2.047 Å. The Eu^{III} cation is coordinated to two O-phenoxo donors that act as a bridge with the Zn^{II} cation, two O-methoxy donors and three bidentate nitrate ligands. The O2/O3/Eu1 plane and the mean plane defined by the base of the coordination polyhedron of the Zn^{II} cation (N_2O_2 plane) dihedral angle is 23.6° and the Eu^{III} cation is placed 0.77 Å out of the main molecular plane. The presence of methanol molecules in the structure generates a set of hydrogen bonds between the coordinate methanol, the crystallization solvent and one nitrate of the neighbour molecule and leads to the formation of one-dimensional zigzag AB chains running parallel to the crystallographic *c* axis, as it is shown in **Figure 6.6**. Interactions between chains consist of CH-π (ring) interactions established between two H-atoms of the methyl groups of the coordinated methanol and the phenyl rings of the neighbour molecule, with distance to the centroids of the rings of 3.025 and 3.275 Å, **Figure AIII.2**.

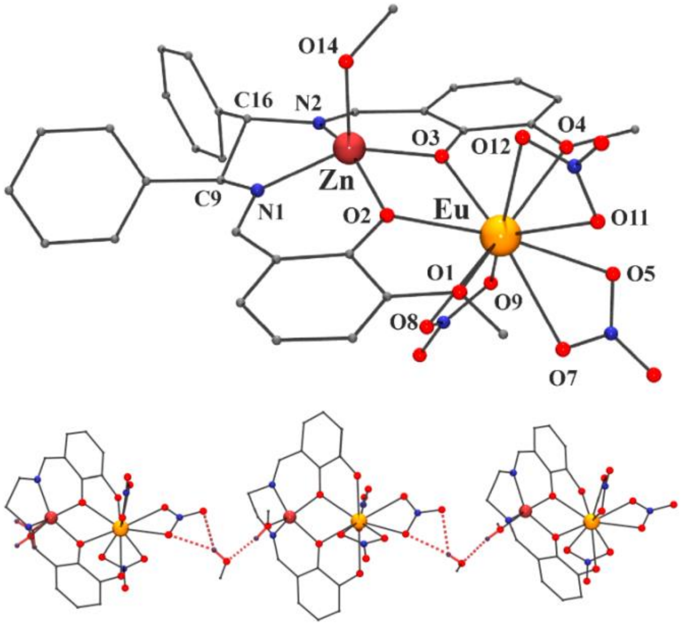

Figure 6.6 Top, partially labelled plot of the molecular structure of complex **[32*SS*]**. Bottom, 1D arrangement of dinuclear units linked by H-bonds mediated by the crystallization methanol molecules. Phenyl rings and methoxy groups have been suppressed for clarity.

[ZnEu(L12)(MeOH)(NO_3)$_3$]·1/2 MeOH [32*SS*b·0.5MeOH]. The structure of complex **32*SS***·MeOH after exposition to open air during 48h is practically equal to **[32*SS*]** at molecular level. The Zn^{II} and Eu^{III} environments are very close to the above described and the changes in the bond parameters are minimal. The structure is shown in **Figure AIII.3**

of Appendix III and bond parameters are summarized in **Table AIII.4**. The main difference between **[32*SS*b]** and **[32*SS*]** consist of the loss of one half of the crystallization methanol molecules involved in the intramolecular H-bonds that determine the 1-D arrangement of dimers. In this case one of the interactions remains like in **[32*SS*]** but the partially loss of solvent promotes the direct H-bond between the methanol molecule coordinated to the Zn^{II} cation with one nitrate anion coordinated to the neighbouring molecule, resulting in a chain of dimers linked alternatively by the two kind of H-bonds, **Figure 6.7**.

Eu(1)-O(1)	2.703(4)	Zn(1)-N(1)	2.045(4)
Eu(1)-O(2)	2.337(3)	Zn(1)-N(2)	2.020(4)
Eu(1)-O(3)	2.368(3)	Zn(1)-O(2)	1.981(3)
Eu(1)-O(4)	2.608(3)	Zn(1)-O(3)	1.991(4)
Eu(1)-O(5)	2.543(4)	Zn(1)-O(14)	2.006(4)
Eu(1)-O(7)	2.568(4)	Zn(1)-O(2)-Eu(1)	108.2(1)
Eu(1)-O(8)	2.487(6)	Zn(1)-O(3)-Eu(1)	106.6(1)
Eu(1)-O(9)	2.469(5)	Zn(1)···Eu(1)	3.503(1)
Eu(1)-O(11)	2.446(4)		
Eu(1)-O(12)	2.505(4)		

Table 6.2. Selected bond distances (Å) and angles (º) for the A-molecule of **[32*SS*].**

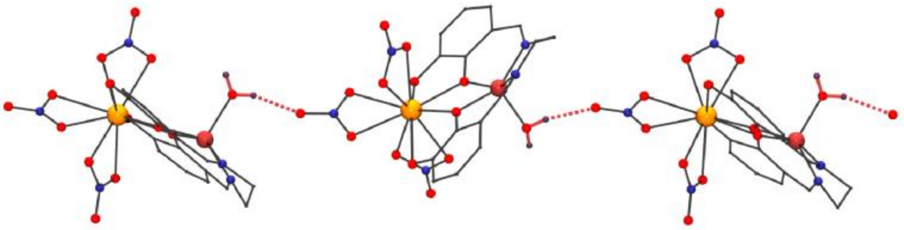

Figure 6.7. 1D arrangement of dinuclear units linked by H-bonds mediated by the crystallization methanol molecules alternated with direct H-bonds for **[32*SS*b]**. Phenyl rings and methoxy groups have been suppressed for clarity.

[ZnEu(L12)(H_2O)(NO_3)$_3$]·H_2O (32*SS*c·H_2O). The structure of **[32*SS*]** after air exposition for one week shows a similar dinuclear molecular structure but with different environment around the Zn^{II} cation, which in this case shows a water molecule coordinated in the apical position of its square pyramidal environment. A labelled plot of the structure is depicted in **Figure 6.8** and main bond parameters are summarized in **Table 6.3**. The Zn^{II} cation is placed 0.53 Å over the N_2O_2 base of the square pyramid and the Eu^{III} cation 0.60 Å over this plane. All the crystallization methanol molecules are lost and a crystallization water molecule has been incorporated to the structure. The crystallization water molecule forms two strong intramolecular H-bonds with the coordinated water and one O-atom from one of the nitrates with O14···O1W and O12···O1W distances of 2.66(2) and 2.62(2) Å respectively. The dinuclear entities are in this case linked in a regular fashion by H-bonds between the coordinated water molecule and one O-atom of one of the nitrates of the neighbouring molecule, **Figure 6.8**, forming a chain of dinuclear complexes linked by H-bonds that runs along the *c* crystallographic axis.

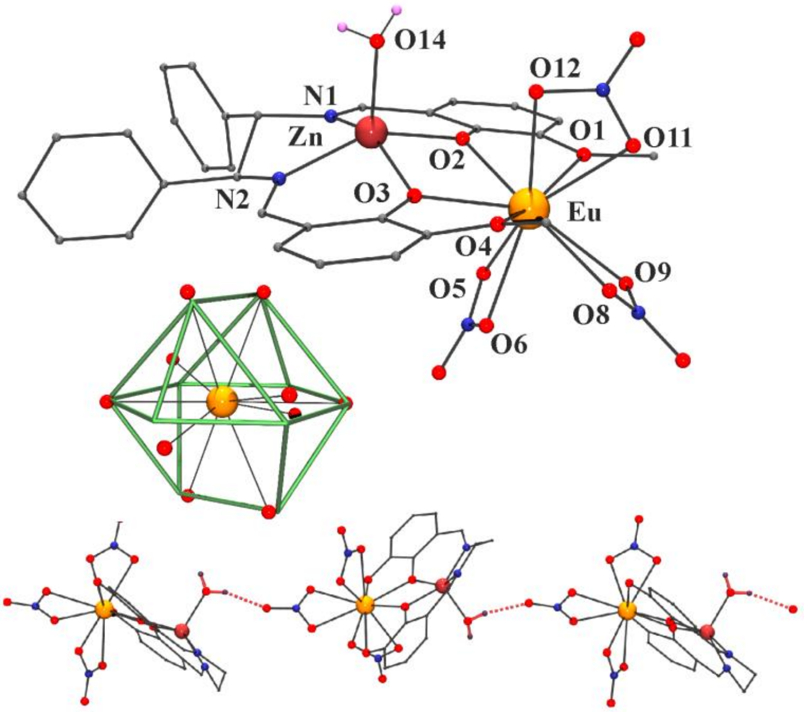

Figure 6.8. Top, partially labelled plot of the molecular structure of complex **[32*SS*c]**. Down, ideal coordination polyhedron *vs*. real O-donors sites for the Eu^{III} cation and regular 1D arrangement of dinuclear units linked by direct H-bonds. Phenyl rings and methoxy groups have been suppressed for clarity.

Eu(1)-O(1)	2.606(7)	Zn(1)-N(1)	1.98(1)
Eu(1)-O(2)	2.380(7)	Zn(1)-N(2)	2.067(7)
Eu(1)-O(3)	2.348(6)	Zn(1)-O(2)	1.988(7)
Eu(1)-O(4)	2.693(8)	Zn(1)-O(3)	1.995(8)
Eu(1)-O(5)	2.454(9)	Zn(1)-O(14)	1.990(9)
Eu(1)-O(6)	2.444(9)	Zn(1)-O(2)-Eu(1)	106.8(3)
Eu(1)-O(8)	2.537(9)	Zn(1)-O(3)-Eu(1)	107.8(3)
Eu(1)-O(9)	2.554(8)	Zn(1)···Eu(1)	3.515(1)
Eu(1)-O(11)	2.47(1)		
Eu(1)-O(12)	2.52(1)		

Table 6.3. Selected bond distances (Å) and angles (°) for the A-molecule of **[32*SS*c]**.

SHAPE[107] calculations indicate that the coordination polyhedron around the Eu^{III} cation is closer in this case to an ideal tetradecahedron (TD-10) (C_{2v}, CShM = 2.78, Appendix III, **Table AIII.3**), distorted due to the low bite of the bidentate nitrato ligands, **Figure 6.8**. Comparison with the structure of complexes **[38]** evidences a key point for the further magnetic studies: the substitution of the Zn^{II} by Ni^{II} is far to be innocent because induces changes in the planarity and conformation of the ligand, on the coordination sphere of the lanthanide and mainly, in the intermolecular interactions.

6.4.1. Ligand conformation.

For the chiral (*R*,*R* / *S*,*S*) ligands there are two conformational possibilities related to the relative position of the phenyl rings, that can be placed on the main molecular plane or perpendicular to this plane, as occurs for the [$Zn^{II}Eu^{III}$] and [$Ni^{II}Eu^{III}$] complexes, **Figure 6.9.** The in-plane conformation seems to be the most usual and has been observed in several mononuclear complexes containing VO^{II}, octahedral V^{IV} or dinuclear $Cu^{II}Gd^{III}$ or $Zn^{II}Dy^{III}$ dimers[103c,109] whereas the perpendicular arrangement of the phenyl groups has only been observed in one case for Ni^{II}.[110] This difference does not come from the crystallization process of the dinuclear complex and must be related to the formation of the NiL12 or ZnL12 precursor because the free rotation around the C-C bond is only possible while the ligand remains in solution until it reacts with the corresponding cation and adopts a fixed conformation.

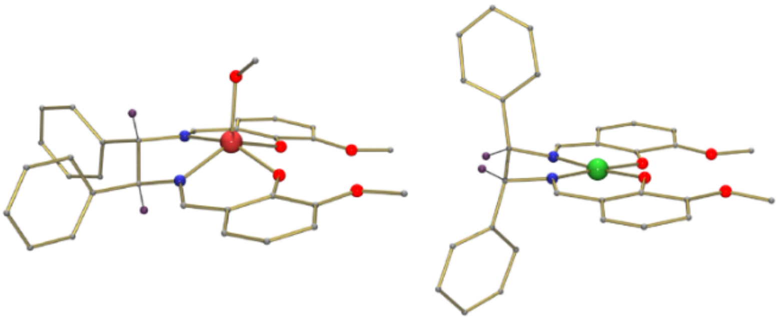

Figure 6.9. Conformations of the phenyl rings for the **L12**$^{2-}$ ligand: in plane for the coordinated Zn^{II} (left) and perpendicular for the Ni^{II} (right).

6.5. CHIRALITY TRANSFER AND ELECTRONIC CIRCULAR DICHROISM.

Transference of chirality from the chiral ligand to the metallic centres is poor in this case because in spite that the coordination polyhedra around the cations show a mirror image between the ***RR*** and ***SS*** complexes, there are minimal differences as for a square planar (Ni^{II}) or square pyramidal (Zn^{II}) environments. Equally the differences around the lanthanide cation are small and limited to the relative torsion of the nitrato groups and thus, the chiroptical properties must be mainly related to the ligands. Electronic circular dichroism (ECD) spectra in dichloromethane or methanolic solution were performed for the representative enantiomeric pairs of **[32]** and **[38]** respectively. The spectra of **[38]** show the same bands than **[32]** but shifted 25 nm to larger wavelengths and with different intensity that must be attributed to the different conformation of the phenyl rings, **Figure 6.9**. The representative ECD spectra for the pairs of complexes **[38*RR*]** / **[3*SS*]** and **[32*RR*]** / **[32*SS*]** are plotted in **Figure 6.10** and their mirror image confirms the enantiomeric nature of the reported complexes. The spectrum for the $Ni^{II}Eu^{III}$ complexes was poor due to the low solubility of the complexes but exhibits positive Cotton effect at λ_{max} = 410, 370(sh) and 290 nm and a negative band at 325 nm for **[38*RR*]** and the bands with opposite sign for **[38*SS*]**. The spectrum of the Zn^{II}Eu^{III} complex **[32*RR*]** shows positive Cotton effect at 218, 265, 342 and 395 nm a weak negative band at 235 and an intense absorption at 300 nm for **[32*RR*]** and a mirror image for **[32*SS*]**.

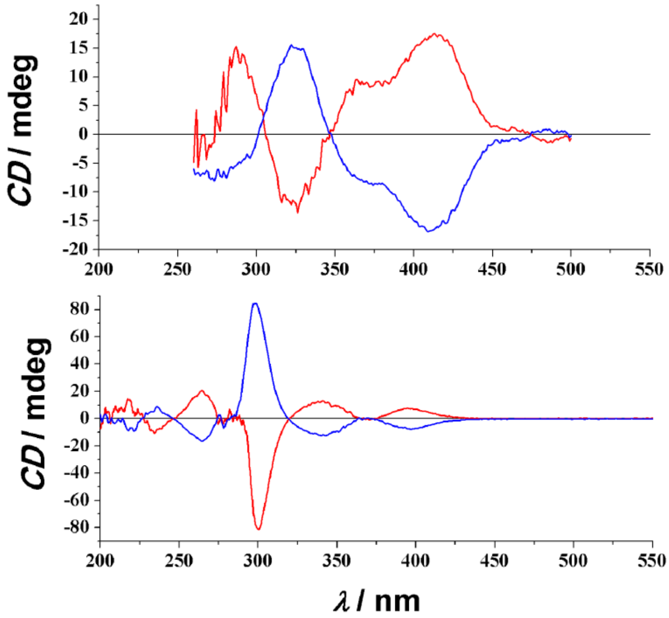

Figure 6.10. Solution EDC spectra for the Ni^{II}Eu^{III} pair of complexes **[38*RR*]** and **[38*SS*]** (top) and the Zn^{II}Eu^{III} pair **[32*RR*]**, **[32*SS*]** (bottom). (*R*,*R*) enantiomers, red lines; (*S*,*S*) enantiomers, blue lines.

6.6. LUMINESCENCE MEASUREMENTS

The Zn^{II} complexes with Schiff bases are good antenna to transfer energy to the Ln^{III} cations and often the [Zn^{II}Ln^{III}Zn^{II}] or [Zn^{II}Ln^{III}] related systems have shown luminescence.[102,103] The emissive properties of the reported complexes and the [NiL12] and [ZnL12] precursors were checked in the NIR and in the visible region. Unfortunately, only the [ZnL12] mononuclear complex exhibits the typical green luminescence with an emission band centred at 489 nm under excitation at 380 nm, **Figure AIII.4**, and for the dinuclear complexes the Ln^{III} emission was completely quenched.

6.7. MAGNETIC MEASUREMENTS

The magnetic susceptibility for complexes **[30]-[41]** in the form of $\chi_M T$ product *vs.* temperature performed on polycrystalline samples in the 2-300 K range is shown **Figure AIII.5**. $\chi_M T$ at room temperature are close to the expected values for the corresponding magnetically independent lanthanide cations $^2F_{5/2}$ (Ce^{III}, 0.80 cm^{3}mol^{-1}K), $^4I_{9/2}$ (Nd^{III}, 1.60 cm^{3}mol^{-1}K), (Dy^{III}, 14.17 cm^{3}mol^{-1}K) $^4I_{15/2}$ (Er^{III}, 11.48 cm^{3}mol^{-1}K) and $^2F_{7/2}$ (Yb^{III}, 2.57 cm^{3}mol^{-1}K), in agreement with the null contribution of the diamagnetics square planar Ni^{II} and square pyramidal Zn^{II} cations. In all cases, the $\chi_M T$ product remains almost constant until the temperature arrives to 150 K, where the values start to steadily decrease for complexes **[30], [31], [33], [34], [35], [36], [37], [39], [40]** and **[41]** due to the progressive depopulation of the M_J states and, at low temperature, the possibility of weak antiferromagnetic interactions between molecules, tending to finite values.[111] Theoretically, the Eu^{III} analogues, **[32]** and **[38]**, should not exhibit any magnetic moment because Eu^{III} has a $^7F_0$ ($J = 0$), although some contribution from thermally accessible levels appear as usual at high temperature, and $\chi_M T$ tends to zero at low T.

Recently Lloret et *al*,[112] reported a series of lanthanide-containing complexes with an ideal D_{3h} symmetry (trigonal axial symmetry) where the magnetic properties can be simplified supposing implicitly a regular distribution of the M_J states using the Hamiltonian:

$$\mathcal{H} = \lambda LS + \Delta[L_z^2 - L(L+1)/3] + \beta H(-kL+2S) \qquad \mathbf{(6.1)}$$

in which the first term describes the spin-orbit coupling, the second one is about the axial ligand field component and the third one is the Zeeman effect, parameterized with the spin-orbit coupling parameter λ, the gap between M_L components, Δ, and the orbital reduction parameter, k. To check if the above Hamiltonian is able to reproduce the experimental data in lower symmetries giving information of the ground M_J state, we implemented it in PHI program.[85] This Hamiltonian is not enough accurate in low symmetry but the $\chi_M T$ simulations were surprisingly good for the most of the complexes, **Figure-AIII.5**. In our opinion the absolute fit values must be assumed with large caution, but allowed us to give a reliable indication about the sign of Δ, profiting that different Δ sign gives clearly different shaped $\chi_M T$ vs temperature curves, **Figure AIII.6**

In order to study the dynamic magnetic properties, temperature and frequency variable ac measurements were performed on polycrystalline samples of all the compounds. No maxima appear in the χ_M'' vs. T measurements above 1.8 K for any of the [$Zn^{II}Ln^{III}$] or [$Ni^{II}Ln^{III}$] compounds indicating that the magnetic moments completely follow the magnetic field due to the fast reversal of the magnetization. Because of tunnelling is a common effect in lanthanide complexes in very distorted environments, we decided to explore the effect of an external dc field on the relaxation processes trying to avoid the QTM. The preliminary measurements were performed scanning at 10 Hz and 1000 Hz frequencies under different dc fields between 500 and 2000 G and selecting the field that induces the clearest signal, **Figure AIII.7**. In light of these measurements fields of 500 G were selected for **[36]** and **[41]**, 2000 G for **[31]** and 1000 G for the remainder compounds. Under the indicated fields, clear dependence of the out-of-phase signal *vs* frequency and temperature was found for the two series of complexes for the cations Ce^{III} (**[30], [36]**), Nd^{III} (**[31]**, **[37]**), Dy^{III} (**[33]**, **[39]**) and only for the for the Er^{III} (**[40]**) and Yb^{III} (**[41]**) derivatives for the [$Ni^{II}Ln^{III}$] series (**Figure 6.11** and **AIII.8-AIII.9**, evidencing the suppression of a faster relaxation path in Kramers doublets. Only very weak tails were observed for the Er^{III}, **[34]** and Yb^{III}, **[35]**, [$Zn^{II}Ln^{III}$] complexes.

Since the discover of the slow relaxation of the magnetization in coordination compounds,[17] the magnetic memory has been attributed to complexes with a negative anisotropy like **[33]** or **[39]**, due to the presence of energy barriers separating states with opposite spin orientations along the anisotropy axis. However, complexes **[30], [31], [36], [37], [40]** and **[41]** present slow relaxation of the magnetization under an applied dc field even that their ground state has a major contribution of the lower M_J value, as has previously observed following our approximation calculating the sign of D. The fact that a cluster with an easy plane anisotropy can behave as a single molecule magnet under an external dc field was demonstrated some time ago by Long and co-workers for a Co^{II} complex [113].

At this point, two different approaches that require different treatment of the data, were used for the calculation of the single-molecule magnet parameters of the systems, **Table 6.4**: a first kind of compounds show peaks above 2 K in the frequency range 10-1488 Hz. In these cases, an Arrhenius dependency fitting was used as a first step to calculate the relaxation time (τ_0) and the relaxation barrier (U_{eff}) (**Figure AIII.10**), by means of the equation:

$$ln(1/(2\pi\omega) = ln(1/\tau_0) - U_{eff}/(k_B T) \qquad \mathbf{(6.2)}$$

which supposes the so-called Orbach relaxation,[32] which is produced at relatively high temperature by means of involving two phonons in a spin-lattice relaxation trough real states (see Section 1.1.3.4.). Other compounds do not show maxima in the χ_M'' vs. temperature representations, but there is a clear dependence of χ_M'' with temperature. In these cases, the so-named *generalized Debye model* was employed (**Figure AIII.10**), to find the SMM parameters according to the expression:[54]

$$ln(\chi_{\mathrm{M}}''/\chi_{\mathrm{M}}') = ln(\omega\tau_0) - U_{\mathrm{eff}}/(k_{\mathrm{B}}T) \qquad \mathbf{(6.3)}$$

It is important to mention, that complexes **[30]**, **[31], [36], [37]** and **[41],** joint to the scarce number of molecules with slow relaxation of the magnetization prepared with lanthanides known as "*uncommon magnetic lanthanides*".[99,114,115]

In last years hundreds of articles appeared about lanthanide clusters presenting slow relaxation of the magnetization, the vast majority of them with Tb^{III} and Dy^{III} cations, being Dy^{III} the favourite by large due to its high magnetic moment and its Kramers ion condition, which makes it a very good candidate for achieving SMM behaviour.[103]

Complex	Ueff (K)	τ_0 (s)	Complex	Ueff (K)	τ_0 (s)
[NiCe] **[36]**	$8.7^{\ddagger}$	$7.7\cdot10^{-5}$	[ZnCe] **[30]**	$4.7^{\ddagger}$	$2.5\cdot10^{-5}$
[NiNd] **[37]**	$9.2^{\ddagger}$	$1.9\cdot10^{-5}$	[ZnNd] **[31]**	$15.9^{\ddagger}$	$3.7\cdot10^{-6}$
[NiDy] **[39]**	$9.3^{\ddagger}$	$2.1\cdot10^{-5}$	[ZnDy] **[33]**	$17.7^{¥}$	$8.3\cdot10^{-7}$
[NiEr] **[40]**	$18.4^{¥}$	$1.7\cdot10^{-6}$	[ZnEr] **[34]**	---	---
[NiYb] **[41]**	$18.1^{\ddagger}$	$2.1\cdot10^{-6}$	[ZnYb] **[35]**	---	---

‡ generalized Debye model fit; $^{¥}$ Arrenhius fit

Table 6.4. Slow relaxation of the magnetization parameters for the complexes with ac response.

However, all lanthanides can present SMM behaviour in an appropriate environment by a proper design of the ligand field[44,114,115] by differentiating the oblate or prolate character of the different lanthanide(III) cations. Among the uncommon lanthanides, Ce^{III} is an attracting cation to work[102b,e] because it does not present nuclear spin. Even Ce^{III} has only one electron in the 4*f* shell ($4f^1$, $^2F_{5/2}$), it has a strong enough spin-orbit coupling to allow magnetic anisotropy (see Chapter 8 for a more detailed discussion about the Ce^{III} magnetic behaviour). Ac susceptibility measurements were carried out for complexes **[30]** and **[36]**, and, as was mentioned before, no signature of slow relaxation was found under zero applied field. This is due to the fact that in these compounds Δ is positive, with the probably Stark doublet M_J=±1/2 being the low-lying level which promotes significant QTM.[102] Even a positive Δ supposes no barrier related with D because the spin is free to rotate, an easy plane anisotropy is derived from the very low symmetry.

About Nd^{III}, its electronic configuration ($4f^3$, $^4I_{9/2}$) allows enough spin-orbit coupling to permit the needed anisotropy for a slow relaxation of the magnetization and the positive Δ of compounds **[31]** and **[37]** doesn't allow relaxation under zero dc field. To end with the uncommon lanthanides, only the Yb^{III} derivative with Ni^{II} presents slow relaxation of the magnetization under an external magnetic field strong enough to quench the quantum tunnelling of the magnetization (**Figure 6.11** and **AIII.8-AIII.9**). Although Yb^{III} is highly anisotropic, there is a scarce number of SMM reported,[116] even is by far the most popular of the "*uncommon lanthanides*". We calculated a positive Δ value for the Yb^{III} derivatives, so again, the ground state should be M_J = ±1/2. However, the reported Yb^{III} complexes in the literature with slow relaxation of the magnetization under a dc external field support in most of the cases a M_J = ±5/2 as the ground doublet[99a] calculated by means of the Stevens operators (see Appendix I), ac data and luminescence spectra, even all of them present higher symmetry conditions.

Turning now to the most common lanthanides, Dy^{III} and Er^{III}, they did not present neither signs of slow relaxation of the magnetization under a zero dc field. For complexes **[33]**, **[34]**, **[39]** and **[40]**, evidence of induced SIM behaviour was only observed under applied dc external field. The Dy^{III} ($4f^9$, $^6H_{15/2}$) derivatives **[33]** and **[39]** showed a Δ negative value, so we can assume that the higher M_J state is the ground one, with a probably mixing with the low lying excited states due to the low symmetry, but allowing an enough large barrier to the relaxation. For the Er^{III} derivatives ($4f^{11}$, $^4I_{15/2}$), with positive Δ, only compound **[40]** from the Ni^{II} family presents slow relaxation of the magnetization.

The calculated values of the energy barriers for all the compounds, **Table 6.4** are too low by far than the first excited state for any Ln^{III} cation and so, an over barrier relaxation is not allowed. This is a usual discrepancy in the *f*-elements magnetic molecules, and is attributed to dipolar interactions between paramagnetic canters and a mixing of the low lying excited states.

Due to the low symmetry environment around the lanthanide cations and due to the fact that all of them present fast relaxation of the magnetization under a zero dc field, in all of the here reported complexes we assume a mixing of the low lying excited states, independently of the sign of Δ as direct consequence of the low environment symmetry.

Cole-Cole[55] plots of **[30]**, **[31]**, **[33]**, **[34], [36]**, **[37]**, **[39]**, **[40]** and **[41]** (**Figures AIII.11** and **AIII.12** were fitted using CCfit software and the generalized Debye model[33]:

$$\chi(\omega)=\chi_S+(\chi_T+\chi_S)/(1+i\omega\tau)^{1-\alpha} \qquad \textbf{(6.4)}$$

where χ_S and χ_T are the adiabatic and thermal susceptibilities respectively, τ is the average relaxation time and α is a parameter ranging from 0 to 1 which quantifies the width of the relaxation time distribution. For all of them, the Cole-Cole plots result in only one semicircle supposing a single relaxation process for each complex yielding in an α value

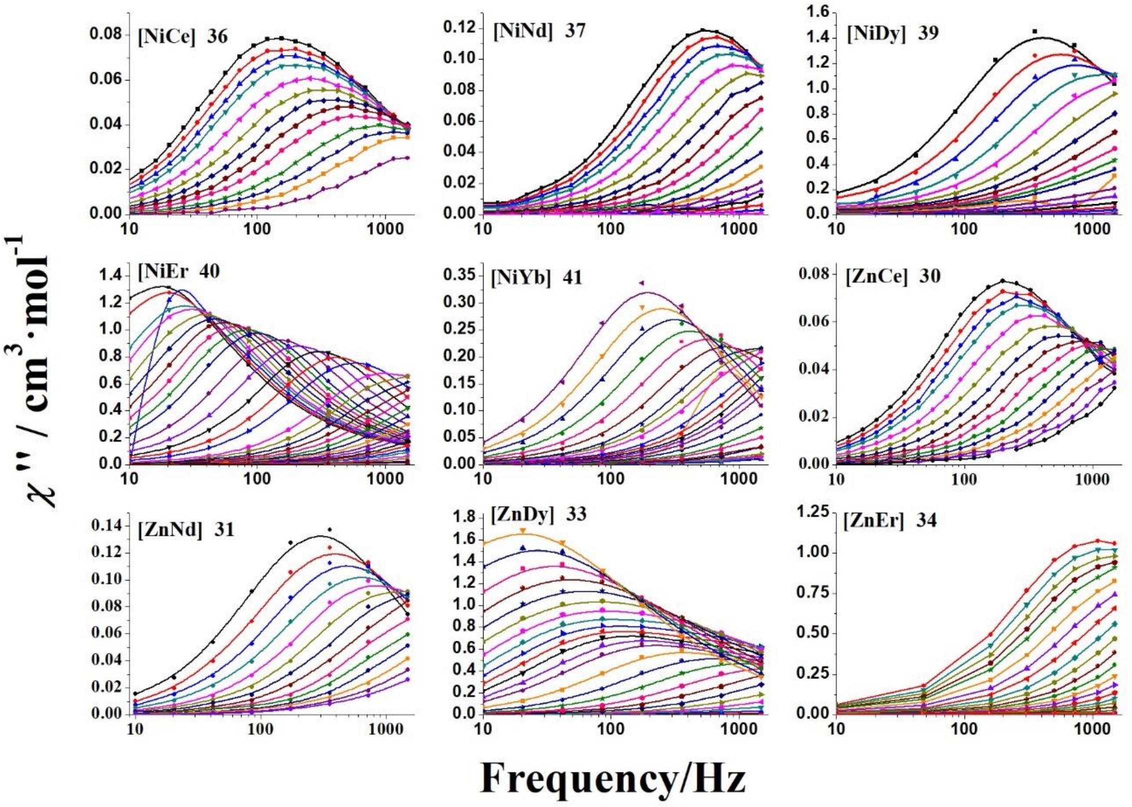

Figure 6.11. Dependence of out-of-phase susceptibility data for complexes **[30[, [31], [33], [36], [37],-39], [40]** and **[41]** measured under dc field of 500 Oe for **[30]** and **[36]**, 2000 G for **[31]** and **[37]** and 1000 Oe for the remainder complexes.

lower of 0.3 for all of them indication a relatively narrow distribution of the relaxation times. For complexes **[30]**, **[31]**, **[36]**, **[37]**, **[39]**, **[40]** and **[41]**, the representation of τ^{-1} *vs*. T shows that for all of these cases, the relaxation rate decreases when decreasing temperature, but no exponential law can simulate this dependence in all the temperature range evidencing that the Orbach relaxation may be mixed with a faster relaxation process. In the representation of $ln(\tau)$ vs the inverse of the temperature (**Figure AIII.13**, insets), there is no evidence of a temperature-independent plateau at low temperatures, indicating that the relaxation process is still dependent on temperature, so QTM as a secondary relaxation path must be excluded above 2K, the minimum temperature allowed by the instrument. Even that the fit parameters are poorly reliable in absolute terms,[38.] the plots have been fitted following a Raman and Arrhenhius dependence, **Figure AIII.13**.

These complexes have an Arrhenius dependency of the relaxation time with temperature (**Figure AIII.13**), but at the same time, the relaxation barrier calculated by means of this dependency is too low to overcome the anisotropy barrier. Below 3K, no maxima appear in the χ_M'' *vs*. temperature plots for the vast majority of the complexes and the linear dependency between τ and T disappears, meaning that below this temperature relaxation between Kramers states cannot be supposed Orbach-like relaxation, but some kind of temperature dependency remains (**Figure AIII.8**).

For this reason, we suppose that there is a non-complete Van Vleck cancellation, and Raman relaxation is the only possible relaxation path.[29,117] Complex **[33]** shows a slightly different behaviour in the relaxation features, as can be seen clearly in the representation of χ'' vs temperature in **Figure AIII.9**, where two maxima appear. The apparition of two processes is usually attributed to two crystallographically independent Dy^{III} cations in the unit cell. Even there are two different molecules in the same unit cell, the quasi identical environment and consequently, crystal field around the cations, do not support this hypothesis in this case. This feature for Dy^{III} has been reported in numerous cases[118] and the low temperature processes have been attributed to direct relaxation under dc field.[104,119]

Summarizing the above results, there are several experimental features that deserves a final comment. 1) These systems present QTM and the barriers of reversal of the magnetization are low in all cases and comparable to the few bibliographic examples (only Dy^{III} and Tb^{III}) with similar ligands. This fact must be attributed to the low symmetry of the coordination polyhedron around the Ln^{III} cations. 2) Due to the low symmetry environment and the positive *D* value in most of them, supports the low barrier related to *E*, which must be, always, lower than a barrier related with *D*. 3) Interestingly, the oblate ions Ce^{III}, Nd^{III} and Dy^{III} does not show a significant difference of behaviour when Zn^{II} is changed by Ni^{II}, presenting all of them similar response and values of the relaxation parameters, suggesting that the change of the diamagnetic cation does not promotes differences in the ligand field of these lanthanides. In contrast, the prolate cations Er^{III} and Yb^{III} clearly show better response for the [Ni^{II}Ln^{III}] family. Has been proved that the diamagnetic cation can modify the electronic density and the field promoted by the μ-O bridges[104] and in our case, the prolate cations must be more sensitive to changes in the environment due to the distribution of the field around the lanthanide cation: the O-donors with negative charge are roughly placed in a plane with the neutral ones placed axially, **Figure 6.12**. Better isolation of the dimers and the change of the diamagnetic cation suggest that in this case promotes different response for oblate/prolate lanthanides.

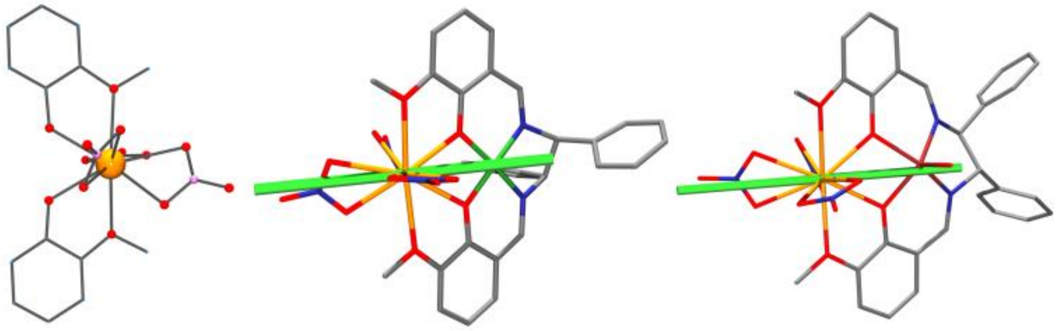

Figure 6.12. A view of the charged O-donors "belt" around the Ln^{III} ions and the axial neutral O-donors (left). Plot of the anisotropy axis cations (green lines, Magellan program) calculated for the [Ni^{II}Dy^{III}] (centre) and [Zn^{II}Dy^{III}] (right) showing that the distribution of the charge around the lanthanide is more adequate for the prolate-like lanthanides.

CHAPTER 7. PURELY LANTHANIDE COMPOUNDS.

In this chapter are going to be reported the syntheses, characterization, structural description and magnetic and spectroscopic studies of two families of complexes derived from the chiral ligand **L6** (**Figure 7.1)** using different lanthanides as paramagnetic centers (Ln= Ce^{III}, Nd^{III}, Eu^{III}, Dy^{III}, Tb^{III}, Er^{III}, Yb^{III}). In light of the structural features, the chapter is going to be divided in three sections: 7.1 that includes the synthetic aspects and spectroscopic characterization, 7.2 containing the $[Ln_2]$ dinuclear complexes derived from Ce^{III} **[42]**, Nd^{III} **[43]** and Sm^{III} **[44]** and a third section 7.3, which is about the mononuclear lanthanide complexes derived from Eu^{III} **[45]**, Tb^{III} **[46]**, Dy^{III} **[47]**, Er^{III} **[48]** and Yb^{III} **[49]**, the [Ln] family.

7.1. SYNTHESES AND CHARACTERIZATION.

7.1.1. Syntheses.

The complete synthesis is represented in **Figure 7.1**. The Schiff base **L6** was prepared in situ and the ligand solution was employed directly to synthesize the corresponding complexes. The syntheses of the ligand were common for the (*RR*) and for the *(SS*) enantiomers: 0.053 g (0.5 mmol) of 2-pyridinecarboxaldehyde and 0.053 g (0.25 mmol) of (1*R*,2*R*) or (1*S*,2*S*)-1,2-diphenylethylendiamine were dissolved in 20 mL of methanol and stirred at room temperature for three hours.

The general procedure for the synthesis of the lanthanide complexes started by adding 20 mL (0.25 mmol) of the previously prepared solution of the ligand (**L6**) to an equimolar quantity of the $LnCl_3·xH_2O$ (0.25 mmol). The resulting solution was stirred for one hour at room temperature. Crystals suitable for X-Ray diffraction were obtained from the crystallization by slow diffusion with Et_2O.

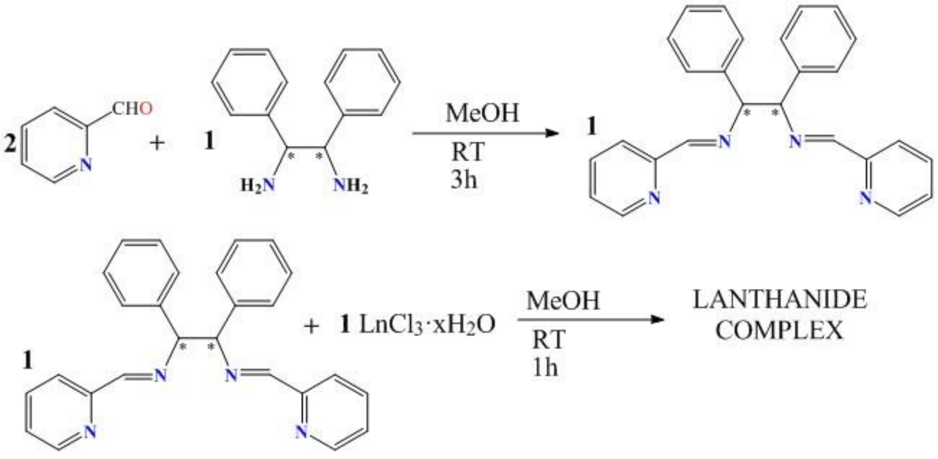

Figure 7.1. Top, synthesis of the chiral ligand **L6** from the condensation of 2-pyridinecarboxaldehyde and (1*R*,2*R*) or (1*S*,2*S*)-1,2-diphenylethylendiamine. Down, preparation of the lanthanide complexes. The chiral centres are marked with (*).

Is going to be shown that, depending on the used lanthanide the final complexes have two different types of structures: dinuclear compounds for the light lanthanides with formula **$[Ln_2(L6)_2(Cl_6)]\cdot MeOH\cdot 1.5H_2O$** (Ln=$Ce^{III}$, Nd^{III}, Sm^{III}) and mononuclear compounds with formula **$[Ln(L6)(Cl_3)]$** (Ln=Eu^{III}, Tb^{III}, Dy^{III},Er^{III}, Yb^{III}) for the heavy ones. Due to this difference, the shape and the crystallinity of the crystals is different: the good shape as polyhedral blocks of the light lanthanide complexes allowed to perform monocrystal measurements on them, like EPR spectra and CTM, while it was not possible to perform monocrystal measurements for the needle shaped crystals of the heavy lanthanide complexes. The two series were characterized by IR, UV-Vis, ECD and monocrystal and powder X-ray diffraction.

7.1.2. Spectroscopic characterization.

Infrared spectra were very practically identical for the two series as can be expected from the similar arrangement of the ligands, **Figure 7.2**.

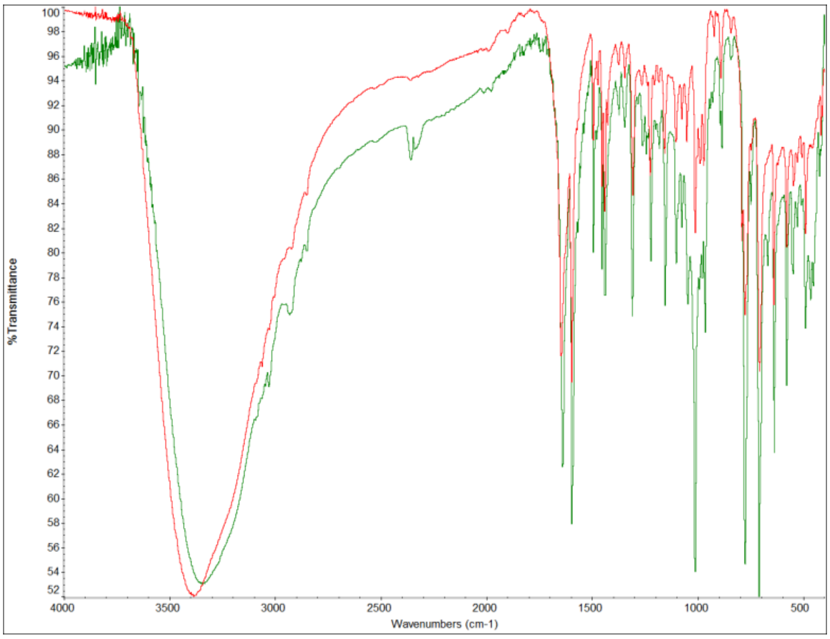

Figure 7.2. Representative spectra of the [Ln_2] (green plot) and the [Ln] (red plot) families of complexes **[42]**-[**49**].

In contrast, UV-Vis and ECD spectroscopy were more sensitive allowing to the differentiation of the two series in solution. UV-Vis spectra are dominated by the transitions related to the ligand in the 200-325 nm range with one absorption at 206 nm due to the $\pi \rightarrow \pi^*$ transitions of the aromatic rings and one band at 250 nm (265, shoulder) related to the iminic group, **Figure 7.3**. The dinuclear complexes show a similar spectrum (205 and 260, 268 shoulder) whereas the mononuclear systems maintain the absorption at 205 but the second band is shifted to 287 and 300 nm.

In the same way the electronic circular dichroism spectra in methanolic solution were also enough different to differentiate the two families of complexes and to check that the structure is maintained in solution, **Figure 7.4**. The mirror-image spectra show similar absorptions with the same sign around 270 and 300 nm but become clearly different in the region below 250 nm.

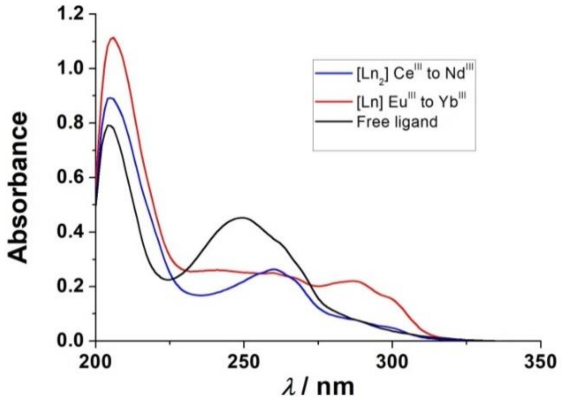

Figure 7.3. Representative UV-Vis spectra for the two families of [Ln_2] **[42]-[44]** and [Ln] **[45]**-[**49]** complexes.

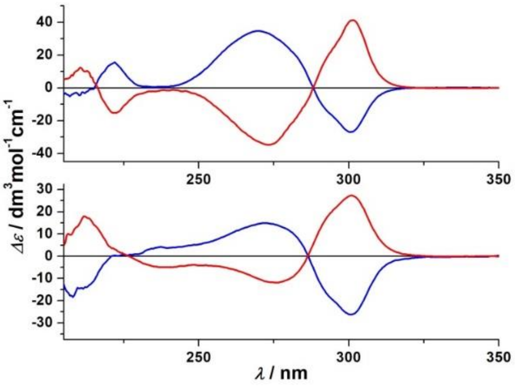

Figure 7.4. Representative ECD spectra for the dinuclear Nd^{III} **[43*RR*]** and **[43*SS*]** complexes (top) and the mononuclear Tb^{III} **[46*RR*]** and **[46*SS*]** complexes (bottom). Red line, *RR* enantiomers; blue lines, *SS* enantiomers.

7.2. DINUCLEAR COMPOUNDS DERIVED FROM Ce^{III}, Nd^{III} and Sm^{III} (THE [Ln_2] FAMILY).

7.2.1. Structural description.

Because both enantiomers are isostructural a common description for the *RR* and *SS* Nd^{III} derivatives is provided in order to avoid repetitive descriptions.

[$Nd_2(L6)_2(Cl_6)$]·MeOH·1.5H_2O. (**43*RR*** and **43*SS***). A view of the molecular structure is shown in **Figure 7.5** and the main bond parameters are summarized in **Table 7.1**. The structure consists of neutral dinuclear Nd^{III} complexes in which the two cations are linked by two μ-Cl bridges. Each cation is octacoordinated by the four N-atoms of one **L6** ligand, two terminal chloro ligands and two bridging chloro donors. The **L6** ligand is planar but the pyridyl groups are slightly bent with respect to the main plane with a dihedral angle between the pyridyl mean planes of 21.8º (around Nd1) and 14.3º (around Nd2). The neighbor N-donors of **L6** determine low N-Nd-N bond angles, close to 62º-65ºallowing to place one of the chloro ligands in the same plane of the coordination polyhedron. The two μ-Cl bridges and the second chloro ligand are placed in the axial positions above and below the NdN_4Cl plane. The shorter bond distances correspond to the Nd-N bonds whereas the larger ones are those related to the Nd-(μ)-Cl bonds. Nd1-Cl-Nd2 bond angles takes a value around 109.7º.

There is a complex set of intra and intermolecular weak CH···Cl and CH···O H-bonds that relates the dimers and the solvent molecules. Among them, the intramolecular CH···Cl H-bonds between H-atoms from the pyridinic groups and the bridging chloro ligands becomes relevant because determine the 1-D arrangement of dimers in the network, **Figure 7.5**. Parallel alignment of these chains gives planes of dimers isolated by layers of solvent molecules **Figure 7.6**. Transference of chirality to the coordination polyhedron around the metallic cation or to the network is not relevant in these structures.

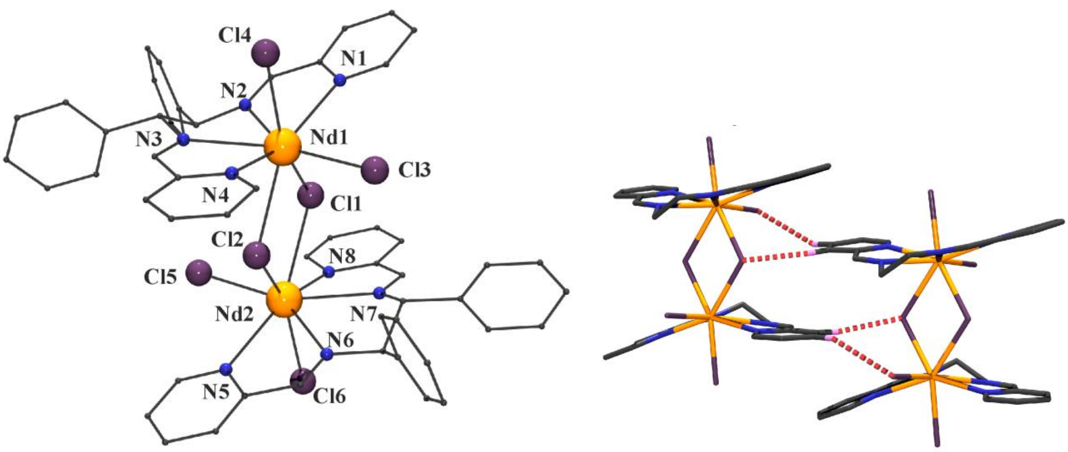

Figure 7.5. Left, partially labeled plot of compound **43*RR***. Right, intermolecular CH···Cl H-bonds that determines the network arrangement (red dotted bonds).

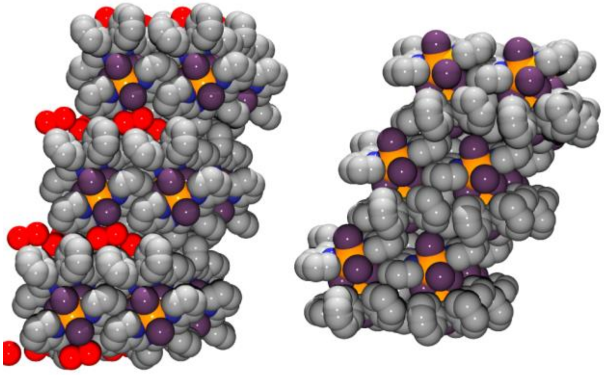

Figure 7.6. Spacefill plot of the structures of $[Nd_2(L6)_2(Cl_6)]\cdot MeOH\cdot 1.5H_2O$ (left) showing the layers of crystallization molecules in the *ab* plane of the cell and $[Sm_2(L6)_2(Cl_6)]$ (right) showing its compact structure

	[43*RR*]	**[43*SS*]**
Nd1-N1	2.660(10)	2.666(8)
Nd1-N2	2.547(9)	2.603(6)
Nd1-N3	2.586(8)	2.547(10)
Mn1-N4	2.603(9)	2.543(6)
Nd1-Cl1	2.805(3)	2.812(3)
Nd1-Cl2	2.893(2)	2.905(2)
Nd1-Cl3	2.699(3)	2.713(3)
Nd1-Cl4	2.741(3)	2.713(5)
Nd2-N5	2.676(9)	2.70(1)
Nd2-N6	2.593(9)	2.537(12)
Nd2-N7	2.566(8)	2.595(7)
Nd2-N8	2.575(10)	2.74(2)
Nd2-Cl1	2.901(3)	2.897(3)
Nd2-Cl2	2.808(3)	2.807(3)
Nd2-Cl5	2.704(3)	2.697(3)
Nd2-Cl6	2.739(3)	2.754(2)
Nd1-Cl1-Nd2	109.67(9)	109.80(9)
Nd1-Cl1-Nd2	109.84(9)	109.71(8)

Table 7.1. Selected bond distances (Å) and angles (°) for compounds **[43*RR*], [43*SS*]**.

The powder diffraction spectra for the three dinuclear complexes (Ce^{III}, Nd^{III} and Sm^{III}) demonstrate that they are isostructural but surprisingly, the spectra were completely different of the simulated spectrum from the monocrystal structure of **[43*RR*] or** [**43*SS***]. To check if the changes were due to loss of solvents, the analogous Sm^{III} complex **[44]** was prepared and the crystals were maintained at open air for 48 h. The crystals do not suffer apparent changes but the structure confirms the loss of solvents. The crystallographic data appears in Appendix IV.

[$Sm_2(L6)_2(Cl_6)$] [44*SS*]. The molecular structure obtained after 48 h of open air exposure of the crystals is identical in their general trends to the above described for Nd^{III}, including bond parameters and the arrangement of dimers in 2D planes. However, the layers methanol and water molecules of crystallization placed in the *ab* plane of the previous structure are completely lost and thus, the *a* and *b* parameters remain practically identical (9.714 and 11.173 *vs*. 9.708 and 11.853 Å) but the *c* parameter of the cell is 2.645Å shorter (12.592 vs. 15.137 Å) than the (*SS*)-**[$Nd_2(L6)_2(Cl_6)$]·MeOH·1.5H_2O** structure.

The simulated powder X-Ray spectrum match perfectly with those obtained from the powdered samples, evidencing two different structures for the fresh complexes and for the samples exposed to open air, **Figure 7.7**. In light of these data, for the further measurement on powdered samples the second structure and molecular weight must be assumed.

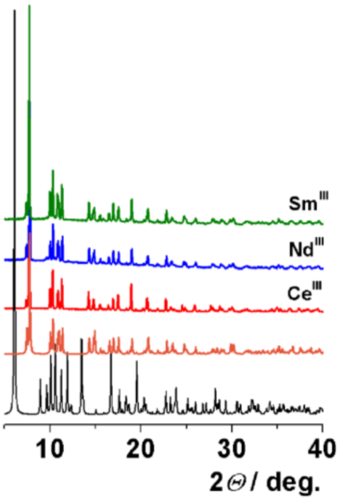

Figure 7.7. In black is represented the simulated powder spectra from the monocrystal structure of the complex **[43]** with contains crystallization solvent molecules. Orange pattern represents the simulation of the desolvated structure [**44]** which matches perfectly with the powder spectra of Ce^{III}, Nd^{III} and Sm^{III} derivatives.

7.2.2. Magnetic studies.

7. 2. 2. 1. Static magnetic properties.

The magnetic susceptibility for complexes **[42]** and **[43]** in the form of $\chi_M T$ product *vs.* temperature, performed on polycrystalline samples in the 2-300 K range, is shown in **Figure 7.8**. $\chi_M T$ at room temperature is close to the free ion values for the two corresponding magnetically independent lanthanide cations ($^2F_{5/2}$ for Ce^{III} and $^4I_{9/2}$ for Nd^{III}).

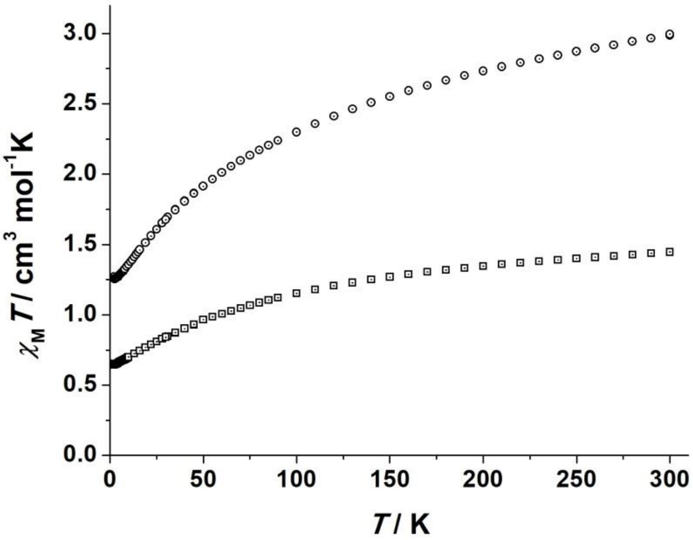

Figure 7.8. $\chi_M T$ vs. T for the dimeric complexes **[Ln$_2$(L6)$_2$(Cl$_6$)] [42]** (Ln = Ce^{III}, squares) and **[43]** (Ln = Nd^{III}, circles).

When temperature is lowered, $\chi_M T$ product reduces for both compounds reaching a final value of 0.64 cm^{3}mol^{-1}K for **[42]** and 1.26 cm^{3}mol^{-1}K for **[43]**. This decrease can be attributed to the thermal depopulation of the energy levels of the ground *J* multiplet split by Crystal Field effects. At the lower temperature, a contribution to the decrease might involve the existence of intramolecular antiferromagnetic interactions, which are expected to be rather weak in these systems.

The field dependent magnetization was measured in the range 0-5 T and at three different temperatures (**Figure 7.9).** Magnetization does not saturate and the reduced magnetization shows quasi superimposable plots, as expected, because only the ground doublet is populated.

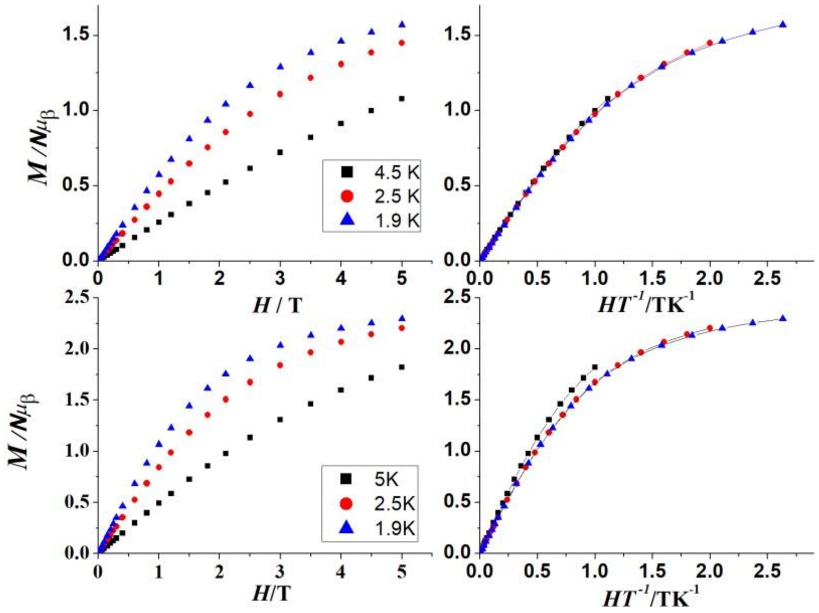

Figure 7.9. Magnetization *vs*. field and reduced magnetization for the dimeric complexes **$[Ln_2(L6)_2(Cl_6)]$ [42]** (Ln = Ce^{III}, top) and **[43]** (Ln = Nd^{III}, bottom).

7. 2. 2. 2. Dynamic magnetic properties.

To study the dynamic magnetic properties, temperature and frequency variable ac measurements were performed on polycrystalline samples of **[42]** and **[43]**. No maxima appear in the χ_M'' vs. *T* measurements above 1.8 K for anyone of the two compounds in zero dc field indicating that the magnetic moments completely follow the magnetic field due to a fast reversal of the magnetization. To explore the effect of an external dc field on the relaxation processes and to see if an applied field is able to slow down the relaxation process, measurements scanning between 10-10000 Hz under different fields (500, 1000, 2000 and 3000 G) were performed. As a result, noisy and poorly defined out-of-phase susceptibility was observed for the Ce^{III} derivative **[42].** These measurements were performed in a PPMS instrument first, and then, in the most sensitive SQUID device where, even weak, it was possible to measure the ac response for the Ce^{III} complex **[42]** under a field of 500 G and the 10-1500 G range of frequencies. (**Figure 7.10**). Well-defined signals and dependency of the out-of-phase signal *vs*. frequency and temperature for the Nd^{III} complex, **[43]**, were observed, **Figure 7.11**.

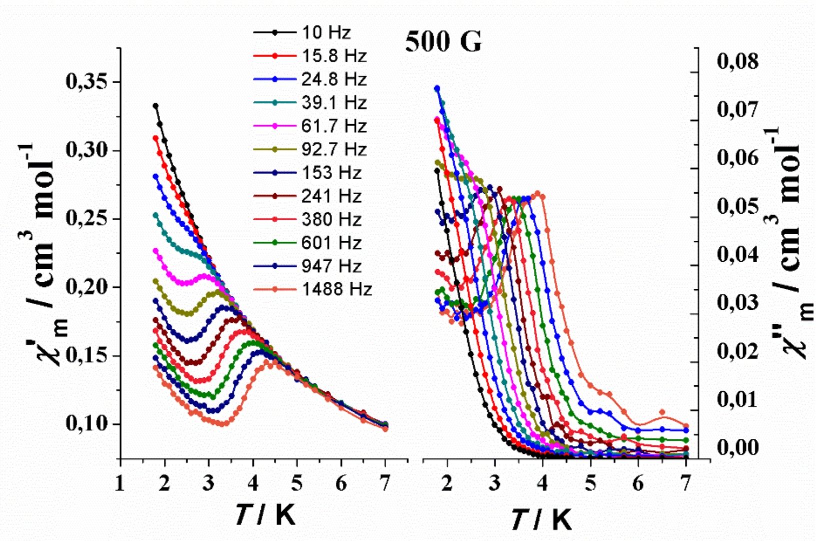

Figure 7.10. χ_M' and χ_M'' vs. *T* under a dc field of 500 G for the Ce^{III}_2 complex **[42]**.

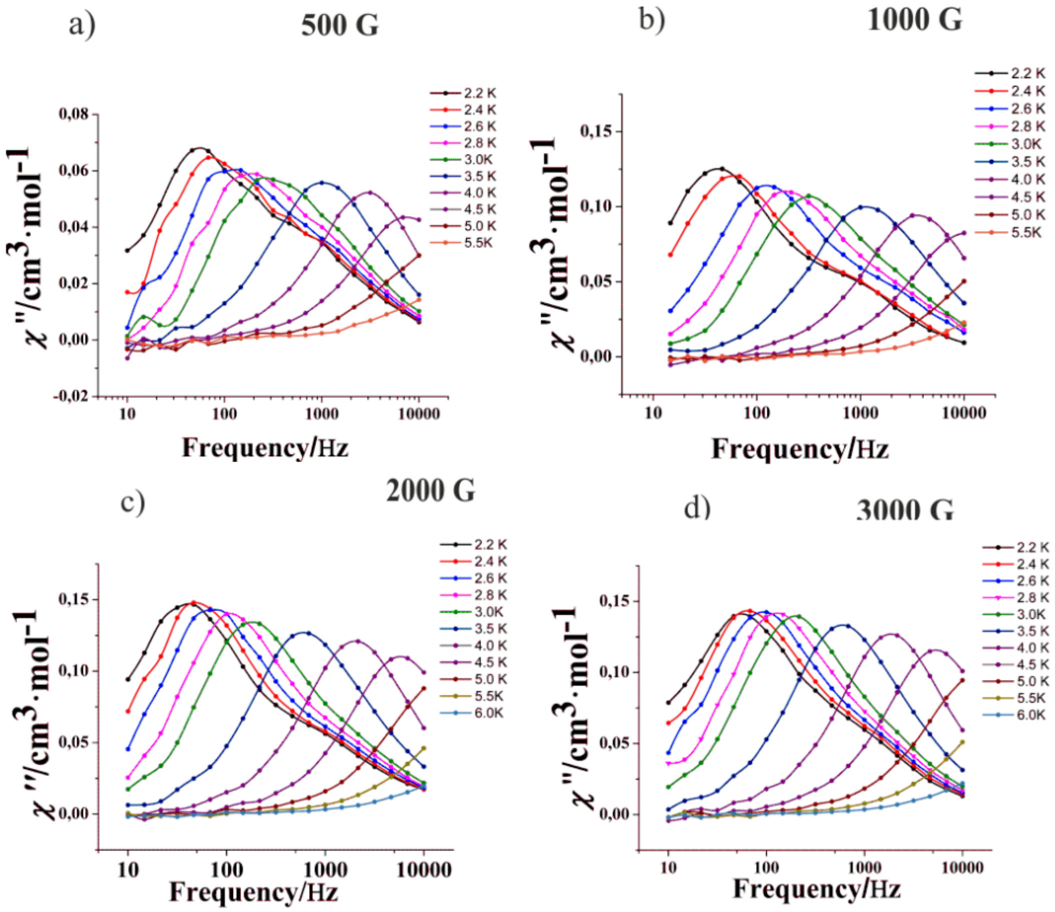

Figure 7.11. χ_M'' *vs*. frequency for complex **[43]** under different dc applied fields, showing peaks in all the cases. Complete dynamic measurements can be found in **Figure AIV. 1** in Appendix IV.

There are hundreds of articles about lanthanide clusters presenting slow relaxation of the magnetization, the vast majority of them with Tb^{III} and Dy^{III} ions, being Dy^{III} the favorite by large due to its high magnetic moment and its Kramers ion condition, which make it a very good candidate for achieving SMM behavior. However, any lanthanide can present SMM behavior in an appropriate environment by a proper design of the ligand field[44,45] by differentiating the oblate or prolate character of the different lanthanide (III) cations. Among the uncommon lanthanides, Ce^{III} has been defined in the previous chapter as an attracting cation to work because it does not present nuclear spin and makes zero field QTM less efficient, in principle.[120] Even if Ce^{III} has only one electron in the *4f* shell ($4f^1$, $^2F_{5/2}$) it has enough spin-orbit coupling to allow relevant magnetic anisotropy of its ground J=5/2 ground state.

However, Nd^{III} has non-zero nuclear spin for the relevant fraction of natural abundance, so there is the possibility, in principle, of efficient QTM between doublets. Its electronic configuration ($4f^3$) results in a $^4I_{9/2}$ ground configuration which is subject to the effect of crystal field thus resulting in magnetic anisotropy and, potentially, in slow relaxation of the magnetization. Complexes **[42]** and **[43]** joint to the scarce number of Ce^{III} and Nd^{III} compounds reported to now that present slow relaxation of the magnetization under certain conditions.

Cole-Cole[55] plots were only performed for complex **[43]** and fitted using CCfit software and the generalized Debye model[33]

$$\chi(\omega)=\chi_S+(\chi_T+\chi_S)/(1+i\omega\tau)^{1-\alpha} \quad \mathbf{(7.1)}$$

where χ_S and χ_T are the adiabatic and thermal susceptibilities, respectively, τ is the average relaxation time and α is a parameter ranging from 0 to 1 which quantifies the width of the relaxation time distribution giving values below 0.3 for the Nd^{III} derivative. What is observed in the representations at 500, 1000, 2000 and 3000 G is that there are two different semicircles in the plot of χ'' vs. χ' which means two different relaxation processes (**Figure 7.12**). This feature is especially visible in the 1000 G field at low temperatures.

In a first stage, we used an Arrhenius dependency fitting to calculate the relaxation time (τ_0) and the relaxation barrier (U_{eff}) by means of the equation:

$$ln(1/(2\pi\omega) = ln(1/\tau_0) - U_{eff}/(k_BT) \quad \mathbf{(7.2)}$$

This supposes the so-called Orbach relaxation[32] which involves relaxation trough real excited states and is a two phonons relaxation process, especially of relevance at high temperature. Arrhenius fitting of the weak signals of complex **[42]** yields in the relaxation parameters τ_0 = 1.50x10^{-7} s and U_{eff} = 17.77 cm^{-1}. **Figure 7.13** shows the linear part of the plots while **Table 7.2** indicates the relaxation parameters (U_{eff} and τ_0) for complex **[43]** at different applied magnetic fields.

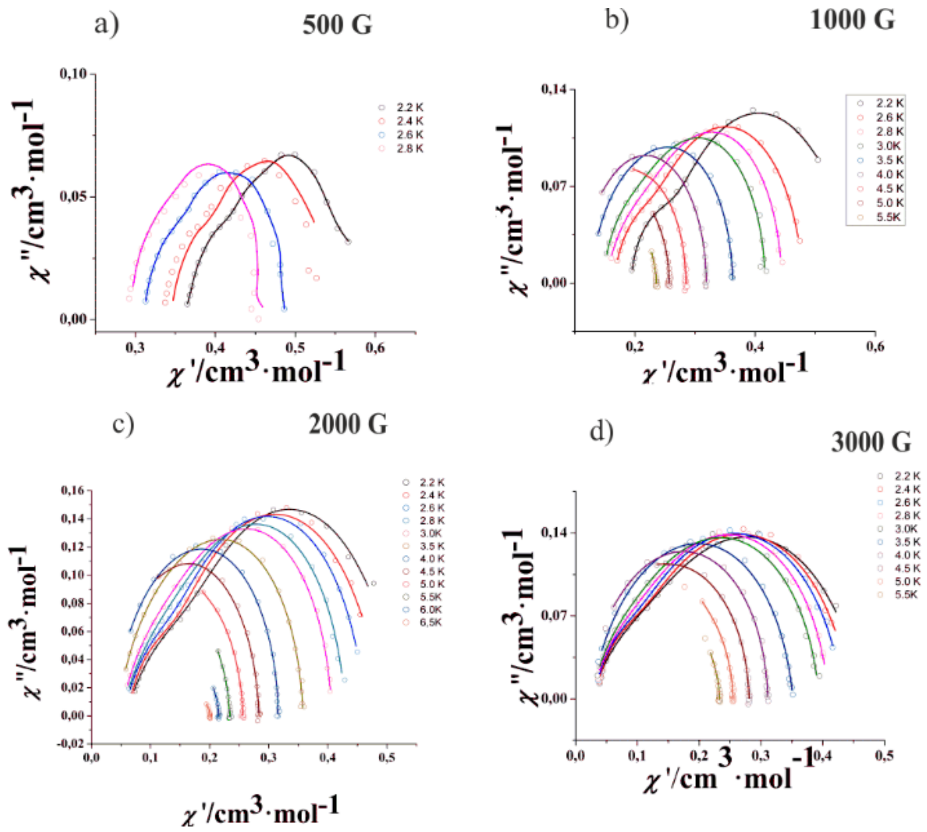

Figure 7.12. Fitted Argand plots for complex **[43]** at different fields.

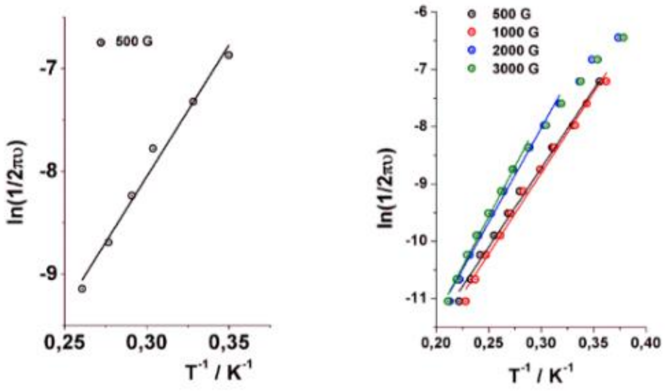

Figure 7.13. Left, Arrhenius plot for complex **[42]**, and right, Arrhenius plot for complex **[43]** at different dc applied external fields

	τ_0 (s)	U_{eff} (cm^{-1})	U_{eff} (K)
500 G	4.24E-8	19.1	27.5
1000 G	3.18E-8	19.6	28.2
2000 G	1.70E-8	22.9	32.9
3000 G	1.10E-8	24.3	35.0

Table 7.2. Relaxation parameters for complex [43] under different applied magnetic fields.

The values for the energy barriers of complex **[42]** are by far lower than the energy of the first excited doublet as is demonstrated by the CTM (see below) so, an over barrier relaxation not to be considered as the dominant mechanism while no values of the energy of the excited states were obtained for complex **[43]** from the CTM measurements. Furthermore, the standard Arrhenius plot is clearly not linear in the investigated temperature range, suggesting the importance of another relaxation process. This is now considered as usual in the magnetic relaxation of *f*-elements magnetic molecules. Due to the low symmetry environment around the lanthanide cations and since all of them present slow relaxation of the magnetization under a zero dc field, in complexes **[42]** and **[43]** we assume an obvious mixing of the low-lying excited states as a direct consequence of the low symmetry. The mixing of low lying excited states is confirmed in the CTM measurements for complex **[42]** (see below).

To confirm the occurrence of two different relaxation mechanisms, an example of the representation of *ln(τ)* vs. the inverse of the temperature is shown in **Figure 7.14** for 3000 G dc field. All the curves at all the fields have the same shape where two different slopes of the curve can be observed, which is an indication of two different relaxation processes. Same behaviour is confirmed by representing the *log log* plots **(Figure 7.15)**. At this point, a distinction between relaxation *process* and relaxation *mechanism* is needed.

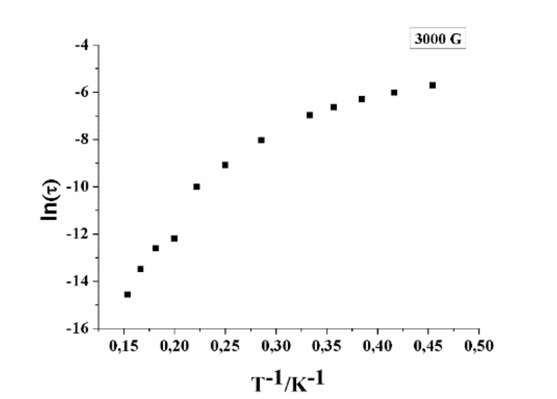

Figure 7.14. Representation of the lnτ *vs.* 1/*T* indicating the occurrence of two different relaxations. To avoid repetitive graphs, only this one has been included as an example.

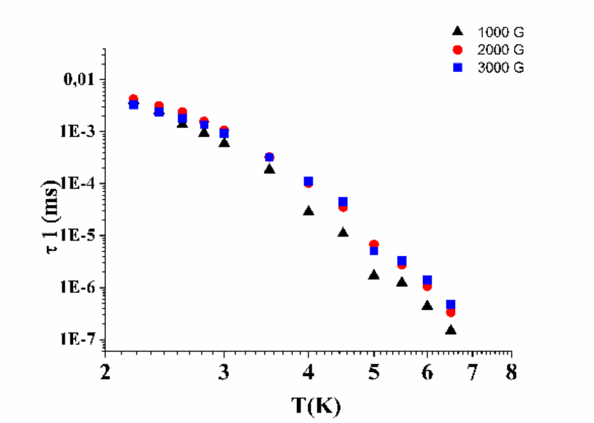

Figure 7.15. Representation of the *log log* plot where is confirmed the two types of regimes for the relaxation. The two involved processes may be a mixture of Raman+Orbach (due to the linear fitting of part of the curve) or more probably a mixture of Raman+direct since it is in-field and the contribution of Orbach mechanism is insignificant for the first fit (Raman+Orbach).

The relaxation mechanism involves different ways of relaxation (i.e. direct, Orbach, Raman) while process involves different magnetic centres. In complexes **[42]** and **[43]**, because this double slope is observed for all the fields even fitting the Cole-Cole plots supposing two different mechanisms/processes, we can say that the molecule has two different relaxation processes, one for each of the centres or much probably, one process which is monomolecular and a second process which should be collective. These two will occur at different temperature regions with different efficiency, depending on which mechanism dominates.

7.2.3. Electronic Paramagnetic Resonance (EPR) studies.

As discussed in Section 1.3.2.1. the possibility of intramolecular interactions can alter the magnetic properties either by providing alternative relaxation pathways by mixing of low-lying states, or act as a sort of bias field, in both cases strongly affecting the QTM. Even if in lanthanide complexes superexchange interactions are weak as a consequence of the inner nature of 4*f* orbitals, their large magnetic moment results in large and highly anisotropic dipole interactions.

Due to the characteristics of [Ln_2] series containing anisotropic lanthanide cations and being dinuclear compounds with the possibility of intramolecular interactions, magnetic anisotropy and exchange interactions were investigated at low temperature using CW-EPR at two frequencies (X-band ~9 GHz and W-band ~94 GHz). All the simulations were performed using the EasySpin software.[121]

Figure 7.16 shows the experimental powder EPR spectra of complex **[42]** at 5 K in X-band. The spectrum shows an absorption band around 1000 G and another one around 9500 G. The shape of the spectrum is in agreement with a Ce^{III} ion with a well isolated ground doublet in a distorted environment, while there are no evidences of intramolecular exchange or dipolar interactions. In this framework, the first resonance occurs for the crystals with the easy axis component of the ground doublet oriented along the magnetic field. The shape of the spectrum suggests the second resonance is the component of a rhombic system rather than the perpendicular one in an axial system.

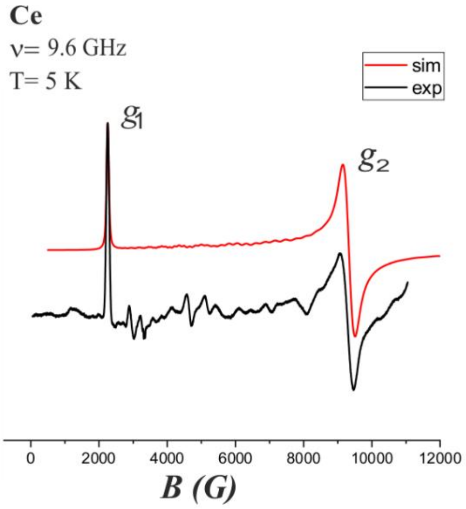

Figure 7.16. Experimental (black) and red (simulated) X-band EPR spectrum of compound **[42]**.

The first model used to study the Ce^{III} spectrum was only considering the ground doublet which allowed to define the anisotropy of the effective g factor for the ground doublet with $g_1 = 2.98$, $g_2 = 0.72$ and $g_3 < 0.5$. Experimentally, g_3 is not observed as it occurs at too high field (**Figure 7.16**).

Taking into account the data extracted from CTM (see Section 1.3.1.2.) another model was used to reproduce the EPR spectrum for complex **[42]**. Since CTM data in whole temperature range were fitted considering the total J=5/2 multiplet with gJ =6/7, D and E, same model was used to simulate the EPR spectrum. Using this second model, the simulation reproduces the main features of the spectrum: i.e. an easy axis system with relevant rhombicity, but the results clearly overestimates the rhombicity of the system. Indeed, using an E parameter somehow lower than the one obtained from CTM provides an improved simulation (**Figure 7.17**). It is further to be noted that the discrepancy in the resonance field of the low field feature is clearly to be attributed to the oversimplification of the model used to reproduce the CTM results, which is just based on a second order Spin Hamiltonian.

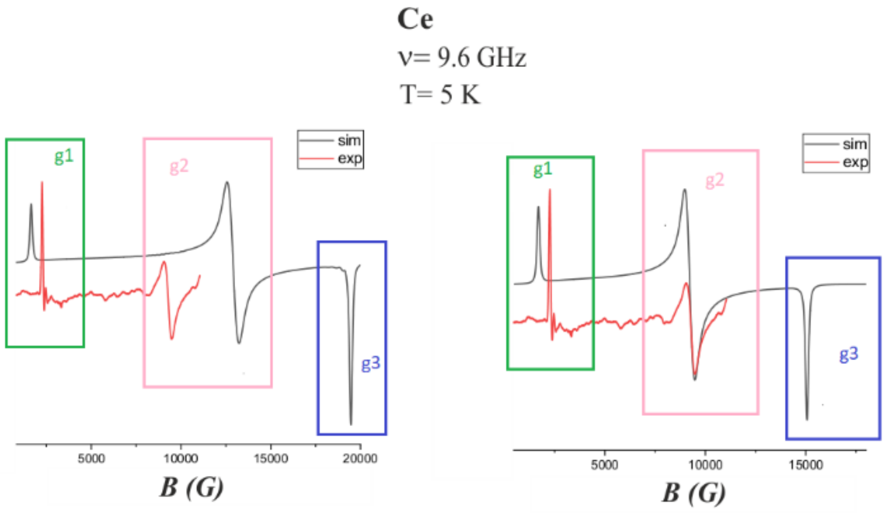

Figure 7.17. Red line corresponds to the experimental EPR spectra while the black line corresponds to the simulation. Left, the fitting using the E parameter directly extracted from CTM (E= 9.6 cm^{-1}). Right, simulation performed changing the E parameter (E=7.75 cm^{-1}), which allows a better simulation demonstrating that CTM overestimated E. In both cases, g_3 appears in the simulated spectra but not in the experimental one. The green box contains g_1, the pink box contains g_2 and the blue box in the spectra contains g_3.

For the Nd^{III} derivative, complex **[43]**, the powder X-band EPR spectra at 5K is depicted in **Figure 7.18,** left. The spectrum shows a number of lines that is not compatible with a simple ground doublet with g. The extra bands in the spectrum can be mainly due to the presence of low-lying excited states (which can allow intradoublet transitions) or due to anisotropic interactions (either dipolar or exchange in nature).

To further characterize the magnetic properties of the Nd^{III} derivative, W-band (ca. 94 GHz) spectroscopy was performed at 14 K, **Figure 7.18,** right. Line-line separation due to the intramolecular interactions should remain the same at any frequency, while if the separation is due to intermultiplet transitions within each centre it should vary while varying frequency. Looking at **Figure 7.18** it is clear that the split of the two lowest field lines remains constant on varying the frequency, thus pointing to an intramolecular interaction along that direction of a magnitude which is on the order of the line-line separation. In much the same way, the partially structured feature observed in the W-band spectrum at ca. 42000 G can be attributed to the same component, split by interaction, of the features centred at 4200 G in the X-band spectrum. Finally, this interpretation allows to simulate the spectra at the two frequencies on the basis of the following spin Hamiltonian

$$\mathrm{H} = \mu_B \boldsymbol{B}\cdot\boldsymbol{g}^{eff}\cdot(\boldsymbol{S}_1+\boldsymbol{S}_2) + J\boldsymbol{S}_1\cdot\boldsymbol{S}_2 + \boldsymbol{S}_1\,\boldsymbol{D}\,\boldsymbol{S}_2 \qquad \textbf{(7.3)}$$

where we assumed the two Nd^{III} centres as equal, with an effective spin S=1/2 and D is a traceless tensor considered as collinear to g_{eff}. The best simulation was obtained with principal g values of $g_1 = 4.16$ $g_2 = 1.52$ $g_3 = 1.08$, an isotropic ferromagnetic exchange of J=0.08 cm^{-1} and a dipolar anisotropic interaction between Nd^{III} ions of [-0.16 0.08 0.08] cm^{-1}. It is worth stressing that the ferromagnetic character of the isotropic contribution is unequivocally established by the relative intensity of the two components of the low field feature in W-band, which would result inverted in the case of antiferromagnetic coupling.

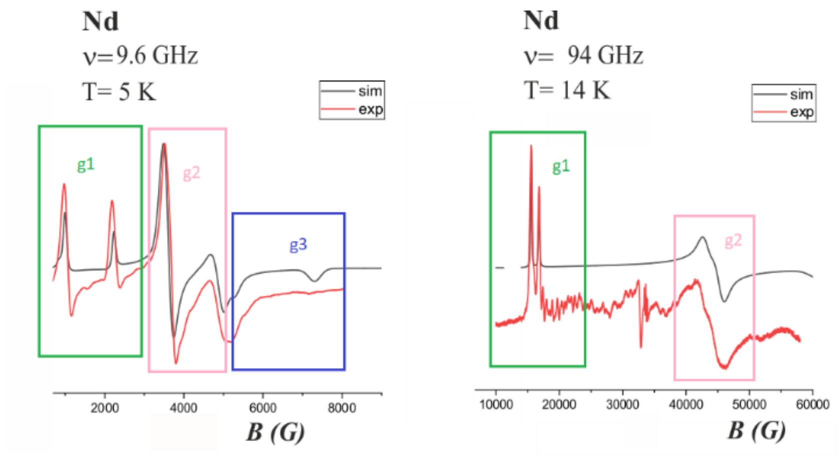

Figure 7.18. Left, powder X-band EPR spectrum performed at 5K of the Nd^{III} compound **[43]** and right, W-band powder X-band spectrum of the same compound performed at 14 K. In both cases there are represented the experimental spectra (red line) and the simulation (black line). The green box contains g_1, the pink box contains g_2 and the blue box in the X-band spectrum contains g_3.

Finally, we performed a single rotation of single crystal EPR spectrum to check whether the assumption of collinearity of the g and D tensor is reasonable, **Figure 7.19**. The expected resonance field were then simulated considering the orientation of the g (and consequently D) tensors obtained by CTM. The comparison between calculated and observed resonant fields indicate that the assumption is quite sound, thus lending further support to the electronic structure of Nd$^{III}_2$ obtained by the combined analysis of CTM and EPR spectra.

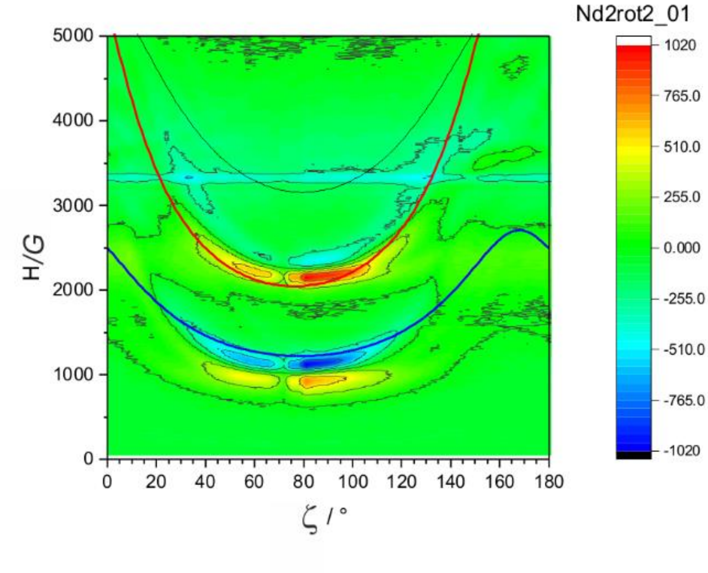

Figure 7.19. Representation of the monocrystal EPR spectrum of complex **[43]**. Solid lines show the calculated resonance fields.

7.2.4. Cantilever Torque Magnetometry (CTM) measurements.

CTM is a technique that allows to determine magnetic anisotropy of coordination compounds and its relation with the molecular structure. This is of paramount importance to understand the origin of slow relaxation of the magnetization, which is too often attributed, without further characterization, to the existence of a magnetic anisotropy barrier. CTM is especially useful in lanthanide compounds, due to the non-easily predictable nature of their magnetic anisotropy and to the low symmetry effect of the ligand field. In this work, this technique was employed to characterize the magnetic anisotropy of the [Ln_2] family (Ln = Ce^{III} **[42]**, Nd^{III} **[43]**).

Square-shaped crystals were used with a previous indexation in a single crystal X-Ray diffractometer to correlate the crystallographic reference frame (*ab'c**) with the laboratory one (*XYZ*). The rotation in the CTM is always around *Y*.

The experimental data for complex **[42]** is represented in **Figure 7.20.** In the first rotation a zero is observed around 25º and another around 115º. For the second rotation, the zeros are around 55º and 145 º. The more abrupt slope indicates the hard direction in the plane. In the second rotation the system looks quite rhombic (no slope difference). Note that increasing the temperature the zero position shifts, indicating the population of the excited states.

Figure 7.20, top, represents the fitting of the torque measurements obtained for the first rotation of Ce_2 in two different temperature ranges (2-5 K and 50-80 K) and **Figure 7.20**, bottom, the fits for the second rotation. Two different models have been used to fit the data. The first one was starting from the EPR *g* values and fitting the angles. This model showed poor agreement with experimental data at high temperature. The second model consists in fixing the angles and in the introduction of J=5/2 and $gJ'=6/7$, D and E to be refined. This second model provides a very good simulation in the whole temperature range yielding in a rhombic system with anisotropy parameters D = 34.5 cm^{-1} and E = 9.6 cm^{-1}. Even this good fitting in the whole temperature range by using the second model, as been said previously in the EPR section, the value of E=9.6 cm^{-1}

resulted to be overestimated to fit the EPR spectra of complex **[42]**. For this reason, a lower value of *E* is probably more correct.

Same procedure was made for complex **[43]**, the Nd^{III} derivative with CTM measurements represented in **Figure 7.21** for rotation 1 and rotation 2. What is observed in this case is a zero around 55º and 150º for the first rotation and at 15º and 100º for the second rotation.

For complex **[43]**, the used model was to fit the data by using an effective spin S=1/2 and fixing the g values obtained from the EPR. No possibility to probe the higher energy doublets due to the fact that there is not enough signal at high temperature.

What can be observed from the comparison between the Ce^{III} and Nd^{III} derivatives is that $\boldsymbol{\tau}$ has slightly different phase in the 180º periodicity, which means that the two cations have a different distribution of the electronic charge, but not opposite.

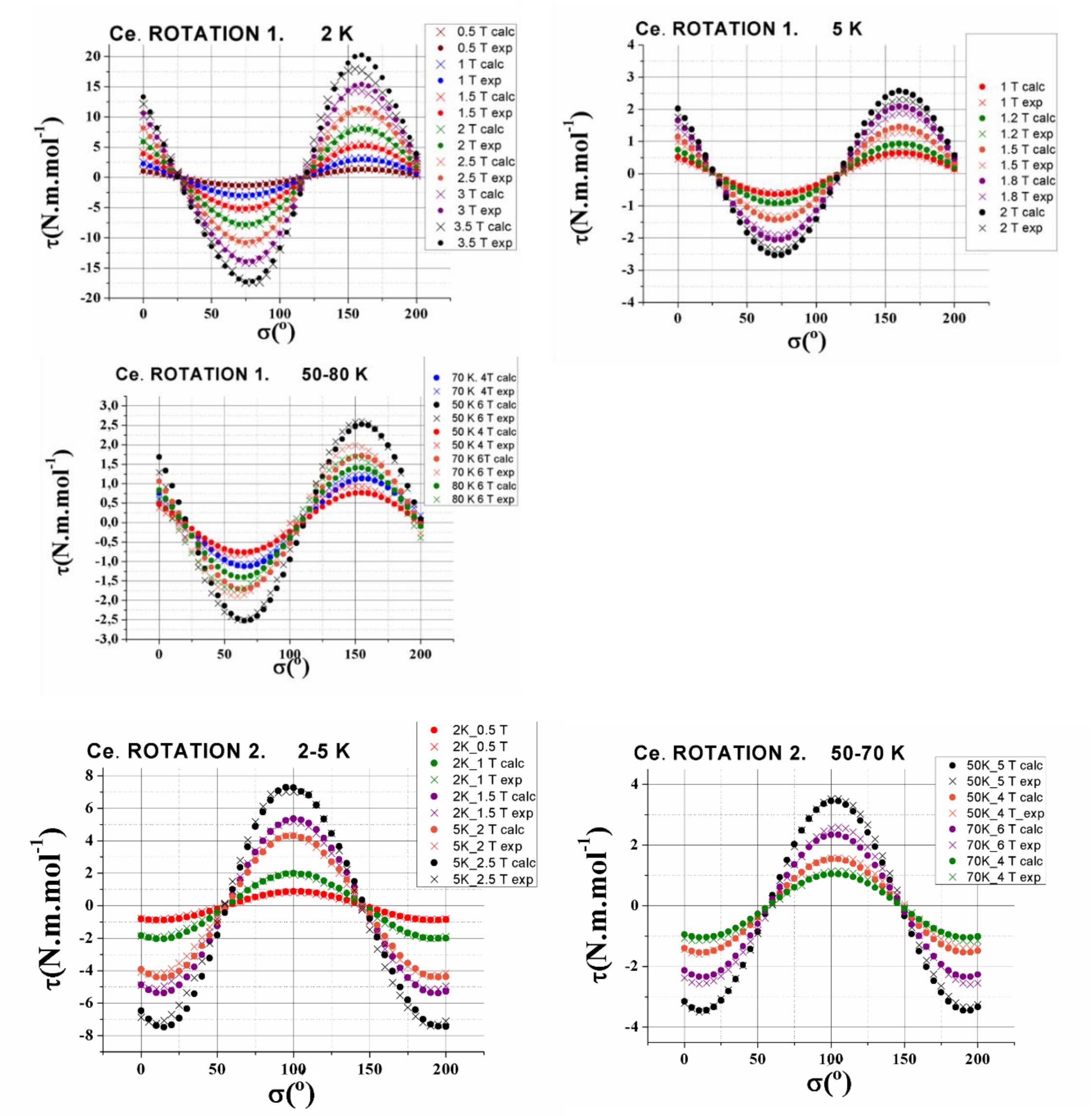

Figure 7. 20. Rotation 1 and rotation 2 in CTM of complex **[42]** at different temperatures.

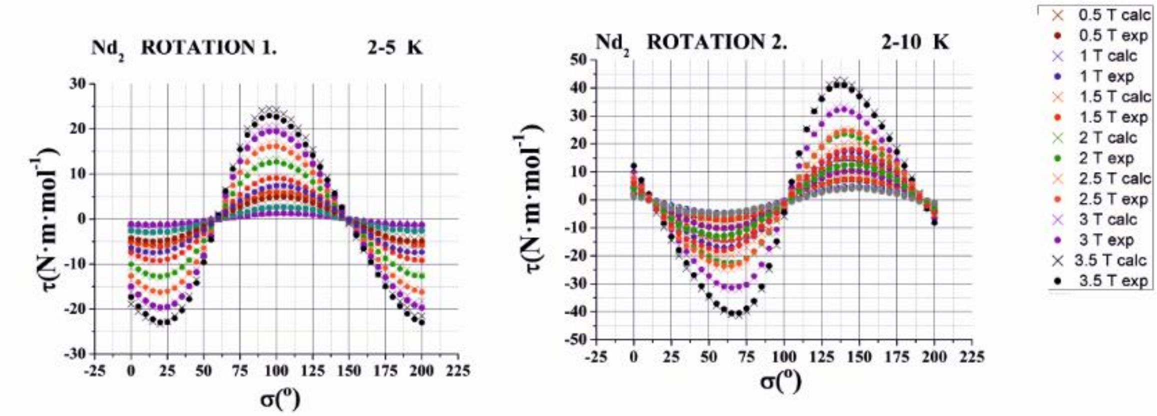

Figure 21. Rotation 1 and rotation 2 for complex **[43]** in the CTM at different temperatures

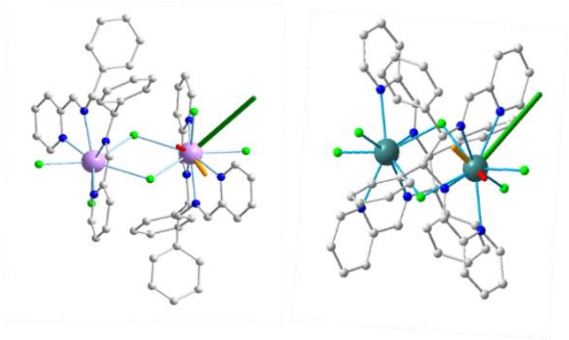

Figure 7. 22 shows the position of the easy, intermediate and hard axis for each molecule. Left, **[42]** and right, **[43].**

The fitting of the CTM allowed to extract the information about the anisotropy axes of **[42]** and **[43]** in the director cosines in *ab*'*c** reference framework: For **[42]:** Hard axis (-0.62413 0.097627 0.77519) Intermediate (-0.78122 -0.062441 -0.62112) and Easy axis (-0.012234 -0.99326 0.1152397). For **[43]**, the axes were represented by using the *g* factors from the EPR, orientation of g tensor in *ab*'*c**: Easy axis (-0.09698 -0.3653 -0.9258), Intermediate axis (0.47415 0.8009 -0.3657, Hard axis (0.87509 -0.47444 0.09555) which come from the fitting with g_1, g_2 and g_3. Easy axis is almost perpendicular to Nd-Cl5, i.e. it lies in the Nd-bridging chlorine plane. There is no other evident relation to structural features.

7.3. MONONUCLEAR COMPOUNDS DERIVED FROM Eu^{III}, Tb^{III}, Dy^{III}, Er^{III} and Yb^{III} ([Ln] FAMILY).

7.3.1. Structural characterization.

Like in the case of the dinuclear compounds, one of the structures was solved by single crystal X-ray diffraction (the Tb^{III} derivatives **[46*RR*]** and [**46*SS***]) whereas the other complexes were characterized by powder X-ray diffraction.

[Tb(L6)(Cl$_3$)] [**46**]. The coordination sphere of the terbium cation is a pentagonal bipyramid and thus, it is heptacoordinated. First, Tb^{III} is bonded to the tetradentate ligand **L6**, which occupies the equatorial positions of the complex. The bond of the metal with the ligand is via the four N-donors of the ligand, that form N_{py}-Tb-N_{imina} angles much lower than 90º ranging from 63.22º to 66.33º in the case of compound **[46*SS*]**, while in the case of **[46*RR*]** from 64.27º to 65.47º (see Table 9, Appendix 4), that provides enough space to coordinate a chloride ligand (Cl1) to be placed in the same plane. Then there are also two more chloride ligands occupying the axial positions forming a Cl2-Tb1-Cl3 bond angle close to 180º. In compound **[46*SS*]**, the stated angle is 170.03º and for compound **[46*RR*]**, 165.52º. This affects the geometry of the molecule by having a slightly distorted pentagonal bipyramid.

The structures of compounds **[46*RR*]** and **[46*SS*]** show a mononuclear neutral complex of Tb^{III}, whose crystalline system is triclinic. In the unit cell there are four non-equivalent molecules (labelled A to D) with similar structures, the data given above refer to molecule C. These four molecules differ only slightly by the bond distances and angles. In the following **Figure 23** it can be seen a labelled plot of the molecular unit and the arrangement of the four molecules inside the cell and **Table 7.3** reports the main bond parameters.

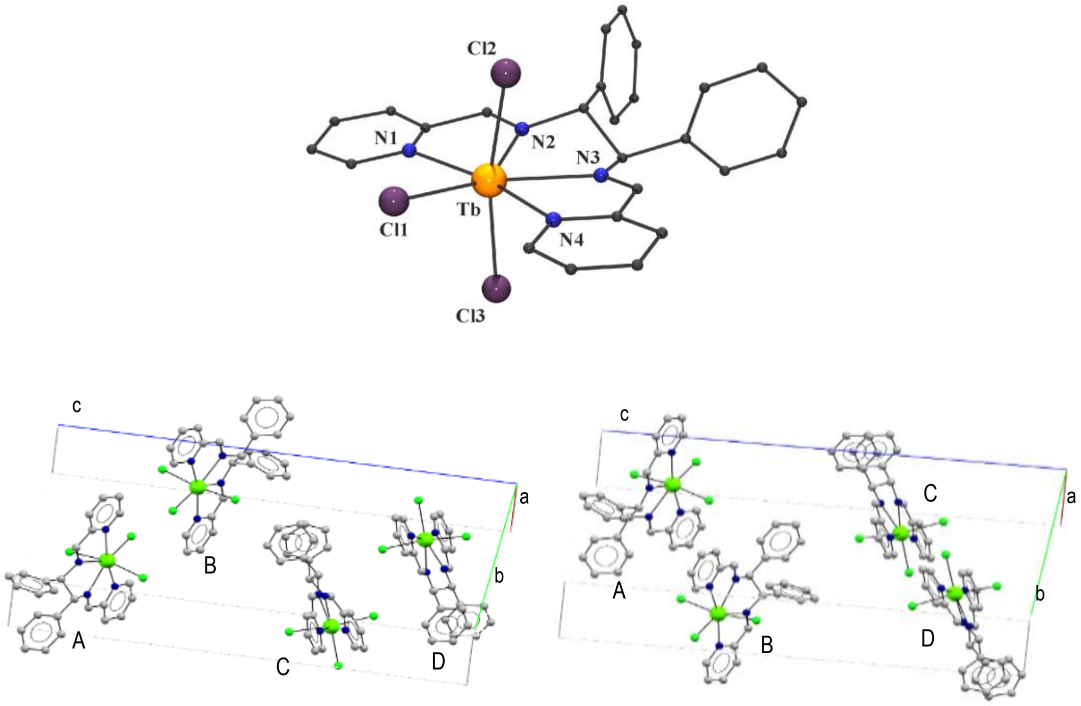

Figure 7.23. Top, labeled plot of the molecular structure of complex **[46]**. Space distribution of the four molecules in the unit cell for complex~~es~~ **[46].** Bottom left, *RR* enantiomer and bottom right, *SS* enantiomer.

There are no relevant intermolecular hydrogen bonds as consequence of the lack of crystallization solvents, O-donors or accessible N-atoms. The only interactions are promoted by weak CH···Cl contacts between the coordinated chloro ligands and the nearest H-atoms from pyridinic fragments of the nearby molecule, with C···Cl distances around 3.5 Å optimizing the maximum possible packaging.

	[46*RR*]				**[46*SS*]**			
	A	B	C	D	A	B	C	D
Tb1 - N1	2.578	2.630	2.575	2.601	2.556	2.572	2.551	2.566
Tb1 - N2	2.520	2.505	2.545	2.495	2.515	2.543	2.508	2.498
Tb1 - N3	2.521	2.519	2.501	2.542	2.522	2.528	2.518	2.532
Tb1 - N4	2.583	2.548	2.542	2.518	2.579	2.553	2.575	2.568
Tb1 - Cl1	2.6130	2.6188	2.6133	2.6048	2.6323	2.6150	2.6147	2.5937
Tb1 - Cl2	2.6089	2.6109	2.5909	2.6325	2.6034	2.6071	2.6342	2.6133
Tb1 – Cl3	2.6471	2.6051	2.6327	2.6154	2.3096	2.6332	2.6025	2.6316
N1 - Tb1 - N2	63.22	65.29	63.24	66.33	64.44	64.27	65.47	64.74
N2 - Tb1 - N3	65.49	64.70	65.53	65.85	64.89	65.33	65.00	64.31
N3 - Tb1 - N4	65.14	64.32	65.05	65.06	64.69	64.78	64.36	65.27
N1 - Tb1 - Cl1	83.23	82.94	84.78	80.68	83.42	82.88	83.11	82.94
N4 - Tb1 - Cl1	83.44	83.58	82.51	82.88	83.67	83.80	82.64	83.81
Cl2 - Tb1 -Cl3	167.75	171.84	170.03	166.43	172.02	168.09	165.52	169.93

Table 7.3. Distances and angles for the Tb^{III} derivative as a representative example of the mononuclear compounds.

The powder X-ray diffraction spectra for the complete series of the mononuclear [Ln] complexes **[45]**-**[49]** (**Figure 7.24**), show the full agreement of the experimental diffraction patterns with the spectrum calculated from the single crystal structures of compounds **[46]** evidencing that compounds **[45]**-**[49]** are isostructural. In this case, the lack of crystallization solvent molecules gives stable crystals in ambient conditions. Crystallographic data appears in Appendix IV.

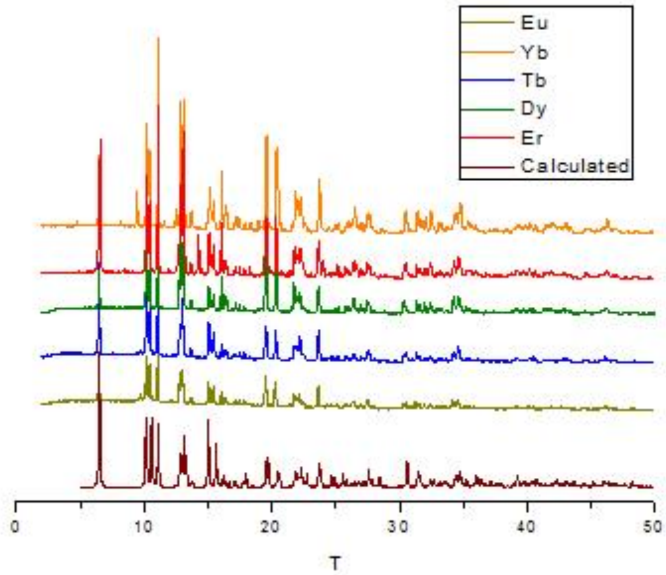

Figure 7.24 Powder XDR diffraction pattern obtained for compounds **[45]-[49]** (above) and calculated spectrum for compound **[46]** (bottom).

7.3.2. Magnetic studies.

7.3.2.1. Dynamic magnetic properties.

To study the dynamic magnetic properties of complexes **[47]**, **[48]** and **[49]** (Dy^{III}, Er^{III} and Yb^{III} respectively) were performed on polycrystalline samples and, like in the [Ln_2] series, no maxima appear in the χ_M'' vs. T measurements above 1.8 K at zero dc field for any on the compounds.

For the Dy^{III} derivative, complex **[47]**, a dc field of 1000 G was selected after a preliminary study of the out-of-phase signal under different fields. Its out-of-phase susceptibility dependence in front of the frequency between 10 and 1488 Hz is represented in **Figure 7.25**.

As is shown in **Figure 7.25**, the relaxation occurs by a lonely process, supposed to be Arrhenius relaxation. By using **Eq. X**, the fitting process yield to plot depicted in **Figure 7.25** right, with the parameters $\tau_0 = 3.22x10^{-6}$ s and $U_{\text{eff}} = 10.58$ cm^{-1}.

Cole-Cole plots were performed for complex **[47]** showing that effectively the relaxation occurs through only one mechanism in the whole temperature range. The Argand plot was also fitted using the CCfit software yielding in an average α value of 0.6, indicating and intermediate distribution of the relaxation times. **Figure 7.26** shows the fitted Argand plot.

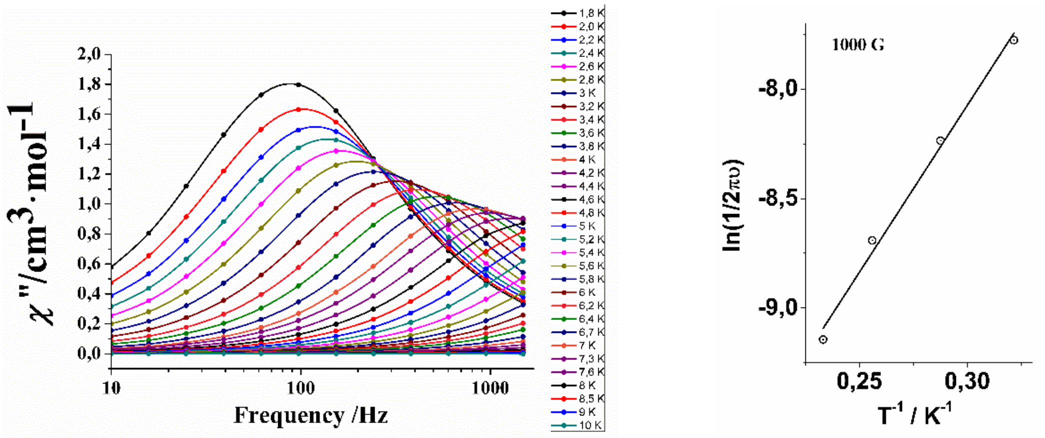

Figure 7.25. Left, representation of the out-of-phase susceptibility for the Dy^{III} complex **[47]** in the frequency range 10-1488 Hz. Right, Arrhenius plot of complex **[47]**.

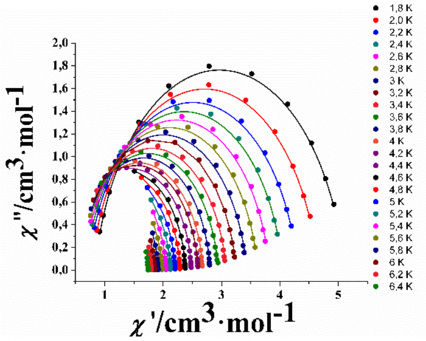

Figure 7.26. Cole-Cole fitted plot of complex **[47]** indicating a lonely relaxation mechanism.

The Er^{III} derivative **[48]** was investigated under the application of different magnetic fields. **Figure 7.27** shows the dependency of the out-of-phase susceptibility for complex **[48]** in front of the frequency under a static dc field of 500, 1000, 2000 and 3000 G.

In a first stage, we used an Arrhenius dependency fitting to calculate the relaxation time (τ_0) and the relaxation barrier (U_{eff}) by means of **Eq. 7.1**. The linear fits are depicted in **Figure 7.28** and the relaxation parameters summarized in **Table 7.4**. The relaxation parameters at 500, 1000 and 2000 G are very similar (the linear fittings are almost superimposed) while a huge difference is observed for an external applied field of 3000 G.

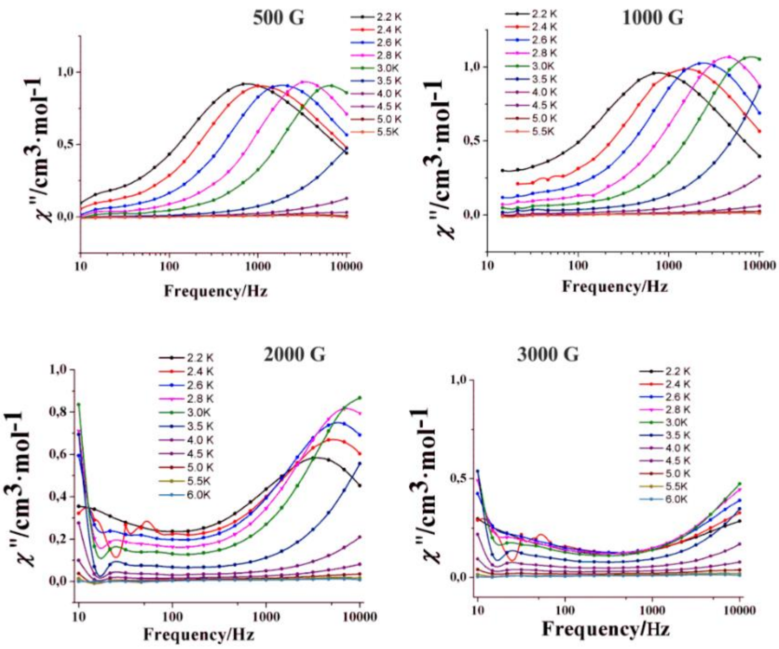

Figure 7.27. Representation of the imaginary part of the susceptibility for complex **[48]** at different applied magnetic fields.

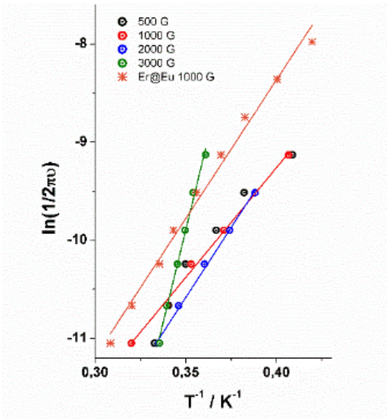

Figure 7.28 Arrhenius plot of complex [**48**], the Er^{III} derivative under different dc applied fields and Er@Eu at 1000 G.

	τ_0 (s)	U_{eff} (cm^{-1})	U_{eff} (K)
500 G	1.27E-8	15.7	22.6
1000 G	1.24E-8	15.5	22.4
2000 G	1.18E-9	19.8	28.5
3000 G	1.54E-16	52.7	75.8
Er@Eu 1000 G	2.87E-9	19.6	28.3

Table 7.4. Relaxation parameters for complex **[48]**, the Er^{III} derivative and for the magnetic dilution of Er@Eu under a dc field of 1000 G.

The measurements of complex **[48]** at 3000 G provide values with extremely large uncertainties, since there are no peaks in χ'' *vs.* ω curves. The reason for this behavior is that the direct process (the efficiency of which scales with the field) is quite efficient, so, on increasing the field, the relaxation goes much faster.

Due to the anomalous behavior of the dynamic magnetic properties of complex **[48]**, two different trials have been done. The first one was to measure the dynamic properties of the complex at low frequencies (between 0.12 and 997 Hz) to try to see if the estrange behavior at low frequencies can be elucidated with more detail. The in-phase and the out-of-phase susceptibility plots are depicted in **Figure 7.29**, showing that the behavior observed in the first measurement cannot be studied in more detail because at low frequencies the χ'' dependency with temperature and frequency vanishes.

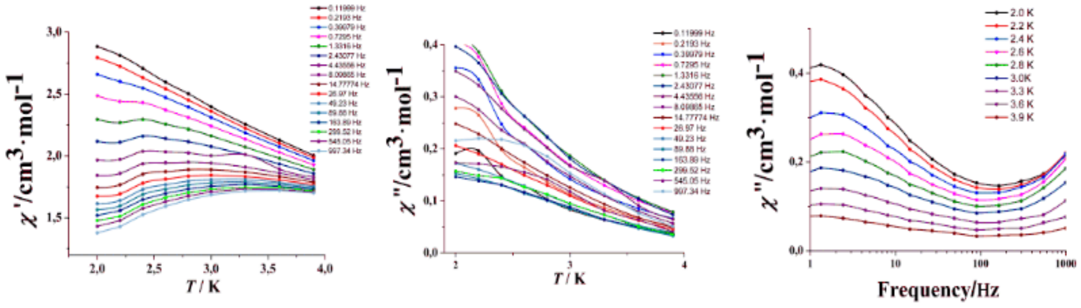

Figure 7.29. χ' and χ'' vs. temperature and χ'' vs. frequency dependence for complex **[48]** measured under a dc field of 3000 G.

The second trail was to prepare a magnetic dilution of the Er^{III} derivative. The first choice for the magnetic dilution was to prepare the Er@Y derivative with a 5% of Er^{III} in the sample. However, this synthesis was not successful (further trials demonstrates that the Y^{III} complex was not formed) and we decided to use Eu^{III} as a magnetic dilutor taking into account that this cation is diamagnetic at the investigated temperatures. **Figure 7.30** shows the susceptibility dependency *vs*. frequency under dc fields of 500 and 1000 G. As was expected the magnetic dilution enhances the magnetic relaxation of the compound due to the diminishing of the intermolecular interactions. The magnetic relaxation parameters for the Er@Eu complex are in **Table 7.4** which are almost equal to the values of the pure Er^{III} compound.

The direct term is quite efficient even in the diluted sample, at 1000 G is faster than 500 G.

The magnetic dilution Er@Eu was also useful to observe the EPR spectrum, which was not observed in the pure Er^{III} complex **[48]. Figure 7.31** shows the EPR spectrum of Er@Eu which shows a general *g* parallel feature at low field (with signals from both I=0 and I=7/2 isotopes) and an intense perpendicular feature partially split, rhombicity, at high field.

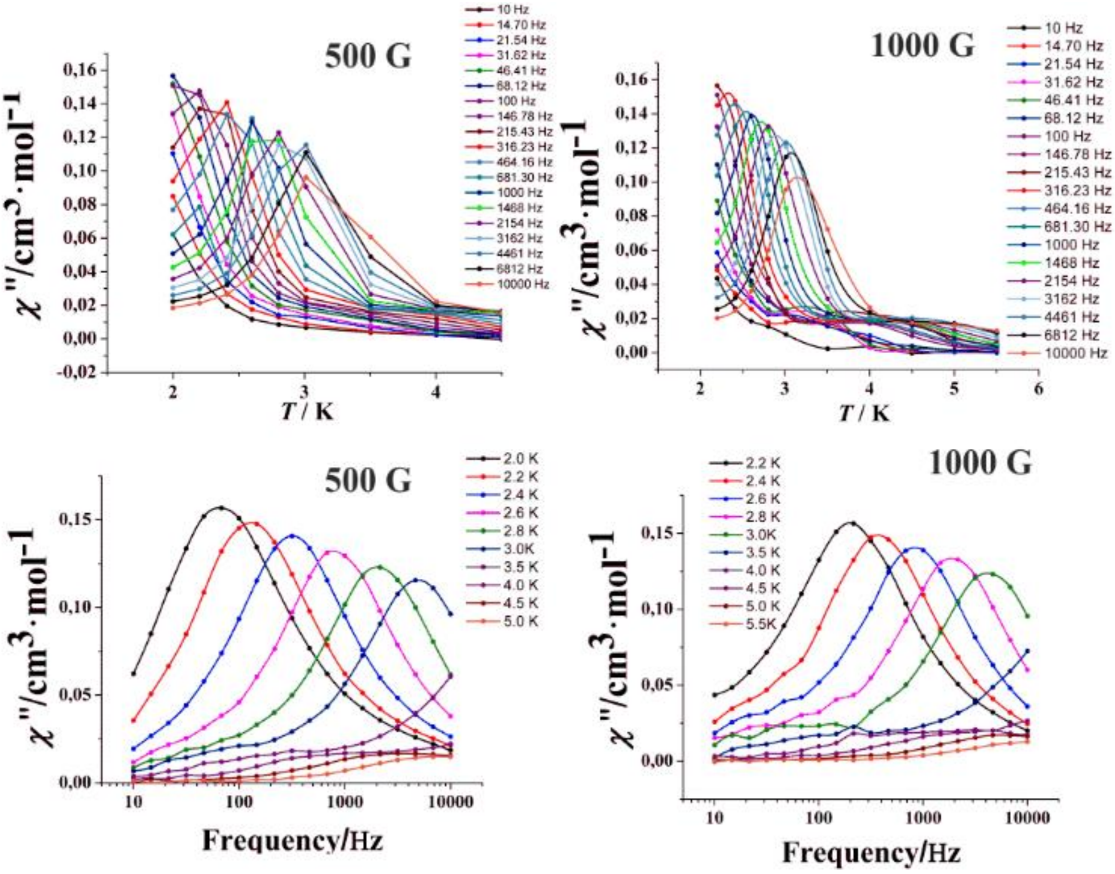

Figure 7.30. Er@Eu dependency of the χ'' vs. frequency and temperature between 10 and 10000 Hz and between 2 and 4.5 K.

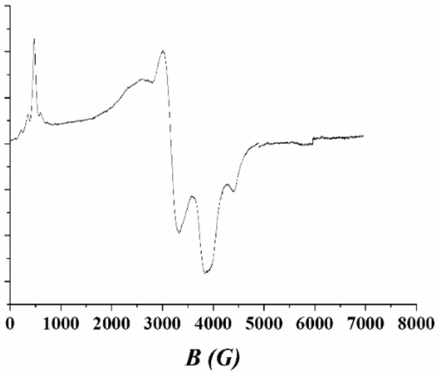

Figure 7.31. EPR spectrum of the Er@Eu complex at 5 K, where the magnetic dilution in Eu^{III} demonstrates to be effective to define the Er^{III} spectrum.

The same ac measurements were performed for complex **[49]**, the Yb^{III} derivative. **Figure 7.32** shows the χ'' vs. frequency dependence between 10 and 10000 Hz at different applied magnetic fields.

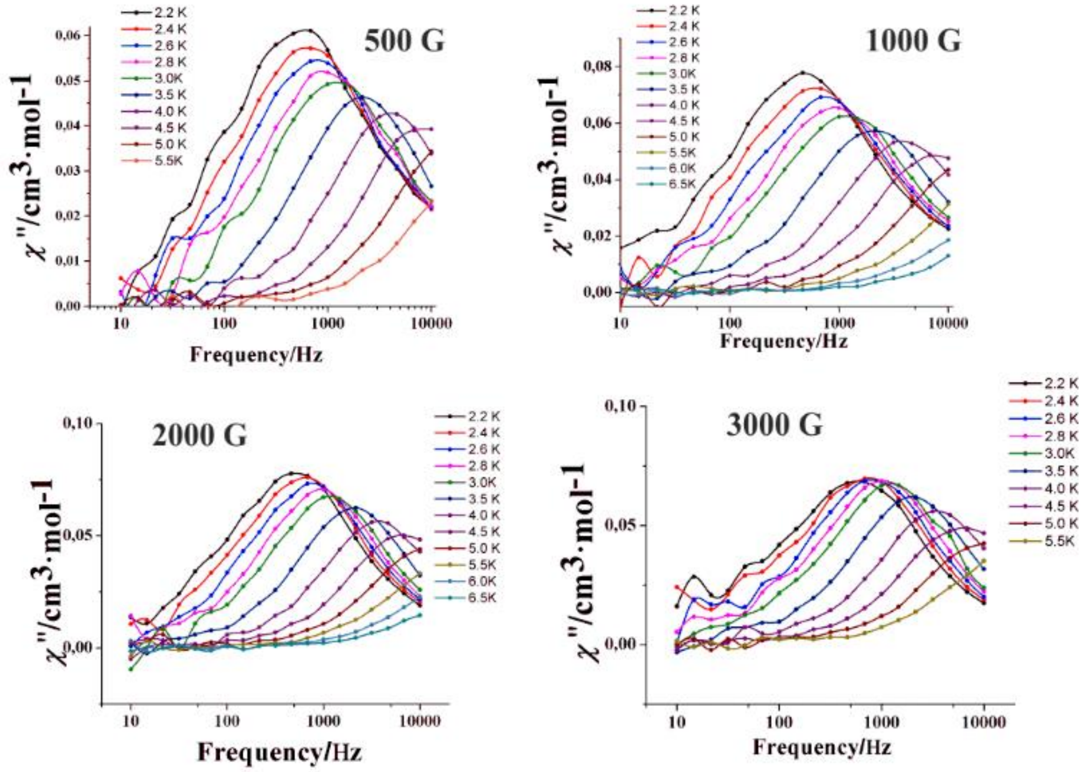

Figure 7.32. χ'' vs. frequency plots of Yb^{III} complex **[49]** at different applied dc fields.

Like in complex **[43]**, the fitting of the Argand plots was performed giving in this case only one relaxation process by using **Eq. 1, Figure 7.33** and with the relaxation parameters in **Table 7.5**

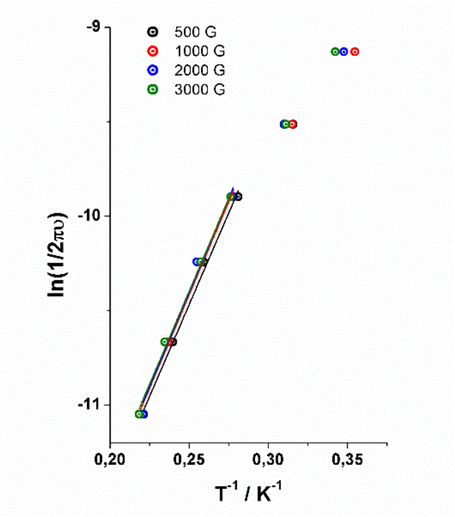

Figure 7.33. Arrhenius representation for the Yb^{III}, complex **[49]** at different applied magnetic fields.

	τ_0 (s)	U_{eff} (cm^{-1})	U_{eff} (K)
500 G	2.21E-7	13.5	19.4
1000 G	2.16E-7	13.7	19.7
2000 G	2.07E-7	13.9	20.0
3000 G	2.24E-7	13.7	19.7

Table 7.5. Relaxation parameters for complex **[49]**, the Yb^{III} derivative.

However, like in previous cases, the representation of lnτ *vs*. the inverse of the temperature derived from the Argand representations (**Figure 7.34** and **7.35**, respectively**)** yields in two different slopes confirming again the presence of more than one relaxation mechanism. Fitting was performed supposing Orbach+Raman relaxation and Raman+direct relaxation giving again negligible values for the Orbach relaxation.

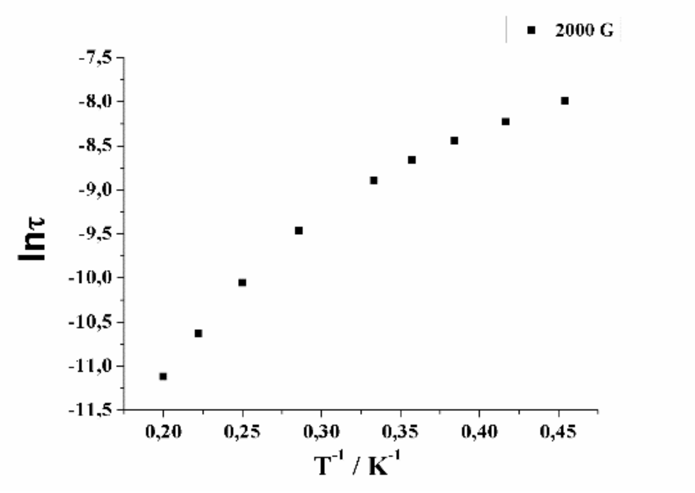

Figure 7.34. lnτ *vs*. 1/*T* plot demonstrating that there are also two relaxation mechanisms for the Yb^{III} derivative **[49]**.

The dynamic magnetic measurements demonstrate the slow relaxation of the magnetization for complexes **[42], [43], [47]**, **[48]** and **[49]**, even all of them only under the application of an external magnetic field.

The different relaxation in dinuclear and mononuclear complexes was demonstrated in the case of complex **[43]**, which shows two different relaxation processes, while only one relaxation process was confirmed for the mononuclear complexes **[47]** and **[49]**. The estrange behavior of **[48]** was not fully understood even the measurements at very low frequency either diluting with europium.

EPR and CTM for **[42]** confirmed the presence of low lying excited states, making impossible the relaxation by an over-barrier process, even at high temperatures, while the EPR in the case of **[43]** confirmed the existence of a weak ferromagnetic coupling between the two Nd^{III} cations. On Nd^{III} derivative we only have low temperature data (powder EPR and CTM), so it is only possible to know the orientation of the anisotropy axis at low temperature.

At low temperature only the ground doublet is populated, and its magnetic anisotropy is described by the different *g* values in the three directions: This system responds to an applied field in different directions.

For the dinuclear complexes **[42]** and **[43]**, the fitting performed in the CTM allowed to elucidate the direction of the easy and hard anisotropy axes.

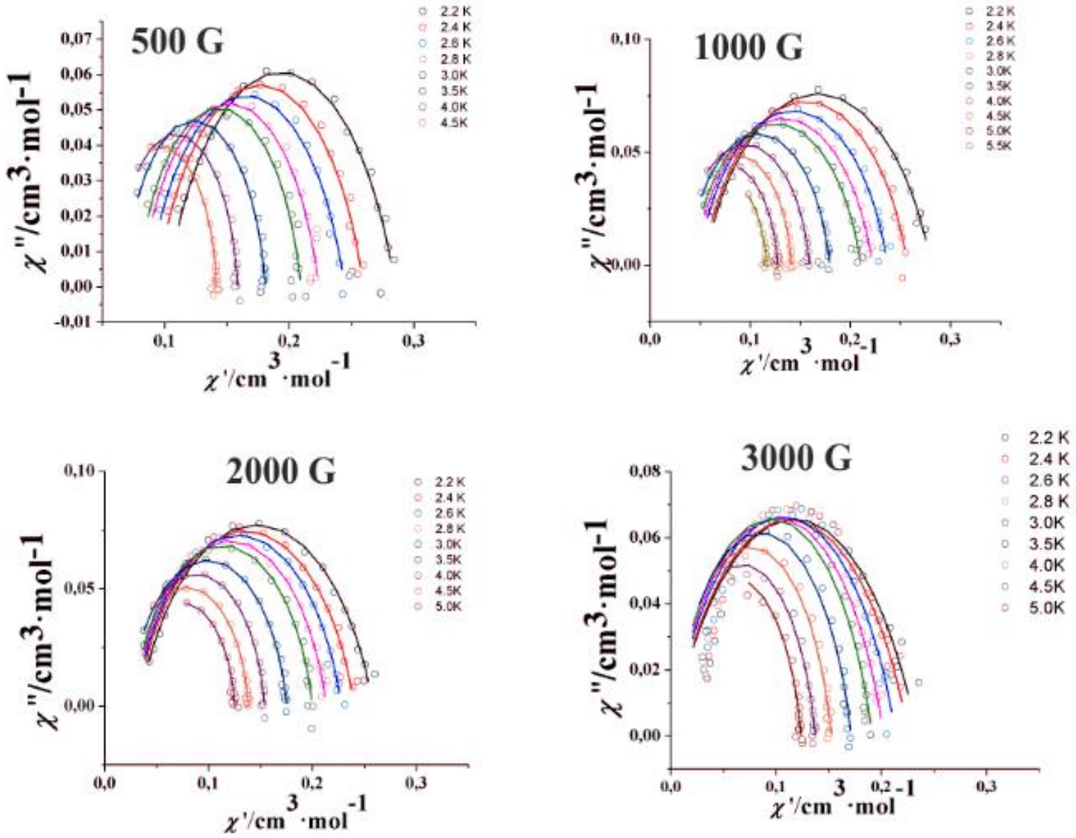

Figure 7.35. Argand plots of complex **[49]** fitted supposing only one relaxation mechanism.

CHAPTER 8. FINAL REMARKS.

Even the large number of compounds present is this thesis, it not that hard to extract general conclusions if we take into account that the nature of the ligands is the same in all the cases. I would like to start by exposing general conclusions about the behaviour of the ligands in different conditions like the used metal, the counter ion or the source of the basic medium. Due to the novelty of most of the products is important to have a systematization of the ligand behaviour for further work. Among this, and because of the main part of the thesis is about magnetism I would like to review why in most of the cases the complexes fail as SMMs or SIMs, if we assume that the expression "Single Molecule/Ion Magnet" is only assumable when no external applied field is applied to promote the magnetic relaxation. Another point that, in my opinion, is extremely important, and this is a point that for me has been the hardest part of the thesis, is the ways in which the magnetic relaxation can occur. At this moment, seems that there is a little bit of controversy about how the magnetic molecules relax. On the other hand, one of the most gratifying parts of this work has been the supramolecular chemistry involved in the structures.

To remark all the parts of my work that are a mixing between a rigorous scientific work and personal impressions of being involved in this kind of chemistry for a while, here, in the final remarks I would like to point out the most relevant conclusions. On the other hand, along an experimental work always there are unsuccessful reactions, non-reproducible syntheses or new series of potentially interesting complexes that at the end of the work are discarded or is planned that will be developed in the future. As part of this chapter, together with the overall view of the positive results of the work of the thesis, information about failed reactions or future perspectives are also reported.

8.1. THE SCHIFF BASES

An overview about this kind of ligands has been included in CHAPTER I, so, at this point I would like to discuss specifically their behaviour in the specific syntheses of the thesis by dividing them in the Schiff bases containing one or two imine functions.

8.1.1. Schiff bases with a lonely imine group and NO_2 or NO_3 donor sets.

In **Figure 8.1,** a representation of the used Schiff bases which contain only one imine function are depicted. All of them have been synthesized from the condensation of one aldehyde functional group and the amino group from an aminoalcohol.

These ligands are dianionic in its deprotonated L^{2-} form and exhibit excellent coordination ability with a wide variety of cations. The double C=N bond confers rigidity to the molecules that usually link one cation in *mer*- coordination sites by means of the N-iminic and the deprotonated O-alcoxo and O-phenoxo donors. The deprotonated oxygen atoms can bind up to three cations and thus these ligands can have a large number of coordination modes that increases if the ligand is prepared instead salicylaldehyde from *o*-vanillin that provides an additional neutral O-donor.

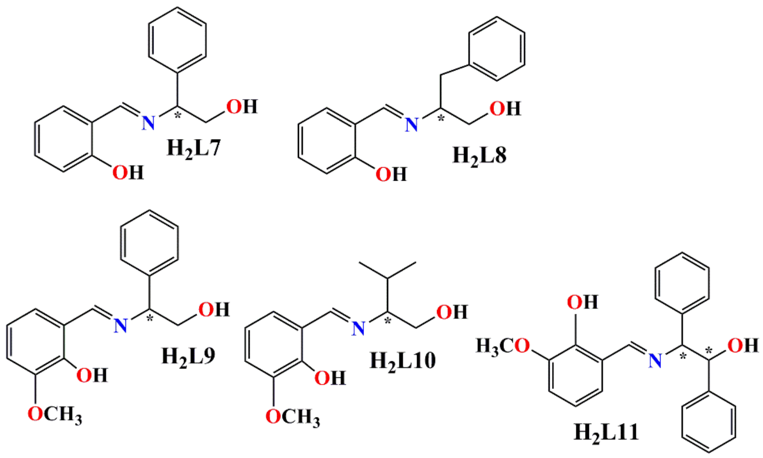

Figure 8.1. Ligands used in the thesis from the condensation of an aldehyde functional group with a chiral aminoalcohol.

Ligands **H_2L7** and **H_2L8** with NO_2 donor atoms have exclusively been used in the synthesis of products belonging to ***Publication #4*** comprising only manganese chemistry (complexes **[6]**, **[7]** and **[8]**) which are the first polynuclear derivatives of these ligands. The found coordination mode for all of them is shown in **Figure 8.2**.

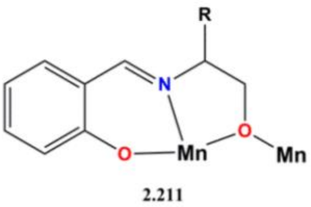

Figure 8.2. Coordination mode of **H_2L7** and **H_2L8** in complexes **[6]**, **[7]** and **[8]**.

For the reaction with manganese carboxylates the R group does not affect the coordination mode or the Mn^{III}-Mn^{II}-Mn^{III} core because, as is said in ***Publication #4***, this trinuclear topology derived from carboxylates is an extremely common and stable structure (**Figure 8.3**), and the only variable that modifies the final structure was the change in the counterion (see below).

Even it was not allowed to crystallize any other product with a different R derived from **H_2L7** and **H_2L8**¸ this behaviour suggests that the trinuclear structure will be obtained with any other R while using a carboxylate manganese salt as a reactant.

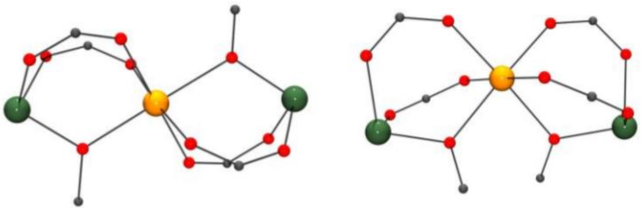

Figure 8.3. Core of complexes **[6]** and **[7]** showing the typical linear trinuclear structure which appears with the use of manganese carboxylates and Schiff bases.

The **H_2L9**, **H_2L10** and **H_2L11** ligands have an additional methoxide function in a third position of the ring. From the result of preliminary reactions with several bases changing the R- substituent on the ethylene fragment (-Ph, -CH_2-Ph, Me, *i*-Pr) it was possible to conclude that **H_2L9** confers better crystallinity to the derived complexes and has been undoubtedly the star of this thesis, giving interesting clusters with nickel, iron, manganese and heterometallic manganese-lanthanide systems. In contrast, only some few positive results have been obtained with **H_2L10** and **H_2L11.** All the found coordination modes along the present work for these ligands and different cations are depicted in **Figure 8.4**.

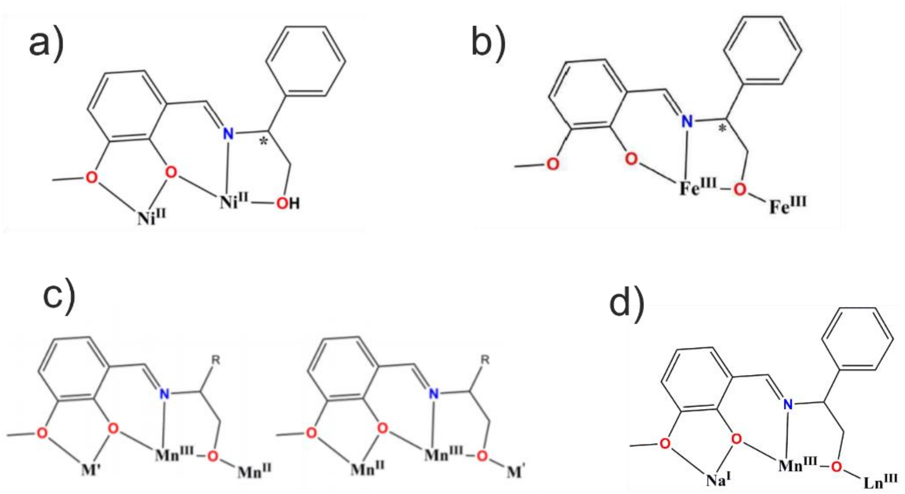

Figure 8.4. Coordination modes of **H_2L9, H_2L10** and **H_2L1.** a) in complex **[5],** b) in complex **[18]**, c) in **[10]-[15]** (R= ph**,** M'=Na^{I}, Ca^{II}, Mn^{II}**.** R= *i*-Pr, M'=Na^{I} in **[16]** and **[17]** and d) for complexes **[20]-[29]**.

Employment of the ligand **H_2L9** in nickel chemistry yielded the enantiomeric pair of tetranuclear complexes **[5]** reported in ***Publication #2.*** Similar Ni_4 or new Ni_2 clusters were obtained during the trials with other ligands but were discarded due to the difficulty to obtain good crystals (all attempts to solve single crystal structures failed allowing only to partial information) and that were poorly reproducible syntheses.

Similar problems were found in the trials to react these ligands in Fe^{III} chemistry. Reaction of **H_2L9** with Fe^{III} salts yields the enantiomeric pair of iron stars **[18]**. The reaction and crystallization was clean and reproducible whereas with the remainder ligands, the products were extremely soluble and poorly crystalline. Only for **H_2L11** it was possible to isolate a mononuclear derivative.

Preliminary trials to obtain $Fe^{III}_3Ln^{III}$ stars have been performed with **H_2L9**. Until now only trinuclear $Fe^{III}_2Ln^{III}$ systems have been characterized, being a promising series of heterometallic clusters to be magnetically studied in the future, **Figure 8.5**.

The larger number of complexes have been obtained in manganese chemistry and, as in the other cases, mainly by employment of **H_2L9,** yielding the enantiomeric pairs **[9]-[15]** reported in ***Publications #5*** and **#7**. The robust $[Mn^{II}Mn^{III}_3M']$ core with the cations in a trigonal bypyramidal core allowed to play with the M' cation or the base employed to deprotonate the ligand, giving new examples of the $[Mn^{II}Mn^{III}_3Na^{I}]$ and $[Mn^{II}Mn^{III}_3Ca^{II}]$ clusters and the first examples of the $[Mn^{II}_2Mn^{III}_3]$ core or the double system sharing the central cation $[Mn^{II}Mn^{III}_6Na^{I}_2]$

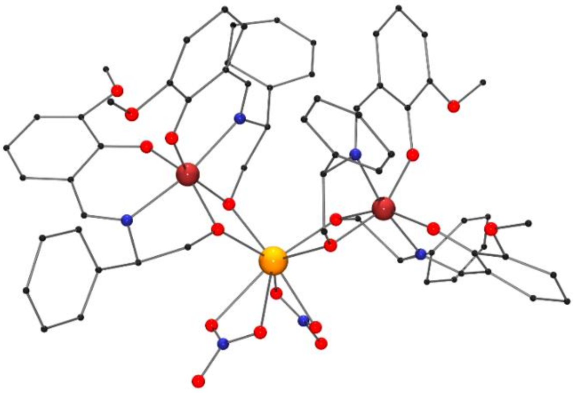

Figure 8.5. Preliminary structure of the new heterometallic $Fe^{III}_2Dy^{III}$ cluster.

The mixture of manganese with lanthanides yield in the successful series of clusters **[19-27]** with $[Ln^{III}Mn^{III}_6Na^{I}_2]$ core, closely related to complexes **[9-10]** by substitution of the central Mn^{II} by one Ln^{III} cation. These complexes provide an interesting case of unprecedented meso-chiral isomerism which is described in deep in CHAPTER 5.

It is remarkable that the change of the reaction conditions opens the possibility to reach substitution on the central Mn^{III} cations by lanthanide ones as was characterized in one $[Tb^{III}_2Mn^{II}_2Mn^{III}_4Na^{I}_2]$ system derived also from **H_2L9, Figure 8.6.** This line has not been included in the work and will be developed in the future.

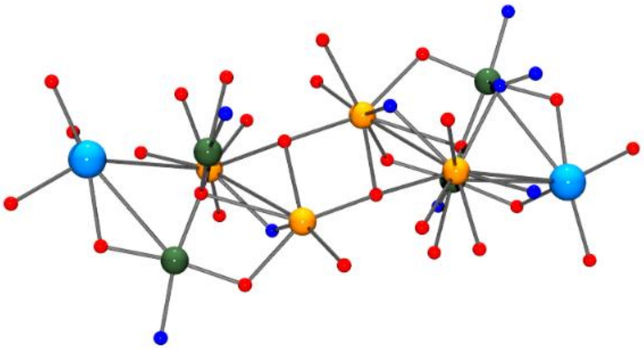

Figure 8.6. Core of the new series of complexes derived from **H_2L9.** Color code: Green, Mn^{III}; orange, Ln^{III}, blue, $Na^{I.}$

The only manganese systems characterized with a ligand different to **H_2L9** was obtained with **H_2L10**. The change in the R substituent of the ligand promotes a different topology in which two $[Mn^{II}Mn^{III}_3Na^{I}]$ fragments are linked by triple chloro, bromo or azido bridges resulting the decanuclear complexes **[16-17]** with core $[Mn^{II}_2Mn^{III}_6Na^{I}_2]$ described in ***Publication #6***. This result suggests that even similar complexes could be obtained, the R group is not innocent in the crystallization of the clusters, probably due to different solubility.

8.1.2. Schiff bases with two imine groups and a N_4 donor set.

The ligands employed in this thesis containing two imine groups and a N_4 donor set are depicted in **Figure 8.7**.

This family of **L1 - L6** ligands exhibit some common characteristics: they are neutral, they are able to coordinate either 3*d* or 4*f* cations, contain a more or less flexible ethylene spacer and the pyridyl groups linked directly to the cations could act as antenna in luminescent systems. For this kind of ligands, we can expect two main coordination possibilities: as tetradentate or bis-bidentate ligands, **Figure 8.8**.

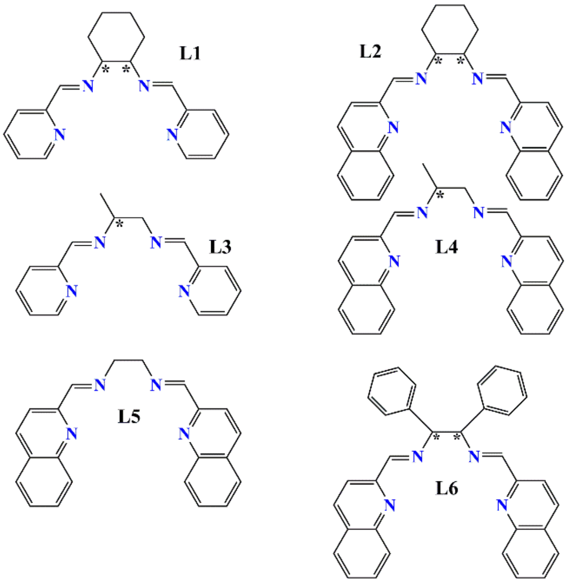

Figure 8.7. Ligands used in the thesis from the condensation of an aldehyde functional group with a chiral diamine.

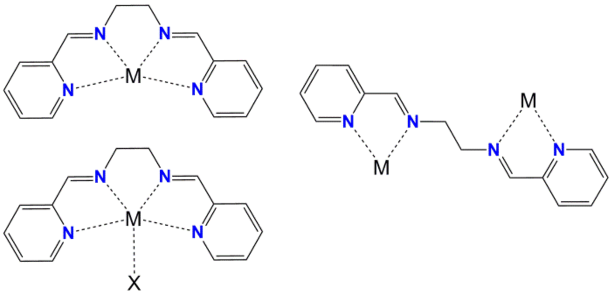

Figure 8.8. Typical coordination modes as tetradentate or bis-bidentate ligands for **L1**-**L6**.

When this kind of ligands acts as tetradentate donors they cover four coplanar coordination sites. The bite between neighbour donors determines low N-M-N bond angles (< 70º) that allow the possibility to incorporate a fifth donor in the available space, **Figure 8.8**. This fact is common for large cations (lanthanides as example) or Mn^{II} which possesses a plastic coordination sphere derived from its d^5 configuration. For 3*d* cations its tetradentate coordination, plus two axial monodentate ligands, usually gives octahedral environments.

The bis-bidentate coordination can be done between two cations that fulfil their coordination spheres with other coligands and then, the bis-bidentate ligand acts as simple bridge. More interesting is the case in which two ligands are coordinated to two cations giving mesocates or helicates as has widely studied with cations with tetrahedral environment such as the divalent ion Cu^{II} or the monovalent ions Ag^{I} and Cu^{I}.

In this thesis we have exploited the above possibilities working with a divalent 3*d* cation (Ni^{II}) or larger trivalent lanthanide ions.

Ligands **L1**, **L2, L3, L4** and **L5** have been used in ***Publication #1*** to study how they affect the supramolecular features of a dinuclear Ni^{II} complex (**[1]-[4]**) demonstrating that the flexibility of the central spacer and the size of the aromatic groups influence the final structure allowing to the fine tuning of the mesocate-helicate configurations.

Things change when we are talking about these ligands and its reaction with lanthanide cations. For the larger Ln^{III} cations the *chelate* effect predominates and the tetradentate coordination was found in all cases yielding the series of complexes **[42]-[49]** with formula $[Ln_2(L6)_2(Cl_6)]$ or $[Ln(L6)(Cl_3)]$ reported in Chapter VII.

Noteworthy, the syntheses of **[42]-[49]** with the diphenyl ligand **L6** were clean and gave easily crystalline compounds whereas the employment of ligands **L1-L4** gave in all cases negative results. Any defined complex was obtained with the ligands containing the quinoline fragment due to the probable solvolysis of the ligands and only for the methyl derivative **L3** some compounds were partially characterized. Their crystallinity was low, the syntheses were not always reproducible and complexes like those shown in **Figure 8.9** were discarded for further measurements in this thesis.

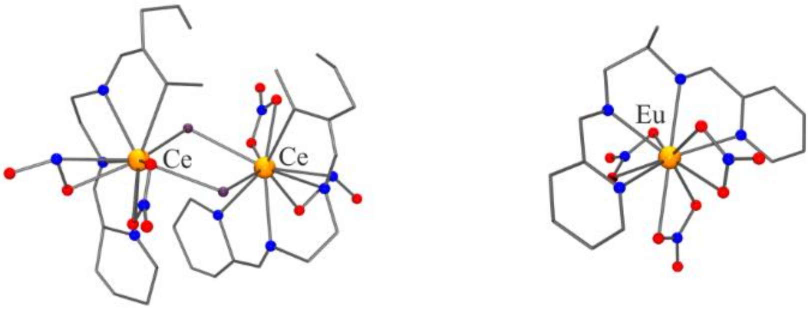

Figure 8.9. Preliminary structures of complexes derived from the reaction of **L3** and $Ln(NO_3)\cdot xH_2O$, yielding in topologies very similar to the ones presented in CHAPTER VII for the light and heavy lanthanides. The μ-Cl bridges come from the diamine hydrochloride starting reagent.

8.1.3. Compartmental Schiff bases with two imine groups and a N_2O_4 donor set.

The compartmental ligands are classical ligands in the synthesis of heterometallic systems and one of the most exploited are those derived from the condensation of diamines with salicylaldehyde or *o*-vanillin. The (*RR*) and (*SS*)-$\mathbf{H_2L12}$ ligands belong to this kind of Schiff bases, and become chiral by substitution on the two C-atoms of the ethylene fragment by phenyl groups, **Figure 8.10**. The inner cavity with a set of N_2O_2 donors is smaller than the outer cavity with a set of O_4 donors and thus, the adequate choice of the cations can predetermine its selective linkage and the composition of the heterometallic system. The binucleation by using the sets of different donor atoms[87] with two well differentiate cavities allows to easy and reproducible syntheses.

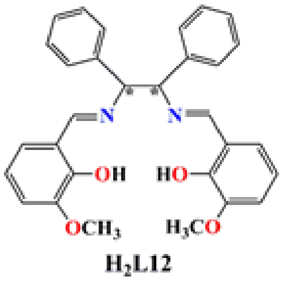

Figure 8.10. Compartmental **H_2L12** ligand.

These compartmental ligands are very useful for the syntheses of compounds combining a 4*f* lanthanide with a 3*d* cations [ref]: The $O_2O'_2$ compartment can easily accommodate the large oxophilic lanthanide and the inner and smaller N_2O_2 pocket hosts adequately the 3*d* metal [ref Andruh] even there are few examples where the nitrogen atoms do not coordinate the *d* metal NOHNIH) and others which are able to coordinate the lanthanide even using the nitrogen (CETPUM, BICKIJ, CICHED, GAJGOQ, IYOXEA, JUQFUW, NOCROM), these complexes must be assumed as unusual.

The strong ligand field promoted by the inner cavity gives square planar complexes when the cation is Ni^{II}. This property, *a priory* unfavourable in a work about magnetic properties, can be an alternative to the usual Zn^{II} cation to promote magnetic dilution. In this thesis the ligands (*RR*) and (*SS*)-**H_2L12** has been successfully employed to prepare the series of $[Zn^{II}Ln^{III}]$ and $[Ni^{II}Ln^{III}]$ complexes in which the 3d cation is diamagnetic, that have been described in CHAPTER VI.

In addition to these complexes, the rol of the Cd^{II} cation was explored. This cation is larger than the divalent 3d cations but smaller than the lanthanides and its soft character seems to favour its coordination in the inner sphere of the ligand. The experimental reaction in the same conditions that the $[Zn^{II}Ln^{III}]$ complexes allowed to the crystallization of a helical 1-D system with formula $[Cd(H_2L12)(NO_3)_2]_n$ in which, surprisingly, the coordination sphere of the Cd^{II} is fulfilled exclusively by O-donors, **Figure 8.11**. Due to its fully diamagnetic character, the study of this system has not been included in the thesis.

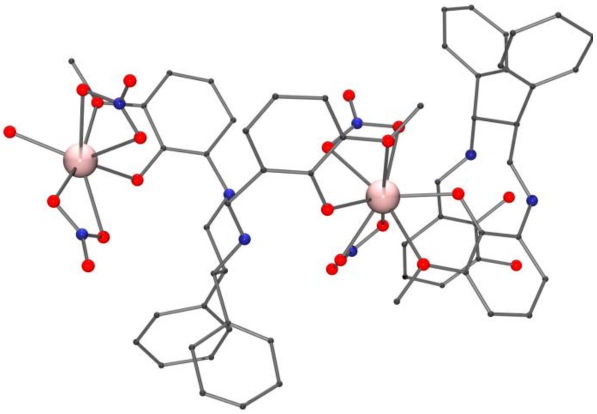

Figure 8.11. Plot of the $[Cd(H_2L12)(NO_3)_2]$ chain.

8.1.4. Solvolysis of the Schiff bases.

It is well known that the Schiff bases are susceptible to solvolysis of the double C=N recovering the starting reagents by reversing the condensation reaction or in other cases, yielding new fragments. The presence of polarizing cations linked to the iminic function favours the attack of the solvent and by example, the breaking of the double bond of the Schiff base is usual in the reaction with lanthanide cations.

Along the present work, the employed bases shown to be stable in the most of the reactions but solvolysis were observed in some cases. Breaking of the ligands is usually a disadvantage and in fact, the reactions of **L2** and **L4** ligands containing the quinoline fragment were unsuccessful in the most of the cases. However, in a serendipitous manner, breaking of the ligands can give unexpected and positive results.

One example is provided by the trinuclear Mn^{III} complexes **[8]** obtained from **H$_2$L8** (***Publication #3***). The Mn^{III} triangle has the molecular monoanionic formula $[\mathrm{Mn^{III}}_3(\mathrm{L8})_3(\mu_3\text{-Cl})\mathrm{Cl}_3]^-$ and the negative charge is balanced by one cationic protonated aminoalcohol that helps to stabilize the cluster, **Figure 8.12**. This aminoalcohol was generated by the partial breaking of the **H$_2$L8** ligand, which in this case was the key to the characterization of these SMMs.

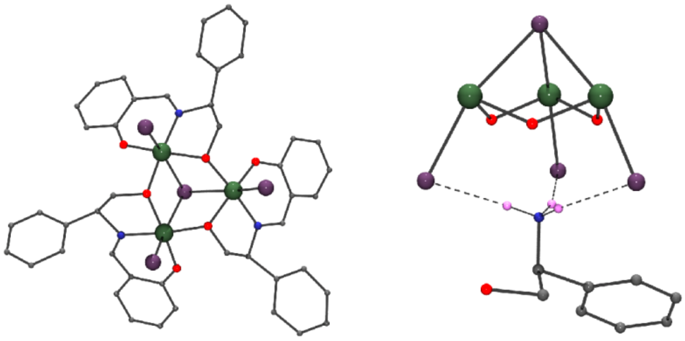

Figure 8.12. Trinuclear structure of the anionic triangular complexes **[8]** (left) and its interaction with the protonated aminoalcohol from partial solvolysis that counterbalance the charge.

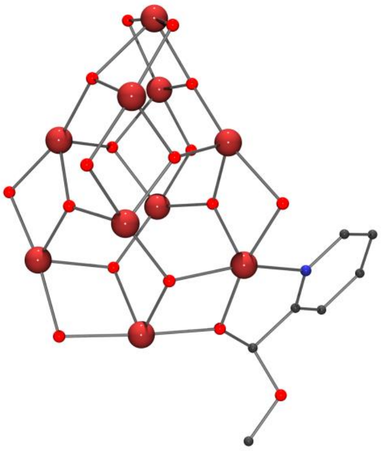

Figure 8.13. $\mathrm{Fe_{10}O_{16}}$ core of the iron cluster obtained by the breaking of the initial Schiff base showing one of the L = methoxy-(2-hydroxymethylpyridine) ligands.

A second interesting case of serendipitous synthesis of a new type of cluster is provided by the reaction of the neutral ligands derived from **L5** with Fe^{III} salts in methanolic medium. In this case the attack of the solvent to the iminic function yields the unexpected ligand methoxy-(2-hydroxymethylpyridine) and the decanuclear $[Fe_{10}(L)_8(NO_3)_7(OH)(O)_7]$ cluster, **Figure 8.13**. In this case, the breaking of the ligand yielded an interesting cluster, because is the larger nuclearity reported to now in 2-hydroxymethylpyridine/iron chemistry. The new ligands are chiral but the cluster contains four (*R*) and four (*S*) ones resulting the meso complexes. This series of achiral complexes has not been included in the thesis and will be studied in a near future.

8.2. THE EFFECT OF THE COUNTERION AND THE BASE

Often the change of the reaction variables such the solvents, anions or the employed base, if needed, to deprotonate the organic ligands are not innocent and can have a direct influence on the topology or nuclearity of the final cluster.

The effect of the counteranion has not been relevant for the nickel complexes (***Publication #1***) because the very stable structure of the $[Ni_2(L)_2(N_3)_2]^{2+}$ dimers can be obtained from different anions without changes in the structure. In the same way, the neutral Fe$^{III}_4$ stars (***Publication #3***) were insensitive to the starting iron salt employed in the synthesis. As was previously indicated for the series of complexes **[6]**, **[7]** and **[8]**, ***Publication #4***, the structures were determined by the employment of carboxylates (Mn^{III}-Mn^{II}-Mn^{III} linear clusters) or chloride (the first discrete Mn$^{III}_3$ triangle with a μ_3-Cl). However, for the remainder clusters reported in this thesis the metallic starting salt was carefully selected to obtain specific features in their structures or properties.

For all the series comprising complexes **[9]** to **[27]** the starting counterions were chloride or bromide in all cases. These complexes with trigonal bipyramidal arrangement of the cations needs three bridging ligands to fulfil the axial coordination sites of the trivalent manganese cations placed in the equatorial plane. This triangle tends to be asymmetric for systems in which there are several coligands or even if the ligands have several coordination modes as can be seen for carboxylates or azides among others. **Figure 8.14** shows some examples of reported asymmetric triangles.

To obtain symmetric equatorial planes the employment of the halide ligands is a good choice because they have the adequate size to bridge the axial positions of the Mn^{III} cations and do not possesses alternative coordination modes, **Figure 8.14**. The main goal by using Cl$^-$ and Br$^-$ is that the triangle becomes strictly (C_3 axis) or practically equilateral, which is an enormous advantage to work with the spin Hamiltonian to avoid the over parametrization in the magnetic analysis. For practically all complexes **[9]** to **[27]** the magnetic analysis was performed with only two coupling constants, one to parametrize the interaction inside the triangle and a second one to parametrize the Mn$^{III}\cdots$Mn^{II} interactions.

Finally, for the lanthanide series presented in CHAPTER 6 the selected salt was the nitrate to avoid bridges between the Zn^{II} and the Ln^{III} cations such often occurs for carboxylates and on the other hand, to cover the remainder coordination sites of the lanthanides avoiding larger nuclearities.

In contrast for the systems reported in CHAPTER VII the selected anion was chloride to favour the dinuclear systems such was obtained for the lighter lanthanides.

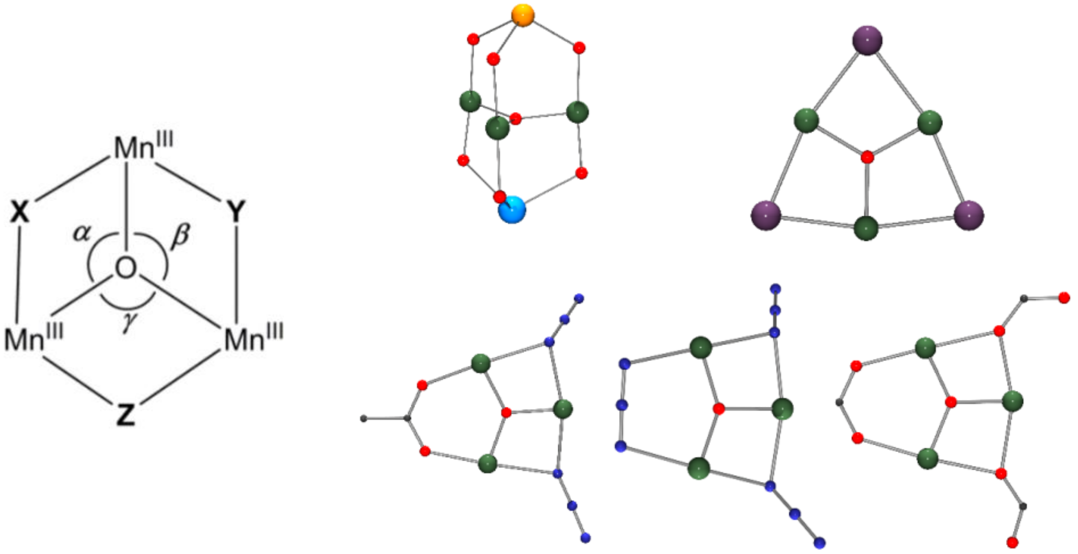

Figure 8.14 Left, the bridges to link the Mn^{III} triangle. Right, some examples of linkages found in the literature that allow to non-equilateral triangles.

About the use of a base to deprotonate the ligands, Et_3N has been employed as a constant along the work. However, in some selected cases in which the idea was that one additional cation could play a role in the final structure participating of the final nuclearity, alkaline salts or hydroxides (or calcium methoxide in the case of compounds **[14]** and **[15]**), were employed.

Na^{I} cation participates in a large number of clusters of this thesis. It appears in complexes **[9], [10], [11], [16], [17]** and **[20]-[29]**. The trial to obtain isostructural complexes of **[9], [10], [11], [16], [17]** by changing the Na^{I} cation by Li^{I}, K^{I} and Cs^{I} failed in all the cases**.** Use of Li(OH) as a base didn't yield to any characterizable product while the use of potassium and cesium salts (azide and methoxide, respectively) or their hydroxides yield to the formation of the pentanuclear [$Mn^{II}_2Mn^{III}_3$] complexes **[12]** and **[13]**, indicating that the cavity that was previously hosting the Na^{I} cation is too small for a K^{I} or Cs^{I} and the inclusion of a smaller Mn^{II} cation was preferred.

For the family of complexes derived from **H$_2$L10**, complexes **[16]** and **[17]**, were only achieved by using NaOH. The introduction of Na^{I} cation in form of NaN_3 yield to the product depicted in **Figure 8.15**, where the triple halide bridge of **[16]** and **[17]** has been substituted by a triple azido bridge. In this structure, there is also an asymmetry between the bridges linking the two Mn^{III} triangles: only one side has the above descripted Mn^{III} triangle linked by three halide bridges whereas the other Mn^{III} triangle is linked by three methoxide bridges.

Azide ion was also an active player in the syntheses of Ni^{II} complexes belonging to ***Publication #1***, complexes **[1], [2], [3]** and **[4]**, where the N_3^- clearly promotes the double helicate/mesocate shape of the structures covering specific coordination sites of the Ni^{II} cations.

For the Ni^{II} complexes derived from **H$_2$L9** and included in ***Publication #2***, azide was used as a base and it was introduced in the compounds as a coligand by bridging the Ni^{II} cations and promoting ferromagnetic interactions. Similar syntheses using trimethylamine as a base instead of azide have been tried with Ni^{II} and **H$_2$L9** yielding in the dinuclear complex depicted in **Figure 8.16**, left, and with **H$_2$L10** yielding in complex depicted in complex depicted in **Figure 8.16**, right. These two compounds have been excluded of this thesis due to the irreproducible synthesis. The fact that only the Ni^{II} complexes containing azide in their structure were obtained in clean and reproducible syntheses confirms the well-known affinity between Ni^{II} and azido.

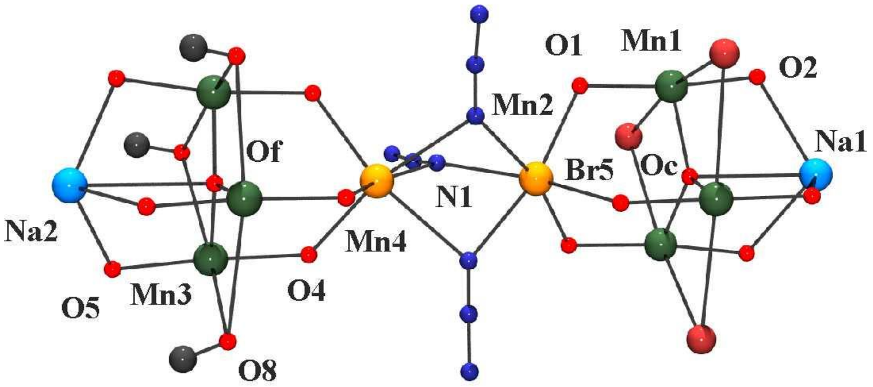

Figure 8.15. Product obtained when NaN_3 was used as a base to deprotonate the ligand in the syntheses of complexes **[16]** and **[17]**.

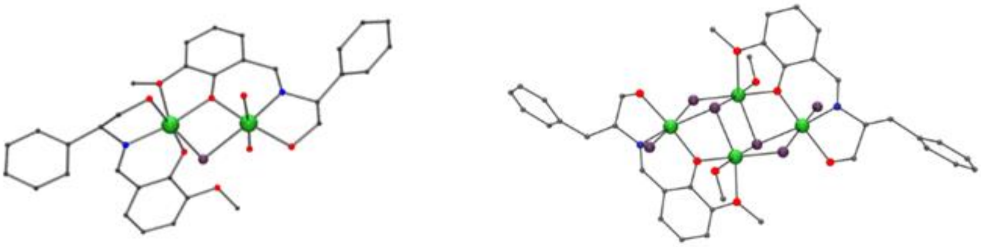

$[Ni_2(L)_2(OH)_2Cl]$ $[Ni_4(L)_2(CH_3O)_2(Cl)_6]$

Figure 8.16. Discarded complexes derived from Ni^{II} without using NaN_3. Left, a complex derived from **H_2L9**, and right, derived from **H_2L10**.

8.3. THE USE OF ELECTRONIC CIRCULAR DICHROISM IN THE STRUCTURAL CHARACTERIZATION.

The use of Electronic Circular Dichroism (ECD) spectroscopy in this work was in all the cases as a characterization technique. Even it can be used to deeply structurally characterize the products, a complementation with theoretical calculations is needed. In ***Publication #1*** there is a theoretical study of the ECD of the complexes by using time-dependent DFT calculations, however, this has not been a common procedure in this work due to the complication of studying theoretically molecules with large nuclearity.

The technique was used here as a corroboration that the structure of the products remains in solution (no differences have been observed in the comparison between the solid state and solution spectra). The most of the ECD spectra were measured in methanolic solution except in some specific cases where the measurements were performed in other solvents for solubility reasons.

8.4. SUPRAMOLECULAR CHIRALITY. CHIRALITY TRANSFER.

What has to be elucidated at this point about the supramolecular chemistry of coordination clusters is if is possible to assembly molecules in such a way that their physical properties could be predicted. I dare to say that the use of enantiopure organic ligands to synthesize the coordination compounds simplified the prediction about what was going to happen in the molecule. The first point is that. For sure, if we use chiral reactants, the product will be chiral. The only question is: at which level of chirality would we arrive?

If we take a look to ***Publication #1*** ¸where the common thread of the paper is the achievement of different types of supramolecular structures while doing slightly changes in the ligand, we can say that it was possible to control the final structure by choosing adequately the building blocks, **Figure 8.17**. It's important to remember that the control of the structures can only be done after a previous step of always pure serendipity.

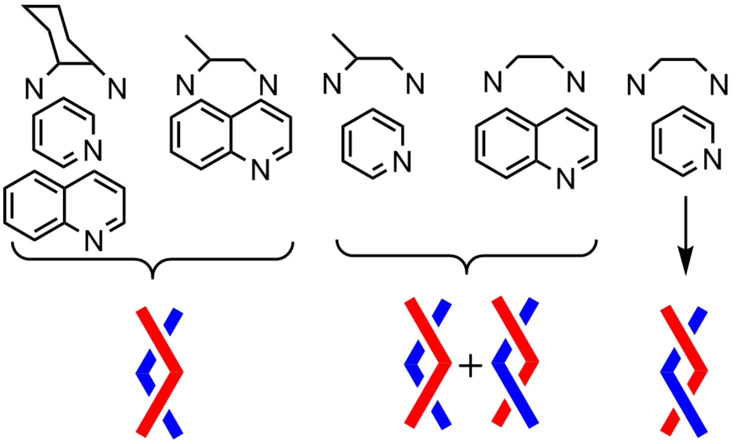

Figure 8.17. Helicate to mesocate transition as a function of the spacer and ring size of the Schiff bases.

It is known from the literature that in all the reported cases for octahedral and tetrahedral metallic centers, when one uses an enantiopure organic ligand, the final clusters becomes in a chiral supramolecular structure (helicates for related examples). Because what we have done is to use chiral ligands to synthesize achiral supramolecular forms (the mesocates) so it can be said that I *fought* against chirality transfer and I won.

Among the control of the chirality transfer from ligand to metal, what is very interesting from the compounds included in ***Publication #1***, is the way how the unit cells ordinate when they can choose between symmetry and asymmetry. If we remember complex **[4]**, its structure contains a centrosymmetric mesocate with two helicates with opposite Δ/Λ helicity. The intermolecular interactions provide an exceptional example of supramolecular chiral recognition in an achiral network. The mesocates from layers of parallel chains linked by π-π stacking of the aromatic rings of the quinolyl groups. Between the mesocate planes there are layers of helicates formed by homochiral parallel chains (ΔΛ or ΛΛ) dimers related by inversion centers (**Figure 8.18)**.

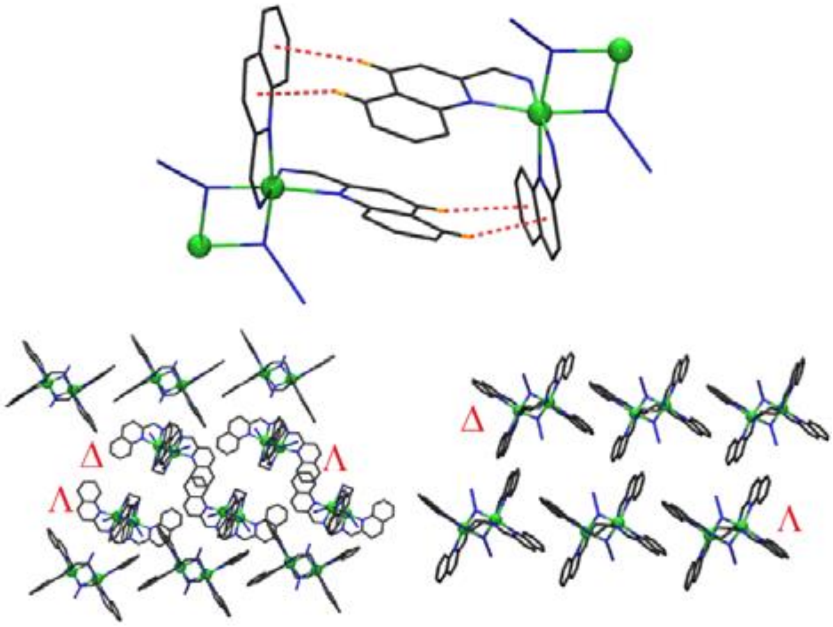

Figure 8.18. Top, intermolecular interactions of complex **[4]** (CH···π-ring, indicated as dotted lines). Bottom (left), one layer of chains of Δ and Λ dimers between layers of parallel chains of mesocates. Botton (right) a lateral view of the parallel Δ and Λ chains of the helical dimers.

The pair of [$Mn^{II}Mn^{III}_3Na^{I}$] enantiomers **[11]** shows the conventional and expected transference of chirality from the chiral ligands to the metallic centres and the molecule. In fact, the clusters are helicates with opposite helicity and the Na^{I} cations are Λ or Δ in one or other enantiomer, **Figure 8.19**. In contrast, the chirality is not transferred to the network arrangement.

The series of manganese-based complexes **[9]** to **[27]** with trigonal bipyramidal common core combined as basic fragment offer a variety of chiral responses that are quite unusual in some cases.

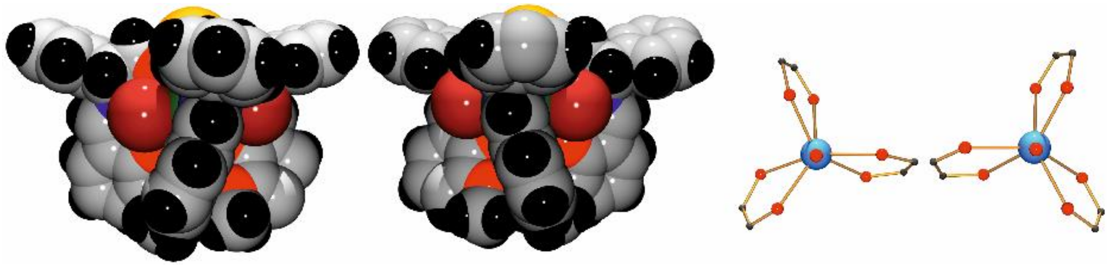

Figure 8.19. Left, a spacefill view of the two pentanuclear enantiomers of **1*R*** and **1*S*** showing the helical arrangement of the ligands. Right, Na^{I} environment for **1*R*** (Λ) and **1*S*** (Δ).

In light of **[11]**, it could be expected that the [$Mn^{II}Mn^{III}_6Na^{I}_2$] clusters **[9]** and **[10]**, the [$Mn^{II}_2Mn^{III}_6Na^{I}_2$] **[16]** and **[17]** and the series of [$Ln^{III}Mn^{III}_6Na^{I}_2$] **[19]** to **[27],** will be also helicates. However, the helicity turns in *opposite* sense in each half of the molecule containing the ligand with the *same* chirality and the Na^{I} cations show Λ or Δ stereochemistry inside the *same* molecule. This feature is extremely unusual and it means that the more obvious transference of chirality is not present in these cases. In contrast, there is a small transference on the central cation for the prismatic rotation, that slightly turns right or left for each enantiomer, probably favouring the network chirality and a best molecular packing, **Figure 8.20**.

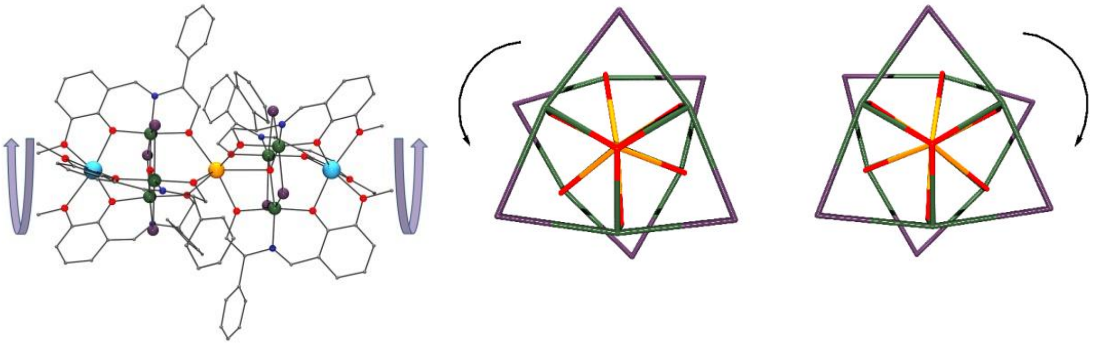

Figure 8.20. Left, example of opposite helicity for the two fragments of the same molecule. Right, trigonal rotation of the central Mn^{II}/Ln^{III} coordination spheres that determine a sligth Λ or Δ conformation for (*R*) (left) or (*S*)-**L9** (right) ligands.

Also, the pentanuclear complexes **[12]** to **[15]** with formula [Mn^{II}Mn$^{III}_{3}$M’] M’=Mn^{II}, Ca^{II} show a rare arrangement of the ligands. One of the three L9^{2-} ligands is reversed, **Figure 8.21**, left, and turns in *opposite* sense to the other two ligands. Consequently, the molecule is a rare helicate in which each kind of ligand turns different and it is not possible to classify it as Λ or Δ. The same feature is transferred to the cation linked by two bidentate fragments that rotate in opposite sense. However, the packing in the network consist of molecules flipped 180º and then, all the equivalent ligands in the net turn in the same sense.

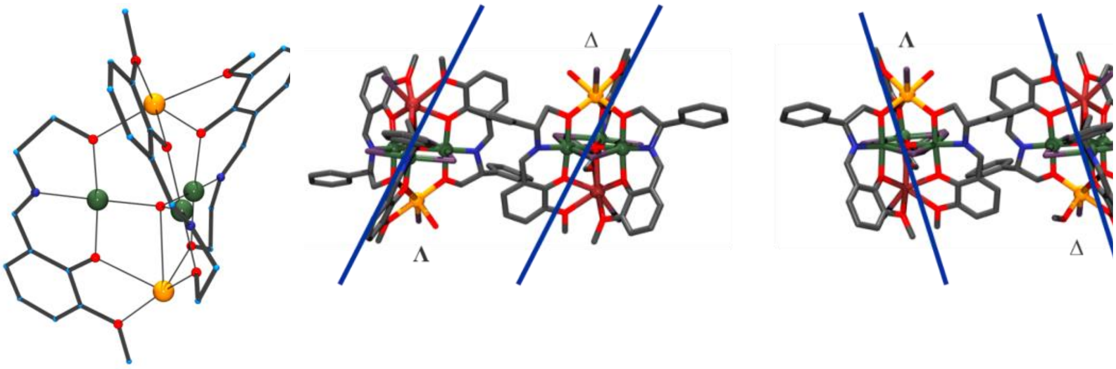

Figure 8.21. Left, view of one molecular unit of [Mn$^{III}_{3}$Mn^{II}M’] M’=Mn^{II}, Ca^{II} complexes showing one reversed ligand. Right, packing of the two enantiomers with all the equivalent ligands turning in the same sense in the network.

Finally, even is not strictly a transference of chirality between enantiomers, the case of complexes with general formula [$Ln^{III}Mn^{III}_6Na^{I}_2$] **[19]-[27]** is exceptional. The chiral enantiomers are asymmetric with the lanthanide in heptacoordinated apicated octahedron environment, whereas the racemic cluster is centrosymmetric with the lanthanide in a compressed octahedral environment. It is a relevant fact that, as is explained in CHAPTER V, the symmetric form is preferred even in 2:1 excess of one of the enantiomers, confirming the preference of the nature to be symmetric when there is the opportunity. It is remarkable that in the literature there is not an equivalent example of meso-chiral isomerism involving rearrangement and change of coordination number of the cations. **Figure 8.22** shows the different environment of the Ln^{III} cation in the racemic or chiral forms.

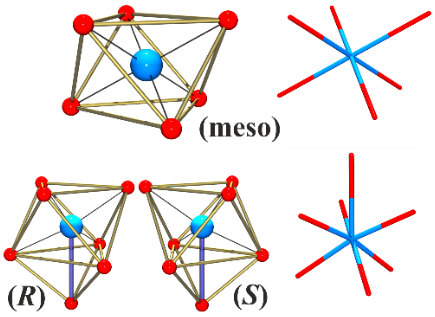

Figure 8.22. Environment around the Ln^{III} cation in meso and chiral forms.

Moving to the iron star, complex **[18],** there is a nice discussion about the chirality transfer to the Fe^{III} central cation of the star which, in spite of its very small deviation from a trigonal prims topology, shows opposite distortion sense for each enantiomer **(Figure 8.23,** top**)**

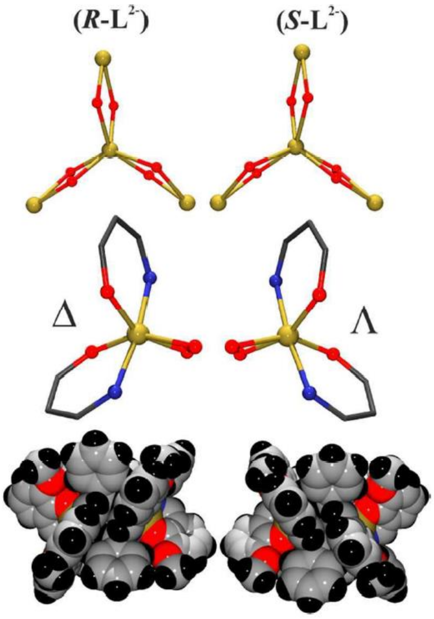

Figure 8.23. Chirality transfer in complex **[18]**.

Also chirality transfer, occurs for the peripheral Fe^{III} cations which show octahedral environment with opposite configurations for each enantiomer (**Figure 23**, middle). The tilted planes of the ligands with respect to the Fe$^{III}_4$ plane determines the propeller shape of the cluster with opposite helicities for each enantiomer.

8.5. MAGNETISM

8.5.1. Magnetic behaviour.

8.5.1.1. Static properties.

Magnetism is complicate. The intrinsic serendipity in coordination chemistry makes difficult to predict in advance the final structure of the synthesized complexes. Moreover, when one is finally able to observe the final structure, the prediction of the magnetic behaviour of the complexes is, at least, changeling.

About the magnetic properties of the complexes presented in ***Publication #1***, **[1], [2], [3]** and **[4]** and in ***Publication #2,*** complex **[5]**, the magnetic behaviour was easy to predict because of the presence of azide making the bridge between two Ni^{II} cations, which is a deeply studied magnetostructural correlation.

The synthesis with manganese was completely different because most of the topologies are completely new. For the linear trinuclear Mn^{III}-Mn^{II}-Mn^{III} complexes **[6]** and **[7]** the behaviour was predicted due to the high number of similar complexes in the literature, while the SMM behaviour of **[8]** was a surprise due to the novelty of the triple chloride bridge, indicating a correct arrangement of the Mn^{III} anisotropy axis. On the contrary, the other Mn^{III} triangles of complexes **[9]-[19]** have a completely different arrangement of the anisotropy axis **(Figure 8.24)** which blocks the SMM behaviour.

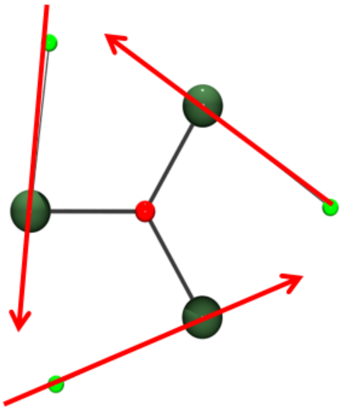

Figure 8.24. Direction of the anisotropy axes of the Mn^{III} triangles bridged by halide atoms in complexes **[9]-[19]**.

To try to achieve SMM behaviour, a lanthanide was introduced yielding in complexes **[20]-[29]**. Unfortunately, no slow magnetic relaxation was observed, but nice magnetic fittings of the static properties were done. For complexes **[9], [10], [20]-[29]**, the static magnetic properties have to take into account the interaction between the two Mn^{III} triangles present in the structure, as has been explained in ***Publication #7***, and for complexes **[16]** and **[17]** it is important to mention that the static magnetic behaviour was fitted for the very first time in all the temperature range.

About the proposition of using the Hamiltonian proposed by Lloret et *al.* to fit the susceptibility curves, the fact that in the case of the ions with positive Δ present slow relaxation of the magnetization must be due to the presence of rhombicity, that means the existence of E.

8.5.2. Magnetic relaxation in lanthanide compounds.

Finally, slow relaxation of the magnetization was achieved when using only lanthanides as paramagnetic cations. Slow magnetic relaxation under certain conditions is present in complexes **[30]-[35]**, where a lanthanide and the diamagnetic Zn^{II} cation are within the same molecule, and the same for complexes **[36]-[41]**, where the lanthanide shares the molecule with a diamagnetic square-planar Ni^{II} cation. For these series of compounds, only the Kramers lanthanides have been magnetically explored. The complexes made of pure lanthanides, **[42]-[49]** present slow magnetic relaxation in the case of the Ce^{III} **[42]**, Nd^{III} **[43]**, Dy^{III} **[47]**, Er^{III} **[48]** and Yb^{III} **[49]** derivatives. It is important to mention that both series of complexes include slow magnetic relaxation with the so-called *unusual magnetic lanthanides* and a brief commentary about Ce^{III} is needed at this point.

As has been said in the text, Ce^{III} has no nuclear spin, and for this reason, its behaviour must be considered apart from the rest of the Kramers ions used in this work. As has been explained by Ruiz and co-workers[117] the not complete Van Vleck cancellation must be related with the apparition of a interaction that breaks the selection rule of the spin-phonon relaxations. This interaction should be the hyperfine coupling, but due to the nature of Ce^{III} this is not valid for complexes **[30]**¸**[36]** and **[42]** of this thesis. Another explanation comes from the fact that Ce^{III} and Tb^{III} have very similar magnetic behaviours because seven of the eight electron of Tb^{III} are distributed in a spherical way around the cation, so Tb^{III} behaves as a $4f^{1}$ lanthanide.[102e] This supposition does not fit in the complexes **[30]** and **[31]**, because the Tb^{III} analogues did not present slow relaxation of the magnetization under any condition.

As has been usual for a vast majority of lanthanide complexes, the perception of that the energy barrier is the only factor to be taken into account is starting to be obsoleted and the idea that coupling of the vibrations with the spin states is the key factor to enhance the slow relaxation of the magnetization is running up.

Has been pointed out at the introduction (CHAPTER 1) that the low operating temperatures of the "magnetic molecules" are a big obstacle for the implementation of single molecular magnets in real technologies even new hopes became with the use of SMMs in quantum computing,[109-110] the implementation of the first Single Atom Magnet (SAM), a Ho atom adsorbed on a magnesium oxide film[111] or the discovery that dysprosocenium presents magnetic hysteresis at 60 K.[112] In CHAPTER VII, which is devoted to exclusively pure lanthanide complexes, when studying the relaxation dynamics, in all the cases an Orbach relaxation has been supposed at "high" temperatures even the height of the barrier is always higher than the calculated *Ueff*. This was assumed because it was true for the Mn$_{12}$ and its derivatives and quite common in 3*d* clusters. In some cases, also Raman or direct relaxations (the latter in dc field) are added to the total relaxation mechanism. This incongruence in the interpretation of the results shows that the understanding of the spin dynamics is still a big problem today.

In the introduction of the thesis I just described the state of the art in SMMs by explaining the different types of relaxations that can occur, but there is a lot of literature about the problems that the study of magnetic relaxation presents.

The features of the relaxation of Mn_{12} and other SMMs are not useful when the anisotropy required for the SMM behavior comes from the single ion, which is exactly what happens when lanthanide cations are involved in the magnetic properties. Their anisotropy comes from a mixture of the SOC and CF effects.[33,113] The CF parameters are the key factor to describe the intrinsic structure of the energy levels, and this is specific for each compound. To do it correctly, the complete determination of the CF structure implies the determination of a large number of crystal field parameters (see Appendix I). To completely characterize the barrier, the determination of this parameters is mandatory. In theory, the experimental characterization of the complexes should allow the determination of this parameters, but a mixture of techniques is required. In the case of complexes **[43]** and **[44]** which have been spectroscopically studied, the idea was to use this experimental spectroscopic data together with the CTM to elucidate the structure of the energy levels. The problem in my case, was that the luminescence data was lacking due to the impossibility of do the measurements at the required temperatures.

Even the experimental limitations, is sure the presence of low-lying excited states in the case of complex **[42]** as is demonstrated by the unsaturated magnetization curves and by the CTM experiments,where the position of the zero shifts when increasing temperature. The CTM fitting with the model with J=5/2, D and E using the parameters extracted from the EPR measurements yields in the values for the excited states of 0, 108 and 233.8 cm^{-1} clearly evidencing the impossibility of an over-barrier relaxation path. However, for complex **[43]¸**the Nd derivative, not much information was obtained about the excited states with the CTM.

The second problem about the parametrization of the magnetic relaxation is the so-called number and types of involved processes, that I differentiate in this thesis as *processes* which distinguish between different environments (different CF) and *mechanisms*, which differentiate between different ways of relaxation (i.e. Orbach, Raman and direct). Unfortunately, due to the very weak signals of the out-of-phase susceptibility of complex **[42]**, only the relaxation processes and mechanisms of complex **[43]** were studied.

The Argand plots for **[44]** were fitted using the CCfit software and supposing two different relaxation processes (because two semicircles appeared in the plots) yielding in $\tau 1$ and $\tau 2$. However, when we represent $\tau 1$ vs T in different ways, two different slopes appear: that means that we still having two different mechanisms involved in the process with the relaxation rate $\tau 1$. This is why we suppose the existence of a monomolecular process and a collective process which take place at different temperature range.

For all of these reasons, is evident that the actual model proposed to explain the relaxation mechanism is still far of giving a full answer to the dynamic properties of the magnetic molecules.

8.5.3. Fit of the magnetic measurements.

The fit of the calculated complexes has been performed by means of PHI program[85]. Due to the interdependence of D and zJ' parameters, determination of D from susceptibility measurements is usually poorly reliable in absolute value. On the other hand, only for medium-low nuclearities is possible to introduce a D parameter in the fitting procedure due to computational limitations.

By this reasons the susceptibility measurements have been fitted as possible with isotropic Hamiltonians to obtain the coupling constant values and the calculated *D* parameters have been calculated from reduced magnetization measurements that offers a higher degree of reliability.

CONCLUSIONS

- Schiff bases are relatively easy tunable ligands which have been useful to synthesize a wide range of products involving different metals and different nuclearities.
- The condensation of a chiral amine, diamine or aminoacohol with an aldehyde group has been demonstrated to be an effective system for the obtention of chiral coordination compounds.
- The *R* substituent in the ligands has been demostrated to be non-innocent in crystallization and solubility, showing that the best option of the used ligands was **H_2L9**.

- For Ni^{II} double helicates/mesocates of ***Publication #1***, the directed tailoring of the spacer flexibility combined with the size of the aromatic groups have been demonstrated to be a efficient form of the control of the supramolecular structure of the molecules.
- The transfer of chirality from ligand to metal is not a rule. In complexes derived from ***Publication #1***, the transfer of chirality has been controlled, and for the complexes belonging to CHAPTER 4, the transfer of chirality has not been achieved spontaneously.
- The chirality can be transferred from the ligand to the system in two different ways: to the complex or to the network.
- The use of chiral or its isostructural ligand should not yield in exactly the same final structure, as has been demonstrated in CHAPTER V by changing the geometry of the central Ln^{III} cation.

- The magnetism of all the complexes presented in CHAPTERS 5 and 6, which have in common the [Mn$^{III}_3$(μ_3-O)(μ-Cl)$_3$] triangles, has been simplified by the use of axial Cl$^-$ as bridges because the magnetic fitting has been achieved by using only 2 different superexchange parameters.
- The [Mn$^{III}_3$(μ_3-O)(μ-Cl)$_3$] triangles are always ferromagnetic in systems with a C_3 axis, while are antiferromagnetic when this axis is not present.
- The diamagnetic square-planar Ni^{II} cation has been useful to promote a magnetic dilution, and has been demonstrated that the use of different diamagnetic *d* cations as magnetic dilutors, changes the magnetic properties of the systems.
- The introduction of a lanthanide cation, with its intrinsic anisotropy, in the systems of CHAPTER 5 has not been enough to achieve slow relaxation of the magnetization due to the unfavorable disposition of the CF around the Ln^{III} cation.
- Cantilever Torque Magnetometry has been useful to determine the magnetic anisotropic axes of intermediate anisotropic cations, being used for the very first time with Ce^{III} and Nd^{III} complexes.
- Even the isostructurality of complexes **[42]** and **[43]**, the intramolecular magnetic properties have been showed to be completely different, with intramolecular coupling elucidated only for the Nd^{II} derivative.
- The Debye model that is used today to explain the relaxation of the lanthanide cations in magnetic molecules is not completely fitting the reality and a new model to explain the slow relaxation of the magnetization in molecular compounds is needed.

APPENDIX I. ELECTRONIC STRUCTURE OF LANTHANIDE IONS IN A LIGAND FIELD.

When one places a lanthanide in a ligand field with not spherical symmetry, the energy of the partially filled 4*f* orbitals splits the 2*J*+1 degeneracy of the free ion states due to this crystal field.

Following Bethe,[127] the placement of a cation in the middle of the crystal field lowers the symmetry. As has been said in the text, the effect of the ligand can be described as an operator, U_{CF}:

$$U_{CF} = -e\sum_{j=1}^{n} U_j = -e\sum_{j=1}^{n}\int \frac{\rho(R)}{|R-r_i|}dv \qquad \textbf{(A.1)}$$

Where n is the number of electrons and $\rho(R)$ is the charge distribution at a distance r_i.

The evaluation of the crystal field created by the ligands comes with the solution of the matrix $<\varphi_l|U_{CF}|\varphi_k>$ where $<\varphi_l|$ and $\varphi_k>$ are the eigenfunctions of the free ion, which are spherically symmetric. Two different formalisms have been developed to calculate the matrix elements of **Eq A.1.** Both formalisms require the decomposition of free ion terms.

STEVEN'S FORMALISM [128]

The electrostatic potential with the symmetry requirements of the lanthanide can be expressed as the product of a radial function. In this approach, the matrix elements can be computed if mixing between different J multiplets is neglected. The expression of **Eq. A.1** using the Steven's formalism is:

$$U_{CF} = H_{CF}^{Stevens}\sum_{k=2,4,6}\rho^k\sum_{q=-k}^{k}\int A_k^q < r^k > \hat{\underset{\cdot}{O}}{}_k^q \qquad \textbf{(A. 2)}$$

Where A_k^q is a parameter, $\hat{\underset{\cdot}{O}}{}_k^q$ is the operator of the CF potential and ρ^k is a number which is different for each 4*f* configuration. The number of q terms that must be included in each case is limited by the point group of the rare earth site (CF Hamiltonian must be invariant under the symmetry operations of the point group).

WYBOURNE'S FORMALISM [129]

Steven's formalism is very powerful as long as only the ground $^{2S+1}L_J$ multiplet is considered. So. It is used for EPR studies, while is not successful to use in optical spectroscopy: when excited multiplets are involved, Wybourne's formalism must be used.

$$U_{CF} = H_{CF}^{Wybourne} = \sum_{k=0}^{\infty}[B_0^0C_0^0(i) + \sum_{q=1}^{k} B_q^k(C_{-q}^k(i) + \left(-1)^qC_q^k(i)\right) + iB'^k_q(C_{-q}^k(i) - \left(-1)^qC_q^k(i)\right)] \qquad \textbf{(A.3)}$$

where B_q^k and B'^k_q are the CF coefficients and C_q^k are the tensor operators. Like in the Steven's formalism, the terms of the equation are well-defined values of k and q.

The CF levels can be found diagonalizing the corresponding matrix derived from the approach. The coefficients are transformed to CF parameters by multiplying them by the radial part of the wavefunctions.

It is important to mention that the CF parameters depend on the choice of the coordinate system, so a convention is needed: the *z*- direction must be the principal symmetry axis, and *y*-axis must coincide with a two-fold symmetry axis, if it is present, while *x*- axis is perpendicular to both. When there is no two-fold symmetry axis, a non-zero imaginary contribution is introduced in the ligand-field Hamiltonian. If the experimentally determined parameters do not conform the convention, a rotation of the reference system is needed: the standardized form of the CF parameters.

This two approaches require a large number of parameters to be determined. However, for low point symmetry the number of CF parameters is determined to be 27, which is still too large. Some approximations can be done to reduce this number.

1. The point-charge electrostatic model, which parametrizes the CF effect generated by *n* atoms coordinated to the lanthanide by using *n* point charges. By using this model, we arrive to:

   $$U_{CF} = \sum_{j=1}^{n} \sum_{i=1}^{lig} \frac{Z_i e^2}{r_{ij}} \qquad \textbf{(A. 4)}$$

   Which is the Hamiltonian for the CF included in the text.

2. The radial effective charge model, where the point charge is situated to a smaller distance than the real one.

3. The angular-overlap model, where the parameters describing the interaction between the ligand and the lanthanide are related with the bonding ability of the ligands. It allows to calculate the effect of the ligand by using the real coordination geometry around the metal ion site,[130]

APPENDIX II. CRYSTALLOGRAPHIC DATA FROM CHAPTER 5

Table AII.1. Crystal data and structure refinement for coordination compounds **[25*S*]** and **[25*RAC*]**.

	[25*S*]	**[25*RAC*]**
Formula	$\mathrm{C_{96}\,H_{103}\,Cl_6\,Gd\,Mn_6\,N_6\,Na_2\,O_{25}}$	$\mathrm{C_{100.5}\,H_{110}\,Cl_6\,Gd\,Mn_6\,N_6\,Na_2\,O_{25.5}}$
FW	2486.41	2555.51
System	Trigonal	Trigonal
Space group	R3	R -3
a/Å	19.6406(6)	19.4486(6)
b/Å	19.6406(6)	19.4486(6)
c/Å	28.447(1)	28.7046(9)
α/deg.	90	90
ß/deg.	90	90
γ/deg.	120	120
V/ Å^3	9503.4(7)	9402.8(7)
Z	3	3
T, K	100(2)	100(2)
λ(MoKα), Å	0.71073	0.71073
ρcalc, g·cm^{-3}	1.303	1.354
μ(MoK$_\alpha$), mm^{-1}	1.289	1.305
R	0.0329	0.0692
ω*R*^{2}	0.0904	0.2011

Table AII.2. Cell parameters for complexes **[20]-[29]**

Complex	***a*** **(Å)**	***b*** **(Å)**	***c*** **(Å)**	**group**
(*S*)-Mn$_6$Na$_2$**Y [20]**	19.6090(9)	19.6090(9)	28.451(2)	*R*3
(*S*)-Mn$_6$Na$_2$**Ce [21]**	19.5854(7)	19.5854(7)	28.541(1)	*R*3
(*S*)-Mn$_6$Na$_2$**Pr [22]**	19.6055(8)	19.6055(8)	28.440(1)	*R*3
(*S*)-Mn$_6$Na$_2$**Gd [25]**	19.6406(6)	19.6406(6)	28.447(1)	*R*3
(*S*)-Mn$_6$Na$_2$**Tb [26]**	19.5945(5)	19.5945(5)	28.3967(7)	*R*3
(*S*)-Mn$_6$Na$_2$**Er [28]**	19.5873(5)	19.5873(5)	28.5718(7)	*R*3
(*S*)-Mn$_6$Na$_2$**Yb [29]**	19.5660(4)	19.5660(4)	28.4759(7)	*R*3
(*S*)-Mn$_6$Na$_2$**Tb (Br)**	19.9312(3)	19.9312(3)	28.8052(8)	*R*3
(*R*)-Mn$_6$Na$_2$**Nd [23]**	19.870(3)	19.870(3)	28.846(6)	*R*3
(*R*)-Mn$_6$Na$_2$**Eu [24]**	19.6360(5)	19.6360(5)	28.3767(7)	*R*3
(*R*)-Mn$_6$Na$_2$**Tb [26]**	19.585(1)	19.585(1)	28.518(2)	*R*3
(*R*)-Mn$_6$Na$_2$**Dy [27]**	19.6197(7)	19.6197(7)	28.503(1)	*R*3
Rac-Mn$_6$Na$_2$**Ce [21]**	19.370(2)	19.370(2)	28.747(3)	*R*-3
Rac-Mn$_6$Na$_2$**Gd [25]**	19.4486(6)	19.4486(6)	28.7046(9)	*R*-3
Rac-Mn$_6$Na$_2$**Tb [26]**	19.4240(8)	19.4240(8)	28.5924(10)	*R*-3

APPENDIX III. SUPPLEMENTARY INFORMATION TO CHAPTER 6. FIELD INDUCED SINGLE ION MAGNET COMPLEXES DERIVED FROM KRAMERS IONS

Table AIII.1. Crystallographic collection data for complexes **[38*RR*]** and **[38*SS*]**.

Parameter	**[38*RR*]**	**[38*SS*]**
Formula	$C_{30}H_{26}EuN_5NiO_{13}$	$C_{30}H_{26}EuN_5NiO_{13}$
FW / g mol^{-1}	875.23	875.23
Crystal system	Monoclinic	Monoclinic
Space group	*C*2	*C*2
a / Å	19.125(1)	19.098(1)
b / Å	15.5700(8)	15.5383(7)
c / Å	22.084(1)	22.039(1)
α / º	90	90
β / º	99.096(2)	99.059(2)
γ / º	90	90
V / Å^3	6493.4(6)	6458.5(6)
Z	8	8
T / K	100.0(2)	100.0(2)
ρ_{calc} / g cm^{-3}	1.791	1.800
μ / mm^{-1}	2.569	2.583
θ range / °	2.016 - 30.603	2.160 - 26.448
Index ranges	$-27 \le h \le 27$ $-22 \le k \le 22$ $-31 \le l \le 31$	$-23 \le h \le 23$ $-19 \le k \le 18$ $-27 \le l \le 27$
Collected reflections	98906	40759
Independent reflections	19717 (R_{int} = 0.0700)	13171 (R_{int} = 0.0422)
Flack parameter	0.13(2)	0.01(2)
Final $R^{b,c}$ indices [$I>2\sigma(I)$]	$R1$ = 0.0387 w$R2$ = 0.0991	$R1$ = 0.0313 w$R2$ = 0.0714
$(\Delta\rho)_{max,min}$ / e Å^{-3}	1.956, -1.203	1.038, -0.959

Table AIII.2. Crystallographic collection data for **[32*RR*]**, **[32*SS*]**, [**32*SSb*]** and [**32*SSc*]**.

Parameter	**32*RR***	**32*SS***	**32*SS*b**	**32*SS*c**
Formula	$C_{32}H_{34}EuN_5O_{15}Zn$	$C_{32}H_{34}EuN_5O_{15}Zn$	$C_{63}H_{64}Eu_2N_{10}O_{29}Zn_2$	$C_{30}H_{30}EuN_5O_{15}Zn$
FW / g mol^{-1}	945.97	945.97	1859.90	917.92
Crystal system	Monoclinic	Monoclinic	Monoclinic	Monoclinic
Space group	*P21*	*P21*	*P21*	*P21*
a / Å	9.2811(4)	9.2850(6)	9.209(1)	9.062(1)
b / Å	16.2336(8)	16.239(1)	16.418(3)	17.159(2)
c / Å	23.407(1)	23.453(2)	23.140(4)	22.414(2)
α / °	90	90	90	90
β / °	95.232(2)	95.284(2)	95.496(6)	97.001(4)
γ / °	90	90	90	90
V / Å^3	3512.0(3)	3521.2(4)	3482	3459.1(6)
Z	4	4	2	4
T / K	100.0(2)	100.0(2)	100(2)	100.0(2)
ρ_{calc} / g cm^{-3}	1.789	1.784	1.774	1.763
μ / mm^{-1}	2.532	2.526	2.551	2.568
θ range / °	2.151 - 30.592	2.148 - 30.558	2.160-25.943	2.544-30.539
Index ranges	$-13 \leq h \leq 12$	$-11 \leq h \leq 13$	$-10 \leq h \leq 11$	$-12 \leq h \leq 10$
	$-23 \leq k \leq 23$	$-23 \leq k \leq 23$	$-20 \leq k \leq 20$	$-24 \leq k \leq 23$
	$-33 \leq l \leq 33$	$-33 \leq l \leq 33$	$-28 \leq l \leq 27$	$-31 \leq l \leq 31$
Coll. Reflections	149772	117630	31197	42189
Indep. Reflections	21530	21475	12529	18446
	(R_{int} = 0.0682)	(R_{int} = 0.0308)	(R_{int} = 0.0956)	(R_{int} = 0.0592)
Flack parameter	0.015(5)	0.017(9)	0.29(4)	0.14(2)
Final $R^{b,c}$ indices	$R1$ = 0.0359	$R1$ = 0.0281	$R1$ = 0.0737	$R1$ = 0.0435
$[I > 2\sigma(I)]$	w$R2$ = 0.0667	w$R2$ = 0.0662	w$R2$ = 0.1773	w$R2$ = 0.0996
$(\Delta\rho)_{max,min}$ / e Å^{-3}	0.991, -1.374	0.968, -2.201	3.731, -2.214	2.672, -2.547

Table AIII.3. SHAPE CShM parameters for the A-molecule of complexes **1*RR*** and **2*SS*-c**. The topology for both complexes is intermediate to JSPC-10, SDD-10 and TD-10

			1*RR*	**2*SS*c**
DP-10	D10h	Decagon	36.370	36.223
EPY-10	C9v	Enneagonal pyramid	23.701	25.930
OBPY-10	D8h	Octagonal bipyramid	16.198	15.675
PPR-10	D5h	Pentagonal prism	8.931	11.193
PAPR-10	D5d	Pentagonal antiprism	9.812	12.382
JBCCU-10	D4h	Bicapped cube J15	9.216	10.237
JBCSAPR-10	D4d	Bicapped square antiprism J17	5.134	4.682
JMBIC-10	C2v	Metabidiminished icosahedron J62	6.146	7.348
JATDI-10	C3v	Augmented tridiminished icosahedron J64	17.626	19.313
JSPC-10	C2v	Sphenocorona J87	***3.241***	***3.360***
SDD-10	D2	Staggered Dodecahedron (2:6:2)	***4.578***	***3.438***
TD-10	C2v	Tetradecahedron (2:6:2)	***4.219***	***2.782***
HD-10	D4h	Hexadecahedron (2:6:2) or (1:4:4:1)	6.119	6.986

Table AIII.4. Selected bond parameters for the A-molecule of **[32*SS*b]**.

Eu(1)-O(1)	2.60(2)	Zn(1)-N(1)	2.10(2)
Eu(1)-O(2)	2.41(1)	Zn(1)-N(2)	2.02(2)
Eu(1)-O(3)	2.34(1)	Zn(1)-O(2)	1.96(1)
Eu(1)-O(4)	2.69(2)	Zn(1)-O(3)	2.08(1)
Eu(1)-O(5)	2.48(2)	Zn(1)-O(14)	2.06(2)
Eu(1)-O(6)	2.41(2)	Zn(1)-O(2)-Eu(1)	106.9(6)
Eu(1)-O(8)	2.57(2)	Zn(1)-O(3)-Eu(1)	105.7(6)
Eu(1)-O(9)	2.41(1)	Zn(1)···Eu(1)	3.519(3)
Eu(1)-O(11)	2.52(2)		
Eu(1)-O(12)	2.49(2)		

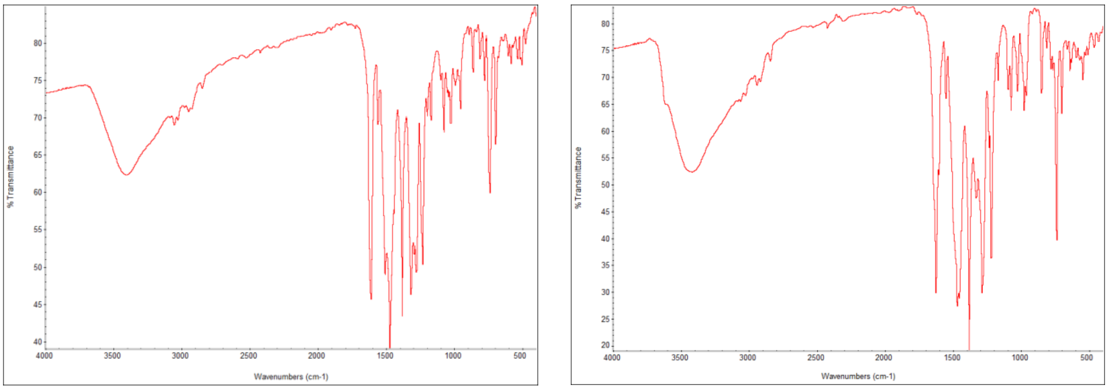

Figure AIII.1 IR spectra for the for the representative [Ni^{II}Eu^{III}] complexes **[38],** (left) and [Zn^{II}Eu^{III}] **[32]** (rigth). The spectra are similar but not identical due to the different conformation of the phenyl rings of the ligands.

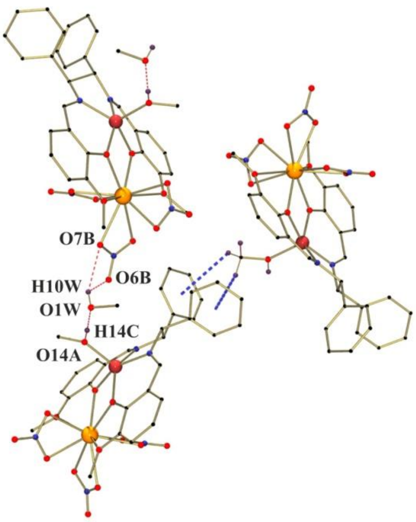
O7B
O6B
H10W
O1W
H14C
O14A

Figure AIII.2. Intermolecular interactions for complex **[32*SS*]**: 1-D arrangement of H-bonds and interchain CH-π(ring) contacts.

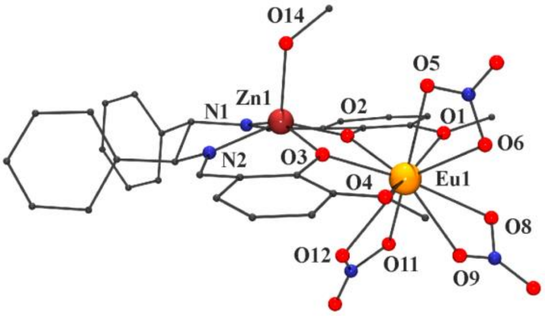
O14
O5
Zn1
N1
O2
O1
O6
O3
N2
O4
Eu1
O8
O12
O11
O9

Figure AIII.3. Labelled view of the A-molecule of structure **[32*SS*b]**. At molecular level is practically identical to the structure of the fresh crystal **[32*SS*]**. The main differences are found in the intermolecular interactions.

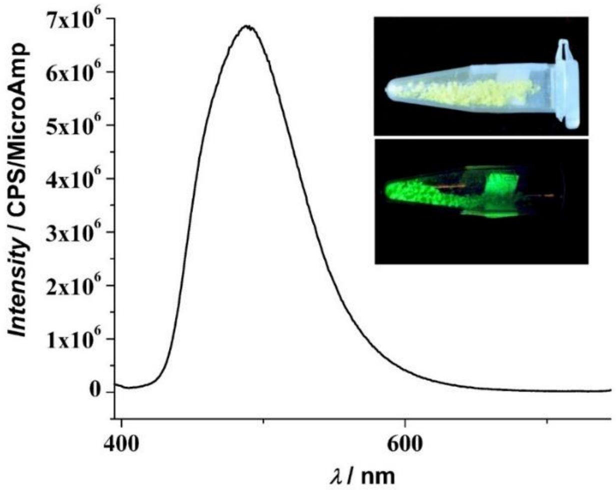

Figure AIII.4. Emission spectrum for the mononuclear precursor [$\mathrm{Zn^{II}L}$]. Inset, the sample under white and UV (400) lamp.

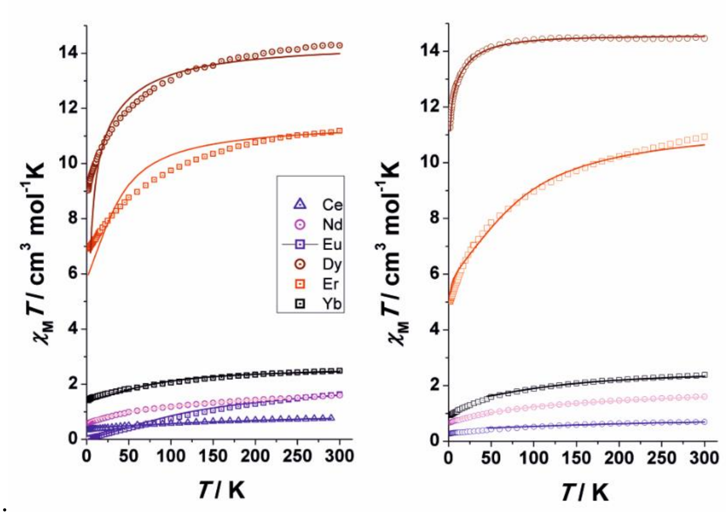

Figure AIII.5. $\chi_M T$ product vs. Temperature for the [Ni^{II}Ln^{III}] (left) and [Zn^{II}Ln^{III}] compounds (right). Solid lines show the best simulation.

In our opinion the absolute fit values must be assumed with large caution, but allowed us to give a reliable indication about the sign of *Δ*, profiting that different Δ sign gives clearly different shaped $\chi_M T$ vs temperature curves, Fig. S5.[27]

Δ > 0 means that the smallest value of M_J corresponds to the lowest energy state, and so, the lowest spin-orbit $\pm M_J$ states (±1/2 for Kramers ions) will be the ground one, while the opposite for Δ < 0. Reasonable fits of the experimental data were reproduced for negative *Δ* values for Dy^{III} complexes and positive ones for Ce^{III}, Nd^{III}, Er^{III} and Yb^{III}. Although in low symmetry environment, different M_J values can be mixed, and this is probably the reason why the lanthanide Kramers cations with a large number of M_J mixed states have more discrepancies with the fitting Hamiltonian (Dy^{III} and Er^{III}). The method seems to provide a simple alternative to approach the lowest M_J state.

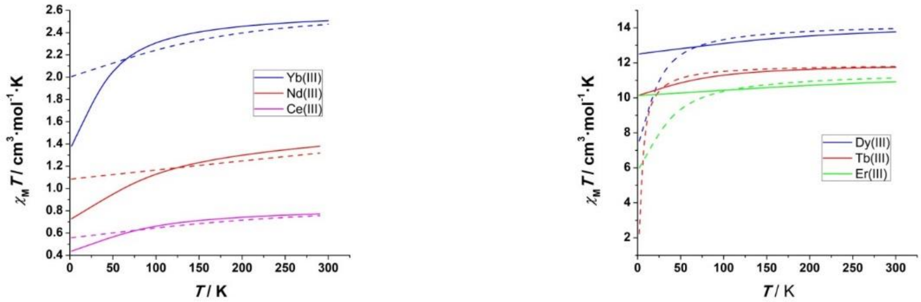

Figure AIII.6. Simulated $\chi_M T$ plots for a mononuclear Ln^{III} for *Δ* = +25 cm^{-1} (solid lines) and *Δ* = -25 cm^{-1} (dotted lines).

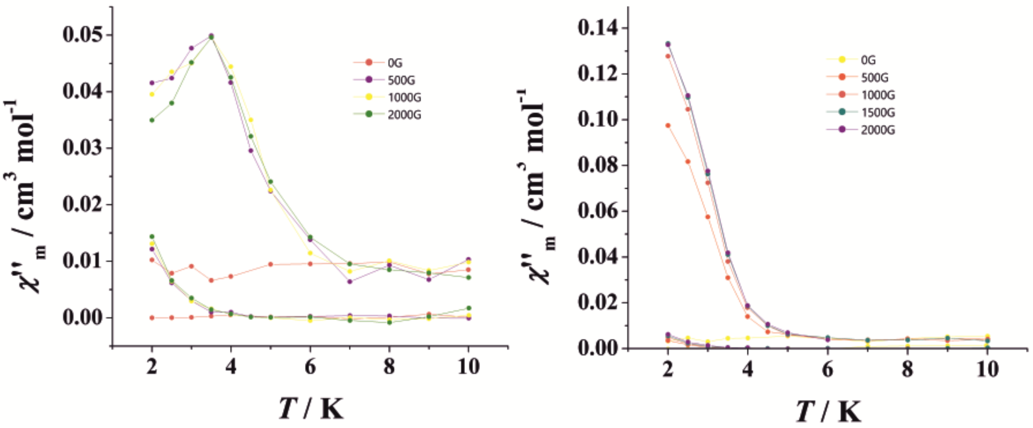

Figure AIII.7. AC measurements for the [ZnCe] complex **[30]** (left) and the [NiNd] complex **[31]** (right) at variable field. The field that gives the maximum dependence of the ac signal was selected in all cases to perform the complete measurements.

χ'*M *vs. T	***χ''*M *vs. T***

[Ni^{II}Ce^{III}] (**36*RR***)

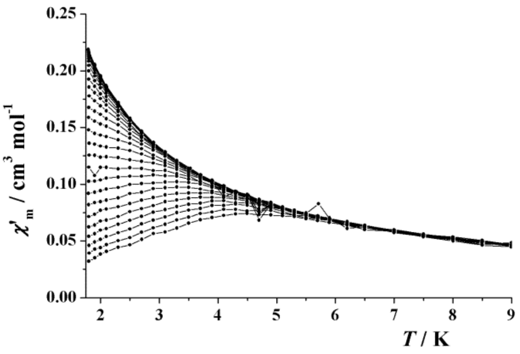

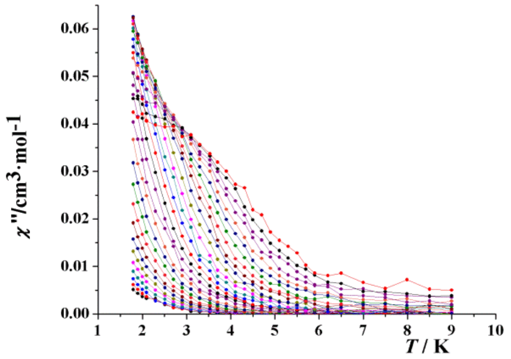

[Ni^{II}Nd^{III}] (**37*RR***)

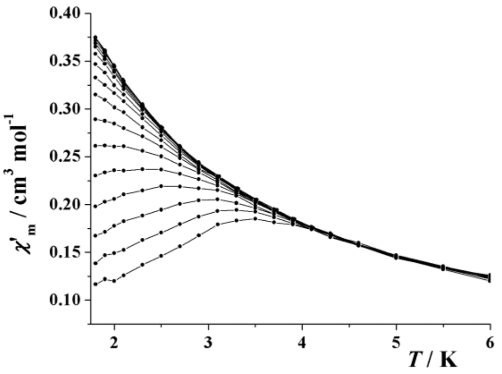

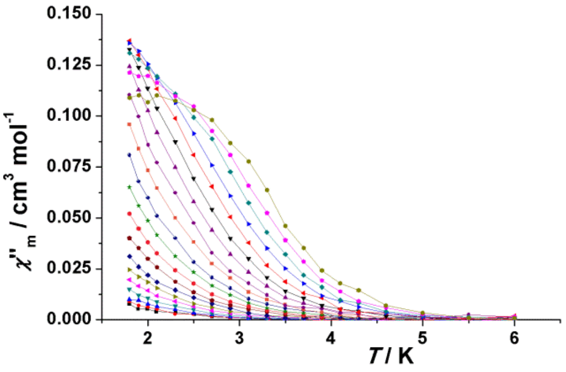

[Ni^{II}Dy^{III}] (**39*RR***)

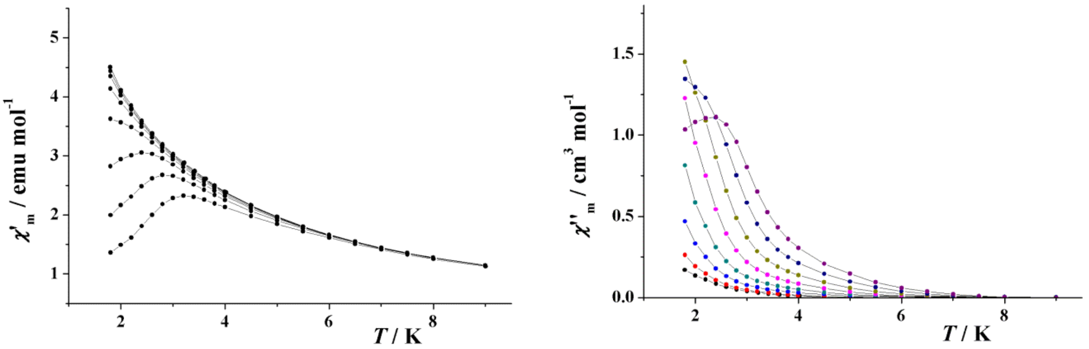

[Ni^{II}Er^{III}] (**40*SS***)

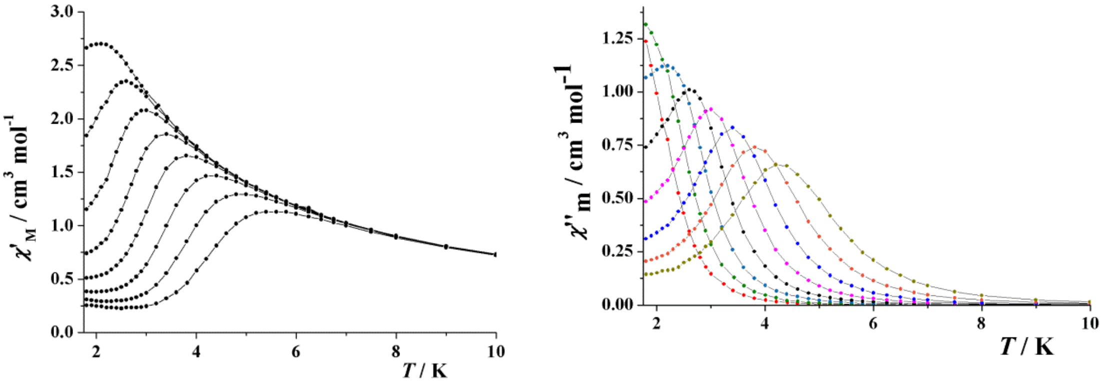

[Ni^{II}Yb^{III}] (**41*SS***)

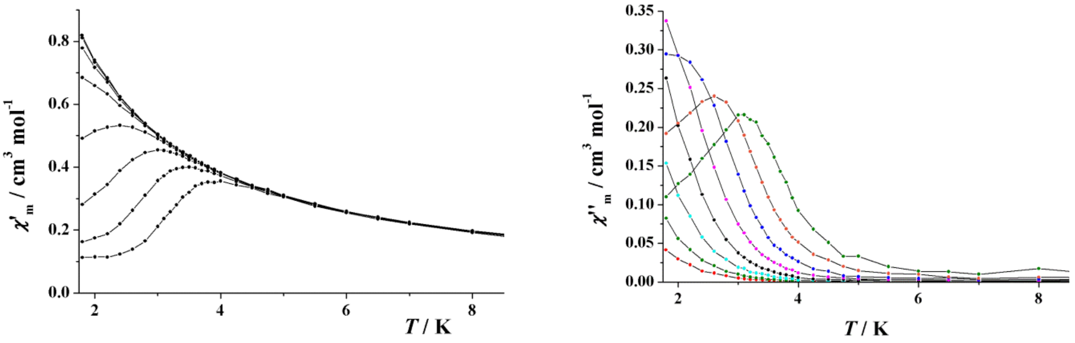

Figure AIII.8. χ_M' and χ_M" vs. *T* plots for the [Ni^{II}Ln^{III}] complexes **[36]**-[**41]**. Complex **[38]** is the Eu^{III} derivative.

χ'_M **vs. *T***	χ''_M **vs. *T***
$[Zn^{II}Ce^{III}]$ (**30*RR***) 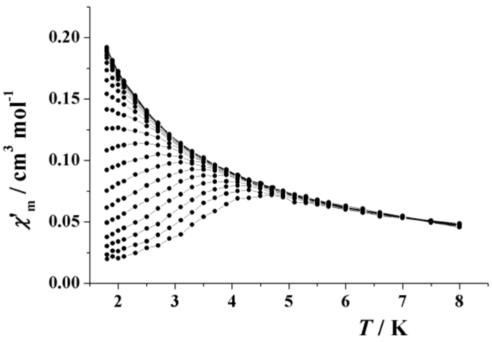	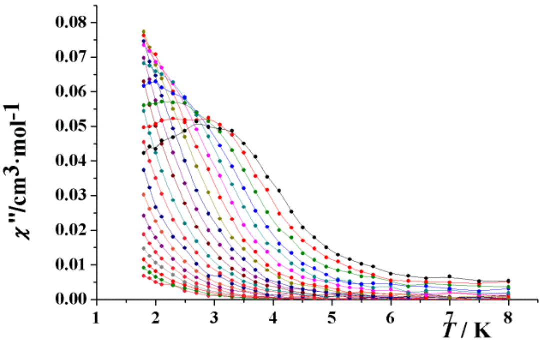
$[Zn^{II}Nd^{III}]$ (**31*RR***) 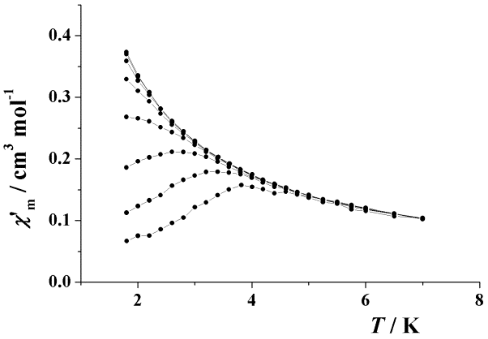	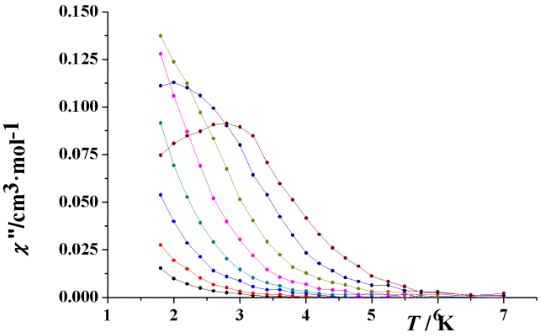
$[Zn^{II}Dy^{III}]$ (**33*SS***) 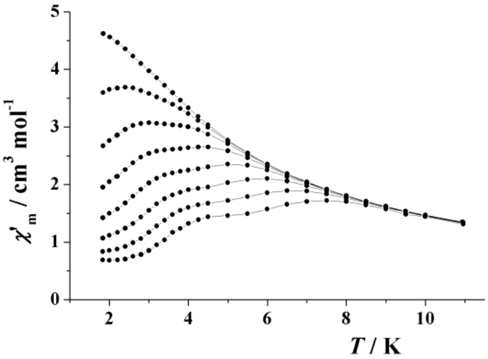	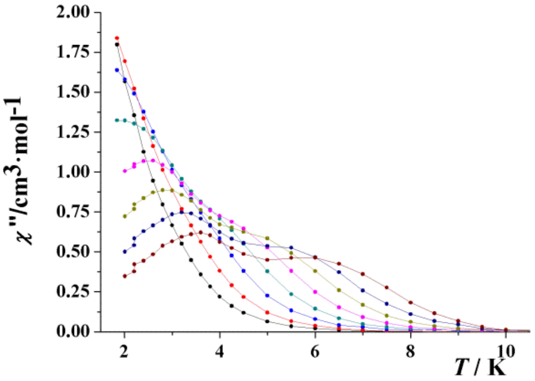
$[Zn^{II}Er^{III}]$ (**34*SS***) 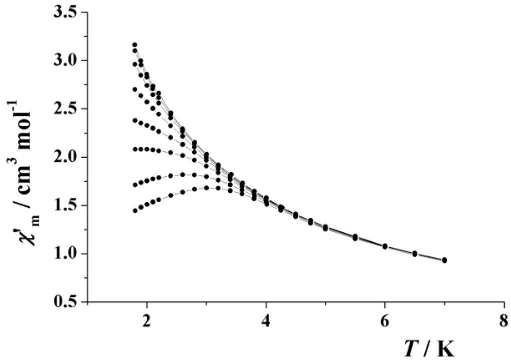	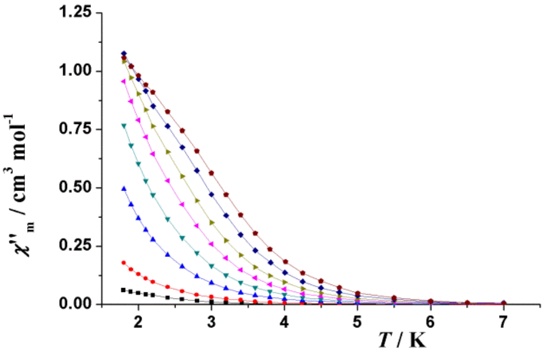

Figure AIII.9. χ_M' and χ_M" vs. *T* plots for the $[Zn^{II}Ln^{III}]$ complexes **[30]** –**[34]**. Complex $[Zn^{II}Yb^{III}]$ (**[35]**) do not shows ac response. **[32]** is the Eu^{III} derivative.

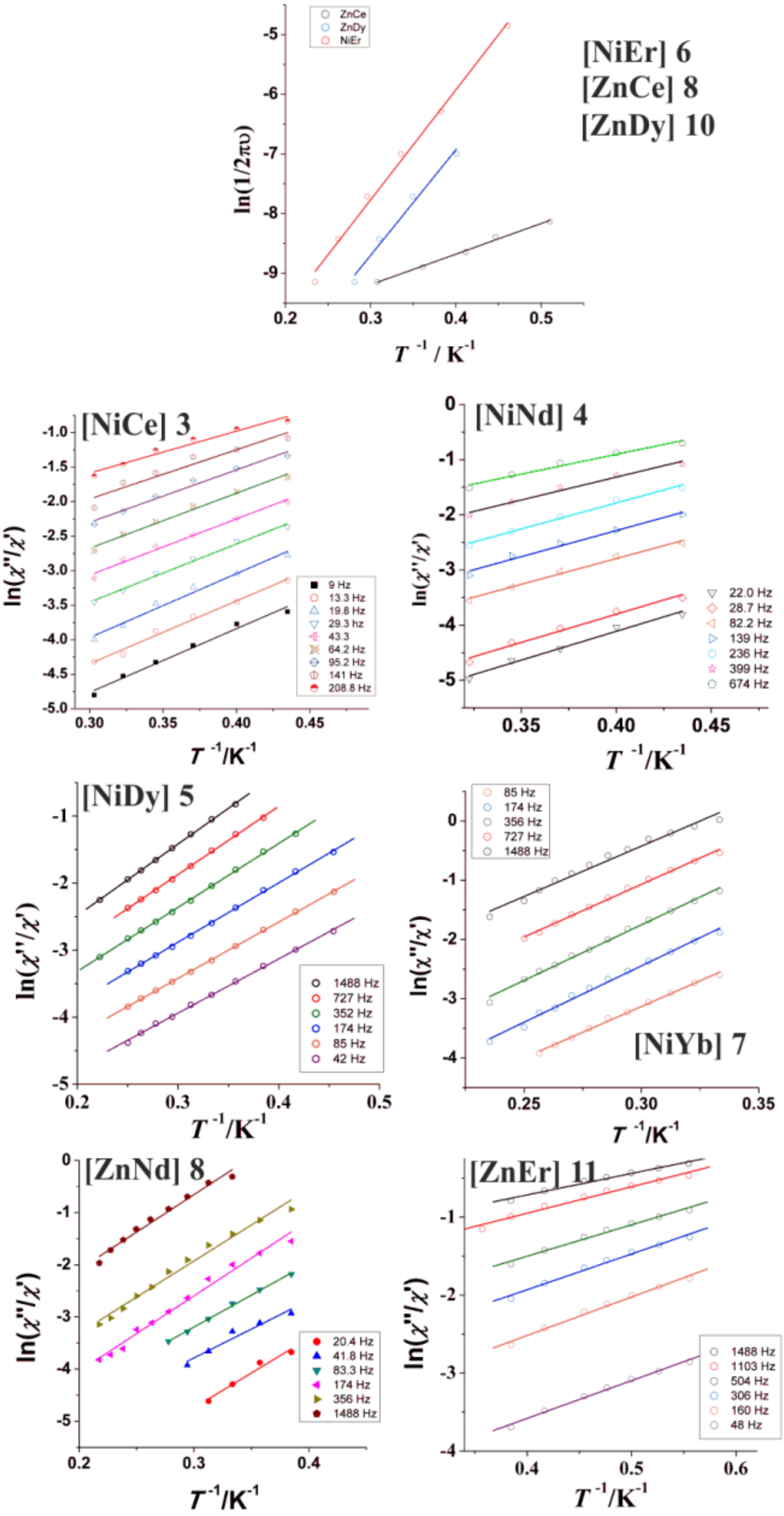

Figure AIII.10. Fit of the ac data for complexes **[36], [30]** and **[33]** ($\ln(1/(2\pi\omega) = \ln(1/\tau_0) - U_{eff}/(k_B T)$) and for **[36]**, **[37]**, **[39]**, **[41]**, **[31]** and **[34]** ($\ln(\chi_M''/\chi_M') = \ln(\omega\tau_0) - U_{eff}/(k_B T)$).

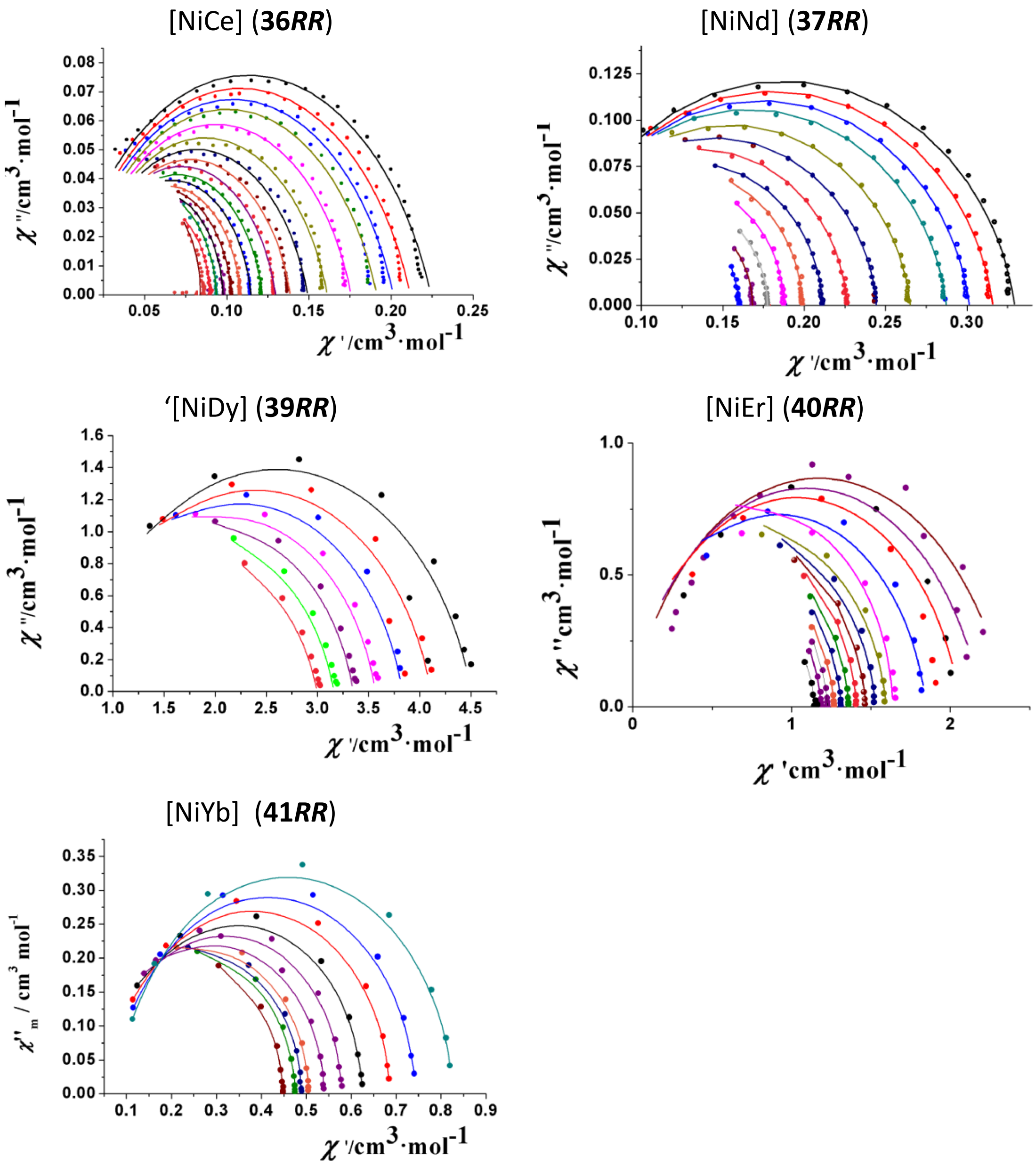

Figure AIII.11. Cole-Cole plots for the [Ni^{II}Ln^{III}] complexes **[36], [37], [39], [40], [41]** measured in the temperature range 1.8-4.5K. The solid lines represent the best fit.

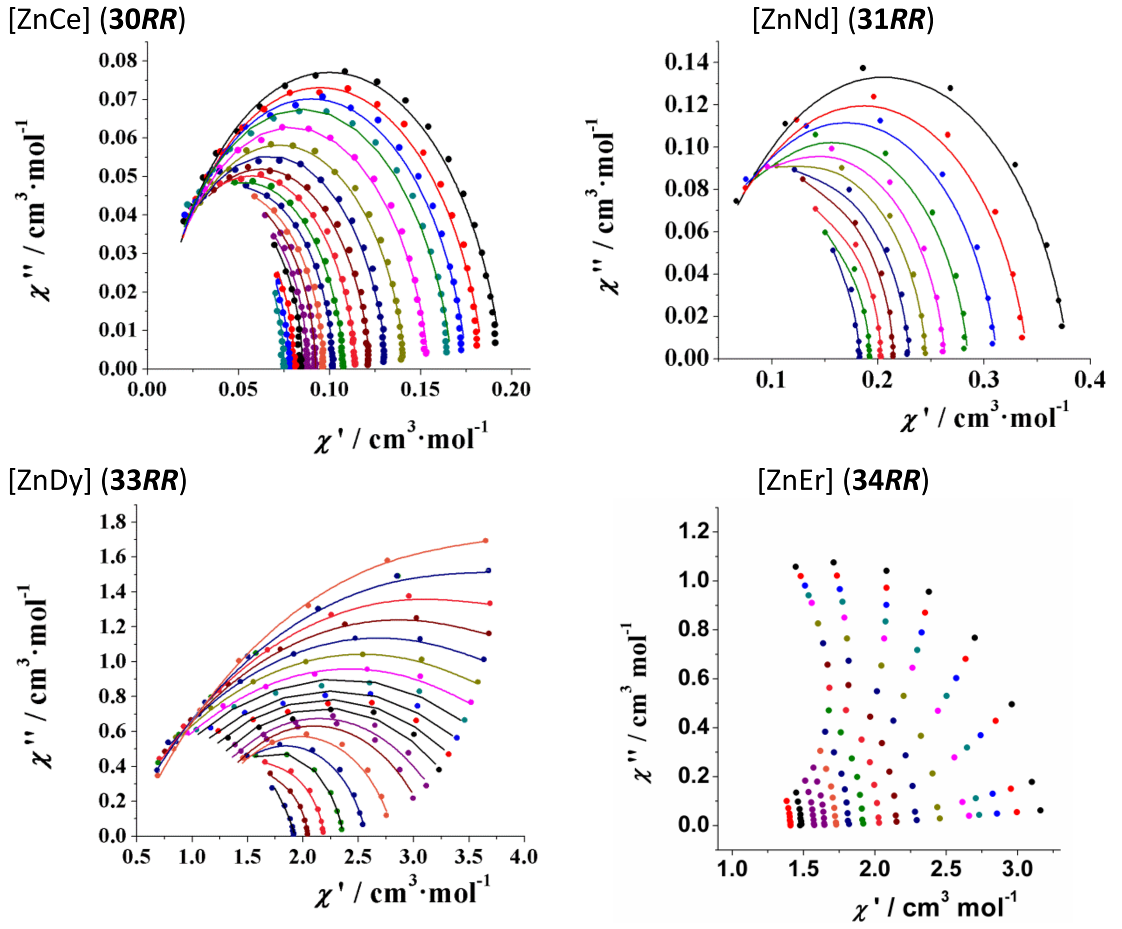

Figure AIII.12.. Cole-Cole plots for the [Zn^{II}Ln^{III}] complexes **[30], [31], [33], [34]** measured in the temperature range 1.8-4.5K. The solid lines represent the best fit except for **10** that are eye guide. Data for complex [Zn^{II}Er^{III}]**[34]** is not enough to fit the data and complex [Zn^{II}Yb^{III}] **[35]** do not shows ac response.

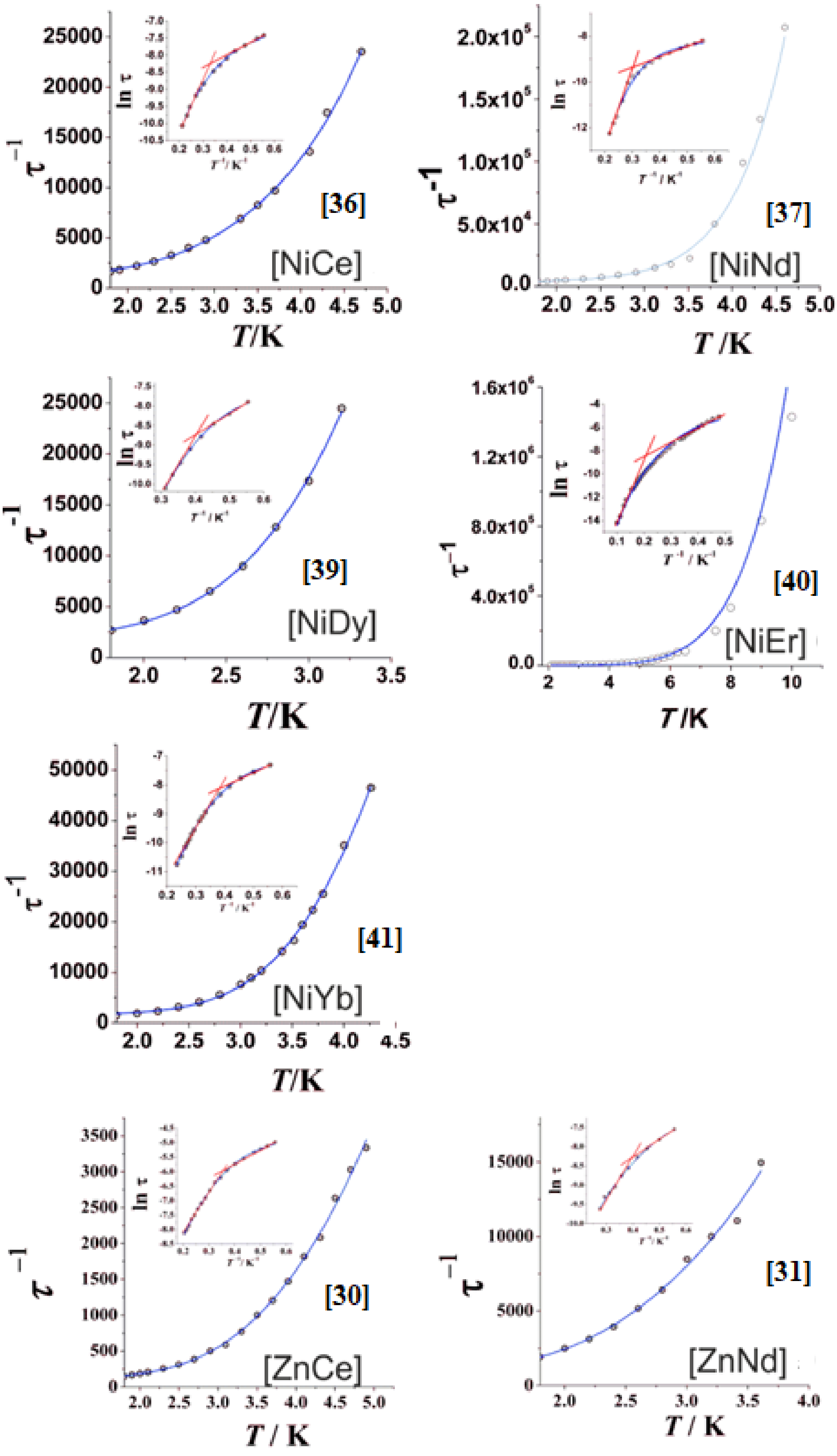

Figure AIII.13. Dependency of the spin-lattice relaxation temperature obtained from Cole-Cole plots under static dc field as τ-1 vs. T or ln(τ) vs T^{-1} (inset). The n values for the term BT^n lies between 6.5-9.1 for all complexes and in agreement with the calculated values by Arrhenius or Debye methods, τ_0 are comprised between 10^{-5}-10^{-7}.

APPENDIX IV. SUPPLEMENTARY INFORMATION TO CHAPTER VII. PURELY LANTHANIDE COMPLEXES.

Table AIV.1. Crystal data and structure refinement for coordination compounds **[43*RR*], [43*SS*]** and **[44*RR*]**

	43*RR*	**43*SS***	**44*RR***
Formula	$C_{53}H_{51}Cl_6N_8Nd_2O_{2.50}$	$C_{52.50}H_{49}Cl_6N_8Nb_2O$	$C_{52}H_{44}Cl_6N_8Sm_2$
FW	1341.20	1206.51	--
System	Triclinic	Triclinic	Triclinic
Space group	P1	P1	P1
a/Å	9.7069(4)	9.7145(5)	9.707(1)
b/Å	11.1708(5)	11.1726(6)	11.853(1)
c/Å	15.1938(7)	15.1362(8)	12.593(1)
α/deg.	73.354(2)	73.452(2)	86.873(4)
ß/deg.	77.880(1)	77.852(2)	70.515(3)
γ/deg.	64.663(1)	64.906(2)	73.949(3)
V/ Å^3	1419.4(1)	1418.5(1)	1311.59
Z	1	1	--
T, K	100(2)	100(2)	100(2)
λ(MoKα), Å	0.71073	0.71073	0.71073
ρcalc, g·cm^{-3}	1.569	1.412	--
μ(MoK$_\alpha$), mm^{-1}	2.138	0.730	--
R	0.0298	0.0388	--
ωR^2	0.0708	0.1115	--

Table AIV.2. Selected bond distances (Å) and angles (°) for compounds **[42*RR*], [42*SS*] and [43*RR*]**.

	[42*RR*]	**[42*SS*]**	**[43*RR*]**	
Nd1-N1	2.660(10)	2.666(8)	Sm1-N1	
Nd1-N2	2.547(9)	2.603(6)	Sm 1-N2	
Nd1-N3	2.586(8)	2.547(10)	Sm 1-N3	
Mn1-N4	2.603(9)	2.543(6)	Sm 1-N4	
Nd1-Cl1	2.805(3)	2.812(3)	Sm1-Cl1	
Nd1-Cl2	2.893(2)	2.905(2)	Sm1-Cl2	
Nd1-Cl3	2.699(3)	2.713(3)	Sm1-Cl3	
Nd1-Cl4	2.741(3)	2.713(5)	Sm1-Cl4	
Nd2-N5	2.676(9)	2.70(1)	Sm2-N5	
Nd2-N6	2.593(9)	2.537(12)	Sm 2-N6	
Nd2-N7	2.566(8)	2.595(7)	Sm 2-N7	
Nd2-N8	2.575(10)	2.74(2)	Sm 2-N8	
Nd2-Cl1	2.901(3)	2.897(3)	Sm 2-Cl1	
Nd2-Cl2	2.808(3)	2.807(3)	Sm 2-Cl2	
Nd2-Cl5	2.704(3)	2.697(3)	Sm 2-Cl5	
Nd2-Cl6	2.739(3)	2.754(2)	Sm 2-Cl6	
Nd1-Cl1-Nd2	109.67(9)	109.80(9)	Sm 1-Cl1-Sm2	
Nd1-Cl1-Nd2	109.84(9)	109.71(8)	Sm1-Cl1-Sm2	

Table AIV.3. Crystal data and structure refinement for coordination compounds **[46*RR*] and [46*SS*].**

	46*RR*)	**46*SS***
Formula	$C_{26}H_{22}Cl_3N_4Tb$	$C_{26}H_{22}Cl_3N_4Tb$
FW	655.74	655.74
System	Triclinic	Triclinic
Space group	P1	P1
a/Å	8.7672(3)	8.7720(3)
b/Å	10.9544(5)	10.9600(4)
c/Å	27.502(1)	27.500(1)
α/deg.	87.262(2)	87.025(2)
ß/deg.	82.056(2)	81.982(2)
γ/deg.	88.241(2)	88.059(2)
V/ Å^3	2612.2(2)	2613.5
Z	4	4
T, K	100(2)	100(2)
λ(MoKα), Å	0.71073	0.71073
ρcalc, g·cm^{-3}	1.667	
μ(MoK$_\alpha$), mm^{-1}	3.036	
R	0.0236	
ωR^2	0.0319	

Table AIV.4. Selected bond distances (Å) and angles (°) for compounds **TbRR,**

	TbRR
Tb1-N1	2.578(5)
Tb1-N2	2.520(5)
Tb1-N3	2.521(4)
Tb1-N4	2.583(6)
Tb1-Cl1	2.613(2)
Tb1-Cl2	2.609(2)
Tb1-Cl3	2.647(2)
N1-Tb-N2	63.2(2)
N2-Tb-N3	65.5(2)
N3-Tb-N4	65.1(2)
N1-Tb-N4	166.6(2)
Cl2-Tb-Cl3	167.75(4)

RESUM.

La present tesi doctoral ha estat duta a terme al Grup de Magnetisme Molecular del Departament de Química Inorgànica i Orgànica de la Universitat de Barcelona.

El Grup de Magnetisme, com el seu nom indica, ha estat bàsicament centrat en l'estudi magnètic de complexes, majoritàriament d'elements de transició, però també amb ions lantànid, que permeten estudis de caràcter magnètic i també luminescent, arribant així a la síntesi de compostos multifuncionals. El grup, també ha tingut interès en la química supramolecular i en la quiralitat.

L'objectiu principal de la tesi ha estat la síntesi i caracterització, magnètica i espectroscòpica, de complexes de coordinació derivats de bases de Schiff quirals, utilitzades com a lligands orgànics. La **Figura R.1** mostra tots els lligands que s'han fet servir, indicant, amb un asterisc, el carboni quiral en cada cas. Com es veu la figura, les bases de Schiff han estat sintetitzades, o bé a partir d'una diamina condensada amb dos grups aldehid, o bé a partir d'un aminoalcohol condensat amb un grup aldehid.

Aquesta sèrie de lligands orgànics, s'ha combinat amb diferents metalls, de transició com ara manganès, ferro i níquel, però també amb ions lantànid i també amb barreges de metalls, donant lloc a clústers combinant un metall 3*d* i un metall 4*f*. La **Figura R.2** mostra una taula periòdica amb els metalls utilitzats durant la tesi i amb quina finalitat cadascun d'ells. Els metalls utilitzats com a cations paramagnètics, s'han fer servir en la recerca de propietats d'imant unimolecular (coneguts per les seves sigles en anglès SMMs, Single Molecule Magnet) i també per a desenvolupar una sèrie de relacions magnetostructurals. En d'altres casos, la part que ens ha interessat del complexes sintetitzats ha estat la seva química supramolecular.

Tots els productes has estat caracteritzats magnèticament, per intentar esbrinar el seu tipus d'interacció magnètica (acoblament ferromagnètic, ferrimagnètic o antiferromagnètic) i, en cas de que presentessin propietats d'imant unimolecular, per esbrinar com era la seva relaxació magnètica. A més a més, per als compostos derivats de ions lantànid, que presenten una elevada anisotropia associada al catió, s'han dut a terme altres tècniques de caracterització magnètica, com l'anomenada *Cantilever Torque Magnetomentry* (CTM), i de caracterització espectroscòpica amb Ressonància Paramagnètica Electrònica (EPR) en banda X i en banda W, tan de compostos en pols com de monocristall.

Degut a la naturalesa quiral dels lligands utilitzats, s'han pogut caracteritzar tots els productes mitjançant Dicroisme Circular Electrònic (ECD), que ens ha servit per demostrar tant la quiralitat dels productes com la seva estructura comparada en sòlid i en dissolució.

Degut a que la tesi ha estat presentada per articles en la seva major part, la divisió dels capítols s'ha fet en funció del metall utilitzat. Així, la tesi es divideix en un primer capítol que conté una introducció teòrica sobre magnetisme i magnetisme molecular, sobre mecanismes de relaxació lenta de la magnetització i sobre anisotropia magnètica, un apartat que parla dels lligands utilitzats, les bases de Schiff, i els metalls amb els que aquestes han estat combinades, i un apartat dedicat a la base teòrica i experimental de les tècniques utilitzades, de caracterització, magnètiques i espectroscòpiques.

El segon capítol de la tesi , inclou les *Publicació #1* i *Publicació #2*, sobre els compostos sintetitzats utilitzant Ni^{II} com a catió metàl·lic. La *Publicació #1* conté una sèrie de complexes dinuclears de níquel, amb acoblament ferromagnètic. La part més remarcable del text és que s'ha aconseguit variar les propietats supramolecular dels compostos mitjançant petites i graduals variacions en una sèrie de lligands. Així, s'ha aconseguit per primera vegada a la literatura la síntesi de *mesocats* quirals, estructures que són típica i intrínsecament aquirals. D'altra banda, la *Publicació #2* conté un parell enantiomèric de clústers de Ni^{II} tetranuclears.

El capítol 3 de la tesi s'ha dedicat a complexes amb bases de Schiff quirals i catió Fe^{III}. Així, s'ha sintetitzat un parell enantiomèric de les conegudes com *Estrelles de Ferro*. Aquests compostos estan inclosos a la *Publicació #3*, que conté, a més de la descripció magnètica i estructural dels productes, un petit *review* sobre altres estrelles de ferro similars presents a la literatura, i sobre com afecta la seva estructura a les seves propietats magnètiques.

El quart capítol de la tesi està exclusivament dedicat a compostos derivats de manganès. S'han fet servir diferents lligands per caracteritzar magnètica i estructuralment una sèrie de complexes que contenen Mn^{II} i Mn^{III} combinats amb altres cations com Na^{I} o Ca^{II}, tot i que generalment, no han presentat propietats d'imant molecular, excepte en un cas particular. Per aquest motiu, s'ha introduït un catió lantànid a les estructures intentant aconseguir una relaxació lenta de la magnetització.

El capítol cinc inclou aquesta sèrie de complexos mixtes 3*d*/4*f*, que malauradament tampoc presenten relaxació lenta de la magnetització. Tot i això, s'ha demostrat que la síntesi de clústers partint d'un lligand enantiomèricament pot portar a estructures diferents que partint del mateix lligand en la seva mescla racèmica.

Continuant amb els compostos mixtes 3*d*/4*f* s'arriba al capítol sis, que està dedicat a l'estudi de compostos amb comportament SIM, de les seves sigles en anglès (Single Ion Magnet) derivats de ions tipus Kramer (Ce^{III}, Nd^{III}, Eu^{III}, Dy^{III}, Er^{III} i Yb^{III}). Tot i que són complexes binuclears, els comportament SIM s'aconsegueix degut a que el catió *d* que incorporen és diamagnètic: Zn^{II} en alguns casos i Ni^{II} pla quadrat en d'altres.

Els últims compostos de la tesi estan inclosos al capítol set i són compostos de coordinació preparats únicament amb ions lantànid. En aquest cas s'ha vist que una mateixa síntesi porta a dos tipus de nuclearitats diferents, dinuclears pel cas dels lantànids lleugers, Ce^{III}, Nd^{III} i mononuclears per als mes pesats, Dy^{III}, Er^{III} i Yb^{III}. Els compostos dinuclears han estat caracteritzats magnèticament i espectroscòpicament, demostrant que relaxen mitjançant més d'un mecanisme. Degut a problemes de cristal·linitat, no s'han pogut fer les mateixes mesures pels compostos mononuclears, únicament s'han pogut estudiar magnèticament, demostrant que, en aquest cas, només involucren un mecanisme de relaxació.

L'últim capítol de la tesi, el capítol vuit, és una visió global de tota la feina feta als capítols anteriors, que ha permès entendre com es comporten aquests tipus de lligands en cada cas, com ha estat la química supramolecular dels productes degut a l'ús de lligands enantiomericament purs i finalment, uns comentaris de magnetisme sobre com els models actuals de relaxació no acaben d'explicar correctament la relaxació dels ions lantànid en una gran majoria de casos.

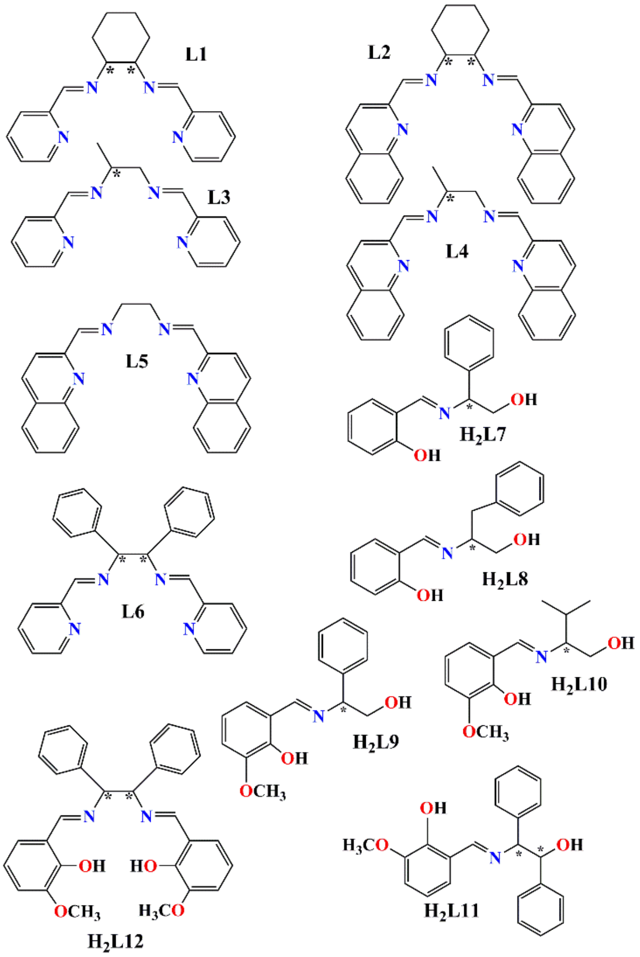

Figura R.1. Lligands utilitzats en la síntesi dels productes. L'asterisc indica en cada cas el carboni quiral.

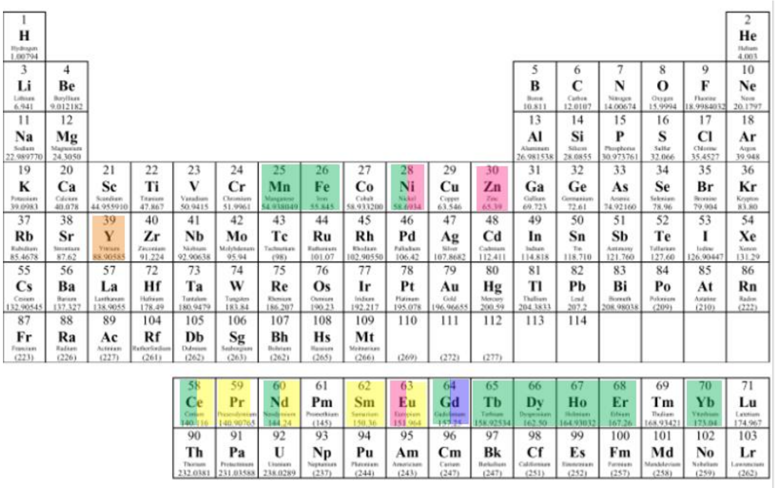

Figura R.2.Taula periòdica amb els metalls pintats de diferents colors segons la seva utilitat als complexes de coordinació. En verd, els metalls utilitzats com a cations paramagnètics, en rosa, els metalls que s'han utilitzat com a diluents magnètics, en groc, elements que permeten luminescència, en blau, el Gd que permet estudiar la diferent relaxació del catió Mn^{III} I en taronja, Y, que s'ha utilitzat com a "lantànid diamagnètic".

BIBLIOGRAPHY

[1] A. Escuer, J. Mayans, M. Font-Bardia. *Dalton Trans.,* **2016**, *45*, 1604.

[2] P. Day. *Notes Rec. R. Soc. Lond.*, **2002**, *56*, 95.

[3] L. Neél. *Ann. Phys.*, **1948**, *3*, 137.

[4] P.W. Anderson. *Magnetism*. **1963**, *1*, 25.

[5] W. Heisenberg. *Z. Phys*., **1926** *38*, 411.

[6] P. A. M. Dirac. *Proc. Roy. Soc. A.* **1929**, *123,* 714,

[7] H. Van Vleck. *The Theory of Electronic and Magnetic Susceptibility*. Oxford University Press. Oxford, **1932**.

[8] (a) J.B. Godenough. *Phys. Rev.*, **1955,** 100, 564**.** (b) J.B. Godenough. *Magnetism and chemical bond*. New York Interscience, **1963**. (c) J. B. Goodenough. *Phys. Chem. Solids.* **1958**, *6*, 287. (d) J. Kanamori. *Phys. Chem. Solids*. **1959**, *10*, 87.

[9] (a) [5] A.N. Holden, B.T. Matthias, P.W. Anderson and H.W. Lewis, *Phys. Rev*., **1956**, *102*, 1463. (b) B.N. Figgis, R.L. Martin. *J. Chem. Soc*., **1956**, 3837. (c) B. Bleaney, K. D. Bowers, *Proc. R. Soc. Lond., A* **1952**, *214*, 451.

[10] B. C. Guha. *Proc. R. Soc. London Ser. A.*, **1951**, *206,* 353.

[11] B. Bleaney, K. D. Bowers. *Proc. R. Soc. London Ser. A.*, **1952**, *214*, 451.

[12] (a) O. Kahn, Y. Pei, M. Verdaguer, J. P. Renard, J. Sletten. *J. Am. Chem. Soc*., **1988**, *110*, 782. (b) Y. Pei, M. Verdaguer, O. Kahn. *J. Am Chem. Soc*., **1986**, *108*, 7428.

[13] (a) T. Mallah, S. Thiebaut, M. Verdaguer, P.Veillet , *Science*, **1993,** *262*, 1554. (b) S. Ferlay, T. Mallah, R. Ouahes, P. Veiellet and M. Verdaguer. *Nature*, **1995,** *378*, 701.

[14] O. Kahn. *Molecular magnetism*. VCH, Weinheim, **1993**.

[15] R. D. Willet, D. Gatteschi, O. Khan. *Magnetostructural correlations in exchange coupled systems*. Reidel Publishing, Dordrecht, **1983**.

[16] M. Verdaguer. *Inorganica Chimica Acta.* **2008**, *361*, 3341.

[17] (a) R. Sessoli, D. Gatteschi, A. Caneschi and M. A. Novak. *Nature*, **1993,** *365*, 141. (b) J. Villain, F. Hartman-Boutron, R. Sessoli and A. Rattori, *Europhys. Lett*., **1994**, *27*, 159.

[18] As some examples: (a) L. Bogani. *Experiments on Molecular Magnets for Molecular Spintronics.* In: S. Gao (eds). *Molecular Nanomagnets and Related Phenomena. Structure and Bonding.* **2014**, *164*, Springer, Berlin, Heidelberg. (b) S. Sanvito. *Handbook of Spin Transport and Magnetism.* **2012**, 649-661. CRC Press, Boca Raton, Fla. (c) L. Bogani, W. Wensdorfer. *Nature Mat.* **2008**, *7*, 179.

[19] (a) C. Chappert, A. Fert, F. N. Van Dau. *Nature Matter*., **2007**, *6*, 813. (b) P. E. Kazin, M. A. Zykin, W. Schnelle, Y. V. Zubavichus, K. A. Bebeshkin, V. a. Tafeenko, C. Felser, M. Jensen. *Inorg. Chem.*, **2017**, *56*, 1232.

[20] As some examples: (a) M. Affronte, F. Troiani, A. Ghirri, S. Carretta, P. Santini, V. Corradini, R. Schuecker, C. Muryn, G. Timco, R. E. Winpenny. *Dalton Trans.*, **2006**, 2810. (b)F. Troiani. M. Affronte. *Chem. Soc. Rev*. **2011**, *40*, 3119. (c) K. S. Pedersen, A.M. Ariciu, S. McAdams, H. Weihe, J. Bondix, F. Tuna, S. Piligkos. *J. Am. Chem. Soc*. **2016**, 5810. (d) G. Lorusso, F. Troiani, V. Bellini, A. Ghirri, A. Candini, S. Carretta, P. Santini, G. Amoretti, W. Wensdorfer, G. Timco, R.E.P. Winpenny, M. Affronte. *Journal of Physics. Conference Series*. **2010**, 012033. (e) M. N. Leuenberger, D. Loss. *Nature*, **2001**, *410*, 789.

[21] D. Gatteschi, R. Sessoli. *Angew. Chem. Int. Ed*., **2003**, *42*, 268.

[22] (a) Y. Mahkliu, G. Schon, A. Shnirman. *Nature*, **1999**, *398*, 305. (b) M. N. Leuenberger, D.Loss. *Nature*. **2001**, *410*, 789.

[23] A. Canneschi, D. Gatteschi, R. Sessoli, A. L. Barra, L. C. Brunel, M. Guillot. *J. Am. Chem. Soc.*, **1991**, *113*, 5873.

[24] A. Bencini, D. Gatteschi. *Electron Paramagnetic Resonance of Exchange Coupled Systems*. Springer-Verlag-Berlin Heidelberg **1990**.

[25] A. Ginsberg. *Inorg. Chim. Acta. Rev*. **1971**, *5*, 45.

[26] J. Tejada, J. M. Hernández, E. del Barco. *J. Magnetism and Molecular Matrials*. **1999**, *196-197*, 552.

[27] J. M. Frost, L. M. Harriman, M. Murugesu. *Chem. Sci*., **2016**, *7*, 2470.

[28] L. T. Anh Ho, L. F. Chibotaru. *Phys. Rev. B*., **2016**, *94*, 104422.

[29] A. Abragam, B. Bleaney. *Electron Paramagnetic Resonance of Transition Ions*. Claredon Press. Oxford, **1970**.

[30] I. Waller. *Z. Phys*., **1932,** *79*, 370.

[31] R. de L. Kronig. *Physica's Grav*., **1939**, *6*, 33.

[32] R. Orbach. *Proc. R. Soc. A*. **1961**, *264*, 458.

[33] (a) P. Debye. *Polar Molecules*. Chemical Catalog Company, New York **1929.** (b) C. Dekker, A. F. Arts, H. W. de Wijn, A. J. van Duyneveldt, J. A. Maydosh. *Phys. Rev. B*., **1989**, *40*, 11243.

[34] (a) C. Milios, A. Vinslava, W. Wensdorfer, S. Moggach, S. Parsons, S. Perlepes, G. Christou, E. K. Brechin. *J, Am. Chem. Soc.*, **2007**¸*129*, 2754. (b) C. Milios, A. Vinslava, W. Wensdorfer, A. Prescimone, P. A. Wood, S. Parsons, S. Perlepes, E. K. Berechin, G. Christou. *J. Am. Chem. Soc*., **2007**, *129*, 6557. (c) C. Milios, A. Vinslava, A. G. Wittaker, S. Parsons, W. Wensdorfer, G. Christou, S. Perlepes, E. K. Brechin. *Inorg. Chem*. **2006**. *45*, 5272.

[35] A. M. Ako, I. J. Hewitt, V. Mereacre, R. Clerac, W. Wensdorfer, C. E. Anson, A. K. Powell. *Angew. Chem. Int. Ed*. **2006**, *45*, 4926.

[36] E. Ruiz, J. Cirera, J. Cano, S. Alvarez, C. Loose, J. Kortus. *Chem. Commun.,* **2008,** *0*, 52.

[37] M. Nakano, H. Oshio. *Chem. Soc. Rev*., **2011,** *40*, 3239.

[38] D. Yoshihara, S. Karasawa, N. Noga. *J. Am. Chem. Soc.*, **2008**, *130*, 10460.

[39] M. Nakano, H. Oshio. *Chem. Soc. Rev*. **2011**, *40*, 3239.

[40] O. Waldmann. *Inorg. Chem*., **2007**, *46*, 10035.

[41] J. Tang, P. Zhang. *Lanthanide Single Molecule Magnets*. Spronger-Verlag GmbH Berlin-Heidelberg **2015**.

[42] N. Ishikawa, M. Sugita, T. Ishikawa, S. Koshihara, Y. Kaizu. *J. Am. Chem. Soc*., **2003**, *125*, 8694.

[43] (a) J. Liu, Y.-C. Chen, J.-L. Liu, V. Vieru, L. Ungur, J.-H. Jia, L. F. Chibotaru, Y. Lan, W. Wensdorfer, S. Gao, X.-M. Chen, M.-L. Tong. *J. Am. Chem. Soc*. **2016**, *138*, 5441

[44] J. D. Reinhart, J. R. Long. *Chem. Sci*. **2011**, *2*, 2078.

[45] N. F. Chilton, D. Collison, E. J. L. McInnes, R. E. P. Winpenny, A. Soncini. *Nat. Commun*., **2013**, *4*, 2551.

[46] Wikipedia. the Free Encyclopedia and references herein.

[47] *The Rare Earth Elements. Fundamentals and Applications*. Ed. David. A. Atwood. **2012**, John Wiley&Sons Ltd.

[48] (a) C. K. Jørgensen, R. Pappalardo, H. H. Schmidtke. *J. Chem. Phys.,* **1963**, *39*, 1422. (b) W. Urland. *Chem. Phys.* **1976**, *14*, 393.

[49] J. M. Lehn. *Supramolecular Chemistry: Concepts and Perspectives*. VCH-Weinheim, **1995**.

[50] A. Dei. *Inorganica Chimica Acta*. **2008**, *361*, 3344.

[51] A. von Zalewsky. *Stereochemistry of coordination compounds.* **1996**, John Wiley & Sons, Chichester.

[52] D. Gatteschi, R. Sessoli, J. Villain. *Single Molecule Mgnets.* Oxford University Press, New York, **2006**.

[53] H. B. G. Casimir, D. Bijl, F. K. du Pré. *Physica (The Hague)*, **1941**, *8*¸449.

[54] J. Bartolomé, G. Filoti, V. Kuncser, G. Schienteie, V. Mereacre, C. E. Anson, A. K. Powell, D. Prodius, C. Turta, *Phys. Rev. B*. **2009**, *80*, 014430.

[55] K. S. Cole, R. H. Cole. *J. Chem. Phys*. **1941**, *9*, 341.

[56] Y.-N. Guo, G.-F. Xu, Y. Guo, J. Tang. *Dalton Trans.* **2011**, *40*, 9953.

[57] R. Argand. *Essai sur une manière de répresenter les quantités imaginaires dans les constructions géométriques.***1971**, Albert Blanchard, Paris.

[58] (a) M. Perfetti, G. Cucinotta, M. E. Boulon, F. E. Hallak, S. Gao, R. Sessoli. *Chem. Eur-J.* **2014**, *20*, 14051. (b) Mauro Perfetti PhD Thesis. *Cantilever Torque Magnetometry: A powerful tool to investigate magnetic anisotropy in crystals and thin films*. **2015**, Università degli Studi Firenze, and references herein.

[59] (a) I. Dzyaloshinkii. *Physics Chemistry of Solids*, **1958**, *4*, 241. (b) I. Dzyaloshinkii, *Phys. Rev*., **1960**, *120*, 91. (c) I. Dzyaloshinkii. *Phys. Rev. Lett*., **1960**, *4*, 228.

[60] *Electron Spin Resonance. Analysis and Interpretation.* Philip H. Reger. **2007**, The Royal Society of Chemistry, Cambridge.

[61] J. T. Vázquez. *Tetrahedron: Asymmetry*. **2017**, *28*, 1199.

[62] P. Crabbé. *Dispersion and Circular Dichroism in Organic Chemistry*. Heyden&Son Ltd. London, **1965**.

[63] N. Harada, K. Nakanishi. *Circular Dichroic Spectroscopy*. *Exciton Coupling in Organic Stereochemistry*. University Science Books. California, **1983**.

[64] R. W. Woody. *Circular Dichroism. Methods in Enzymology*. **1995** *246*¸ 34.

[65] L. Liu, L. Zhang, T. Wang. *Chem. Rev*. **2015,** *115*, 7304.

[66] H. Miyake. *Symmetry*. **2014**, *6*, 880.

[67] J. Crassous. *Chem. Soc. Rev.*, **2009**, *38*, 830.

[68] (a) K. Mikami, M. Lantens. *New Frontiers in Asymmetric Catalysis*, **2007**¸Wiley-Hoboken. (b) R. Gómez-Arrayás, J. Adrio, J. C. Carretero. *Angew. Chem. Int. Ed.*, **2006**, *118*, 7836. (c) T. Katsuki. *Chem. Soc. Rev*. **2004**, *33*, 437.

[69] (a) O. Mamula, A. von Zelewsky. *Coord. Chem. Rev*, **2003**, *242*, 87. (b) D. Amabilino. *Chirality at the Nanoscale, Nanoparticles, Surfaces, Materials and More.* **2009**, Wiley-VCH, Weinheim.

[70] (a) E. Francotte, W. Lindner. *Chirality in Drug Research*, **2006**, Wiley-VCH, Weinheim. (b) K. Szacilowski, W. Mazyk, A. Drzewiecka-Matuszek, M. Brindell, G. Stochel. *Chem. Rev* **2005,** *105*, 2647.

[71] Y. Inoue, V. Ramamurthy. *Chiral Photochemistry*, Marcel Dekker, **2004**, New York, pp. 261-313.

[72] C. Train, M. Gruselle, M. Verdaguer. *Chem. Soc. Rev*. **2011**, *40*, 3297.

[73] Y. Zheng, Y.-Y. Pan, Y.-P. Ren, L.-S. Long, R.-B. Huang, L.-S. Zheng, *Chem. Commun.* **2014**, *50*, 14728.

[74] N. Hoshino, Y. Sekine, M. Nihei, H. Oshio. *Chem. Commun.* **2010**, *46*, 6117.

[75] T. Ueno, T. Fujinami, N. Matsumoto, M. Furusawa, R. Irie. N. Re, T. Kanetomo, T. Ishida, Y. Sunatsuki. *Inorg. Chem*. **2017,** *56*, 1679.

[76] J. Ribas Gispert. *Coordination Chemistry,* **2008**, WILEY-VCH Verlag GmbH&Co, KGaA, Weinheim.

[77] A. Escuer, J. Mayans, M. Font-Bardia, M. Górecki, L. Di Bari. *Dalton Trans.* **2017**, *46*, 6514.

[78] R. Ramesh, N. A. Spaldin. *Nat. Mater.* **2007**, *6*, 21.

[79] S. Horiuchi, Y. Tokura. *Nat. Mater*, **2008**¸*7*, 357. (b) T. Akutagawa, H. Kishinaka, D. Sato, S. Takeda, S.-I. Noro, H. Tkahashi, R. Kumai, Y. Tokura, T. Nkamura. *Nat. Mater.* **2009**, *8*, 342.

[80] E. Pardo, C. Train, H. Liu, L.M. Chamoreau, B. Dkhil, K. Boubekeur, F. Lloret, K. Nakatani, H. Tokoro, S.-I. Ohkoshi, M. Vedaguer *Angew. Chem. Int. Ed*. **2012**, *51*, 8356.

[81] P. Curie. *J. Phys. Theor. Appl*., **1894**, *3*, 393.

[82] *Molecular Magnetic Materials. Concepts and Applications.* E.D. Barbara Sieklucka and David Pinkowicz. **2017**, Wiley-VCH Verlag GmbH & Co.

[83] J. Mayans, M. Font-Bardia, L. Di Bari. M. Gorecki, A. Escuer. *Chem. Eur-J.* Web published. DOI: 10.1102/chem.201803730

[84] C. Ding, C. Gao, S. Ng, B. Wang, Y. Xie. *Chem-Eur. J.* **2013**, *19*¸ 9961.
[85] N. F. Chilton, R. P. Anderson, L. D. Turner, A. Soncini and K. S. Murray, *J. Comp. Chem*., **2013**, *34*, 1164.
[86] I. Bertini, C. Luchinat. *Coord. Chem. Rev*., **1996**, *150*, 77.
[87] C. Atzeri, V. Marzaroli, M. Quaretti, J. R. Travis, L. Di Bari, C. M. Zaleski, M. Tegoni. *Inorg. Chem*, **2017**, *56*, 8257.
[88] S. Di Pietro, S. Lo Piano, L. Di Bari. *Coord. Chem. Rev*. **2011**, *255*, 2810.
[89] X. Yang, S. Wang, T. King, C. J. Kerr, B. Blanchet, D. Svergun, R. Pal, A. Beeby, J.Vadivelu and K. A. Brown, *Faraday Discussions*, **2016**, *191*, 465.
[90] D. T. Thielman, A. T. Wagner, E. Roesch, D. K. Koelmel, J. G. Heek, B. Rudat, M. Naeumaier, C. Feldman, U. Sheepers, S. Brase, *J. Am. Chem. Soc*., **2013**, *135*, 7454.
[91] K.-Y. Zhang, Q. Yu, H. Wei, S. Liu, Q. Zhao, W. Huang, *Chem. Rev*., **2018**, *118*, 1770;
[92] (a) G. Xiao, B. Yan, R. Ma, W.-J. Jin, X.-Q. Lu, L.-Q. Ding, C. Zeng, L.-L. Chen, F. Bao, *Polym. Chem*., **2011**, *2*, 659; (b) W.-J. Jin, L.-Q. Ding, Z. Chu, L.-L. Chen, X.-Q. Lue, X.-Y. Zheng, J.-R. Song, D.-D. Fan, *J. Mol. Catal. A: Chem*., **2011**, *337*, 25; (c) O. V. Amirkhanov, O. V. Moroz, K. O. Znovjyak, T. Y. Sliva, L. V. Penkova, T. Yushchenko, L. Szyrwiel, I. S. Konovalova, V. V. Dyakonenko, O. V. Shishkin , V. M. Amirkhanov, *Eur. J. Inorg. Chem*., **2014**, 3720.
[93] Y.-Z. Zheng, E. M. Pineda, M. Helliwell and R. E. P. Winpenny, *Chem-Eur. J.*, **2012**, *18*, 4161.
[94] F. Zinna and L. Di Bari, *Chirality*, **2015**, *27*, 1.
[95] S. I. Weissman, *J. Chem. Phys*., **1942,** *10*, 214.
[96] F. Habib, M. Murugesu. *Chem. Soc. Rev*. **2013**, *42*, 3278
[97] J. D. Rinehart, M. Fang, W. J. Evans, J. R. Long. *Nature Chem*. **2011**, *3*, 538.
[98] H. L. C. Feltham, S. Brooker. *Coord. Chem. Rev*. **2014**, *276*, 1.
[99] F. Pointillart, O. Cador, B. Le Guennic, L. Ouahab. *Coord. Chem. Rev*. **2017**, *346*, 150.
[100] (a) M. Andruh. *Dalton Trans*., **2015**, ***44***, 16633. (b) M. Andruh, *Chem. Comm*., **2011**, ***47***, 3025.
[101] (a) A. Caneschi, L. Sorace, U. Castellato, P. Tomasin, P. A. Vigato, *Eur. J. Inorg. Chem*., **2004**, 3887; (b) T. D. Pasatoiu, C. Tiseanu, A. Madalan, B. Jurca, C. Duhayon, J. P. Sutter, M. Andruh, *Inorg. Chem*., **2011**, *50*, 5879; (c) V. Bereau, H. Bolvin, C. Duhayon and J. P. Sutter, *Eur. J. Inorg. Chem*., **2016**, 4988; (d) K. Griffiths, J. Mayans, M. A. Shipman, G. J. Tizzard, S. J. Coles, B. A. Blight, A. Escuer and G. E. Kostakis, *Cryst. Growth&Des*., **2017**, *17*, 1524; e) M. Fondo, J. Corredoira-Vazquez, A. M. Garcia-Deibe, J. Sanmartin-Matalobos, J. M. Herrera and E. Colacio, *Inorg. Chem*., **2017**, *56*, 5646.
[102] (a) M. Maeda, S. Hino, K. Yamashita, Y. Kataoka, M. Nakano, T. Yamamura and T. Kajiwara, *Dalton Trans.*, **2012**, *41*, 13640; (b) P.-L. Then, C. Takehara, Y. Kataoka, M. Nakano, T. Yamamura, T. Kajiwara, *Dalton Trans*., **2015**, *44*, 18038; (c) W.-B. Sun, P.-F. Yan, S.-D. Jiang, B.-W. Wang, Y.-Q. Zhang, H.-F. Li, P. Chen, Z.-M. Wang, S. Gao, *Chem. Sci*., **2016**, *7*, 684; (d) A. L. Boukedid, J. Long, C. Beghidja, Y. Guari, A. Beghidja, J. Larionova, *Dalton Trans*., **2018**, *47*, 1402; (e) S. Hino, M. Maeda, K. Kataoka, M. Nakano, T. Yamamura, T. Kajiwara, *Chem. Lett*., **2013**, *42*, 1276; (f) C. Takehara, P.-L. Then, Y. Kataoka, M. Nakano, T. Yamamura, T. Kajiwara, *Dalton Trans*., **2015**, *44*, 18276.
[103] (a) J. Long, R. Vallat, R. A. S. Ferreira, L. D. Carlos, F. A. Almeida Paz, Y. Guari, J. Larionova, *Chem. Commun*., **2012**, *48*, 9974; (b) P. Zhang, L. Zhang, S.-Y. Lin and J. Tang, *Inorg. Chem*., **2013**, *52*, 6595; (c) J. Rouquette, J. M. Thibaud, R. A. S. Ferreira, L. D. Carlos, B. Donnadieu, V. Vieru, L. F. Chibotaru, L. Konczewicz, J. Haines, Y. Guari and J. Larionova, *Angew. Chem. Int. Ed*., **2015**, *54*, 2236.
[104] (a) A. Chakraborty, J. Goura, P. Kalita, A. Swain, G. Rajaraman and V. Chandresekhar, *Dalton Trans*., **2018**, *47*, 8841; (b) A. Upadhyay, C. Das, S. Vaidya, K. S. Sing, T. Gupta, R.

Mondol, S. K. Lagnley, K. S. Murray, G. Rajaraman and M. Shanmugam, *Chem-Eur. J.*, **2017**, *23*, 4903.

[105] (a) A. Upadhyay, S. K. Singh, C. Das, R. Mondol, S. K. Langley, K. S. Murray, G. Rajaraman, M. Shanmugam, *Chem. Commun.*, **2014**, *50*, 8838; (b) C. Das, A. Upadhyay, S. Vaidya, S. K. Singh, G. Rajaraman and M. Shanmugam, *Chem. Commun.*, **2015**, *51*, 6137; (c) J.-L. Liu, Y.-C. Chen, Y.-Z. Zheng, W.- Q. Lin, L. Ungur, W. Wernsdorfer, L. F. Chibotaru and M.-L. Tong, *Chem. Sci.*, **2013**, *4*, 3310.

[106] H.-R. Wen, S.-J. Liu, X.-R. Xie, J. Bao, C.-M. Liu and J.-L. Chen *Inorg. Chim. Acta.*, **2015**, *435*, 274.

[107] (a) S. Zabrodsky, S. Peleg and D. J. Avnir, *J. Am. Chem. Soc.*, **1992**, *114*, 7843; (b) J. Cirera, P. Alemany, S. Alvarez, *Chem. Eur-J.*, **2004**, *10*, 190; (c) SHAPE version 2.0: M. Llunell, D. Casanova, J. Cirera, P. Alemany, S. Alvarez, Barcelona, **2010**.

[108] T. Gergaly, G. Simeon, P. Anh, G. Probst, *Current Pharm. Design*, **2007**, *13*, 3476.

[109] (a) H. Schmidt, D. Rehder, *Inorg. Chim. Acta*, **1998**, *267*, 229; (b) O. Margeat, P. G. Lacroix, J. P. Costes, B. Donnadieu, C. Lepetit, K. Nakatani, *Inorg. Chem.*, **2004**, *43*, 4743; (c) W.-Y. Bi, X.-Q. Lu, W.-L. Chai, J.-R. Song, W.-Y. Wong, W.-K. Wong, R. A. Jones, *J. Mol. Struct.*, **2008**, *891*, 450.

[110] Y. Sui, D.-P. Li, C.-H. Li, X.-H. Zhou, T. Wu and X.-Z. You, *Inorg. Chem.*, **2010**, *49*, 1296.

[111] (a) N. C. Anastasiadis, C. M. Granadeiro, N. Klouras, L. Cunha-Silva, C. Raptopoulou, V. Psycharis, V. Bekiari, S. S. Balula, A. Escuer, S. P. Perlepes, *Inorg. Chem.*, **2013**, ***52***, 4145; (b) N. C. Anastasiadis, C. D. Polyzou, G. E. Kostakis, V. Bekiari, Y. Lan, S. P. Perlepes, K. K. Konidaris and A. K. Powell, *Dalton Trans.*, **2015**, *44*, 19791; (c). X.-C. Huang, V. Vieru, L. F. Chibotaru, W. Wernsdorfer, S.-D. Jiang and X. Y. Wang, *Chem. Commun.*, **2015**, *51*, 10373.

[112] M. V. Marinho, D. O. Reis, W. X. C. Oliveira, L. F. Marques, H. O. Stumpf, M. Déniz, J. Pasán, C. Ruiz-Pérez, J. Cano, F. Lloret, M. Julve. *Inorg. Chem.*, **2017**, *56*, 2108.

[113] J. M. Zadrozny, J. Liu, N. A. Piro, C. J. Chang, S. Hill, J. R. Long. *Chem. Commun.*, **2012**, *48*, 3927.

[114] S. K. Sing, T. Gupta, L. Ungur and G. Rajaraman, *Chem. Eur-J.*, **2015**, *21*, 13812.

[115] (a) J. D. Reinhart and J. R. Long, *Dalton Trans.*, **2012**, *41*, 13572; (b) S. D. Gupta, T. Rajeshkumar, G. Rajaraman and R. Murugavel, *Chem. Commun.*, **2016**, *52*, 7168.

[116] (a) P.-H. Lin, W.-B. Sun, Y.-M. Tian, P.-F. Yan, L. Ungur, L. F. Chibotaru, M.Murugesu, *Dalton Trans.*, **2012**, *41*, 12349; (b) M. A. Aldamen, S. Cardona-Serra, J. M. Clemente-Juan, E. Coronado, A. Gaita-Ariño, F. Martin-Gastaldo and F. Luis, *Inorg. Chem.*, **2009**, *48*, 3467; (c) H. L. C. Feltham, F. Klower, S. A. Cameron, D. S. Larsen, Y. Lan, M. Tropiano, S. Faulkner, A. K. Powell and S. Brooker, *Dalton Trans.*, **2011**, *40*, 11425; (d) M. Sugita, N. Ishikawa, T. Ishikawa, S. Koshinara and Y. Kaizu, *Inorg. Chem.*, **2006**, *45*, 1299.

[117] S. Gómez-Coca, A. Urtizberea, E. Cremades, P. J. Alonso, A. Camón, E. Ruiz, F. Luis. *Nature Commun.*, **2014**, *5*, 4300.

[118] (a) P. E. Car, M. Perfetti, M. Mannini, A. Favre, A. Caneschi , R. Sessoli, *Chem. Commun.*, **2011**, *47*, 3751; b) M. Jeletic, P.-H. Lin, J. J. Le Roy, I. Korobkov, S. I. Gorelsky, M. Murugesu, J. Am. Chem. Soc., **2011**, *133*, 19286; c) J. Ruiz, A. J. Mota, A. Rodriguez-Dieguez, S. Titos, J.-M. Herrera, E. Ruiz, E. Cremandes, J.-P. Costes and E. Colacio, *Chem. Commun.*, **2012**, *48*, 7916.

[119] M. M. Hanninen, A. J. Mota, D. Aravena, E. Ruiz, R. Sillanpaa, A. Camon, M. Evangelisti and E. Colacio, *Chem. Eur. J.*, **2014**, *20*, 8410.

[120] F. Pointillart, K. Bernot, S. Golhen, B. Le Guennic, T. Guizoguarn, L. Ouahab, O. Cador. *Angew. Chem. Int. Ed.*, **2015**, *54*, 1504.

[121] EasySpin Software for MatLab.

[122] R. Sessoli. *ACS Cent. Sci.*, **2015**, *1*, 473.

[123] R. Sessoli. *Nature*, **2017**, *548*, 400.

[124] F. Donati, S. Rusponi, S. Stepanow, C. Wackerlin, A. Singha, L. Persichetti, R. Baltic. K, Diller, F. Patthey, E. Fernandes. J. Dreiser, Z. Slijvancanin, K. Kummer, C. Nistor, P. Gambardella, H. Brune. *Science*, **2016,** *352*, 318.

[125] (a) C. A. P. Goodwin, F. Ortu, D. Reta, N. F. Chilton, D. P. Mills, *Nature*, **2017**, *548*, 439. (b) F. S. Guo, B. M. Day, Y. C. Chen, M. L. Tong, A. Mansikkamaki, R. A. Layfield. *Angew, Chem. Int. Ed*. **2017**, *56*, 11445.

[126] R. Sessoli, A. K. Powell. *Coord. Chem. Rev*. **2009**, *253*, 2328.

[127] H. Bethe. *Ann. Phys.* **1929**, *395*, 133.

[128] K.W.H. Stevens. *Proc. Phys. Soc. London, Sect. A*, **1952**, *65*, 209.

[129] B. G. Wybourne. *Spectroscopic Properties of Rare Earths*. John Wiley & Sons, Inc. New York, **1965.**

[130] *Lanthanides and Actinides in Molecular Magnetism.* Ed. R. E. Layfield, M. Murugesu. **2015-**Wiley-VCH Verlag GmbH & Co.